UDC 524.728 ISSN 0373-3742

ПУБЛИКАЦИЈЕ АСТРОНОМСКЕ ОПСЕРВАТОРИЈЕ У БЕОГРАДУ
PUBLICATIONS OF THE ASTRONOMICAL OBSERVATORY OF BELGRADE
Св. 84 No. 84

24th Summer School and
International Symposium on
the Physics of Ionized Gases
August 25-29, 2008, Novi Sad, Serbia

CONTRIBUTED PAPERS

&

ABSTRACTS of INVITED LECTURES,
TOPICAL INVITED LECTURES and PROGRESS REPORTS

Editors:
Gordana Malović
Luka Č. Popović,
Milan S. Dimitrijević

БЕОГРАД
2008

PUBL. ASTRON. OBS. BELGRADE No. 84, 1-525 BELGRADE, JULY 2008

PUBLICATIONS OF THE ASTRONOMICAL OBSERVATORY OF BELGRADE

FOUNDED IN 1947

Published and copyright © by Astronomical Observatory, Volgina 7, 11160 Belgrade 74, Serbia

Director of the Astronomical Observatory: Dr. Zoran Knežević

Typesetting: Tatjana Milovanov

Internet address `http://www.aob.bg.ac.yu`

ISBN 978-86-80019-27-7

The publication of this issue is financially supported by the Serbian Ministry of Science.

Sponsor:

Number of copies / тираж : 500

Production: "TULI" Printing Office, Vršac, Beogradska b.b.

Publ. Astron. Obs. Belgrade No. 84 (2008), 13 *Invited Lecture*

LOW ENERGY LEPTON SCATTERING – RECENT RESULTS FOR ELECTRON AND POSITRON INTERACTIONS

J. P. SULLIVAN, V. VIZCAINO, S. MONDAL, J. C. LOWER, A. JONES,
P. CARADONNA, C. MAKOCHEKANWA and S. J. BUCKMAN

Centre for Antimatter-Matter Studies,
Research School of Physical Sciences and Engineering
The Australian National University, Canberra, 0200, Australia
E–mail: Stephen.buckman@anu.edu.au

Abstract. The interaction of low energy electrons with atoms, molecules and materials underpin a large number of technological, environmental and biomedical processes that impact on our everyday lives. Many of these areas have been well studied over the years and in some cases a large body of important and relevant cross section data has been gathered to assist in the understanding and development of the technology or phenomena. A perfect example of this is the area of low energy gaseous electronics where microscopic cross section information for a whole host of scattering processes (vibrational and electronic excitation, dissociation, ionization) have been critical to an understanding of the macroscopic behaviour of a range of gas discharge environments – large area plasma processing discharges being a case in point.

More recently there has been a realisation that fundamental information about both low energy electron and positron interactions also have significant bearing on issues of radiation damage in biological materials. Low energy electrons have been shown to cause significant damage to DNA strands, for instance, as a result of processes such as dissociative attachment – a process which can occur at energies down to 0 eV. These processes result from the production of copious low energy electrons (< 20 eV) when high energy ionizing radiation thermalises in the body. This realisation has provided an enormous boost to the field of low energy electron physics and spawned an enormous number of new studies of interactions with biologically relevant molecules.

In a similar fashion, low energy positron interactions are thought to be fundamentally important for an understanding of the atomic and molecular processes that underpin technologies such as Positron Emission Tomography (PET). PET scans image the coincident 511 keV γ-rays that arise form the annihilation of an electron-positron pair. During a PET scan, high energy positrons thermalise in the body through scattering (ionization and excitation of molecules) until their energy is low enough (typically below ~ 100 eV) for positronium formation, quickly followed by annihilation, or free electron annihilation, to occur. Essentially no information exists on the fundamental positron scattering processes from important biological molecules that lead to the γ-ray emission.

This talk will attempt to provide an overview of these aspects of the field of low energy lepton interactions with atoms and molecules and discuss some recent experimental advances in the field.

Publ. Astron. Obs. Belgrade No. 84 (2008), 14 *Invited Lecture*

MODELING OF ANOMALOUS DOPPLER BROADENED LINES, THERMALIZATION OF ELECTRONS AND THE ROLE OF RADICALS IN DISCHARGES AT HIGH E/N

Z. Lj. PETROVIĆ, Ž. NIKITOVIĆ and V. D. STOJANOVIĆ
Institute of Physics, Pregrevica 118, 11080 Zemun, Serbia
E–mail: stoyanov@phy.bg.ac.yu

Abstract. Observations of anomalously broadened hydrogen lines in gas discharges were made in 60s and the explanations that followed were mainly based on dissociative processes. However, some observations, especially those of Benesch and Li (1984) could not be explained without evoking the directionality of the motion of ions. First full explanation of the effect and observations of energies exceeding few tens of eV were made on the basis of a swarm experiment carried out by Petrović et al. (1992) which revealed the need to include a new effect, that of the reflection of fast neutrals from the cathode with sufficient energies to produce hydrogen radiation. The model that was developed although having a correct physical phenomenology was based on approximate treatment of non-hydrodynamic transport, i.e. essentially on a beam like treatment of energy distribution functions with the mean energy calculated from the energy balance. In the meantime the set of pertinent atomic collisions has become much more complex and we have based the calculations on a Monte Carlo simulation which gives exact energy distributions. We will present the results on all details of kinetics of relevant particles, from electrons to ions, molecules and atoms. We will also stress the need to model more accurately the heavy particle collisions, especially the angular anisotropy of scattering.

Thermalization of electrons produced by cosmic rays from very high energies and the resulting emission of nitrogen radiation has been proposed as a means to detect properties of extremely high energy elementary particles. The process is exactly the opposite to that taking place in high E/N discharges and may be treated exactly by a similar Monte Carlo code if the applied cross sections are correct.

Finally we will discuss how dissociated fragments affect the transport properties of electrons having in mind applications such as plasma etching of SiO_2 where abundances of radicals of CF_x are of the order of several percent. The principal effect of radicals on electron transport in pure CF_4 or in CF_4/Ar mixtures is through very different attachment rates which leads to orders of magnitude different effective attachment rate for the mixture with radicals as compared to the properties of pristine buffer gas. Thus one may conclude that even the electronegative nature of the plasma may be changed due to the presence of different radicals, especially of CF_2.

References

Benesch, W., Li, E.: 1984, *Opt. Lett.*, **9**, 338.
Petrović, Z. Lj., Jelenković, B. M., Phelps, A. V. : 1992, *Phys. Rev. Lett.*, **68**, 325.

Publ. Astron. Obs. Belgrade No. 84 (2008), 15 *Invited Lecture*

THERMALISATION OF HIGH ENERGY ELECTRONS AND POSITRONS IN WATER VAPOUR

A. MUÑOZ[1], F. BLANCO[2], P. LIMAO-VIEIRA[3], P. A. THORN[4], M. J. BRUNGER[4], S. J. BUCKMAN[5] and G. GARCÍA[6]

[1]*Centro de Investigaciones Energéticas, Medioambientales y Tecnológicas, Avenida Complutense 22, 28040 madrid, Spain*
[2]*Departamento de Física Atómica, Molecular y Nuclear, Universidad Complutense de Madrid, Avenida Complutense s.n., 28040 madrid, Spain*
[3]*Atomic and Molecular Collisions Laboratory, Department of Physics, New University of Lisbon, Campus de Caparica, 2829-516 Caparica, Portugal*
[4]*ARC Centre for Antimatter-Matter Studies, SoCPES, Flinders University, G.P.O. Box 2100, Adelaide, South Australia 5001, Australia*
[5]*RC Centre for Antimatter-Matter Studies, RSPhysSE, Australian National University College of Science, Canberra, ACT 0200, Australia*
[6]*Instituto de Física Fundamental, Consejo Superior de Investigaciones Científicas, Serrano 113-bis, 28004 Madrid, Spain*
E–mail: g.garcia@imaff.cfmac.csic.es

Abstract. In this study we describe a method to simulate single electron tracks of electrons in molecular gases, particularly in water vapour, from relatively high energies, where Born(Inokuti 1971) approximation is supposed to be valid, down to thermal energies paying special attention to the low energy secondary electrons which are abundantly generated along the energy degradation procedure. Experimental electron scattering cross sections (Muñoz et al. 2007) and energy loss spectra(Thorn et al. 2007) have been determined, where possible, to be used as input parameters of the simulating program. These experimental data have been complemented with optical potential calculation (Blanco and García 2003) providing a complete set of interaction probability functions for each type of collision which could take place in the considered energy range: elastic, ionization, electronic excitation, vibrational and rotational excitation. From the simulated track structure(Muñoz et al. 2005) information about energy deposition and radiation damage at the molecular level can be derived.

A similar procedure is proposed to the study of single positron tracks in gases. Due to the lack of experimental data for positron interaction with molecules, especially for those related to energy loss and excitation cross sections, some distribution probability data have been derived from those of electron scattering by introducing positron characteristics as positroniun formation. Preliminary results for argon are presented discussing also the utility of the model to biomedical applications based on positron emitters.

References

Blanco, F. and García, G.: 2007, *Phys. Rev.* A, **67**, 022701.
Inokuti, M.: 1971, *Rev. Mod. Phys.*, **43**, 297.
Muñoz, A., Oller, J. C, Blanco, F., Gorfinkiel, J. D., Limao-Vieira, P., Garcia, G.: 2007, *Phys. Rev.* A, **76**, 052707.
Muñoz, A., Pérez, J. M., García G. and Blanco F.: 2005, *Nucl. Instrum. Meth.* A, **536**, 176.
Thorn, P. A., Brunger, M. J. et al.: 2007, *J. Chem. Phys.*, **126**, 064306.

Publ. Astron. Obs. Belgrade No. 84 (2008), 16 *Invited Lecture*

ATOMIC AND MOLECULAR SYSTEMS IN INTENSE ULTRASHORT LASER PULSES

A. SAENZ

Humboldt-Universität zu Berlin, Institut für Physik,
AG Moderne Optik, Hausvogteiplatz 5-7, 10117 Berlin, Germany
E–mail: Alejandro.Saenz@physik.hu-berlin.de

Abstract. The full quantum mechanical treatment of atomic and molecular systems exposed to intense laser pulses is a so far unsolved challenge, even for systems as small as molecular hydrogen. Therefore, a number of simplified qualitative and quantitative models have been introduced in order to provide at least some interpretational tools for experimental data. The assessment of these models describing the molecular response is complicated, since a comparison to experiment requires often a number of averages to be performed. This includes in many cases averaging of different orientations of the molecule with respect to the laser field, focal volume effects, etc. Furthermore, the pulse shape and even the peak intensity is experimentally not known with very high precision; considering, e. g., the exponential intensity dependence of the ionization signal. Finally, experiments usually provide only relative yields. As a consequence of all these averagings and uncertainties, it is possible that different models may successfully explain some experimental results or features, although these models disagree substantially, if their predictions are compared before averaging. Therefore, fully quantum-mechanical approaches at least for small atomic and molecular systems are highly desirable and have been developed in our group. This includes efficient codes for solving the time-dependent Schrödinger equation of atomic hydrogen, helium or other effective one- or two-electron atoms as well as for the electronic motion in linear (effective) one-and two-electron diatomic molecules like H_2.Very recently, a code for larger molecular systems that adopts the so-called single-active electron approximation was also successfully implemented and applied.

In the first part of this talk popular models describing intense laser-field ionization of atoms and their extensions to molecules are described. Then their validity is discussed on the basis of quantum-mechanical calculations. Finally, some peculiar molecular strong-field effects and the possibility of strong-field control mechanisms will be demonstrated. This includes phenomena like enhanced ionization and bond softening as well as the creation of vibrational wavepacket in the non-ionized electronic ground state of H_2 by creating a Schrödinger-cat state between the ionized and the non-ionized molecules. The latter, theoretically predicted phenomenon was very recently experimentally observed and lead to the real-time observation of the so far fastest molecular motion.

Publ. Astron. Obs. Belgrade No. 84 (2008), 17 *Invited Lecture*

INVESTIGATING FEW PARTICLE DYNAMIC - ATOMS AND MOLECULES UNDER THE REACTION MICROSCOPE

M. S. SCHÖFFLER[1,2], J. TITZE[1], T. JAHNKE[1], L. Ph. H. SCHMIDT[1], O. JAGUTZKI[1], T. WEBER[2], H. SCHMIDT-BÖCKING[1] and R. DÖRNER[1]

[1] *Institut für Kernyphsik, University Frankfurt, Max-von-Laue-Str. 1, 60438 Frankfurt, Germany*
E–mail: schoeffler@atom.uni-frankfurt.de

[2] *Lawrence Berkeley National Laboratory, One Cyclotron Road, 94720 Berkeley, CA, USA*

Abstract. The reaction microscope or the so called COLTRIMS-technique (COLd Target Recoil Ion Momentum Spectroscopy) is a novel momentum imaging technique to investigate the dynamics of ionization processes of atom, molecules and clusters, induced by particle impact or single/multiple photon absorption. Thereby the particle can either be a charged ion or electron, but also a neutral fast moving projectile. It allows the measurement of the full three dimensional momentum vector of all during the ionization process ejected charged particles (ions and electrons as well) with a 4π acceptance angle to provide kinematically complete experiments. We review the technical development from the last 15 years and give an overview of the key experiments performed with this technique. These studies opened a new window onto the correlated motion of the fragments of atomic and molecular breakup processes, super high resolution, detail and completeness. Finally we give an outlook on the exciting future prospects of this method for atomic and molecular physics.

Publ. Astron. Obs. Belgrade No. 84 (2008), 18 *Topical Lecture*

LOW ENERGY POSITRON SCATTERING FROM HELIUM

J. P. SULLIVAN, C. MAKOCHEKANWA, A. JONES, P. CARADONNA
and S. J. BUCKMAN
Centre for Antimatter-Matter Studies
RSPhysSE, Australian National University, Canberra ACT 0200, Australia
E–mail: jps107@rsphysse.anu.edu.au

Abstract. Positron scattering from helium has been historically limited to experiments with energy resolution of 0.5 eV or worse. A new apparatus has been developed that allows the investigation of scattering processes with an energy resolution as good as 30 meV, allowing new experimental insight into positron helium interactions. The experiment is based on the buffer gas trap techniques developed in San Diego by Cliff Surko. A moderated positron beam is magnetically confined and directed into a series of electrodes forming a potential well structure. Positrons are trapped in the potential well through collisions with a buffer gas of N_2 and cool to room temperature through further collisions with the N_2 and CF_4. This cooled reservoir of positrons forms the source for a high resolution beam which can be used to probe low energy scattering processes.

The present work has determined the cross sections for positron scattering from helium from 1 to 60 eV, for a range of different scattering processes. Low energy scattering cross sections have been determined and compared to recent results which suggested the presence of resonances in the elastic scattering channel. Cross sections above the positronium formation threshold have been measured, and are compared to previous measurements as well as theoretical calculations. The positronium formation cross section has also been investigated and is in some disagreement with previous measurements. The likely reason for this disagreement will be discussed. High resolution measurements around various inelastic thresholds will also be presented and compared to predictions for a cusp in the total elastic scattering cross at the positronium formation threshold.

Publ. Astron. Obs. Belgrade No. 84 (2008), 19 *Progress Report*

THE MULTI TERM BOLTZMANN EQUATION ANALYSIS OF NON-CONSERVATIVE ELECTRON TRANSPORT IN TIME-DEPENDENT ELECTRIC AND MAGNETIC FIELDS

S. DUJKO[1,2] and R. D. WHITE[2]

[1] *Institute of Physics, University of Belgrade, Pregrevica 118, Zemun, Serbia*
E–mail: sasa.dujko@jcu.edu.au

[2] *ARC Centre for Antimatter-Matter Studies, School of Mathematics, Physics and IT, James Cook University, Townsville 4811, QLD, Australia*
E–mail: ronald.white@jcu.edu.au

Abstract. A multi term technique for solving the Boltzmann equation has been developed to investigate the time-dependent behavior of charged particle swarms in an unbounded neutral gas under the influence of spatially uniform time-dependent electric and magnetic fields (Dujko 2008). The hierarchy resulting from a spherical harmonic decomposition of the Boltzmann equation in the hydrodynamic regime is solved numerically by representing the speed dependence of the phase-space distribution function in terms of an expansion in Sonine polynomials about a Maxwellian velocity distribution at an internally determined time-dependent temperature. This technique avoids restrictions on the electric and magnetic field amplitudes and frequencies and/or the charged particle to neutral molecule mass ratio traditionally associated with many investigations. To our knowledge, it represents the first rigorous treatment of the explicit effects of non-conservative processes on transport coefficients in ac electric and magnetic fields. The variation of the transport coefficients with electric and magnetic field strengths, field frequency, phase difference between the fields and angle between the fields is addressed using physical arguments. Results are given for electron swarms in certain model and real gases. The errors associated with the two term approximation for solving the Boltzmann equation and inadequacies of the Legendre polynomial expansion procedure are highlighted. The results of the Boltzmann equation analysis are compared with those obtained by a Monte Carlo simulation code. The comparison validates the basis of transport theory and numerical integrity of both approaches.

References

Dujko S.: 2008, PhD Thesis, School of Mathematics, Physics and IT, James Cook University, Townsville, Australia, 2008.

Publ. Astron. Obs. Belgrade No. 84 (2008), 20 *Progress Report*

MODELING OF TOWNSEND DISCHARGES AT HIGH E/N AND LOW PRESSURE

V. D. STOJANOVIĆ
Institute of Physics, Pregrevica 118, 11080 Zemun, Serbia
E–mail: stoyanov@phy.bg.ac.yu

Abstract. Nonequilibrium manifestations in electron and heavy particle transport in gaseous discharges are standard part of all devices that uses such a plasma. Nonequilibrium effects are related to collective behavior of these particles in gas that deviates from the hidrodynamic regime. In that sense phenomena presented in this work are part of the swarm physics for which it is characteristic that particles do not interact with particles of the same kind but only with the unpertrbed background gas particles. Only partial information is avaliable on elementary collisional processes that are important for modelling of gas discharges. As a result all the research on gas discharges is to a large degree conected to the fundamental studies in atomic and molecular physics.

Aim of this work is to investigate complex behavior of electrons and ions by the most precise possible method - Monte Carlo simulations. Although recognized as a relatively simple for implementation it is, at the same time, difficult to test and verify. In any case, this method is revealed as a right choice for modelling of Townsend discharges. This work begins with selection of input data and benchmarking of the codes. Main results are modelling of Townsend discharges in nitrogen and argon at low pressures and at consequently at very high E/N. We include description of effects of ions and fast neutrals to kinetics of excitation, description of nonhydrodinamic effects in the vicinity of electrodes and at the high E/N the runaway of electrons and ions. We also present description of impulse discharges and time resolved current impulses under similar conditions. In addition we have compiled cross section sets that may serve for discharge modelling in argon and nitrogen in broad range of conditions and discussed numerous approximations that were recently used in modelling of plasmas.

Publ. Astron. Obs. Belgrade No. 84 (2008), 21 - 22 *Progress Report*

THE EXPERT SYSTEMS FOR ANALYSIS OF ELECTRON ENERGY-LOSS SPECTRA

V. PETROVIĆ, V. BOČVARSKI and I. PETROVIĆ

Department of Physics, Faculty of Science, Kragujevac University, R. Domanovića 12, 34000 Kragujevac, Serbia

Abstract. The expert systems for analysis of energy-loss spectra are developed with aim to enable qualitatively and quantitatively improvement of process analysis spectra which are obtained in collision processes between electron and atoms or molecules. The expert system contribute to process of spectra analysis firstly in parts of spectra where are many structures and where subjective estimation of a person that performs an experiment can limit a precision of analysis regarding a quantity of obtained data, and also regarding a quality of interpreted results.

The expert systems shown in this paper are developed on the base of backward chaining methodology, and for their development is used ESBT I2+. The process of development of expert system was done in phases. In the first phase the expert system was oriented on atom spectra analysis (Petrović and Bočvarski 2003). The application of thusly developed expert system has given very satisfying results. So we decided to upgrade existing expert system in order to enable analysis of molecule spectra which are far more complex then atomic (because they, beside the peaks of discrete states, also contain peaks of vibrational levels).

On the Fig. 1 is given part of characteristic SO_2 molecule threshold spectrum.

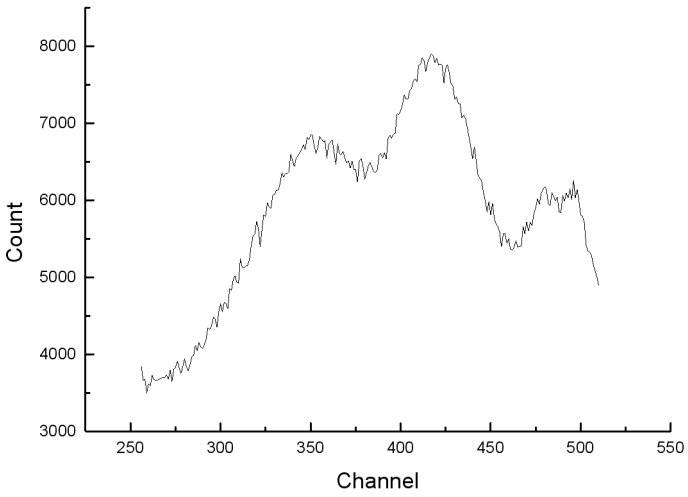

Figure 1: Characteristic SO_2 molecule threshold spectrum in the energy range x-x.

The process of analysis done by expert system should solve the problem of working with complex, compound structures, which stems from overlapping of large number of vibrational level peaks, which are characteristic for this kind of spectra.

In order to solve the aforementioned problem, in first stage of development we started with two-atomic molecules, because their spectra, although complex, are well structurally defined, and also there is a multitude of data for these molecules (Petrović and Bočvarski 2005). This enabled the verification of certain ideas that were later used in analysis of three-atomic spectra (Petrović et al. 2007). This has a special relevance, because it enabled us to obtain certain amount of information from those parts of spectra that remained unanalyzed.

References

Petrović, V. and Bočvarski, V.: 2003, *Int. J. Mod. Phys.* C, **14**, 433.
Petrović, V. and Bočvarski, V.: 2005, *Int. J. Mod. Phys.* C, **16**, No. 9, 1395.
Petrović, V., Bočvarski, V. and Petrović, I.: 2007, *Int. J. Mod. Phys.* C, **18**, No. 7, 1133.

Publ. Astron. Obs. Belgrade No. 84 (2008), 23 - 26 *Contributed Paper*

RELAXATION OF LOW ENERGY POSITRONS IN MOLECULAR GASES

A. BANKOVIĆ[1], J. P. MARLER[2], Z. Lj. PETROVIĆ[1], S. DUJKO[1], R. D. WHITE[3] and G. MALOVIĆ[1]

[1] *Institute of Physics, Pregrevica 118, 11080 Zemun, Serbia*

[2] *University of Aarhus, Aarhus, Denmark*

[3] *ARC Centre for Antimatter-Matter Studies, School of Mathematics, Physics and IT, James Cook University, Townsville 4810, Australia*

Abstract. The calculations of thermalization times and spatial relaxation profiles of the positron transport properties in H_2, N_2 and in mixture of N_2 and CF_4 are presented. Recently, the data needed to compile comprehensive set of cross sections for these gases became available which made our calculations possible. The main difference between positron and electron transport is the existence of the effect of positronium (Ps) formation which changes the number of particles and has a strong energy dependence. The relative magnitude of positronium formation to electronic excitations and the relative positions of their thresholds control the efficiency of thermalization and non-conservative transport phenomena. The effect of vibrational and rotational excitations on thermalization has been considered and relative contributions were determined. Our calculated thermalization data are in reasonably good agreement with the experimental data of Al-Qaradawi et al. (2000).

1. INTRODUCTION

The investigation of low energy positron interactions with matter is of great interest in areas of atomic physics, condensed matter physics and gamma-ray astronomy. There is also a need to understand these interactions for technological applications including mass spectroscopy, characterization of solid surfaces and for biomedical diagnostics. Progress in positron-matter interaction research has been limited by the availability of high flux positron sources and bright low-energy positron beams. The development of efficient positron traps (e.g. the Penning-Malmberg-Surko trap) changed this situation.

The development of low energy positron traps opened a possibility of measuring the low energy cross sections for positron scattering on numerous gases and allowed us to revisit the studies of positron transport and possible interpretations of past and future swarm experiments. We have compiled reasonably complete sets of cross sections for several gases such as nitrogen, hydrogen, water vapor and argon (see Šuvakov et al. (2008) and Banković et al. (2008)) and performed calculations of transport coefficients.

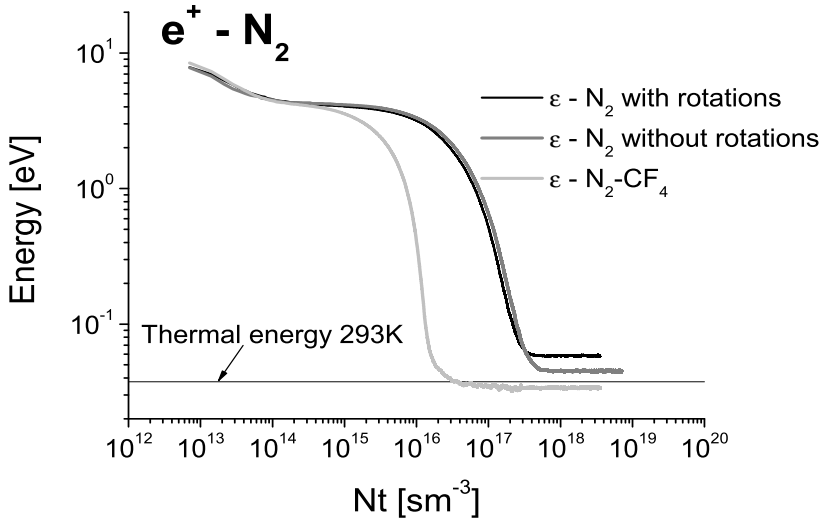

Figure 1: Thermalization of the mean energy of positrons from a Maxwellian initial distribution with a mean starting energy of 10 eV in N_2 and N_2-CF_4 mixture.

2. TEMPORAL RELAXATION

We have performed Monte Carlo simulation of thermalization for the energy range relevant to the Penning-Malmberg-Surko trap at the room temperature (293 K). The main goal of this work was to give the estimate of thermalization times for positrons in different gases and perhaps to open a possibility to optimize gas composition and performance of these traps. Thermalization time has been defined as the time it takes positrons to reach the energy 50% above the thermal equilibrium energy in gases but for practical purposes we took it to mean the time it takes to reach twice the thermal energy. The results have been compared with experimental measurements of Al-Qaradawi et al. 2000. who used the positron lifetime spectroscopy in order to obtain the thermalization times. When making comparisons such as this, one should bear in mind that it is very difficult to provide identical definition of the boundary for thermalization when time is determined in two approaches.

Temporal relaxation of positrons from Maxwellian with the mean starting energy of 10 eV in nitrogen is presented in Figure 1. In the same Figure, it is shown how rotational excitations affect the thermalization of positrons. The rotational excitations are quite small in nitrogen and they make little contribution even below 100 meV. Here we have assumed that the cross sections for rotational excitation are the same as for non-resonant rotational excitation by electrons. Addition of other molecular gases such as CF_4 with large vibrational cross sections speeds up thermalization while the overall losses to Ps formation are not increased significantly. In Figure 1 the thermalization in mixture of N_2 with 10% of CF_4 is presented. We observe that the time of thermalization becomes shorter by an order of magnitude when CF_4 is added to the molecular nitrogen.

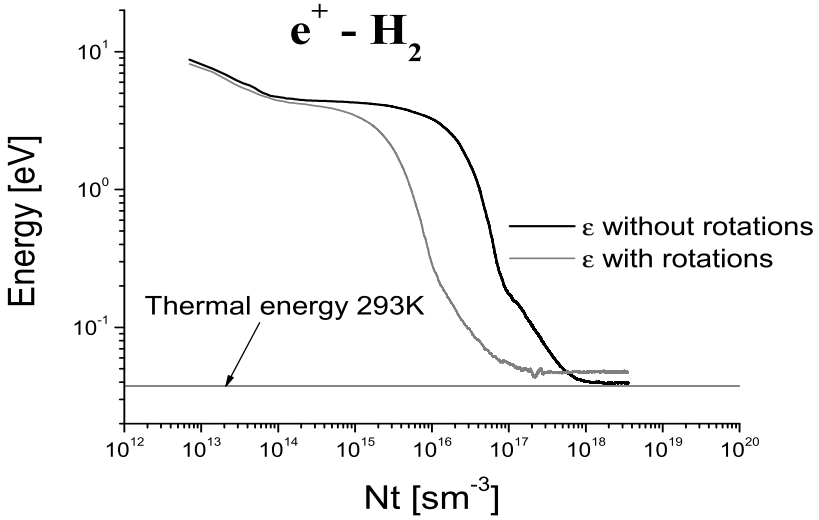

Figure 2: Thermalization of the mean energy of positrons from a Maxwellian initial distribution with a mean starting energy of 10 eV in H_2.

In Figure 2 the similar results for positrons in hydrogen are presented. The rotational excitations in hydrogen are much larger then those in nitrogen so their influence on the thermalization time is significantly larger and it becomes essential for thermalization to energies below 100 meV, making hydrogen almost as effective in thermalization as the mixture of N_2 and CF_4. The main reason why it is more convenient to use molecular nitrogen as buffer gas in positron traps than molecular hydrogen is the relative position of the threshold for Ps formation to electronic excitations threshold. In H_2 the threshold for Ps formation is lower than the thresholds for electronic excitations and thereby losses of positrons during thermalization will be far greater as compared to nitrogen.

The thermalization time has been extracted from Figures 1 and 2. The moment when positrons are in thermal equilibrium with surrounding gas has been defined as the time that positron need to reach the half of the thermal energy above $3kT/2$. Thermalization times measured by Al-Qaradawi et al. 2000. have been given originally in units of ns Amagat (1 Amagat $= 2.69 \times 10^{25}$ sm^{-3}) and here these units are converted to sm^{-3}. The comparison between our Monte Carlo calculations and experimental results is presented in Table 1. One should bear in mind that in experiment the limiting time is determined by the energy resolution of the experiment. Our choice of the energy 50% above the thermal energy is rather arbitrary but it was selected to reduce uncertainties in determination where the slope of the curve is still high. The experimental data are in good agreement with our data but are more consistent with resolution of the order of 20% above the thermal energy. In any case we may state that our results are in good agreement with the experiment.

When considering comparisons with the thermalization times in Surko trap one should redefine the calculation to use initial distribution (of velocities) that is more appropriate to the trap.

Table 1: Comparison between the thermalization times calculated using our Monte Carlo code and measured by Al-Qaradawi et al. 2000

gas	Nt (sm^{-3}) Present results	Nt (sm^{-3}) Al-Qaradawi et al
N_2	2.5×10^{17}	3.8×10^{17}
N_2-CF_4	1.4×10^{16}	X
H_2	4.5×10^{16}	6.5×10^{16}

3. SPATIAL RELAXATION

A standard Surko trap belongs to Steady state Townsend (SST) experiments in strongly non-hydrodynamic conditions, i.e. with very few collisions bordering on beam experiments. We have treated spatial relaxation of the initial distribution paying special attention to the mean energies and average velocities. The data were obtained by our steady-state Townsend (SST) Monte Carlo simulation code. Both the mean energy and average velocity exhibit a damped oscillatory relaxation along a decaying profile for E/N >0.25 Td. The nature of the spatial relaxation profiles of positron transport properties is dependent as the interplay between the power dissipated in elastic collisional processes, power dissipated in inelastic collisions and power deposited into the swarm by the field. For certain gases there exist a window of E/N strengths where the relaxation profiles are damped oscillatory in nature, and outside this window the profiles are monotonic.

4. CONCLUSION

In our attempt to apply modern tools for a treatment of the electron swarms to positron transport, we have performed calculations for thermalization of positrons at sub excitation (less than 10 eV) energies. Our calculated results provide a tool for optimizing the collisional traps and thermalization/annihilation experiments. The calculated thermalization times are in good agreement with experimental data giving support to the selected set of cross sections as the numerical technique has been verified independently.

References

Al-Qaradawi, I., Charlton, M., Borozan, I., Whitehead, R.: 2000, *J. Phys. B: At. Mol. Opt. Phys.*, **33**, 2725.

Banković, A., Marler, J. P., Šuvakov, M., Malović, G., Petrović, Z. Lj.: 2008, *Nuclear Inst. and Methods*, B **266/3**, 462.

Šuvakov, M., Petrović, Z. Lj. Marler, J. P., Buckman, S. J., Robson, R. E. and Malović, G.: 2008, *New J. Phys.*, **10**, 053034.

Publ. Astron. Obs. Belgrade No. 84 (2008), 27 *Contributed Paper*

ELECTRON IMPACT EXCITATION IN COMETARY COMAS

L. CAMPBELL and M. J. BRUNGER
ARC Centre for Antimatter-Matter Studies, SoCPES, Flinders University, GPO Box 2100, Adelaide SA 5001, Australia
E–mail: laurence.campbell@flinders.edu.au

Abstract. The role of electron impact excitation in comets is investigated, particularly with regard to recent laboratory measurements of electron impact cross sections.

1. INTRODUCTION AND REVIEW

Molecules, such as water, carbon monoxide and carbon dioxide, vaporise from comet nuclei and are then dissociated or ionised by sunlight. Photoionisation produces photoelectrons which, along with electrons in the solar wind, can produce excitation of atoms and molecules and subsequent emissions. These excitations are considered to be negligible compared to other processes for all but a few transitions (Feldman, 2006). However, with many recent measurements of both cometary spectra and of electron impact excitation cross sections, it is timely to review the role of electron impact excitation in cometary emissions. The particular electron impact excitations which are considered to be important in producing emissions in comets are outlined and evidence for them in observations is reviewed.

2. ANALYSIS

We use recent measurements of electron impact integral cross sections for H_2O (Brunger *et al.* 2008), CO (Kato *et al.* 2007) and CO_2 (Campbell *et al.* 2008), plus literature values for O atom excitation. A statistical equilibrium calculation is performed to find the balance between excitation and various radiative decay paths and so predict emissions. The results are compared with measurements, with particular emphasis on cases where more than one transition of interest is available in a measured spectrum.

References

Brunger, M. J., Thorn, P. A., Campbell, L., Diakomichalis, N., Kato, H., Kawahara, H., Hoshino, M., Tanaka, H., Kim, Y.-K.: 2008, *J. Mass Spect.*, **271**, 80.
Campbell, L., Brunger, M. J., Rescigno, T. N.: 2008 *J. Geophys. Res.*, submitted.
Feldman, P. D.: 2006, Handbook of Atomic, Molecular and Atomic Physics, ed. G. W. F. Drake, 1247–1258, New York: Springer.
Kato, H., Kawakara, H., Hoshino, M, Tanaka, H., Brunger, M. J., Kim, Y.-K.: 2007, *J. Chem. Phys.*, **126**, 064307.

Publ. Astron. Obs. Belgrade No. 84 (2008), 29 - 33 *Contributed Paper*

CONTRIBUTION OF AUTOIONIZING PROCESS INTO POTASSIUM ATOM IONIZATION BY ELECTRONS

I. V.CHERNYSHOVA, J. E. KONTROS, O. B. SHPENIK
Institute of Electron Physics, National Academy of Sciences of Ukraine,
21 Universitetska str., Uzhgorod 88017, Ukraine
E–mail: an@zvl.iep.uzhgorod.ua

Abstract. Ionization cross-section of potassium atom by electrons is studied in the range from the ionization threshold to 26 eV. A resonance structure in the ionization cross-section is observed near 19 eV related to the contribution of autoionizing states. The energy position of the structure is shown to be in a good agreement with the one predicted theoretically (Roy and Rai 1973), though its absolute value is much smaller. Besides, the determined autoionizing contribution into the potassium atom ionization cross-section correlates well with the recently measured (Evrij et al. 2005) total autoionizing cross-section.

1. INTRODUCTION

It is known (Brink 1962) that potassium atom ionization can proceed in two independent channels. The mechanism of simple ionization corresponds to the transition of a valence electron from the ground state of $3p^5 4s$ configuration to a continuum with the formation of an ionic ground state $3p^6$ which can be also achieved by autoionizing via the excited $3p^5 4s^2$ state of the atom. The threshold of the second process is about 19 eV; at this value a break is revealed in the potassium atom ionization curve (Zapesochny and Aleksakhin 1968).

Roy and Rai (1973) were the first to take into account the contribution of the autoionizing processes into the total ionization cross-section. As a result, a fine structure in the potassium atom ionization function was revealed which had not been observed experimentally before.

Measurements of potassium atom ionization cross-section by electrons (Nygaard 1975), performed using the crossed-beam technique, give the experimental confirmation of the calculation data. In these studies the length of the overlap area of the atomic and the electron beam was 25 mm, this being much higher than in the preceding experiments of other authors. As stated by the author, this is one of the reasons explaining why they were able to observe the structure at 19 eV, not observed in other experiments. Note that the energy values at which Nygaard (1975) observed the autoionizing peaks, are in a good agreement with those of Roy and Rai (1973); however, this is not the case for the theoretically predicted absolute cross-section value.

Recently a crossed-beam experiment (Evrij et al. 2005), using a 127^o electrostatic cylindrical analyser, enabled the total autoionizing cross-section to be determined

from the spectra of the emitted electrons, measured at the angle 54.7^o for various incident electron energies. The authors supposed that the autoionizing contribution into the ionization cross-section should be somewhat higher than the one observed by Nygaard (1975). Additional studies were required to check this statement.

Here we report on the studies of total cross-section of potassium atom ionization by slow monoenergetic electrons in the near-threshold energy range. A considerable attention was paid to the range from 18 to 23 eV where the highest autoionizing contribution should be expected.

2. EXPERIMENT

The studies were performed using a setup with a vapour-filled cell. An electron beam from an oxide cathode was formed by a hypocycloidal electron monochromator (a detailed description is given by Romanyuk et al. 1993), passed through the vapour-filled cell and was detected by a deep Faraday cup. A uniform axial magnetic field with a strength of about 150 OE, formed by Helmholtz rings, was applied for the spectrometer functioning. Due to a rather small intensity of the useful signal near the ionization threshold, the incident electron current was chosen within $0.5 \div 1\ \mu A$. The electron energy spread in the beam did not exceed 0.20 eV (FWHM).

Potassium vapour was delivered to the cell from a separate reservoir whose temperature was kept by 30^oC below that of the vapour-filled cell in order to avoid precipitation of the substance under investigation on the spectrometer surface that could finally result in undesirable changes of the contact potential difference during the measurements.

A positive ion detector was located directly inside the cell and was performed as a flat electrode, protected by a metal grid and located at a distance of 5 mm from the electron beam. Positive ions were ejected from the interaction area by a slight electric field ($\sim$ 1.5 V) and detected by a V7-30 picoammeter. Using a voltage-to-currency converter, the analog signal from the picoammeter was transformed into pulses for subsequent storage by the registration system.

3. RESULTS AND DISCUSSION

Figure 1 shows the obtained energy dependence of total ionization cross-section for the potassium atom in the energy range from the threshold to 26 eV. The curve obtained by Nygaard (1975) is also shown for comparison, our data at $E = 8.5$ eV being normalized by this curve. A rather good agreement with our results is seen to be observed.

The energy dependence of the ionization cross-section was measured by scanning over the electron energy with a step of 0.05 eV and acquisition time at each point of $\sim 3{-}5$ s. The energy scale was set from the initial part of the $I{-}V$ characteristic of the electron current at the primary beam collector and from the spectroscopic threshold of the atom ionization ($E_i = 4.34$ eV) (NIST AtData). The position of the atom ionization threshold was determined by linear extrapolation of the experimentally measured initial part of the ionization curve and corrected using the method proposed by Lossing et al. (1971).

As seen from Figure 1, the ionization cross-section increases rather steeply near the threshold (from 4.34 to 8 eV) and at 8.5 eV a distinct maximum is observed, followed

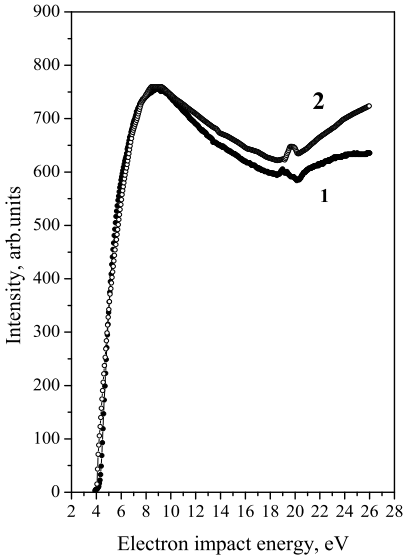

Figure 1: Potassium atom ionization cross-section: curve 1 - our experimental data, curve 2 - data of Nygaard (1975).

by a gradual decrease to the energy of ~ 18 eV, at $E \sim 19$ eV a slight maximum is observed, again followed by the cross-section increase.

It is reasonable to ascribe the first maximum in the ionization curve at 8.5 eV to the direct ionization of the s-electron as follows:

$$A + e \rightarrow A_s^+ + 2e, \tag{1}$$

where A and A_s^+ are a neutral atom and a conventional ion, respectively.

Note that the position of this maximum in our curve agrees well with the data of Zapesochny and Aleksakhin (1968) and Nygaard (1975).

In the energy dependence of the potassium atom ionization cross-section we have observed a structure with a maximum near 19 eV, which have not been observed in earlier experiments (Zapesochny and Aleksakhin 1968, Brink 1962). However, it was clearly revealed by Nygaard (1975). The absence of this structure in the study by Zapesochny and Aleksakhin (1968) can be explained by the incident electron energy scanning with a large step. Nygaard (1975) ascribes the appearance of this structure to the excitation of $3p^5 4s^2\ ^2P_{3/2,1/2}$ levels (at 18.72 and 18.98 eV) with subsequent decay and emission of electrons.

In order to determine the energy position and character of this structure more accurately as well as to determine its contribution into the ionization cross-section, we have additionally performed thorough measurements of the ionization function in the energy range from 19 to 23 eV with a smaller step of energy scan and higher acquisition time at each point. The parameters of the observed cross-section features were determined using the approximation method with a fitting function in the framework

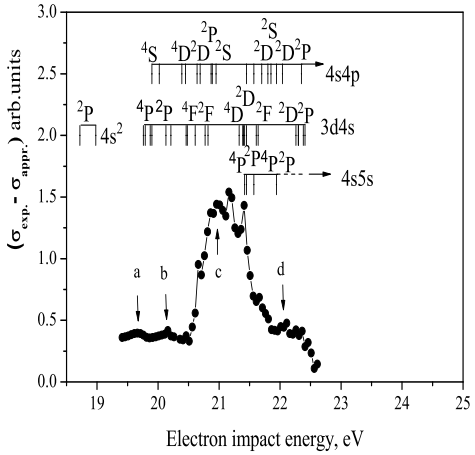

Figure 2: Structure in the total ionization cross-section.

of Origin 7.5 with subsequent subtraction of the smoothed curve from the measured one ($\sigma_{exp.} - \sigma_{appr.}$). The obtained ($\sigma_{exp.} - \sigma_{appr.}$) curve is shown in Figure 2. The positions and notations of the lowest $3p^5 n_1 l_1 n_2 l_2$ autoionizing levels (Mansfield and Ottley 1979, NIST AtData) are also shown in the figure. It is seen that for the collision energies below 20.5 eV the decay of $3p^5 4s^2\ ^2P$ and $3p^5 3d4s\ ^4P$ levels contributes to the ionization cross-section. The predominant feature is observed above 20.5 eV. Evidently, this results from the strong resonance excitation of the lowest $3p^5 3d4s\ ^4F,^2F$ and ^4D autoionizing levels (Evrij et al. 2005 and references therein). These levels and, partially, autoionizing quartets of the $3p^5 4s4p$ configurations mainly determine the potassium atom ionization in the whole collision energy range 20.5-24.4 eV. It is also seen from Figure 2 that in the range from 19 to 23 eV four well-resolved features (a, b, c, and d) are revealed, located at 19.55, 20.07, 21, and 22.04 eV, respectively. The a feature can be attributed to the formation and decay of a short-lived state of the negative ion at 19.47 eV, observed at the excitation of the $3p^5 4s^2\ ^2P_{3/2}$ level (Borovik et al. 2005).

The d feature corresponds to the negative ion resonance state, observed at 22.09 eV in the excitation function of the $3p^5 3d4s\ ^4D$ level (Borovik et al. 2005).

In Figure 3 our results are compared with the data of Evrij et al. (2005). Our data are normalized with respect to those of Evrij et al. (2005) at $E = 21$ eV. A good agreement of these data is seen to be observed. This agreement in the range from 19 to 22.5 eV once more demonstrates the presence of the autoionizing process contribution into the ionization cross-section.

Thus, the measurements performed have shown that the autoionizing contribution is clearly revealed in the cross-section of potassium atom ionization by electrons in the energy from 19 to 23 eV. However, the comparison has shown this contribution to be smaller than the one predicted theoretically (Roy and Rai 1973).

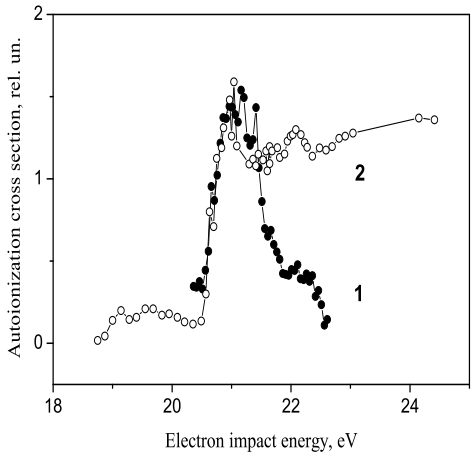

Figure 3: Comparison of the structure, revealed in the total ionization cross-section, with the total autoionizing cross-section by Evrij et al. (2005).

References

Borovik, A. A., Grum-Grzhimailo, A. N., Zatsarinny, O. I., Bartschat, K.: 2005, *J. Phys. B*, **38**, 1081.

Brink, G. O.: 1962, *Phys. Rev.*, **127**, 1204.

Evrij, M. J., Borovik, A. A. (Jr.), Shimon, L. L., Kontros, J. E., Borovik, A. A.: 2005, *NIMB*, **233**, 280.

Lossing, F. P., Emmel, R. H., Giessner, B. G., Meisels, G. G.: 1971, *J. Chem. Phys.*, **54**, 5431.

Mansfield, M. W. D., Ottley, T. W.: 1979, *Proc. R. Soc. Lond.*, **A365**, 413.

NIST AtData: http://physics.nist.gov/cgi-bin/AtData/main_asd.

Nygaard, K. J.: 1975, *Phys. Rev. A*, **11**, 1475.

Romanyuk, N. I., Shpenik, O. B., Mandi, I. A., et al.: 1993, *Zh. Tekh. Fiz.*, **63**, 138 [1993, Tech. Phys. 38, 599].

Roy, N., Rai, D. K.: 1973, *Phys. Rev.*, **A8**, 849.

Zapesochny I. P., Aleksakhin I. S.: 1968, *Soviet JETP*, **55**, 76 (in Russian).

Publ. Astron. Obs. Belgrade No. 84 (2008), 35 - 38 *Contributed Paper*

ELECTRON-SCATTERING TOTAL CROSS SECTIONS FOR COMPLEX MOLECULES: GROUP ADDITIVITY RULE

A. DOMARACKA, P. MOŻEJKO, E. PTASIŃSKA-DENGA and Cz. SZMYTKOWSKI
Atomic Physics Group, Faculty of Applied Physics and Mathematics
Gdańsk University of Technology, ul. G. Narutowicza 11/12, 80-952 Gdańsk, Poland
E–mail: domaracka@mif.pg.gda.pl

Abstract. Absolute electron-scattering total cross sections (TCSs) for nitrogen containing [$N(CH_3)_3$, NH_2CH_3, NH_3] and for cyclic-ether molecules [$(CH_2)_nO$, n=2–4] have been measured with transmission technique. The TCSs are compared to study how the number of methyl and/or methylene groups within molecule reflects in TCS energy function.

1. INTRODUCTION

Electron-driven low-energy processes play a key role in planetary physics, biology, and nowadays advanced technologies (e.g. Christophorou and Olthoff, 2004), just to cite a few. Recently, it has been also shown that low-energy electrons can initiate amino acid synthesis in the interstellar medium (Lafosse *et al.*, 2006). For understanding and modelling electron-induced reactions comprehensive sets of scattering data are needed. Unfortunately, in spite of great experimental and theoretical effort, data for compounds of current scientific and technological interest, especially those in absolute scale, are rather scarce. Deficiency of results is connected partly with experimental as well as theoretical difficulties. Some help in estimation of required data may come from regularities observed in cross sections which are already known for other molecules. Such trends in electron-scattering total cross section (TCS) energy dependence have already been noticed in our laboratory for hydro- and perfluorocarbon target families: isomer effect (e.g. Szmytkowski and Kwitnewski, 2002) and perfluorination effect (e.g. Szmytkowski and Ptasińska-Denga, 2001). Recently, our studies focused on determining TCS for polyatomic molecules have been extended to nitrogen containing molecules [$N(CH_3)_3$, NH_2CH_3, NH_3] and cyclic ethers series [$(CH_2)_nO$, n=2–5]. These series have been chosen to examine how the number of CH_3 and CH_2 groups, respectively, reflects in the shape and magnitude of TCS energy function.

2. EXPERIMENTAL AND COMPUTATIONAL PROCEDURES

2. 1. EXPERIMENT

The absolute total cross sections for studied molecules have been measured using the electron-transmission method in linear configuration (Bederson and Kieffer, 1971). The electron beam of required energy E and resolution of about 100 meV—prepared by electron gun, followed with 127° cylindrical electrostatic monochromator, and lens systems—is directed into scattering cell filled with target under study. The electrons emerging through the exit slit are energy discriminated by a retarding-field analyzer and eventually collected with a Faraday cup.

To determine the total cross section value, the Bouguer-de Beer-Lambert attenuation formula, in which the thermal transpiration effect was accounted for, is used

$$\mathrm{TCS}(E) = \frac{k\sqrt{T_c T_m}}{pL} \ln \frac{I(E,0)}{I(E,p)},$$

where: $I(E,p)$ and $I(E,0)$ are the transmitted electron currents taken in the presence and absence of the target in the cell, respectively. The other quantities measured directly are: p – the pressure of investigated gas in the scattering cell of the length L; T_m – the temperature of the mks absolute manometer head, and T_c – the temperature of the collision chamber; k is the Boltzmann constant. The energy scale was calibrated by the reference to the well-known resonant oscillatory structure of N_2 appearing near 2.3 eV. The final TCS value at each electron energy is a weighted mean of results from several series carried out at different target pressures and electron-beam controlling conditions.

2. 2. COMPUTATIONS

Elastic cross section (ECS) for electron collisions with complex molecules has been calculated with the independent atom method, while the ionization cross section (ICS) has been obtained within the binary-encounter-Bethe formalism. The theoretical total cross section, as shown in Fig. 2, is the sum (ionization+elastic) of calculated partial cross sections. More details about computational procedures can be found in Możejko *et al.* 2006, and references therein.

3. RESULTS AND DISCUSSION

Figure 1 shows the absolute total cross sections for electron scattering by nitrogen containing molecules: ammonia (NH_3), methylamine (NH_2CH_3) with one hydrogen atom replaced by methyl group, and trimethylamine ($N(CH_3)_3$) – permethylated analogue of ammonia. The variation of TCS magnitude across this series can be associated with the geometrical size of molecules. Regarding the shape, the TCSs are basically similar—they all have maximum located within 7–9 eV range. The only difference is observed below 2 eV, where TCS functions for NH_3 and NH_2CH_3 are rising with energy decrease, while TCS for $N(CH_3)_3$ is nearly constant. The detailed analysis of TCS curves for nitrides family, based on geometrical considerations, shows that TCS of any of three molecules can be estimated as combination of TCSs for molecular fragments: e.g. $\mathrm{TCS}_{NH_2CH_3} = 1/3{\times}\mathrm{TCS}_{N(CH_3)_3} + 2/3{\times}\mathrm{TCS}_{NH_3}$. We have also noticed that the TCS for trimethylamine can be reasonably estimated as a sum of TCSs for

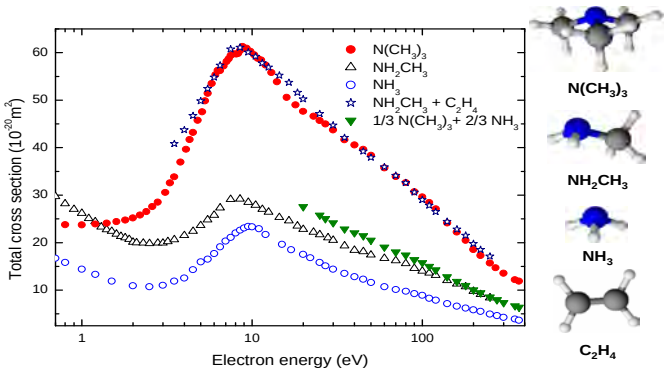

Figure 1: Total cross sections for e^--collision with: NH_3 (Szmytkowski *et al.* 1989, Szmytkowski, *at al.* 2004), NH_2CH_3 (Szmytkowski and Krzysztofowicz 1995) and $N(CH_3)_3$ (Szmytkowski *et al.* 2007). Presented are also examples of TCS estimation for: $N(CH_3)_3$, as the sum of TCSs values for NH_3 and C_2H_4 (Szmytkowski *et al.* 2003), and for NH_2CH_3 - composed as $1/3\times TCS_{N(CH_3)_3}+2/3\times TCS_{NH_3}$. The geometries of considered molecules are shown as well.

NH_2CH_3 and C_2H_4. It means that having data for appropriate molecular fragments, it is possible to estimate roughly the cross section before performing measurements or calculations.

That conclusion is also confirmed by our very recent study concerning cyclic ethers $(CH_2)_nO$ (n=2–4) family. The ring of studied molecules is composed of n methylene groups and one oxygen atom (cf. Fig. 2). Measured TCSs curves are compared to find out how the increasing number of CH_2 groups within molecule reflects in the TCS function. The inspection of data reveals that above 20 eV the TCS is in direct proportion to the number of CH_2 groups. Figure 2 shows the estimated TCS values for methylene group and oxygen atom, as well as the estimated TCS for each studied molecules, e.g.: $TCS_{(CH_2)_3O} = 3\times TCS_{CH_2} + TCS_O$. The agreement of estimated and experimental TCS data is excellent. Having in hand the partial contributions we are able to estimate TCS for c-$C_5H_{10}O$ molecule, the next member of the ethers family. As no data can be found in the literature for the electron c-$C_5H_{10}O$ collision, we check the correctness of estimated cross section by comparing it with our theoretical TCS being a sum of ICS and ECS. Above 40 eV, the estimated TCS is consistently lower (3-11%) than computed one, however this difference does not exceed much the typical– experimental TCS uncertainty.

4. CONCLUSION

Based on our intermediate-energy TCS results for nitrides and cyclic ethers we have shown that molecular TCS can be decomposed into cross sections of sub-molecular units. Using these effective partial TCS contributions it is possible to estimate TCS for other complex molecules with reasonable accuracy.

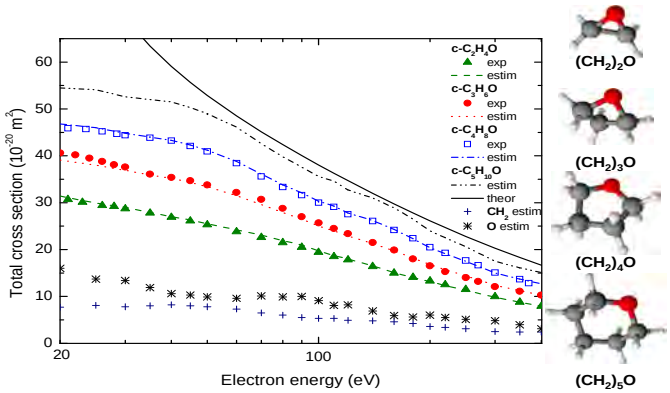

Figure 2: Comparison of the experimental or calculated TCSs with those estimated from group additivity rule for e^--scattering by $(CH_2)_nO$, n=2–5. Experimental data: c-$(CH_2)_2O$ (Szmytkowski *et al.* 2008a), c-$(CH_2)_3O$ (Szmytkowski *et al.* 2008b) and c- $(CH_2)_4O$ (Możejko *et al.* 2006). Theoretical TCS for c- $(CH_2)_5O$ is the sum of elastic and ionization cross sections. Molecule pictographs are included.

Acknowledments

This work is part of the MNSzW program 2007-2008 and is supported by the Polish Ministry of Science and Higher Education (project no. N202 110 32/2862).

References

Bederson, B., Kieffer, L. J.: 1971, *Rev. Mod. Phys.* **43**, 601.
Christophorou, L. G., Olthoff, J. K.: 2004, Fundamental electron interactions with plasma processing gases, Kluwer, New York.
Lafosse, A., Bertin, M., Domaracka, A., Pliszka, D., Illenberger, E., Azria, R. : 2006, *Phys. Chem. Chem. Phys.*, **8**, 5564.
Możejko, P., Ptasińska-Denga, E., Domaracka, A., Szmytkowski, Cz.: 2006, *Phys. Rev. A*, **74**, 012708.
Szmytkowski, Cz., Domaracka, A., Możejko, P., Ptasińska-Denga, E.: 2007, *Phys. Rev. A*, **75**, 052721.
Szmytkowski, Cz., Domaracka, A., Możejko, P., Ptasińska-Denga, E.: 2008a, *J. Phys. B*, **41**, 0652004.
Szmytkowski, Cz., Domaracka, A., Możejko, P., Ptasińska-Denga, E.: 2008b, *J. Chem. Phys.*, submitted.
Szmytkowski, Cz, Krzysztofowicz, A. M.: 1995, *J. Phys. B*, **28**, 4291.
Szmytkowski, Cz., Kwitnewski, S.: 2002, *J. Phys. B*, **35**, 2613, 3781.
Szmytkowski, Cz., Kwitnewski, S., Ptasińska-Denga, E.: 2003, *Phys. Rev. A*, **68**, 03715.
Szmytkowski, Cz., Maciąg, K., Karwasz, G., Filipović, D.: 1989, *J. Phys B*, **22**, 525.
Szmytkowski, Cz., Piotrowicz, M., Domaracka, A., Kłosowski, Ł., Ptasińska-Denga, E., Kasperski, G.: 2004, *J. Chem. Phys.*, **121**, 1790.
Szmytkowski, Cz., Ptasińska-Denga, E. : 2001, *Vacuum*, **63**, 545.

Publ. Astron. Obs. Belgrade No. 84 (2008), 39 - 44 *Contributed Paper*

RECOMBINATION OF D_3^+ IONS WITH ELECTRONS IN LOW TEMPERATURE PLASMA

I. KOROLOV[1,2], T. KOTRÍK[2], P. DOHNAL[2], R. PLAŠIL[2] and J. GLOSÍK[2]

[1] *Research Institute for Solid State Physics and Optics, Konkoly-Thege M. 29-33, Budapest, Hungary*
E–mail: Ihor.Korolov@mff.cuni.cz

[2] *Charles University Prague, Faculty of Mathematics and Physics, V Holešovičkách 2, Prague 8, Czech Republic*
E–mail: Juraj.Glosik@mff.cuni.cz

Abstract. The flowing afterglow study of recombination of D_3^+ ions with electrons and measurements of recombination rate coefficients in He-Ar-D_2 plasma at several temperatures and buffer gas pressures, and over a wide range of deuterium number densities are reported. The influence of helium number density on overall recombination rate coefficient was observed. The results indicate the multicollision character of the recombination process in D_3^+ dominated low temperature plasma. The obtained binary and ternary recombination rate coefficients are: $\alpha_{\rm bin}(250\ {\rm K}) = (4.1 \pm 1.2) \times 10^{-8}\ {\rm cm^3 s^{-1}}$, $K_{\rm He}(250{\rm K}) = (2.1 \pm 0.7) \times 10^{-25}\ {\rm cm^6 s^{-1}}$.

1. INTRODUCTION

Interactions of electrons with H_3^+ and D_3^+ ions is of fundamental importance for plasma physics, physical chemistry, astrophysics and for quantum theory. From first study of H_3^+ recombination in 1949 to present days there was over 50 attempts to measure recombination rate coefficients of H_3^+ and D_3^+ ions (see reviews Johnsen et al. 2005, Plasil et al. 2002, Larson et al. 2008). Up to 2001 the measured values of the recombination rate coefficients of H_3^+ and D_3^+ ions were scattered over several orders in magnitude and they were in contradiction with available theoretical predictions. In 2001 inclusion of non-Born-Oppenheimer Jahn-Teller coupling significantly improved the theory (Kokoouline et al. 2001). After further refinement the cross sections and the rate coefficients for H_3^+ and D_3^+ recombination were calculated (Kokoouline et al., 2003). The most recent theoretical values of the recombination rate coefficients for dissociative recombination of H_3^+ and D_3^+ ions are $\alpha_{H_3^+}(300\ {\rm K}) = 5.6 \times 10^{-8}\ {\rm cm^3 s^{-1}}$ and $\alpha_{D_3^+}(300\ {\rm K}) = 4 \times 10^{-8}\ {\rm cm^3 s^{-1}}$ respectively (Kokoouline et al., 2003, Santos et al. 2007, Kokoouline 2008). These values are in good agreement with the recent storage ring experiments (McCall et al. 2003, 2004, Kreckel et al. 2005). But the disagreement between multi- and single-collisional experiments (Plasil et al. 2002, Poterya et al. 2002) has not been solved until now. Note that in the plasmatic (mul-

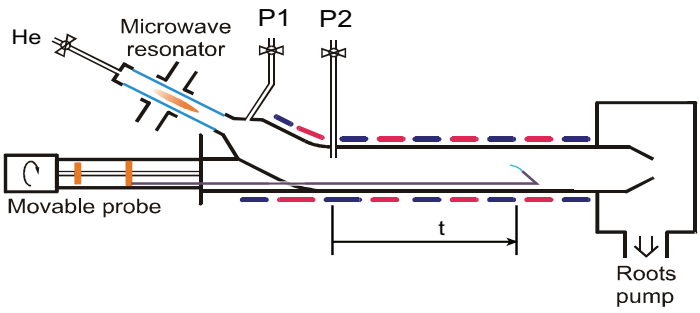

Figure 1: Schema of temperature variable Flowing Afterglow with Langmuir probe (FALP).

ticollisional) experiments plasma is usually formed in the ambient gas (He in present experiments) and small amount of hydrogen or deuterium is added to form H_3^+ or D_3^+ dominated plasma. Moreover, in plasmatic experiments in order to minimize diffusion losses the ambient gas pressure is high (100-2000 Pa) and the ions have multiple collisions with neutral particles prior to their recombination. In beam experiments there is single collision of electron with ion and ion do not collide with neutral particles. If in electron-ion interaction long-lived intermediate neutral molecule is formed, as it is in case of H_3^+ or D_3^+ ions, then we can also expect collisions of this molecule with the atoms of ambient gas. These collisions can influence the process of recombination and as a result measured overall recombination rate coefficient $\alpha_{\rm eff}$ will be dependent on the pressure. The presented studies concentrated on recombination of D_3^+ and on measurements of the pressure dependence of $\alpha_{{\rm eff}D_3^+}$.

2. EXPERIMENT

The recombination rate coefficients were measured with flowing afterglow apparatus (FALP technique) (Novotny et al. 2006). The present version of the experimental apparatus is designed and constructed for measurement of small recombination rate coefficients (down to 5×10^{-9} cm^{3}s^{-1}) at relatively high buffer gas pressure (up to 2000 Pa), the details are described elsewhere (Korolov et al. 2006, Plasil et al. 2008). Schematic diagram of FALP is shown in Figure 1.

Helium as a buffer gas flows through the glass discharge tube where He^+ ions and He^m metastables are formed. Downstream from the discharge region argon gas is added (port P1, see Figure 1) to quench helium metastables and to form Ar^+ dominated plasma. Further downstream hydrogen (or deuterium) is added via port P2 to already relaxed plasma (Glosik et al. 1999) and D_3^+ dominated plasma is formed via the reaction sequence:

$$Ar^+ \xrightarrow{D_2} (ArD^+, D_2^+) \xrightarrow{D_2} D_3^+ \qquad (1)$$

The kinetics of formation of D_3^+ ions in deuterium containing plasmas is sufficiently well understood and has been described several times (see e.g. (Poterya et al. 2002)). In the present experiments electron number density evolution (decay) along the flowing afterglow plasma is measured using the axially movable Langmuir probe (from

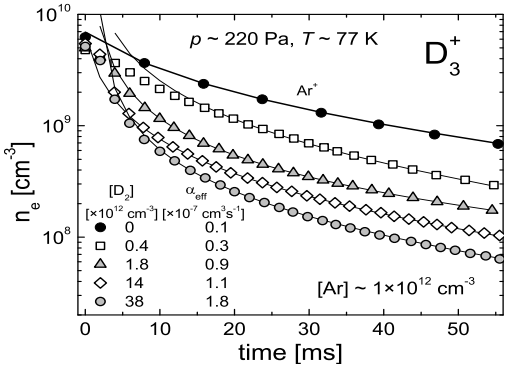

Figure 2: Measured electron density decays along the Flow Tube in He-Ar-D_2 plasmas at several concentrations of D_2. The solid lines represent fits of the data sets; the obtained rate coefficients are indicated.

the P2 port down to the end of the flow tube; 35 cm). The examples of measured electron density decays along the Flow Tube at several concentrations of D_2 (at $T =$ 77 K) are shown in Figure 2. The indicated values of α_{eff} were calculated from the decay curves using advanced data analysis (for details see (Korolov et al. 2008)).

3. RESULTS AND DISCUSSION

In Figure 3, the obtained effective recombination rate coefficients (α_{eff}) are plotted as a function of deuterium concentration ([D_2]). The previous AISA data (Poterya et al. 2002) were also included in the figure. The observed difference between the rate coefficients measured at $T = 250$ K in AISA and FALP experiments is given by the difference in helium number densities in these experiments.

Because of large extend of deuterium densities the plasmas at low [D_2] differ substantially from plasma at high [D_2]. The difference is in number of collisions (N) of ion with deuterium molecule prior to its recombination with electron. Figure 3 is divided into three sections. In the left section with $[D_2] \leq 1 \times 10^{12}$ cm^{-3} ion has typically less than 1 collision with D_2 prior to recombination N < 1. In the right section $D_2 > 1 \times 10^{13}$ cm^{-3} ion has many collisions with D_2, N $>> 1$, at used temperatures and helium pressures D_5^+ ions are formed in three-body association. As a consequence decay of the plasma is influenced by recombination of D_5^+ ions and measured α_{eff} is increasing with increasing [D_2] (Novotny et al. 2006). In the middle section (1×10^{12} cm^{-3} $< [D_2] < 1 \times 10^{13}$ cm^{-3}) D_3^+ ion will collide several times with D_2 before recombining with electron, N > 1. We will denote these condition as "saturated region". In these collisions ion (D_3^+) will be thermalized (internal excitation). The kinetic energy of D_3^+ will be thermalized immediately after its formation in collisions with He atoms (He density is higher by many orders of magnitude). Because of these fast relaxation processes the plasma is in the conditions corresponding to the middle section in thermodynamic equilibrium. We have studied temperature and pressure dependence of the value of recombination rate coefficient in this plasma. Figure 4

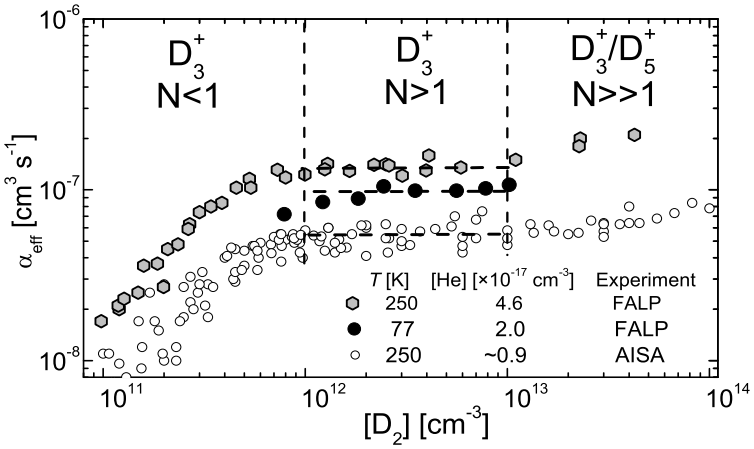

Figure 3: The effective recombination rate coefficients measured over a broad range of deuterium number densities. The dashed lines indicate values of recombination rate coefficients considered to conditions in "saturated region", i.e. in conditions where ions D_3^+ have many collisions with D_2 and the decaying plasma is in thermodynamic equilibrium with helium and deuterium.

shows the dependence of recombination rate coefficients on helium number density. The plotted rate coefficients were measured in different experiments at two different temperatures and at deuterium densities corresponding to the "saturated region". The figure also includes the calculated value of the recombination rate coefficient for binary dissociative recombination of D_3^+ at 250 K (Kokoouline et al. 2008).

The linear dependence of $\alpha_{\rm eff}$ on helium density is obvious. Therefore, the dependence of measured aeff on helium number density can be written as:

$$\alpha_{\rm eff} = \alpha_{\rm bin} + \alpha_{\rm ter} = \alpha_{\rm bin} + K_{\rm He}[{\rm He}] \tag{2}$$

From the data corresponding to 250 K and 200 K we obtained: $\alpha_{\rm bin}(250\ {\rm K}) = (4.1 \pm 1.2) \times 10^{-8}\ {\rm cm^3 s^{-1}}$ $\alpha_{\rm bin}(200\ {\rm K}) = (4.7 \pm 1.4) \times 10^{-8}\ {\rm cm^3 s^{-1}}$. These values agree with the values calculated for binary dissociative recombination (DR) of the corresponding ions (Kokoouline 2008). We assume that ternary channel is coupled with formation of long-lived highly exited Rydberg molecules (D_3^*) in the interaction of electrons with D_3^+ ions. If average lifetime of D_3^* is long, then this highly excited molecule can eventually collide with buffer gas atom, affecting the recombination process:

$$\begin{array}{l} {\rm D}_3^+ + e^- \rightleftarrows {\rm D}_3^* \rightarrow neutrals\ Binary \\ \qquad\qquad\quad \downarrow {\rm He} \\ \qquad\qquad\quad \rightarrow neutrals\ Ternaty \end{array}$$

The obtained values of ternary rate coefficient $K_{\rm He}$ for 250 K and 200 K are $(2.1 \pm 0.7) \times 10^{-25}\ {\rm cm^6 s^{-1}}$ and $(3.5 \pm 1.1) \times 10^{-25}\ {\rm cm^6 s^{-1}}$ respectively.

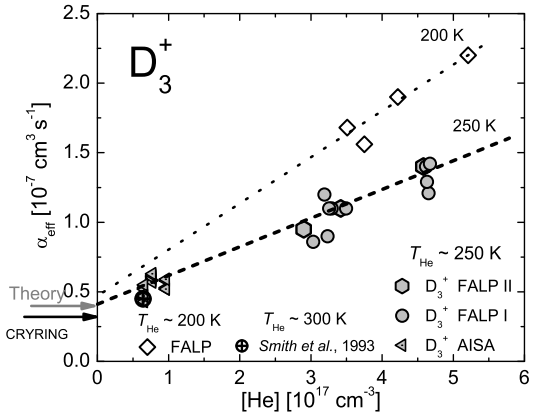

Figure 4: Effective recombination rate coefficients of D_3^+ measured in He-Ar-D_2 afterglow experiments. The arrow "Theory" indicates calculated values for 250 K (Kokoouline 2008). The dashed and dotted line connect measured data with theoretical value of rate coefficient for binary dissociative recombination (Kokoouline et al. 2008) for 250 K and 200 K. The arrow "Cryring" indicates the value of recombination rate coefficient obtained from the cross section measurements in CRYRING experiment (Padellec et al. 1998, Larsson et al. 1997). The thermal value obtained by Smith and Spanel in FALP experiment (300 K) is also included.

4. CONCLUSIONS

The measurements of recombination rate coefficient of D_3^+ ion at well defined conditions of afterglow plasma in a FALP experiment were performed. We observed strong pressure and temperature dependence of the rate coefficient indicating the existence of ternary channel in the overall recombination process. The observed ternary process is 100 times faster than previously observed three body recombination (Cao et al. 1991) and indicates extraordinary mechanism of D_3^+ recombination. The study of temperature dependence of the ternary channel of D_3^+ recombination process is in progress. The dependence of the effective rate coefficient on the D_2 density at $[D_2] < 1 \times 10^{12}$ cm^{-3} can indicate that different rotational and nuclear spin states of D_3^+ are not at the equilibrium on the timescale of the present experiment.

Acknowledgements

This work is a part of the research plan MSM 0021620834 financed by the Ministry of Education of the Czech Republic and was partly supported by GACR (202/07/0495, 202/08/H057) by GAUK 53607, GAUK 124707 and GAUK 86908.

References

Cao, Y. S. and Johnsen, R.: 1991, *J. Chem. Phys.*, **94**, 5443.

Glosik, J., Bano, G., Plasil, R., Luca, A., Zakouril, P.: 1999, *Int. J. Mass Spectrom.*, **189**, 103.

Johnsen, R.: 2005, *J. Phys.: Conf Series*, **4**, 83.
Kokoouline, V., Greene, C. H., Esry, B. D.: 2001, *Nature (London)*, **412**, 891.
Kokoouline, V., Greene, C. H.: 2003, *Phys. Rev. A*, **68**, 012703.
Kokoouline, V.: 2008, *private communication*.
Korolov, I., Novotny, O., Kotrik, T., Plasil, R., Varju, J., Hejduk, M., Glosik, J.: 2008, *Contrib. Plasma Phys.*, in print.
Korolov, I., Novotny, O., Plasil, R., Hlavenka, P., Kotrik, T., Tichy, M., Kudrna, P., Glosik, J., Luca, A.: 2006, *Czech. J. Phys.*, **56**, 854.
Kreckel, H. et al.: 2005, *Phys. Rev. Lett.*, **95**, 263201.
Larsson, M. and Orel, A.E.: 2008, Dissociative Recombination of Molecular Ions, Cambridge University Press, Cambridge.
Larsson, M., Danared, H., Larson, A., Le Padellec, A., Peterson, J. R., Rosen, S., Semeniak, J., Stromholm, C.: 1997, *Phys. Rev. Lett.*, **79**, 395.
McCall, B. J. et al.: 2003, *Nature*, **422**, 500.
McCall, B. J. et al.: 2004, *Phys. Rev. A*, **70**, 052716.
Novotny, O., Plasil, R., Pysanenko, A., Korolov, I. and Glosik, J.: 2006, *J. Phys. B: At. Mol. Opt. Phys.*, **39**, 2561.
Padellec, A., Larsson, M., Danared, H., Larson, A., Peterson, J. R., Rosen, S., Semeniak, J., Stromholm, C.: 1998, *Phys. Scripta*, **57**, 215.
Plasil, R., Glosik, J., Poterya, V., Kudrna, P., Rusz, J., Tichy, M. and Pysanenko, A. : 2002, *Int. J. Mass. Spectrom.*, **218**, 105.
Plasil, R., Korolov, I., Kotrik, T., Glosik, J.: 2008 *Int. J. Mass Spectom. Ion Process.*, in print.
Poterya, V., Glosik, J., Plasil, R., Tichy, M., Kudrna, P. and Pysanenko, A.: 2002, *Phys. Rev. Lett.*, **88**, 044802.
Santos, S. F., Kokoouline, V. and Greene, C. H.: 2007, *J. Chem. Phys.*, **127**, 124309.
Smith, D. and Öpatnel, P.: 1993, *Int. J. Mass Spectrom. Ion Process.*, **129**, 163.

Publ. Astron. Obs. Belgrade No. 84 (2008), 45 - 48 *Contributed Paper*

RELATIVE ANGLE-DIFFERENTIAL CROSS SECTIONS FOR ELASTIC ELECTRON SCATTERING FROM PYRIMIDINE

J. B. MALJKOVIĆ, A. R. MILOSAVLJEVIĆ, D. ŠEVIĆ and B. P. MARINKOVIĆ

Laboratory for Atomic Collision Processes, Institute of Physics, Pregrevica 118, 11080 Belgrade, Serbia
E–mail: djurdja@uranus.phy.bg.ac.yu

Abstract. Angle-differential cross sections for elastic scattering of electrons from pyrimidine are reported for the incident energies from 50-300 eV. Measurements were performed using a cross-beam technique, for scattering angles from 20^o to 110^o. Experimental relative elastic differential cross sections are compared with recent theoretical results for uracil, which is a pyrimidine base and a component of ribonucleic acid.

1. INTRODUCTION

The investigation of electron interaction with molecules which are analogue to DNA components has been motivated in recent years by the research of radiation damage in biomolecular systems (Boudaiffa et al. 2000). Since a large number of secondary low-energy electrons are formed on the track of primary high-energy ionizing particles they carry most of energy and play particulary important role in the final radiation damage, ascribed to the primary ionizing particle. To improve our understanding of the chain of the reactions leading to DNA and RNA damage (Hassan et al. 2000,Boudaiffa et al. 2000, Michael et al. 2000) and postulate new reaction models, spectroscopic data and cross section values for electron impact on DNA and RNA are needed. The pyrimidine (Py) molecule is akin to cytosine and thymine in DNA as well as uracil in RNA and therefore may serve as a model compound to investigate differential cross sections for elastic scattering of electrons from constituents of these biomolecules (Levesque et al. 2005). Pyrimidine ($C_4H_4N_2$) is a heterocyclic aromatic organic compound containing two nitrogen atoms at positions 1 and 3 of the six-member ring (Gilchrist 1997, see Figure 1). Three nucleobases found in nucleic acids, namely cytosine ($C_4H_5N_3O$), thymine ($C_5H_6N_2O_2$) and uracil ($C_4H_4N_2O_2$) are pyrimidine derivatives. Because of its similarity to nucleotide ring system, Py has been used as a simple theoretical model of the ring conformations in nucleotides (Lesyng et al. 1984, Herzyk et al. 1989,Berthier 1997). Levesque et al. 2005 have reported low-energy vibrational and electronic electron- energy-loss (EEL) spectra of pyrimidine condensed on a thin film of solid argon held at 18 K, for incident energy range of 2-12 eV. According to our knowledge, no theoretical results concerning elastic electron scattering from Py have been published. However, Možejko and Sanche 2003 have calculated differential cross

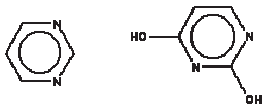

Figure 1: Structural formulae of pyrimidine (left) and uracil (right) molecules.

sections (DCSs) for elastic electron collisions with uracil, cytosine, guanine, adenine and thymine, using the independent atom method (IAM) with a static-polarization model potential, for incident energies ranging from 50-4000 eV. Total cross sections have also been calculated with the binary-encounter-Bethe model from the ionization threshold up to 5000 eV. The highest values of the elastic DCSs are obtained for the largest molecule (guanine) and the lowest for uracil which is smallest investigated molecule. Thus, the absolute elastic DCS value is connected with number of electrons in molecule and molecular size, while angular dependence of the elastic DCSs is related to molecular geometry.

In the present contribution, experimental results on elastic electron scattering from pyrimidine molecule have been reported. The experimental relative DCSs are obtained for 50, 100, 200 and 300 eV in the angular range from 20^o to 110^o. We have compared our results for pyrimidine ($C_4H_4N_2$) with calculations of Možejko and Sanche 2003 for the uracil molecule. Shapes of DCS curves show similarities at all impact energies.

2. EXPERIMENTAL

A detailed description of the present crossed-beam experimental set-up has been given elsewhere (Milosavljević et al. 2006). Briefly, an electron gun produces a nonmonochromated, well collimated incident electron beam, which is crossed perpendicularly by a molecular beam produced by a stainless still needle. The gun can be rotated around the needle in the angular range fr om about -40^o to 120^o. The scattered electrons are retarded and focused by a four-element cylindrical electrostatic len s into a double cylindrical mirror analyzer, followed by three-element focusing lens and a single channel electron multiplier. The base pressure of about 4×10^{-7} mbar was obtained by a turbo-molecular pump. The working pressure was usually less than 3×10^{-6} mbar and was checked for each experimental point. The uncertainty of the incident energy scale was determined to be less than ± 0.4 eV, by observing a threshold for He^+ ions yield. The best energy resolution is about 0.5 eV, limited by a thermal spread of primary electrons. The angular resolution was better than $\pm 2^o$. The experimental procedure was checked according to benchmark DCSs for elastic electron scattering by Ar. The anhydrous Py was purchased from Aldrich with declared purity better than 99 %.Py posses high vapor pressure, but the sample cointainer was still heated during a measurement at the temperature of about 50-60^{o}C, because of system stability and further improvement of the signal. The temperature of the needle and pipes were around 70 ^{o}C and 60 ^{o}C, respectively. The background contributions, which were typically below 15 %, have been subtracted from the measured electron yields. The errors for the relative DCSs measured as a function of scattering angle include statistical errors (0.1-3 %) according to Poisson's distribution and short-term

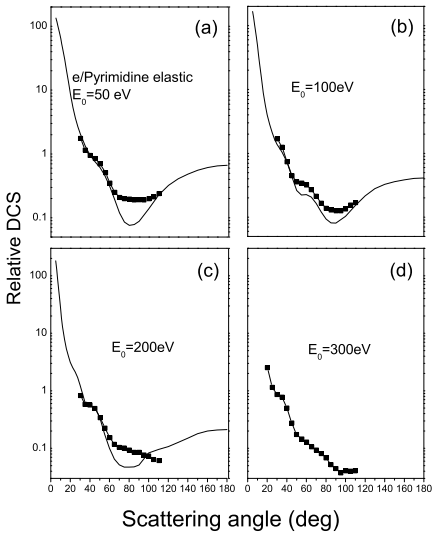

Figure 2: Angular dependence of relative DCSs for elastic electron scattering from Py molecule (▪, present experiment) and uracil (-, theory by Možejko and Sanche 2003). The DCSs are normalized at 40^o for 50 eV, at 30^o for 100 eV and at 50^o for 200 eV.

stability errors (1-12 %), according to discrepancy of repeated measurements at the same incident energy and scattering angle.

3. RESULTS and DISCUSSION

The experimental relative DCSs are obtained for the incident electron energies of 50, 100, 200 and 300 eV, in the angular range from 20^o to 110^o (for 300 eV), and from 30^o to 110^o (for 50, 100 and 200 eV). The DCSs, experimental for pyrimidine and theoretical for uracil (Možejko and Sanche 2003), are normalized and presented in Figure 2. Theoretical results for uracil are based on the IAM approximation, where the electron-molecule collisions are reduced to the problem of collision with individual atoms by assuming that each atom of the molecule scatters independently and that redistribution of atomic electrons due to the molecular binding is unimportant. The theoretical DCSs for uracil are similar to experimental DCSs for pyrimidine for 50 eV and 100 eV, but at 200 eV DCSs do not seem to agree very well. The theoretical calculations for pyrimidine are under way (Garcia 2008). IAM technique gives more pronounced minima in the angular range from 60^o to 100^o, for all energies. The DCS at 100 eV is characterized by a minimum at about 90^o, which disappears with increasing electron energy. At 300 eV the electron beam was better focused and experimental results exist down to 20^o, but there are no calculations for uracil at this energy.

4. CONCLUSION

To conclude, the elastic scattering of electrons from Py has been investigated. The measurements were performed using cross-beam technique, for incident electron energies of 50, 100, 200 and 300 eV, and scattering angles from 20^o to 110^o. Expe rimental elastic differential cross sections are compared with recent theoretical results for similar molecule uracil ($C_4H_4N_2O_2$), available at 50, 100 and 200 eV. The shape of the present experimental DCSs for elastic electron-Py scattering shows resemblance with the calculations at 50 and 100 eV for uracil.

Acknowledgments

We are very grateful to Dr Pawel Možejko from Gdansk University of Technology for sending us calculated results in numerical form. This work has been supported by Ministry of Science of Republic of Serbia under project 141011. We are also pleased to recognize support of EU/ESF COST Action P9 on Radiation Damage and the European Science Foundation EIPAM Programme.

References

Boudaiffa, B., Cloutier, P., Hunting, D., Huels, M. A. and Sanche, L.: 2000, *Science*, **287**, 1658.

Berthier, G., Cadioli, C., Gallinella, E., Aamouche, A. and Ghomi, M.: 1997, *J. Mol. Struct.*, **390**, 11.

Garcia, G.: 2008, private comunication.

Gilchrist Thomas, L.: 1997, Heterocyclic Chemistry (3rd Edition) ISBN 0-582-27843-0.

Hassan, A. C., Dugal, P.C. and Sanche, L.: 2000, *Radiat. Res.*, **153**, 23.

Herzyk, P. and A. Rabczenko, A.: 1989, *J. Chem. Soc., Perkin Trans.*, **2**, 209.

Lesyng, B. and Saenger, W.: 1984, *Carbohydr. Res.*, **133**, 187.

Levesque, P. L., Michaud, M. and Sanche, L.: 2005, *J. Chem. Phys.*, **122**, 094701.

Michael, B. D. and Neil, P. O.: 2000, *Science*, **287**, 1603.

Milosavljević, A. R., Mandžukov, S., Šević, D. I., Čadež, I., Marinković, B. P.: 2006, *J. Phys. B: At. Mol. Opt. Phys.*, **39**, 609.

Možejko, P., Sanche, L.: 2003 *Radiat.Environ.Biophys.*, **42**, 201.

Publ. Astron. Obs. Belgrade No. 84 (2008), 49 - 52 *Contributed Paper*

ELECTRON IMPACT EXCITATION OF Ag ATOM: ENERGY-LOSS SPECTROSCOPY

S. D. TOŠIĆ[1], D. ŠEVIĆ[1], V. PEJČEV[1,2], D. M. FILIPOVIĆ,[1,3]
and B. P. MARINKOVIĆ[1]

[1] *Institute of Physics, Belgrade, Serbia*
E–mail: bratislav.marinkovic@phy.bg.ac.yu

[2] *Faculty of Natural Sciences, University of Kragujevac, Radoja Domanovića 12, 34000 Kragujevac, Serbia*

[3] *Faculty of Physics, University of Belgrade, P. O. Box 368, 11001 Belgrade, Serbia*

Abstract. Here we present the results of electron spectroscopy measurements of electron collisions with Ag atom at medium electron impact energies up to 100 eV. Data obtained include the energy-loss spectra of Ag recorded at different scattering angles using a crossed electron-atom beam technique in the electron spectrometer ESMA that operates in energy-loss mode.

1. INTRODUCTION

Electron energy-loss spectroscopy (EELS) is based on measuring the energy which electron loses in inelastic electron-atom scattering. Since the electron excitation process is energy dependent, EELS is recognized to be very useful tool for the investigation and determination of atomic excited states. If a target atom is in the ground state, lines observed in the energy-loss spectra are directly attributed to their excited states. Generally, EELS technique is important in many applications ranging from various surface science researches to medical diagnosis. It is widely employed for the study of electronic structures, electronic correlation and elemental composition of different materials (Hebert et al. 2006, Schone et al. 2003, Salaita et al. 2000), as well as for analyzing biological structures and detection of a single atom contained in the macromolecule assembly (Leapman 2003). In comparison with optical spectroscopy and optical-like spectra, electron spectroscopy has worse resolution. On the other hand, the EEL spectra obtained at different energies and observation angles can focus either on the optically allowed or optically forbidden transitions. Allowed transition will dominate the spectrum for higher incident energies and smaller scattering angles while the forbidden transitions could dominate at lower energies and larger scattering angles. To the best of our knowledge, there are no studies of EEL spectra resulting for electron excitation of Ag atom. The reason for the lack of experimental investigations on this topic could be the high working temperature (approximately 1300 K) which is necessary for vaporization of the silver sample and for production

of well collimated effusive atomic beam. In this paper we present the results of experimental investigation of the unresolved silver resonance lines ($4d^{10}5p\ ^2P_{1/2,3/2}$) excited by electron impact using EEL spectroscopy. We have employed an electron spectrometer in a crossed-beam arrangement to record energy-loss spectra over the range of incident electron energies from 10 to 100 eV at various scattering angles.

2. EXPERIMENT AND PROCEDURE

EEL spectra were measured with the hemispherical electron spectrometer ESMA described earlier (Tošić et al. 2008). In brief, the experiment was carried out by utilizing a crossed electron-atom beam technique. A hairpin thermoelectron source was used and electron beam was formed by the electron monochromator which consists of systems of cylindrical electrostatic lenses and hemispherical electrostatic energy selector. Inelastically scattered electrons were detected by the hemispherical electron energy analyzer with a channel electron multiplier as a single-electron detector at the end. Analyzer is of the same type as the monochromator and it can rotate around the atomic beam axis from -30^o to 150^o with respect to the incoming electron beam. The spectrometer operates in energy-loss mode. Typical overall energy resolution (full width at half maximum FWHM) was 120 meV while the angular resolution of the spectrometer is estimated to be 1.5^o. The position of the zero scattering angle was determined according to the symmetry of angular distribution of scattered electrons at negative and positive scattering angles (from -10^o to +10^o) around the instrumental zero. An atomic oven heated by two resistive bifilar heaters was used to produce well collimated effusive Ag vapor beam. The working temperature was about 1300 K and it was controlled by two thermocouples (top and bottom). Transfer of heat and radiation losses from the oven are minimized and reduced by additional foil shields. Overheating of surrounding components was avoided by additional water-cooling. A liquid-nitrogen cold trap was placed above the oven and interaction region in order to prevent contamination of the chamber. Background pressure was of the order of 10^{-5} Pa.

3. RESULTS AND DISCUSION

We have recorded electron energy-loss spectra of Ag at incident electron energies of 10, 20, 40, 60, 80 and 100 eV and various scattering angles. Figure 1 shows an energy loss spectrum taken for primary electron beam energy of 60 eV and small scattering angle of 6^o. The assignment of atomic energy states is given following Moore (1958). Under these conditions (impact energy, scattering angle) the allowed transitions are somewhat favoured, but other contributions, i.e. other peaks, each characteristic of particular forbidden transitions can also be present in the spectrum. As one can see, this EEL spectrum of silver shows structures which are related to the electron excitation of the first excited states and also covers the autoionization region from the first ionization limit of 7.57623 eV (Sansonetti and Martin 2005) up to 10.5 eV. At the overall energy resolution mentioned above, the spectrum contains well resolved feature that corresponds to the elastic scattering (zero energy-loss). It is also evident that the low energy region of this spectrum is dominated by an intense and sharp excitation at about 3.7 eV. The EEL spectrum is obtained under the conditions where we could not separate $4d^{10}5p\ ^2P_{1/2}$ and $4d^{10}5p\ ^2P_{3/2}$ levels (energy losses of 3.664 and 3.778

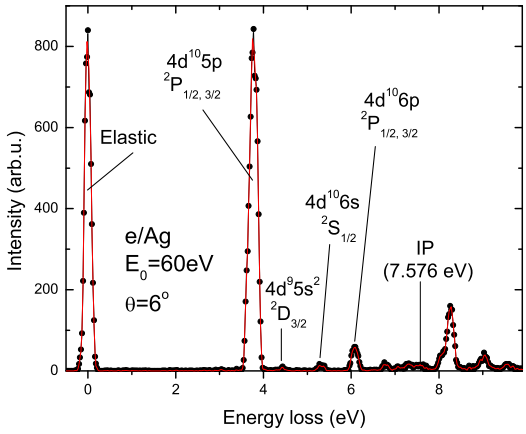

Figure 1: Energy-loss spectra of silver at 60 eV electron impact energy and scattering angle of 6^o.

eV). Energy resolution was not high enough not only to resolve these two states but also to enable their decomposition so we obtained only one feature at about 3.7 eV that corresponds to the summed $4d^{10}5p\ ^2P_{1/2,3/2}$ excitation. On the other side, this structure is clearly resolved from the other ones in the spectrum. Below the first ionization limit, spectrum contains at least three more features. The features at 4.304 and 5.276 eV correspond to the electron excitation of the $4d^95s^2\ ^2D_{3/2}$ and $4d^{10}6s\ ^2S_{1/2}$ states but, as one can see, their intensities are more than 50 times smaller than that of unresolved silver resonant line. The excited state at about 6 eV is labeled as $4d^{10}6p\ ^2P_{1/2,3/2}$. The $4d^{10}6p\ ^2P_{1/2}$ and $4d^{10}6p\ ^2P_{3/2}$ states (energy losses of 5.988 and 6.013 eV) are separated by only 25 meV and overall energy resolution of 120 meV was not sufficient to resolve them. The features in the energy-loss region above first ionization potential (7.57623 eV) correspond to the autoionization processes. In order to experimentally investigate electron impact excitation of silver, we have also recorded autoionizing energy-loss spectra for energies between 10 and 100 eV. As one can see clearly resolved lines that appear in autoionization region of the EEL spectra at 60 eV (Figure 1). As shown in Figure 2, the same energy- loss structures occur at the silver EEL spectrum taken at 40 eV electron impact energy and scattering angle of 10^o, again with the very similar intensity ratios.

4. CONCLUSION

Electron impact excitation from the ground state of silver has been studied with electron energy-loss spectroscopy. We have recorded energy-loss spectra for incident electron energies between 10 and 100 eV at different scattering angles using the electron spectrometer with crossed electron-atom beams. Here we have presented EEL spectra recorded at 60 eV and 6^o, i.e. at 40 eV and 10^o. Both spectra show the same

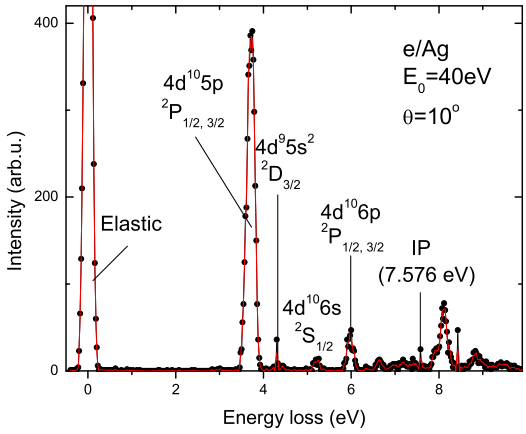

Figure 2: Energy-loss spectra of silver at 40 eV electron impact energy and scattering angle of 10^o.

features with very similar intensity ratios, including the lines in the autoionization region covered by these spectra from the first ionization limit (7.57623 eV) up to 10.5 eV. Currently, detailed analysis of the spectra taken at higher electron impact energies and different scattering angles are underway. The obtained data will give more insight into the electronic structure of Ag atom and give the basis for a further detailed study of the electron-Ag scattering processes.

Acknowledgments

This work has been carried out within project 141011 financed by Ministry of Science of Republic of Serbia.

References

Hebert, C., Schone, W. D., and Su, S. S.: 2006, *Ultramicroscopy*, **106**, 1115.
Leapman, R. D.: 2003, *J. Microsc.*, **210**, 5.
Moore, C. E.: 1958, Atomic Energy Levels, vol III, Natl. Bur. Stand. Circ. 467, Washington DC: US Govt Printing Office.
Salaita, G. N., Hazos, Z. F., and Hoflund, G. B.: 2000, *J. Elect. Spectros. Rel. Phenom.*, **107**, 73.
Sansonetti, J. E., and Martin, W. C.: 2005, *J. Phys. Chem. Ref. Data*, **34**, 2009.
Schone, W. D., Su, S. S., and Ekardt, W.: 2003, *Phys. Rev. B*, **68**, 115102.
Tošić, S. T., Rabasović, M. S., Šević, D., Pejčev V., Filipović, D. M., Sharma Lalita, Tripathi, A. N., Srivastava Rajech, and Marinković, B. P.: 2008, *Phys. Rev. A*, **77**, 012725.

Publ. Astron. Obs. Belgrade No. 84 (2008), 53 - 56 *Contributed Paper*

ELECTRON IMPACT EXCITATION OF YTTERBIUM

B. PREDOJEVIĆ[1,2], D. ŠEVIĆ[1], V. PEJČEV[1,3], D. M. FILIPOVIĆ,[1,4]
and B. P. MARINKOVIĆ[1]

[1] *Institute of Physics, Belgrade, Serbia*
E–mail: bratislav.marinkovic@phy.bg.ac.yu

[2] *Faculty of Natural Sciences, University of Banja Luka, Republic of Serpska, Bosnia and Herzegovina*

[3] *Faculty of Natural Sciences, University of Kragujevac, Radoja Domanovića 12, 34000 Kragujevac, Serbia*

[4] *Faculty of Physics, University of Belgrade, P. O. Box 368, 11001 Belgrade, Serbia*

Abstract. The energy-loss spectra of Ytterbium in energy-loss ranges from 3.30 to 3.75 eV, scattering angles 6^o, 10^o, 20^o at incident electron energies of 20 eV, and from 3.75 to 6.50 eV, scattering angle 0^o at incident electron energies of 40, 60, 80 eV, have been recorded. These spectra are analysed and compared with other available measurements.

1. INTRODUCTION

The Ytterbium is a heavy atom (Z = 70) with a closed-shell, two (6s) valence electron ground state configuration [Kr] $4f^{14}6s^2\ {}^1S_o$. The electronic structure of Ytterbium makes this atom very interesting for investigations of a number electron atom collision processes. The transitions below the first ionization limit can be divided in two classes. The transitions corresponding to the excitation of the 6s-electrons give the simple spectra and transitions due to excitations of one of the $4f^14$ electrons give the complex spectra.

An electron energy-loss spectrum of Ytterbium was initially reported by Kazakov and Hristoforov (1983). The spectrum has been recorded at incident electron energy of $E_o = 14$ eV and scattering angle of 90^o. Mandy et al. (1993) have presented energy-loss spectra and a threshold excitation spectrum. Johnson et al. (1998) presented an electron energy-loss spectrum at incident electron energy $E_o = 40$ eV and scattering angle of 10^o recorded with overall energy resolution of 80 meV. In our previous papers (Predojević et al. 2005a, 2005b) we also presented several energy-loss spectra at impact energies of 20 eV and different scattering angles.

In this contribution we present and analyse the parts of energy-loss spectra of Yb which were not enough considerated in previous articles, mainly because of insufficient energy resolution of spectrometers. In this paper, atomic levels of Yb are identified according to the NIST Atomic Spectra Database (2008).

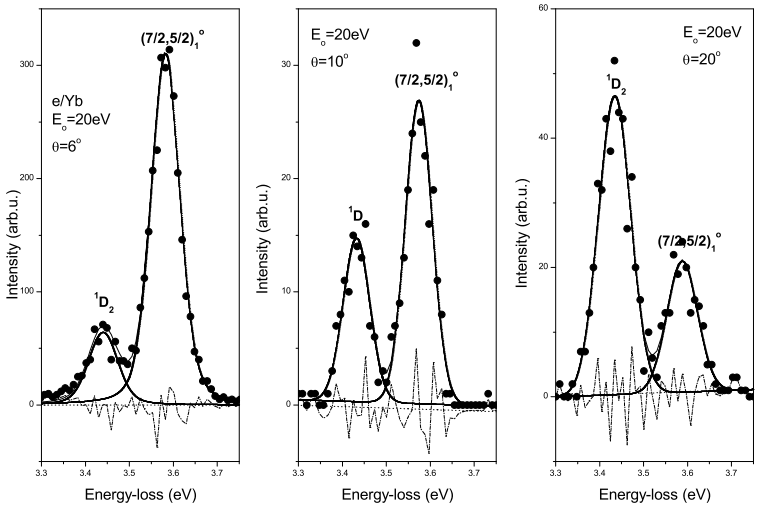

Figure 1: Decomposed energy-loss spectra of Yb at E_o = 20 eV (θ = 6^o, 10^o, 20^o): full circles, raw data; line, synthetic spectrum; dashed line, decomposed states; dots, baseline; dash-dot line, difference between raw data and the synthetic spectrum (residuum).

2. THE EXPERIMENT

The apparatus used for the measurements is a conventional cross-beam electron spectrometer described elsewhere (Predojević et al. 2005a, 2005b), operated in energy-loss mode. Overall system energy resolution (as FWHM) was estimated of 65 meV. The energy scale was calibrated against the structure at 4.03 eV attributed to the 4 ^{3}P excitation threshold in Zn (Predojević et al. 2003). The uncertainty of the scale was estimated to be less than 0.01 eV.

Construction of the vapour source as well as the production and the control of the vapour beam have been described in detail in (Predojević et al. 2005a). The measurements are performed at temperature of 870 K for 99,99% purity Ytterbium. This temperature corresponds to a metal-vapour pressure of about 5.2 Pa, at which ytterbium effused through the cylindrical channel (aspect ratio $\gamma = 0.075$) in the cap of crucible.

3. RESULTS

The spectra of Yb recorded at incident electron energy of 20 eV in the energy- loss range from 3.30 to 3.75 eV and scattering angles 6^o, 10^o and 20^o are shown in Fig 1. As one can see the states $4f^{14}5d6s\ ^1D_2$ and $4f^{13}5d6s^2\ (7/2,\ 1/2)_1$ are resolved with energy resolution of 65 meV.

The states are decomposed and fitted using two Gaussian profiles and synthetic spectra are obtained as sum of these profiles. The values of residuum show that we

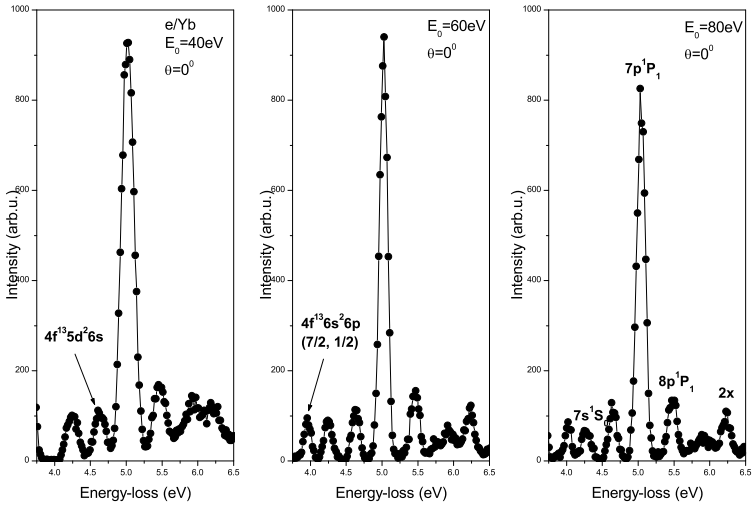

Figure 2: The energy-loss spectra of Yb atom at scattering angle $\theta = 0^o$ and incident electrons energies $E_o = 40$, 60 and 80 eV.

have quite good agreement between the row data and synthetic spectra. Shimon et al. (1981) emphasize that $4f^{14}6s^2\ {}^1S_0 \rightarrow 4f^{13}5d6s^2\ (7/2, 1/2)_1$ transition have third intensity among 36 optical excitation functions determined in their measurements. These states as an unresolved feature are identified in (Johnson et al. 1998) and marked as $^1D_2$, the same designation was used by Kazakov and Hristoforov (1983) for structure at right side of the resonance line (transition $4f^{14}\ 6s^2\ {}^1S_0 \rightarrow 4f^{14}6s6p\ {}^1P_1$). It could be observed that in selected energy-loss range intensity ratio $I(^1D_2)/I((7/2,1/2)_1)$ increases with scattering angle. The differential cross sections for electron impact excitation of the $4f^{14}5d6s\ {}^1D_2$ and $4f^{13}5d6s^2\ (7/2, 1/2)_1$ states at incident electron energies of $E_o = 10$, 20 eV where published in (Predojević et al. 2005b).

The energy-loss spectra at incident electron energies of 40, 60 and 80 eV and scattering angle of 0^o and in energy-loss range from 3.75 to 6.50 eV are presented in Fig 2. At $E_o = 60$ and 80 eV the spectra contain well-resolved feature at 3.980 eV. According with NIST tables this energy belongs to the state with configuration $4f^{13}6s^26p$ (7/2, 1/2); consequently, we have the spectral line from complex part spectra of Yb. At 40^o this state is absent and also has not been identified in previous measurements (Kazakov and Hristoforov 1983).

In all spectra in Fig 2. we find the feature at 4.259 eV.

To this energy, according with NIST tables and previous measurements (Kazakov and Hristoforov 1983), the $4f^{14}6s7s\ {}^1S_0$ state is designated. Similarly to the atoms of the IIb group, the (n+1) $^1S_0$ states have significantly stronger intensities compared to the close (n+1) $^3S_0$ states. Also, in all the spectra appears the spectral line at 4.639 eV. This line corresponds to the $4f^{14}6s^2\ {}^1S_0 \rightarrow 4f^{13}6s^26p$ transition and did not appear in previous energy-loss measurements. If we accept this classification then this state together with the state at 3.980 eV belongs to the complex spectra of Yb. The

state at 5.030 eV is optically allowed transition ($4f^{14}6s^2\ ^1S_0 \rightarrow 4f^{14}6s7p\ ^1P_1$) and this line is strongest in the selected energy- loss range. The differential cross sections for electron impact excitation of the $4f^{14}6s7p\ ^1P_1$ state at incident electron energies of $E_o = 20$, 40 eV where published in our previous paper (Predojević et al. 2005b). The next line at 5.457 eV also belongs to the optically allowed transition ($4f^{14}6s^2\ ^1S_0 \rightarrow 4f^{14}6s8p\ ^1P_1$) and to the simple spectra of Yb. The broad feature in energy-loss range from 5.600 to 6.070 eV consists of many transitions but the energy resolution in our spectrometer was not high enough to resolve these states. In our opinion the feature at 6.20 eV, which exists at all spectra, probably arises due to double scattering of incident electrons after successive excitation of the $4f^{14}6s6p\ ^1P_1$ resonance state at 3.108 eV.

Finally, in energy-loss range from 3.30 to 6.50 eV, we have detected the transitions belonging to both, the simple and complex spectra of Yb. The intensities of lines from these spectra are comparable, as is expected for heavy atoms.

4. CONCLUSION

We presented the preliminary results of decomposed energy-loss spectra of Ytterbium atom. Differential cross sections of higher excited states should be determined experimentaly in near future.

Acknowledgments

This work has been carried out within project 141011 financed by Ministry of Science of Republic of Serbia and bilateral project Serbia Rapublic of Srpska, BH, No. 06/6-020/961-25/05.

References

Johnson, P. V,, Li, Y., Zetner, P. W., Csanak, G., Clark, R. E. and Abdallah, J.: 1998, *J. Phys. B: At. Mol. Opt. Phys.*, **31**, No. 13, 3027.

Kazakov, S. M. and Hristoforov, O. V.: 1983, *Opt. Spektrosk.*, **54**, 750.

Mandy, J. A., Romanyuk, M. I., Papp, F. F. and Shpenik, O. B.: 1993, Proceedengs of the 18th Int. Conf. Physics of Electronic and Atomic Collisions, Eds. Anderson, T., Folkmann, F., and Knudsen, H., Aarhus, Denmark, (Bristol: Hilger) Abstracts p. 167.

NIST: 2008, Atomic Spectra Database of the Physics Laboratory of the National Institute of the Standards and Technology, USA.

Predojević, B., Šević, D., Pejčev V., Marinković, B. P. and Filipović, D. M.: 2003, *J. Phys. B: At. Mol. Opt. Phys.*, **36**, No. 11, 2371.

Predojević, B., Šević, D., Pejčev V., Marinković, B. P. and Filipović, D. M.: 2005a, *J. Phys. B: At. Mol. Opt. Phys.*, **38**, No. 8, 1329.

Predojević, B., Šević, D., Pejčev V., Marinković, B. P. and Filipović, D. M.: 2005b, *J. Phys. B: At. Mol. Opt. Phys.*, **38**, No. 19, 3489.

Shimon, L. L., Golovchak, N. V., Garga, I. I. and Kurta, I. V.: 1981, *Opt. Spektrosk.*, **50**, 1037.

Publ. Astron. Obs. Belgrade No. 84 (2008), 57 - 60 *Contributed Paper*

CROSS SECTIONS FOR SCATTERING OF ELECTRONS ON BF_3

M. RADMILOVIĆ-RADJENOVIĆ[1], H. N. VARAMBHIA[2], M. VRANIĆ[1],
J. TENNYSON[2] and Z. Lj. PETROVIĆ[1]

[1] *Institute of Physics Belgrade, Pregrevica 118, 11080 Zemun, Serbia*
E–mail: marija@phy.bg.ac.yu

[2] *Department of Physics and Astronomy, University College London, London WC1E 6BT, UK*
E–mail: hemal@theory.phys.ucl.ac.uk

Abstract. We calculate cross sections for elastic scattering and electronic excitation of BF_3 molecules by low energy electrons. The R-Matrix code Quantemol-N has been used for calculations. The cross sections indicate the presence of a shape resonance of symmetry B_1 (A_2" in D_{3h}) at around 4.5 eV.

1. INTRODUCTION

Collisions of electrons with atoms and molecules represent the interaction that determines the behaviour of plasmas. Therefore, studying electron scattering has attracted considerable attention over the years (see e.g. Morrison 1983). Boron trifluoride (BF_3) is used in instruments such as neutron counters (Chen and Chung 1997) and in plasma doping (Radovanov 2005). The importance of further optimization of plasma doping sources dictated the need for the present study as measured properties of discharge afterglows and discharge periods require more direct modeling.

This work dealing with BF_3 is focused on computing the total (integrated) electron scattering cross-sections. This data will enable more accurate calculation of the transport coefficients. Whereas to date there has been no theoretical study on this topic, the most recent experimental enquiry was that of Szmytkowski et. al. (2004).

The R-matrix method has already been successfully applied to a number of molecules, including CF_3 (Rozum et al. 2003), NH_3 (Munjal and Baluja 2006) and O_3 (Gupta and Baluja 2005). Here we employ the Quantemol-N system developed at UCL (Tennyson at al. 2007)

2. THE R-MATRIX METHOD

The molecular R-matrix method (Burke and Berrington 1993, Burke and Tennyson 2005) is a variational technique that relies on the partitioning of configuration space into an inner and an outer part. The boundary is a sphere whose center is located at the center of mass of the molecule. The radius is chosen so that the molecular electron cloud is fully contained within the sphere (here $a = 10a_0$). In the inner

region, exchange and electron-electron correlations are considerable. As a result, the collision problem within a finite volume can be treated as a molecular bound state problem, by constructing and diagonalizing a Hamiltonian matrix. To meet the boundary conditions, the Bloch operator (Bloch 1957) is added to the diagonalized inner region Hamiltonian. In the outer (asymptotic) region, exchange and electron-electron correlations are not considered to be important, and one need only account for the long-range multi-polar interactions between the scattering electrons and the target. Hence the problem can be reduced to solving a set coupled second order equations, which is in practice done by propagating the R-matrix and matching to the asymptotic expansion of the solution (Morgan et al. 1998) to obtain the scattering observables.

In the inner region the scattering wavefunction Ψ_k^{N+1} is expressed through a close-coupling (CC) expansion:

$$\Psi_k^{N+1} = A \sum_i \psi_i^N(x_1, x_2, \ldots, x_n) \sum_j \kappa_j(x_{N+1}) a_{ijk} + \sum_l \chi_l(x_1, x_2, \ldots, x_{n+1}) b_{lk} \quad (1)$$

where A is the anti-symmetrization operator and $x_i = r_i\sigma_i$ is the spin-space coordinate of the i-th electron, ψ_k^N is the target wavefunction, κ_j is the j-th continuum orbital spin coupled with the scattering electron and χ_l are square integrable configurations in which all electrons are placed in target molecular orbitals (Varambhia and Tennyson 2007). Gaussian-type orbitals were used to represent the target molecular orbitals.

All these steps are now embedded within a package for general purpose calculations Quantemol-N, which was employed to carry out the calculations presented here.

3. RESULTS

The quantum chemistry and scattering models employed in the present work were automatically generated by the application. The calculations were carried out in the abelian C_{2v} sub-group of D_{3h}, the natural point group at the equilibrium geometry of BF_3 (NIST 2008).

Calculations were performed for BF_3 using Gaussian-type basis sets $6-311G^*$ and DZP. The configuration interaction method was used to construct the molecular (target) ground and electronically-excited state wavefunctions. The complete active space (CAS) involved freezing eight electrons in the $1a_1$, $2a_1$ $3a_1$ and $1b_2$ orbitals in all reference determinants, and allowing the remaining twenty-four electrons to be distributed freely among 4–$9a_1$, $1b_1$, $2b_1$, $3b_1$, 2–$5b_2$, and $1a_2$ molecular orbitals. A number of test calculations were carried out which retained an increasing number of target electronic states (closed channels) in the close-coupling expansion (1): 15, 48 and 56 states in both inner and outer regions. The scattering orbitals used by Quantemol-N were those appropriate for radius a=$10a_0$, where the partial wave expansion was up to and including g-wave. One virtual orbital was allocated to each symmetry where target orbitals were available. In the computation of the scattering observables the R-matrix was propagated to a radial distance of $100.1a_0$.

Quantemol-N generates graphs of cross section (Figure 1) and eigenphase (Figure 2). The calculation predicts the existence of a $^2B_1$ ($^2A_2$") shape resonance. The shape nature of the resonance was confirmed by the fact that it appeared in the basic

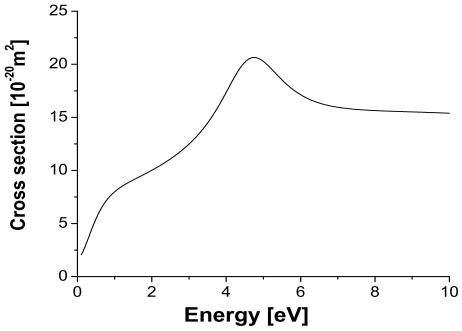

Figure 1: Cross sections for elastic scattering obtained by the 48-state close-coupling calculation for BF_3.

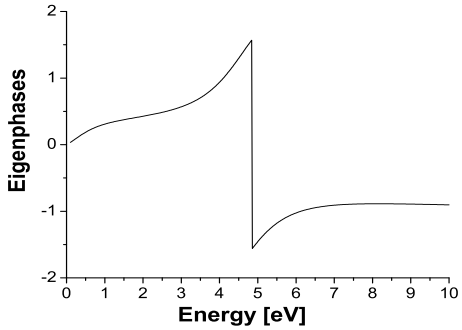

Figure 2: $^2B_1$ ($^2A_2$") eigenphases from the 48-state close-coupling calculation for BF_3.

1-state static exchange (SE) calculation, which is not discussed in the present work. The resonance obtained at above 4.5 eV has been observed experimentally but at a somewhat lower energy: 3.6 eV (Szmytkowski et. al. 2004). The latter of the two figures indicates more accurately the position of this resonance.

Results for the cross section were tested for convergence of the polarisation interaction by retention of more closed channels in expansion (1) and the outer region. Results obtained using 48 and 56 states appear to be almost identical and further changes do not appear to be likely. The parameters of the resonance yielded by these two computations differ considerably from the values obtained using only 15 states, as can be seen from Table 1. This is to be expected as there are markedly fewer closed channels retained.

Table 1: Quantemol-N results for the positions and widths (in eV) of the resonance obtained by using different number of target states.

Resonance Parameter	15 states	48 states	56 states
E_r	5.09	4.56	4.56
Γ_r	1.65	2.17	2.18

Acknowledgements

This work was funded under project 141025 of the Serbian Ministry of Science.

References

Burke, P. G., Berrington K. A.: 1993, Atomic and Molecular Processes (Bristol IOP).
Burke, P. G., Tennyson, J.: 2005, *Molecular Physics*, **103**, No. 18, 2537.
Chen, C. Y., Chung: 1997, *Nucl. Instrum. Methods Phys. Res.*, **40**, 1211.
DeCorpo, J. J., Franklin, J. L.: 1971, *J. Chem. Phys.*, **54**, 1885.
Farber, M., Srivastava, R. D.: 1984, *J. Chem. Phys.*, **81**, 241.
Gupta, M., Baluja, K. L.: 2005, *J. Phys. B: At. Mol. Opt. Phys. A*, **395**, 195.
MacNeil, K. A. G., Thynne, J. C. J.: 1970, *J. Chem. Phys.*, **74**, 2257.
Morgan, L. A., Tennyson, J., Gillan, C. J.: 1998, *Comput. Phys. Commun.*, **114**, 120.
Munjal, H., Baluja, K. L.: 2006, *Phys. Rev. A*, **74**, 032712.
Morrison, M. A.: 1983, *Aust. J. Phys.*, **36**, 239.
NIST: 2008, http://cccbdb.nist.gov/
Radovanov, S., Godet, L., Dorai, R., Fang, Z. Koo, B. W., Cardinaud, C., Cartry, G., Lenoble, D, Grouillet, A.: 2005, *J. Appl. Phys.*, **98**, 13307.
Stockdale, J. A., Nelson, D. R., Davis, F. J., Compton, R. N.: 1972, *J. Chem. Phys.*, **56**, 3336.
Szmytkowski, C., Piotrowicz, M., Domaracka, A., Klosowski, L., Ptasinska-Denga, E., Kasperski, G.: 2004, *J. Chem. Phys.*, **121**, 4.
Tennyson, J., Brown, D. B., Munro J. J., Rozum, I., Varambhia, H. N. and Vinci, N.: 2007, *J. Phys.: Conference Series*, **86**, 012001.
Varambhia, H. N., Tennyson, J.: 2007, *J. Phys. B: At. Mol. Opt. Phys.*, **40**, 1211.

Publ. Astron. Obs. Belgrade No. 84 (2008), 61 - 64 *Contributed Paper*

PHOTODETACHMENT OF 2p SHELL OF THE CHLORINE NEGATIVE ION

V. RADOJEVIĆ[1], J. JOSE[2], G. B. PRADHAN[2], P. C. DESHMUKH[2] and S. T. MANSON[3]

[1] *Institute of Physics, P. O. Box 57, 11001 Belgrade, Serbia*
E–mail: vradoje@phy.bg.ac.yu

[2] *Department of Physics, Indian Institute of Technology - Madras, Chennai 600 036, India*
E–mail: pcd@physics.iitm.ac.in

[3] *Department of Physics and Astronomy, Georgia State University, Atlanta, Georgia 30303, U. S. A.*
E–mail: smanson@gsu.edu

Abstract. The photodetachment cross sections are calculated for intermediate, $2p$ shell of the chlorine negative ion in the relativistic random-phase approximation (RRPA) to account for relativistic effects and many electron correlations, and in modified RRPA (RRPA-R) to additionally account for relaxation of atomic core in the photodetachment process. The results of calculations with and without relaxation effects are compared.

1. INTRODUCTION

There has been relatively recently rapid development in the physics of negative ions, particularly in investigations of many body effects in electron structure and photodetachment process (Ivanov, 1999, 2004, and references therein). One of the approaches that has been rather successful in describing the photoionization process of neutral atoms and positive ions, and that takes into account the many-electron correlations, is the random-phase approximation (RPA) in nonrelativistic form (usually refered to as RPAE) (Amusia and Cherepkov, 1975, Wendin, 1976) and and its relativistic version (RRPA) (Johnson and Lin, 1979, Johnson et al. 1980). The RRPA has been applied to photodetachment of negative halogen ions (Radojević et al. 1987) and the agreement with a limited amount of experimental data available has been quite reasonable.

However, the RPA (whether it is RPAE or RRPA) does not include the effects of a relaxation of remaining atomic core in the photoionization process. It has been demonstrated that by applying modified RPAE to include relaxation effects (GRPAE) (Amusia et al. 1976) as well as modified RRPA (RRPA-R) (Radojević et al. 1989) that these effects are significant for some inner shells of neutral atoms and mostly in an energy region close to the ionization threshold of the considered shell. The RRPA-R has been also applied to photodetachment of outer shells of I^- (Z=53) (Radojević, 1992), Br^- (Z=35) (Altun and Radojević, 1992), F^- (Z=9) and Br^- (Z=35) (Robertson, et al. 2000), and Cl^- (Z=17) (Kutzner et al. 2000).

There were until recently few calculations of the inner-shell photodetachment from negative ions (Ivanov 2004), and the applications of the RRPA and RRPA-R were mostly done for photodetachment of valence shells. In a few applications of RRPA and RRPA-R to photodetachment of valence shells of negative ions, some intermediate shells were treated, like I^- 4d (Radojević and Kelly, 1992) and Br^- 3d (Altun and Radojević, 1992).

In the present study the RRPA and RRPA-R are applied to the photodetachment of the inner $2p$ shell of Cl^-. Unfortunately, there are no experimental data known to us for the processes treated in the present work, with which we could compare our results.

2. METHODS AND CALCULATIONS

Dipole excitations from the $3p$, $3s$, $2p$, and $2s$ shells have been included in our calculations, thereby producing 14 jj-coupled channels. The channels arising from the excitations of the innermost $1s$ shell have been omitted (truncated RRPA) as there is very small interaction (coupling) of this shells with those included. We performed some calculations with inclusion of the channels arising from excitation of the $1s$ shell, and the results are practically the same as without its inclusion.

The relaxation effects were included in RRPA-R by performing the RRPA-type calculations and computing the excited-state orbitals in the field of self-consistently calculated orbitals for relaxed neutral atom (V^{N-1} potential), i.e. the neutral atom with the hole in the shell which is the origin of a given channel.

In our study of the photodetachment of the $2p$ shell the hole state of the relaxed atom may be placed either in the $np_{3/2}$ or in $np_{1/2}$ subshell. We have chosen to place it in the $np_{3/2}$ subshell since it has a lower ionization energy and has the greater degeneracy. It was found in some earlier calculations (Radojević et al. 1989, Kutzner et al. 1989) that the results depend weakly on which subshell is chosen.

Overlaps between orbitals of the relaxed atom and those of the ground state of negative ion multiply the dipole matrix elements (Radojević et al. 1989) in the RRPA-R calculations and this leads to the reduction in the np cross section by approximately 20% for. The theoretical values of the channel thresholds in the strict RRPA are the absolute values of the Dirac-Hartree-Fock eigenvalues. In the relaxed-core calculations, the differences between the total energies calculated self-consistently for the relaxed neutral atom with a hole in a considered subshell and the ground state of the negative ion (ΔE_{SCF} values) are used for the thresholds. The relevant calculated threshold energies are presented in Table 1.

Table 1: The photodetachment thresholds of Cl^- in a.u. used in present work. Presented are Dirac-Hartree-Fock values (DHF) used in RRPA and ΔE_{SCF} values used in RRPA-R calculations.

Subshell	DHF	ΔE_{SCF}
$3p_{3/2}$	0.1480	0.0927
$3p_{1/2}$	0.1532	0.0969
$3s_{1/2}$	0.7398	0.6660
$2p_{3/2}$	7.6762	7.2214
$2p_{1/2}$	7.7410	7.2832
$2s_{1/2}$	10.2981	9.8776

The threshold energies, as well as all the orbitals used in present work were calculated using the Oxford multiconfiguration Dirac-Fock package by Grant et al. (1980). These orbitals and energies could be calculated using any other, even single configuration Dirac-Fock code, and interfacing the RRPA-R code appropriately.

3. RESULTS

The results of our RRPA and RRPA-R calculations for partial cross sections are shown in Fig. 1. The length and velocity form results in our (truncated) RRPA practically coincide in our calculations. All calculated partial cross sections vanish (or seems to vanish) at the corresponding threshold, satisfying (or showing the tendency) to satisfy the Wigner threshold law for negative ions (Wigner 1948), according to which the cross section vanish at the corresponding threshold. Let us note that the RRPA and RRPA-R codes cannot run at the very threshold. Each partial cross section increases with increase of the photon energy in the very vicinity of its threshold, then reaches a maximum relatively close to the threshold, and at higher energies decreases monotonically. One notices a big difference between both types of calculations (RRPA and RRPA-R) in the region of energies around the corresponding maximum of the cross section and in the vicinity of the threshold. This difference cannot be completely ascribed to the reduction of transition matrix elements when relaxation of atomic core is taken into account in the RRPA-R calculations.

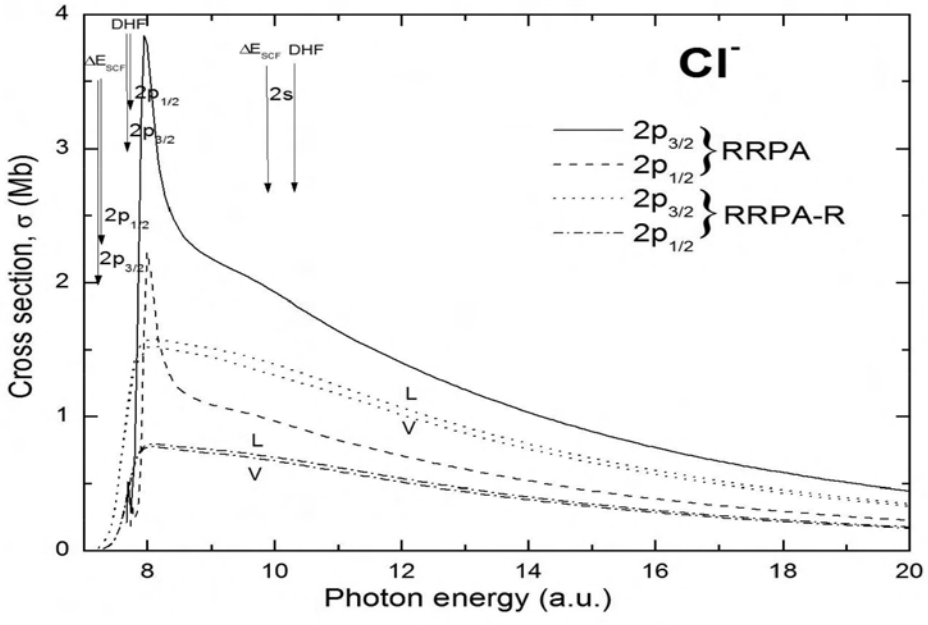

Figure 1: Photodetachment partial cross sections of Cl^- 2p shell in RRPA and RRPA-R.

4. CONCLUDING REMARKS

In our present calculations, relativistic effects and significant interchannel correlations are included. Furthermore, in the RRPA-R calculations are included the effects of relaxation of the atomic core in the photodetachment process. Through the inclusion of the overlaps, transfers of the oscillator strengths from the main channels to doubly excited channels are approximately accounted (Kutzner et al 1989). However, it is assumed in our approach with the RRPA-R that the atomic core is fully relaxed during the photodetachment process, although relaxation is in general less than complete, and the degree of relaxation changes during the process. Perhaps the incomplete relaxation is responsible for the big difference between the RRPA and RRPA-R results, although all the reasons for this difference are not clear. It is already found in photoionization calculations that the RPA results close to the channel threshold are notably larger than the results with the relaxation effects included (Amusia et al. 1976, Radojević et al. 1989). Experimental data are extremely desirable to determine whether for the negative ions the results with relaxation effects included agree better than the results without, as has been found to be the case for photoionization of atoms (Amusia et al. 1976, Radojević et al. 1989).

Acknowledgments

This work was supported by a research grant from the Department of Science and Technology, Government of India. One of the authors (V.R.) wishes to acknowledge the hospitality extended by the Department of Physics at the Indian Institute of Technology -Madras, where the present work was carried out, and to the partial support of the Ministry of Science of the Republic of Serbia through the project No. 141029.

References

Altun, Z., Radojević, V.: 1992, *J. Phys B: At. Mol. Opt. Phys.*, **25**, 3757.
Amusia, M. Ya., Cherepkov, N. A.: 1975, *Case Stud. At. Phys.*, **5**, 47.
Amusia, M. Ya., Ivanov, V. K., Chernysheva, L. V.: 1976, *Phys. Let.*, **59A**, 191.
Grant, I. P., McKenzie, B. J., Norrington, P. H., Meyers, D. F., Pyper, N. C.: 1980, *Comput. Phys. Commun.*, **21**, 207.
Ivanov, V. K.: 1999, *J. Phys B: At. Mol. Opt. Phys.*, **32**, R6 7.
Ivanov, V. K.: 2004, *Rad. Phys. Chem.*, **70**, 345.
Johnson, W. R., Lin, C. D.: 1979, *Phys. Rev. A*, **20**, 964.
Johnson, W. R., Lin, C. D., Cheng, K. T., Lee., C. M.: 1980, *Phys. Scr.*, **21**, 409.
Kutzner, M., Radojević, V., Kelly, H. P.: 1989, *Phys. Rev. A*, **40**, 5052.
Kutzner, M., Robertson, J. A., Pelley, P.: 2000, *Phys. Rev. A*, **62**, 062717.
Radojević, V., Kelly, H. P., Johnson, W. R.: 1987, *Phys. Rev. A*, **35**, 2117.
Radojević, V., Kutzner, M., Kelly, H. P.: 1989, *Phys. Rev. A*, **40**, 727.
Radojević, V., Kelly, H. P.: 1992, *Phys. Rev. A*, **46**, 662.
Robertson, J. A., Kutzner, M., Pelley, P.: 2000, *Phys. Rev. A*, **63**, 042715.
Wendin, G.: 1976, In: Photoionization and Other Probes of Many-Electron Interactions, ed. F. J. Wuilleumier, p. 61, New York: Plenum.
Wigner, E. P.: 1948, *Phys. Rev.*, **73**, 1002.

Publ. Astron. Obs. Belgrade No. 84 (2008), 65 - 68 *Contributed Paper*

LOW ENERGY ELASTIC SCATTERING OF ELECTRON ON THE NEGATIVE IONS

A. R. TANČIĆ[1] and M. NIKOLIĆ[2]

[1] *VINČA Institute for Nuclear Sciences, P.O.Box 522, 11001 Beograd, Serbia*
E–mail: atancic@rt270.vin.bg.ac.yu.

[2] *The Faculty of natural Sciences and Mathematics, P.P.Box xxxx, 18000 Niš, Serbia*
E–mail: mnikolic@pmf.ni.ac.yu.

Abstract. In the framework of the many body theory we presented the method and results of calculations of the electron scattering on the negative ions. As an example we calculated the differential and total cross sections of the low energy elastic scattering of electrons on the negative ion Li^-.

1. INTRODUCTION

There have been a great interest for investigating photo absorption processes by negative ion lately (Buckman and Clark 1994, Ivanov 2004). This is connected with a great role of many electrons correlations and also with the appearance of lot of new characteristics related to the same processes with neutral atom. Electron scattering processes are less studied than processes of photodetachment. Scattering processes are interesting above all because of different polarization effects.

Regardless to Coulomb repulsion between the incident electron and ion, ion polarization influence special phase and cross section behaviour.

In this paper we have investigated elastic scattering electron on negative ions. The elastic electron scattering on Li^- is calculated here as an example. We used many-body theory method. The polarization effect is calculated t by solving Dyson equation (Amusia and Chernisheva 1997) and using improved random phase approximation which is developed in our early papers (Tančić et al. 1989). Because Li^- ion has closed shell and spherical symmetry the calculation is very simplified. In the paper, we used atomic system units.

2. THEORY

In the framework of the one particle model, the ground state wave functions are calculated in Hartree-Fock (HF) approximation. In this way we have taken into account only a part of many-electron correlations. In this calculation the HF approximation is initial approximation for developing different many-electron calculation. Total cross section for elastic scattering of electron with energy E and momentum $k = \sqrt{E}$ is

(Mott and Massey 1965)

$$\sigma(E) = \frac{\pi}{k^2} \sum_{\ell=0}^{\infty} (2\ell + 1) \left| 1 - \exp(2i\delta_\ell(k)) \right|^2, \tag{1}$$

where $\delta_\ell(k)$ is scattering phase of ℓ partial wave. The phase is determined by asymptotic form of scattered particle wave function (Drukarev G.F.: 1978)

$$\Psi_k(\vec{r}) = \frac{i}{2kr} \sum_i (2\ell + 1) P_\ell(\cos\theta) \left[(-1)^\ell \exp(-ikr) - \exp(2i\delta_\ell(k) + ikr) \right] \tag{2}$$

There are two ways to calculate the scattering phase: 1. by solving HF equations for incident electron in the negative ion frozen core field, 2. by solving the integral equation which takes into account the core potential. The scattering phase is defined by the standard expression:

$$\delta_\ell = \arcsin \left(-\sqrt{\pi/k} \int_0^\infty J_\ell(kr) V(r) P_{N+1}(r) dr \right). \tag{3}$$

$J_\ell(kr)$ is the Bessel function, $V(r)$ scattering potential and $P_j(r)$ $j \in [1, S]$ (S is the number of the subshell in the ground ion state) is the radial function.

The polarization of core by incident electron is neglect in the HF approximation. The negative ion has a big polarisability because the external electrons are weakly bounded. The dynamic polarisability has calculated by Dyson equation method. The Dyson equation for the reducible self energy part $\tilde{\Sigma}$ of the one particle Green function has the form (Tančić and Nikolić 2002)

$$\left\langle E_1\ell | \tilde{\Sigma}(E) | E_2\ell \right\rangle = \langle E_1\ell | \Sigma(E) | E_2\ell \rangle + vp \int \langle E_2\ell | \Sigma(E) | E'\ell \rangle \left\langle E'\ell | \tilde{\Sigma}(E) | E_2\ell \right\rangle \frac{dE'}{E - E'}, \tag{4}$$

where $|E\ell\rangle$ are one electron wave functions. The $\langle\, |\Sigma(E)|\, \rangle$ is the irreducible self energy part of the Green function and may be derived in the form (Amusia et al. 1976):

$$\Sigma(E) = \Sigma^{HF}(E) + \Sigma^{cor}(E). \tag{5}$$

The matrix element $\Sigma^{cor}(E)$ in the lowest order on the perturbation theory (PT) of the Coulomb interaction is described by the diagrams of the second order (the first order of the PT is taken into account in the HF approximation). We have taken into account some important third order diagrams, too (improved version of the RPA method). The correction to the HF phase is defined by the expression:

$$\Delta\delta_\ell(E) = \arctan\left(-\pi \left\langle E\ell | \tilde{E}(E)\ell \right\rangle \right) \tag{6}$$

In the calculation of the phase correction (6) we used modified computer program (Amusia and Chernisheva 1997, Amusia et al. 1976). First the wave function for NI lithium ion ground state in HF approximation is calculated. Wave function and scattering phases of incident electron are determined in frozen field HF lithium negative ion. This function is used for the calculation of the matrix elements $\Sigma^{cor}(E)$ with $\Delta\ell = 0, 1, 2$. The scattering phases are determined by solving integral equation (4).

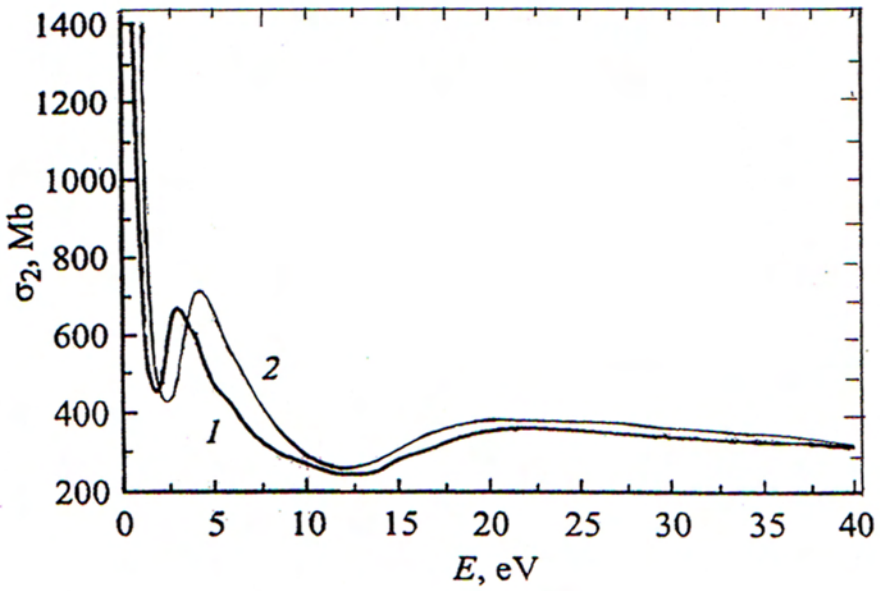

Figure 1: The total cross section of the electron elastic scattering on the litium negative ion. 1- Semennikhina V. Ivanov V.K., Lapkin C.V. 2004, 2- our improved calculations.

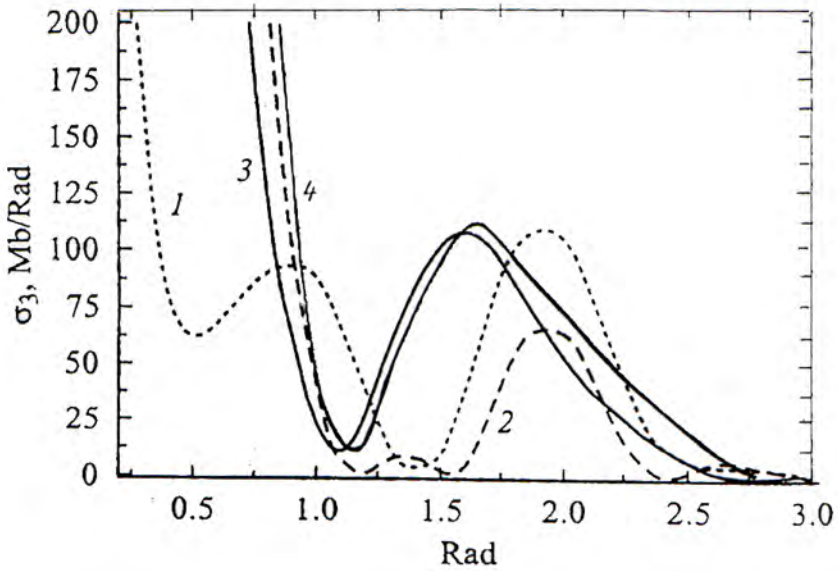

Figure 2: The differential cross section of the electron elastic scattering on the lithium negative ion at the electron energies: E=5 eV (1), E=15.5 eV (2), E=36 eV (3) Semennikhina et al. 2004. Our result (4) correspond to E=36 eV.

3. RESULTS AND CONCLUSIONS

Comparing the calculations of partial wave scattering phase on the repulsion Coulomb potential (CP) with HF calculations we can see: -Partial wave scattering phase on the CP is a smooth curve as function of incident electron energy. However, HF calculations of p and d partial waves show rough character of scattering phase. Leap appeared in p and d phase in order $\pi/4$ and $\pi/6$ respectively. This behaviour results from electron waves diffractions on space structure of negative ion.

The accounts achieved by Dyson equation method show that polarization potential changes essentially the behaviour of partial scattering phase: the leap in p-phase is now increased to $\pi/2$ order, while for d-phase that leaps is $\pi/3$ order when energy is $\approx 13.6eV$, and it practically cames only from many electron correlations. The influence of polarization potential decreases quickly with increasing of ℓ.

The behaviour of d phase is especially important because of many electron effects with energy $\approx 2.8eV$, interference minimum appears (when $\delta_d = \pi$, Fig. 1.).

As a conclusion we may notice that very interesting effects of electron scattering on negative ion are got and proved. The appearance of diffraction in electron scattering on negative ion leads to important changes in the scattering processes characteristics. The results show that it is very important to take into account the many body electron correlations. This account my be used on the other negative ions and negative charge clusters.

References

Amusia, M. Ya., Chernisheva, L.: 1997, Computation of Atomic Processes, London: IOP Publiching.

Amusia, M. Ya., Cherpkov, N. A., Shapiro, S., Tančić, A. R.: 1976, *Sov. Phys. JETP*, **41**, 185.

Buckman, S., Clark, C. W.: 1994, *Rev. Mod. Phys.*, **66**, 539.

Drukarev, G. F.: 1978, Stolkovenie elektronov s atomami i molekulami, Moskva, Nauka.

Ivanov, V. K.: 2004, *Rad. Phys. and Chem.*, **70**, 345.

Mott, N. F., Massey, H. S. W.: 1965, The Theory of Atomic Collisions, Oxford.

Semennikhina, V., Ivanov, V. K., Lapkin, C.V.: 2004, *Proc. PSIE*, **5400**, 46.

Tančić, A. R., Amusia, M. Ya., Cherepkov, N. A., Nikolić, M.: 1989, *Phys. Lett. A*, **140**, 503.

Tančić, A. R. and Nikolić, M,: 2002, *Facta universitatis: Series Physics, Chemistry and Thecnology*, **2**, 185.

Publ. Astron. Obs. Belgrade No. 84 (2008), 69 - 74 *Contributed Paper*

IONIZATION AND DISSOCIATIVE IONIZATION OF GLYCERIN MOLECULES BY ELECTRON IMPACT NEAR THRESHOLD

A. N. ZAVILOPULO, O. B. SHPENIK, L. G. ROMANOVA

Institute of Electron Physics, Ukr. Nat. Acad. Sci.,
21 Universitetska str., Uzhgorod 88017, Ukraine
E–mail: an@zvl.iep.uzhgorod.ua

Abstract. Method of measurement of functions of dissociative ionization of glycerin molecules is described, their relative cross-sections being obtained. The experiment was carried out by the method of crossing electron and molecular beams using a setup with a monopole mass spectrometer. A secondary electron multiplier was used for ion detection. The glycerin molecule mass spectrum is presented as well as the energy dependences of disociative ionization cross-sections in the range $5 - 40\ eV$, from which the fragment ion appearance thresholds are determined.

1. INTRODUCTION

Here we present the results of experimental studies of dissociative ionization of glycerin (1,2,3-trihyroxypropane, $C_3H_8O_3$) molecule by electron impact in the near-threshold energy range. Along with methanol, ethanol, methyl and ethyl esters of fatty acids as well as terpenoids, glycerin is treated as a potential fuel to replace the oil product fuel. Glycerin is the simplest representative of triatomic alcohols. Due to the presence of three OH groups in the molecule, it gives threerows of derivatives. Note that the mono- and di-derivatives can exist in the form of two structural isomers and the derivatives of $CH_2XCHOHCH_2OH$ or $CH_2XCHXCH_2OH$-type – in the form of optical isomers. Ionization of molecules by electron impact plays an important role in the processes in low-temperature plasma, especially in non-equilibrium gas discharge plasma. The products of dissociative ionization of multiatomic molecules can be various atomic and molecular ions being contained in the initial molecule:

$$e + \mathrm{XYZ} \Longrightarrow (\mathrm{XY})^+ + \mathrm{Z} + 2e \quad \text{or} \quad e + \mathrm{XYZ} \Longrightarrow \mathrm{X} + (\mathrm{YZ})^+ + 2e. \quad (1)$$

As a rule, at a collision of an electron with a molecule, an unstable molecular ion is formed which subsequently decays into more simple fragments, fragment ions, neutral residue. Therefore, dissociative ionization of multiatomic molecules can proceed in different channels, producing different dissociation products: fragment ions and neutral atoms or molecules.

A number of papers has been devoted to theoretical and experimental studies of ionization of complex organic compounds by electron impact; however, they are

mainly concentrated on the determination of ionization potentials (IPs) of the parent molecule and appearance potentials (APs) of fragment ions being formed due to the dissociative ionization. Allam et al. (1982) have analyzed the initial sections of the ionization curves of some molecules in order to use them to determine the APs of fragment ions. As regarding investigation and analysis of the threshold behaviour of the fragment ions being formed as a result of the dissociative ionization, there are much less data available and there a practically no data for alcohol molecules. The most efficient method of studies of ionization, including dissociative ionization, is mass spectrometry, enabling both the information on the mass spectrum of the molecule under investigation to be obtained and the relative contribution of each of the dissociated fragments into the formation of ions to be evaluated at the same experimental conditions.

2. EXPERIMENT

The experiment was carried out using a setup with a monopole mass spectrometer, the method of crossing electron and molecular beams being employed (Zavilopulo et al. 2002). The molecular beam was formed by evaporating the investigated substance from a liquid state using an effusive multichannel source of neutral particles. The concentration o molecules in the area of interaction with the electron beam was not lower than $10^{11} - 10^{12}\ cm^{-3}$ at the residual gas pressure in the setup of $\sim 10^{-6}\ Torr$. In order to avoid condensation of the substance under investigation on the vacuum chamber walls and the mass spectrometer electrodes, the mass analyzer chamber was heated to the temperature $\sim 150 - 200^{o}C$. Molecules become ionized in an ion source with electron bombardment. This source enables the electron beams of controlled energy to be obtained in the electron current stabilization mode at the current values $0.5 - 1.5\ mA$ at the energy spread not worse than $\triangle E = 500\ meV$ (full width at half maximum). The ions, extracted from the source, are focused into a beam, move to the analyzer (mass filter) electrode area, separated according to their mass and detected by a secondary electron multiplier or an ion collector in the form of a Faraday cup. The mass scale was calibrated using the mass lines of N_2, Ar, and Kr.

3. DISCUSSION

Aliphatic polyols are easily decomposed, the decomposition being accompanied by dehydratation and dehydration. A specific feature of their mass spectra is a low intensity of the molecular ion peak or its total absence. The most common trend of fragmentation is simple breakdown of hydrocarbon skeleton bonds with the formation of oxonium type ions as well as dehydratation of the molecular and fragment ions. Formation of oxonium ions at the fragmentation of aliphatic alcohols can be a result of charge localization on the oxygen atom and β-decay of the molecular ion (with respect to the heteroatom). Processes of formation of water and oxonium cations are competitive, in this case not only the molecular ion, but also the hydroxyl-containing ions being subject to dehydratation (Zenkevich et al. 1986).

In the glycerin molecule mass spectrum, experimentally obtained at the ionizing electron energy 70 eV (Fig.1), there is no molecular ion at all. The high specific fragmentation depth of the initial molecule is confirmed by the formation of fragments with small masses, and low selectivity of the spectrum shows the absence of predomi-

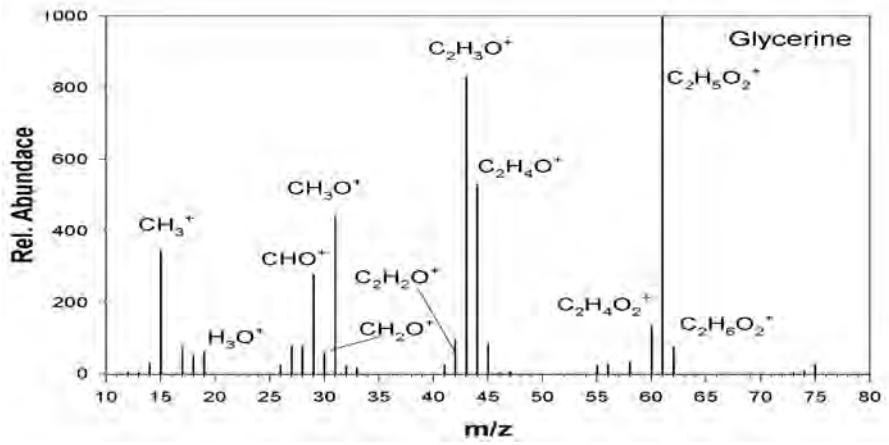

Figure 1: Glycerin molecule mass spectrum ($E = 70\ eV$).

nant trends of decomposition of the molecular ion. The most intense peaks correspond to the peaks of the oxonium ion $[HOCH_2CH{=}OH]^+$ with $m/z = 61$, $[H_2C{=}C{=}OH]^+$ ($m/z = 43$), $[H_2CCH{=}OH]^+$ ($m/z = 44$), and $[H_2C{=}OH]^+$ ($m/z = 31$) as well as to the products of secondary fragmentation of $[CO]^+$ and $[CH_3]^+$ fragment ions. High hygroscopicity of glycerin and the presence of three OH groups in a molecule result in the formation of considerable amounts of molecular water and hydroxonium ions ($m/z = 18$ and 19). The maximal intensity in the mass spectrum corresponds to the $[C_2H_5O_2]^+$ ion with $m/z = 61$ which is complementary to the $[CH_3O]^+$ ion ($m/z = 31$). This pair of ions is formed at a simple breakdown of the C–C bond of the glycerin molecule, the charge being localized mostly at a fragment with larger molecular mass. The low probability of fragmentation processes, in which the single-charged molecular ion is decomposed into a light uncharged ion and a heavy charged ion according to Afrosimov et al. (2006), is explained by the fact these processes having higher ionization threshold energy than the processes with the formation of a light charged fragment and a light neutral fragment.

Having tuned the spectrometer for transmission of ions of a certain mass, we have measured the energy dependences of cross-section of dissociative ionization of fragments in the energy range $5 - 40\ eV$, a special attention being given to the initial parts of the ionization curve. Energy scale calibration was performed by measuring well known threshold parts of ionization functions for nitrogen molecule and krypton atoms (Zavilopulo at al. 2002). The calibration procedure was repeated at each measurement cycle, thus providing energy scale determination accuracy comparable with the half-width of the energy spread for the electrons within the beam.

As known from Cherny at al. (1995), determination of the ionization energy for organic molecules is a complicated problem. Among the two known methods, photoionization (PI) and electron-impact ionization (EI), the second one is more universal and can be applied for a wide class of atoms and molecules. Besides, the PI methods has essential restrictions regarding the studies of dissociative ionization process. The EI method is based on the determination of a point in the energy dependence of the

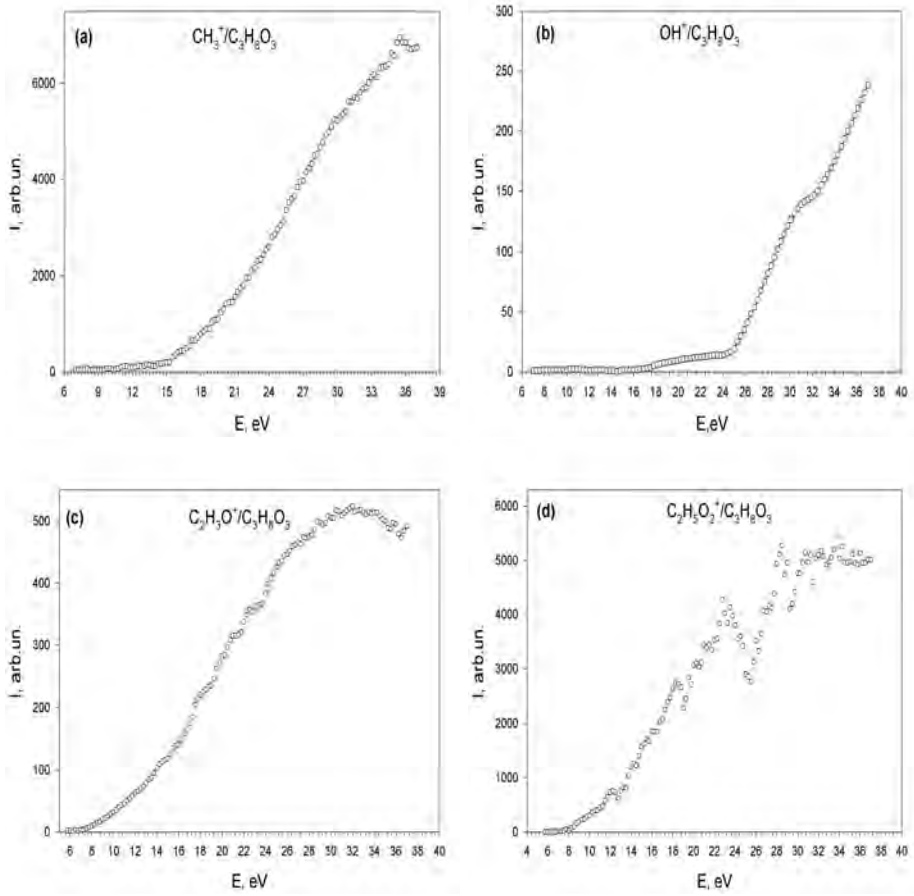

Figure 2: Energy dependenes of relative cross-sections of dissociative ionization of some child ions of the glycerin molecue.

ionization cross-section, starting from which the cross-section becomes non-zero. The accuracy of determination of this energy is affected by three main factors:

- ionization cross-section rate versus bombarding electron energy;
- electron monoenergetic beam;
- accuracy of electron energy scale calibration.

Thus, a certain procedure should be applied to the measured energy dependence of the cross-section of dissociative ionization of a fragment, minimizing the effect of these factors. One of the most well known is the procedure of double differentiation of the initial parts of ionization functions using the Lossing method with digital filtration and fitting of the obtained curve according to the Breit-Wigner formula. The most exact and widely applied is a least-square method of fitting of the initial part of the ionization curve using the Marquardt-Levenberg algorithm proposed by Fiegele et al. (2000).

Table 1: Appearance potentials of ion fragments at the dissociative ionization of glycerin molecules

fragment ions	m/z	E_{ap} (eV)
CH_3^+	15	15.31 ∓ 0.25
OH^+	17	18.12 ∓ 0.25
H_3O^+	19	12.12 ∓ 0.25
CO^+	28	10.89 ∓ 0.25
CHO^+	29	12.20 ∓ 0.25
CH_3O^+	31	12.37 ∓ 0.25
$C_2H_2O^+$	42	7.80 ∓ 0.25
$C_2H_3O^+$	43	7.23 ∓ 0.25
$C_2H_4O^+$	44	7.60 ∓ 0.25
$C_2H_4O_2^+$	60	8.10 ∓ 0.25
$C_2H_5O_2^+$	61	7.43 ∓ 0.25
$C_2H_6O_2^+$	62	7.27 ∓ 0.25

Energy dependences of relative cross-sections of dissociative ionization of some child ions of the glycerin molecule in the energy range $5 - 40$ eV are shown in Fig. 2. These dependences were used to determine the appearance potentials (E_{ap}) for practically all fragment ions using the method proposed by Fiegele et al. (2000) (See Table 1). One should pay attention to the low values of appearance thresholds for dissociative ionization fragments $[C_2H_3O]^+$ and $[C_2H_5O_2]^+$. Evidently, the formation of the fragment ion with $m/z = 43$ occurs at the elimination of a water molecule from the $[C_2H_5O_2]^+$ ($m/z = 61$) ion. Such low values of the appearance potentials for these fragments are explained by a change of geometry and interatomic distances in an ionized molecule in comparison with a neutral one, resulting in an essential decrease of the C–C binding energy in the ionized molecules (Afrosimov et al. 2006, Johnstone 1972). Note that the behaviour of relative ionization cross-sections in the energy range $5 - 40$ eV for these fragment ions is different (Fig. 2c, d): while for the $[C_2H_3O]^+$ fragment ion a gradual growth is observed with a smooth maximum at $E_i = 32$ eV, for $[C_2H_5O_2]^+$ several distinct maxima at $E_i = 12, 18, 24, 28$, and 32 eV are revealed.

The energy dependence of the relative cross-section of dissociative ionization of the $[OH]^+$ ion (Fig.2,b) is stepwise, the threshold value E_{ap} for this ion corresponding to the appearance threshold for the $[OH]^+$ ion at dissociative ionization of water molecule. A sharp increase of yield of this ion at 24 and 32 eV, probably, corresponds to stage-like splitting this ion off the products of primary dissociative ionization of the glycerin molecule. The appearance potential of the $[CH_3]^+$ ion also testifies for the formation of this fragment as a result of secondary dissociation, accompanied by migration of a proton. For the energy dependence of this fragment ion yield an almost linear growth is observed from the appearance potential to 36 eV (Fig. 2, a).

Thus, we present the first data regarding the appearance thresholds for fragments of dissociative ionization of the glycerin molecule. Splitting the electron off the neutral $C_2H_5O_3$ molecule at the ionization results in an essential relaxation of interatomic

bonds in the hydrocarbon skeleton which affects the threshold parts of the energy dependences and the absolute values of appearance potentials of the fragment ions measured.

References

Afrosimov, V.V, Basalaev, A. A., Berezovskaya, E. A., Panov, M. N., Smirnov, O. V., Tulub, A. V.: 2006, *Technical Physics*, **51**, 1553.

Allam, S.,. Migahed,M., -Khodary, A.: 1982, *Egypt. J. Phys.*, **13**, 167.

Cherny, G., Losev, S.: 1995, Physical and Chemical Processes in Gas Mechanics, Moscow University.

Fiegele, T., Hanel, G., Torres, I., Lezius, M. and Mark, T.: 2000, *J. Phys. B*, **33**, 4263.

Jonstone, R.: 1992, Mass-spectrometry for organic chemists, Cambridge University Press.

Zavilopulo, A.,. Snegursky, A.: 2002, *Techn. Phys. Lett.*, **28**, 913.

Zenkevich, I., Ioffe, B.: 1986, Interpretation of mass spectra of organic compounds, Khimiya, Leningrad (in Russian).

Publ. Astron. Obs. Belgrade No. 84 (2008), 75 - 78 *Contributed Paper*

EXCITATION CROSS SECTIONS AND POLARIZATION OF EMISSION IN Ar-Ar COLLISIONS

S. Yu. KURSKOV[1] and A. S. KASHUBA[2]

Department of Physics and Engineering, Petrozavodsk State University, Lenin 33, 185910 Petrozavodsk, Russia

E–mail: [1]*kurskov@psu.karelia.ru*

E–mail: [2]*alekscomp@onego.ru*

Abstract. The present work is devoted to study of $Ar(3p^5 4p)$ states excitation in binary low-energy Ar–Ar collisions. The results of the experimental investigation of excitation cross sections of Ar I $4p'[1/2]_1$, $4p'[3/2]_1$, $4p'[3/2]_2$ and $4p[3/2]_2$ levels in the collision energy range from threshold up to 500 eV (centre of mass system) and degree of polarization for $4s[3/2]_2^0 - 4p'[1/2]_1$ and $4s[3/2]_2^0 - 4p[3/2]_2$ transitions in this energy range are represented.

1. INTRODUCTION

The importance of the study of non-elastic collisions of argon atoms was conditioned by their significant role in different scientific and technical applications. Among the numerous research aspects of non-elastic collision of neutral particles the determining of quantitative scattering characteristics in the conditions of a beam experiment plays considerable role. The low collision energy range is a special interest since the theoretical treatment of non-elastic processes at such energies is rather complicated and, therefore, the quantitative data as well as the information on mechanisms of population of atomic levels can be obtained in an experiment mainly (see e.g. Breno et al. 1975, Kempter et al. 1976). The development of plasma physics, plasma chemistry, and astrophysics requires clarification of the idea of lowenergy atoms interactions, that is a significant interest of quantum theory of scattering.

The purpose of this work is the research of mechanisms of $Ar(3p^5 4p)$ atomic levels excitation at collision energies that corresponds of the adiabatic approximation conditions.

2. SETUP AND MEASUREMENT PROCEDURE

The measurements of the cross sections at interaction of an atomic beam with a gas target were carried out by optical methods on setup, controlled by computer. Experimental setup outline is shown on figure 1.

The neutral atoms beam was produced by means of charge exchange of Ar ions in own gas in an extending electrode channels of ion source. The density of the atom

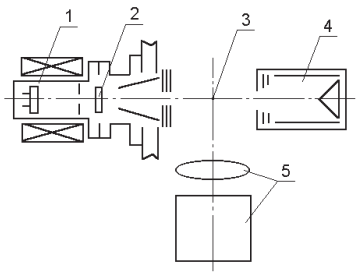

Figure 1: Experimental setup: 1 – ion source; 2 – multi-channel charge exchange cell; 3 – gas target; 4 – detector of fast atoms; 5 – optical recording system.

beam was defined by secondary electron emission from the detector surface. The dependence of the secondary emission coefficient from the energy of atoms was measured. The flux density of fast atoms in the collision chamber reached 10^{16} particle/(m^{2}s). The angular divergence of the neutral beam did not exceed 3×10^{-4} sr.

The target gas pressure in the collision chamber was equal to 4.5×10^{-1} Pa, the residual gas pressure did not exceed 3×10^{-4} Pa. The gas pressure at the ion source varied in the range $10 \div 20$ Pa.

The emission of exited particles was observed at right angle respectively to the atomic beam; therefore, radiating particles of the beam and the target were not distinguished.

The analysis of polarization was implemented using the Glan – Taylor prism. The compensators from the quarter-wave mica plates were applied to remove the influence of polarizing effect of the optical monochromator.

The measurement procedure was described in detail in the work (Kurskov 1995).

The emission cross section was measured in the experiment directly. Note that the emission cross section is determined by measuring of the spectral line intensity, the flux density of fast atoms and target particle density (Wolterbeek Muller et al. 1970).

With taking angular divergence of the dipole radiation into account, emission cross section is equal to

$$\sigma_{ij} = \frac{4\pi}{\Omega} \frac{S(\lambda)}{K(\lambda)} \frac{G}{I_p N_t L} \frac{1}{1+\eta} \,, \tag{1}$$

where Ω – a solid angle, defined by the optical system aperture; $S(\lambda)$ – photon count rate; $K(\lambda)$ – absolute sensitivity of the registration system at the given wavelength; I_p – beam intensity of the fast particles; N_t – target particle density, and L – observation zone length. The coefficient G – considers the angular distribution of dipole emission:

$$G = \frac{3-P}{3(1-P\cos^2\Theta)} \,, \tag{2}$$

where P – a degree of polarization, Θ – an angle between a beam of fast particles and an optical axis of system. The degree of polarization is determined by the following expression

$$P = (P_\parallel - P_\perp)/(P_\parallel + P_\perp) \,, \tag{3}$$

where $P_\parallel$ and $P_\perp$ – intensities of components which are polarized in parallel and transversely to the beam of fast particles respectively. The value η – takes into

account a part of the excited fast atoms, which irradiate before leaving the observed zone. It is equal to

$$\eta = 1 - \frac{x_i}{L} exp(-l/x_i)(1 - exp(-L/x_i)) \ , \tag{4}$$

where l – the distance between the point of fast particles enter the collision chamber before the observation zone and $x_i = v\tau_i$, where v – colliding particle velocity, τ_i – excited state life time. The multiplier $1/(1+\eta)$ was obtained from the condition that excitation cross sections of fast and slow particles in symmetric collisions are equal.

The atom beam intensity in the observation zone was defined in the following way:

$$I_p = \frac{J}{e\gamma^0(E) exp(\sigma_s(E) N_t d)} \ , \tag{5}$$

where J – detector current, e – charge of electron, $\gamma^0(E)$ – coefficient of secondary electron emission from the detector surface under the action of fast atoms, $\sigma_s(E)$ - cross section of decrease of fast atoms from atomic beam, d – a distance from the observation zone up to the detector surface.

3. RESULTS AND DISCUSSION

The excitation cross sections of Ar I $4p'[1/2]_1$, $4p'[3/2]_1$, $4p'[3/2]_2$ and $4p[3/2]_2$ levels and degree of polarization for $4s[3/2]_2^0 - 4p'[1/2]_1$ and $4s[3/2]_2^0 - 4p[3/2]_2$ transitions are represented in the figures 2 – 5.

Taking into account the inaccuracy of measurements of the absolute spectral sensitivity, the inaccuracy of the definition of the secondary electron yield from the detector surface of the fast particles, and the inaccuracy of the definition of the gas pressure of the target the systematic error could reach $\pm 55\,\%$.

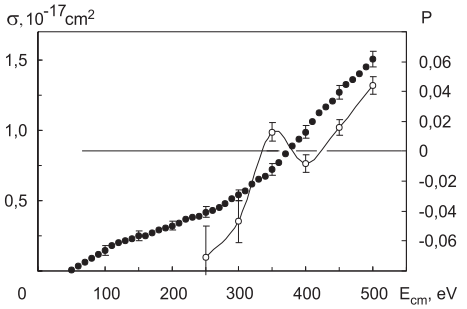

Figure 2: Ar I $4p'[1/2]_1$ level excitation cross section (•) and degree of polarization for $4s[3/2]_2^0 - 4p'[1/2]_1$ transition (○) plotted against collision energy of Ar atoms.

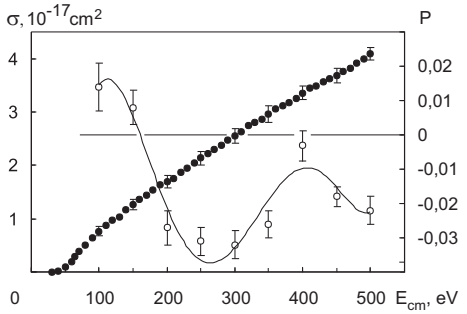

Figure 3: Ar I $4p[3/2]_2$ level excitation cross section (•) and degree of polarization for $4s[3/2]_2^0 - 4p[3/2]_2$ transition (○) plotted against collision energy of Ar atoms.

The obtained results demonstrate that the polarization degree of emission significantly depends on collision energy – when the latter goes up, the former changes its sign. The fact that the sign of the polarization degree changes, as well as does

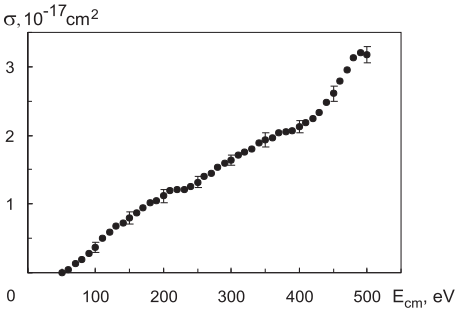

Figure 4: Ar I $4p'[3/2]_1$ level excitation cross section plotted against collision energy of Ar atoms.

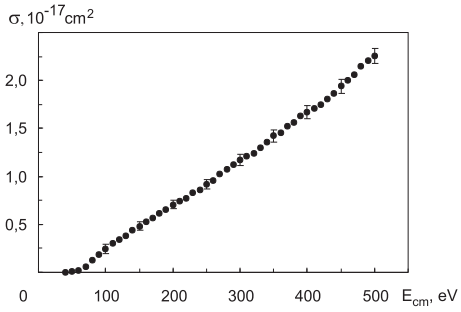

Figure 5: Ar I $4p'[3/2]_2$ level excitation cross section plotted against collision energy of Ar atoms.

interaction energy, proves that the mechanism of level population changes too (Blum 1981).

For instance, since the angular momentum of $4p'[1/2]_1$ excitation level is equal to 1, the positive polarization degree shows that the magnetic sublevel σ_0, that is zero momentum projection onto internuclear axis of the Ar_2 quasimolecule, is mostly populated. Negative polarization degree, in its turn, means that there is a dense population at magnetic sublevels σ_1, corresponding to ± 1 projections. Therefore, according to the data obtained, if collision energy is higher than 400 eV, the population at the mentioned above level is determined by $\Sigma_g - \Sigma'_g$ transactions. If collision energy is equal to or lower than 300 eV, level population is guided by $\Sigma_g - \Pi_g$ transactions due to radial coupling of even terms of the Ar_2 quasimolecule.

It is important to note that since output Σ_g terms of the Ar_2 quasimolecule are actually double excited terms, supposedly, the other interacting atom is excited too. This fact agrees with Wigner's law (system spin unchanged at collision) and with the research results described in works (Martin et al. 1978, Moorman et al. 1987).

The diabatic molecular orbital diagram for homonuclear system (Barat et al. 1972) and measurement results of the polarization of emission lead to the following conclusion: if collision energy is less or equal to 300 eV, the population of $4p'[1/2]_1$ level is determined by $4p\sigma - 4p\pi$ transactions due to rotational coupling at small nuclear distances. In case of higher energies, the population is governed by $5f\sigma - 5d\sigma$ transactions due to non-adiabatic radial coupling.

References

Barat, M., Lichten, W.: 1972, *Phys. Rev.*, **A6**, 211.
Blum, K.: 1981, Density Matrix Theory and Applications, New-York: Plenum Press.
Breno, J. C., Dhuicq, D., Gauyacq, J. P. et al.: 1975, *Phys. Rev.*, **A11**, 1245.
Kempter, V., Riecke, G., Veith, F., Zehnle, L.: 1976, *J. Phys.*, **B9**, 3081.
Kurskov, S. Yu.: 1995, *PhD thesis*, Petrozavodsk State University, Petrozavodsk.
Martin, P. J., Riecke, G., Hermann, J. et al.: 1978, *J. Phys.*, **B11**, 1991.
Moorman, L., van Hoegaerden, V., van Eck, J. et al.: 1987, *J. Phys.*, **B20**, 6267.
Wolterbeek Muller, L., de Heer, F. J.: 1970, *Physica*, **48**, 345.

Publ. Astron. Obs. Belgrade No. 84 (2008), 79 - 82 *Contributed Paper*

CHARGE TRANSFER IN ENERGETIC $Li^{2+} - H$ COLLISIONS

I. MANČEV

Department of Physics, Faculty of Sciences and Mathematics,
P.O. Box 224, 18000 Niš, Serbia
E–mail: mancev@pmf.ni.ac.yu

Abstract. The total cross sections for charge transfer in $Li^{2+} - H$ collisions have been calculated, using the four-body first Born approximation with correct boundary conditions (CB1-4B) and four-body continuum distorted wave method (CDW-4B) in the energy range 10 - 5000 keV/amu. Present results call for additional experimental data at higher impact energies than presently available.

1. INTRODUCTION

The theoretical total cross sections for single electron capture in $Li^{2+} - H$ collisions are reported. Data for this process are of particular interest in fusion research. Heretofore there has been very little theoretical work especially for high impact energies. For $Li^{2+} - H$ collisions, previous theoretical work consists of calculations performed employing the following methods: three-body continuum distorted wave (CDW-3B) of the Belkić 1991, coupled-channel calculations in 'perturbative one-and-a-half-centre' (POHCE) formulation (Ford et al. 1982), modified continuum distorted wave (Crothers and Todd 1980), Oppenheimer-Brinman-Kramers approximation (Eichler et al. 1981). All quoted models reduced four-body problem to a three-body problem. Although some of these three-body models show a satisfactory agreement with experimental data, these methods completely neglect dynamic (i.e. collisional) correlations.

A substantially different approaches to the problem of high-energy electron capture from one- and multielectron atoms by hydrogen-like projectiles have recently been undertaken by Mančev, who introduced the four-body corrected first Born approximation (CB1-4B) approximation (Mančev 1995, 1996) and four-body Continuum Distorted Wave (CDW-4B) method (Mančev 2007). Different quantum-mechanical four-body methods for high-energy ion-atom collisions have recently been extensively discussed in review paper of Belkić et al. (2008).

Four-body treatments allow one to study the effects of the electron-electron correlation in single capture. Along this line the CDW-4B and CB1-4B approximations are utilized for investigating $Li^{2+} - H$ collisions, since the evidence of correlation effects in this process has not been previously assessed.

Atomic units will be used throughout unless otherwise stated.

2. THEORY

We examine single electron capture in collision between hydrogen-like projectiles:

$$(Z_P, e_1) + (Z_T, e_2) \longrightarrow (Z_P, e_1, e_2) + Z_T. \tag{1}$$

The parentheses $(\ldots)$ symbolize the bound states. Let $\vec{s}_1$ and $\vec{s}_2$ ($\vec{x}_1$ and $\vec{x}_2$) be position vectors of the first and second electrons (e_1 and e_2) relative to the nuclear charge of the projectile Z_P (target Z_T). Further, let us denote by $\vec{R}$ the position vector of the Z_T with respect to Z_P. The vector of the distance between the two active electrons (e_1 and e_2) is denoted by $\vec{r}_{12} = \vec{x}_1 - \vec{x}_2 = \vec{s}_1 - \vec{s}_2$. In the entrance channel, it is convenient to introduce $\vec{r}_i$ as a the position vector between the center of mass of (Z_P, e_1) and target system. Symmetrically in the exit channel, let $\vec{r}_f$ is the position vector of the center of mass of (Z_P, e_1, e_2) system relative to Z_T. The transition amplitudes in the prior (-) and post (+) forms in the CDW-4B theory can be written as (Mančev 2007):

$$\begin{aligned} T_{if}^{+(CDW-4B)} &= N^{-*}(\nu_T)N^{+}(\nu_P)\int\int\int d\vec{x}_1 d\vec{x}_2 d\vec{R}\, e^{i\vec{\alpha}\cdot\vec{s}_2 + i\vec{\beta}\cdot\vec{x}_2}\varphi_P(\vec{s}_1)\varphi_T(\vec{x}_2) \\ &\times F(i\nu_P, 1, ivs_2 + i\vec{v}\cdot\vec{s}_2)\left\{ Z_T\left(\frac{1}{R} - \frac{1}{x_1}\right)\varphi_f^*(\vec{s}_1, \vec{s}_2)F(i\nu_T, 1, ivx_2 + i\vec{v}\cdot\vec{x}_2)\right. \\ &\left. - \nabla_{s_2}\varphi_f^*(\vec{s}_1, \vec{s}_2)\cdot\nabla_{x_2}F(i\nu_T, 1, ivx_2 + i\vec{v}\cdot\vec{x}_2)\right\}, \end{aligned} \tag{2}$$

$$\begin{aligned} T_{if}^{-(CDW-4B)} &= N^{-*}(\nu_T)N^{+}(\nu_P)\int\int\int d\vec{x}_1 d\vec{x}_2 d\vec{R}\, e^{i\vec{\alpha}\cdot\vec{s}_2 + i\vec{\beta}\cdot\vec{x}_2}\varphi_f^*(\vec{s}_1, \vec{s}_2) \\ &\times F(i\nu_T, 1, ivx_2 + i\vec{v}\cdot\vec{x}_2)\left\{\left[Z_T\left(\frac{1}{R} - \frac{1}{x_1}\right) + \frac{1}{r_{12}} - \frac{1}{s_2}\right]\varphi_P(\vec{s}_1)\varphi_T(\vec{x}_2)\right. \\ &\left. \times F(i\nu_P, 1, ivs_2 + i\vec{v}\cdot\vec{s}_2) - \varphi_P(\vec{s}_1)\nabla_{x_2}\varphi_T(\vec{x}_2)\cdot\nabla_{s_2}F(i\nu_P, 1, ivs_2 + i\vec{v}\cdot\vec{s}_2)\right\}. \end{aligned} \tag{3}$$

The corresponding expressions for transition amplitudes in the CB1-4B approximation are given by (Mančev 1995, 1996):

$$\begin{aligned} T_{if}^{+(CB1-4B)} = \quad & Z_T\int\int\int d\vec{s}_1 d\vec{s}_2 d\vec{R}\, e^{i\vec{\alpha}\cdot\vec{s}_2 + i\vec{\beta}\cdot\vec{x}_2}\varphi_f^*(\vec{s}_1, \vec{s}_2) \\ & \times\left(\frac{2}{R} - \frac{1}{x_1} - \frac{1}{x_2}\right)\varphi_P(\vec{s}_1)\varphi_T(\vec{x}_2), \end{aligned} \tag{4}$$

$$\begin{aligned} T_{if}^{-(CB1-4B)} = \quad & \int\int\int d\vec{s}_1 d\vec{x}_2 d\vec{R}\, e^{i\vec{\alpha}\cdot\vec{s}_2 + i\vec{\beta}\cdot\vec{x}_2}\varphi_f^*(\vec{s}_1, \vec{s}_2) \\ & \times\left(\frac{Z_T + Z_P - 1}{R} - \frac{Z_T}{x_1} - \frac{Z_P}{s_2} + \frac{1}{r_{12}}\right)\varphi_P(\vec{s}_1)\varphi_T(\vec{x}_2), \end{aligned} \tag{5}$$

where $\varphi_f(\vec{s}_1, \vec{s}_2)$ is the bound state wave function of the atomic system (Z_P, e_1, e_2), whose binding energy is ε_f. The hydrogen-like wave functions of the (Z_P, e_1) and

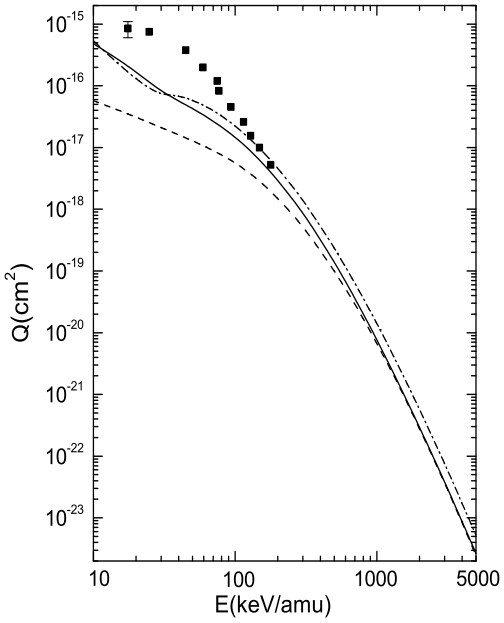

Figure 1: Total cross sections $Q(cm^2)$ as a function of laboratory incident energy $E(keV/amu)$ for charge transfer in $Li^{2+} - H$ collisions. The solid line represents the results of the prior form of the CDW-4B method, whereas singly chained curve is due to the the post version of the CDW-4B theory. The dashed curve represents the cross sections of the CB1-4B approximation. All computations have been performed using the two-parameter Silverman et al. (1960) wave function. Experimental data: ■ Shah et al. (1978).

(Z_T, e_2) systems are respectively denoted as $\varphi_P(\vec{s}_1)$ and $\varphi_T(\vec{x}_2)$. The corresponding binding energies are ε_P and ε_T. The momentum transfers $\vec{\alpha}$ and $\vec{\beta}$ are defined by $\vec{\beta} = -\vec{\eta} - \beta_z\hat{\vec{v}}$, $\vec{\alpha} = \vec{\eta} - \alpha_z\hat{\vec{v}}$, $\vec{\alpha} + \vec{\beta} = -\vec{v}$, $\alpha_z = v/2 - \Delta\varepsilon/v$, $\beta_z = v/2 + \Delta\varepsilon/v$, $\Delta\varepsilon = \varepsilon_P + \varepsilon_T - \varepsilon_f$. The transverse component of the change in the relative linear momentum of a heavy particle is denoted by $\vec{\eta} = (\eta\cos\phi_\eta, \eta\sin\phi_\eta, 0)$. The incident velocity vector $\vec{v}$ is chosen as $\vec{v} = (0, 0, v)$. The symbol ${}_1F_1(a, b, z)$ stands for the regular confluent hypergeometric function.

It should be recalled that both CDW-4B and CB1-4B models satisfy correct boundary condition according to principles of scattering theory (Belkić 2004). The proper connection between long-range Coulomb distortion effects and accompanying perturbation potentials are established. It must be emphasized that imposing the proper Coulomb boundary conditions in the entrance and the exit channels is of crucial importance for ion-atom collisions (Belkić 2008). Experience has shown that if this requirement is disregarded, serious problems may arise and such models are generally inadequate for description of experimental findings (Belkić 2008).

As shown (Mančev 2007), after analytical calculations performed by means of standard Nordsieck technique, the expressions for the total cross sections for the CDW-4B model can be reduced to a four-dimensional numerical integral. In the case of CB1-4B model (post version), the total cross sections are expressed (Mančev 1995) via a three-dimensional quadrature, whereas prior version of the CB1-4B approximation requires an additional three-dimensional integral due to term $1/r_{12}$ in the perturbation potential.

3. THE RESULTS OF THE NUMERICAL COMPUTATIONS

In this work, the explicit calculation of the matrix elements for single electron capture are carried out by using the two-parameter wave function of Silverman et al. (1960) for the final state of lithium ion: $\varphi_i(\vec{s}_1,\vec{s}_2) = N[e^{-\alpha_1 s_1-\alpha_2 s_2}+e^{-\alpha_2 s_1-\alpha_1 s_2}]/\pi$, where $N=\left[1/\alpha_1^3+1/\alpha_2^3+16/(\alpha_1+\alpha_2)^3\right]^{-1/2}$. Despite its very simple form in this function Silverman et al. (1960) the radial static correlations are taken into account to within nearly 90%.

Numerical computations of the total cross sections are presently carried out for the following charge exchange reaction:

$$Li^{2+}(1s)+H(1s)\longrightarrow Li^{+}(1s^2)+H^{+}. \tag{6}$$

The explicit computations of the total cross sections are carried out only for capture into the final ground state $1s^2$. In Fig. 1 we compare our theoretical results for prior (solid line) and post (dot-dashed line) CDW-4B cross sections, together with CB1-4B results (dashed line).

Our total cross sections are also compared with the experimental data of Shah et al. (1978). A comparison of the CDW-4B and CB1-4B models with measurements Shah et al. (1978) shows that the theoretical curves underestimate experimental data, especially at lower impact energies. Unfortunately the measurements of Shah et al. (1978) are limited up to 178 keV/amu, and this is only marginally within the considered range $10 \leq E \leq 5000 keV/amu$. However, we recall that CDW-4B and CB1-4B models are high-energy approximations and we expect better agreement at larger impact energies. New measurements for the considered reaction are needed for a better assessment of the validity of the CDW-4B and CB1-4B models.

References

Belkić, Dž.: 1991, *Phys. Scr.*, **43**, 561.
Belkić, Dž.: 2004, Principles of Quantum Scattering Theory, Institute of Physics, Bristol.
Belkić, Dž.: 2008, Quantum Theory of High-Energy Ion-Atom Collisions, Taylor & Francis, London.
Belkić, Dž., Mančev, I and Hanssen, J.: 2008, *Rev. Mod. Phys.*, **80**, 249.
Crothers, D. S. F., and Todd, N. R.: 1981, *J. Phys. B*, **14**, 1035.
Eichler, J. K. M., Tsuji, A. and Ishihara T.: 1981, *Phys. Rev. A*, **23**, 2833.
Ford, A. L., Reading, J. and Becker R. L.: 1982, *J. Phys. B*, **15**, 3257.
Mančev, I.: 1995, *Phys. Scr.*, **51**, 762.
Mančev, I.: 1996, *Phys. Rev. A*, **54**, 234.
Mančev, I.: 2007, *Phys. Rev. A*, **64**, 012708.
Silverman, J. N., Platas, O. and Matsen, F. A.: 1960, *J. Chem. Phys.*, **32**, 1402.
Shah, M. B., Goffe T. V. and Gilbody, H. B.: 1978, *J. Phys. B*, **11**, L233.

Publ. Astron. Obs. Belgrade No. 84 (2008), 83 - 86 *Contributed Paper*

ARIBE: A LOW ENERGY ION BEAM FACILITY IN CAEN

V. BERNIGAUD, O. KAMALOU, A. ŁAWICKI, M. CAPRON, R. MAISONNY,
B. MANIL, L. MAUNOURY, J. RANGAMA, P. ROUSSEAU,
J.-Y. CHESNEL, L. ADOUI and B. A. HUBER

Centre de recherche sur les ions, les matériaux et la photonique (CIMAP) – CEA - CNRS - ENSICaen - Université de Caen – Boulevard Henri Becquerel BP5133 F-14070 Caen cedex 05 France
E–mail: prousseau@ganil.fr

Abstract. Beams of low-energy ions are specific tools for interdisciplinary research allowing for preparing and studying the properties of complex systems like (bio)molecules, clusters and surfaces. In particular highly charged ions can induce strong electronic excitations as they are carriers of a large amount of potential energy up to the high keV range. But also other types of ion beams, like size-selected cluster beams or beams of biomolecular species, are useful for preparing and structuring surfaces or performing collision experiments. The ARIBE facility, located in Caen, which is part of the distributed European Facility LEIF, delivers such types of beams. In the present contribution recent technical developments and typical results are discussed.

1. INTRODUCTION

The ARIBE installation, located in Caen, is part of the Distributed European Low Energy Ion beam Facility (LEIF). Other access-giving partners are H-EBIT from the MPIK in Heidelberg, the ZERNIKE-LEIF installation from KVI in Groningen, the ELISA infrastructure at the University of Aarhus, and the QU-LEIF installation at Queen's University in Belfast. These installations are devoted to study the interaction of low energy ion beams with matter. The ARIBE facility distributes different kinds of low-energy ion beam. A well-established high intensity low energy ion beamline delivers a beam of multiply charged ions (MCI) in high charge states produced by an electron cyclotron resonance (ECR) ion source. To study very low energy interactions involving multiply charged ion, a beam line has been installed which decelerates ions down to kinetic energies of a few eV (typically 5 eV) per charge. Very recently a size-selected cluster ion beamline and an electrospray ion source coupled with a quadrupole mass filter allowing for the production of beams of complex systems have been developed. These latter beamlines are mobile and can be coupled and crossed with the beamlines of multiply charged ions. Thus, the study of stability and fragmentation of complex systems, charged during the interaction with MCI, becomes feasible. As part of the ITS LEIF Integrated Infrastructure Initiative and of the GANIL pluridisciplinary facility, external users are encouraged to apply for beam

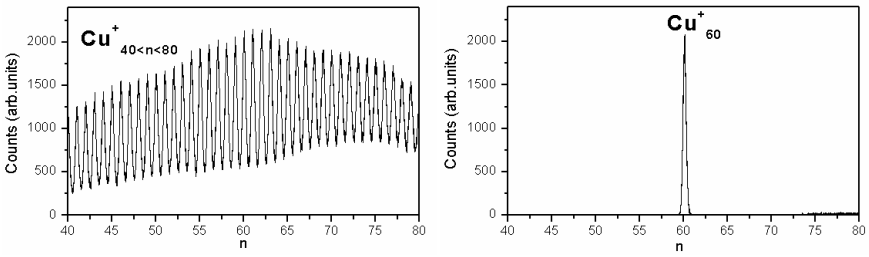

Figure 1: Mass spectra of copper clusters without mass selection (left) and of a size-selected cluster beam of Cu_{60}^{+} by using time-of- flight mass selection (right).

time and to send in scientific proposals. In order to apply for beam time at one of the five infrastructures one might contact the website: `http://www.its- leif.org`, where more information on the modalities and where the application forms are given.

2. BEAMLINES

There are seven high intensity beamlines supplied by a Supershypie ECR ion source which is able to produce multiply charged ions (A^{q+}) in high charge states with high intensity. Typical beam intensities of eμA are reached for Xe ions in charge states q up to 30+. The kinetic energy of the multiply charged ions can be varied between 3 $q$keV and 25 $q$keV. Among the seven beamlines available, two are entirely magnetic; one of them is equipped with a complete installation to study the fragmentation of clusters induced by multiply charged ions. This instrument has been widely used to study the interaction of multiply charged ions with fullerenes, fullerenes clusters (Manil et al. 2003), and biomolecules (Schlathölter et al. 2006). After a switching magnet, five more beamlines with electrostatic optics are available. Each of the seven beamlines is equiped with diagnostics tools, steerers, and movable apertures.

The very low energy beamline is connected to a Caprice ECR ion source which is able to provide multiply charged ions in high charge state (up to Xe^{30+}). There is a diagnostic chamber to characterize the ion beam and to prepare its shape before entering the decelerating lens system. This ion optical system serves to slow down the ions and to focus them at an image plan, which can be moved in a range of 20 cm. It is possible to decelerate the beam starting from 20 keV/q down to a few eV/q with a size of about 3 mm (Lebius et al. 2003).

The beamline of size-selected cluster ions has been recently developed at the CIMAP laboratory (Kamalou et al. 2008). A magnetron discharge sputters a metallic or semiconducting target and sputtered particles are then aggregated in a liquid nitrogen-cooled condensation zone. A heat bath situated after the cluster source allows controlling the temperature of the clusters, i.e. the cluster internal energy. An octupole ion guide helps to transport cluster ions to the mass filter. Mass selection is obtained by using a Wiley-McLaren time- of-flight mass spectrometer. Pulsed ion beams of size-selected clusters $A_n^{+,-}$ are available with sizes varying from several atoms up to $n = 10000$ with a typical kinetic energy of 3 keV. In order to separate neutral clusters from charged ones, the cluster ions are 90°- deflected by a quadrupolar electrostatic

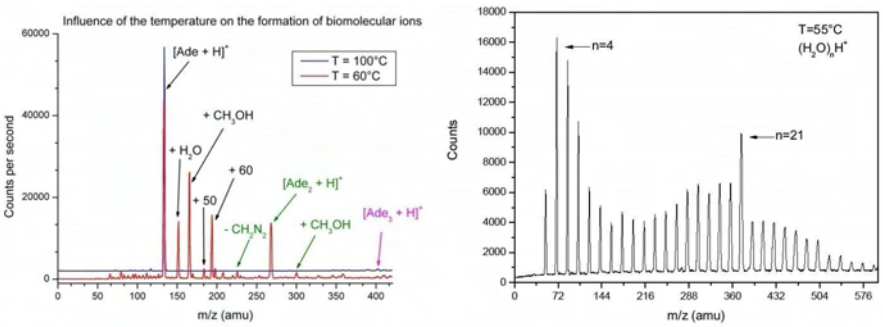

Figure 2: Mass spectrum of protonated adenine (left) and of water clusters (right) obtained with the electrospray ion source.

deviator. A typical mass spectrum obtained with copper clusters is shown in the left part of figure 1. We observed separated peaks of Cu_n^+ cluster ions for $40 \leq n \leq 80$. On the right part of figure 1, a mass-selected Cu_{60}^+ cluster beam is obtained by using mass filtering by time-of-flight.

With the increasing interest for biomolecular studies and the need to produce biomolecules in the gas phase, which are too fragile to be evaporated by using an oven device, the electrospray ion source (Fenn et al. 1989) appears to be most appropriate to obtain large biomolecules in the gas phase. We have recently built an electrospray ion source at the ARIBE facility in collaboration with the Aarhus group. This source is coupled to a quadrupole mass filter in order to produce a beam of mass-selected biomolecular ions. First mass spectra have been obtained in spring 2008. A typical mass spectrum of the protonated adenine ($[AdeH]^+$) is displayed on figure 2. Furthermore, we have been able to produce water clusters ($[(H_2O)_nH]^+$) by using a corona discharge instead of the spray technique, as shown in the right part of fig. 2.

3. RECENT RESULTS

As an example, we will discuss in the following two type of experiments. The first one concerns the deposition of mass-selected clusters on a substrate. Deposition experiments of mass-selected copper clusters with a deposition energy of about 0.7 eV/atom have been performed on highly oriented pyrolytic graphite (HOPG) and on SiO_2 substrates. Pictures obtained with an Atomic Force Microscopy (AFM), shown below (figure 3), indicate that copper clusters are evidently mobile on the HOPG surface and that they finally stick only along cleavage steps, dislocation lines or other surface defects. When deposited on a SiO_2 substrate, copper clusters do not move, they stay at their landing position.

A second example concerns the fragmentation of FeTPPCl molecules. Figure 4 shows a typical mass spectrum of FeTPPCl when ionised in collisions with O^{3+} ions at 30 keV. The singly charged intact molecule is found to be the most abundant in contrast to experiments with electrons (Feil et al. 2006). The intact molecule is observed in charge states up to $q = 3$. However, with increasing charge state the loss of the Cl atom becomes more and more important. Figure 4 shows that in addition to the loss of the Cl atom also the loss of 1 or 2 phenyl groups (peaks labelled a

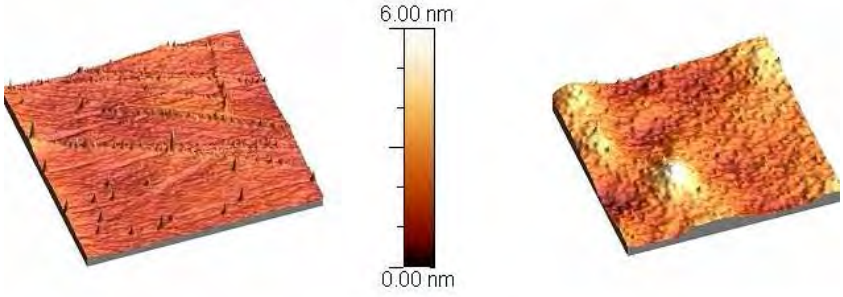

Figure 3: 3D AFM pictures of positive Cu clusters deposited on a HOPG surface (left side) and on a SiO_2 surface (right side).

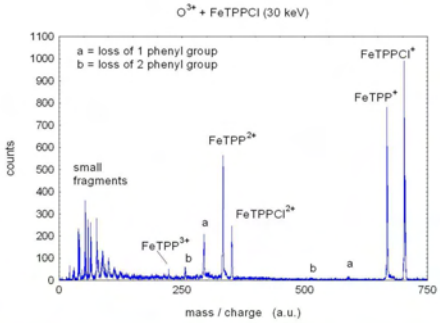

Figure 4: Typical fragmentation spectrum obtained in 30 keV-collisions of O^{3+} ions with FeTPPCl molecules. The peaks characterised by a and b correspond to the loss of 1 and 2 phenyl groups in addition to the Cl-atom, respectively.

and b) becomes increasingly important with the charge state of the ionised molecule. Finally, small fragments are observed which are due to a more complete break-up of the multi-ionised molecule.

The presented results have been obtained at the ARIBE facility, a part of the distributed infrastructure LEIF; the support by the ITS LEIF Project 026015 is gratefully acknowledged.

References

Feil, S., Winkler, M., Sulzer, P., Ptasinska, S., Denifl, S., Zappa, F., Krńutler, B., Märk, T. D., Scheier, P.: 2006, *Int. J. Mass Spectrom.*, **255-256**, 232

Fenn, J. B., Mann, M., Meng, C. K., Wong, S. F., Whitehouse, C. M.: 1989, *Science*, **246**, 64.

Kamalou, O., Rangama, J., Huber, B. A.: 2008, *Rev. Sci. Instrum.*, accepted for publication.

Lebius, H., Brenac, A., Huber, B. A., Maunoury, L., Gustavo, F., Cornier, D.: 2003, *Rev. Sci. Instrum.*, **74**, 2273.

Manil, B., Maunoury, L., Huber, B. A., Jensen, J., Schmidt, H. T., Zettergren, H., Cederquist, H., Tomita, S., Hvelplund, P.: 2003, *Phys. Rev. Lett.*, **91**, 215504.

Schlathölter, T., Alvarado, F., Bari, S., Lecointre, A., Hoekstra, R., Bernigaud, V., Manil, B., Rangama, J., Huber, B. A.: 2006, *Chem. Phys. Chem.*, **7**, 2339.

Publ. Astron. Obs. Belgrade No. 84 (2008), 87 - 90 *Contributed Paper*

THE EFFECT OF ANISOTROPY OF THE SCATTERING OF HEAVY PARTICLES ON MODELLING OF THE DOPPLER PROFILE IN PURE H_2 DISCHARGE

V. D. STOJANOVIĆ, Ž. D. NIKITOVIĆ and Z. Lj. PETROVIĆ
Institute of Physics, Pregrevica 118, 11080 Zemun, Serbia
E–mail: zeljka@phy.bg.ac.yu

Abstract. The Effect of anisotropy of vibrational excitation by heavy particle scattering (fast H_2, H^+ and H_2^+) on Doppler profile and spatial distribution of emission in pure H_2 is studied by Monte Carlo technique by using simple differential cross sections (DCS) in the center of mass system (CMS). Electron and heavy particle collisions are represented by the latest cross section sets compiled by Phelps. For the conditions of very high reduced electric fields nonequilibrium electron transport should necessarily be modelled by anisotropic scattering.

1. INTRODUCTION

The first interpretations of unusually high Doppler broadening of hydrogen lines in non-equilibrium plasmas were based on possible dissociative processes, recombination and excitation (Capelli et al. 1985). The experiments, especially the experiments performed at dc fields revealed a large asymmetric component with energies exceeding the energy available from the repulsive potentials of the dissociating molecules (Barbeau and Jolly 1990, Konjević and Kuraica 1992). The explanation of such results was found in a specially designed high E/N swarm experiment (Petrović et al. 1992, Petrović and Phelps 1991) which gave a proof that, to the largest degree the excitation is due to collisions of fast neutrals formed in charge transfer collisions of the feed gas with fast ions. At high E/N, which can only be achieved under breakdown conditions at the left branch of the Paschen curve, the mean free paths are sufficiently high to allow large energy gain by ions and consequently formation of very fast neutrals with comparable energies. In addition it is possible to have reflection and neutralization of ions with reflection as fast neutrals, which leads to different components in blue and red wings of the Doppler profile (Petrović et al. 1992).

Some alternative explanations of anomalous Doppler profiles were offered in the literature (Mills et al. 2002), but all reliable measurements performed so far (Jovićević et al. 2004, Tatarova et al. 2007a, Tatarova et al. 2007b) do not require more than a combination of ionization and acceleration of the resulting ions in high fields leading to heavy particle (predominantly fast neutral) excitation. High, DC, E/N swarm experiment (self sustained discharge operating in the Townsend regime) may

be modeled directly and exactly as it does not require self consistent calculation of the electric field and is thus open to a simple Monte Carlo simulation (MCS) that may include maximum complexity in the representation of collisions.

Vibrational excitation is a significant momentum and energy loss process for H^+ in H_2 at energies between 10 and 100 eV and potentially important process for H_2^+ in H_2 and H_2 in H_2 (Phelps 1990). Usual assumption for plasma models treating vibrational excitation is that scattering anisotropy for vibrational excitation by heavy particles is forward scattering although precise calculations (Krstić and Schultz 1999) exist. For both proton and neutral atom impact the scattering angles following vibrational excitation are shifted significantly towards larger values in comparison with the data due when only elastic scattering is involved.

In this paper we show results of simple modeling of heavy particles induced spatially resolved emission intensity or the Doppler profile in pure H_2 discharge when scattering anisotropy is included in the model.

2. DATA AND SIMULATION TECHNIQUE

The Monte Carlo code (Petrović and Stojanović 2008) based on null collision technique was used to follow electrons and heavy particles (H^+, H_2^+, H_3^+, fast H and fast H_2) between collisions with H_2 or with the cathode surface for the conditions of high electric field (E) to gas density (N) ratios E/N. We followed trajectories of all reaction fragments until they neutralized or thermalized below the H_α excitation energy. Conditions of simulation are appropriate for very high E/N (E/N =10 kTd, p =145 mTorr, interelectrode distance is d =4 cm) and are selected from experimental Townsend discharges in pure H_2 (Petrović et al. 1992). Effect of anisotropy of vibrational excitation by heavy particle scattering (fast H_2, H^+ and H_2^+) on Doppler profile, and spatial distribution of emission in pure H_2, is studied by using differential cross sections (DCS) in the center of mass system . One model of vibrational excitation was chosen to be isotropic below 30 eV in CMS and forward for the energies over 30 eV (this combination was marked as VA in this text) the other as forward scattering at all energies. All other processes have the same anisotropy as the model of Phelps (1990).

3. RESULTS AND DISCUSSION

Simulations are performed for the cases with vibrational excitation is included or excluded in the cross section set and when we use different models of scattering anisotropy. We used the model of Phelps (Phelps 2006) which includes vibrational excitation only by H^+ ions on H_2 from Phelps (1990) as the starting point and in that model at all energies forward scattering is assumed. Results obtained with these data compared to experimental results and other calculations are shown by dashed lines in Figs. 1. and 2. In both figures the same factor (F) is used to fit the intensity from the MCS to EXP. Effect of anisotropy of vibrational excitation by H^+ ions obtained by using VA differential cross section is shown in Fig. 1 by the thin solid line. If vibrational excitation proceeds with the VA model for H^+ ions than the Doppler peak due to particles moving towards the cathode is significantly shifted towards lower energies and so is the backward peak (reflected from the cathode). If one wants to compare these results to scale with experiment (EXP) than normalization factor

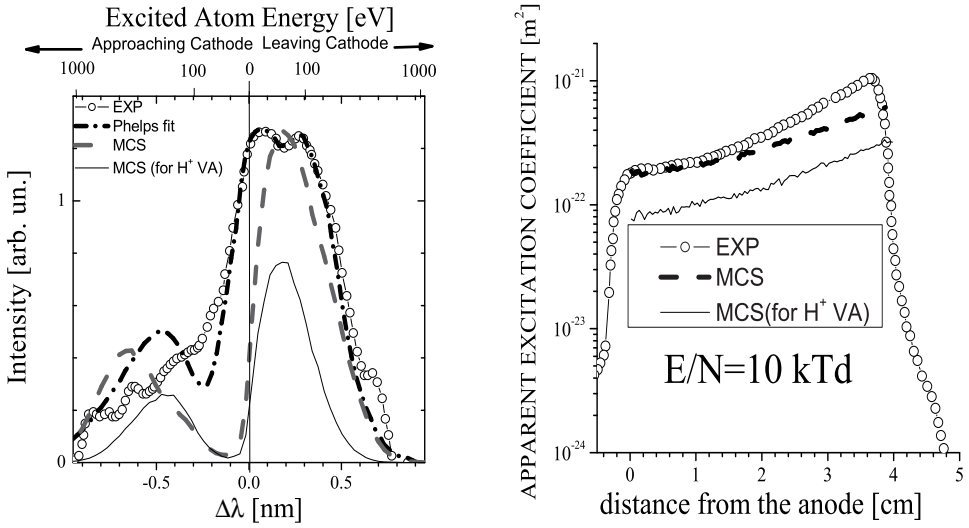

Figure 1: a) Doppler broadened profile, b) spatial distribution of emission, at very high E/N. "Phelps fit" and "EXP" are results published by Petrović et al. (1992).

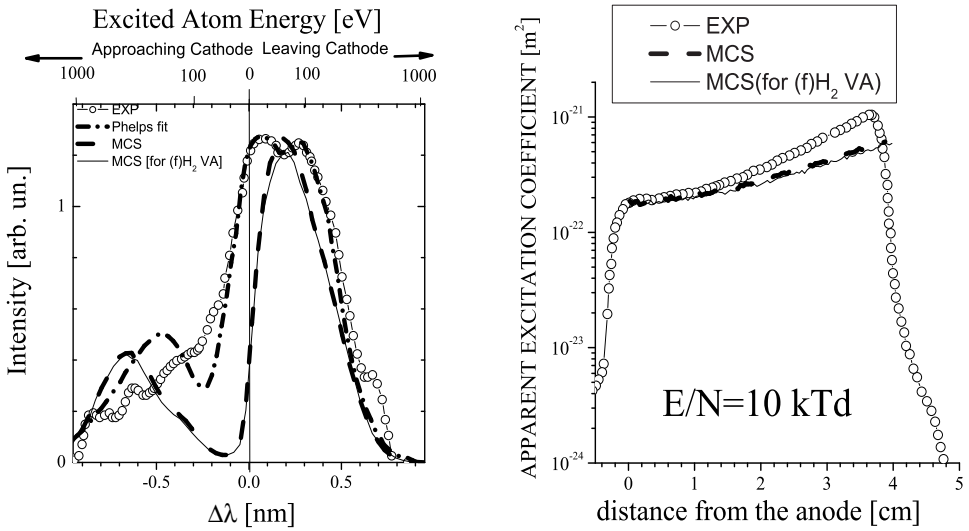

Figure 2: a) Doppler broadened profile, b) spatial excitation coefficient. "for (f)H_2" - MCS results for case where cross section for vibrational excitation by (f)H_2 from Phelps (1990) is included in the model while vibrational excitation for other heavy particles on H_2 is excluded.

F*1.7 (thin line in Fig 1.) should be applied. At the same time vibrational anisotropy shifts down the results for spatially resolved emission by a factor of two.

Introduction of vibrational excitation by H_2^+ and/or (f)H_2 collisions with buffer gas molecules with forward scattering (Phelps 1990) into our Monte Carlo simulation affects neither Doppler profile nor spatial profile of H_α emission intensity. Only minor changes can be observed with VA scattering anisotropy. Results for the e case where only vibrational excitation by (f)H_2 (Phelps 1990) is taken into account are shown in Fig. 2. MCS results are fitted to EXP by the same normalization factor.

Acknowledgments

Work at the Institute of Physics is supported by the MNRS, under grants 141025.

References

Barbeau, C., Jolly, J.: 1990, *J. Phys. D*, **23**, 1168.
Capelli, A. I., Gottscho, R. A., Miller, T. A.: 1985, *Plasma Chem. Plasma Process*, **5**, 317.
Jovicević, S., Ivković, M., Konjević, N., Popović, S., Vušković, L.: 2004, *J. Appl. Phys.*, **95**, 24.
Konjević, N., Kuraica, M.: 1992, *Phys. Rev. A: At. Mol. Opt. Phys.*, **46**, 4429.
Krstić, P. S., Schultz, D. R.: 1999, *J. Phys. B: At. Mol. Opt. Phys.*, **32**, 2415.
Mills, R. L., Raz, P. C., Dhandapani, B., Mayo, R. M., He, J.: 2002, *J. Appl. Phys.*, **92**, 7008.
Petrović, Z. Lj., Jelenković, B. M., Phelps, A. V. : 1992, *Phys. Rev. Lett.*, **68**, 325.
Petrović, Z. Lj., Stojanović, V. D.: 2008, AIP CP938, Spectral Line Shapes in Astrophysics-VI-Serbian Conference (VI SCLSA) ed. By L.Č. Popović and M.S. Dimitrijević, p. 237.
Petrović, Z. Lj., Phelps, A. V.: 1991, *Proc. of the Internatonal Seminar on Reactive Plasmas*, **E-3**, 351.
Phelps, A. V.: 2006, unpublished
Phelps, A. V.: 1990, *J. Phys. Chem. Ref. Data*, **19**(3), 653.
Tatarova, E., Dias, F. M., Ferreira, C. M., Puač, N.: 2007a, *J. Appl. Phys.*, **101**(6), 063306.
Tatarova, E., Dias, F. M., Puač, N., Ferreira, C. M.: 2007b, *Plasma Sources Sci. Technol.*, **16**, S52.

Publ. Astron. Obs. Belgrade No. 84 (2008), 91 - 94 *Contributed Paper*

ELECTRON DETACHMENT OF H^- IONS IN HYDROGEN DISCHARGE

V. D. STOJANOVIĆ[1], Z. M. RASPOPOVIĆ[1], J. V. JOVANOVIĆ[2],
Ž. D. NIKITOVIĆ[1] and Z. Lj. PETROVIĆ[1]
[1] *Institute of Physics, Pregrevica 118, 11080 Zemun, Serbia*
E–mail: zeljka@phy.bg.ac.yu
[2] *Faculty of Mechanical Engineering, Kraljice Marije 16, Belgrade, Serbia*
E–mail: jjovanovic@mas.bg.ac.yu

Abstract. We present results of Monte Carlo simulation (MCS) for detachment rate coefficient for H^- ions in H_2 and for modeling of spatiall dependence of apparent detachment excitation coefficient at very high E/N in a Townsend discharge.

1. INTRODUCTION

H^- transport in discharges has an important role in plasma physics, ionospheric and flame chemistry and astrophysics. The transport is strongly affected by the large detachment cross section in the energy range of interest for those applications.

Negative ions in hydrogen discharges have been of particular interest as a source of ion beams that are to be neutralized to produce fast neutral beams that may be used for heating in fusion devices. However, hydrogen discharges have become interesting recently also for the etching of organic low-k dielectrics (Nagai et al. 2002) and possible conversion of negative ions to fast neutrals may be the origin of charging free plasma etching procedure for organic dielectrics. The mixtures containing H_2 are widely utilized as a working gas in different glow discharges for spectroanalytical sources, laser media, etc.

Goal of the present work is to model H^- transport in Townsend discharges in H_2 when the main source of H^- ion is not dissociative electron attachment (DEA) but heavy particle collisions. One may expect such situations at very high E/N where heavy particle excitation becomes dominant and mean electron energies are considerably larger than DEA threshold.

2. MONTE CARLO SIMULATION

Calculations were performed by using our Monte Carlo technique for electron transport that has been verified against all relevant swarm benchmarks (Raspopović et al. 2000, Petrović and Stojanović 1998). We followed between 10^6 - 10^7 electrons with the initial energy of 1 eV. Gas number density was 3.54 10^{22} m^{-3}. Nonequilibrium conditions for H^- transport were selected from experimental results of (Petrović et al. 1992).

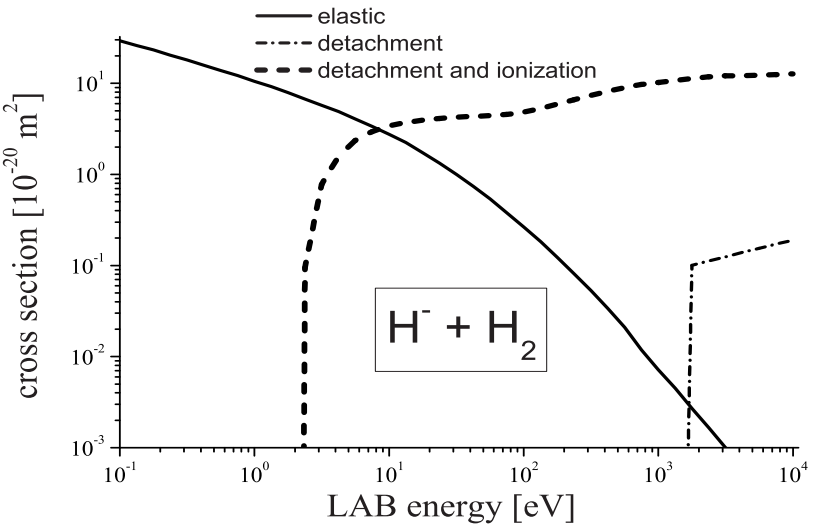

Figure 1: Cross section set for scattering H^- ions on H_2 [3].

We assumed that negative ions are produced in fast H collisions with H_2 according to probability given by Phelps (Phelps 1990) and assuming that H^- after collision is moving in the same direction as that of fast H before collision with H_2. Townsend discharge model at very high E/N based on heavy particles excitation is used (Phelps 2006) to calculate fluxes of H^- ions and production of electrons by electron detachment. H^- production was obtained by introducing cross section for H^- production. We also accounted for surface interaction of H^- ions in the same way as for H^+ neutralization and reflection at the cathode surface (Stojanović et al. 2007). Note that according to the present model, the anode surface is not reflective for fast H and fast H_2. Approximately 60 % of H^- ions are reflected as fast H at the anode surface.

There is a large number of theoretical and experimental cross sections for H^- ions in H_2. The cross sections for H^- in H_2 that have been evaluated and tested have been proposed in the review article of Phelps (1990). That cross section set frpm (Fig. 1) is used in our calculations.

3. RESULTS

In Fig. 2 we show results for drift velocity obtained by Monte Carlo simulation. Splitting of flux and bulk values is a consequence of electron detachment which is one example of nonconservative collisions. Rate coefficients are calculated as a number of collisions per observation time divided by a number of electrons and gas density. In Fig. 3a) we show total rate coefficient and detachment rate coefficient as a function of E/N. Spatial excitation coefficient can be obtained by dividing rate coefficient with drift velocity of ion.

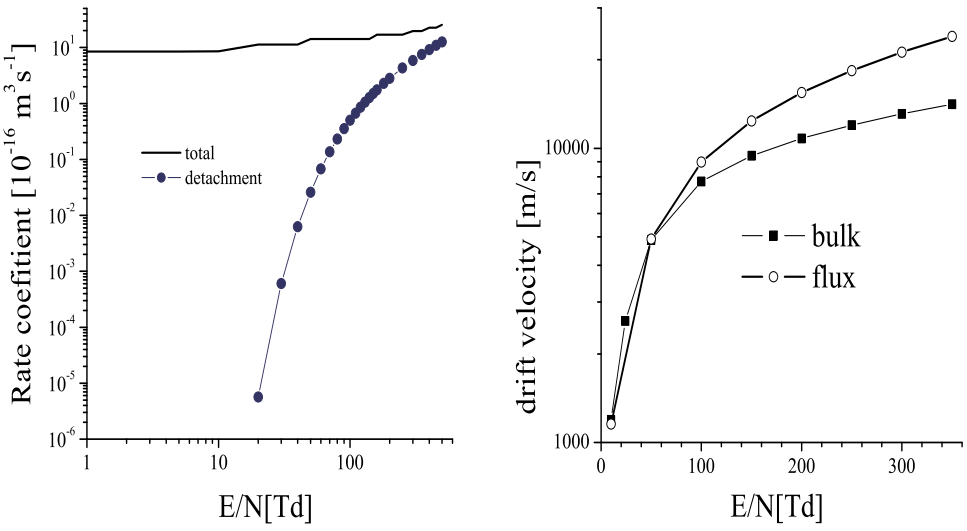

Figure 2: a) Drift velocity, b) Rate coefficient for H^- negative ion in pure H_2 discharge.

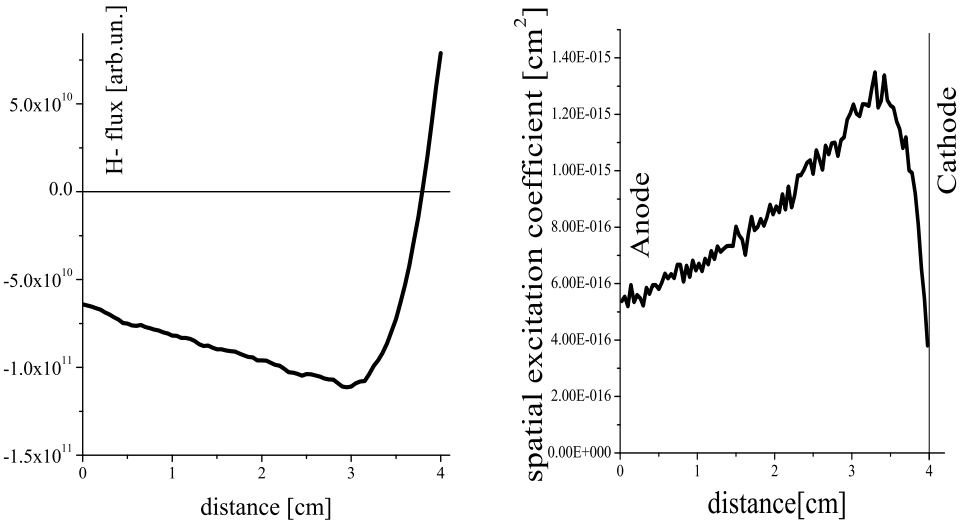

Figure 3: a) Flux of H^- ions in interelectrode space. b) Apparent detachment coefficient for H^- ions in H_2. E/N = 10 kTd, p =145 mTorr.

At very high E/N between two plan-parallel plates H^- ions exhibit non-equilibrium behavior similar to the positive ions (Stojanović et al. 2007). In order to calculate flux of negative ions we sum velocities whenever particle crossed a membrane (Stojanović and Petrović 1998) assuming positive ion fluxes towards cathode. Spatial dependent flux of H^- ion is shown in Fig. 3.a). Maximum flux intensity is obtained in the middle between electrodes while fluxes of opposite sign were obtained close to the cathode and anode. Positive flux close to the cathode is a result of significant production of H^- ions by the fast H neutrals. In the direction of the anode strong detachment rate is reducing intensity of H^- flux. High energy H^- ions are efficiently removed from the H^- beam towards anode. One has to be aware that presented H^- flux consist of two components, one due to the large flux of fast H in the direction of cathode and other due to the acceleration of H^- ions in the direction of the anode.

Apparent detachment coefficient for H^- ions in H_2 is shown in Fig. 3.b). Intensity is placed on the absolute scale by using normalization to the H^- detachment excitation coefficient at the anode (see Stojanović and Petrović 1998).

Total yield of secondary electrons produced in H^- collisions with H_2 is proportional to detachment cross section so one may expect that maximum electron production due to the H^- detachment on H_2 is close to the cathode.

Acknowledgments

Work at the Institute of Physics is supported by the MNRS, under grants 141025.

References

Nagai, H., Takashima, S., Hiramatsu, M., Hori, M., Goto, T.: 2002, *J. Appl. Phys.*, **91**, 2615.
Petrović, Z. Lj., Jelenković, B. M., Phelps, A. V.: 1992, *Phys. Rev. Lett.*, **68**, 325.
Petrović, Z. Lj., Stojanović, V. D.: 1998 *J. Vac. Sci. Technol A*, **16**, 329.
Phelps, A. V.: 1990, *J. Phys. Chem. Ref. Data*, **19**, No. 3., 653.
Phelps A. V.: 2006, unpublished.
Raspopović, Z., Sakadžić, S., Petrović, Z. Lj., Makabe, T.: 2000 *J. Phys. D*, **33**, 1298.
Stojanović, V.D., Petrović, Z. Lj.: 1998 *J. Phys. D: Appl. Phys.*, **31**, 834.
Stojanović, V., Nikitović, Ž, Petrović, Z.: 2007, *Bul. Am. Phys. Soc.*, **52** No. 8.

Publ. Astron. Obs. Belgrade No. 84 (2008), 95 - 98 *Contributed Paper*

TEMPORAL RELAXATION OF ELECTRON SWARMS: THE EFFECTS OF NON-CONSERVATIVE COLLISIONS AND ANGLE BETWEEN THE ELECTRIC AND MAGNETIC FIELDS

S. DUJKO[1,2], R. D. WHITE[2], K. F. NESS[2] and Z. Lj. PETROVIĆ[1]

[1] *Institute of Physics, University of Belgrade, Pregrevica 118, Zemun, Serbia*
E–mail: sasa.dujko@jcu.edu.au

[2] *ARC Centre for Antimatter-Matter Studies, School of Mathematics, Physics and IT, James Cook University, Townsville 4811, QLD, Australia*

Abstract. A multi-term solution of the Boltzmann equation has been developed and used to investigate the temporal relaxation of charged-particle swarms under the influence of electric and magnetic fields crossed at arbitrary angles. We present results for the ionization model of Lucas and Saelee highlighting the explicit influence of the electric and magnetic field strengths, angle between the fields and non-conservative collisions on temporal relaxation characteristics, including the existence of transiently negative electron diffusivity.

1. INTRODUCTION

Studies of transport processes of a swarm of charged particles in neutral gases under the influence of electric and magnetic fields crossed at arbitrary angle is a topic of great interest both as a problem in basic physics and for its potential for application to modern technology. One of the major challenges in these investigations is an accurate representation of temporal relaxation of charged-particle swarms. Relaxation processes of a swarm of charged particles are related to various problems of gaseous electronics such as modeling of non-equilibrium plasma discharges, high-speed switching technique, swarm physics and physics of gas lasers (see Winkler et al. 2002). The knowledge of temporal relaxation is essential for a better understanding of electron-molecule interaction as well as for a better understanding of transient transport phenomena in gases such as transient negative electron mobility (Warman et al. 1985) or transient negative electron diffusivity (White et al. 2008). In addition, to fully appreciate the complex structure of the transport properties in radio-frequency (rf) electric and magnetic fields, a systematic investigation of the temporal relaxation of a swarm of charged particles in dc electric and magnetic fields is required.

We begin this paper with a brief review of multi term theory for solving the Boltzmann equation valid for both electrons and ions in time-dependent electric and magnetic fields. We investigate the temporal relaxation of electron swarms and focus on the effects of non-conservative collisions and angle between the electric and magnetic

fields on temporal relaxation profiles of both the *bulk* and *flux* electron transport properties.

2. THORETICAL METHOD

The behavior of charged particles in neutral gases under the influence of electric and magnetic fields is described by the phase-space distribution function $f(\vec{r},\vec{c},t)$ representing the solution of the Boltzmann equation

$$\frac{\partial f}{\partial t}+\vec{c}\cdot\frac{\partial f}{\partial \vec{r}}+\frac{q}{m}\Big[\vec{E}(t)+\vec{c}\times\vec{B}(t)\Big]\frac{\partial f}{\partial \vec{c}}=-J(f,f_o)\ , \tag{1}$$

where $\vec{r}$ and $\vec{c}$ denote the position and velocity co-ordinates while q and m are the charge and mass of the swarm particle and t is the time. The right-hand side of $J(f,f_o)$, denotes the linear charged particle-neutral molecule collision operator, accounting for elastic, inelastic, and non-conservative (e.g. ionizing or attaching) collisions. The electric and magnetic fields are assumed to be spatially homogeneous and time-dependent. In what follows, we employ a co-ordinate system in which $\vec{E}$ defines the z-axis while $\vec{B}$ lies in the $y-z$ plane, making an angle ψ with respect to the $\vec{E}$.

In the present approach equation (1) is solved by decomposing $f(\vec{r},\vec{c},t)$ in terms of spherical harmonics in velocity space and powers of the gradient operator acting on the number density $n(\vec{r},t)$ in real space, i.e

$$f(\vec{r},\vec{c},t)=\sum_{l=0}^{\infty}\sum_{m=-l}^{l}\sum_{s=0}^{\infty}\sum_{\lambda=0}^{s}\sum_{\mu=-\lambda}^{\lambda}f(lm|s\lambda\mu;c,t)Y_m^{[l]}(\hat{\mathbf{c}})G_\mu^{(s\lambda)}n(\vec{r},t)\ , \tag{2}$$

where $Y_m^{[l]}(\hat{\mathbf{c}})$ denotes the spherical harmonics and $G_\mu^{(s\lambda)}$ denotes the sth application of the gradient operator in irreducible tensor notation. The speed dependence is treated as follows:

$$f(lm|s\lambda\mu;c,t)=\omega(\alpha(t),c)\sum_{\nu=0}^{\infty}F(\nu lm|s\lambda\mu;\alpha(t),t)R_{\nu l}(\alpha(t)c)\ , \tag{3}$$

where $\alpha(t)^2=m/kT_b(t)$ and $\omega(\alpha(t),c)$ is a Maxwellian,

$$R_{\nu l}(\alpha(t)c)=N_{\nu l}\left[\frac{\alpha c}{\sqrt{(2)}}\right]^l S_{l+\frac{1}{2}}^{(\nu)}(\alpha(t)^2c^2/2) \tag{4}$$

$$N_{\nu l}^2=\frac{2\pi^{3/2}\nu!}{\Gamma(\nu+l+3/2)}\ , \tag{5}$$

and $S_{l+\frac{1}{2}}^{(\nu)}$ is a Sonine polynomial. Using the above decompositions of f and implicit finite difference evaluation of time derivatives, the Boltzmann equation is transformed into a hierarchy of doubly infinite coupled inhomogeneous matrix equations for the time-dependent moments. Finite truncation of both the Sonine polynomial and spherical harmonic expansions permits solution of this hierarchy by direct numerical inversion. Having obtained the moments, the transport coefficients and other transport properties may be calculated.

3. RESULTS AND DISCUSSION

In this section we consider the effect of the angle between the electric and magnetic fields on temporal relaxation of the electron transport properties under hydrodynamic conditions. Similar studies have been published previously using the two term approximation for solving the Boltzmann equation (see Loffhagen et al. 1999) and multi term theory for solving the conservative Boltzmann equation (White et al. 2008). We extend these studies by: (i) overcoming the inherent inaccuracies of the two term approximation; (ii) addressing the temporal relaxation of spatial inhomogeneities through a study of the diffusion tensor and (iii) highlighting the explicit effects of non- conservative collisions on temporal relaxation profiles of various transport properties. We consider the temporal relaxation processes of the electrons for the ionization model of Lucas and Saelee (see Lucas and Saelee (1975)). The initial conditions represent the steady state magnetic field free case where the electron swarm is acted on solely by a dc electric field. At time $t = 0$, a magnetic field is switched on while the electric field is left unaltered. The relaxation properties of the electron swarm is monitored as a function of normalized time (Nt). The relaxation process is followed until the steady- state is reached. We consider the electric field strength of 10 Td (1 Td = 10^{-21} Vm^2) and the reduced magnetic field strength of 500 Hx (1 Hx = 10^{-27} Tm^{-3}).

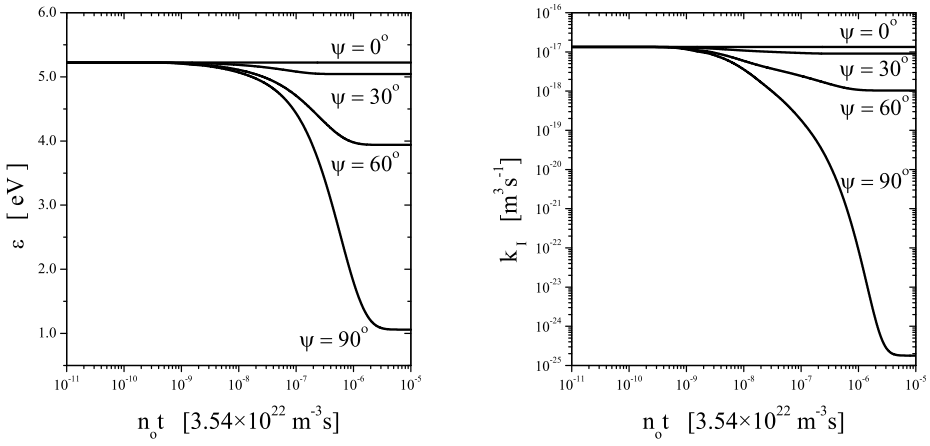

Figure 1: Temporal relaxation of the mean energy and ionization rate as a function of ψ.

In Figures 1 and 2 we show the influence of ψ on the temporal relaxation process associated with the mean energy (ε), ionization rate (k_I), longitudinal drift velocity component (W_z) and diffusion coefficient along the y-direction ($n_0 D_{yy}$). We observe that all transport properties show high sensitivity with respect to ψ. Note that as ψ increases, ε and k_I decrease markedly as a consequence of the magnetic field cooling effects. For parallel fields ($\psi = 0°$), ε, k_I and W_z are not affected by the magnetic field in accordance with the symmetry properties (White et al. 1999). While ε and k_I

exhibit monotonic relaxation for all ψ considered, $n_0 D_{yy}$ shows the same monotonic relaxation profile only for perpendicular fields. For an orthogonal field configuration the Lorentz force does not act in this direction and hence there are no imprinted oscillations on the diffusion coefficient in this direction. On the other hand, for small angles between the fields, the electrons are under the action of Lorentz force producing the oscillatory relaxation profiles which can lead to the transiently negative diffusivity.

It is interesting to consider the differences between the bulk and flux components associated with W_z and $n_0 D_{yy}$. In the early and intermediate stages of the relaxation process, the significant deviations between the bulk and flux components associated with both W_z and $n_0 D_{yy}$ can be observed. This is a clear indication that the initial distribution function and its initial evolution is significantly affected by the ionization processes. However, for an increasing ψ, as the relaxation process proceeds in time, the distinction between the bulk and flux values for W_z diminishes until reaching the steady state where differences between the bulk and flux values are negligible. Similar but not identical behavior shows $n_0 D_{yy}$. These results suggest that due to the complex interplay of the action of the magnetic field and the energy and momentum dissipation of the electrons in collisions, a complicated redistribution of high energetic electrons occurs.

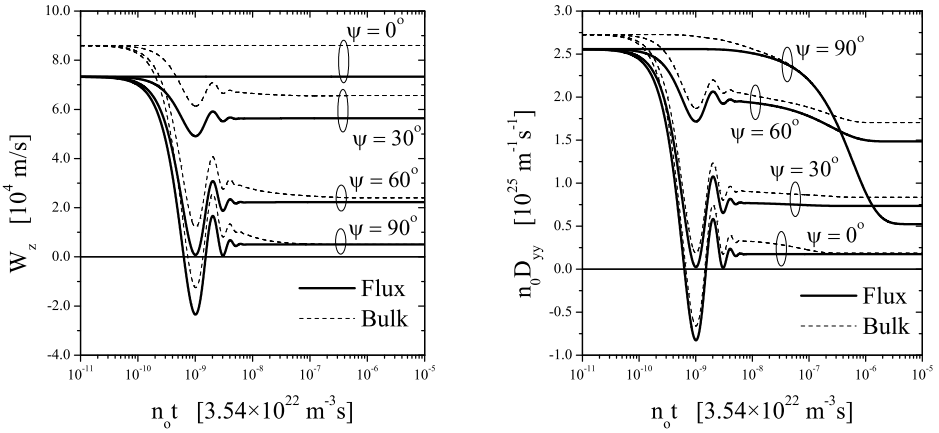

Figure 2: Temporal relaxation of the longitudinal drift velocity component and diagonal element D_{yy} of the diffusion tensor as a function of ψ.

References

Loffhagen, D., Winkler, R.: 1999, *IEEE Trans. Plasma Sci.*, **27**, 2231.
Lucas, J. and Saelee, H. T.: 1975, *J. Phys. D: Appl. Phys.*, **8**, 640.
Warman, J. M., Sowada, U., De Haas, M. P.: 1985, *Phys. Rev. A*, **31**, 1974.
White, R. D., Dujko, S., Ness, K. F., Robson, R. E., Raspopović, Z. M., Petrović, Z. Lj.: 2008, *J. Phys. D: Appl. Phys.*, **41**, 025206.
White, R. D., Ness, K. F., Robson, R. E., Li, B.: 1999, *Phys . Rev. E*, **60**, 2231.
Winkler, R., Loffhagen, D., Sigeneger, F.: 2002, *Appl. Surf. Sci.*, **192**, 50.

Publ. Astron. Obs. Belgrade No. 84 (2008), 99 - 102 *Contributed Paper*

DIELECTRONIC RECOMBINATION MEASUREMENTS OF IRON M-SHELL IONS MOTIVATED BY ACTIVE GALACTIC NUCLEI X-RAY ABSORPTION FEATURES

D. V. LUKIĆ[1,2], M. SCHNELL[1,3], D. W. SAVIN[1], C. BRANDAU[4,5], E. W. SCHMIDT[4], S. BÖHM[4,6], A. MÜLLER[4], S. SCHIPPERS[4], M. LESTINSKY[7,1], F. SPRENGER[7], A. WOLF[7], Z. ALTUN[8] and N. R. BADNELL[9]

[1] *Columbia Astrophysics Laboratory, Columbia University, New York, NY 10027, USA*

[2] *Institute of Physics, 10001 Belgrade, Serbia*

[3] *Carl Zeiss NTS GmbH, Oberkochen D-73447, Germany*

[4] *Institut für Atom- und Molekülphysik, Justus-Liebig-Universität, D-35392 Giessen, Germany*

[5] *Gesellschaft für Schwerionenforschung (GSI), Darmstadt, D-64291, Germany*

[6] *Department of Atomic Physics, Stockholm University, S-106 91 Stockholm, Sweden*

[7] *Max-Planck-Institut für Kernphysik, D-69117 Heidelberg, Germany*

[8] *Marmara University, Istanbul 81040, Turkey*

[9] *Department of Physics, University of Strathclyde, G4 0NG Scotland, UK*

Abstract. XMM-Newton and Chandra observations of active galactic nuclei (AGN) show rich spectra of X-ray absorption lines. These observations have detected a broad unresolved transition array (UTA) between 15-17 Å. This is attributed to inner-shell photoexcitation of M-shell iron ions. Modeling these UTA features is currently limited by uncertainties in the low-temperature dielectronic recombination (DR) data for M-shell iron. In order to resolve this issue, and to provide reliable iron M-shell DR data for plasma modeling, we are carrying out a series of laboratory measurements using the heavy-ion Test Storage Ring (TSR) at the Max-Plank-Institute for Nuclear Physics in Heidelberg, Germany. Currently, laboratory measurements of low temperature DR can only be performed at storage rings. We use the DR data obtained at TSR, to calculate rate coefficients for plasma modeling and to benchmark theoretical DR calculations. At temperatures where these ions are predicted to form in photoionized gas, we find a significant discrepancy between our experimental results and previously recommended DR rate coefficients. Here we report our recent experimental results for DR of Mg-like Fe XV forming Al-like Fe XIV.

1. INTRODUCTION

A new absorption feature between 15-17 Å has been detected in recent Chandra and XMM Newton X-ray observations of active galactic nuclei (AGNs). This has been identified as an unresolved transition array (UTA) due mainly to 2p $\rightarrow$ 3d inner shell absorption in M-shell iron ions. AGN photoionization models generally match

spectral features from abundant second and third row elements but over-predict the average iron ionization stage derived from these UTAs. This is believed to be due to an underestimation of the relevant low temperature dielectronic recombination (DR) rate coefficients for M-shell iron (Netzer 2004; Kraemer et al. 2004). To address this issue we have initiated a series of laboratory DR measurements for iron M-shell ions. Here we report our recent progress.

DR is a two-step recombination process which begins when a free electron collides with an ion, collisionally excites a bound electron in the target, and is simultaneously captured in the Rydberg level n. The electron excitation can be labeled $Nl_j \rightarrow N'l'_{j'}$ where N is the principal quantum number of the core electron, l its orbital angular momentum, and j its total angular momentum. The resulting doubly-excited state lies in the continuum of the recombined system. This intermediate state can either autoionize (the time reverse of the capture process) or decay by emitting a photon. DR is complete when the intermediate state emits a photon, thereby reducing the total energy of the system to below the ionization threshold of the recombined system.

2. HEAVY ION STORAGE RING EXPERIMENTS

At the Test Storage Ring (TSR) of the Max-Plank-Institute for Nuclear Physics in Heidelberg, Germany, electron-ion collision experiments are performed using the merged electron-ion beams technique. Measurements can be carried out for most ions of the cosmically abundant elements H, He, C, N, O, Ne, Na, Mg, Al, Si, S, Ar, Ca, Fe, and Ni. Ions are injected into the ring, stored, and their initial energy spread is reduced using electron cooling. The electrons and ions are merged over a distance of 1.5 m. After cooling, electrons and ions possess the same relative velocity. In contrast to previous experiments, where the electron beam of the cooler was also used as an electron target for recombination experiments, in the present experiments a newly installed separate electron beam (Sprenger et al., 2004) was used. This additional electron beam is hereafter denoted as the electron target.

For the DR measurements the electron energy of the electron target beam was alternatingly chopped between measurement and reference energies by switching the acceleration voltage for the target electron beam accordingly. The number of recombined ions is recorded as a function of the corresponding relative energy. The measured recombination signal, normalized to the primary electron and ion beam intensities, represents the DR cross section times the relative velocity averaged over the relative velocity spread between the electrons and ions (i.e., a merged-beams rate coefficient). There are advantages when a separate electron target is used for recombination measurements. First, the electron cooler can be used continuously for the cooling of the ion beam. Thus, the low velocity and spatial spread of the ion beam is maintained at all times. Second, the electron target was specifically designed for providing an electron beam with a very low initial energy spread (Sprenger et al., 2004). Both of these results in a higher experimental resolving power in the present measurement as compared to previous measurements with the electron cooler.

3. RECENT LABORATORY RESULTS

As an example of our recent results, the measured merged-beams dielectronic recombination rate coefficient for Fe XV forming Fe XIV via $\Delta N = 0$ core electron

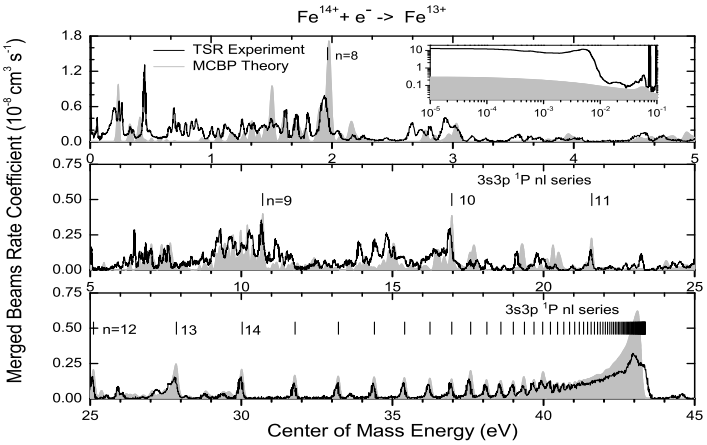

Figure 1: Measured DR resonance spectrum for Fe^{14+} forming Fe^{13+} via $\Delta N = 0$ core electron excitations (thick solid curve). The energy range spans from zero relative energy up to the $3s3p(^1P_1)nl$ DR series limit at 43.6 eV. The gray shaded curve is our calculated multiconfiguration Breit-Pauli (MCBP) results for ground state Fe^{14+}.

excitations (Lukic et al. 2007) is shown in Fig.1 The energy range spans from zero relative energy up to the $3s3p(^1P_1)nl$ DR series limit at 43.6 eV. This exceedingly rich resonance structure shows the importance of DR laboratory measurements and has triggered new theoretical studies. We have convolved our merged-beams DR data with a Maxwellian energy distribution to produce a plasma rate coefficient. As detailed by Schippers et al. (2004), there are three issues in deriving the cross section that require special consideration: the experimental energy spread, the recombination rate enhancement at low energies, and field ionization of high Rydberg states in the storage-ring bending magnets.

In Fig. 2 we compare our experimentally-derived plasma recombination rate coefficient with the DR rate coefficient of Arnaud & Raymond (1992). In the temperature range where Fe XV is expected to form in a photoionized plasma (Kallman & Bautista 2001), the experimentally-derived plasma rate coefficient is several orders of magnitude larger than the presently available theoretical DR data of Arnaud & Raymond (1992). In order to improve agreement between AGN models and observations Netzer (2004) arbitrarily increased the low temperature DR rate coefficient for all the M-shell iron ions. Our experimentally derived rate for Fe XV is still about an order of magnitude larger than his deliberate modification of the theoretical DR data. The estimated rate coefficient of Kreamer at al. (2004) is a factor of over three times smaller. As a reference we show the recommended RR rate coefficient of Arnaud & Raymond (1992). The RR contribution is insignificant relative to DR at all temperatures considered here.

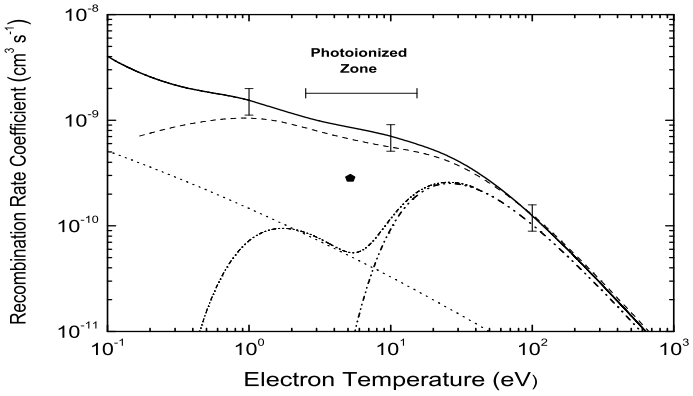

Figure 2: Maxwellian-averaged $3 \rightarrow 3$ DR rate coefficients for Fe XV forming Fe XIV. The thick solid curve represents our experimentally derived rate coefficient plus the theoretical estimate for unmeasured contributions due to capture into states with $n > 80$. The error bars show our estimated total experimental uncertainty of $\pm 29\%$. Also shown is the recommended DR rate coefficient of Arnaud & Raymond (1992; thick dot-dot-dashed curve) and its modification by Netzer (2004; thin dot-dot-dashed curve). The filled pentagon at 5.2 eV represents the estimated rate coefficient from Kraemer et al. (2004). The dashed curve shows our MCBP calculations for $n_{max} = 1000$. As a reference we show the recommended RR rate coefficient of Arnaud & Raymond (1992; dotted curve). The horizontal line shows the temperature range over which Fe XV is predicted to form in photoionized gas (Kallman & Bautista 2001).

4. CONCLUSION

We are in the process of carrying out DR measurements for other M-shell iron ions. As they become available, we recommend that these experimentally-derived plasma rate coefficients be incorporated into future models of AGN spectra in order to arrive at more reliable results.

This work has been supported in part by NASA, the German Federal Ministry for Education and Research, and the German Research Council under contract no. Schi 378/5.

References

Arnaud, M., Raymond, J.: 1992, *Astrophys. J.*, **398**, 394.
Kallman, T. R., Bautista, M.: 2001, *Astrophys. J. Suppl. Series*, **133**, 221.
Kraemer, S. B. et al.: 2004, *Astrophys. J.*, **604**, 556.
Lukić, D. V. et al.: 2007 *Astrophys. J.*, **664**, 1244.
Netzer, H.: 2004, *Astrophys. J.*, **604**, 551.
Schippers S. et al.: 2004, *Astron. Astrophys.*, **421**, 1185.
Sprenger F. et al.: 2004, *Nucl. Instrum. Methods A*, **532**, 298.

Publ. Astron. Obs. Belgrade No. 84 (2008), 103 - 106 *Contributed Paper*

MODELING OF HIGH E/N IN MIXTURES OF CF_4 AND ITS RADICALS

Ž. D. NIKITOVIĆ, V. D. STOJANOVIĆ and Z. Lj. PETROVIĆ
Institute of Physics, Pregrevica 118, 11080 Zemun, Serbia
E–mail: zeljka@phy.bg.ac.yu

Abstract. We present transport coefficients for electrons in mixtures of CF_4 with its radicals for ratios of the electric field to the gas number density E/N from 1 Td to 1000 Td (1 Td=10^{-21} Vm^2). Our analysis of non-conservative collisions revealed a range of E/N where electron attachment introduced by radicals significantly changes electron kinetics obtained for pure CF_4 gas. Results are obtained by using simple solutions for Boltzmann's equation.

1. INTRODUCTION

Carbon tetrafluoride is one of the most often used gases in todays semiconductor industry. It is primarily applied for etching of substrates of different materials where the most important is SiO_2 . It is also for formation of fluorinated polymer films. CF_4 has an important role in technological applications such as development of gaseous circuit breakers (Hunter et al. 1985) and for development of particle detectors (James et al. 1980, Kopp et al. 1982, Yamashita et al. 1992). CF_4 belongs to freons that unfortunately significantly affect global warming of our planet. Its atmospheric halftime estimated to over 50 000 years and it has a large potential to global warming. Because of that it is important to continue research related to removal of this freon from the atmosphere by applying gas discharges (e.g. by focused microwave radiation (Bzenić et al. 1995). CF_4 has advantage with respect to other gases primarily due to the low level of toxicity and relatively low cost. At room temperature it has low reactivity in its electronic ground state. Because no stable excited states exist it dissociates in plasma treatments where it becomes a source of reactive particles (ions, neutrals, radicals). In CCP (capacitively coupled plasma) (Nakano and Samukawa 1999) and ICP (inductively coupled plasma) (Hioki et al. 2000) etching reactors dominant reactive radical is CF_2. Recent advances in measurements and calculations of electron scattering cross sections (Rozum et al. 2006) on CF_4 radicals in the energy domain relevant to non-equilibrium plasmas have shown that probabilities for many processes are significantly larger than for CF_4 itself. It is even likely that CF_2 radical may reclaim a dominant role for certain processes in plasma. It is now possible to build more precise quantitative picture about rate coefficients in realistic gas mixtures and improve control of radical concentration in order to optimize these processes. In this work we calculated electron transport coefficients for mixtures of CF_4/CF_2 in order

to estimate radical concentrations at which dominant radical influence is achieved in collisions of electrons with CF_4.

2. MONTE CARLO CODE AND TWO TERM APPROXIMATION

A description of electron kinetics in non-equilibrium plasma modeling necessarily includes calculation of transport coefficients which are usually based on compilations of cross sections from different sources (Kurihara et al. 2000). Requirement to establish reliable transport coefficients for CF_4 plasmas is especially demanding for conditions that include many reactive species. Free radical species, such as CF_y (y = 1–3) and fluorine atoms, play important but complex roles in plasma processing. We calculated electron transport coefficients for pure CF4 and in X/CF_4 mixtures (X= F, F_2, CF, CF_2 and CF_3) for the conditions overlapping with those found in plasma technologies for semiconductor production. Set of cross sections for CF, CF_2 and CF_3 is based on the work of Rozum et al. (2006). Set of cross sections for molecular fluorine is from Morgan (1992) and for atomic fluorine is according to Gudsmundsson et al. (2002). We calculated attachment and ionization rate coefficients for 0.01 %, 0.1 %, 1 % and 10 % of the radical species X in CF_4. Transport coefficients are obtained by using numerical solution of Two Term approximation to Boltzmann equation (Morgan et al. 1990).

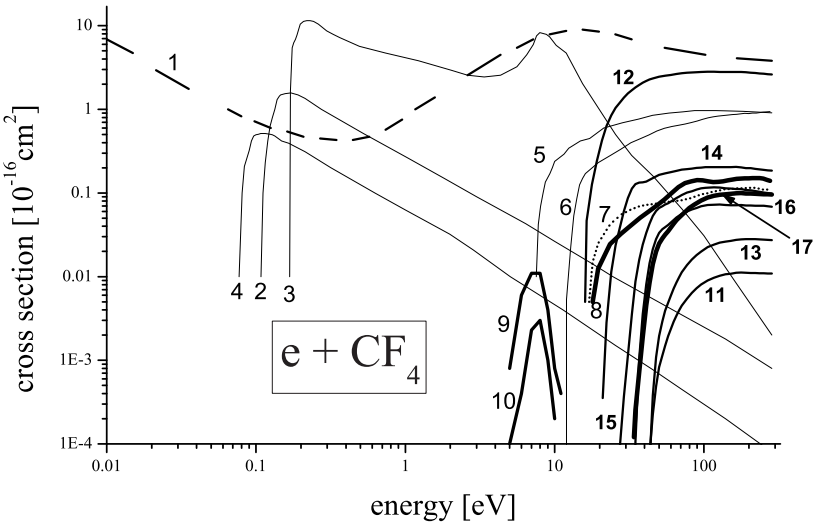

Figure 1: Electron impact cross sections for scattering on CF_4 (1 - elastic momentum transfer, 2 - vibrational excitation v=1, 3 - vib. excitaton v=3, 4 - vib. excitation v=4, 5 - electron excitation, dissociation to products CF_3 (6), CF_2 (7), CF (8), 9 - dissociative electron attachment(DEA) (F^-), 10 - DEA (CF_3^-), 11 - CF_3^+ + F + 2e (ionization), 12-17 other channels of ionization.

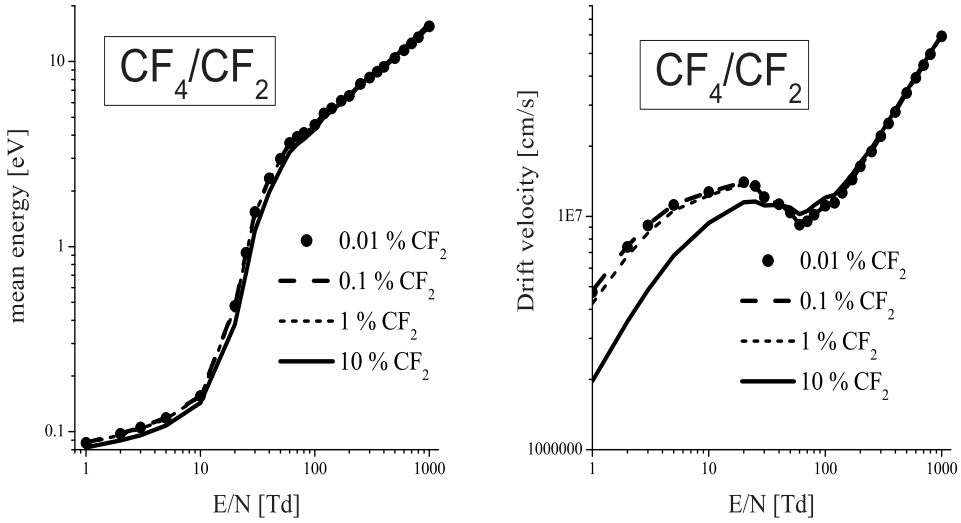

Figure 2: Mean energy and drift velocity as a function of E/N for CF_4/CF_2 mixture.

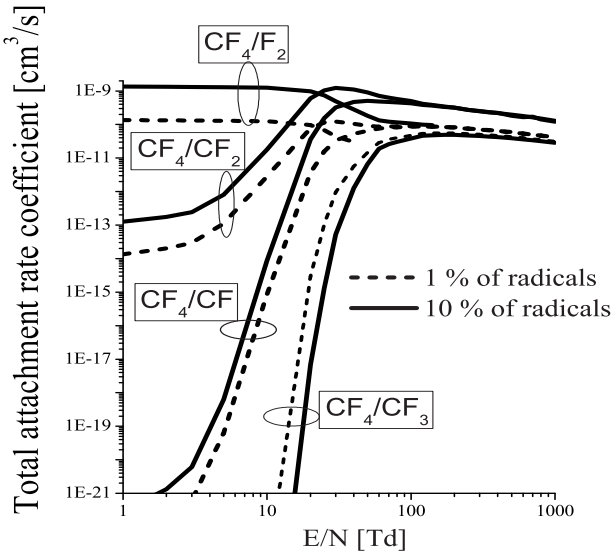

Figure 3: Comparison of total attachment rate coefficient for 1 % s and 10 % of radicals.

3. RESULTS AND DISCUSSION

The basic cross sections of pure CF_4 were used from Kurihara et al. (2000) and are modified (Donko 2006) in order to include production of CF_3^- ions. Complete cross section set is shown in Fig. 1.

Electron mean energy and electron drift velocity in mixtures CF_4/CF_2 as a function of E/N are shown in Fig. 2. Effect of adding less than 0.01 %, 0.1 %, 1 % and 10 % is significant only at the level of few percent.

Total rate coefficient for electron attachment, obtained as a sum of electron attachment contributions to CF_4 and one of its radicals according to the assumed abundance is shown in Fig. 3.

Large variations of attachment coefficient are observed below 10 Td even for concentrations of added radicals below 1 %. In these conditions one should not expect large changes in electron kinetics. Adding CF_3 radical in mixture with CF_4 decreases total attachment rate coefficient due to the increased rate for elastic collisions and lack of attachment for the radical. Total attachment rate coefficient for both CF_2 and CF radicals in 10 % mixture with CF_4 are quite similar in magnitude for $E/N > 100$ Td which is the result of CF_4 ionization.

Acknowledgments

Work at the Institute of Physics is supported by the MNRS, under grants 141025.

References

Bzenić, S., Manola, S. S., Petrović, Z. Lj.: 1995, Proceedings of the 25th European Microwave Conference, Swanley Nexus, Bologna, Italy, 856.

Donko, Z.: 2006, personal communication.

Gudmundsson, J. T.: 2002, *J. Phys. D: Appl. Phys.*, **35**, 328.

Hioki, K., Hirata, K., Nakano, N., Petrović, Z. Lj., Makabe, T.: 2000, *J. Vac. Sci. Technol. A*, **18**, 864.

Hunter, S. R, Carter, J. G., Christophorou, L. G.: 1985, *J. Appl. Phys.*, **58**, 3001.

James, D. R., Christophorou, L. G., Mathis, R. A.: 1980, "New unitary and multicomponent gaseous dielectrics" in Gaseous Dielectrics II (ed. Christophorou, L. G.) Pergamom, New York, 115.

Kopp, M. K., Valentine, K. H., Christophorou, L. G., Carter, J. G.: 1982, *Nucl. Instrum. Methods*, **201**, 395.

Kurihara, M., Petrović, Z. Lj., Makabe, T.: 2000, *J. Phys. D: Appl. Phys.*, **33**, 2146.

Morgan, W. L.: 1992, *Plasma Chemistry and Plasma Processing*, **12**, 449.

Morgan, W. L., Penetrante, B. M.: 1990, *Computer Physics Communications*, **58**, 127.

Nakano, T., Samukawa, S.: 1999, *J. Vac. Sci. Technol. A*, **17**, 686.

Rozum, I., Limao-Vieira, P., Eden, S., Tennyson, J., Mason, N. J.: 2006, *J. Phys. Chem. Ref. Data*, **35**, No. 1, 267.

Yamashita, T., Kurashige, H., Morii, M. M., Nakamura, T. T., Nomura, T., Sasao, N., Shibata, K., Fukushima, Y., Ikegami, Y., Kobayashi, H., Taniguchi T.: 1992, *Nucl. Instrum. Methods Phys. Res. A*, **317**, 213.

Publ. Astron. Obs. Belgrade No. 84 (2008), 107 - 110 *Contributed Paper*

SELE HEM: ADJUSTING THE PARAMETERS

D. ŠEVIĆ[1], A.R. MILOSAVLJEVIĆ[1], I. ČADEŽ[2]
and B. P. MARINKOVIĆ[1]
[1] *Institute of Physics, Belgrade, Serbia*
E–mail: sevic@phy.bg.ac.yu
[2] *Institut Jožef Stefan, Ljubljana, Slovenia*

Abstract. This paper presents preliminary results of adjusting parameters of Hypocycloidal Electron Monochromator in Stepwise Electron Laser Excitation (SELE) experiment at the Institute of Physics, Belgrade.

1. INTRODUCTION

In our SELE experiment the cylindrical electron monochromator (see Marinković et al. 1992) is utilized for low energy (0.3-20 eV) electron beam formation. Crossed magnetic and electric field in cylindrical symmetry are used to select the electrons having energy in the narrow interval. For this kind of monochromator, the uniform magnetic field is one of the basic requirements. Because of the large range (20 cm) in which uniform magnetic field is required in our experiment, the most common solution of using Helmholtz pair (because of large dimensions of coils) has been abandoned. Our five-coil system is described in Marinković et al. 2006 and Šević et al. 2008.

In this paper we describe preliminary results of adjusting the parameters of our cylindrical monochromator. Simultaneously with assembling the apparatus, we did SIMION simulations to have some insight into behavior of electrons, i.e. to have some starting values of electron optics voltages. We have obtained the electron beam in the target area by playing it by ear, i.e. optimizing the HEM electrodes voltages by manually turning the knobs, guided by readouts of digital electrometer measuring the beam current. Magnetic field was 30G, obtained by setting coil currents to the values from numerical calculation and verified by measurement with Gaussmeter. Slight tunning of currents with respect to the predicted values was needed in order to maximize output beam current.

Our monochromator was called cylindrical (cylindrical trochoidal electron monochromator, CTEM, Marinković et al. 1992), because of geometry of the electrodes. In (Smialek at al. 2005) and (Smialek at al. 2007) the same type of monochromator is called hypocycloidal electron monochromator (HEM) because of the shape of electron trajectories. From now on, we will use the name HEM, also. First, we will shortly review the theoretical basics of HEM as presented in Smialek at al. 2005. Then, we

will present some preliminary results of our SIMION simulations of HEM. Finally, we will describe some of the first adjustments of monochromator.

2. THE CYLINDRICAL ELECTRON MONOCHROMATOR

In the HEM, the electrostatic field is produced by two cPoaxial cylindrical electrodes, the inner and outer electrodes with radii R_1 and R_2, respectively. The magnetic field is directed along the axis of the HEM. Potential distribution is:

$$V(r) = V_0 - \frac{V_1 - V_2}{\ln(R_2/R_1)} \ln(2r/(R_1 + R_2) \tag{1}$$

The electrons drift in HEM describing hypocycloidal trajectories on the surface perpendicular to the direction of the magnetic field. The radius of the hypocycloids is about two orders of magnitude smaller than the mean radius $R_0 = (R_1 + R_2)/2)$. The electrons drift with a approximately constant velocity:

$$v_d \approx \frac{E_r}{B} \tag{2}$$

where $E_r = (V_1 - V_2)/(r \ln(R_2/R_1))$ is electrostatic field, and B is the magnetic field strength.

At the exit plane of the monochromator the electrons are deflected by an angle ϕ_d:

$$\phi_d = \frac{LE_r}{Brv_z} \tag{3}$$

where L is HEM length, and v_z is constant velocity component along the axis of the HEM.

For optimum energy resolution of the HEM, as shown by Smialek at al. 2005, a higher polarization potential should be applied to the inner cylindrical electrode.

In our apparatus, emitting cathode is a thoria-coated iridium filament. Elements of our cylindrical monochromator have names as follows. Potential of the filament center is denoted by V_n. Filament housing is denoted by V_f. First beam forming electrode is V_k. Beam is then focused by electrodes S_1, S_2 and S_3. Entrance and exit electrodes are N_1 and N_2, respectively. Between N_1 and N_2 are cylindrical electrodes V_1 and V_2. Length of cylindrical electrodes is 126 mm, inner and outer radii are 8.8 mm and 22 mm, respectively. Just before exit aperture on N_2, there is an electrode S_p for collecting nonmonochromated electrons.

Set of the starting electrode voltages was obtained by SIMION simulations.

An illustration of electron trajectories simulation is presented in Fig 1.

3. ADJUSTING THE MONOCHROMATOR

After "guessing" the initial values as determined by SIMION simulations, fine adjustments were made by tuning the electrode voltages.

Electron optics electrode voltages, after optimization, are presented in Table 1.

Two sets (for two combinations of cylindrical electrode voltages) of ilustrative experimental results are presented in Table 2. ICC and OCC denote inner and outer coil current, respectively. IEV and OEV denote voltages of inner and outer cylindrical electrode of HEM. Electron beam current is denoted by EBC. Beam is collected

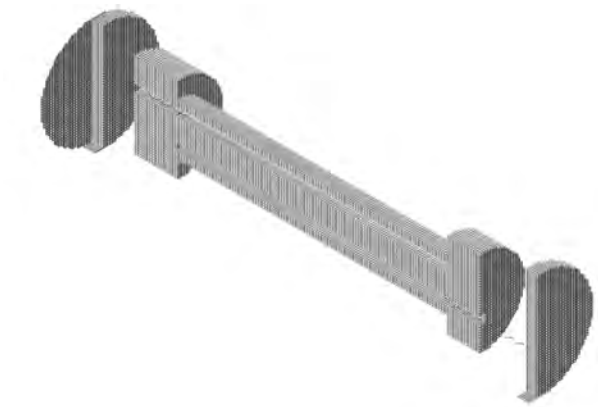

Figure 1: An illustration of electron trajectories simulation.

Table 1: Electron optics electrode voltages.

electrode	voltage [V]
V_n	-13.4
V_f	4.7
V_k	-12.69
S_1	1.32
S_2	5.75
S_3	-7.46
N_1	5.63
N_2	-1.89
S_P	-1.26
V_1	-10.44
V_2	-11.40

by a round electrode (diameter 38 mm) placed in the target area. The electrode is grounded via digital electrometer. All voltages are measured with respect to ground.

Determination of electron beam energy resolution using retarding potentials method is planned in near future.

Table 2: Parameters of HEM and electron beam current(EBC).

IEV [V]	OEV [V]	OCC [A]	ICC [A]	EBC [100pA]
-10.44	-11.40	0.95	1.48	8.5
-10.44	-11.40	0.95	1.57	9.5
-10.44	-11.40	0.95	1.66	10.5
-10.44	-11.40	0.95	1.76	10.5
-10.44	-11.40	0.95	1.85	10.6
-10.44	-11.40	0.95	1.82	10.2
-10.44	-11.40	0.95	1.90	10.1
-10.44	-11.40	0.95	2.00	10.0
-10.44	-11.40	0.95	2.30	8.0
-2.95	-2.10	0.95	0.87	4.9
-2.95	-2.10	0.95	1.01	6.0
-2.95	-2.10	0.95	1.12	8.8
-2.95	-2.10	0.95	1.23	9.4
-2.95	-2.10	0.95	1.41	9.8
-2.95	-2.10	0.95	1.51	11.3
-2.95	-2.10	0.95	1.70	8.0
-2.95	-2.10	0.95	1.80	7.5
-2.95	-2.10	0.95	1.90	5.5
-2.95	-2.10	0.95	2.01	4.6

4. CONCLUSION

We presented the preliminary results of adjusting parameters of our SELE HEM. Although it is relatively easy to obtain the electron beam, the problem of optimization of its characteristics faces us in near future. First of all, electron beam energy resolution should be determined using retarding potential method.

Acknowledgments

This work has been carried out within project 141011 financed by Ministry of Science of Republic of Serbia and bilateral project Serbia - Slovenia 2008-2009 ("Electron induced fragmentation of organic molecules and small hydrocarbons").

References

Marinković, B., Wang, P., and Gallagher, A.: 1992, *Physical Review A*, **46**, No. 5, 2553.
Marinković, D, Milosavljević, A, Marušnik, D. and Šević, D.: 2006, Proceedengs of the 23rd SPIG, August 28 - September 1, Kopaonik, Serbia, pp. 97-100.
Šević, D., Milosavljević, A., Marinković, B.: 2008, Proceedengs of the 1st CEAMPP, 15- 18 May, Zaječar, Serbia, pp. 45-46.
Smialek, M., Dydycz, A., Mielewska, B., Feyer, V. and Zubek, M.: 2005, *Measurment Science and Technology*, **16**, 2275.
Smialek, M., Mielewska, B. and Zubek, M.: 2007, *Radiation Physics and Chemistry*, **76**, 599.

Publ. Astron. Obs. Belgrade No. 84 (2008), 111 - 114 *Contributed Paper*

CHARACTERISTIC FEATURE OF $2p \rightarrow 2s$ TRANSITION IN SPHERICALLY CONFINED HYDROGEN ATOM

Lj. STEVANOVIĆ[1] and K. D. SEN[2]

[1] *Department of Physics, Faculty of Sciences and Mathematics, University of Niš, Niš, Serbia*
E–mail: ljstevanovic@junis.ni.ac.yu

[2] *School of Chemistry, University of Hyderabad, Hyderabad 500 046, India*
E–mail: sensc@uohyd.ernet.in

Abstract. The electronic transition $2p \rightarrow 2s$ absent in the free hydrogen atom due to the Coulomb degeneracy becomes feasible when the atom is embedded inside a spherical cavity with impenetrable walls. We show, for the first time, that the oscillator strength corresponding to this transition in the confined state attains its maximum value at the characteristic confinement radius of 2 a.u. at which simultaneous degeneracy also takes place between the confined $[ns, (n+1)d]$ levels with $n \geq 2$.

1. INTRODUCTION

Model of spatially confined hydrogen atom (CHA in the text bellow) was introduced in physics in order to simulate the high pressure effects on dipole polarizability of hydrogen gas (Michels et al. 1937). Over the years, this model has been applied in many diverse fields of physics and chemistry. For example, the model of hydrogen atom confined in a hard spherical box was used in the study of partially ionized plasma (Harris et al. 1960) as well thermodynamic properties of non-ideal gases (Graboske et al. 1969) and atoms embedded in neutral media (Tabbert et al. 1997, Saha et al. 2002). Other important applications of confined CHA model deal with the study of hydrogenic impurity in semiconductor nanostructures like quantum dots, quantum wells and quantum well wires (see e.g. Moriarty 2001). An exhaustive account of diverse applications of the CHA model can be found in the available review articles (Jaskólski 1996, Dolmatov et al. 2004).

As compared to the unconfined (free) hydrogen atom, UHA, the superimposition of spatial confinement potential significantly changes the structure of the eigen-spectrum and other properties of the CHA. Hydrogen atom when placed at the center of the spherical well with impenetrable walls, does not exhibit any Coulomb degeneracy of levels. As a consequence of such confinement, the (nl) states with the same quantum number n and $l = 0, 1, \ldots, n-1$ are separated on the energy scale. Thus, newer allowed transitions appear in the CHA absorption spectrum which are generally absent in the UHA.

In this paper we focus on one such transition in the CHA given by $2p \rightarrow 2s$ transition and report the corresponding transition energy and oscillator strength as a function of the confinement radius. Our aim is to examine if there exists any characteristic feature in the variation of the chosen spectroscopic properties of the CHA. The paper is organized as follows. In section 2 the theoretical model is outlined. In section 3 we present the results for oscillator strength of $2p \rightarrow 2s$ transition and half-lifetime of the $2s$ state. Section 4 closes the paper summarizing the main results.

Atomic units ($m_e = e = \hbar = 1$) are used throughout the paper.

2. THEORY

In the CHA model considered here, the atomic nucleus is placed at the center of spherically symmetric potential well with impenetrable walls. Accordingly, electronic potential is given by

$$V(r) = \begin{cases} -\frac{1}{r}, & r < r_0 \\ \infty, & r \geq r_0 \end{cases} . \tag{1}$$

Spherical symmetry of the potential (1) allows factorization of the wave function into the radial and angular parts: $\Psi(\mathbf{r}) = \frac{1}{r} P_{nl}(r) Y_{lm}(\theta, \phi)$. Radial wave function is the solution of the radial Schrödinger equation

$$\left\{ -\frac{1}{2} \left[\frac{d^2}{dr^2} - \frac{l(l+1)}{r^2} \right] + V(r) \right\} P_{nl}(r) = 0 \tag{2}$$

with the imposed Dirichlet boundary condition

$$P_{nl}(r_0) = 0 \tag{3}$$

and requirement of the condition at $r = 0$ given by $P_{nl}(0) = 0$.

3. RESULTS AND DISCUSSION

3. 1. OSCILLATOR STRENGTH FOR $2p \rightarrow 2s$ TRANSITION

The required eigenvalue problem (2)-(3) is solved applying Numerov-Cooley method (Numerov 1933, Cooley 1961) with given accuracy $\epsilon = 1 \cdot 10^{-9}$ and 50000 grid points at every confinement radius value r_0. For more details on the method and avoiding the singularity at the origin see e.g. (Jensen 1983). Oscillator strength for $2p \rightarrow 2s$ transition in dipole approximation is given by

$$f = \frac{2}{3} \Delta E S_{2p \rightarrow 2s} , \tag{4}$$

where

$$S_{2p \rightarrow 2s} = \left| \int_0^{r_0} r P_{2p}(r) P_{2s}(r) dr \right|^2 \tag{5}$$

and ΔE is a transition energy

$$\Delta E = E_{2s} - E_{2p} . \tag{6}$$

All the spectroscopic properties stated above are the functions of confinement radius.

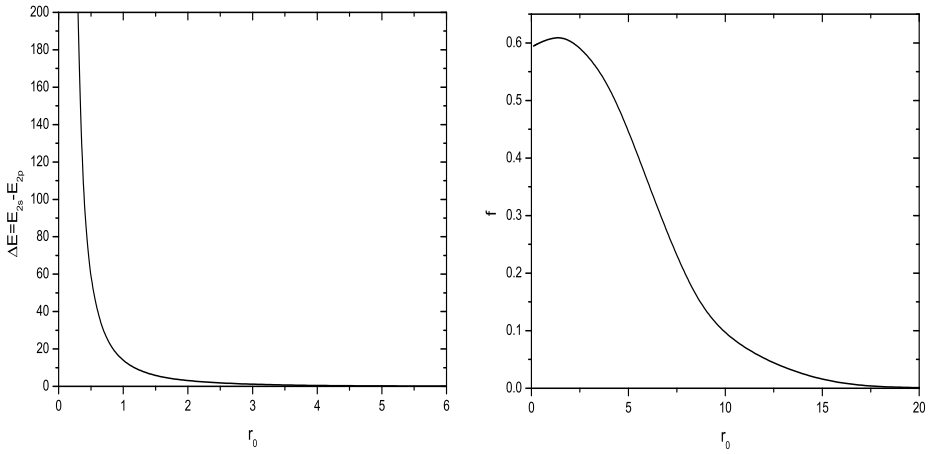

Figure 1: Transition energy (left panel) and oscillator strength (right panel) of the $2p \rightarrow 2s$ transition as a function of confinement radius.

Our results for transition energy and oscillator strength are shown in Figure 1. It is evident that the transition energy ΔE is a monotonically decreasing function of r_0.In the limit of infinite confinement radius the CHA energy levels approach the UHA levels, and $2s$ and $2p$ states become degenerate. In this limit, as given by (4), the oscillator strength approaches zero. It is interesting to note that this quantity is increasing function at small r_0 values which passes through a maximum value and then decreases at larger values of confinement radius. This behavior is reasonable since transition energy is decreasing function and quantity $S_{2p\rightarrow 2s}$ is increasing function of r_0. The oscillator strength maximal value is at $r_0 = 2$, the same value at which the simultaneous degeneracy occurs (see e.g. Scherbinin et al. 1997) between the confined states given by the pairs $[ns, (n+1)d]$ with $n \geq 2$.

3. 2. HALF-LIFETIME OF $2s$ STATE

In dipole approximation $2s$ state of the UHA has an infinite lifetime due to the fact that (1) transition $2s \rightarrow 1s$ is forbidden in this approximation, (2) transition $2s \rightarrow 2p$ is absent due to Coulomb degeneracy (transition energy is zero). In the CHA, the first transition is still not allowed, but the second transition becomes feasible giving the way of $2s$ state radiative decay. Half-lifetime τ (in s) of the CHA $2s$ state is determined by

$$\tau = \frac{1}{P_{2s\rightarrow 2p}}\,, \tag{7}$$

where transition probability for spontaneous emission $2s \rightarrow 2p$ is given by

$$P_{2s\rightarrow 2p} = C(\Delta E)^3 S_{2s\rightarrow 2p}\,. \tag{8}$$

Here, C is a constant $C = 2.1417 \cdot 10^{10} s^{-1}$ and $S_{2s\rightarrow 2p}$ and ΔE are given by the same expressions (5) and (6) as for absorption $2p \rightarrow 2s$.

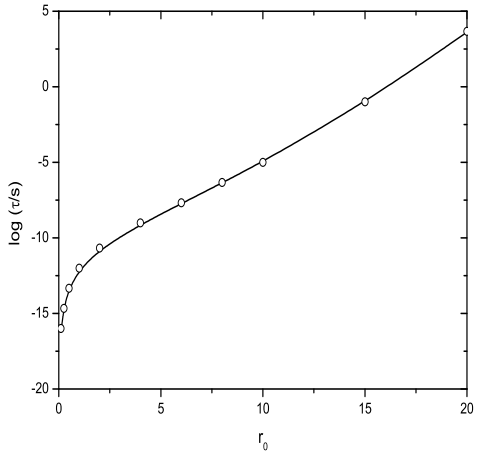

Figure 2: Half-lifetime of $2s$ state of CHA as a function of confinement radius. Line: present calculation, open circle (○): results from (Goldman et al. 1992).

In Figure 2 the $\log \tau$ is shown as a function of confinement radius r_0 together with the other available estimates (Goldman et al. 1992).

4. SUMMARY

The oscillator strength for $2p \rightarrow 2s$ absorption transition in the CHA at different confinement radius values is reported for the first time in the literature. A characteristic feature showing its maximum value at $r_0 = 2$ has been demonstrated numerically. It is of interest to examine the oscillator strength for other transitions $(nl) \rightarrow (n, l \pm 1)$, not appearing in the UHA, and check if the similar behavior is also displayed therein.

References

Cooley, J. W.: 1961, *Math. Comp.*, **15**, 363.
Dolmatov, V. K., Baltenkov, A. S., Connerade, J.-P., Manson, S. T.: 2004, *Rad. Phys. Chem.*, **70**, 417.
Goldman, S., Joslin, C.: 1992, *J. Phys. Chem.*, **96**, 6021.
Graboske, H. C., Harwood, Jr., D. J., Rogers, F. J.: 1969, *Phys. Rev.*, **186**, 210.
Harris, G. M., Roberts, J. E., Trulio, J. G.: 1960, *Phys. Rev.*, **119**, 1832.
Jaskólski, W.: 1996, *Phys. Rep.*, **271**, 1.
Jensen, P.: 1983, *Comp. Phys. Rep.*, **1**, 1.
Michels, A., De Boer, J., Bijl, A.: 1937, *Physica*, **4**, 271.
Moriarty, P.: 2001, *Rep. Prog. Phys.*, **64**, 297.
Numerov, B.: 1933, *Publs. Observatoire Central. Astrophys. Russ.*, **2**, 188.
Saha, B., Mukherjee, P. K., Diercksen, G. H. F.: 2002, *Astron. Astrophys.*, **396**, 337.
Scherbinin, A. V., Pupyshev, V. I., Ermilov, A. Yu.: 1997, Physics of Clusters, pp. 273-292, World Scientific, Singapore.
Tabbert, B., Günther, H., Zu Putlitz, G.: 1997, *J. Low Temp. Phys.*, **109**, 653.

Publ. Astron. Obs. Belgrade No. 84 (2008), 115 - 118 *Contributed Paper*

THEORETICAL STUDY OF BOUND STATES SUPPORTED BY THE $I'^1\Pi_g$ OUTER POTENTIAL WELL IN HD

T. P. GROZDANOV[1] and R. McCARROLL[2]

[1] *Institute of Physics, P.O. Box 57, 11001 Belgrade, Serbia*
E–mail: tasko@phy.bg.ac.yu

[2] *Laboratoire de Chimie Physique-Matière et Rayonnement, (UMR 7614 du CNRS), Université Pierre et Marie Curie, 75231-Paris Cedex 05, France*
E–mail: mccarrol@ccr.jussieu.fr

Abstract. The bound states of HD close to the n=2 dissociation limit are strongly affected by non-adiabatic coupling which breaks the gerade-ungerade (g-u) symmetry in HD. The coupled-states formalism is used to describe loosely bound rovibrational states in the $I'^1\Pi_g$ outer potential well. For f -parity states it was sufficient to take into account the constant asymptotic g-u coupling with $C^1\Pi_u$ state. In the case of e -parity states, besides the g-u coupling, the asymptotically strongest rotational coupling with $GK^1\Sigma_g^+$ was also taken into account. The calculated binding energies are in excellent agreement with data obtained in XUV+IR multistep laser experiments.

1. INTRODUCTION

The states close to the $n = 2$ dissociation limit of HD are particularly interesting because they are markedly different from their homonuclear analogues. There are actually two different dissociation limits corresponding to H($n = 1$)+D*($n = 2$) and H*($n = 2$)+D($n = 1$), separated by an energy gap of 22.38 cm^{-1}. One of the Born-Oppenheimer (BO) potentials from the $n = 2$ manifold is the $II'^1\Pi_g$ double well potential. Recently, very precise and systematic measurements of the rovibrational states corresponding to the outer well ($I'^1\Pi_g$) have been reported as results of XUV+IR multistep laser experiments (De Lange et al. 2000, Pielage et al., 2002). In order to interpret their results the authors have constructed a semi-empirical potential (De Lange et al., 2000) which incorporates the effects of the nonadiabatic g-u coupling with the nearby lying $C^1\Pi_u$ state. The aim of the present work is to go beyond the notion of a single effective potential by considering the minimal sets of coupled BO states necessary to accurately describe bound states of the $I'^1\Pi_g$ potential well.

Atomic units are used throughout, except when explicitly stated.

2. HAMILTONIAN AND COUPLED EQUATIONS

We neglect the spin-orbit and hyperfine interactions as they are much smaller than g-u coupling, concentrate on singlet states of HD and therefore ignore the spin variables. After the separation of the center-of-mass motion, introduction of the internuclear vector $\vec{R} = \vec{R}_D - \vec{R}_H$ with spherical polar coordinates $\{R, \theta, \phi\}$ and using the relative position vectors $\vec{r}_1$ and $\vec{r}_2$ of the electrons with respect to the geometric center between the nuclei, the non-relativistic Hamiltonian of HD molecule is :

$$H = T_R + H_{gu} + H_{mp} + H_e, \tag{1}$$

where T_R, the nuclear kinetic energy term and H_{gu}, the g-u coupling (cross derivative) term are

$$T_R = -\frac{1}{2\mu}\nabla_R, \quad H_{gu} = -\frac{1}{2\mu_a}\nabla_R \cdot \sum_{j=1,2} \nabla_j, \tag{2}$$

H_{mp}, the mass polarization term and and H_e, the (BO) electronic Hamiltonian

$$H_{mp} = -\frac{1}{8\mu}\left(\sum_{j=1,2} \nabla_j\right)^2, \quad H_e = -\frac{1}{2}\sum_{i=1,2} \nabla_i^2 + V(\vec{R}, \vec{r}_1, \vec{r}_2). \tag{3}$$

In the equations (2-3), the reduced mass of the nuclei is given by $\mu = m_D m_H/(m_D + m_H) = 1223.8988$ and the mass asymmetry is defined by $\mu_a = m_D m_H/(m_D - m_H) = 3674.1340$.

The exact integrals of motion, commuting with the Hamiltonian (1) are the square of the total angular momentum $\vec{J}^2$, its projection J_Z onto the space-fixed Z-axis and the parity operator i corresponding to inversion of all (nuclear and electronic) space-fixed coordinates. So, we can consider the subspaces with the corresponding fixed angular momentum quantum numbers J, M and parity $(-1)^{J+\tilde{p}} = \pm 1$, where $\tilde{p} = 0$ corresponds to so called e-parity states and $\tilde{p} = 1$ to f-parity states.

The total molecular wavefunction can then be expanded as :

$$\Psi^{\tilde{p}JM}(R, \theta, \phi, \vec{r}_1, \vec{r}_2) = \frac{1}{R}\sum_{\alpha} \chi_\alpha(R)\Phi_\alpha^{\tilde{p}JM}(\theta, \phi, \vec{r}_1, \vec{r}_2; R), \tag{4}$$

where the basis functions $\Phi_\alpha^{\tilde{p}JM}(\theta, \phi, \vec{r}_1, \vec{r}_2; R)$ are symmetrized products of Wigner rotational functions and BO electronic eigenfunctions (the eigenfunctions of (3) in body-fixed coordinate framwe which parametrically depend on R), (for details see Grozdanov et al., 2008).

Restricting our basis to electronic BO states which correlate to n=2 dissociation limit, we find that there are two f -symmetry basis functions related to $\mathrm{II}'^1\Pi_g$ and $\mathrm{C}^1\Pi_u$ BO states and six e -parity basis states related to $\mathrm{B}^1\Sigma_u^+$, $\mathrm{II}'^1\Pi_g$, $\mathrm{EF}^1\Sigma_g^+$, $\mathrm{B}'^1\Sigma_u^+$, $\mathrm{C}^1\Pi_u$ and $\mathrm{GK}^1\Sigma_g^+$ BO states. The label α used above corresponds to set of quantum numbers: $\alpha = \{s, l, \Lambda\}$ where $s = g, u$ is related to gerade-ungerade symmetry, $l = 1, 0$ is the asymptotic atomic orbital angular momentum quantum number of the excited (n=2) electron and $\Lambda = 0, 1$ is the modulus of the projection of the orbital electronic angular momentum onto the internuclear axis.

Table 1: Energies (in cm^{-1}) of the $I'^1\Pi_g$ e-parity levels relative to the $X^1\Sigma_g^+(v = 0, J = 0)$ ground state. E^a_{calc} - present results , E^b_{calc} - results obtained by using a semi-empirical potential . E_{obs} - experimental data.

J	E_{obs}	E^a_{calc}	E^b_{calc}	$E_{obs} - E^a_{calc}$	$E_{obs} - E^b_{calc}$
$v = 0$					
1	118548.14	118548.18	118548.33	-0.04	-0.19
2	552.92	552.88	553.11	0.04	-0.19
3	560.05	560.00	560.20	0.05	-0.15
4	569.30	569.32	569.55	-0.02	-0.25
$v = 1$					
1	118614.17	118614.23	118615.36	-0.06	-1.19
2	618.43	618.44	618.81	0.01	-0.38
3	623.75	623.71	623.89	0.04	-0.14
4	630.38	630.13	630.50	0.24	-0.12
$v = 2$					
1	118650.51	118650.34	118650.13	0.17	0.38
2	652.89	652.71	652.26	0.18	0.63
3	655.15	655.08	655.31	0.07	-0.16
4	659.26	659.07	659.14	0.19	0.12
$v = 3$					
1	118663.650	118663.493	118663.42	0.157	0.230
2	664.544	664.359	664.29	0.185	0.254

The calculation of the molecular spectrum is then reduced to set of coupled equations for vibrational wavefunctions:

$$\left(-\frac{1}{2\mu}\frac{\partial^2}{\partial R^2} + \frac{J(J+1)}{2\mu R^2} + V_{\alpha\alpha}(R) - E\right)\chi_\alpha(R) + \sum_{\beta\neq\alpha} V_{\alpha\beta}(R)\chi_\beta(R) = 0. \quad (5)$$

The diagonal potentials are sums of the BO potentials and the so called adiabatic corrections:

$$V_{\alpha\alpha}(R) = V^{BO}_\alpha(R) + V^{ad}_\alpha(R), \quad (6)$$

$$V^{ad}_\alpha(R) = \langle\psi_\alpha| - \tfrac{1}{2\mu}\tfrac{\partial^2}{\partial R^2} + \tfrac{L_x^2+L_y^2-L_z^2}{2\mu R^2} + H_{mp}|\psi_\alpha\rangle \quad (7)$$

where $\psi_\alpha(\vec{r}_1, \vec{r}_2; R)$ are the BO electronic wavefunctions and $L_i, i = x, y, z$ are body-fixed components of the electronic orbital angular momentum. The off diagonal coupling terms (operators $V_{\alpha\beta}(R)$) are defined by

$$V_{\alpha\beta}(R)\chi_\beta = \langle\Phi^{\tilde{p}JM}_\alpha|RH\frac{1}{R}\Phi^{\tilde{p}JM}_\beta\chi_\beta\rangle. \quad (8)$$

3. RESULTS AND DISCUSSION

The binding energies of f -parity rovibrational states localized in the outer well of the $\mathrm{II}'^1\Pi_g$ potential have been calculated by solving two coupled equations (5) with $\alpha, \beta = 1, 2$. The index "1" is identified with the set of quantum numbers $1 \equiv \{s = g, l = 1, \Lambda = 1\}$ (that is with the $\mathrm{II}'^1\Pi_g$ potential) and index "2" with the set of quantum numbers $2 \equiv \{s = u, l = 1, \Lambda = 1\}$ (that is with the $\mathrm{C}^1\Pi_u$ potential). While for the BO potentials and adiabatic corrections there are *ab initio* (Dressler et al. 1984, Wolniewicz et al. 2003) and asymptotic (Stephens et al. 1974) results in the literature , this is not the case for the coupling matrix element (8) which in this case involves only H_{gu}. Since we are interested here in the states localized in the outer well of the $\mathrm{II}'^1\Pi_g$ potential , that is at large internuclear distances, we shall replace $V_{12}(R)$ with their (constant) asymptotic values at $R \to \infty$ (Grozdanov et al. 2008):

$$V_{12}(R) = V_{21}(R) \asymp V_{12}(\infty) = \frac{3}{16\mu_a} = 11.20 \text{ cm}^{-1}, \tag{9}$$

Similarly, when treating e -parity states we include only the dominant direct couplings of the $\mathrm{II}'^1\Pi_g$ e-parity state at large internuclear separations. This includes, beside the constant g-u coupling (9) with $C^1\Pi_u$ e-parity state, the rotational coupling with the $\mathrm{GK}^1\Sigma_g^+$ state, which has an R^{-2} dependence. All other couplings fall off more rapidly, like R^{-4} and faster (see Grozdanov et al, 2008) and are therefore neglected. The third basis function is labeled by index "3" identified with quantum numbers $3 \equiv \{g, l = 1, \Lambda = 0\}$ (corresponding to the $\mathrm{GK}^1\Sigma_g^+$ potential). The $V_{33}(R)$ potential was constructed using the *ab initio* data from (Wolniewicz et al. 1994) and asymptotic multipole expansions taken from (Stephens et al. 1974). The $\mathrm{GK}^1\Sigma_g^+$ - $\mathrm{II}'^1\Pi_g$ rotational coupling is given by

$$V_{13}(R) = V_{31}(R) = -[2J(J+1)]^{\frac{1}{2}} \frac{S(R)}{2\mu R^2}, \tag{10}$$

with $S(R) = \langle \psi_1 | L_+ | \psi_3 \rangle$ taken from *ab initio* data (Dressler et al. 1984). We have set $V_{23}(R) = V_{32}(R) = 0$ since this interaction actually falls off like R^{-4}.

Table 1 shows results of calculated term values for the e -parity states, with the assumed dissociation energy D=118664.80 cm^{-1} . It can be seen that the agreement with experiments (De Lange et al. 2000, Pielage et al. 2002) is excellent and that the close-coupling method is superior to calculations using a single semiempirical potential (De Lange et al. 2000).

References

Dressler, K., Wolniewicz, L.: 1984, *Can. J. Phys.*, **62**, 1706.
Grozdanov, T. P., McCarroll, R.: 2008, *J. Chem. Phys.*, **128**,114317.
de Lange, A., Reinhold, E., Hogervorst W., Ubachs, W.: 2000, *Can. J. Phys.*, **78**, 567.
Pielage, Th. G. P., De Lange, A., Brandi F., Ubachs, W.: 2002, *Chem. Phys. Lett.*, **366**, 583.
Stephens, T. L., Dalgarno, A.: 1974, *Mol. Phys.*, **28**, 1049.
Wolniewicz, L., Staszewska, G.: 2003, *J. Mol. Spectrosc.*, **220**, 45.
Wolniewicz, L., Dressler, K.: 1994, *J. Chem. Phys.*, **100**, 444.

Publ. Astron. Obs. Belgrade No. 84 (2008), 119 - 122 *Contributed Paper*

INFLUENCE OF SUBVALENCE nd^{10} SHELL ON THE EXCITATION OF RESONANCE LINES OF Al^+ SUBGROUP IONS

A. GOMONAI, E. OVCHARENKO, A. IMRE, Yu. HUTYCH

Institute of Electron Physics, Ukrainian National Academy of Sciences, 88017 Uzhgorod, Ukraine
E–mail: dep@mail.uzghorod.ua

Abstract. The results of comparative analysis of energy dependences of effective cross-sections for electron-impact excitation of resonance $nsnp\ ^1P_1 \rightarrow ns^2\ ^1S_0$ transitions in ions of Al^+ subgroup are presented. The values of excitation cross-sections for the Ga^+, In^+ and Tl^+ ion resonance lines are found to be comparable in the entire energy range under investigation. The increase of the atomic number of an ion is shown to result in the increase of contribution of the resonance processes into the effective electron-impact excitation cross-sections for resonance line due to the increasing role of relativistic and correlation effects. Correlations not only within closed s^2 and d^{10} shells, but also between them are shown to be significant.

1. INTRODUCTION

Data for the electron-impact excitation of positive ions are necessary to model and diagnose high-temperature plasmas important in controlled-fusion research and astrophysics. Single- and multiply-charged ions occur in these environments and it is important to have knowledge of collision cross sections for the analysis and diagnostics of such plasmas. Most of the existing data for electron-impact excitation of positive ions come from theoretical calculations. Experimental measurements are needed to provide tests of the theoretical methods.

A first stage of beam studies has resulted in the elucidation of the general regularities of electron scattering by ions and in the determination of effective cross sections, primarily for light single-charged ions. The development of experimental techniques in recent years has rendered the detailed study of scattering cross sections of electrons by heavy ions and particularly their resonance structure increasingly practicable. This structure is caused by the dielectronic capture of the incident electron by the excited-ion target into a short-lived autoionizing states (AIS) followed by autoionization to an excited state (resonance excitation). However, heavy many-electron ions have not been studied nearly as much, and discrepancies are found between experimental measurements and various predictions.

Despite the active experimental investigations in different scientific teams world-wide, that began with the first precise experiments using crossed beams, as well as the sound theoretical work on the resonance account, reliable data on electron

collisions with ions have been obtained only for a limited number of ionic targets. With limited data, a comprehensive, systematic and consistent interpretation of electron-ion scattering mechanisms has yet to be achieved – and can only be realized by in-depth studies involving electron correlation effects.

Our recent investigations of Zn^+ (see, e.g. Imre et al. 2000) and Cd^+ (see, e.g. Gomonai 2003) ions with filled subvalent nd^{10} shell show that in this case the resonance processes are substantially complicated due to the intershell interaction and relativistic effects. Up to now these and another new high-order effects are not fully explained. In this connection, the studies of the excitation processes in the collisions of slow electrons with ions of Al^+ subgroup seem to be of a particular interest.

In this paper, we report on the results of comparative analysis of the experimental resonance line electron-impact excitation cross-sections for In^+ ion investigated by our group (Gomonai et al. 2005), Ga^+ (Stefani et al. 1982) and Tl^+ (Imre et al. 1989) ions. These ions are the heaviest homologue in the group II-B alkaline-earth Zn-, Cd- and Hg-like systems, which have the $(n-1)d^{10}ns^2$ ground configurations.

2. EXPERIMENTAL APPARATUS AND PROCEDURE

The measurements were performed using a crossed-beam technique with an apparatus previously described elsewhere (Gomonai 2003). The experiment including metal indium is a complicated and laborious task for a number of reasons: (i) desired indium atom vapor pressure in the ion source ($10^{-3}-10^{-2}\ Torr$) is reached at high temperatures ($900-1000$) ^oC, while indium melting point is 156 ^oC; (ii) at such temperatures this metal is chemically aggressive that results in the destruction of ion source parts and intense production of liquid metal phase at the ceramic insulators; (iii) when the ion source operates in the discharge mode, the low-lying metastable $^3P^o_{0,2}$ -states of In^+ ion could be produced effectively. The above peculiarities put strict requirements on the ion source design. We have developed new design of the ion source (Gomonai et al. 2005), which allowed one to take into account these requirements and obtain a stabilized In^+ ion beam ($E_i = 700\ eV$, $I_i = 2\times10^{-6}\ A$). Electron beam current in the energy region of $E_e = (7-300)\ eV$ was $I_e = (7-30)\times10^{-5}\ A$ at the energy spread (FWHM) of $\triangle E_{1/2} = 0.4\ eV$. Spectral separation of radiation was carried out by means of a vacuum monochromator based on the Seya-Namioka scheme. The inverse linear dispersion of monochromator was $d\lambda/dl = 1.7\ nm/mm$. A cooled solar-blind photomultiplier was used to detect radiation. Modulation of both beams by square voltage pulses phase-shifted by 1/4 of the modulation period was used to extract the signal due to the process under study against the total background. The signal of the $(1-0.2)\ s^{-1}$ magnitude was extracted against the background at the signal to background ratio 1/10 to 1/30. The process of the measurements and analysis of results were automated using an IBM PC. The electron energy scale was calibrated with the 0.1 eV accuracy.

3. RESULTS AND DISCUSSION

The results of the Ga^+, In^+ and Tl^+ ($nsnp\ ^1P^o_1 \rightarrow ns^2\ ^1S_0$) resonance line emission cross-section measurements are shown in Fig. 1. The energy dependences of the cross-sections behavior at threshold are consistent with an infinitely steep rise folded with

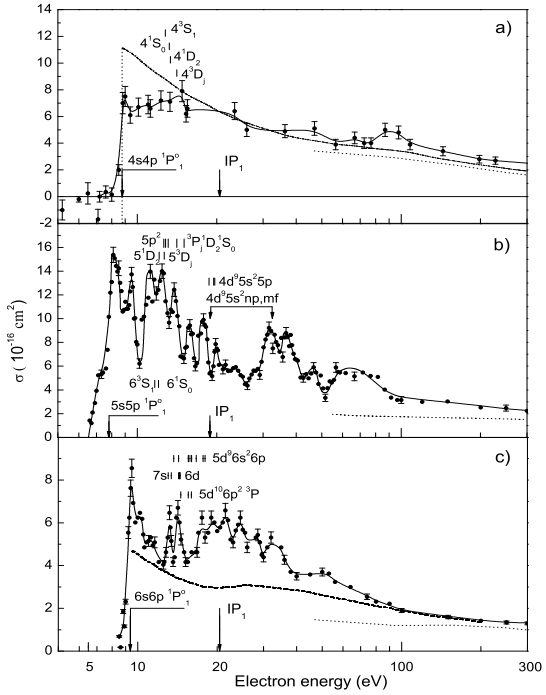

Figure 1: Electron excitation functions for the resonance lines: a) Ga^+ ion; b) In^+ ion; c) Tl^+ ion (dots - experiment data; dotted lines - calculation by Van-Regemorter formula; chain line - calculation by the g-factor formula; long dotted line - close-coupling approximation).

the 0.6 eV (Ga^+), 0.4 eV (In^+) and 0.5 eV (Tl^+) energy spread of the electron beam. Above 100 eV the data fall off with the predicted lnE/E energy dependence.

The absolute value of the emission excitation cross-sections for the resonance $\lambda =$ 158.6 nm line of In^+ ion was obtained by normalizing the experimental excitation functions to the semi-empirical calculation by the Van-Regemorter formula at the 300 eV electron energy (see Fig. 1b, dotted curve). The uncertainty of the absolute effective excitation cross-section determination was about 30 percent.

The absolute cross-section for Ga^+ ion resonance line was obtained by normalizing the excitation function to the experimentally determined absolute excitation cross-section standard at the energy 6.9 ± 0.5 eV ($\sigma = (5.0 \pm 0.6) \times 10^{-16}$ cm^2) (Stefani et al. 1982) and for Tl^+ ion – by normalizing to the theoretical calculation at the 100 eV energy using the close-coupling method taking into account two stages ($\sigma =$ $(1.9 \pm 0.8) \times 10^{-16}$ cm^2) (Imre et al. 1989).

As seen from Fig. 1, the excitation cross-section values for the Ga^+, In^+ and Tl^+ ion resonance lines are comparable in the entire energy range under study, and the maximum of the effective excitation cross-sections was observed for In^+ ion, that, probably, can be explained by the lowest value of the $5s5p\ ^1P^o_1$ resonance level

excitation energy. Peculiarities revealed in the excitation functions result from both the resonance contribution due to formation and decay of short-lived AIS of Ga (Dunn et al. 1993), In (Bhatia 1978), Tl (Baig et al. 1992) atoms and cascade transitions from higher ion levels. As seen from Fig. 1a, the contribution of these processes is the smallest for the Ga^+ ion resonance line effective cross-section. In our opinion, this is due to the fact that for this ion, as the lightest one ($Z = 31$), the resonance contribution can result only due to correlation effects inside the valence s^2 closed shell. In this case, the influence of the subvalence d^{10} shell is not determinative because, as the estimative calculations of the average radii of the valence and subvalence shells of Ga^+ ion using Hartree-Dirac formula show, the above shells are located at large distances from each other.

For a heavier In^+ ion ($Z = 49$), the peculiarities in the energy dependence of the effective electron-impact excitation cross section for the resonance line are, first of all, due to the resonance processes with the essential role being played by correlation effects both inside the valence s^2 shell (as observed below 12 eV) and between the valence s^2 and subvalence shells (above 12 eV) due to the close electron binding energies in these shells.

For the heaviest Tl^+ ion ($Z = 81$) the effect of configuration interaction is larger, and correlation and relativistic effects are more essential. In this ion, the presence of the $4f^{14}$ shell in the total configuration of the electron core results in a strong screening of the Tl^+ ion nucleus. As a result, the electron trajectories in the valence and subvalence shells overlap (their average radii differ less than twice). As shown in (Deselaux and Yong-Ki Kim 1975), the binding energies of the $6s^2$-electrons increase to 30 percent and for the $5d^{10}$-electrons decrease to 15 percent as compared to non-relativistic case, i.e. the role of the $5d^{10}$ shell in the excitation process significantly increases. In case of Tl^+ ion the AIS formed at the excitation of one of the $5d^{10}$-electrons are located lower and they are an important channel of the resonant contribution to the excitation of these ionic resonance levels.

Resonance phenomena strongly affect all collision processes and can considerably influence their cross sections, especially in the near-threshold region. The resonance contributions dominate over the direct scattering in this energy region and strongly depend on Z. The mechanisms of both direct and resonance collision processes are considerably complicated by the relativistic and correlation effects, which are extremely essential in the complex multielectron systems characterized by effectively excited nd- subvalence shell.

This work was supported in part by Ukrainian National Academy of Sciences Young Scientist Grant No 0107U008526.

References

Baig, M. A. et al.: 1992, *J. Phys. B: At. Mol. Opt. Phys.*, **25**, 1119.
Bhatia, K. S.: 1978, *J. Phys. B: Atom. Molec. Phys.*, **11**, 2421.
Deselaux, J.P. and Yong-Ki Kim.: 1975, *J. Phys. B: Atom. Molec. Phys*, **8**, 1117.
Dunne, P. et al.: 1993, *Phys. Rev. A*, **48**, 4358.
Gomonai, A. N.: 2003, *Optics and Spectroscopy*, **94**, 488.
Gomonai, A. et al.: 2005,*Nucl. Instr. and Meth. in Phys. Res. B*, **233**, 250.
Imre, A. I. et al.: 1989, *Abstracts of Contributed Papers XVI ICPEAC, New-York, USA*, 876.
Imre, A. I. et al.: 2000, *Optics and Spectroscopy*, **89**, 179.
Stefani, G. et al.: 1982, *Phys. Rev. A*, **25**, 2996.

Publ. Astron. Obs. Belgrade No. 84 (2008), 123 - 126 *Contributed Paper*

DOUBLY EXCITED STATES OF He IN A DC FIELD

S. I. THEMELIS

Technological Educational Institute of Chalkis, Department of Applied Sciences, GR-34400 Psahna - Evia, Greece
E–mail: sthemelis@teihal.gr

Abstract. The effects of strong electric fields on the doubly excited states of He are investigated. Strong electric-field strengths up to F=0.02 a.u. are used in the present study. Intrashell doubly excited states are chosen as prototype states for studying these effects. The solution of the Complex Eigenvalue Schrödinger equation is obtained using and appropriate partitioning of the wave-function and the complex rotation method. Energy shifts and field induced widths, as a function of the external field strength, are presented and analyzed.

1. INTRODUCTION

The effects of electric fields on ground or low-lying states of atoms and molecules have been studied for many years (Ryde 1976). Likewise, the doubly excited states of H^- are particularly sensitive to external electric fields and the DC-field effects on these states have been studied fairly well (Halka 2006). The effects of electric fields on the doubly excited states of He have only recently been considered by experiments (Harries et al. 2003, Halka 2006). Some recent advances in the experimental methods have given us the opportunity to study the energy shift and the field induced width of the doubly excited states of He and the modifications appearing in the photoionization cross section. The calculation of these properties and of the profile shapes is a testing case for the advanced many-body theories. The problem is more difficult than the calculation of the tunneling rates in effective one-electron systems. The semi classical theory is useful for, essentially, hydrogen-like states, whereas for a more complicated system, the formulation suggested by Fisher, Maron and Pitaevskii (1998) could be applied. A thorough and effective approach is required far from the semi-classical limit. A first principles approach, in the context of density functional approach, has been proposed by Otobe et al. (2004), but applications on non-stationary states are not reported.

The *ab initio* theoretical approach introduced by Themelis and Nicolaides (2000, 2001) is the background for the recent study. A general and computationally feasible theoretical approach has been developed for the study of the Stark effect on many electron atomic systems, in both ground and in excited states. The complex coordinate rotation method is used for the solution of the Complex Eigenvalue Schrodinger Equation. The main characteristic of the present approach is the partitioning of the function space used for the description of the atomic or molecular states, with or

without the existence of an external perturbation. Application of the theory has been reported for ground or excited states and the present problem is a natural generalization.

For non-stationary states there is already a finite lifetime whereas the application of an electric field can increase or decrease it, as a function of the applied field strength. For the width of an autoionizing state in a DC field we can write:

$$\Gamma(F) = \Gamma_{aut} + \Gamma_{DC}(F). \tag{1}$$

Γ_{aut} is the autoionization width and the problem here is actually the determination of the field induced width, $\Gamma_{DC}(F)$. For a bound state the usual dependence of the field-induced width on the field strength F is $\Gamma_{DC}(F) \sim e^{-k/F}$, where k is a parameter depending on the ionization potential, the angular momentum of the escaping electron etc. We will see that this rule does not apply in the case of the doubly excited states (DES) of He. An old suggestion made by Khomskii (1965) and reinvented by Davis and Jacobs (1975), brings forth a dependence of Γ_{DC} on F^2 and describes fairly well the exact values of the width in a large interval of values of F.

2. THEORY AND METHODOLOGY

The calculation of field-induced properties of atoms or molecules, in the present approach is formulated as a problem of solving variationally a complex eigenvalue Schrodinger equation (Kukulin et al. 1988):

$$(\widehat{H} - \epsilon)\Psi = 0, \tag{2}$$

where: $\widehat{H} = \widehat{H}_{atom} + \sum_i \vec{r}_i.\vec{F}$ and $\epsilon = E_0 + \Delta(F) - \frac{i}{2}\Gamma(F)$. H_{atom} is the free-atom Hamiltonian and $\vec{F}$ the external dc-field. E_0 is the field-free energy of the state of interest, described by the field-free wave-function Ψ_0, while $\Delta(F)$ and $\Gamma(F)$ are the field-dependent energy shift and width. Resonances are eigenvalues of $\widehat{H}$ with ϵ=complex energy ($\Gamma > 0$). A straightforward description of such states are difficult because their wave functions are exponentially divergent in the asymptotic region. In this method the eigenvalue problem of a transformed Hamiltonian

$$\widehat{H}_\theta = \widehat{U}(\theta)\widehat{H}\widehat{U}^{-1}(\theta) \tag{3}$$

is solved, instead of the original $\widehat{H}$. The effect of the complex scaling transformation, in equation (3), is that the positive-energy continuum of $\widehat{H}$ gets rotated down into the complex energy plane, while the wave function of any resonance becomes square-integrable (if $0 < \theta < \pi/3$).

The trial wave-function Ψ, which will be computed by a variational procedure, is expanded in a function space that is divided into two nonorthogonal parts Q and P. The Q space, in general, contains correlated wave-functions belonging to the bound spectrum. The P space contains states that represent the multichannel continuous spectrum. These states are expanded in terms of L^2 functions, since the complex coordinate transformation $\widehat{U}(\theta)$ makes them square integrable. The Stark Hamiltonian matrix which is derived from this choice of the basis functions is:

$$\mathbf{H} = \begin{pmatrix} H_{QQ} & H_{QP} \\ H_{PQ} & H_{PP} \end{pmatrix} \tag{4}$$

H is diagonalized repeatedly in respect to changes of the non-linear parameters in the basis set of the space P and in the rotation angle θ, until the root having the maximum overlap with Ψ_0 is stabilized.

2. 1. APPLICATION TO DES OF HE

For the calculation of the localized part of the autoionizing states, we use a multi-configuration Hartree-Fock (MCHF) approximation. For example, the $2s2p\ ^3P^o$ state can be described accurately by a 3×3 minimal approximation to the wave-function: $\Psi(2s2p\ ^3P^o) = 0.992\ (2s2p) - 0.118\ (2p3d) + 0.049\ (3s3p)$ The energy that corresponds to the expectation value of $\widehat{Q}\widehat{H}\widehat{Q}$ for this wave-function is: $E_0(2s2p\ ^3P^o) = -0.760935$ a.u. For the description of the nearby lying non-relativistically bound state $2p^2\ ^3P$, we use an approximation of a similar accuracy. The energy that results from the calculation for this state is $E_0(2p^2\ ^3P) = -0.710190$ a.u. The function space Q for the manifold of the triplet-spin states is not consisted only by these two states. The states that are also included in our calculation are:

i. the singly excited states 1snℓ, $n \leq 6$ and $\ell \leq n-1$.

ii. intershell autoionizing and bound states lying below the threshold n=2 of He^+, that is $2\ell n\ell'$, $2 \leq n \leq 6$ and $\ell, \ell' \leq 5$.

iii. higher lying double excited states of the form $n'\ell' n''\ell''$, with $3 \leq n' \leq n'' \leq 6$, lying below higher thresholds of He^+.

Singly excited states are represented by compact but accurate MCHF expansions or by their HF functions. The doubly excited states are represented by CI expansion in a hydrogenic basis set, which proved to provide an accurate description of the localized part of these states. The symmetry of all of the above cited doubly excited states is for limited values of the total angular momentum $L \leq 4$.

All the above singly and doubly excited states are the members of the Q-space included in our calculations. However, in order to have a complete description of the field-free or non-zero field problem, we have to include the multichannel continuum described by the complementary function space P. The open channel components of the resonant wave-functions are represented as: $X(n\ell\varepsilon\ell'\ ^{2S+1}L^\pi) = \hat{\mathcal{A}}\,(\phi_{n\ell}(\vec{r_1})u_{\epsilon\ell'}(\vec{\rho_2})) = \hat{\mathcal{A}}\,(\phi_{n\ell}(\vec{r_1})\sum_i c_i\chi_i(\rho_2^*)Y_{\ell m}(\Omega_2))$ $\hat{\mathcal{A}}$ is an antisymmetrizer and $\phi_{n\ell}$ are hydrogen-line states with Z=2 and $u_{\epsilon\ell'}$ are states belonging to the continuum represented as a linear combination of $\chi_i(\rho^*) = (\rho^*)^{k_i}e^{-a_i\rho^*}$. In the variant of the complex-coordinate approximation followed here, for $\chi_i(\rho^*)$ the radial coordinate takes the form $\rho_i^* = r_i e^{-i\theta}$. The non-linear parameters a_i and the expansion coefficients c_i are subject to a variational optimization for the calculation of the complex energy eigenvalues pertaining to the autoionizing and field induced resonant states.

3. RESULTS

In the case of the absence of electric field, for the triplet-spin states of interest, we have found for their energy position the following results: E($2s2p\ ^3P^o$) = -0.760150 a.u. and E($2p^2\ ^3P$) = -0.710218 a.u.. The energy width of the autoionizing state is: $\Gamma(2s2p\ ^3P^o) = 0.0003126$ a.u.. In Fig. (1a) we show the movement of the resonance poles for the $2s2p\ ^3P^o$ and $2p^2\ ^3P$ states ($M = 0$ and $M = \pm 1$) when the external electric field is turned on. For the field-free case, the $2s2p\ ^3P^o$ state lies at a position of ~ 0.05 a.u. lower than the $2p^2\ ^3P$ state. When the external electric field is turned

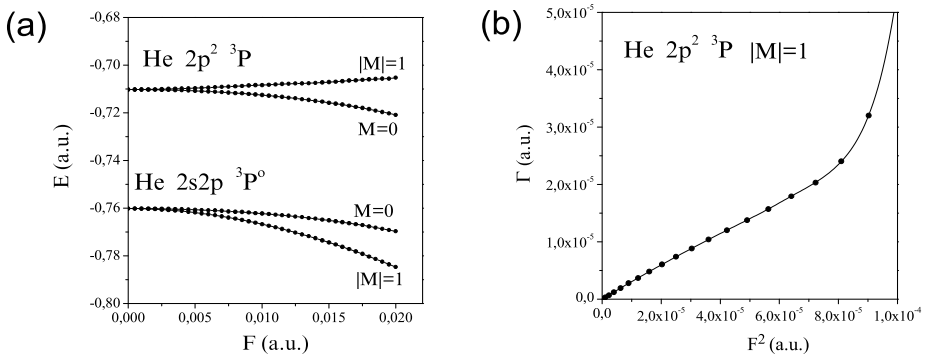

Figure 1: Energies and widths as functions of the DC-field.

on, the interaction between the two resonant poles having $M = \pm 1$ is evident, as they start to repel each other in the complex-energy plane. This is not the case for the states with $M = 0$ since, according to the selection rules for the external perturbation, they do not interact. The width for the $2s2p\ ^3P^o$ states decreases for small values of F whereas for higher values of F starts to increase. At the same time, the width for the $2p^2\ ^3P$ state increases when the field strength is increased. In Fig. (1b) we show the change in width of the state $2p^2\ ^3P$, $M = \pm 1$ as a function of the squared external electric-field strength F. Its is clear that for low values of F the width has a linear dependence on F^2. This dependence has been predicted many years ago by Khomskii (1965). It is further noted that when the external electric-field strength is greater than 8×10^{-5} a.u. approximately, the width for the $2p^2\ ^3P$, $M = \pm 1$ state increases quite rapidly. At the high-field region, the effective potential barrier, formed by the combination of the atomic potential and the external DC field, would become narrower as the external electric-field strength is increased further.

References

Davis, J. and Jacobs, V. L.: 1975, *Phys. Rev.*, **A12**, 2017.
Fisher, D., Maron, Y., and Pitaevskii, L. P.: 1998, *Phys. Rev.*, **A58**, 2214.
Halka, M.: 2006, *J. Rad. Phys. Chem.*, **75**, 2228.
Harries, J. R. et al.: 2003, *Phys. Rev. Lett.*, **90**, 133002.
Khomskii, D. I.: 1965, *Opt. and Specrtosc.*, **18**, 297.
Kukulin, V. I., Krasnopol'sky, V. M. and Horáček, J.: 1988, Theory of Resonances: Principles and Applications, Kluwer Academic, Dordrecht.
Otobe, T., Yabana, K., and Iwata, J.-I.: 2004, *Phys. Rev.*, **A69**, 053404.
Ryde, N.: 1976, Atoms and Molecules in Electric Fields, Almqvist & Wiksell International, Stockholm.
Themelis, S. I. and Nicolaides, C. A.: 2000, *J. Phys. B*, **33**, 5561.
Themelis, S. I. and Nicolaides, C. A.: 2001, *J. Phys. B*, **34**, 2905.

Publ. Astron. Obs. Belgrade No. 84 (2008), 127 - 130 *Contributed Paper*

ELECTRON IMPACT VIBRATIONAL EXCITATION RATES OF CO_2 MOLECULE

G. B. POPARIĆ[1], M. M. RISTIĆ[2] and D. S. BELIĆ[1]

[1] *Faculty of Physics, University of Belgrade, Studentski trg 12, P.O. Box 368, 11000 Belgrade, Serbia*
E–mail: goran_poparic@ff.bg.ac.yu

[2] *Faculty of Physical Chemistry, University of Belgrade, Studentski trg 12, P.O. Box 137, 11000 Belgrade, Serbia*
E–mail: ristic@ffh.bg.ac.yu

Abstract. Integral cross sections (ICS) for electron impact vibrational excitation of CO_2 molecule have been used to calculate electron energy transfer rate coefficients for the equilibrium electron energy distribution conditions. Symmetric stretch vibrational excitation cross sections are measured by using our high resolution trochoidal electron spectrometer. ICS for bending and asymmetric vibration of CO_2 have been adopted from previous results. Total and partial electron energy transfer rate coefficients for vibrational excitations are calculated by use of the Maxwellian electron energy distribution function (EEDF) and by direct numerical integration of experimental cross sections. These preliminary calculations have been compared with the previous results.

1. INTRODUCTION

Electron collision processes with the carbon-dioxide molecules are important in many naturally occurring phenomena and also in plasma devices and laser technology. In particular, CO_2 has been intensively studied as a dominant constituent of the Earth's atmosphere responsible for the greenhouse effects. For modeling all of these phenomena, one needs to know cross sections and rate coefficients for various involved processes. At low electron energies vibrational excitation is dominating process of energy transfer. In order to determine rate coefficients for these processes it is necessary to have accurate absolute integral cross sections for vibrational excitation.

Vibrational excitation of the CO_2 molecule has two significant resonant contributions at low energy: $^2\Pi_u$ shape resonance (Bonnes and Schulz, 1974) with the maximum between 3 and 4 eV and a virtual state below 2 eV (Morrison 1982, Herzenberg 1984, Kochem et al. 1985, Estrada and Domcke 1985, Morgan 1998, Rescigno et al. 1999, Mazevet et al. 2001, Field et al. 2001) which causes ICSs for (100) and (020) vibrational transitions to rise steeply above threshold energy.

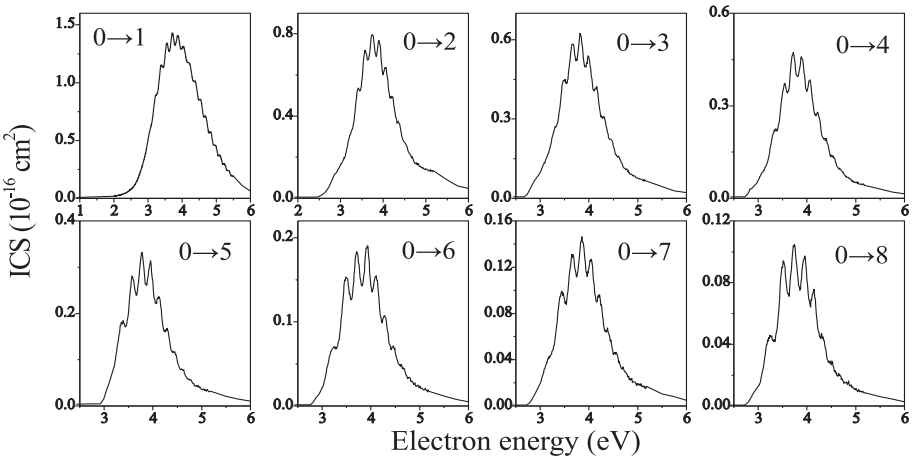

Figure 1: ICS for symmetric stretch vibrational excitation of CO_2.

2. VIBRATIONAL EXCITATION CROSS SECTIONS OF CO_2

Low energy electron impact vibrational excitation cross sections of CO_2 are measured by use of a high resolution crossed-beams double trochoidal electron spectrometer. Experimental procedure has been described in detail by Vićić et al. 1998 and only a brief outlook will be given here. The electron beam is prepared by using a trochoidal electron monochromator (TEM), and is crossed at right angles with the gas beam, introduced by one-dimensional capillary array, aligned along the electron beam trajectory, in the collision region. After the collision, inelastically scattered electrons are analyzed by use of a double TEM device. Selected electrons are detected by use of a channel electron multiplier, counted and the results are stored in an on line-computer.

We have focused our attention to measure the excitation functions from the ground level of the CO_2 molecule to the first 8 vibrationally excited symmetric stretch levels via the $^2\Pi_u$ shape resonance. In order to normalize our results to the absolute scale, we have used absolute ICS value of $1.33 * 10^{-16} cm^2$ at 3.8 eV in the v = 1 excitation channel, obtained by the recent measurements of Kitajima et al 2001. Our result for $v = 1$ excitation channel is normalized, and other results are scaled relative to the $v = 1$ by using number of counts for each particular vibrational channel under the same experimental conditions. This normalization is performed under the assumption of the angular distributions being the same for all vibrational levels and independent of the electron energy, that is of constant ratios of differential and integral cross sections. Our normalized results for the symmetric stretch vibrational excitation of the first eight levels are shown in figure 1.

ICSs for bending mode and asymmetric stretch have been determined from differential cross sections published by Katajima et al. 2001. For bending mode, only (010) and (020) ICSs have been determined because ICSs for higher levels are much lower. For the same reason, only (001) ICS is determined for asymmetric stretch. A contribution of the virtual state resonance below 2 eV to all ICSs is taken into account separately, using the experimental data of Morgan et al. 1997.

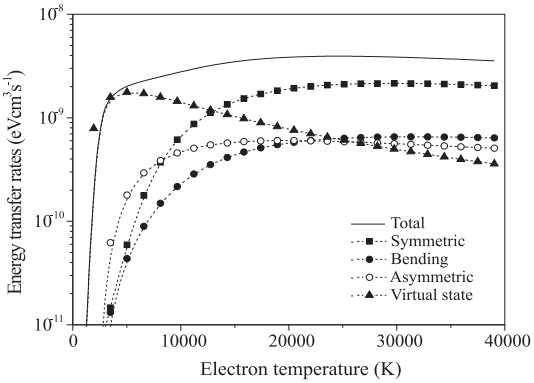

Figure 2: Electron energy transfer rate coefficients for bending, symmetric, asymmetric vibrations and virtual state contributions.

3. RATE COEFFICIENTS CALCULATION

The energy transfer rate coeffcient, K, for vibrational excitation is given by Campbell et al. 2004:

$$K(\bar{E}_{\rm el}) = \epsilon_{thres.}\sqrt{2/m_e}\int_{\epsilon_{thres.}}^{+\infty}\sigma_v(\epsilon)\sqrt{(}\epsilon) f_e(\bar{E}_{\rm el},\epsilon)d\epsilon \tag{1}$$

where $\bar{E}_{\rm el}$ is the mean electron energy, $\sigma_v(\epsilon)$ is the vibrational excitation cross section, $\epsilon_{thres.}$ is the threshold energy for vibrational excitaion and $f_e(\bar{E}_{\rm el},\epsilon)$ is the normalized electron energy distribution function (Chantry P., 1987, Belić D. S., 1989):

$$\int_0^{+\infty} f_e(\bar{E}_{\rm el},\epsilon)d\epsilon = 1. \tag{2}$$

For the equilibrium case, the electron energy distribution function is given by the Maxwellian equation:

$$f_e(\bar{E}_{\rm el},\epsilon) = 2\pi^{-1/2}(3/2\bar{E}_{\rm el})^{+3/2}\sqrt{\epsilon}\exp\left(-3\epsilon/2\bar{E}_{\rm el}\right) \tag{3}$$

For this case the energy transfer rate coefficients are determined by the direct numerical integration of integral cross sections multiplied by the Maxwellian electron energy distribution function, for a wide electron energy range. The energy transfer rate coecients are calculated for each vibrational mode and separately for contribution of the virtual state below 2 eV to all ICSs. Calculations are performed for the mean electron energies up to 5 eV, which correspond to the mean electron temperatures up to 40000 K. Obtained results are shown in figure 2.

4. RESULTS AND DISCUSSION

As it can be seen from figure 2, the maxima of the partial energy transfer rates range from 0.3 to $1*10^{-9}eVcm^3s^{-1}$, for excitation of bending, over symmetric, asymmetric

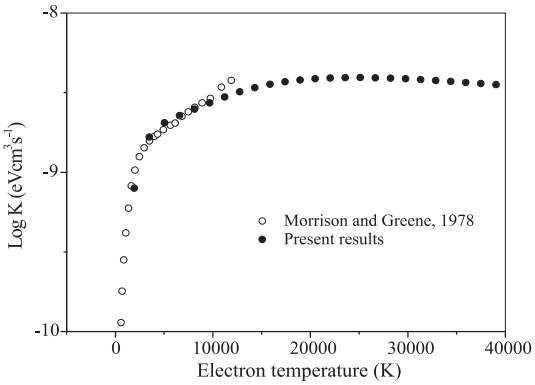

Figure 3: Comparison of our total electron energy transfer rate coefficients with the data of Morrison and Greene, 1978.

vibrations and virtual state contributions, respectively. At low electron temperatures, contribution of virtual state resonance is dominant. The higher contribution in the region from 1 to 5 eV (10000-40000 K) is that of symmetric vibration via the $^2\Pi_u$ resonance.

Our results are compared with the previous results published by Morrison and Greene, 1978. Comparison is shown in figure 3. and as it can be seen, our results are in very good agreement with these data.

References

Belić D. S.: 1989, *Chem. Phys.*, **130**, 141.
Campbell, L., Brunger, M. J., Cartwright and Teubner P. J. O.: 2004, *Planet. Space Sci.*, **52**, 815.
Chantry P.: 1987, *Final Technical Report ARPA*, Order No 3342.
Estrada, H. and Domcke, W: 1985, *J. Phys. B: At. Mol. Phys.*, **18**, 4469.
Field, D., Jones, N. C., Lunt, S. L. and Ziesel, J. P.: 2001, *Phys. Rev. A*, **64**, 022708.
Herzenberg, A.: 1984, Vibrational excitation of molecules by slow electrons Electron molecule collisions ed. I Shimamura and K Takayanagi (New York: Plenum) ch. 3, 191.
Kitajima, M., Watanabe, S., Tanaka, H., Takekawa, M., Kimura, M. and Itikawa, Y.: 2001, *J. Phys. B: At. Mol. Opt. Phys.*, **34**, 1929.
Kochem, K. H., Sohn, W., Nebel, N., Jung, K. and Ehrhardt, H.: 1985, *J. Phys. B: At. Mol. Phys.*, **18**, 4455.
Mazevet, S., Morrison, M. A., Morgan, L. A. and Nesbet, R. K.: 2001, *Phys. Rev. A*, **64**, 040701.
Morgan, L. A.: 1998, *Phys. Rev. Lett.*, **80**, 1873.
Morgan, L. A., Gillan, C. J., Tennyson, J. and Chen, X.: 1997, *J. Phys. B*, **30**, 4087.
Morrison, M. A.: 1982, *Phys. Rev. A*, **25**, 1445.
Morrison, M. A. and Greene, A. E.: 1978, *J. Geophys. Res.*, **83**, 1172.
Rescigno, T. N., Byrum, D. A., Isaacs, W. A. and McCurdy, C. W.: 1999, *Phys. Rev. A*, **60**, 2186.
Vićić, M., Poparić, G. B. and Belić, D. S.: 1998, *Rev. Sci. Instrum.*, **34**, 1996.

Publ. Astron. Obs. Belgrade No. 84 (2008), 131 - 134 *Contributed Paper*

THE EXPERT SYSTEMS FOR ANALYSIS OF ATOM AND MOLECULE THRESHOLD SPECTRA

I. PETROVIĆ, V. BOČVARSKI and V. PETROVIĆ
Faculty of Science, R. Domanovića 12, 34000 Kragujevac, Serbia

Abstract. In this paper is presented development of the expert systems for threshold spectra analysis, starting from firstly developed expert system for atom threshold spectra analysis, up to the expert system for analysis more complex molecule threshold spectra (firstly two-atomic and then tree-atomic molecules). The goal of the expert systems application is to automate, speed up and improve process of spectra analysis. Interest for threshold spectra originates from the fact that, by studding them, it is possible obtained information about processes which happened on energies near reaction threshold. Also, in these spectra can be seen peaks that correspond to forbidden transitions and which can't be seen in the optical spectroscopy. For testing of the expert systems, we used the threshold spectra for the He atom, and N_2 and SO_2 molecules. All these spectra are obtained on threshold spectrometer which is situated in Institute for Physics in Zemun.

1. INTRODUCTION

The main characteristic of threshold spectra is possibility to detect electrons with low energy i.e. electrons which are loosed almost of their incident energy in collisions with atoms or molecules. Advantage of this method in relation to optical spectroscopy method, is possibility for detections and studying optical forbidden transitions.

The spectra used for development and testing of the expert system are obtained by using threshold method spectroscopy which is developed by Cvejanovic and Read (1974). This method is known as method of "field penetration". The essence of this method is penetration of external electrical field in the area where is performed collision between electron and atom or molecule beams. Aforementioned electrical field creates, in the center of area such potential, which can extract electrons with zero energy. Threshold spectra used for development and testing of expert systems are result of detection of these electrons. All mentioned spectra are obtained on threshold spectrometer that is situated in Institute for Physics in Zemun.

2. EXPERT SYSTEMS

The expert systems used for threshold spectra analysis and described in this paper, are developed by using expert system building tool I2+, which in conclusion process enables the backward changing method. The advantage is avoiding of conflict resolution, which can be very complicated factor in process of practical exploitation of an

expert system. The knowledge is presented in form of production rules with structure IF-THEN-ELSE.

The first expert system is developed with aim to automate the process of atom threshold spectra analysis (Petrović and Bočvarski 2003). Actually, we used He atom threshold spectra, but it should be emphasized that the expert system can be adapted to make spectra analysis of the other atoms. Beside identification of states, which is necessary step in process of analysis, the additional task for expert system is identification of resonances in these spectra. Resonances are non stable, short-lived states created by electron capture by atom or molecule, and they are characteristic for threshold spectra. After the short time the electron leaves atom or molecule and gives contribution to peak of other state. In this way, in the case of atom spectra, these electrons are disturbing the rule that the peaks which correspond to states of one group (peaks that have been determined with same value of principal quantum number form one group) must form a growing array, looking from a point of view of peak intensity. Deviations in spectra are consequence of resonance influence on some states. Because of that, detection of this influence on a peak of state is one of the most important steps in process of spectra analysis. On Figure 1 is given a part of characteristic spectrum of He atom. This spectrum represents a second group of peaks, which is determined by a value of principal quantum number $n = 2$, and where can be seen the aforementioned deviation.

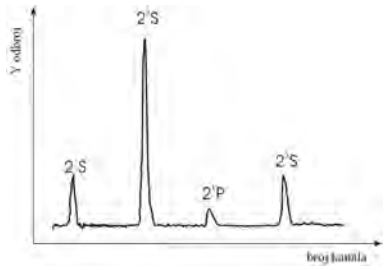

Figure 1: The second group of characteristic spectrum of He.

Application of the expert system in process of the threshold spectra analysis has fulfilled our expectations, and enabled us to upgrade an expert system for analysis of more complex spectra, i.e. the molecule threshold spectra.

Besides peaks which arise from discrete states and resonances, in molecule threshold spectrum is characteristic an appearance of vibrational level peaks. Vibrational movement in molecules is consequence of oscillation of atoms around position of equilibrium which represents the most probable distance between atoms. This is the reason why in the total sum of molecular energy there is always an oscillation energy, i.e. energy of vibrational movement.

Vibrational levels can be observed on almost all peaks which correspond to electronical transitions. For vibrational levels is characteristic that they appear on almost identical energy distances. In the first phase we limited ourselves on two-atomic molecule spectra, actually on molecules of nitrogen (Petrović and Bočvarski 2005).

On the Figure 2 is given characteristic threshold spectrum of N_2 molecule. In the structure of this spectrum it can be seen that the every state has exactly determined

number of vibrational levels. On the higher energies, overlapping of vibrational levels forms the complex structures. Qualitative improving of process analysis can be seen at those structures where the peaks can't be separated and where they are often in form of "shoulders" on higher energy side of most intense peaks of states. Such appearance of spectra makes their analysis and states identification very difficult by classical methods.

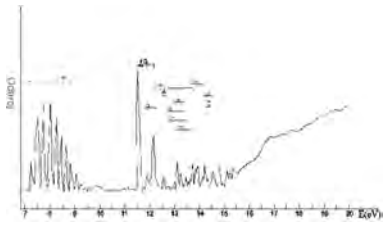

Figure 2: Characteristic threshold spectrum for N_2 molecules.

Molecules of N_2 are chosen for development and testing of an expert system because their spectra are very well examined. Because of that they can be used for checking the same ideas and principles which were necessary in the process of searching a correct methodology for analysis of polyatomic molecules by expert system. For development and testing of the expert system for polyatomic molecules we used the SO_2 molecules threshold spectra (Petrović and Bočvarski 2007). On the Figure 3 is given part of characteristic threshold spectrum for SO_2 molecules.

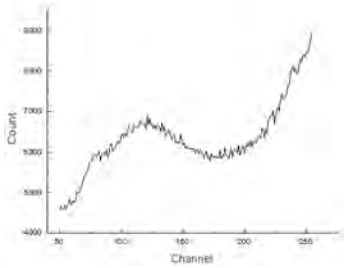

Figure 3: Characteristic threshold spectrum for SO_2 molecules (energy range 5,5 - 8 eV).

For those spectra is characteristic non existence or very small existing of determined structures which are necessary for calibration process.

In order for expert system to work, beside energy levels tables of atom and molecule states, we also formed tables of energy levels of corresponding vibrational levels and resonances.

After the input of initial data, calibration of energy scale and estimation of resolution, the expert system starts with identification and classification of peaks of states, and by the same principle makes identification of vibrational levels (Petrović and Bočvarski 2003, 2005, 2007).

In the process of calibration and identification, each peak obtains corresponding mark, depending of its nature. Aforementioned marks will be written by expert

system, in collaboration with appropriate Pascal program, in corresponding field in the table with spectrum.

Where atom and two-atom spectra are concerned, the process of analysis is finished.

However, in tree-atom molecule spectra, regarding of density and overlapping of peaks, especially at higher energy intervals, it is necessary to make some additional analyses.

Additional analysis should solve two problems. First problem originates from fact that the number of vibrational levels isn't always known. Second problem is consequence of the fact that the distance between vibrational levels isn't always known also. Additional problem is disturbance of equidistance between vibrational levels that originates from different influences. Development of the expert system should show if, on base the known minimum data, the expert system can generate spectrum which will correspond, in principle, to experimentally obtained spectrum.

These problems have been solved by using the process of peak generation in form of a Gaussian, after identification of peak of states and separated vibrational levels. The parameters for Gaussian are obtained based on the characteristic peak which represents structure the most intense and defined in spectrum. Generating is performed by using the Pascal program on the channels at which the expert system positioned itself, based on the characteristic number of channels. After the correction of peak intensity, the expert system checks the position of peaks and, if necessary, moves a spectrum on left or right side. After that, the expert system generates additional peaks with aim to obtain overlapping structures which, in principle, correspond to real spectrum. The Figure 4 illustrates aforementioned processes.

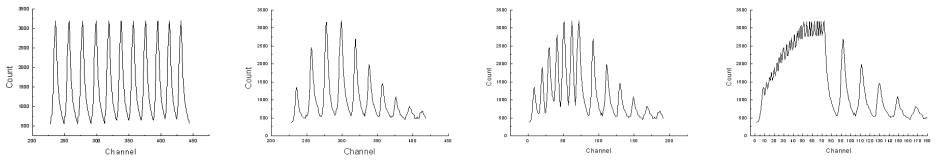

Figure 4: Generating of peaks of vibrational levels on equal distance, correction of peak intensity, and addition of peaks.

3. CONCLUSION

Application of expert system in processes of spectra analysis gave expected results. Quantitatively and qualitatively, improvement of analysis process completely vindicated a further work on development of expert systems which would find their application in processes of spectra analysis.

References

Cvejanović, S. and Read, F. H.: 1974, *J. Phys. B: Atom. Molec. Phys.*, **7**, 1180.
Petrović, V. and Bočvarski, V.: 2003, *Int. J. Mod. Phys.* C, **14**, 433.
Petrović, V. and Bočvarski, V.: 2005, *Int. J. Mod. Phys.*, **16**, No. 9, 1395.
Petrović, V. and Bočvarski, V.: 2007, *Int. J. Mod. Phys.*, **16**, No. 9, 1395.

Publ. Astron. Obs. Belgrade No. 84 (2008), 137 - 138 *Invited Lecture*

CHARACTERIZATION TECHNIQUES FOR NANO-ELECTRONICS, WITH EMPHASIS TO ELECTRON MICROSCOPY.

The role of the European Project ANNA

A. ARMIGLIATO

CNR-Istituto IMM, Sezione di Bologna, Via P.Gobetti, 101 - 40129 Bologna, Italy
E–mail: armigliato@bo.imm.cnr.it

Abstract. In the present and future CMOS technology, due to the ever shrinking geometries of the electronic devices, the availability of techniques capable of performing quantitative analyses of the relevant parameters (structural, chemical, mechanical) at a nanoscale is of a paramount importance. The influence of these features on the electrical performances of the nanodevices is a key issue for the nanoelectronics industry.

In the recent years, a significant progress has been made in this field by a number of techniques, such as X-ray diffraction, in particular with the advent of synchrotron sources, ion-microbeam based Rutherford backscattering and channeling spectrometry, and micro Raman spectrometry. In addition, secondary ion mass spectrometry (SIMS) has achieved an important role in the determination of the dopant depth profile in ultra-shallow junctions (USJs) in silicon.

However, the technique which features the ultimate spatial resolution (at the nanometer scale) is scanning transmission electron microscopy (STEM). In this presentation it will be reported on the nanoanalysis by STEM of two very important physical quantities which need to be controlled in the fabrication processes of nanodevices: the dopant profile in the USJs and the lattice strain that is generated in the Si electrically active regions of isolation structures by the different technological steps. The former quantity is investigated by the so-called Z-contrast high-angle annular dark field (HAADF-STEM) method, whereas the mechanical strain can be two-dimensionally mapped by the convergent beam electron diffraction (CBED-STEM) method. A spatial resolution lower than one nanometer and of a few nanometers can be achieved in the two cases, respectively.

To keep the pace with the scientific and technological progress an increasingly wide array of analytical techniques is necessary; their complementary role in the solution of present and future characterization problems must be exploited. Presently, however, European laboratories with high-level expertise in materials characterization still operate in a largely independent way; this adversely affects the competitivity of European science and industry at the international level.

For this reason the European Commission has started an Integrated Infrastructure Initiative (I3) in the sixth Framework Programme (now continuing in FP7) and funded a project called ANNA (2006-2010). This acronym stands for European Integrated **A**ctivity of Excellence and **N**etworking for **N**ano and Micro- Electronics **A**nalysis. The consortium includes 12 partners from 7 European countries and is coordinated by the Fondazione B.Kessler (FBK) in Trento (Italy); CNR-IMM is one of the 12 partners.

Aim of ANNA is the onset of strong, long-term collaboration among the partners, so to form an integrated multi-site analytical facility, able to offer to the European community a wide variety of top-level analytical expertise and services in the field of micro- and nano-electronics. They include X-ray diffraction and scattering, SIMS, electron microscopy,

medium-energy ion scattering, optical and electrical techniques. The project will be focused on three main activities: Networking (standardization of samples and methodologies, establishment of accredited reference laboratories), Transnational Access to laboratories located in the partners' premises to perform specific analytical experiments (an example is given by the two STEM methodologies discussed above) and Joint Research activity, which is targeted at the improvement and extension of the methodologies through a continuous instrumental and technical development. It is planned that the European joint analytical laboratory will continue its activity beyond the end of the project in 2010.

Publ. Astron. Obs. Belgrade No. 84 (2008), 139 *Invited Lecture*

THEORETICAL STUDY OF EXCITED ELECTRONIC STATES AT SURFACES, LINK WITH PHOTO-EMISSION AND PHOTO-DESORPTION EXPERIMENTS

J. P. GAUYACQ[1,2], A. G. BORISOV[1,2] and A. K. KAZANSKY[3]

[1] *CNRS, Laboratoire des Collisions Atomiques et Moléculaires, UMR 8625, Université Paris-Sud, Bâtiment 351, 91405 Orsay Cedex, France*
E–mail: jean-pierre.gauyacq@u-psud.fr

[2] *Université Paris-Sud, Laboratoire des Collisions Atomiques et Moléculaires, UMR 8625, Bâtiment 351, 91405 Orsay Cedex, France*

[3] *Fock Institute of Physics, State University of Saint Petersburg, Saint Petersburg 198504, Russia*

Abstract. Excited electronic states at surfaces are very often invoked as intermediates in reaction mechanism at solid surfaces. Indeed, formation of an excited state brings energy into the system and, most importantly, opens the way toward rearrangement processes: the potential energy surfaces describing the heavy particle motion are different for the ground and excited electronic states, so that electronic excitation triggers a motion of the atoms at the surface. In that context, the lifetime of the excited state as well as its coherence time are key parameters for the reaction mechanisms: they determine the extent to which a given excited state can induce a reaction or possibly lead to its quantum control. Various experimental techniques yielded many detailed results on the excited electronic states and their dynamical properties (energy, lifetime and coherence time): time-resolved 2-photon photo-emission (TR-2PPE) in the fs-domain and scanning tunnelling spectroscopy (STS) with atomic resolution.

The talk will review a series of results on excited electronic states at noble metal surface systems(Gauyacq et al, 2007). Based on theoretical results, it will show how the presence of a projected band gap on certain noble metal surfaces qualitatively influence the dynamics of the excited electronic states and in particular how it partly blocks the electron transfer between an adsorbate and the surface, allowing the existence of long-lived electronic states localized on the adsorbates. In the alkali/noble metal systems, the formation of the long-lived state corresponds to the transient capture of an electron by the adsorbate and the change of charge state of the adsorbate induces an outward motion of the adsorbate from the surface. Recent results on these photo-induced adsorbate vibration and desorption processes will be presented.

References

Gauyacq, J. P., Borisov, A. G. and Bauer, M.: 2007, *Prog. Surf. Sci.*, **82**, 244.

Publ. Astron. Obs. Belgrade No. 84 (2008), 140 *Invited Lecture*

INTERACTIONS OF IONS WITH CARBON NANO-STRUCTURES

Z. L. MIŠKOVIĆ

Department of Applied Mathematics, University of Waterloo, Waterloo, Ontario, Canada N2L 3G1
E–mail: zmiskovi@math.uwaterloo.ca

Abstract. Investigation into the properties of carbon nano-structures, involving fullerene molecules, carbon nanotubes, and the most recently contrived graphene, has been growing at a relentless rate over the past decade or so owing to prospects of their applications in nanotechnology. While interactions with particle beams have been an important part of this research endeavor in the context of various spectroscopic techniques (TEM, EELS, ...), the use of energetic electron and ion beams has recently emerged as a novel engineering tool for modifications of atomic structure and electronic properties of carbon nano-structures (Krasheninnikov and Banhart 2007).

In that context, the most widely studied themes in literature are concerned with changes in carbon nanotubes upon exposure to the ion-beam irradiation at energies ranging from several tens of eV to some MeV. On the other hand, the empty cylindrical space in individual carbon nanotubes, and a high degree of their ordering and alignment in structures called ropes or bundles, provide unique means for achieving the effect of ion channeling. Prospects of realization and a range of possible applications of ion channeling through carbon nanotubes at energies from keV to TeV have stimulated an active research area, which was recently reviewed (Artru et al. 2005, Mišković 2007).

After assessing some key experimental facts and the status of computer simulations of ion irradiation effects on carbon nanotubes, I shall discuss several problems arising in modeling of ion interactions with carbon nanotubes (Mowbray et al. 2006) and with graphene (Radović et al. 2008) in the medium-to-low range of ion energies, where the dielectric response of those carbon nano-structures plays a significant role. Special attention will be payed to calculations of the stopping and image forces on ions due to plasmon excitations in carbon nanotubes and graphene, with an emphasis to scattering geometries of relevance to ion channeling.

References

Artru, X., Fomin, S. P., Shulga, N. F., Ispirian, K. A., Zhevago, N. K.: 2005, *Phys. Rep.*, **412**, 89.
Krasheninnikov, A. V., Banhart, F.: 2007, *Nature Materials*, **6**, 723.
Mišković, Z. L.: 2007, *Radiat. Eff. Def. Solids*, **162**, 185.
Mowbray, D. J., Mišković, Z. L., Goodman, F. O. : 2006, *Phys. Rev. B*, **74**, 195435.
Radović, I., Hadžievski, Lj., Mišković, Z. L.: 2008, *Phys. Rev. B*, **77**, 075428.

Publ. Astron. Obs. Belgrade No. 84 (2008), 141 *Invited Lecture*

PLASMA-SURFACE INTERACTIONS

M. J. GOECKNER, C. T. NELSON, S. P. SANT, A. K. JINDAL, E. A. JOSEPH,
B. S. ZHOU, G. PARDON-WELLS, B. JARVIS, R. PIERCE and L. J. OVERZET
Department of Electrical Engineering, University of Texas at Dallas
E–mail: goeckner@utdallas.edu

Abstract. Materials processing is at a crossroads. Currently much of industrially viable materials processing is via plasmas. However as this processing has reached the nano-scale, development of industrially viable processes has become more and more difficult. In part this is because of all of the free parameters that exist in plasmas. To overcome this economic issue, tool vendors and semiconductor companies have turned to complex computational models of processing plasmas. For those models to work, one requires a through understanding of all of the gas-phase and surface-phase processes that are exhibited in plasmas. Unfortunately, these processes are not well understood.

Fortunately, one can examine the influence the plasma properties on the desired surface processes and through this ultimately optimize manufacturing. It is well known that the surface processes (etch or deposition), occur in the top few mono-layers of the surface. For example, growth of a film will require that molecules from the gas-phase land and bond on the surface. In order to understand the mechanism of deposition and etch on a surface, we begin with a basic reaction rate density

$$R_{\text{particle}} = \int_0^\infty \sigma(\varepsilon, T) n_{bonds} v_{particle} n_{particle} f_{particle}(\varepsilon) d\varepsilon \tag{1}$$

Here $\sigma(\theta, \varepsilon, T)$ is defined as the cross section of a particle either filling or creating an available bond site on the a surface of temperature T, n_{bonds} is the density of surface bonds, $v_{particle}$ is the gas particle velocity, $n_{particle}$ is the gas particle density and $f_{particle}(\varepsilon)$ is the gas energy distribution function. Assuming that the fraction of bond sites that are open is Θ, then at any given time the open bond density will be $\Theta\ n_{bonds}$ and the closed bond density is $(1-\Theta)\ n_{bonds}$. Under the assumption that most of these processes occur at open bond sites, our group has arrived at a general formula for the process rate (here applied to C_xF_y etch of SiO_2) of:

$$\text{Process Rate} = \left[\begin{array}{l} \sum \frac{K_{ions}}{\rho_{C_xF_y}} \langle \Gamma_{ions} \rangle S.C_{ions} + \sum\limits_{deposit} \frac{K_{C_xF_y}}{\rho_{C_xF_y}} \langle \Gamma_{C_xF_y} \rangle S.C_{C_xF_y} \\ - \sum \frac{K_{ions}}{\rho_{C_xF_y}} \langle \Gamma_{ions,FC} \rangle Y_{ions,FC} - \sum\limits_{etches} \frac{K_{C_xF_y}}{\rho_{C_xF_y}} \langle \Gamma_{C_xF_y} \rangle Y_{C_xF_y} \\ - \sum \frac{K_{C_xF_y}}{\rho_{SiO_2}} \langle \Gamma_{ions,SiO_2} \rangle Y_{ions,SiO_2} - \sum\limits_{etches} \frac{K_{C_xF_y}}{\rho_{SiO_2}} \langle \Gamma_{C_xF_y} \rangle Y_{C_xF_y,SiO_2} \end{array} \right] \tag{2}$$

Here, S.C or Y $\approx \langle R_{particle} \Theta * n_{surface} \rangle$ is the deposition sticking coefficient or etch yield, K_X is a species dependent proportionality constant, $\langle \Gamma_X \rangle$ is the particle flux, and ρ_X is the surface material density.

In this paper we will examine the implications of Equation 2. Specifically we will examine how the surface interactions set how process tools work. From this we will examine the potential future of the plasma-processing field.

Publ. Astron. Obs. Belgrade No. 84 (2008), 142 *Topical Lecture*

SURFACE AND THIN FILM ANALYSIS USING GRAZING INCIDENCE FAST ATOM DIFFRACTION (GIFAD)

H. KHEMLICHE, P. SOULISSE, N. BUNDALESKI and P. RONCIN[1]

Laboratoire des Collisions Atomiques et Moléculaires,
UMR 8625 CNRS-Université Paris Sud, Orsay, France
E–mail: philippe.roncin@u-psud.fr

Abstract. Grazing collisions at surfaces offer rather contrasted conditions. For well ordered flat surfaces, the scattering is spread among several lattice sites, each of which produces only a tiny elementary deflection. If, in addition, the atomic projectile is aligned along a crystallographic direction, the surface appears as made of parallel furrows which act as a diffraction grating for the atomic wave. We will show that the analysis of characteristic diffraction pattern recorded on the position sensitive detector located downstream allow a sensitive measure of the shape of the surface electronic density. At variance, if a terrace edge or an ad-atom is sitting on the surface along the trajectory, a quasi-binary collision will follow in which energy and momentum conservation allow identification of the mass of the collision partner.

[1]To whom any correspondence should be addressed.

Publ. Astron. Obs. Belgrade No. 84 (2008), 143 *Topical Lecture*

FUNDAMENTAL ASPECTS IN THE PLASMA SURFACE INTERACTION DURING PLASMA STERILIZATION

A. VON KEUDELL

Ruhr-University Bochum, 44780 Bochum, Germany
E–mail: Achim.vonKeudell@rub.de

Abstract. The inactivation of bacteria in oxygen or hydrogen containing low pressure plasmas is investigated by mimicking the plasma exposure with a dedicated beam experiment employing argon ions, oxygen molecules/atoms and hydrogen atoms . Thereby, fundamental inactivation mechanisms can be revealed. It is shown that the impact of O atoms or H atoms has no effect on the viability of bacterial spores and that no etching of the spore coat occurs up to an O and H atom fluence of 3.5×10^{19} cm^{-2}. The impact of argon ions with an energy of 200 eV does not cause significant erosion for fluences up to 1.15×10^{18} cm^{-2}. However, the combined impact of argon ions and oxygen molecules/atoms or H atoms causes significant etching of the spores and significant inactivation. This is explained by the process of chemical sputtering, where an ion induced defect at the surface of the spore reacts with either the incident bi-radical O_2 or with an incident O atom or H atom. This leads to the formation of CO, CO_2 and H_2O and thus to erosion. This beam results are compared to a broad sterilization campaign using an ICP reactor in a European round robin experiment BIODECON. Strategies for optimizing the plasma sterilization processes will be presented.

Publ. Astron. Obs. Belgrade No. 84 (2008), 144 *Topical Lecture*

SIMULATION OF STREAKING EXPERIMENTS AT SURFACES

C. LEMELL[1], B. SOLLEDER[1], K. TŐKÉSI[2], and J. BURGDÖRFER[1]

[1] *Inst. for Theoretical Physics, Vienna Univ. of Technology, Vienna, Austria*
E–mail: lemell@concord.itp.tuwien.ac.at

[2] *ATOMKI, H–4001 Debrecen, P.O.Box 51, Hungary*

Abstract. Recently, first streaking experiments at a tungsten surface (Cavalieri et al. 2007; "streaking": Kienberger et al. 2004) were performed. An XUV laser pulse was directed on a tungsten surface together with a collinear ultrashort near infrared probe pulse. Surprisingly large run-time differences of 110 ± 70 as for different regions of the electron spectrum were observed.

In our simulation of this experiment we model first electron excitation by the XUV laser pulse. We determine the energy distribution and emission depths of excited electrons from material and laser-pulse properties. These electrons are then propagated in the target material by a classical transport simulation. Along their trajectory, electrons undergo elastic and inelastic collisions with the target material (Solleder et al. 2007). Furthermore, trajectories are deflected due to the probe laser field penetrating into the metal. Electrons escaping the target are subject to the laser field in vacuum and may eventually reach the detector mounted perpendicular to the surface.

A lower bound for the run-time difference within the target material for electrons from the conduction band and 4f electrons of about 20 as can be derived. Inelastic scattering events increase the observed run-time difference. Depending of the dispersion relation used in our model values of up to 85 as were found.

References

Cavalieri, A. L., Müller, N., Uphues, Th., Yakovlev, V. S., Baltuska, A., Horvath, B., Schmidt, B., Blümel, L., Holzwarth, R., Hendel, S., Drescher, M., Kleineberg, U., Echenique, P. M., Kienberger, R., Krausz, F., Heinzmann, U.: 2007, *Nature*, **449**, 1029.

Kienberger, R., Goulielmakis, E., Uiberacker, M., Baltuska, A., Yakovlev, V., Bammer, F., Scrinzi, A.,Westerwalbesloh, Th., Kleineberg, U., Heinzmann, U., Drescher, M., Krausz, F.: 2004, *Nature*, **427**, 817.

Solleder, B., Lemell, C., Tökesi, K., Hatcher, N., Burgdörfer, J.: 2007, *Phys. Rev. B*, **76**, 075115.

Publ. Astron. Obs. Belgrade No. 84 (2008), 145 *Progress Report*

DECOHERENCE IN THE DIFFRACTION OF HELIUM AT SURFACES

F. AIGNER[1], N. SIMONOVIĆ[2], B. SOLLEDER[1] and J. BURGDÖRFER[1]

[1]*Institute for Theoretical Physics, Vienna University of Technology, A-1040 Vienna, Austria, EU*
E–mail: aigner@concord.itp.tuwien.ac.at

[2]*Institute of Physics, P.O. Box 57, 11001 Belgrade, Serbia*
E–mail: simonovic@phy.bg.ac.yu

Abstract. Scattering of fast neutral atoms with keV kinetic energies at alkali-halide surfaces under grazing angles displays intriguing diffraction patterns (Schüller, Wethekam and Winter 2007, Roisseau et al. 2007). In spite of the impulsive interaction with a surface at elevated temperature, which results in phonon excitation, quantum coherence evidently persists. To quantitatively study this remarkable survival of coherence, we present an ab initio simulation of the quantum diffraction of fast helium beams at a LiF (100) surface in the $\langle 110 \rangle$ direction and compare with recent experimental diffraction data.

Decoherence is analyzed employing a quantum trajectory Monte Carlo method (Minami, Reinhold and Burgdörfer 2003), calculating the ensemble average over solutions of a stochastic linear Schrödinger equation. The evolution of the atomic wavepacket is governed by a sequence of stochastic collisions and continuous propagation in the He-LiF surface potential. We find near-perfect agreement between the resulting diffraction patterns and experimental results (Schüller, Wethekam and Winter 2007) without using any adjustable parameters.

The question, whether the LiF surface features "buckling", (i.e. vertical surface reconstruction where the F atoms are displaced relative to the Li atoms) has been addressed in the past (de Wette, Kress and Schröder 1985). However, experimental uncertainties were of the same order as the displacement amplitude itself. In atom-surface diffraction at a grazing angle, surface reconstruction drastically changes the diffraction patterns. By comparison of numerical and experimental results, the buckling amplitude can be determined with unprecedented accuracy.

References

de Wette, F., Kress, W. and Schröder, U.: 1985, *Phys. Rev. B*, **32**, 4143.
Minami, T., Reinhold, C. and Burgdörfer, J.: 2003, *Phys. Rev. A*, **67**, 022902.
Rosseau, P., Khemliche, H., Borisov, A. and Roncin, P.: 2007, *Phys. Rev. Lett.*, **98**, 016104.
Schüller, A., Wethekam, S. and Winter, H.: 2007, *Phys. Rev. Lett.*, **98**, 016103.

Publ. Astron. Obs. Belgrade No. 84 (2008), 146 *Progress Report*

CHANNELING OF PROTONS THROUGH CARBON NANOTUBES

D. BORKA[1,2], D. J. MOWBRAY[2], Z. L. MIŠKOVIĆ[2], S. PETROVIĆ[1] and N. NEŠKOVIĆ[1]

[1] *Laboratory of Physics (010), Vinča Institute of Nuclear Sciences, P. O. Box 522, 11001 Belgrade, Serbia*
E–mail: dusborka@vin.bg.ac.yu

[2] *Department of Applied Mathematics, University of Waterloo, Waterloo, Ontario, Canada N2L3G1*

Abstract. We investigate how dynamic polarization of carbon valence electrons influences both the angular and spatial distributions of protons channeled in a (11, 9) single-wall carbon nanotube placed in vacuum and in different dielectric media. Proton speeds between 3 and 10 a.u., corresponding to energies of 0.223 and 2.49 MeV, are chosen with the nanotube length varied between 0.1 and 1 μm (Borka et al. 2006, 2008). In all performed calculations we describe the interaction between proton and carbon atoms on the nanotube wall using the Doyle-Turner potential. The image force on proton is calculated using a two-dimensional hydrodynamic model for the dynamic response of the nanotube valence electrons and the dielectric media surrounding the nanotube. The angular distributions of channeled protons are generated using a computer simulation method which solves the proton equations of motion in the transverse plane numerically. The best level of ordering and straightening of carbon nanotube arrays is often achieved when they are grown in a dielectric matrix, so such structures present the most suitable candidates for future channeling experiments with carbon nanotubes. Consequently, we investigate here how the dynamic polarization of carbon valence electrons in the presence of various surrounding dielectric media affects the angular distributions of protons channeled through (11, 9) single-wall carbon nanotubes. Our analysis shows that the inclusion of the image interaction causes qualitative changes in the proton deflection function, giving rise to a number of rainbow maxima in the corresponding angular and spatial distribution. We propose that observations of those rainbow maxima could be used to deduce detailed information on the relevant interaction potentials, and consequently to probe the electron distribution inside carbon nanotubes. Also, our analysis shows that the presence of dielectric media surrounding the nanotube influences both the positions of extrema in the proton deflection functions and the positions and appearance of rainbows in the corresponding angular and spatial distributions. In addition, we analyze the possibility of production of nano-sized beams by carbon nanotubes.

References

Borka, D., Mowbray, D. J., Mišković, Z. L., Petrović, S. and Nešković, N.: 2008, *Phys. Rev. A* **77**, 032903.

Borka, D., Petrović, S., Nešković, N., Mowbray, D. J. and Mišković, Z. L.: 2006, *Phys. Rev. A*, **73**, 062902.

Publ. Astron. Obs. Belgrade No. 84 (2008), 147 *Progress Report*

COLLISIONS OF IONS WITH INSULATOR SURFACES: CHARGING AND DISCHARGING DYNAMICS

N. BUNDALESKI[1*], H. KHEMLICHE[1], P.ROUSSEAU[2], A. CASSIMI[2],
P. SOULISSE[1] and P. RONCIN[1]

[1] *Laboratoire des Collisions Atomiques et Moléculaires,*
UMR 8625 CNRS-Université Paris Sud, Orsay, France
E–mail: nenad.bundaleski@u-psud.fr

[2] *Centre de Recherche sur les Ions, les Matériaux et la Photonique,*
UMR 6252 CNRS-ENSICAEN-CEA-Université Caen Basse-Normandie, Caen, France

Abstract. The guiding of ions in keV to MeV energy range by insulator microcappilaries opens interesting perspectives such as direct injection of ions inside a living cell or formation of surface nano-structures, etc. (see e.g. ITS-LEIF news letter #4 http://www.its-leif.org/NEWSPRESS/newspress.html). We have studied the dynamic behaviour of charge deposition and beam deflection on insulators having well defined planar geometry when the exact number of charges implanted into the surface, as well as the time evolution of the beam deflection, can be monitored. Depending on temperature of the sample, surface composition and structure, discharging time constant varies by orders of magnitude, giving rise to different guiding effects in insulator microcappilaries.

[1*]To whom any correspondence should be addressed.

Publ. Astron. Obs. Belgrade No. 84 (2008), 148 - 150 *Progress Report*

UNRAVELING THE IMPORTANCE OF SURFACE ASSOCIATION TO THE FORMATION OF MOLECULES IN A RECOMBINING N_2/O_2 PLASMA

R. ZIJLMANS[1,*], S. WELZEL[2], O. GABRIEL[1], J. H. VAN HELDEN[1,**], J. RÖPCKE[2], D. C. SCHRAM[1] and R. ENGELN[1]

[1] *Departement of Applied Physics, Eindhoven University of Technology, Eindhoven, The Netherlands*
E–mail: r.engeln@tue.nl

[*] *Present address: Sensor Sense B.V., Toernooiveld 1, Nijmegen, The Netherlands (www.sensor-sense.nl)*

[**] *Present address: Physical and Theoretical Chemistry Laboratory, Oxford University, United Kingdom*

[2] *INP-Greifswald, Friedrich-Ludwig-Jan-Str. 19, D-17489, Greifswald, Germany*

1. INTRODUCTION

The interaction of reactive species, like atomic or molecular radicals, with a surface is a very general phenomenon. In plasma processing it is this interaction that leads to the modification of surfaces, i.e. deposition or etching (van de Sanden et al. 1998, Martinu and Poitras 2000). But also in the plasma assisted conversion of gases the surface plays an important role (Rousseau et al. 2006, Tanaka et al. 1994). In interstellar space it has been recognized that ice or dust particles act as third body in association processes in which not only hydrogen molecules are formed, but also larger molecules (Vidali et al. 2006). How to control the very fast erosion of the carbon tiles due to the plasma-surface interaction in the divertor region of Tokamaks, is one of the most important research questions still to be answered in thermonuclear fusion research (Shimomura 2007).

Next to studies on technological plasmas, also more fundamental studies have been performed to obtain detailed insight in the interaction of radicals with surfaces. In these studies different surface materials are exposed to well-defined atomic and molecular radicals. For example, already in 1971, the formation of NH_3 at different types of surfaces in a plasma created from mixtures of N_2 and H_2 was studied by Eremin et al. (Eremin et al. 1971). They compared the catalytic conversion into NH_3 in a barrier discharge in the presence of metallic palladium, platinum, iron, copper or nickel with clean glass. Differences of a factor of four of production for the various materials is observed. Detailed studies on the plasma assisted ammonia formation from N_2 and H_2 mixtures have been performed also by Vankan (2002) and van Helden

(2007). More recent are studies on photo-catalytic processes, as reported for example by Thevenet et al. (2006). Another example is described by Gatilova et al. (2007), where the formation of NO in a low pressure discharge is investigated. The authors focus mainly on the gas phase formation of NO, but recognize the importance of the surfaces of the plasma reactor. Also Castillo et al. (2005) conclude in their studies that mainly heterogeneous processes are responsible for the formation of NO.

To unravel the contribution of surface related processes to the total kinetics in a low pressure recombining plasma created from mixtures of N_2 and O_2, we measured the abundance of the stable molecules NO, N_2O and NO_2in the plasma by means of IRMA, which is an IR tunable diode laser absorption system (Röpcke et al. 2000), and mass spectrometry (N_2 and O_2). A simulation, developed in CHEMKIN (2004), is used to investigate the effect of radical-surface interactions on the conversion of the feedstock gases.

2. RESULTS

A plasma expansion is created from a flow of 3000 standard cubic centimeters per minute (sccm) argon through a cascaded arc plasma source. A total power of 5 kW (I = 75 A) is used to create the Ar plasma in the arc channel of the source. This plasma expands from the exit of the arc channel into the reactor, which is kept at a pressure of p = 20 Pa or p =100 Pa. A total flow of 1800 sccm of mixtures of N_2 and O_2 is injected directly into the reactor. The molecular abundances of the species formed in the plasma vessel are investigated as function of the ratio of admixed O_2 flow over the total flow of O_2 and N_2.

In Figure 1 the symbols denote the measured mole fractions of Ar, N_2, O_2, NO, N_2O and NO_2, which are plotted on a semi-logarithmic scale. All the species are measured with the quadrupole mass spectrometer, while NO and N_2O are also measured by infrared absorption spectroscopy, using the IRMA system (Röpcke et al. 2000). The results of both the mass spectrometry measurements and tunable diode laser absorption spectroscopy measurements showed good agreement (within 10%). For both pressures the molecules N_2 and O_2 are dominantly present. The abundance of the other types of molecules (NO, NO_2 and N_2O) is at least one to three orders of magnitude lower. Remarkable is the maximum abundance of NO: for both pressures it is close to a mole fraction of 10^{-2}. Furthermore, the abundance of N_2O and NO_2 decreases significantly with an increase of pressure. During the presentation it will be shown that the abundance of NO increases with increasing O_2 admixture only for admixed O_2 fractions higher than 10%. This onset is much more pronounced at a pressure of p = 100 Pa than at p = 20 Pa.

In Figure 1 the lines denote, except for argon, the simulations performed with CHEMKIN (2004), a chemical kinetics model. During the presentation results will be shown that clearly indicate that, especially for the formation of NO_2 and N_2O, the presence of surfaces is essential to explain the observed abundances in the plasma. Also, the rate of surface production of NO was calculated to be the highest for almost all the studied conditions and was found in the same order as the primary dissociation rate of injected gases. The best agreement between calculations and measurements was found for low activation energies and desorption energies of the surface processes and low calculated surface coverage. It will be shown that these results can be explained by assuming that the processes take place on a mobile surface layer.

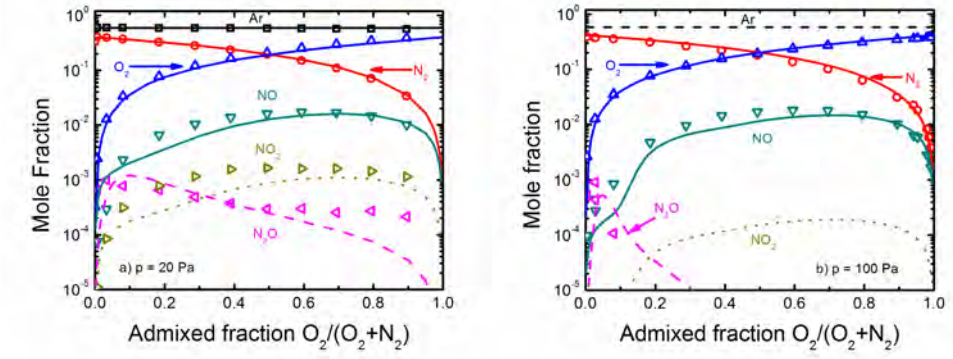

Figure 1: The measured (symbols) and calculated (lines) mole fractions of the molecules in the plasma at two different pressures as a function of the ratio of the flow of O_2 to the total flow of the injected gas mixture of N_2 and O_2. The expanding plasma is generated from 3000 sccm of argon. The total flow of the injected mixture is 1800 sccm.

References

Castillo, M., Méndez, I., Islyaikin, A. M., Herrero V. J. and Tanarro, I.: 2005, *J. Phys. Chem. A*, **109**, 6255.

CHEMKIN®Interface 4 Simulation software: 2004.

Eremin, E. N., Mal'tsev, A. N. and Syaduk, V. L.: 1971, *Russian Journal of Physical Chemistry*, **45**, 635.

Gatilova, L. V., Allegraud, K., Guillon, J., Ionikh, Y. Z., Cartry, G., Röpcke J. and Rousseau, A.: 2007, *Plasma Sources Sci. Technol.*, **16**, S107.

Martinu, L. and Poitras, D.: 2000, *J. Vac. Sci. Technol. A*, **18**, 2619.

Röpcke, J., Mechold, L., Käning, M., Anders, J., Wienhold, G., Nelson D. and Zahniser, M.: 2000, *Rev. Sci. Instrum.*, **71**, 3706.

Rousseau, A., Meshchanov, A. V. and Röpcke, J.: 2006, *Appl. Phys. Lett.*, **88**, 021503.

Shimomura, V.: 2007, *Journal of Nuclear Materials*, **363-365**, 467.

Tanaka, S., Uyama, H. and Matsumoto, O.: 1994, *Plasma Chemistry and Plasma Processing*, **14**, 491.

Thevenet, F., Guaitella, O., Puzenat, E., Herrmann, J.-M., Rousseau A. and Guillard, C.: 2006, *Catalysis Today*, **122**, 186.

van de Sanden, M. C. M., Severens, R. J., Kessels, W. M. M., Meulenbroeks, R. F. G. and Schram, D. C.: 1998, *J. Appl. Phys.*, **84**, 2426.

van Helden, J. H., van den Oever, P. J., Kessels, W. M. M., van de Sanden, M. C. M., Schram, D. C. and Engeln, R.: J. 2007, *Phys. Chem. A*, **111**, 11460.

Vankan, P., Rutten, T., Mazouffre, S., Schram, D. C. and Engeln, R.: 2002, *Appl. Phys. Lett.*, **81**, 418.

Vidali, G., Roser, J. E., Ling, L., Congiu, E., Manicó, G. and Pirronello, V.: 2006, *Faraday Discuss.*, **133**, 125.

Publ. Astron. Obs. Belgrade No. 84 (2008), 151 - 152 *Progress Report*

THE NANOPARTICLE FORMATION IN HYDROCARBON PLASMAS

E. KOVAČEVIĆ[1], I. STEFANOVIĆ [2], J. BERNDT[1], C. GODDE[3], J. WINTER[2] and L. BOUFENDI[1]

[1] *GREMI Université d'Orléans Polytech'Orleans 14 rue d'Issoudun*
E–mail: eva.kovacevic@uni-orleans.fr
E–mail: johannes.berndt@univ-orleans.fr

[2] *Ruhr University Bochum, Institute for Experimental Physics II, Bochum, Germany*
E–mail: Ilija.stefanovic@rub.de
E–mail: joerg.winter@rub.de

[3] *Ruhr University Bochum, Institute for Experimental Physics III, Bochum, Germany*
E–mail: casten.godde@rub.de

Abstract. This work presents controllable plasma polymerization of nanoparticles. Controlled production of nanoparticles with variable characteristics is important for different application fields, from technology to astrophysics. We present changes in material characteristics of nanoparticles due to variations of the gas mixtures, plasma characteristics and especially the role of temperature.

The phenomena related to dusty plasmas have an immense number of facets – from plasma crystals to applications in astrophysics or technology. One of the special aspects of this field is certainly the plasma polymerization of dust particles, resulting from homogeneous or heterogeneous processes, ("Dusty Plasmas", ed. Bouchoule 2003).

We present here results obtained in low–pressure capacitively coupled radiofrequency discharges, with variable gas mixtures. The plasma polymerization process and experimental set up used in our work are in detail described in Kovačević 2006, Berndt 2007. It is possible to claim that such polymerization process posses similarities to stellar outflow conditions (Chiar et al. 1998, Kovačević et al. 2005) and provides a convenient way to produce candidate carbonaceous interstellar dust analogs under controlled conditions and to compare their characteristics to astronomical observations (Kovačević et al. 2005, Stefanović et al. 2005). Moreover low temperature rf plasmas provide an excellent trap for the charged dust particles, enabling different in-situ methods like in-situ extinction measurements on the dust particles (from VUV to IR spectroscopy), mass spectroscopy and optical emission spectroscopy of gas phase species etc.

One of the important results concerns the role of the gas composition on the material characteristics of the nanoparticles. Even changes of the carrier gases (He, Ar, Xe) affect the plasma characteristics, and thus the material characteristics of plasma polymerized nanoparticles. One important direction in our work concerns the role of the gas temperature for the nucleation processes and the material characteristics. Further variations in material characteristics of our nanoparticles are obtained by annealing of collected particles. The temperature aspect is highly interesting for applications in the field of astrophysics (see the results presented recently by Mennella et al. 2008).

References

Berndt, J.: 2007, Reactive Dusty Plasmas, Habilitation, Ruhr-University Bochum, Germany.

Bouchoule. A. ed.: 2003, Dusty Plasmas: Physics, Chemistry and Technological Impacts in Plasma Processing, Wiley & Sons, Chichester, UK.

Chiar, J. E., Pendleton, Y. J., Geballe, T., Tielens, A. G. G. M.: 1998, *Astrophys. J.*, **507**, 281.

Kovačević, E.: 2006, Dissertation, RUB, Bochum, Germany.

Kovačević, E., Stefanović, I., Berndt, J., Pendleton Y. J. and Winter, J.: 2005, *Astrophys. J.*, **620**, 2924.

Manella, V: 2008, see IAU Symposium 251: "Organic Matter in Space", 18-22 Feb. 2008, Hong Kong China, web.science.hku.hk/online/programmes.

Stefanović, I., Kovačević, E., Berndt, J., Pendleton, Y. J. and Winter, J.: 2005, *PPCF*, **47**, A179.

Publ. Astron. Obs. Belgrade No. 84 (2008), 153 - 156 *Contributed Paper*

DECAY RATES OF LARGE-l RYDBERG STATES OF MULTIPLY CHARGED IONS APPROACHING SOLID SURFACES

N. N. NEDELJKOVIĆ[1], M. A. MIRKOVIĆ and D. K. BOŽANIĆ[2]

[1] *Faculty of Physics, University of Belgrade, P.O.Box 368, Belgrade, Serbia*
E–mail: hekata@ff.bg.ac.yu

[2] *Vinča Institute of Nuclear Sciences, P.O.Box 522, Belgrade, Serbia*

Abstract. We investigate the ionization of large-l multiply charged Rydberg ions approaching solid surfaces within the framework of decay model and applying the etalon equation method. The radial coordinate ρ of the active electron is treated as a variational parameter and therefore the parabolic symmetry is preserved in this procedure. The complex eigenenergies are calculated from which the energy terms and the ionization rates are derived. We find that the large-l Rydberg states decay at approximately the same ion-surface distances as the low-l states oriented toward the vacuum and considerably closer to the surface comparing to the low-l states oriented towards the surface.

1. INTRODUCTION

The neutralization and ionization processes of Rydberg ions during the ion-surface interaction represent the complex quantum events that require a detailed description of the intermediate stages of the processes.

Depending on the collision geometry and energy, the charge state of the ionic projectiles, and the quantum state of the active electron these two basic one-electron processes can be treated by rather different theoretical tools. Here we mention the coupled angular mode (CAM) method, see e.g. Borisov et al. (1996).

A specific description of the neutralization can be obtained within the framework of two-state vector model (TVM), see e.g. Nedeljković and Nedeljković (1998) and Nedeljković et al. (2003). The TVM has been applied both to the large-l and low-l cases, where l is the angular momentum quantum number. It was demonstrated that the reionization of the previously populated Rydberg states could play an important role. However, only the low-l ionization and reionization have been considered; the problems have been treated within the framework of etalon equation method (EEM) by Nedeljković and Nedeljković (2003, 2005) and by Nedeljković et al. (2006). The information about the (re)ionization of the large l Rydberg states is still uncomplete.

In the present paper, we analyze the ionization of multiply charged ($Z \gg 1$) ions approaching solid surfaces at velocity v, being initially in the large-l Rydberg states ($n \gg 1, l \approx n-1, m=0$). In contrast to the low-l states, the large-l states evolve, under plausible physical assumptions, into the low-eccentricity parabolic states in the

vicinity of the surface. We consider the ionization as a decay of the formed intermediate state $\bar{\Psi}$; the ionization rates follow directly from the complex eigenenergies corresponding to the eigenfunctions $\bar{\Psi}$. In solving the complex energy eigenvalue problem, we use the EEM adapted for the intermediate states of low-eccentricities.

2. DECAY MODEL

Here we extend the low-l decay model of Nedeljković and Nedeljković (1998, 2003) to the large-l case.

We consider the ionization process $\mathrm{A}^{(Z-1)+} + \mathrm{M} \rightarrow \mathrm{A}^{Z+} + \mathrm{M}(e)$ of the ionic projectile $\mathrm{A}^{(Z-1)+}$ in the large-l Rydberg state (or more precisely, being initially in the large-l state) approaching a solid surface (M) at velocity $v = v_{\perp} = -dR/dt$, along the z axis orthogonal to the surface. At the time $t = t_{in}$ ($R = R_{in} \rightarrow \infty$) the active electron is in the state $\Psi_{\nu,in}$, where $\nu = (n, l, m)$ represents a given set of spherical quantum numbers.

The electron wave function in the absence of ionization evolves according to the law $\Psi(\vec{r}, t) = \hat{U}(t_{in}, t)\Psi_{\nu,in}$, where $\hat{U}(t_{in}, t) = \exp(-i\int_{t_{in}}^{t} \hat{H}dt)$ is the evolution operator and $\hat{H}$ is the corresponding Hamiltonian. Expanding $\Psi_{\nu,in}$ over the parabolic basis $\Psi_{\mu,in}$, characterized by the parabolic quantum numbers $\mu = (n_1, n_2, m)$, where $n_1 + n_2 + |m| + 1 = n$, we get

$$\Psi_{\nu,in} = \sum \langle \mu|\nu\rangle \Psi_{\mu,in}, \tag{1}$$

where $\langle \mu|\nu\rangle$ are the expansion coefficients. In the large-l case ($l \approx n - 1$) and for $m = 0$, the main contribution to the expansion (1) give the terms with $n_1 \approx n_2$, i.e., $n_1 \approx (n-1)/2$. This can be proved if the coefficients $\langle \mu|\nu\rangle$ are expressed via Clebsh-Gordon coefficients; for example, for $l = n - 1$ and $m = 0$ we have

$$\langle \mu|\nu\rangle = \frac{\sqrt{2l+1}}{\sqrt{(2n-1)!}} \frac{[(n-1)!]^2}{n_1!(n-n_1-1)!}. \tag{2}$$

At intermediate stages, the "large-l" wave function $\Psi(\vec{r}, t)$ behaves as a parabolic function corresponding to the intermediate parabolic quantum numbers μ with $n_1 \approx n_2$. On the other hand, the initially low-l Rydberg states evolve into the intermediate parabolic states with $n_1 \approx 0$ (states of large eccentricities oriented toward the surface) and the states with $n_1 \approx n - 1$, which are highly eccentric, but which are oriented toward the vacuum.

The ionization process represents a decay of the function $\Psi(\vec{r}, t)$: $\Psi \rightarrow \bar{\Psi}$, where

$$\bar{\Psi}(\vec{r}, t) = \mathcal{E}_{\mu}(t)\Psi(\vec{r}, t)\Theta(z) + \chi(\vec{r}, t)\Theta(-z). \tag{3}$$

The regions inside and outside the solid ($z < 0$ and $z > 0$) are defined by the Heaviside function $\Theta(z)$. The function $\chi(\vec{r}, t)$ in Eq. (3) stands for the outgoing wave inside the solid. According to expression (3), the state $\bar{\Psi}$ represents a decaying state, with a "parabolic" decay factor of the following form:

$$\mathcal{E}_{\mu}(t) = \exp\left(-\frac{1}{2}\int_{t_{in}}^{t} \Gamma_{\mu}^{I}(t)dt\right), \tag{4}$$

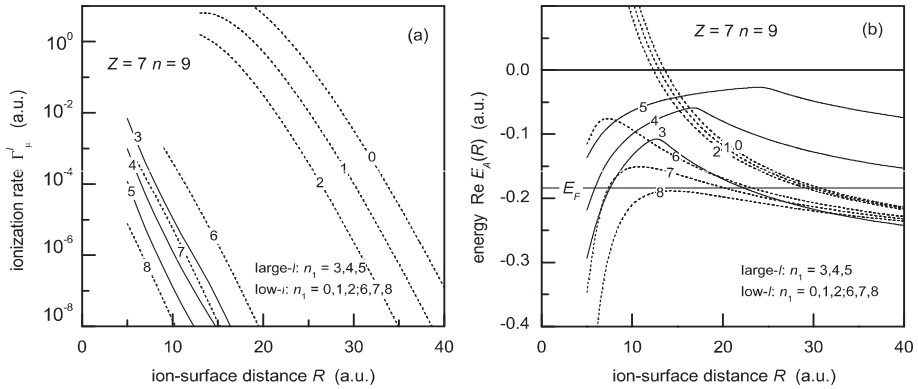

Figure 1: (a) Ionization rates $\Gamma^I_\mu(t)$ for the ion with core charge $Z = 7$ for the large-l Rydberg states $n = 9$, $n_1 = 3, 4$ and 5 and $m = 0$ (full curves) and the low-l states $n = 9$, $n_1 = 0, 1, 2; 6, 7, 8$ (dashed curves) and (b) the corresponding energy terms $\mathrm{Re}E_A(R)$.

where $\Gamma^I_\mu(t)$ is the ionization rate. The quantity $\Gamma^I_\mu(t)$ follows from the complex eigenenergies $E_A = \mathrm{Re}E_A - i\Gamma^I_\mu/2$.

The crucial difference of the large-l case in comparison to the low-l case is the fact that the radial coordinate ρ in the surface potential can not be neglected. For that reason, the separation of variables in the parabolic coordinates is possible only if we consider the variable ρ as parameter ($\rho = \bar{\rho}$). In adapting the EEM to the large-l case, we define the appropriate functional $T[\Phi]$, which is stationary for $\Phi = \bar{\Psi}$. Accordingly, the parameter $\bar{\rho} = \bar{\rho}_0(\mu; R)$ can be derived from the variational requirement $\delta T = 0$. The proposed EEM enables us to evaluate the complex eigenenergies E_A, from which we get the ionization rates $\Gamma^I_\mu(t) = -2\mathrm{Im}E_A$ and the corresponding energies $\mathrm{Re}E_A$ in sufficiently accurate form. The low-l EEM theoretical predictions for the ionization via tunneling mechanism follow from the large-l expressions under the transformation $\bar{\rho}_0 \Rightarrow 0$.

3. RESULTS

According to Eqs. (3) and (4), the problem of ionization in the large-l case is reduced to the analysis of the "parabolic" rate $\Gamma^I_\mu(t)$. The calculation of the quantity $\Gamma^I_\mu(t)$ can be performed in two steps. In the first step we calculate the rates $\Gamma^I_\mu(\bar{\rho}, R)$ with $\bar{\rho}$ as a parameter. In the next step, we calculate the quantity $\bar{\rho} = \bar{\rho}_0(\mu; R)$; in that way we obtain the rates $\Gamma^I_\mu(\bar{\rho}_0(\mu; R), R) \equiv \Gamma^I_\mu(t)$. The EEM yields directly the quantities $\mathrm{Re}E_A(\bar{\rho}, R)$ and $\Gamma^I_\mu(\bar{\rho}, R)$, without explicit calculation of the eigenfunction $\bar{\Psi}$.

In Fig. 1 we present the characteristic behavior of the large-l rates and energies (full curves) via ion-surface distance R, for the Rydberg states $n = 9$, $n_1 = 3, 4$ and 5, $m = 0$ and ion with core charge $Z = 7$. The dashed curves in Fig. 1 represent the rates and energies for the low-l parabolic Rydberg states with $n = 9$, $n_1 = 0, 1, 2, 6, 7$ and 8. By E_F we denote the Fermi level of the Al-surface with work function $\phi = 5$ eV.

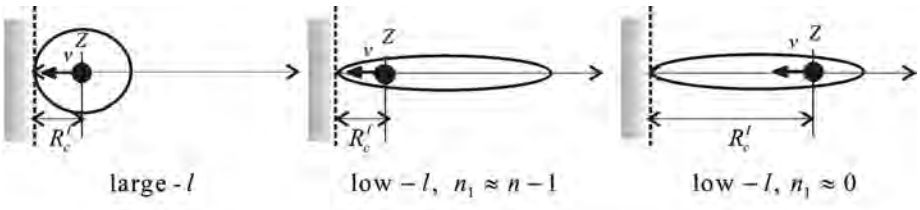

Figure 2: Behavior of the Rydberg states in the decay region $R \approx R_c^I$.

The rates presented in Fig. 1(a) are localized in two separate regions of the ion-surface distances: the large-l rates and the low-l rates with $n_1 \approx n-1$ (I group of states) are localized closer to the surface comparing to the rates corresponding to the low-l case with $n_1 \approx 0$ (II group of states). The discussed positions of the rates indicate that the two group of states (I and II) will decay at separate ion-surface distances R_c^I: the almost spherical large-l states and the eccentric low-l states with $n_1 = 6$ and 7, oriented from the surface toward the vacuum, will decay at smaller ion-surface distances in comparison to the low-l states ($n_1 = 0, 1, 2$) - oriented toward the surface. The CAM-rates of Borisov et al. (1996) are positioned at ion-surface distances just between our large-l and low-l EEM rates.

From Fig. 1(b) we see that the energy terms of the considered two group of states have also different behaviors: the energy terms corresponding to the first group: the large-l energy terms (full curves) and the low-l energy terms for $n_1 \approx n-1$ (dashed curves) have the characteristic increasing-decreasing behavior with decreasing R. On the other hand, the low-l energy terms with $n_1 \approx 0$ increase with decreasing R. The energy terms of CAM method behaves as the low-l terms from the second group of states.

In Fig. 2 we illustrate the ionization of these two group of states within the framework of classical "bubble" picture in which the ionization occurs when the ion touches the surface.

We recall that in the presented decay model the large-l and low-l states are related with the l-values of the initial states; these states evolve into the low- and large-eccentricity intermediate parabolic states, respectively. The quantum number l can be used to characterize the intermediate stages of the electron-exchange process only within the TVM in which the two functions are used to define the quantum state of a single electron.

References

Borisov, A., Zimny, R., Teillet-Billy, D. and Gauyac, J. P.: 1996, *Phys. Rev. A*, **53**, 2457.
Nedeljković, Lj. D. and Nedeljković, N. N.: 1998, *Phys. Rev. B*, **58**, 16455.
Nedeljković, Lj. D. and Nedeljković, N. N.: 2003, *Phys. Rev. A*, **67**, 032709.
Nedeljković, Lj. D., Nedeljković, N. N. and Božanić, D. K.: 2006, *Phys. Rev. A*, **74**, 032901.
Nedeljković, N. N. and Nedeljković, Lj. D.: 2005, *Phys. Rev. A*, **72**, 032901.
Nedeljković, N. N., Nedeljković, Lj. D. and Mirković, M. A.: 2003, *Phys. Rev. A*, **68**, 012721.

Publ. Astron. Obs. Belgrade No. 84 (2008), 157 - 160 *Contributed Paper*

l-DISTRIBUTIONS OF THE FIRST ELECTRON TRANSFERRED TO MULTIPLY CHARGED IONS INTERACTING WITH SOLID SURFACES

M. A. MIRKOVIĆ and N. N. NEDELJKOVIĆ

Faculty of Physics, University of Belgrade, P.O.Box 368, Belgrade, Serbia
E–mail: hekata@ff.bg.ac.yu

Abstract. We analyze the angular momentum distributions of the electron transferred into the Rydberg states of multiply charged ions escaping the solid surfaces. The population probabilities are calculated within the framework of two-state-vector model; in the case of large values of the angular momentum quantum numbers l the model takes into account an importance of a wide space region around the projectile trajectory. The reionization of the previously populated states is also taken into account. The corresponding ionization rates are obtained by the appropriate etalon equation method; in the large-l case the radial electronic coordinate ρ is treated as variational parameter. The theoretical predictions based on the proposed population-reionization mechanism fit the available beam-foil experimental data; the obtained large-l distributions are also used to elucidate the recent experimental data concerning the multiply charged Rydberg ions interacting with micro-capillary foil.

1. INTRODUCTION

For a long time it is known that the Rydberg states of multiply charged Rydberg ions can be populated during the interaction with conducting solid surface. The beam-foil type of experiments, see, e.g. Veje et al. (1985, 1988), and Bashkin et al. (1982), performed at intermediate velocities ($v \approx 1$ a.u.) of the ionic projectiles SVI, ClVII and ArVIII, provide non-linear electron capture probability distributions for both principal and angular momentum quantum numbers, n and l, of the final bound states (n, l, m). Recently, a new type of experiment by Morishita et al. (2004) produced an evidence about the l distributions in the large-l region, for the ions Ar^{7+} and Ar^{8+} at velocities $v \approx 0.2$ a.u. interacting with micro-capillary foil.

The probability distributions P_{nl} for the low-l Rydberg states ($l = 0, 1$ and 2) have been obtained theoretically within the framework of two-state-vector model (TVM) by Nedeljković et al. (1994) and Nedeljković and Nedeljković (1998). The model has been extended to the case of large-l Rydberg states ($l \geq 3$) by Nedeljković et al. (2003). In both cases the reionization was neglected. Effects of reionization in the low-l case have been included in the population process by Nedeljković and Nedeljković (2003); the ionization was considered as a decay process, and the etalon equation method (EEM) was proposed for solving the complex energy eigenvalue problem.

In this paper we include the reionization in the large l region. Just in this region, and for higher n values, the absence of the experimental data in the beam-foil geometry has been previously considered as the existence of the thresholds at $l = l_{thr} < l_{max}$. However, the new experiment with micro-capillary foil gives the nonzero population probabilities in this region. We shall demonstrate that the renormalized probabilities $\bar{P}_{nl}$, obtained by inclusion of reionization in the TVM, reconstruct the entire l distribution of the first electron transferred to the ions in the vicinity of solid surface.

2. RENORMALIZED TVM

We consider the the population-reionization (capture-recapture) process of Rydberg states of multiply charged ions escaping solid surfaces with velocity v. In the large-l case the neutralization process (electron capture from the the solid into the ionic field) can be suppressed by the reionization (electron recapture by the solid). Accordingly, if the reionization is remarkable, only a fraction of the formed Rydberg states survives. The both processes can be incorporated in the two-state vector model.

Applying the TVM, our prime intention has been to learn information about the behavior of the active electron which left the solid surface at the time t_{in}, but which will be detected in the final bound state at the time t_{fin}. To this end, we describe the single active electron simultaneously by two wave functions $\Psi_1(\vec{r},t)$ and $\Psi_2(\vec{r},t)$. The state $\Psi_1(\vec{r},t)$ evolves from an initial state Ψ_{in} labeled by the set of parabolic quantum numbers $\mu_{M,in}$ at the time $t_{in} = 0$. The population process represents a "transition" $\Psi_1(\vec{r},t) \rightarrow \Psi_2(\vec{r},t)$ at the intermediate time $t \approx \tau$, due to the "measurement" of the electron localization in the ionic region. If the reionization could be neglected, the state $\Psi_2(\vec{r},t)$ would evolve into a final bound state determined by the spherical quantum numbers $\nu_{A,fin} = (n,l,m)$ at the time $t_{fin} \rightarrow \infty$. The concept of the mixed flux through a moving Firsov plane S_F, used in the calculation of the two-state amplitude offers the possibility to treat the functions $\Psi_1(\vec{r},t)$ and $\Psi_2(\vec{r},t)$ in the "interaction-free" region. Using the appropriate asymptotic forms of wave functions, the final population probabilities P_{nl} have been obtained for both the low-l and the large-l Rydberg states, see Introduction.

The reionization is included in the model by introducing the "renormalized" wave function $\bar{\Psi}_2(\vec{r},t)$, which represents a decaying state with a decay factor of the following form:

$$\mathcal{E}_{\mu_{A0}}(t) = \exp\left[-\frac{1}{2}\int_{\tau}^{t}\Gamma^{I}_{\mu_{A0}}(t)dt\right], \tag{1}$$

where $\Gamma^{I}_{\mu_{A0}}(t)$ is the reionization rate corresponding to the intermediate parabolic quantum numbers μ_{A0}. The experimentally verifiable renormalized population probability $\bar{P}_{nl}$ is given by

$$\bar{P}_{nl} = \mathcal{E}^2_{\mu_{A0}} P_{nl}, \tag{2}$$

where $\mathcal{E}^2_{\mu_{A0}} = \lim_{t\rightarrow\infty}\mathcal{E}^2_{\mu_{A0}}(t)$, whereas P_{nl} represents the electron capture probability (without reionization) into the final Rydbeg state (n,l,m).

From Eqs. (1) and (2) we see that the problem of reionization is reduced to the calculation of the decay factor $\mathcal{E}_{\mu_{A0}}(t)$, expressed via the ionization rate $\Gamma^{I}_{\mu_{A0}}(t)$. The intermediate parabolic quantum numbers which give the main contribution to the reionization process are determined by the quantum numbers of the most probable populated states: in this interplay of quantum numbers we get that $\mu_{A0} = \{n_1 =$

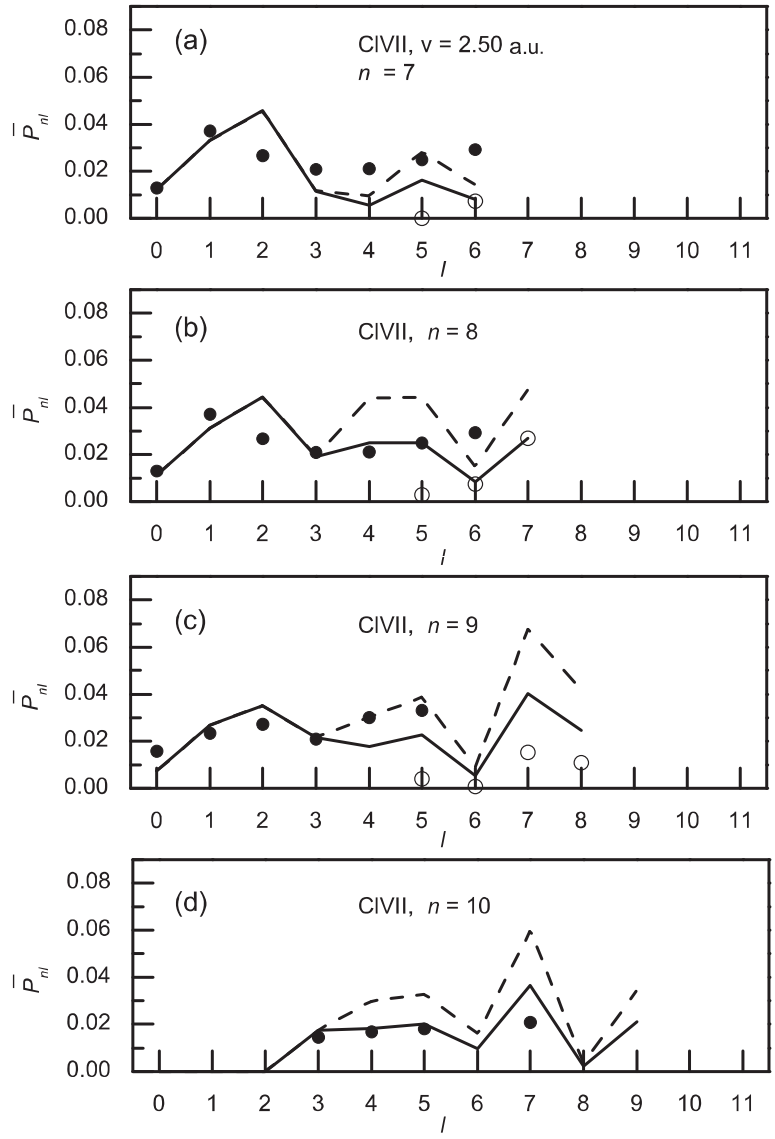

Figure 1: Renormalized population probabilities $\bar{P}_{nl}$ (full curves) and population probabilities P_{nl} (dashed lines) for the ClVII ion, via angular momentum quantum number l, for $7 \leq n \leq 10$ and $v = 2.50$ a.u. The low-l probabilities P_{nl} are obtained by Nedeljković and Nedeljković (1998) and the large-l values P_{nl} are obtained by Nedeljković et al. (2003). Note the existence of the threshold value $n = n_{thr} = 9$ in the low-l region. Dots are the beam-foil experimental data, see, e.g. Veje et al. (1985, 1988); the experimental data obtained in the presence of micro-capillary foil by Morishita et al. (2004), are presented by circles.

$0, n_2 = n-1, m = 0\}$. The ionization rates $\Gamma^I_{\mu_{A0}}(t)$ in the low-l case have been calculated by Nedeljković and Nedeljković (2003). The large-l case was considered by Nedeljković et al. (2008) for the intermediate quantum numbers $\mu_{A0} = \{n_1 \approx (n-1)/2, n_2 \approx (n-1)/2, m = 0\}$ of the Rydberg states of multiply charged ions approaching solid surface; with full analogy with the considered case, one can obtain the rates in the case relevant for the reionization process.

3. RESULTS

The electron exchange during the intermediate stages of the ion-surface interaction results in the final Rydberg system (n, l, m) at $t_{fin} \to \infty$. The experimentally verifiable population probability $\bar{P}_{nl}$, Eq. (2), can be calculated explicitly for all relevant values of the ion-surface parameters.

In Fig. 1, we present the l-distributions of the probabilities P_{nl} and $\bar{P}_{nl}$ for $n = 7-10$ of the ClVII ion ($Z = 7$) escaping the solid surface with the velocity $v = 2.50$ a.u. The population probabilities P_{nl} are presented by dashed curves; the renormalized population probabilities $\bar{P}_{nl}$ obtained by inclusion of reionization are presented by full lines. The low-l probabilities ($l = 0, 1$ and 2) are obtained by Nedeljković and Nedeljković (1998); the probabilities P_{nl} in the large-l case are obtained by Nedeljković et al. (2003). Let us note that, in contrast to the large-l case, the population of the low-l Rydberg states is characterized by the existence of the threshold value of the principal quantum number $n = n_{thr}$, i.e., $\bar{P}_{nl} = 0$ for $n > n_{thr}$.

The properly normalized beam-foil experimental data for the population of the Rydberg levels of ClVII ion, see e.g. Veje et al. (1985, 1988), are presented in Fig. 1 by dots; data are for the ionic velocity $v = 2.50$ a.u. The experimental data for neutralization of the Ar^{7+} ion ($Z = 7$), obtained in the presence of micro-capillary foil by Morishita et al. (2004), are also presented in Fig. 1 (circles). The available experimental data are for $v \approx 0.2$ a.u., so that the experimental results are scaled to the intermediate velocity case (and normalized).

Considering the l distributions presented in Fig. 1 we recognize that the proposed renormalized TVM predictions are in agreement with the both sets of available experimental data. The use of the more accurate l-dependent decay factor $\mathcal{E}^2_{\mu_{A0}}$, as well as the exact scaling factor between the low and the intermediate velocity results, will further improve the presented l-distributions.

References

Bashkin, S., Oona, H. and Veje, E.: 1982, *Phys. Rev. A*, **25**, 417.

Morishita, Y., Hutton, R, Torri, H.A, Komaki, K., Brage, T, Ando, K, Ishii, K., Kanai,Y., Masuda, H., Sekiguchi, M., Rosmej, F. B. and Yamazaki, Y.: 2004, *Phys. Rev. A*, **70**, 012902.

Nedeljković, Lj. D. and Nedeljković, N. N.: 1998, *Phys. Rev. B*, **58**, 16455.

Nedeljković, Lj. D. and Nedeljković, N. N.: 2003, *Phys. Rev. A*, **67**, 032709.

Nedeljković, N. N., Mirković, M. A. and Božanić, D. K.: 2008, *Publ. Astron. Obs. Belgrade*, **84**, 153.

Nedeljković, N. N., Nedeljković, Lj. D., Janev, R. K., Mišković, Z. L.: 1991, *Nucl. Instrum. Methods Phys. Res. B*,

Nedeljković, N. N., Nedeljković, Lj. D. and Mirković, M. A.: 2003, *Phys. Rev. A*, **68**, 012721.

Nedeljković, N. N., Nedeljković, Lj. D., Vojvodić, S. B. and Mirković, M. A.: 1994, *Phys. Rev. B*, **49**, 5621.

Veje, E.: 1985, *Nucl. Instrum. Methods Phys. Res. B*, **8**, 586.

Veje, E. and Winter, H.: 1988, *Zs. f. Phys. D*, **10**, 457.

Publ. Astron. Obs. Belgrade No. 84 (2008), 161 - 164 *Contributed Paper*

NEUTRALIZATION DISTANCES OF Ar^{Z+} RYDBERG IONS INTERACTING WITH SOLID SURFACES

M. D. MAJKIĆ, N. N. NEDELJKOVIĆ and S. M. D. GALIJAŠ

Faculty of Physics, University of Belgrade, P.O.Box 368, Belgrade, Serbia
E–mail: hekata@ff.bg.ac.yu

Abstract. We apply the recently developed time-symmetrized, two-state vector model to investigate the intermediate stages of the electron capture into the Rydberg states of multiply charged Ar^{Z+} ions (core charge $Z \gg 1$, principal quantum number $n_A \gg 1$) escaping Al-solid surface at low velocity. The simple analytical formulae derived for the corresponding neutralization rates enable us to analyze the neutralization distances for the low-l Rydberg states (n_A, l_A, m_A), for different charge states Z of the ion. It is found that the inclusion of core polarization significantly reduces the neutralization distances. The neutralization distances for the highest Rydberg levels that can be populated in the vicinity of solid surface are in agreement with the data deduced from experiments in which the kinetic energy gain due to the image acceleration of the ions is measured.

1. INTRODUCTION

The electron exchange during the interaction of ions with solid surfaces has been intensively studied both theoretically and experimentally; see, e.g. Reviews by Burgdorfer (1993) and Winter (2002). However, the quantum description of the events in the time interval between the initial and final "measurements" is still uncompleted. Recently, this kind of problem has been considered within the framework of two-state vector model (TVM) by Nedeljković and Nedeljković (2007), concerning the neutralization dynamics of the multiply charged ions in the interaction with solid surfaces. The model has been adapted to the intermediate stages of the population dynamics and to the low-velocity regime.

The TVM represents a form of the time-symmetric formulation of quantum mechanics; namely, the state of a single electron is described by two state vectors $|\Psi_1(t)\rangle$ and $|\Psi_2(t)\rangle$. The first state evolves from the initial state $|\Psi_1(t_{in})\rangle$ towards the future, while the second state evolves "teleologically" towards the fixed final state $|\Psi_2(t_{fin})\rangle$ detected in the final time $t = t_{fin}$. The TVM has been applied to the ions ArVIII, KrVIII and XeVIII (all with core charges $Z = 8$), and to the ions SVI, ClVII and ArVIII (with core charges $Z = 6, 7$ and 8, respectively), see e.g. Nedeljković and Nedeljković (2007) and Nedeljković et al. (2008).

In the present paper, we analyze the electron capture (neutralization) into the Rydberg states of multiply charged Rydberg ions escaping solid surfaces at low velocity, considering the ions Ar^{Z+} for $Z = 5 - 10$. We use the simple analytical expressions

for the probabilities and rates obtained by Nedeljković and Nedeljković (2007) to calculate the neutralization distances R_c^N, for the ions finally detected in the spherical Rydberg state $\nu_A = (n_A, l_A, m_A)$ with principal quantum number $n_A \gg 1$, low values of the orbital quantum number l_A, and $m_A = 0$. In the applied TVM treatment of intermediate stages of neutralization, the polarization of the solid, as well as the polarization of the electronic cloud of the ionic core are taken into account. The neutralization distances R_c^N for the particular (critical) Rydberg state $n_A = n_{max}$ can be compared with the values deduced from the measured projectile kinetic energy gains in the step-wise neutralization under grazing incidence, see e.g. Winter (1992) and Winter et al. (1993).

2. NEUTRALIZATION DISTANCES IN TVM

Within the framework of the TVM, the neutralization distances R_c^N are defined via the intermediate neutralization probabilities $P_{\nu_A}(t)$. That is, we use the normalized probability $\tilde{P}_{\nu_A}(t) = P_{\nu_A}/P_{\nu_A}^{fin}$, and the corresponding rate $\tilde{\Gamma}_{\nu_A}(t)$. By definition, the quantity $\tilde{P}_{\nu_A}(t)$ represents the neutralization probability at the time t under the condition that the state $|\nu_A\rangle$ is populated at the time $t \to t_{fin}$ with certain. We note that the TVM is almost independent of the form of the near-surface potential, and a dynamical response of the surface can be neglected, so that the classical electrostatic image potentials can be used outside the surface. The interaction of the active electron with polarized ionic core can be represented by the Simons-Bloch potential, which accounts for the experimentally observed quantum defects of the ionic energy spectra.

Under these conditions we get the following expressions for the probability $\tilde{P}_{\nu_A}(t)$ and the corresponding rate $\tilde{\Gamma}_{\nu_A}(t)$, see e.g. Nedeljković and Nedeljković (2007):

$$\tilde{P}_{\nu_A}(t) = \left[1 - \left(\frac{R}{R_{in}^*}\right)^{\tilde{\alpha}} \mathrm{e}^{-\tilde{\beta}(R-R_{in}^*)}\right]^2, \tag{1}$$

$$\tilde{\Gamma}_{\nu_A}(t) = 2v\left(\frac{R}{R_{in}^*}\right)^{\tilde{\alpha}}\left(\frac{\tilde{\alpha}}{R} - \tilde{\beta}\right)\mathrm{e}^{-\tilde{\beta}(R-R_{in}^*)}\left[\left(\frac{R}{R_{in}^*}\right)^{\tilde{\alpha}} \mathrm{e}^{-\tilde{\beta}(R-R_{in}^*)} - 1\right]. \tag{2}$$

In the above equations we have $\tilde{\beta} = (\gamma_M + \tilde{\gamma}_A)/2$ and $\tilde{\alpha} = Z/\tilde{\gamma}_A - 1/2 + 1/4\gamma_M$, where $\gamma_M = \gamma_A(R)$; by $\tilde{\gamma}_A$ we denoted the energy parameter of the active electron in the field of polarized ionic core, and $\gamma_A = \tilde{\gamma}_A + (2Z-1)/4R$ is the corresponding energy parameter shifted due to the interaction with polarized solid. The quantity R_{in}^* is the minimal ion-surface distance at which the resonant neutralization is allowed.

The rates $\tilde{\Gamma}_{\nu_A}(t)$, are directly related with the problem of localization of the neutralization process. That is, the maxima of the rates $\tilde{\Gamma}_{\nu_A}(t)$ determine the neutralization distances R_c^N for the process $A^{Z+} + M(e) \to A^{(Z-1)+} + M$, i.e.,

$$\left(\frac{d\tilde{\Gamma}_{\nu_A}(t)}{dt}\right)_{R=R_c^N} = 0. \tag{3}$$

We point out that the neutralization distances defined within the framework of the TVM are related to the fraction of ions with a given final state $\nu_A = (n_A, l_A, m_A)$, but with an arbitrary initial states μ_M, thus the neutralization distances R_c^N depend only on n_A and l_A (for $m_A = 0$).

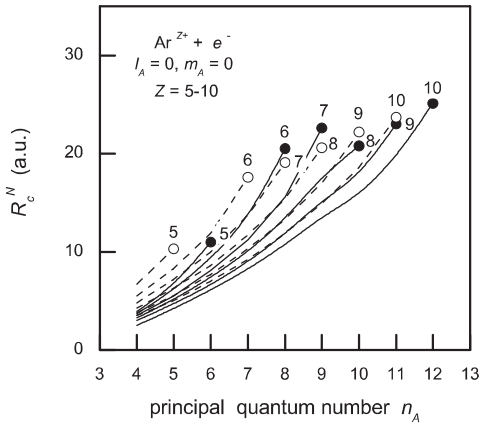

Figure 1: Neutralization distances R_c^N of the ion Ar^{Z+} interacting with Al surface, for the electron capture into the Rydberg states $n_A \leq n_{max}$, $l_A = 0$, $m_A = 0$. Dashed curves correspond to the point-like core case. The quantum numbers n_{max} are marked by dots and circles, for the polarized and non-polarized ionic cores, respectively.

3. RESULTS

We apply the expression (3) to calculate the neutralization distances for the Ar^{Z+} ions with core charges $Z \in [5, 10]$. We consider the Rydberg states (n_A, l_A, m_A) for $n_A \leq n_{max}$ where n_{max}, represents the quantum number n_A of the highest level that can be populated; for the angular momentum quantum number l_A and the quantum number m_A we take the value $l_A = m_A = 0$.

The maximal value of the principal quantum number corresponds to the Rydberg state populated from the vicinity of the Fermi level. Within the framework of the TVM, the quantity n_{max} is defined by the condition: $\gamma_{max}(R_c^N) = \gamma_\phi + \delta\gamma$, where $\gamma_{max}(R)$ is the energy parameter of the active electron in the first scenario (conduction band energy parameter), which gives the main contribution to the population of the considered state, γ_ϕ is the energy parameter of the Fermi level and $\delta\gamma$ is the mean distance between the energy terms. In the low-velocity case considered in the present paper we have the quasi-resonant condition $\gamma_{max}(R) \approx \gamma_A(R)$.

In Fig. 1 we present (full curves) the neutralization distances R_c^N via principal quantum number n_A, for the Ar^{Z+} ion interacting with Al solid surface with work function $\phi = 5$ eV. Dashed curves in Fig. 1 are the neutralization distances obtained in the point-like core case. From Fig. 1 we recognize that the polarization of the ionic cores plays an important role in the considered low-l_A case; the neutralization distances are significantly overestimated if the polarization is neglected. The neutralization distances for the electron capture into the critical Rydberg states with $n_A = n_{max}$ are marked by dots and circles, for the polarized and the point-like core charges Z, respectively. It is intriguing that the R_c^N-curves obtained for the polarized ionic cores with a core charge Z nearly coincide with the curves related to the non-polarized core cases, for the core charges $Z + 1$.

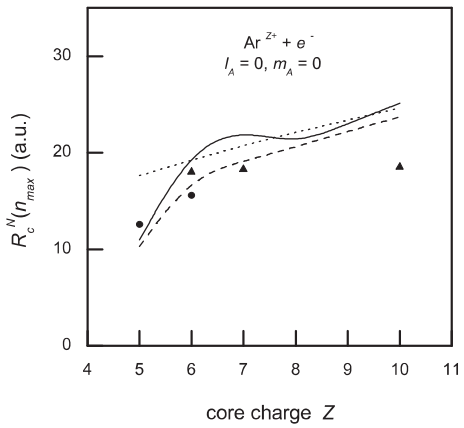

Figure 2: Neutralization distances R_c^N for $n_A = n_{max}$ and $l_A = 0$ of the ion Ar^{Z+} interacting with Al surface. Dashed curve corresponds to the point-like core case. Symbols are the experimental data, see e.g. Winter (1992) and Winter et al. (1993). By dotted line we presented the COB-neutralization distances R_c^{class}.

At present, the experimental evidence of the intermediate stages of the neutralization process of the considered Ar^{Z+} ions exists only for the projectiles impinging the surface under grazing geometry, and only for $n_A = n_{max}$. The corresponding neutralization distances R_c^N can be deduced from the measured projectile kinetic energy gains $\Delta E = Z^2/4R_c^N$, see e.g. Winter (1992) and Winter et al. (1993). In Fig. 2 we present the neutralization distances R_c^N for $n_A = n_{max}$ and $l_A = m_A = 0$ of the ion Ar^{Z+} interacting with Al surface, together with the experimental data for Ar^{Z+} (dots, Winter 1992) and Xe^{Z+} (triangles, Winter et al. 1993). In Fig. 2 we also present the first neutralization distance $R_c^{class} = \sqrt{8Z+2}/2\phi$ proposed for $n_A = n_c^{class}$ by COB method, see e.g. Ducrée et al. (1998) and Burgdörfer and Meyer (1993). From Fig. 2 we recognize the agreement of the TVM theoretical predictions with experiment.

To complete the TVM analysis, it is necessary to extend our considerations to other ions and core charges, for example to the case of Xe^{Z+} ions. Also, it remains to include into the TVM the effect of the parallel velocity, which could play an important role in the grazing geometry under which the experiments were performed.

References

Burgdörfer, J.: 1993, Review of Fundamental Processes and Applications of Atoms and Moleculs, eds. C.D. Lin, Singapore: World Scientific.

Burgdörfer, J. and Meyer, F.: 1993, *Phys. Rev. A*, **47**, R20.

Ducrée, J., Casali, F. and Thumm, U.: 1998 *Phys. Rev. A*, **57**, 338.

Nedeljković, N. N. and Majkić, M. D.: 2007, *Phys. Rev. A*, **76**, 042902.

Nedeljković, N. N., Majkić, M. D., Galijaš, S. M. D. and Mitrović, S. B.: 2008, *App. Surf. Sci.*, **10.1016**, j.apsus.2008.05.274.

Winter, H.: 1992, *Europhys. Lett.*, **18**, 207.

Winter, H.: 2002 *Phys. Rep.*, 367 **586**, 387.

Winter, H., Auth, Ch., Schuch, R. and Beebe, E.: 1993, *Phys. Rev. Lett.*, **71**, 1939.

Publ. Astron. Obs. Belgrade No. 84 (2008), 165 - 168 *Contributed Paper*

RESONANT *vs.* NON-RESONANT NEUTRALIZATION OF MULTIPLY CHARGED IONS IN THE INTERACTION WITH SOLID SURFACES

N. N. NEDELJKOVIĆ, S. M. D. GALIJAŠ and M. B. OBRADOVIĆ
Faculty of Physics, University of Belgrade, P.O.Box 368, Belgrade, Serbia
E–mail: hekata@ff.bg.ac.yu

Abstract. The two-state vector model is used to investigate the intermediate stages of the electron capture into the Rydberg states of multiply charged ArVIII ion, escaping solid surface. Two cases of the ionic velocities are considered: the low velocities ($v \approx 0$ a.u.) and the intermediate velocities ($v \approx 1$ a.u.). Within the framework of the two-state vector description of the neutralization dynamics the two wave functions are used to determine the state of a single active electron. The intermediate stages of the process are characterized by the two-amplitude, the neutralization probability and rate. These quantities are obtained in two different analytical forms in the two considered cases of the projectile velocities. The key difference of the intermediate velocity case in respect to the low-velocity case, is the non-resonant character of the electron transitions. The obtained rates in the low velocity case are well localized. The neutralization rates in the intermediate velocity case are oscillatory in character. At larger ion-surface distances R the neutralization is stabilized; the behavior of the rates becomes similar to that obtained for the low ionic velocities.

1. INTRODUCTION

One of the recently developed model for description of the non-resonant neutralizations process during the interaction of multiply charged ions with the solid surface is the quantum teleological model, known as the two-state vector model (TVM), see e.g. Nedeljković et al. (1994, 2003) and Nedeljković and Nedeljković (1998). This model is appropriate for description of the intermediate stages of the ion-surface interaction, when we consider the problem at which distance from the surface the process is the most probable. Within the framework of TVM, we define the intermediate probabilities and rates, from which the problem of localization of the process can be resolved.

The TVM represents a form of the time-symmetric quantum model in which the two state functions are used for description of a single electron exchange dynamics. The first wave function $\Psi_1(t)$ evolves from the preselected state of the electron, initially localized in the solid, which is described by the parabolic set of quantum numbers $\mu_M = (\gamma_M, n_{1M}, m_M)$. The second wave function $\Psi_2(t)$ describes the state which will evolve into the given postselected final state of the electron bound to the ion, labeled by the spherical quantum number set $\nu_A = (n_A, l_A, m_A)$. In the TVM formalism, the

electron capture process from the solid surface into the moving ion is described via mixed flux through the Firsov plane S_F, separating the solid and the ionic subsystems.

In this paper we consider the neutralization of ArVIII ions in a normal emergence geometry. The main output of this analysis are the normalized neutralization rates for the ions finally detected in a given Rydberg state ν_A. We apply the TVM, considering both the neutralization at small ionic velocities as well as the neutralization process at intermediate projectile velocities.

2. THE TVM OF NEUTRALIZATION

Neutralization process represents the capture of the active electron from the solid surface into the field of moving ion. Within the framework of TVM it can be considered as a transition $\Psi_1(t) \to \Psi_2(t)$ at some intermediate time t, due to the "measurement" of the electron localization in the ionic region V_A.

Hamiltonians $\hat{H}_1$ and $\hat{H}_2$, which determine the evolutions of the states Ψ_1 and Ψ_2 are adapted to the fact that in the first scenario, inside the solid, electron can moves infinitely. Also, in the second scenario and outside the solid, the polarization effect of the ionic core has to be included. Therefore, inside the solid we have $\hat{H}^{(1)} = -(1/2)\nabla^2 - U_0$ and $\hat{H}^{(2)} = -(1/2)\nabla^2 - Z/r_A$, where U_0 is the the mean electronic potential inside the solid, and r_A is the distance of the electron from the ionic core. Outside the solid we have $\hat{H}^{(i)}(R) = -(1/2)\nabla^2 + U_A^{(i)} + U_S^{(i)}$, where $U_A^{(i)}$ is the effective potential energy of the active electron in the field of polarized ionic core; the surface potential $U_S^{(i)}$ is the electron potential energy in the field of polarized solid. In the second scenario the Simons-Bloch potential $U_A^{(2)} = -Z/r_A + \sum_{l'=0}^{\infty}(c_{l'}/r_A^2)\hat{P}_{l'}$ can be used, where $\hat{P}_{l'} = |l'\rangle\langle l'|$ is the projection operator onto the subspace of a given angular momentum l'. The quantity $U_S^{(i)}$ can be expressed in the electrostatic approximation; furthermore, in the low-l case the radial electron coordinate can be neglected in comparison to the ion-surface distance R.

Following the general TVM-formalism, the neutralization is described by the two-state probability amplitude $A_{\mu_M,\nu_A}(t) = \langle\Psi_2(t)|\hat{P}_A(t)|\Psi_1(t)\rangle$, where $\hat{P}_A(t) = \int_{V_A}|\vec{r}_A\rangle\langle\vec{r}_A|$ is the projecting operator onto the ionic region V_A. Using the two-amplitude we can define the intermediate neutralization probability, as well as the normalized probability $\tilde{P}_{\nu_A}(t)$ and the corresponding rate $\tilde{\Gamma}_{\nu_A}(t)$. The advantage of the TVM is that the probabilities and rates can be expressed via mixed flux through the boundary surface S_A of the region V_A, which partially consists of the Firsov plane S_F. In this way, we obtain the relatively simple expressions for the normalized probability and rate; these expressions have different forms in the low and intermediate velocity regions.

The normalized neutralization rate is given by $\tilde{\Gamma}_{\nu_A}(t) = d\tilde{P}_{\nu_A}/dt$. In the low-velocity case for the normalized probability $\tilde{P}_{\nu_A}$ we have, see e.g. Nedeljković and Majkić (2007)

$$\tilde{P}_{\nu_A}(t) = \left[1 - \left(\frac{R}{R_{in}^*}\right)^{\tilde{\alpha}} \mathrm{e}^{-\tilde{\beta}(R-R_{in}^*)}\right]^2, \tag{1}$$

where R_{in}^* is the minimal ion-surface distance at which the resonant neutralization is possible. In the case of intermediate velocities, the expression for the normalized

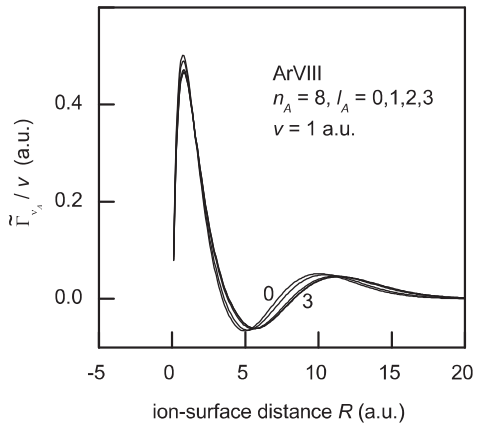

Figure 1: Normalized intermediate rates $\tilde{\Gamma}_{\nu_A}(t)$ (scaled by v) via ion surface distances R for the ArVIII ion escaping the solid surface with velocity $v = 1$ a.u.

probability is more complicated:

$$\tilde{P}_{\nu_A}(t) = 1 + f^2(R) - 2f(R)\cos\left(\frac{w}{v}R + \arg\mathcal{B}\right), \tag{2}$$

where

$$f(R) \approx \left(1 + \frac{|\beta|^{\tilde{\alpha}}}{\Gamma(\tilde{\alpha}+1)}R^{\tilde{\alpha}}\right)e^{-\tilde{\beta}R}, \tag{3}$$

whereas $|\beta| = [\tilde{\beta}^2 + (\omega/v)^2]^{1/2}$, and

$$\arg\mathcal{B} = \arctan\frac{|\beta|^{\tilde{\alpha}}R^{\tilde{\alpha}}\sin[(\tilde{\alpha})\arctan(\omega/v)]}{1 + |\beta|^{\tilde{\alpha}}R^{\tilde{\alpha}}\cos[(\tilde{\alpha})\arctan(\omega/v)]}. \tag{4}$$

The quantities $\tilde{\alpha}$ and $\tilde{\beta}$ are the given functions of the energy parameter $\tilde{\gamma}_A$ for the electron in the field of polarized ionic core and energy parameter γ_M: $\tilde{\alpha} = Z/\tilde{\gamma}_A - 1/2 + 1/4\gamma_M$ and $\tilde{\beta} = \gamma_M + (\tilde{\gamma}_A - \gamma_M)g$. Parameter g defines the kinematics of the Firsov plane, and the quantity w is defined by $w = (1/2)\left(\gamma_M^2 - \tilde{\gamma}_A^2\right) - (v^2/2)(1-2g)$.

3. RESULTS

In Fig. 1. we present the normalized intermediate rates $\tilde{\Gamma}_{\nu_A}(t)$ (scaled by v) via ion-surface distances R, for the ArVIII ion interacting with Al solid surface. We considered the case of the electron capture into the Rydberg state $n_A = 8, l_A = 0-3, m_A = 0$, for the ionic velocity $v = 1$ a.u., which belongs to the domain of intermediate velocities. The case of the point-like core (dashed curve) nearly coincide with the curve obtained for $l_A = 3$. From Fig. 1 we recognize that in the initial stages of the ionic motion, at smaller distances from the surface, we have a kind of instability. That is, the electron is firstly captured (neutralization); after that, the sign of the rate is changed, which means that the electron become partially recaptured by the solid. At larger R, the neutralization process is stabilized.

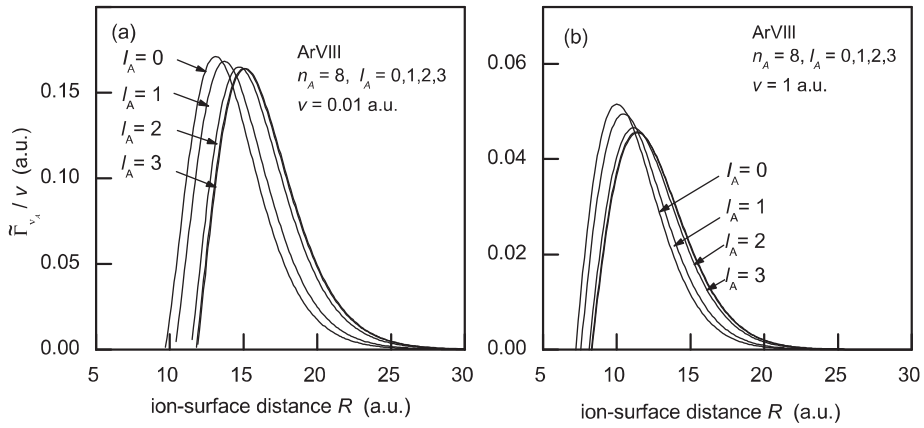

Figure 2: Normalized intermediate rates $\tilde{\Gamma}_{\nu_A}(t)$ (scaled by v) via ion-surface distances R for the ion ArVIII escaping the solid surface with velocity (a) $v = 0.01$ a.u. and (b) $v = 1$ a.u.

In Fig. 2. we present the normalized intermediate rates $\tilde{\Gamma}_{\nu_A}(t)$ (scaled by v) analyzing the cases of small and intermediate ionic velocities, Figs. 2(a) and 2(b), respectively. Again, we consider the electron capture into the Rydberg state $n_A = 8, l_A = 0 - 3, m_A = 0$, for the ionic velocities $v = 0.01$ a.u., see e.g. Nedeljković and Majkić (2007), and Nedeljković et al. (2008) and $v = 1$ a.u. In Fig. 2(b), we present only the stabilized part of the rate, i.e., the last oscillation. We recall that the neutralization of the ionic projectile escaping the surface with small velocity, Fig 2(a), is resonant in type; it begins at the ion-surface distance R^*_{in}, which can be determined on the base of the energy condition. On the other hand, in the case of intermediate velocities, Fig. 2(b), the beginning of the stable regime coincide with the last zero of the rate.

Two effects can be recognize from Fig. 2. First, the rates are shifted toward the smaller R with increasing ionic velocity v. Indeed, the non-resonant transitions ($v = 1$ a.u.) are localized at smaller ion-surface distances R comparing to the resonant transitions ($v = 0.01$ a.u.). Second, the rates are additionally shifted toward the smaller ion-surface distances R due to the ionic core polarization.

We point out that the velocity dependence obtained within the TVM is nontrivial, and different comparing to the velocity dependence obtained within the framework of rate equation.

References

Nedeljković, Lj. D. and Nedeljković, N. N.: 1998, *Phys. Rev. B*, **58**, 16455.
Nedeljković, N. N. and Majkić, M. D.: 2007, *Phys. Rev. A*, **76**, 042902.
Nedeljković, N. N., Majkić, M. D., Galijaš, S. M. D. and Mitrović, S. B.: 2008, *App. Surf. Sci*, **10.1016**, /j.apsus.2008.05.274.
Nedeljković, N. N., Nedeljković, Lj. D. and Mirković, M. A.: 2003, *Phys. Rev. A*, **68**, 012721.
Nedeljković, N. N., Nedeljković, Lj. D., Vojvodić, S. B. and Mirković, M. A.: 1994, *Phys. Rev. B*, **49**, 5621.

Publ. Astron. Obs. Belgrade No. 84 (2008), 169 - 172 *Contributed Paper*

HYPERCHANNELING OF Ne^{10+} IONS THROUGH THE THICK <111> Si CRYSTALS

V. BORKA-JOVANOVIĆ, S. PETROVIĆ, D. BORKA and N. NEŠKOVIĆ

Laboratory of Physics (010), Vinča Institute of Nuclear Sciences,
P. O. Box 522, 11001 Belgrade, Serbia
E–mail: vborka@vin.bg.ac.yu

Abstract. In this work we investigate the angular distributions of Ne^{10+} ions hyperchanneled along the <111> direction in a thick silicon crystals as a function of the reduced crystal thickness. The ion energy is 60 MeV and the reduced crystal thickness, Λ, is varied from 10 to 21, corresponding to the crystal length from 6.2 to 13.1 μm. We follow the ion trajectory in the triangular region of the crystal channel determined by the maximum closed equipotential line around the channel axis, where the hyperchanneling occurs. The Hénon-Heiles type of the ion-crystal interaction potential is used as the model of the continuum interaction potential obtained assuming the Molière expression for the ion-atom interaction potential. The angular distributions are generated using the numerical solution of ion's equations of motion in the transverse plane and the computer simulation method. The obtained results show periodicity of the angular distribution, with the period of 0.5. The values of Λ = 10, 10.5, 11, ..., 21, correspond to the beginnings of periodic cycles of the angular distribution. The effect of zero-degree focusing is observed for these values of variable Λ. Also, one can observe the formation of the symmetrical ridges in the angular distributions around the centre of the scattering angle plane, whose number increases and the average distance between them decreases as the variable Λ increases.

1. INTRODUCTION

Hyperchannelling effect occurs when motion of the channelled ion is restricted to only one crystal channel (Gemmell 1974). The hyperchanneling region is then determined by the maximum closed equipotential line around the channel axis. In this region electron density is low comparing with the rest of the crystal and one can call hyperchanneling the "pure" channeling since the trajectory of channeled ion is always far away from the atomic strings defining the channel.

In this work we investigate the angular distributions of Ne^{10+} ions hyperchanneled along the <111> direction in the thick silicon crystals as a function of the reduced crystal thickness. The ion energy is 60 MeV and the reduced crystal thickness, $\Lambda = f \times L/V_0$, where f is the frequency of transverse ion motion close to the channel axis, L is the crystal thickness, and V_0 is initial ion velocity (Krause et al. 1994; Miletić et al. 1996), is varied from 10 to 21, corresponding to the crystal length from 6.2 to 13.1 μm.

2. THEORY

We consider an ion moving along axial channel in the <111> direction of a thick silicon crystal. The atomic strings defining the channel lie on the x and y axes, and the negative direction of z axis coincides with the channel axis. The origin lies in the entrance plane of the crystal. The initial ion velocity vector is parallel to the channel axis $\vec{v} = -v\vec{e}_z$. We assume that the interaction of the ion and the crystal is elastic and that it can be treated classically. Also, we assume that we can apply the continuum approximation (Lindhard 1965). For the "exact" continuum interaction potential of the ion and i-th atomic string we use the potential based on the Molière's expression for the ion-atom interaction potential (Petrović et al. 2000; Nešković et al. 2000):

$$U_i(\rho) = \frac{2Z_1Z_2e^2}{d} \sum_{i=1}^{3} \alpha_i K_0(\beta_i \frac{\rho}{a_s}) \tag{1}$$

where Z_1 and Z_2 are the atomic numbers of ion and crystal atom, respectively, e is the elementary charge, $a_s = [9\pi^2/(128\,Z_2)]^{\frac{1}{3}} a_0$ is the screening radius, and a_0 is the Bohr radius; $\{\alpha_i\} = \{0.10; 0.55; 0.35\}$ and $\{\beta_i\} = \{6.0; 1.2; 0.3\}$ are the fitting parameters and K_0 is modified Bessel function of the zero order and second kind and ρ is the distance between the ion and the Si atom in the transverse plane. The ion-crystal continuum interaction potential is given by the expression, $U_{tot}(\rho) = \sum_{i=1}^{M} U_i(\rho)$, where M is the number of atomics rows taken into account. We take $M = 36$, i.e. two nearest (relative to the channel axis) triangular coordinate lines.

For the model potential the Hénon-Heiles type potential is used (Hénon & Heiles 1964):

$$V = Z_1Z_2e^2(a(x^2 + y^2) + b(x^3 - 3xy^2)) \tag{2}$$

where a and b are the fitting parameters. The values of the parameters are $a = 4.46 \times 10^{-3}$ and $b = 0.691 \times 10^{-3}$. They are obtained using two independent conditions: (i) frequencies of the transverse motion in the cases of the "exact" and model potentials are equal and (ii) values of the "exact" and model potentials corresponding to the maximum closed equipotential line around the channel axis are equal.

The results presented in this work are obtained using the model potential (2). It is simple, accurate, and efficient considering the computational time.

The transverse components of the ion position, x and y, and ion scattering angle at the exit from the crystal, Θ_x and Θ_y, are determined via the numerical solution of the ion's equations of motion in the transverse plane. The angular distribution of hyperchanneled ions is generated using the computer simulation. The impact parameters of ions are chosen from 2D uniform distribution within the hyperchanneling region. The initial number of ions is around 60 000.

We do not take into account the ion energy loss, the uncertainty of its scattering angle and the change of charge of the ion caused by the collisions with the crystal's electrons since the electron density is low in the hyperchanneling region and the effect of thermal vibrations of the crystal's atoms since the trajectory of the channeled ion is always far away from the atomic strings defining the channel.

3. RESULTS AND DISCUSSION

As it is already mentioned, we study here the dependence of the angular distribution of 60 MeV Ne^{10+} ion hyperchanneled through the <111> Si crystals on the reduced thickness, that varies from 10 to 21, corresponding to the crystal length from 6.2 to 13.1 μm.

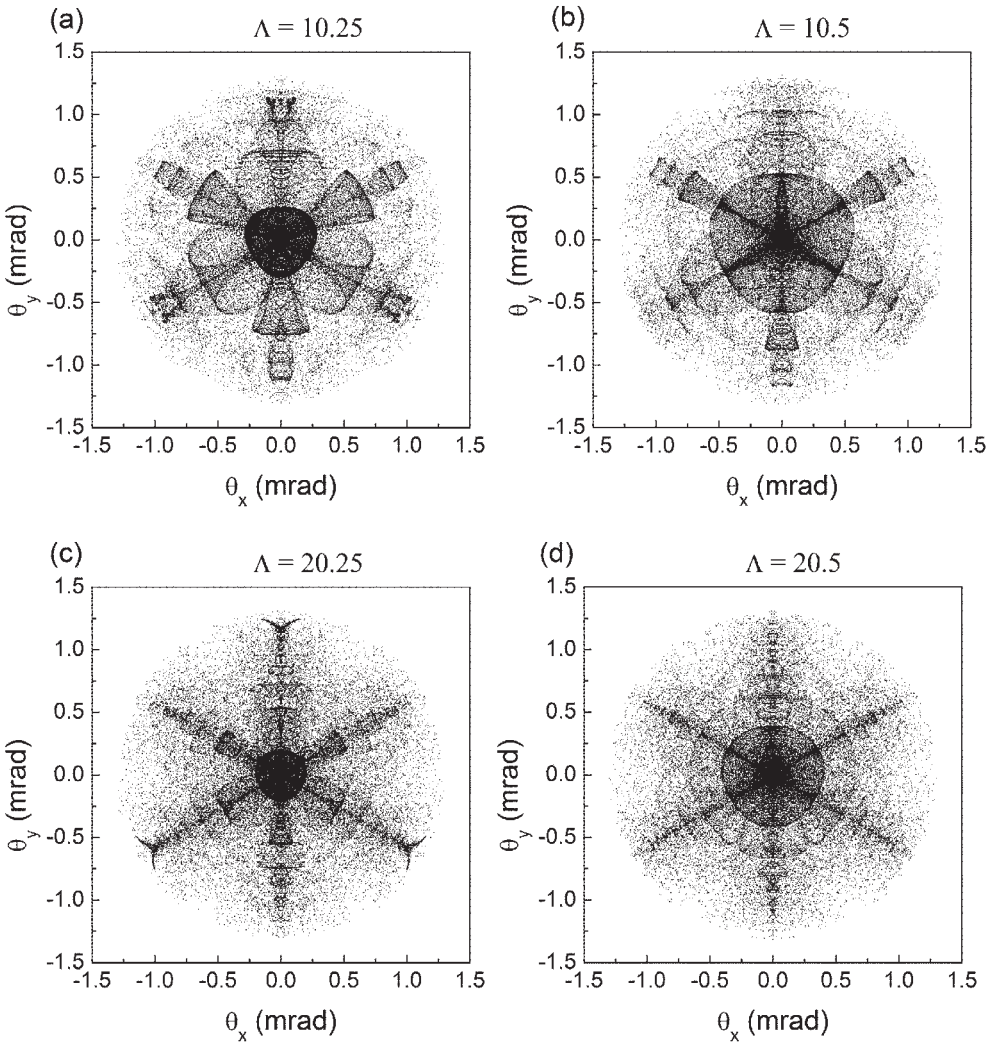

Figure 1: The angular distributions of 60 MeV Ne^{10+} ions hyperchanneled through the <111> Si thick crystals for the reduced thickness of (a) 10.25, (b) 10.50, (c) 20.25 and (d) 20.50.

Figs. 1 (a)-(d) show the angular distributions of the hyperchanneled ions for variable Λ equal to 10.25, 10.5, 20.25 and 20.5, respectively. Comparing the Figs. 1 (a) with (c) and (b) with (d), it is clear that they are qualitatively similar, thus, showing the periodicity of the angular distribution with the period of 0.5. The values of Λ

= 10, 10.5, 11, ..., 21, correspond to the beginnings of periodic cycles of the angular distribution (Krause et al. 1994; Miletić et al. 1996). The analysis shows that for these values of variable Λ there are pronounced and narrow maxima in the central region of the scattering angle plane i.e. the zero-degree focusing effect occurs (Krause et al. 1994; Miletić et al. 1996).

The angular distribution for $\Lambda = 10.25$ is characterized by the pronounced curved triangular structure in the central region of the scattering angle plane and the pronounced maximum at the origin. For $\Lambda = 10.50$, one can observe that the angular distribution contains the less pronounced curved triangular structure and narrow maximum at the origin and the six "arms" structures lying along the lines $\pi/6 + 2n\pi/6$, where n = 0 - 5. The angular distribution for $\Lambda = 20.25$ is characterized by the pronounced curved triangular structure around the origin and the pronounced maximum at the origin. Also, less pronounced "arms" structures lying along the lines $\pi/6 + 2n\pi/6$, where n = 0 - 5. Finally, for $\Lambda = 20.5$ the angular distribution is characterized by the pronounced narrow maximum at the origin and the six "arms" structures lying along the lines $\pi/6 + 2n\pi/6$, where n = 0 - 5.

It should be noted that the angular distributions presented here have the C_{3V} symmetry which is the consequence of the C_{3V} symmetry of the hyperchanneling region.

One can also observe that the angular distributions for $\Lambda = 10.25$ and 10.5 are characterized by four, and, for $\Lambda = 20.25$ and 20.5, by six symmetrical ridges around the centre of the scattering angle plane. The average distance between the four ridges is larger then the average distance between the six ridges. The analysis of the angular distributions for the values of variable Λ under the consideration confirms observed tendency that the number of ridges increases and the average distance between them decreases as the variable Λ increases. It is interesting to note that the same tendency is recently observed for the angular distributions of 1 GeV protons channelled through the long (11, 9) single-wall carbon nanotubes (Petrović et al.).

References

Gemmell, D. S.: 1974, *Rev. Mod. Phys.*, **46**, 129.
Hénon, M., Heiles, C.: 1964, *Astron. J.*, **69**, 73.
Krause, H. F., Barrett, J. H., Datz, S., Dittner, P. F., Jones, N. L., Gomez del Campo, J. and Vane, C. R.: 1994, *Phys. Rev. A*, **49**, 283.
Lindhard, J.: 1965, K. Dan. Vidensk. Selsk., *Mat-Fys. Medd.* **34**, No. 14.
Miletić, L., Petrović, S., Nešković, N.: 1996, Book of Contributed Papers of the 18th Summer School and International Symposium on the Physics of Ionized Gases, eds. Vujičić, B. and Djurović, S., Faculty of Sciences, Novi Sad, p. 161.
Nešković, N., Petrović, S. and Živković, L.: 2000, *Eur. Phys. J. B*, **18**, 553.
Petrović, S., Miletić, L. and Nešković, N.: 2000, *Phys. Rev. B*, **61**, 184.
Petrović, S., Telečki, I., Borka, D., Nešković, N.: submitted for the publication.

Publ. Astron. Obs. Belgrade No. 84 (2008), 173 - 176 *Contributed Paper*

AXIAL CHANNELING OF HIGH ENERGY PROTONS IN CARBON NANOTUBES

I. TELEČKI, S. PETROVIĆ, D. BORKA and N. NEŠKOVIĆ
Laboratory of Physics (010), Vinča Institute of Nuclear Sciences,
P. O. Box 522, 11001 Belgrade, Serbia
E–mail: tigor@vin.bg.ac.yu

Abstract. We have studied theoretically the angular distributions of 1 GeV protons channeled through the long (10, 0) single-wall carbon nanotubes. The nanotube length is varied between 10 and 80 μm. The angular distribution of channeled protons is generated by the computer simulation method using the numerical solution of the proton equations of motion in the transverse plane. The analysis shows that for the nanotube length less then 30μm the transverse geometrical structure of the nanotubes could be deduced from the angular distribution. For the length over 30 μm, the angular distribution is characterized only by the concentric circular ridges. The number of ridges increases and the distance between them decreases as the nanotube length increases. For the nanotube length of 80μm, the circular ridges are no longer visible and the angular distribution becomes equilibrated.

1. INTRODUCTION

Carbon nanotubes were discovered by Iijima in 1991 (Iijima 1991). Soon after nanotubes were discovered, Klimov and Letokhov (Klimov et al. 1996) foresaw the effect of channeling of positively charged particles in them. Petrović et al. applied the theory of crystal rainbows,which has been demonstrated to be the proper theory of ion channeling through thin crystals (Petrović et al. 2000, Nešković et al. 2000) to channeling of 1 GeV protons through the straight and bent (10, 10) single-wall carbon nanotubes (Petrović et al. 2005, Nešković et al. 2005). They showed that the rainbow patterns provide the full explanation of the angular distributions of channeled protons. Recently, in a study of channeling of 0.233 MeV protons through the (11, 9) single-wall carbon nanotubes, Borka et al. demonstrated that the image force acting on the protons gave rise to the additional rainbows in their angular distributions (Borka et al. 2006). Our motivation for the work presented here is to find out how the angular distribution of protons channeled through a (10, 0) carbon nanotube evolves with the nanotube length, and how it looks like when the nanotube is very long.

2. THEORY

The system we investigate is a high energy (relativistic) proton moving through the long (10, 0) single-wall carbon nanotubes. The z axis is taken to be parallel to

nanotube axis and the origin lies in its entrance plane. Each nanotube consists of the straight atomic strings parallel to its axis (Saito et al. 2001). The continuum approximation is assumed (Lindhard 1965), and we use the Molière's expression for the proton-atom interaction potential (Petrović et al. 2000, Nešković et al. 2000, Petrović et al. 2005),

$$V(r) = \frac{Z_1 Z_2 e^2}{r}[0.35exp(-br) + 0.55\exp(-4br) + 0.10\exp(-20br)], \qquad (1)$$

where Z_1 and Z_2 are the atomic numbers of the proton and carbon atom, respectively, e is the elementary charge, r is the distance between the proton and the atom, $b = 0.3/a$, $a = [9\pi^2/(128\,Z_2)]^{\frac{1}{3}} a_0$ is the screening radius, and a_0 is the Bohr radius. The effect of the thermal vibrations of the atoms is included via expression $U_i^{th}(x,y) = U_i(x,y) + (\sigma_{th}^2/2)\,\Delta U_i(x,y)$ where U_i is the continuum potential of the i-th atomic string of the nanotube with the thermal vibrations of the atoms neglected, $\Delta \equiv \partial_{xx} + \partial_{yy}$, x and y are the components of the proton position in the transverse plane, and σ_{th} is the one-dimensional thermal vibration amplitude of the atoms. The continuum potential of the nanotube, U^{th}, is the sum of the continuum potentials of the atomic strings.

For the specific (electronic) proton energy loss we use expression (Gemmell 1974, Petrović et al. 2002)

$$-\frac{dE}{dz} = \frac{4\pi Z_1^2 e^4}{m_e v^2} n_e \left(\ln \frac{2m_e\gamma^2 v^2}{\hbar\omega_e} - \beta^2\right) \qquad (2)$$

where $\omega_e = \left(4\pi e^2 n_e/m_e\right)^{1/2}$ and $n_e = \Delta U^{th}/4\pi$; m_e is the electron mass, v the proton velocity, $\gamma^2 = 1/(1-\beta^2)$, $\beta = v/c$, and c the speed of light; ω_e is the angular frequency of the proton induced oscillations of the electron gas, and $n_e = n_e(x,y)$ is the average (along the z axis) density of the electron gas of the nanotubes. The dispersion of the proton scattering angle due to its collisions with the nanotube electrons is given by expression (Gemmell 1974, Petrović et al. 2002): $\frac{d\Omega_e^2}{dz} = \frac{m_e}{m^2 v^2}\left(-\frac{dE}{dz}\right)$, where m is the (relativistic) proton mass. The corresponding standard deviations of the x and y components of the proton scattering angle, Θ_x and Θ_y, respectively, are $\Omega_{ex} = \Omega_{ey} = \Omega_e/\sqrt{2}$. The proton impact parameter is chosen uniformly within the region of the nanotube. For each impact parameter, the x and y components of the initial proton velocity, v_{0x} and v_{0y}, respectively, are chosen within the Gaussian distributions with the standard deviations $\Omega_{bx} = \Omega_{by} = \Omega_b/\sqrt{2}$, where Ω_b is the divergence of the proton beam.

3. RESULTS AND DISCUSSION

We study here the angular distributions of 1 GeV protons channeled through the long (10,0) single-wall carbon nanotubes. The length is varied between 10 and 80 μm. Since the bond length of two carbon atoms is 0.14 nm, the radius of a nanotube is 0.39 nm and the thickness of one atomic layer is 0.21 nm (Saito et al. 2001). The one-dimensional thermal vibration amplitude of the atoms is estimated, using the Debye approximation, to be 0.0053 nm (Hone et al. 2000). The initial number of protons is 5 000 000. The divergence of the proton beam is set at $\Omega_b = 0.1\Psi_c$ mrad, where $\Psi_c =$

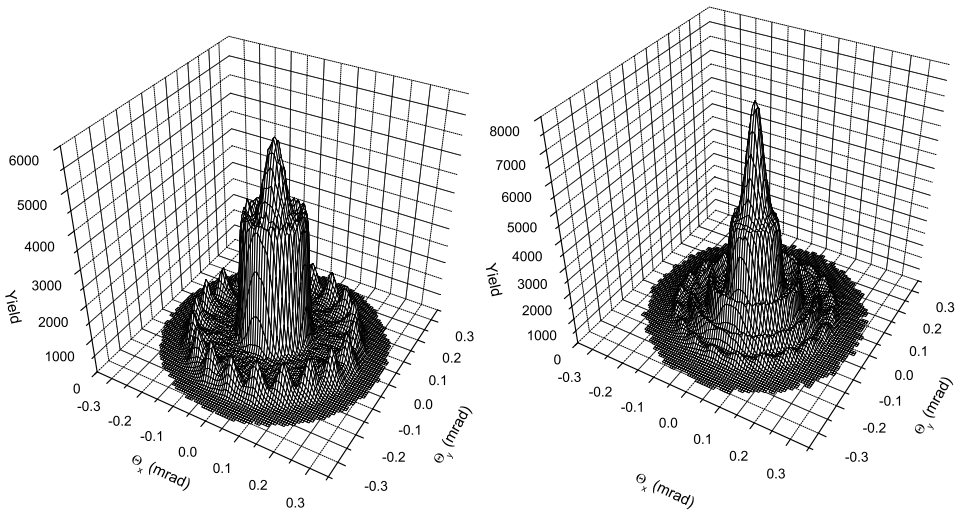

Figure 1: The angular distributions of 1 GeV protons channeled through the (10, 0) single-wall carbon nanotube of the length of 10 μm (*left panel*) and 30 μm (*right panel*).

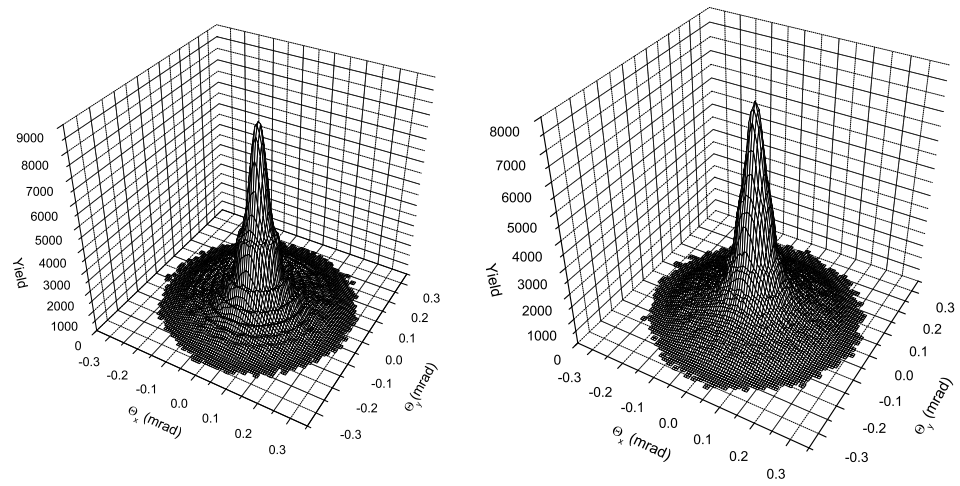

Figure 2: The same as in Fig. 1, but for 50 μm (*left panel*) and 80 μm (*right panel*).

0.0314 mrad is the critical angle for channeling. The proton whose impact parameter happens to be inside one of the circles around the atomic strings of the radius equal to the screening radius is treated as if it is backscattered and is disregarded.

Fig. 1 (left panel) shows the angular distribution of 1 GeV protons channelled through the (10, 0) single-wall carbon nanotube, in the case of nanotube length $L =$ 10 μm. It is characterized by 20 maxima lying on the lines $\Phi = \arctan(\Theta_y/\Theta_x) = (n+1)\pi/10$, $n =$ 0-19, in the peripheral region of the scattering angle plane, one

concentric circular ridge in the central region of the scattering angle plane and the maximum at the origin. The appearance of the 20 maxima is connected to the symmetry of the transverse geometrical structure of the nanotube, which consists of 20 atomic string parallel to the nanotube axis (Saito et al. 2001). For $L = 30$ μm, the angular distribution of 1 GeV protons channelled through the (10, 0) single-wall carbon nanotube is shown in Fig. 1 (right panel). It is characterized by 20 maxima lying on the lines $\Phi = (n+1)\pi/10$, n = 0-19, in the peripheral region of the scattering angle plane, two concentric circular ridge in the central region of the scattering angle plane, and the maximum at the origin. It is clear that the transverse geometrical structure of the nanotube could be deduced from the angular distribution.

Fig. 2 (left panel) shows the angular distribution of 1 GeV protons channelled through the (10, 0) single-wall carbon nanotube, in the case of $L = 50$ μm. One can see that it is characterized by the five concentric circular ridges, and the maximum at the origin. One ridge lies in the peripheral region and the others in the central region of the scattering angle plane. Clearly, the transverse geometrical structure of the nanotube is no longer visible in the angular distribution. It should be noted that the ridges are closer than in the previous case ($L = 30$ μm). Also, the analysis shows that the observed trend in the angular distributions i.e. the increase of the number of concentric ridges and decrease of the average distance between them as variable L increases also holds for $L > 50$ μm. Finally, for $L = 80$ μm, the angular distribution of 1 GeV protons channelled through the (10, 0) single-wall carbon nanotube is shown in Fig. 2 (right panel). The angular distribution is a bell-shaped one with no longer visible circular ridges structure. Hence, the angular distribution becomes equilibrated.

The results presented here indicate how the angular distribution of channeled protons through carbon nanotube could be used for its characterization. Namely, each nanotube presumably has its characteristic pattern of the concentric circular structures in the angular distributions of the channeled protons. Additional way to experimentally distinguish between different nanotubes would be to measure the change of the patterns of concentric circular structures in the angular distributions by changing the proton energy, which is equivalent with the change of nanotube length analyzed here.

References

Borka, D., Petrović, S., Nešković, N., Mowbray, D. J. Mišković Z. L.: 2006, *Phys. Rev. A*, **73**, 062902.

Gemmell, D. S.: 1974, *Rev. Mod. Phys.*, **46**, 129.

Hone, J., Batlogg, B., Benes, Z., Johnson, A. T., Fischer, J. E.: 2000, *Science*, **289**, 1730.

Iijima, S.: 1991, *Nature*, **354**, 56.

Klimov, V. V., Letokhov, V. S.: 1996 *Phys. Lett. A*, **vol 222**, 424.

Lindhard, J.: 1965, K. Dan. Vidensk. Selsk., *Mat-Fys. Medd.*, **34**, No. 14.

Nešković, N., Petrović, S., Živković, L.: 2000, *Eur. Phys. J. B*, **18**, 553.

Nešković, N., Petrović, S., Borka, D.: 2005, *Nucl. Instrum. Meth. Phys. Res. B* **230**, 106.

Petrović, S., Miletić, L., Nešković, N.: 2000, *Phys. Rev. B*, **61**, 184.

Petrović, S., Korica, S., Kokkoris, M., Nešković, N.: 2002, *Nucl. Instrum. Meth. Phys. Res. B*, **193**, 152.

Petrović, S., Borka, D., Nešković, N.: 2005, *Eur. Phys. J. B*, **44**, 41.

Saito, R., Dresselhaus, G., Dresselhaus, M. S. : 2001, *Physical Properties of Carbon Nanotubes*, Imperial College Press, London.

Publ. Astron. Obs. Belgrade No. 84 (2008), 177 - 179 *Contributed Paper*

NON-LINEAR EFFECTS IN INTERACTIONS OF FAST IONS WITH GRAPHENE

I. RADOVIĆ[1], Lj. HADŽIEVSKI[1], N. BIBIĆ[1] and Z. L. MIŠKOVIĆ[2]

[1] *VINČA Institute of Nuclear Sciences, P.O. Box 522, 11001 Belgrade, Serbia*

[2] *Department of Applied Mathematics, University of Waterloo, Waterloo, Ontario, Canada*

Abstract. We study the interactions of fast ions with graphene, describing the high-frequency plasmon excitations of the electron gas by a two-dimensional, two-fluid hydrodynamic model. The Barkas effect on the stopping force and the analogous correction to the image force are evaluated within the second-order perturbation approach to the hydrodynamic equations.

1. INTRODUCTION

Graphene is a single sheet of carbon atoms tightly packed into a two-dimensional (2D) honeycomb lattice (Novoselov et al. 2004). Besides being the fundamental building block of highly oriented pyrolytic graphite (HOPG), carbon nanotubes and fullerene molecules, graphene is currently attracting a great deal of interest on its own right owing to its fascinating physical properties, most notably as a potential basis for the future nano-electronic devices (Geim and Novoselov 2007, Katsnelson 2007, Katsnelson et al. 2006, Novoselov et al. 2006, Niyogi et al. 2006).

In the present paper, we adopt the hydrodynamic model of a 2D electron gas (Hetter 1973) to evaluate the stopping force and the image force which, in the regime of high projectile speeds and large distances from graphene, respectively, describe the dissipation of the projectile's kinetic energy into plasmon excitations in graphene, and the conservative force attracting the projectile towards graphene.

2. BASIC THEORY

We use a three-dimensional Cartesian coordinate system with $\overrightarrow{r} = (\overrightarrow{R}, z)$, where $\overrightarrow{R} = (x, y)$ is position in the graphene plane and z distance from it. Furthermore, we consider the ion to be a point charge Q, moving parallel to the graphene in the upper half-space defined by $z > 0$, with a constant velocity v, at distance z_0. Next, we describe the σ and π electrons in graphene as two fluids occupying the xy plane and having the equilibrium number densities per unit area $n_\sigma^0 \approx 0.321$ and $n_\pi^0 \approx 0.107$, respectively. The perturbations of their densities $n_j^{(1)}(\overrightarrow{R}, t)$ and their velocity fields $\overrightarrow{u}_j^{(1)}(\overrightarrow{R}, t)$, with $j = \sigma, \pi$, satisfy the linearized continuity equation and the linearized momentum-balance equation (Radović et al. 2007). The second-order equations are:

$$\frac{\partial n_j^{(2)}(\overrightarrow{R},\,t)}{\partial t} + n_j^0 \nabla_{||} \cdot \overrightarrow{u}_j^{(2)}(\overrightarrow{R},\,t) = -\nabla_{||} \cdot [n_j^{(1)}(\overrightarrow{R},\,t)\overrightarrow{u}_j^{(1)}(\overrightarrow{R},\,t)] \tag{1}$$

$$\begin{aligned}&\frac{\partial \overrightarrow{u}_j^{(2)}(\overrightarrow{R},t)}{\partial t} = \nabla_{||}\Phi_{tot}^{(2)}(\overrightarrow{R},\,z,\,t)\,|_{z=0} - \frac{\alpha_j}{n_j^0}\nabla_{||} n_j^{(2)}(\overrightarrow{R},\,t) - \gamma_j \overrightarrow{u}_j^{(2)}(\overrightarrow{R},\,t)\\ &-[\overrightarrow{u}_j^{(1)}(\overrightarrow{R},\,t)\cdot\nabla_{||}]\overrightarrow{u}_j^{(1)}(\overrightarrow{R},\,t)\end{aligned} \tag{2}$$

It can be noticed that, in Eqs. (1) and (2), $\nabla_{||} = \partial \Big/ \partial \overrightarrow{R}$ differentiates in directions parallel to the xy plane. The first term on the right-hand side of Eq. (2) is the tangential force on an electron due to the total electric field at $z = 0$, where $\Phi_{tot}^{(2)}(\overrightarrow{R},\,z,\,t) \equiv \Phi_{ind}^{(2)}(\overrightarrow{R},\,z,\,t)$ because we assume that ρ_{ext} is a weak, first-order perturbation of the 2D electron gas. The second term describes the internal interactions in the electron fluids based on the Thomas-Fermi model (van Zyl and Zaremba 1999, Parr and Yang 1989), giving $\alpha_j = \pi n_j^0$. The third term in Eq. (2) represents phenomenologically introduced friction in the electron gas with the friction constant γ_j which we take to be infinitesimally small.

These equations are solved by performing the Fourier transformation in the xy plane and in time ($\overrightarrow{R} \to \overrightarrow{k}$ and $t \to \omega$). After some algebra, one can obtain the Fourier transform of the second-order induced density $n_2(\overrightarrow{k},\,\omega) = n_\sigma^{(2)}(\overrightarrow{k},\,\omega) + n_\pi^{(2)}(\overrightarrow{k},\,\omega)$. By performing the inverse Fourier transformation in the xy plane and in time ($\overrightarrow{k} \to \overrightarrow{R}$ and $\omega \to t$), we obtain the second-order expression for the induced potential as:

$$\begin{aligned}&\Phi_{ind}^{(2)}(\overrightarrow{R},\,z,\,t) =\\ &\sum_{j=\sigma,\pi}\left[\frac{Q^2}{4\pi(n_j^0)^2}\int \frac{(\overrightarrow{k}-\overrightarrow{k}')\cdot\overrightarrow{v}\left[k^2(\overrightarrow{k}'\cdot\overrightarrow{v})\,\overrightarrow{k}'\cdot(\overrightarrow{k}-\overrightarrow{k}')+2(\overrightarrow{k}\cdot\overrightarrow{v}+i\gamma_j)k'^2\,\overrightarrow{k}\cdot(\overrightarrow{k}-\overrightarrow{k}')\right]}{k^3k'^3|\overrightarrow{k}-\overrightarrow{k}'|^3 D(k,\,\overrightarrow{k}\cdot\overrightarrow{v})D(k',\,\overrightarrow{k}'\cdot\overrightarrow{v})D(|\overrightarrow{k}-\overrightarrow{k}'|,(\overrightarrow{k}-\overrightarrow{k}')\cdot\overrightarrow{v})}\right.\\ &\left.\times\chi_j(k,\,\overrightarrow{k}\cdot\overrightarrow{v})\chi_j(k',\,\overrightarrow{k}'\cdot\overrightarrow{v})e^{-(k'+|\overrightarrow{k}-\overrightarrow{k}'|)z_0}e^{-kz}e^{i\overrightarrow{k}\cdot(\overrightarrow{R}-\overrightarrow{v}t)}d^2\overrightarrow{k}\,d^2\overrightarrow{k}'\right]\end{aligned} \tag{3}$$

where $D(k,\,\omega) = 1 + \frac{2\pi}{k}\chi(k,\,\omega)$. The polarization function of graphene is given by $\chi(k,\,\omega) = \sum\limits_{j=\sigma,\pi}\chi_j(k,\,\omega)$ with $\chi_j(k,\,\omega) = \frac{n_j^0 k^2}{\alpha_j k^2 - \omega(\omega+i\gamma_j)}$.

3. RESULTS FOR STOPPING AND IMAGE FORCES

The stopping force is defined by $F_s = -Q\overset{\wedge}{\overrightarrow{v}}\cdot\nabla_{||}\Phi_{ind}(\overrightarrow{R},\,z,\,t)\Big|_{\overrightarrow{R}=\overrightarrow{v}t,\,z=z_0}$, with the derivative $\nabla_{||}\Phi_{ind}(\overrightarrow{R},\,z,\,t)$ taken at the ion position ($\overrightarrow{R} = \overrightarrow{v}t$, $z = z_0$) and $\overset{\wedge}{\overrightarrow{v}}$ being the unit vector in the direction of ion's motion. The image force is defined by $F_{im} = -Q\frac{\partial}{\partial z}\Phi_{ind}(\overrightarrow{R},\,z,\,t)\Big|_{\overrightarrow{R}=\overrightarrow{v}t,\,z=z_0}$.

The second-order expressions for the stopping and image forces are, respectively:

$$F_s^{(2)} = -\sum_{j=\sigma,\pi}\left[\frac{iQ^3}{2\pi v(n_j^0)^2}\int\limits_0^\infty \frac{e^{-kz_0}}{k^2}dk\int\limits_0^\infty \frac{e^{-k'z_0}}{k'^2}dk'\int\limits_{-kv}^{kv}\frac{\omega\chi_j(k,\omega)d\omega}{D(k,\omega)\sqrt{k^2v^2-\omega^2}}\right.$$
$$\left.\times\int\limits_{-k'v}^{k'v}\frac{\chi_j(k',\omega')\left[\frac{A_j\chi_j(B,\omega-\omega')}{B^3D(B,\omega-\omega')}e^{-Bz_0}+\frac{A'_j\chi_j(B',\omega-\omega')}{B'^3D(B',\omega-\omega')}e^{-B'z_0}\right]}{D(k',\omega')\sqrt{k'^2v^2-\omega'^2}}d\omega'\right] \tag{4}$$

$$F_{im}^{(2)} = \sum_{j=\sigma,\pi}\left[\frac{Q^3}{2\pi(n_j^0)^2}\int\limits_0^\infty \frac{e^{-kz_0}}{k}dk\int\limits_0^\infty \frac{e^{-k'z_0}}{k'^2}dk'\int\limits_{-kv}^{kv}\frac{\chi_j(k,\omega)d\omega}{D(k,\omega)\sqrt{k^2v^2-\omega^2}}\right.$$
$$\left.\times\int\limits_{-k'v}^{k'v}\frac{\chi_j(k',\omega')\left[\frac{A_j\chi_j(B,\omega-\omega')}{B^3D(B,\omega-\omega')}e^{-Bz_0}+\frac{A'_j\chi_j(B',\omega-\omega')}{B'^3D(B',\omega-\omega')}e^{-B'z_0}\right]}{D(k',\omega')\sqrt{k'^2v^2-\omega'^2}}d\omega'\right] \tag{5}$$

where $A_j = (\omega - \omega')\left[k^2\omega'\left(\frac{C}{v^2}-k'^2\right)+2(\omega+i\gamma_j)k'^2\left(k^2-\frac{C}{v^2}\right)\right]$ and $B = \sqrt{k^2+k'^2-2C/v^2}$ with $C = \omega\omega'+\sqrt{k^2v^2-\omega^2}\sqrt{k'^2v^2-\omega'^2}$, while in the expressions for A'_j and B' one has to replace C by $C' = \omega\omega' - \sqrt{k^2v^2-\omega^2}\sqrt{k'^2v^2-\omega'^2}$.

Note that the second-order expressions for the stopping and image forces are each proportional to Q^3 (so-called Barkas effect (Barkas et al. 1963)) and are therefore sensitive to the sign of the external charge, in contrast to the first-order expressions for these forces (Radović et al. 2007).

4. CONCLUSION

We have used a simple 2D, two-fluid model to describe the high-frequency collective electron excitations in graphene. The Barkas correction to the stopping force and the analogous corrections to the induced potential and the image force on charged particles moving parallel to graphene have been obtained by means of the second-order perturbation of the hydrodynamic equations. In future work, we shall evaluate numerically expressions (4) and (5) for those forces to establish the range of relevant parameters validating the applicability of the linearized hydrodynamic model.

References

Barkas, W. H., Dyer, N. J. and Heckman, H. H.: *Phys. Rev. Lett.*, **11**, 26.

Fetter, A. L.: 1973, *Ann. Phys.*, **81**, 367.

Geim, A. K. and Novoselov, K. S.: 2007, *Nature Mater.*, **6**, 183.

Katsnelson, M. I.: 2007, *Mater. Today*, **10**, 20.

Katsnelson, M. I., Novoselov, K. S. and Geim, A. K.: 2006, *Nature Phys.*, **2**, 620.

Niyogi, S., Bekyarova, E., Itkis, M. E., McWilliams, J. L., Hamon, M. A., Haddon, R. C.: 2006, *J. Am. Chem. Soc.*, **128**, 7720.

Novoselov, K.S., Geim, A. K., Morozov, S. V., Jiang, D., Zhang, Y., Dubonos, S. V., Grigorieva, I. V. and Firsov, A. A.: 2004, *Science*, **306** 666.

Novoselov, K. S., McCann, E., Morozov, S. V., Falko, V. I., Katsnelson, M. I., Zeitler, U., Jiang, D., Schedin, F. and Geim, A. K.: 2006, *Nature Phys.*, **2**, 177.

Parr, R. G. and Yang, W.: 1989, Density-Functional Theory of Atoms and Molecules, Oxford University Press, New York.

Radović, I., Hadžievski, Lj., Bibić, N. and Mišković, Z. L.: 2007, *Phys. Rev. A*, **76**, 042901.

van Zyl, B. P. and Zaremba, E.: 1999, *Phys. Rev. B*, **59**, 2079.

Publ. Astron. Obs. Belgrade No. 84 (2008), 181 - 184 *Contributed Paper*

BACKSCATTERING OF FAST ELECTRONS FROM SOLIDS WITHIN A MULTIPLE COLLISION MODEL

J. VUKANIĆ and D. M. DAVIDOVIĆ

Vinča Institute of Nuclear Sciences, P.O. Box 522, 11001 Belgrade, Serbia
E–mail: vukanic@vin.bg.ac.yu
E–mail: davidd@vin.bg.ac.yu

Abstract. Reflection of electrons from solids is treated by the approximate analytic solution of the linearized transport equation. Scattering of electrons on target atoms is determined by the screened Coulomb interaction and the energy loss due to interaction with target electrons is defined by Bethe- Bloch formula. The anisotropic P_3 approximation of the collision integral is utilized and the Bolzmann transport equation is Laplace transformed in relative path length and solved by applying the DP0 technique. The approach is applicable in a wide range of electron energy –from several tens of keV to several MeV- and for materials where the mean number of collisions of an electron with target atoms during slowing down is large. Analytic expressions for energy distribution of backscattered electrons as well as for the particle and energy reflection coefficients were derived. Comparison of our results with data of the computational bipartition model is presented.

1. THE BASIC PHYSICAL MODEL

The scattering and slowing down of fast electrons penetrating a solid targe can be desribed by the following expressions:

(a) The transport cross section for a screened Coulomb interaction between a fast electron and target atom can be approximated by the modified Rutherford formula

$$\sigma_1(T) = 2\pi \frac{Z(Z+1)r_e^2}{T^2} \frac{(T+1)^2}{(T+2)^2} L_1(T). \tag{1}$$

with

$$L_1(T) \approx L_1(T_0) = \ln(1+\frac{1}{\eta}) - \frac{1}{1+\eta}. \tag{2}$$

The screeing constant η is determined by the formula of Moliere (see Moliere 1947). Furtermore, $T = E/(m_0c^2)$ is the kinetic energy of the electron expressed in units $m_0c^2 = 510.7keV$, Z is the atomic number of target atom, and r_e is the classic radius of the electron. The cross section (1) incudes relativistic corrections and deflections caused by inelastic collisions between electrons.

(b) For energies $E > 10keV$, specific energy loss of primary electron caused by interaction with target elecrons can be well described by Bethe- Bloch formula (see Berger et al. 1982)

$$\frac{dT}{d\tau} = -NS(T) = -N4\pi Z r_e^2 \frac{(T+1)^2}{T(T+2)} L_{ion}(T) \tag{3}$$

where τ is the path length traveled, and the term $L_{ion}(T)$ varies very slowly with the energy and can be regarded as a constant i.e. $L_{ion}(T) \approx L_{ion}(T_0)$. Then, the total path length has the form

$$\tau_0 = \frac{1}{4\pi N Z r_e^2 L_{ion}(T_0)} \frac{T_0^2}{(1+T_0)}. \tag{4}$$

We treat the case of fast electrons moving in a solid target when the total path length τ_0 is much greater than the transport mean free path $\lambda_1(E_0) = [N\sigma_1(E_0)]^{-1}$. The dimensionless parameter ν

$$\nu = \frac{\tau_0(E_0)}{\lambda_1(E_0)} = N\sigma_1(E_0)\tau_0 \tag{5}$$

gives the mean number of wide angle collisions for the electron before slowing down to rest. According to Eqs. (1), (4) and (5) the parameter ν becomes

$$\nu = \frac{Z+1}{2} \frac{1+T_0}{(2+T_0)^2} \frac{L_1(T_0)}{L_{ion}(T_0)} \tag{6}$$

Eq. (6) gives the mean number of large angle collisions of electrons penetrating different targets, as a function of initial electron energy. It turns out that - except for very light targets-electrons undergo several deflections before coming to rest.

2. SOLUTIONS OF ELECTRON TRANSPORT EQUATION

The basic simplifying assumption entering the model is that the large number of wide angle deflections produce a nearly isotropic distribution of backscattered electrons. This model of backscattering enabled us to use the convenient approximation of the collision integral of the electron transport equation. We expanded the Laplace transformed electron distribution function in series of double Legendre polynomials over the angular variable. In the lowest order of approximation (DP0 method) we obtained Laplace transformed reflection function.

The approximate solution is simple if one assumes inverse square scattering potential for the screened Coulomb interaction between a high energy electron and target atom. Similar procedure was already successfully used for low energy ion reflection from heavy targets(see Vukanić et al. 2001). The reason is that the situation $\nu >> 1$ apears during penetration of low energy light ions through solids.

The scattering cross section can be approximated by the expression

$$d\sigma(T_0, \mu) = \frac{1}{2\sqrt{2}} \frac{\sigma_1(T_0) d\hat{\mu}}{(1-\mu)^{3/2}} \quad . \tag{7}$$

Here, $\sigma_1(T_0)$ is the transport cross section of the first order, determined by the formula of Moliere , given by Eq. (1). By applying Laplace transform in relative path length,

and utilizing further DPN method ,we have found the solution for the half space reflection function in the lowest order of approximation (DP0 approximation) in form of an exponential function.

3. RESULTS AND DISCUSSION

Applying Laplace inversion, we obtained the analytic expression for the path length and angular distribution of backscattered electrons

$$R(\mu_0, \mu, s)\, d\mu\, ds = \frac{h\nu}{\sqrt{\pi}} \frac{\mu}{(\nu s + g)^{3/2}} \exp[-\frac{h^2}{4(\nu s + g)}]\, d\mu\, ds \tag{8}$$

with $h = h(\mu_0) = 3.094\,\mu_0$ and g=g(μ_0) $= -1.72 + 14.44\mu_0^2 - 24.2\mu_0^4 + 11.48\mu_0^6$

Thank to the simplicity of the expression (6) for $R(\mu_0, \mu, s)$, we obtained by simple integrations over all exit directions and all possible path lengths the particle reflection coefficient in the form

$$R_N(\mu_0, \nu) = erfc(\frac{3.094\mu_0}{2\sqrt{\nu + g}}) \tag{9}$$

One can see from Eq. (9) that the particle reflection coefficient appears to be a universal function of the parameter ν which represent the mean number of wide-angle collisions of the ion during slowing down. Fig. 1 shows the universal curve $R_N(1, \nu)$ for electrons incident normally on solid targets. Our results calculated from Eq. (9) are compared with the data obtained from the computational bipartition model (see Luo Zheng-Ming 1985). One can see that the reflection coefficient scales with the characteristic parameter ν. The agreement of the present results with the computational data is good.

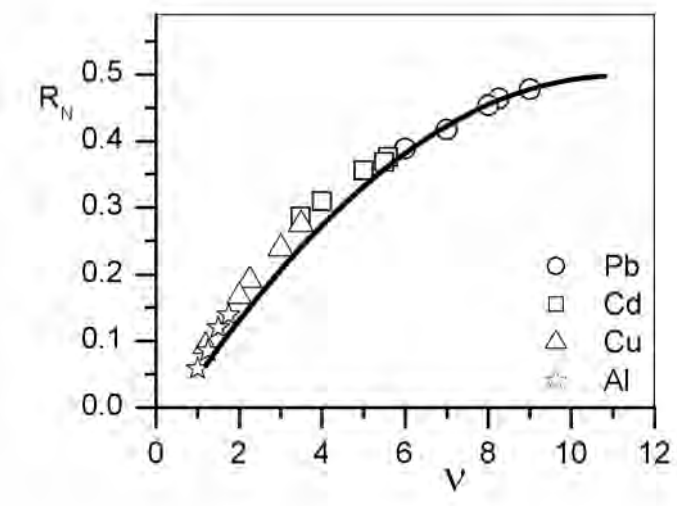

Figure 1: Particle reflection coefficient for electrons incident normally on solid targets. Our universal curve, calculated from Eq.(9) (solid line) is compared with computational data for different materials.

Good agreement of our theoretical estimates for the particle reflection coefficient with the result of computational bipartition model suggests that the obtained formulae describe correctly the backscattering of fast electrons from solids.

References

Berger, M. J., Seltzer, S. M.: 1982, Stopping Powers and Ranges of Electrons and Positrons, National Bureau of Standards Report NBSIR **82-2550**.

Moliere, G. Z.: 1947, *Naturforsch*, **24**, 133.

Vukanić, J., Simović, R.: 2001, *Nuclear Intruments and Methods in Physics Research* B, **179**, 497.

Zheng-Ming Luo: 1985, *Phys. Rev. B*, **32**, 824.

Publ. Astron. Obs. Belgrade No. 84 (2008), 185 - 188 *Contributed Paper*

INVERSE-SQUARE INTERACTION POTENTIAL IN THE MULTIPLE COLLISION MODEL OF LIGHT ION REFLECTION

J. VUKANIĆ[1] and R. SIMOVIĆ[2]

[1] *Lab. for Atomic Physics, Vinča Inst. of Nucl. Sci., P. O. Box 522, 11001 Belgrade, Serbia*
E–mail: vukanic@vin.bg.ac.yu

[2] *Centre for Nucl. Techn. and Res., Vinča Inst. of Nucl. Sci., P. O. Box 522, 11001 Belgrade, Serbia*
E–mail: simovicr@vin.bg.ac.yu

Abstract. The linear Boltzmann transport equation for diffusion and slowing down of low-energy light ions in solids is Laplace transformed in relative path-length and solved by applying the DP0 technique. The ion-target atom interaction potential is assumed to have a form of the inverse-square law and furthermore, the collision integral of the transport equation is replaced by the P_3 approximation in angular variable. The approximative Laplace transformed solution for the reflection function is found and inverted leading to the distribution of backscattered particles in the relative path-length. Analytic expression for the particle reflection coefficient was derived and our result is compared with computer simulation data.

1. INTRODUCTION

In this paper, the energy dependent albedo problem of low energy light ions from heavy targets is considered in a multiple collision model. The ion transport equation is treated with the assumptions that (i) distribution function of reflected ions is almost isotropic and (ii) backscattered particles suffer small energy loss and therefore the transport cross section depends only on initial ion energy. Here we follow the DPN procedure applied in our previous paper (see Simović et al. 1997) improving the model by taking into account the anisotropy effects in ion scattering (Vukanić et al. 2001). This is done by replacing the isotropic approximation of the collision integral in the transport equation with the anisotropic Legendre polynomial approximation of the third order in angular variable.

For ordinary power potentials $V(R) \propto R^{-1/m}$ and the specific case $m = 1/2$, the particle reflection coefficient is found in compact form. The calculated particle reflection coefficient is compared with the results of the Monte Carlo simulations of H, D and He reflection from different targets.

2. PATH-LENGTH DISTRIBUTION OF BACKSCATTERED IONS

In this paper we employ a special power cross section

$$d\sigma(E_0,\hat{\mu}) = \sqrt{2}\,\sigma_1(E_0)\frac{d\hat{\mu}}{(1-\hat{\mu}\,)^{3/2}} \tag{1}$$

which describes scattering in the inverse-square potential $V(R) \propto R^{-2}$. In Eq. (1), $\hat{\mu}$ is the cosine of the scattering angle, E_0 is the ion initial energy and $\sigma_1(E_0)$ is the transport cross section. The scattering cross sections $d\sigma(E_0,\hat{\mu})$ appears appropriate for light ions interacting with heavy target atoms in the energy range of some tens of eV to some tens of keV. The use of Eq. (1) as an input quantity allows simple analytic solutions of the transport equation for the ion reflection.

We have derived the Laplace transformed half space reflection function in DP0 approximation. This procedure gives good results for the reflection function even in the lowest order of approximation (Vukanić et al. 2001)

$$\Re(\mu_0,p) = \frac{1}{1-A}\frac{(\sqrt{1-A\omega(p)}-\sqrt{1-\omega(p)})[\sqrt{1-A\omega(p)}-B(\mu_0)\sqrt{1-\omega(p)}]}{1+2\,\mu_0\sqrt{1-A\omega(p)}\sqrt{1-\omega(p)}} \tag{2}$$

Here μ_0 is the cosine of the angle of incidence and p is the Laplace variable. For the inverse-square scattering potential $A = 41/128$, $B(\mu_0) = (3\,\mu_0 + 35\,\mu_0^3)/32$ and the multiplication factor ω is $\omega(p) = 2\nu/(2\nu+p)$. Moreover, $\nu = N\,\sigma_1(E_0)\,\tau_0$, where N is the density of target atoms and τ_0 is the total path length.

The parameter ν represents the mean number of wide-angle collisions that ions suffer before slowing down to rest. For $\nu \gg 11$, because of large number of scattering events, the initially strongly peaked ion beam becomes more and more isotropic. The complete randomization of the direction of motion occurs already at transport path length much less than the total path length: $\lambda_1(E_0) \ll \tau_0 2$. For relative path lengths $s > \lambda_1\,/\,\tau_0 3$, the ion distribution function is almost isotropic.

For not very oblique incidence, we have approximated the Laplace transformed reflection function by an exponential

$$\Re(\mu_0,p) \approx \exp[-h\sqrt{p/\nu} + g(p/\nu)] \tag{3}$$

with $h = h(\mu_0) = 3.094\,\mu_0$ and $g = g(\mu_0) = -1.72 + 14.44\,\mu_0^2 - 24.2\,\mu_0^4 + 11.48\,\mu_0^6$.

The semi-empirical approximation (3) is very accurate except in the tails of the distribution ($p \gg 1$) when deviations occur. However, the approximations used in the derivation of Eq. (2) become questionable for $p \gg 1$ and the theoretical model applied is not very reliable.

Applying Laplace inversion of the approximative $\Re(\mu_0,p)$, we obtained the path-length distribution of backscatered particles

$$R(\mu_0,s) \approx \frac{h}{2\sqrt{\pi}}\frac{\nu}{(\nu s+g\,)^{3/2}}\exp[-\frac{h^2}{4(\nu s+g)}] \tag{4}$$

where s is the relative path-length travelled.

At normal incidence $\mu_0 = 1$, $g = 0$ and $R(\mu_0,s)$ is the exact inversion of $\Re(\mu_0,p)$. For $\mu < 1$, $g > 0$, but small, and $R(\mu_0,s)$ is the very good approximate inversion of

$\Re(\mu_0, p)$. $R(\mu_0, s)$ is the peak shaped distribution with a sharp peak at $\nu_{S_m} \approx 1.6\,\mu_0^2$, where S_m is the most probable relative path-length.

Figures 1 (a) and (b) compare the universal function $R(\mu_0, s)/\nu$ obtained from the simple expression (4) with the exact solution accomplished by numerical inversion of the original DP0 Laplace transformed solution (2). One can see that the analytical solution is a very good overall approximation of the numerical result for both normal and oblique incidence.

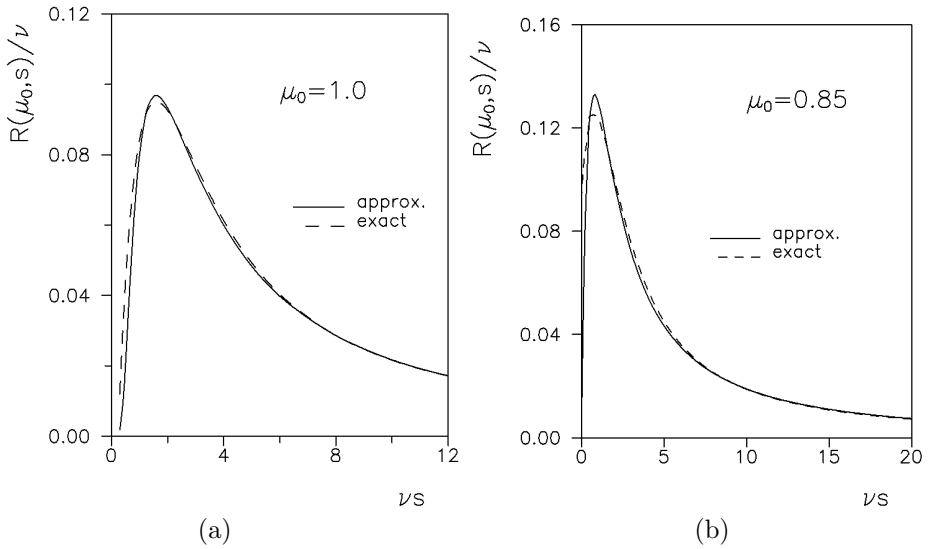

Figure 1: Path-length distributions of backscattered ions calculated for (a) perpendicular incidence and (b) oblique incidence.

3. RESULTS AND DISCUSSION

Thanks to the simplicity of the approximate expression (4) for $R(\mu_0, s)$, we obtained in analytic and condensed form the particle reflection coefficient $R_N(\mu_0, \nu)$

$$R_N(\mu_0, \nu) = \int_0^1 R(\mu_0, s) ds = erfc(u) \tag{5}$$

with $u = 3.094\,\mu_0 / [2\sqrt{(\nu + g)}]$.

One can see from Eq. (5) that particle reflection coefficient depends on initial energy and ion-target combination through the variable ν which represents the mean number of wide-angle collisions that ions suffer before slowing down to rest. The scaling holds at low ion energies ($\nu > 14$) when reflection is determined by multiple collisions, as well as at high energies ($\nu < 15$) when single collisions dominate. It was found recently that the reflection coefficient of heavy ions from solids also scales with the parameter $\nu 6$.

Fig. 2 gives the particle reflection coefficient for light ions incident normally on heavy targets as a function of the parameter ν. The present work is compared with

the Monte Carlo simulations of H, D and He reflection from different targets for a wide range of initial energies (Vicanek et al. 1991).One can see that the agreement of our results with simulated data is good for $\nu > 2$.

Good agreement of our theoretical estimates with computer simulation data suggests that the obtained analytical universal formula describes correctly the low-energy light ion reflection from solids.

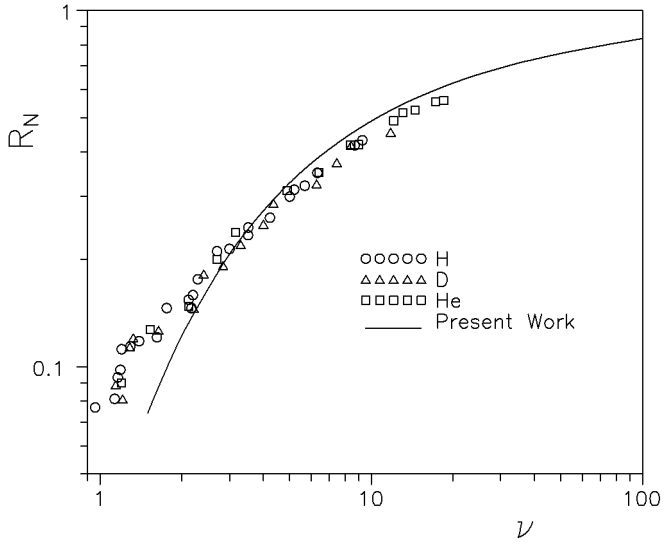

Figure 2: Particle reflection coefficient for light ions incident normally on heavy targets. Comparison of the present work with the computer simulation data of Vicanek et. al.

References

Simović, R., Vukanić, J.: 1997, *J. Phys. D*, **30**, 2331.
Vicanek, M., Urbassek, N. M.: 1991, *Phys. Rev. B*, **44**, No. 14, 7234.
Vukanić, J., Simović, R.: 2001, *Nucl. Instr. and Meth.* B, **179**, 497.

Publ. Astron. Obs. Belgrade No. 84 (2008), 189 - 192 *Contributed Paper*

TRANSMISSION OF ELECTRONS THROUGH Al_2O_3 NANOCAPILLARIES IN THE ENERGY RANGE 2-120 eV

A. R. MILOSAVLJEVIĆ[1], J. JURETA[1], Gy. VÍKOR[1], Z. D. PEŠIĆ[1,2], D. ŠEVIĆ[1], S. MÁTÉFI-TEMPFLI[3], M. MÁTÉFI-TEMPFLI[3] and B. P. MARINKOVIĆ[1]

[1] *Institute of Physics, Pregrevica 118, 11080 Belgrade, Serbia*
E–mail: vraz@phy.bg.ac.yu

[2] *Institute of Ions Beam Physics and Materials Research, Dresden, Germany*

[3] *Unité de Physico-Chimie et de Physique des Matériaux, Université Catholique de Louvain, Place Croix du Sud, 1, B-1348 Louvain-la-Neuve, Belgium*

Abstract. Electron transmission through insulating Al_2O_3 nanocapillaries (diameter 140 nm and aspect ratio 110) has been investigated, for low incident energies from 2 to 120 eV. An energy dependence of the transmission function has been investigated both with and without an energy analysis of the electrons and differences are discussed. Significant intensities of transmitted electrons (without the energy analysis) were observed even at the lowest electron energies.

1. INTRODUCTION

The transmission of charged particles through insulating nanocapillaries has been attracting a great deal of attention in recent years, since Stolterfoht et al. in 2002 reported an experiment showing a guiding of slow positive ions (3 keV Ne^{7+}) through highly insulating nanocapillary foils of polyethylene teraphthalate (PET). The observed phenomenon offered new possibilities for fundamental investigations, characterization of the inner walls of the insulating nanotubes and different applications. Thereafter, an intensive experimental investigation has been reported on the guiding of positive ions, mainly slow HCIs, by insulating nanocapillaries: PET (see Stolterfoht et al. 2008 and references therein), SiO_2 (Sahana et al. 2006) and Al_2O_3 (Mátéfi-Tempfli et al. 2006, Skog et al. 2007, Krause et al. 2007). The experimental work was accompanied by classical trajectory Monte Carlo simulations by Schiessl et al. 2005, 2007, which related the microscopic charge-up with macroscopic material properties.

Using the electrons as projectiles gives new possibilities both for a fundamental understanding of the guiding phenomenon and applications. However, only recently the first results on guided transmission of electrons through insulating nanocapillaries have been reported by Milosavljević et al. 2006 (200-350 eV for Al_2O_3) and Das et al. 2007 (500 and 1000 eV for PET). Both these experiments confirmed an existence of electron guiding, as found for HCIs. Still, they also showed a very small transmissivity of electrons through insulating nanocapillaries in comparison with ions. Furthermore,

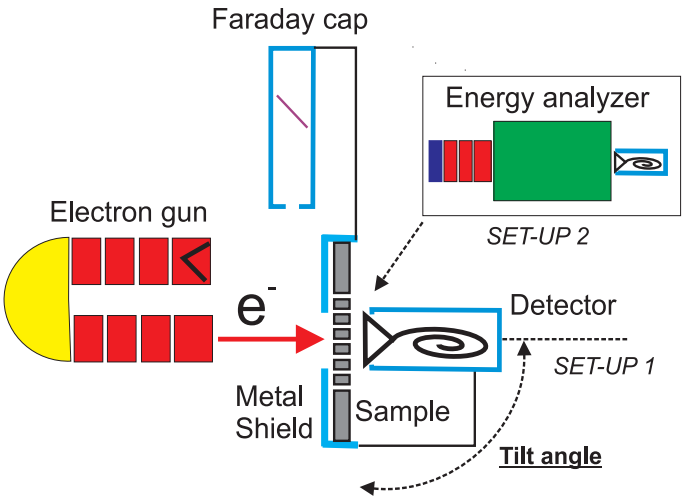

Figure 1: A schematic view of the experimental set-up.

it appears that the transmission rate (even for electrons transmitted along the capillary axis) decreases strongly with decreasing the electron energy. Therefore, the characteristics of electron guiding at very low energies down to a few eVs remained unknown. It is an open question even if it is possible to transmit very slow electrons through the insulating nanocapillaries, considering a significant charge-up of the inner walls. Therefore, we arranged an experimental set-up to investigate transmission of electrons through Al_2O_3 nanocapillary foils for low energies down to almost 0 eV. The next step then would be to investigate guiding phenomenon in this region.

2. EXPERIMENT

A highly ordered hexagonally close-packed Al_2O_3 nanochannels array was prepared using the self-ordering phenomenon during a two-step anodization process of a high purity (99.999%) 0.5 mm tick aluminium foil. To prevent a macroscopic charge-up of the target surface, the niobium layers of 20 nm thickness were deposited by dc-sputtering on both sides of the final well-ordered honeycomb membrane. A more detailed description of the fabrication process has been given by Mátéfi-Tempfli et al. 2006. The diameter of the used Al_2O_3 capillaries is about 140 nm, the intercapillary distance about 320 nm, while the length is 15 μm. The calculated geometrical transparency is about 8.4%.

The measurements were performed on a modified threshold electron impact spectrometer, which was described elsewhere (Cvejanović et al. 1992, Jureta et al. 2004). A schematic view of the present experimental set-up is given in figure 1. Electrons are produced in a Pierce type electron gun and focused by a system of three-element aperture lenses into a hemispherical monochromator. Between the monochromator and the interaction region, the electron beam passes two sets of lenses in order to satisfy the constant focusing in a large incident energy range. Measurements of the incident beam current in the Faraday cup as a function of the electron energy con-

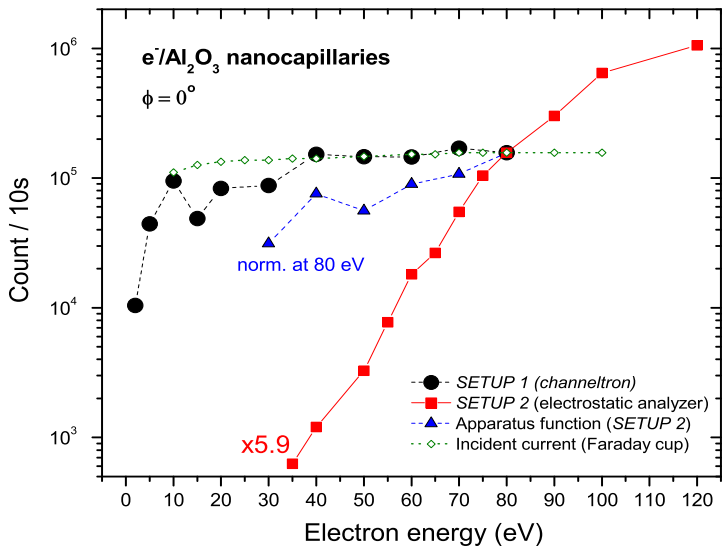

Figure 2: The intensity of the signal of electrons transmitted through Al_2O_3 nanocapillaries in the straightforward direction as a function of the incident energy.

firmed a constant geometry of the incident beam down to about 20 eV. In this energy range, the radius of the incident beam is estimated to be about 1 mm at the position of the sample. The present measurements were usually performed with an incident electron current of 8 nA, thus resulting in about 10 nA/mm^2 of the current density at the nanocapillary foil. The electron energy scale has been previously calibrated according to the positions of the 2^3S and 2^1S resonance structures in the metastable excitation spectrum of helium (19.820 eV and 20.616 eV, respectively). The energy spread in the incident electron beam has been determined to be about 50 meV.

3. RESULTS AND DISCUSSION

Figure 2 shows the transmitted electron current intensity in the straightforward direction as a function of the incident electron energy, for both used experimental configurations - without (*SETUP 1*) and with (*SETUP 2*) the energy analyzer. The *SETUP 1* configuration insures that practically all transmitted electrons are detected, regarding both the angular and the energy spread. For *SETUP 2*, however, detection was limited to the incident energy and a few degrees angular spread around the axis. Even for the *SETUP-UP 2*, the range of the energy of detected electrons transmitted through the insulating nanocapillaries has been significantly extended regarding Milosavljević et al. 2006 down to about 35 eV (red squares in fig. 2). Still, the transmission appears to decrease very quickly with decreasing the electron energy, as it was previously reported. As a consequence, it was impossible to obtain a statistically accurate signal below about 30 eV. Note that the apparatus function (blue triangles in fig. 2) shows significantly different behavior, itself decreasing much slower. Hence, this difference must be ascribed to an influence of the insulating nanocapillaries. How-

ever, placing the detector directly behind the nanocapillary foil (*SETUP-UP 1*) did allow us to measure a significant signal of transmitted electrons even at the lowest used incident energy of 2 eV. Furthermore, the curve representing the energy dependence appears to be rather flat in this case, with a behavior that is similar to the apparatus function (note that the later also includes the transmission of the analyzer, resulting in a steeper slope). At very low energies below about 20 eV, an inevitable geometrical divergence of the incident beam resulted in a lower electron flux at the nanocapillary foil and, hence, a decrees of the signal.

One of the possible explanations for the strong difference of transmission functions with and without an analyzer is, of course, a significant influence of the insulating nanocapillaries to the transmission of the analyzer-detector system, due to an angular divergence of the transmitted electrons. However, an increase of the portion of inelastically scattered electrons from the nanocapillary walls could be a possible contribution to the decrease of the signal in *SETUP-UP 2* configuration, since only the electrons with the incident energies are selected in this case. Note that electrons deflected by the charge deposited on the walls cannot be distinguished from the elastically scattered ones.

To conclude, transmission of electrons through Al_2O_3 nanocapillaries has been measured for the first time at low energies (2-120 eV). The transmission in the straight forward direction strongly depends on a setup of the detector system.

Acknowledgments

We are grateful to Professor Nico Stolterfoht for an useful discussion. This work has been supported by Ministry of Science of Republic of Serbia under project 141011 and by the Interuniversity Attraction Pole Program (P6/42) - Belgian State - Belgian Science Policy.

References

Cvejanović, S., Jureta, J., Minić, M. and Cvejanović, D.: 1992, *J. Phys. B: At. Mol. Opt. Phys.*, **25**, 4337.

Das, S., Dassanayake, B. S., Winkworth, M., Baran, J. L., Stolterfoht, N. and Tanis, A.: 2007, *Phys. Rev. A*, **76**, 042716.

Jureta, J. and Cvejanović, S.: 2004, *Eur. Phys. J. D*, **30**, 37.

Krause ,H. F., Vane, C. R. and Meyer F. W.: 2007, *Phys. Rev. A*, **75**, 042901.

Mátéfi-Tempfli, S. et al.: 2006, *Nanotechnology*, **17**, 3915.

Milosavljević, A. R., Víkor, Gy., Pešić, Z. D., Kolarž, P., Šević, D., Marinković, B. P., Mátéfi-Tempfli, S., Mátéfi-Tempfli, M. and Piraux L.: 2006, *Phys. Rev. A*, **72**, 030901(R).

Sahana, M. B., Skog, P., Víkor, Gy., Rajendra Kumar, R. T. and Schuch, R.: 2006, *Phys. Rev. A*, **73**, 040901(R).

Schiessl, K., Palfinger, W., Tőkési, K., Nowotny, H., Lemell, C. and Burgdörfer, J.: 2005, *Phys. Rev. A*, **72**, 062902.

Schiessl, K., Palfinger, W., Tőkési, K., Nowotny, H., Lemell, C. and Burgdörfer, J.: 2007, *Nucl. Instrum. Methods B*, **258**, 150.

Skog, P., Soroka, I. L., Johansson, A. and Schuch, R.: 2007, *Nucl. Instrum. Methods B*, **258**, 145.

Stolterfoht, N., Bremer, J.-H., Hoffmann, V., Hellhammer, R., Fink, D., Petrov, A. and Sulik, B.: 2002, *Phys. Rev. Lett.*, **88**, 133201.

Stolterfoht, N., Hellhammer, R., Bundesmann, J. and Fink, D.: 2008, *Phys. Rev. A*, **77**, 032905.

Publ. Astron. Obs. Belgrade No. 84 (2008), 193 - 196 *Contributed Paper*

STRUCTURAL AND MAGNETIC PROPERITES OF Xe ION IRRADIATED Co/Si BILAYERS

M. NENADOVIĆ, M. POPOVIĆ, M. NOVAKOVIĆ, N. BIBIĆ and Z. RAKOČEVIĆ
Institute of Nuclear Sciences "Vinča", Laboratory for Atomic Physics, 11001 Belgrade, Serbia

Abstract. Polycrystalline cobalt layers, deposited on Si(110) wafers via electron beam evaporation to a thickness of 55 nm, were irradiated at room temperature with 200 keV Xe ions to fluences of up to 15×10^{15} ions/cm^2.The atomic and magnetic force microscopy (AFM and MFM) were used to investigate the changes in the roughness and magnetic properties of the Co/Si bilayers. Ion beam induced structural changes were correlated with magnetic properties.

1. INTRODUCTION

Tailoring thin films of new materials by ion bombardment of layered structures appears as an interesting alternative to physical or chemical vapor co-deposition, pulsed laser deposition, and other methods of thin-film technology.

Based on the need to tailor shallow $CoSi_2$ junctions as contact metallization, the Co–Si system (Cheng and Chen 2008) has been investigated in much detail, with respect to thermal and ion-induced mixing (Mayer et al. 1981), implantation through metal doping (Bouilla et al. 2006), nano-patterning via focussed ion beams (Mitan et al. 2001) and low-energy and swift heavy-ion mixing (Bhattacharya et al. 2002). Nonetheless, the correlations existing between the microstructural properties of ion-irradiated or ion-mixed metal/silicon bilayers and their magnetic properties (in the case of 3d elements) is far from being understood. Phase transformations in Xe-irradiated Co and Co/Fe films have recently been studied by Zhang and collaborators (2003).

Led by these considerations, we have carried out a series of experiments, in which cobalt films of 55 nm thickness were deposited on crystalline Si wafers and irradiated at room temperature with 200 keV Xe ions to fluences of up to 15×10^{15} ions/cm^2.

2. EXPERIMENTAL PROCEDURE

Co thin films were deposited on Si (100) substrate by e-beam evaporation at the TESLA facility (Bibic et al. 2002). The substrates were cleaned by means of standard procedure, rinsed in diluted HF and in deionized H_2O, and prior to deposition they were sputter-cleaned with a high-intensity 1,5 keV Ar ion beam. The pressure in the chamber during deposition was maintained 1×10^{-6} mbar, and the Co deposition rate

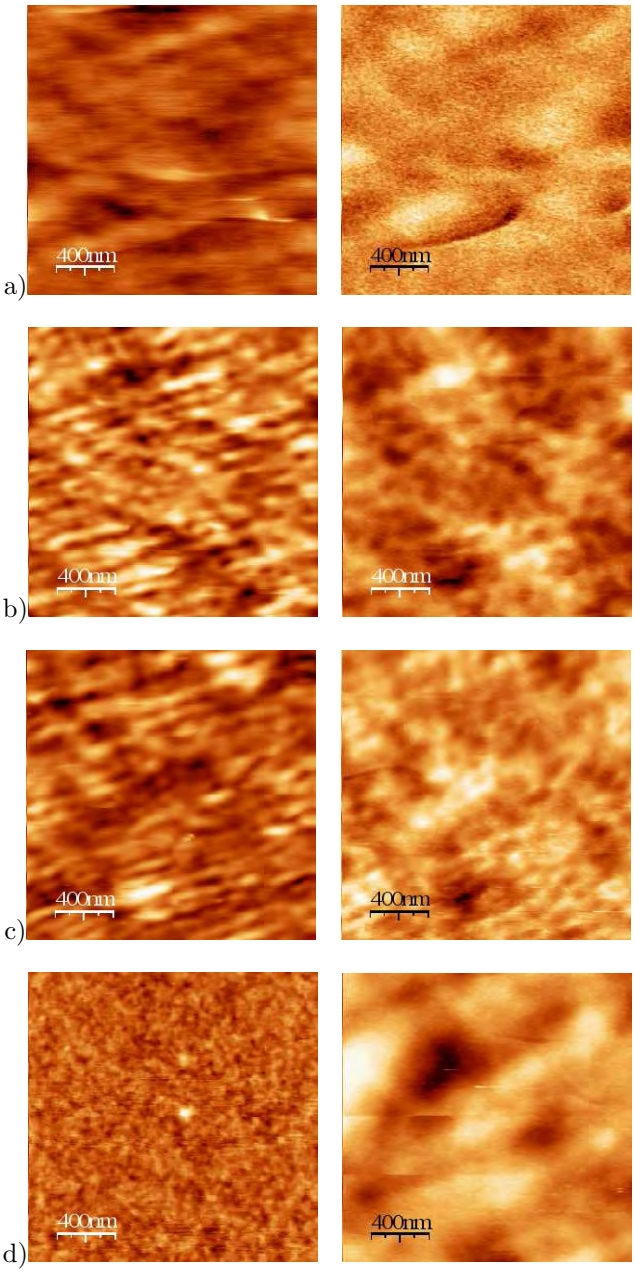

Figure 1: (a-d) Topography(AFM) images (left) and MFM images (right) of Co/Si bilayers: (a) as deposited; (b) irradiated to 5×10^{15} ion/cm^2; (c) 10×10^{15} ion/cm^2 and (d) 15×10^{15} ion/cm^2.

at 0,5 nm/s. The IONAS implanter was used for ion irradiation. A sample area of 1×1 cm^2 was implanted homogeneously at a beam current of 2,5 μA/cm^2. The Co/Si layers were irradiated to (5, 10, 15) $\times$ 10^{15} ions/cm^2 with 250 keV Xe at 550 °C.

The SPM studies were caried out on VEECO MultiMode Quadrex IIIe in the lift mode. In the first step cantilever was tapping the surface and gives topography. In second step cantilever was lifted for 60 nm and it oscilated under the magnetic forces. Changing the oscilating frequency magnetic domains were obtained. Cantilever type is standard MESP-Veeco production. Tip was magnetized in external magnetic field in N direction along vertical axis. Scaned area was 2×2 μm for the all samples.

3. RESULTS AND DISCUSSION

The results of AFM and MFM analyses of Co/Si bilayers before and after irradiation are shown in Figure 1. Topography image(AFM) taken from as deposited Co/Si bilayer clearly show that the mean grains size is about 30 nm, and z-range 9 nm (Fig. 1a left). The specific pattern with the bright and dark regions represents magnetic domain structures (Fig. 1a right). The MFM image indicates that the magnetic domains are in the range of 50 nm.

After irradiation of Co/Si bilayers with 200 keV Xe ions to fluence of 5×10^{15} ion/cm^2 the surface roughness increases to 15 nm z-range (1b left), but the grain size decreases to 25 nm. The MFM image shown in Figure 1b right suggests that Xe ion irradiation induces the change of the local magnetic structure. In fact, the magnetic domains increased to 75 nm (1b right).

Images shown in Figure 1c are from the sample implanted to 10×10^{15} ion/cm. Analysis of this sample in AFM mode showed that the z- range was 22 nm, indicating also slightly smaller grains size of about 20 nm (Fig. 1c left). In this case, the increase of the magnetic domains to 100 nm was observed (Fig. 1c right).

At a highest Xe ions fluence of 15×10^{15} ion/cm^2, the smoothing effects occurred, as shown in Figure 1.d. Namely, the mean grains size is about 15 nm and z-range 8 nm (Figure 1d left). This suggests that high concentration of irradiation induced defects may enhance the atomic mobility, which can result in a change of the crystalline structure. As a consequence the magnetic domains increased to 170 nm (Figure 1d right).

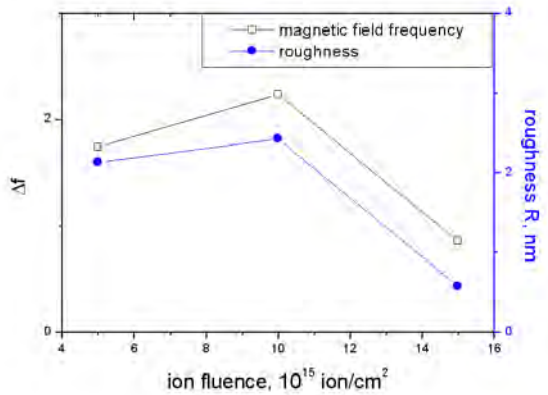

Figure 2: The Xe ion fluence dependence of magnetic frequency (Δf) and roughness (R) of Co/Si bilayers irradiated with 5×10^{15} ion/cm^2, 10×10^{15} ion/cm^2 and 15×10^{15} ion/cm^2.

Figure 2 displays the fluence dependence of magnetic frequency (Δf) and roughness (R) for irradiated Co/Si bilayers. Both curves show very similar behavior. A dramatic change occurred after irradiation to a highest fluence of 15×10^{15} ion/cm^2. This is consistent with the possible changes of the crystalline structure induced by Xe ion irradiation.

4. CONCLUSION

In conclusion, the results obtained with AFM and MFM analyzing techniques are consistent with the changes of crystalline structure in Co/Si bilayers irradiated with 200 keV Xe^+ ions. A possible explanation of this phenomenon has been associated with a high concentration of irradiation induced defects.

References

Bhattacharya, D., Srivastava, S. K., Sahoo, P. K., Principi, G., Kabiraj, D., Som, T., Kulkarni, V. N. and Avashthi, D. K.: 2002, *Surf. Coat. Techn.*, **158/159**, 59.

Bibic, N., Dhar, S., Lieb, K. P., Milosavljevic, M., Schaaf, P., Huang, Y.-L., Seibt, M., Homewood, K. P., McKinty, C.: 2002, *Surface and Coatings Technology*, **158**, 198.

Bouilla, F. A., Skeldon, P., Thompson, G. E., Piekoszewski,J., Chimielewski, A. G., Sartowska,B., Stanislawski, J.: 2006, *Surface and Coating Technology*, **200**, 4684.

Cheng, S. L., Chen, H. Y.: 2008, *Journal of Physics and Chemistry of Solids*, **69**, 441.

Mayer, J. W., Tsaur, B. Y., Lau, S. S., Hung, L. S.: 1981, *Nuclear Instruments and Methods*, **182-183**, 1.

Mitan, M. M., Pivin, D. P., Alford, T. L. and Mayer, J. W.: 2001, *J. Vacuum Sci. Techn. B*, **19**, 2525.

Zhang, K., Gupta, R., Lieb, K. P., Luo, Y., Muller, G. A., Schaaf, P. and Uhrmacher, M.: 2003, *Europhys. Lett.*, **64**, 668; *J. Mag. Mag. Mat.*, **272-276**, 1162.

Publ. Astron. Obs. Belgrade No. 84 (2008), 197 - 200 *Contributed Paper*

SURFACE TEXTURE PARAMETERS IN OPTIMIZING MAGNETIC FORCE IMAGES

M. NENADOVIĆ[1], S. ŠTRBAC[2], Z. RAKOČEVIĆ[1]

[1]*INS Vinča, Laboratory for Atomic Physics, P.O.B. 522, 11001 Belgrade, Serbia*

[2]*ICTM-Institute of Electrochemistry, University of Belgrade, P.O.B. 815, 11001, Belgrade, Serbia*

Abstract. In this work, the optimizing conditions necessary for magnetic field gradient imaging using Atomic Force Microscopy (AFM) and Magnetic Force Microscopy (MFM) in a lift mode have been established. 55 nm thick Co thin film deposited on monocrystalline silicon substrate was used as a sample. The lift height dependence of various surface texture parameters: R_{sk} - the skewness, and R_{ku}- the kurtosis, have been determined. The results have shown that the influence of the substrate and its texture on the magnetic field gradient can be neglected for the lift height above 40 nm, and that the upper lift height limit corresponding to the height where magnetic field lines follow the shape of the field is 100 nm.

1. INTRODUCTION

Various parameters used to determine the real surface can be considered depending on the surface physical properties investigated for specific purpose (Dong et al. 2004). Real surface parameters involve: 3D Surface Texture Parameters, Stylus X and Stylus Y Surface Texture Parameters, S Parameters and Wear Surface Texture Parameters (Cohen 2002, *** 2007). Using a commercial Atomic Force Microscopy (AFM) has emphasized the importance of 3D surface topography and an advent of measurement and characterization of surface topography and magnetic field in three dimensions.

Magnetic images are very complex to define and we used an analogy with a surface 3D topography to obtain reproducible results in this field. Surface parameters used to define magnetic images have to be limited to statistic parameters only where z-axis represents the change in the cantilever oscillation phase due to the magnetic forces between the tip and the sample. Also, some preliminary physical conditions defined by the nature of the measured magnetic field have to be taken into account.

Ferromagnetic materials, bulk and thin solid films, all have magnetic domains whose spatial and surface distribution gives a magnetic field of a material with a given dimensions to be minimal, tending to zero in the case when there is no external magnetic field applied (Hubert and Schafer 2000). This suggests that the image of 3D magnetic field topography should have a Gaussian distribution without a pronounced high peaks and deep valleys. It should be symmetrical with no anomalies in surface height distribution. Taking into account these considerations it can be concluded that

kurtosis parameter should have value of S_{ku}=3, while skewness parameter should be S_{sk}=0.

Magnetic Force imaging is a secondary imaging mode derived from TappingMode AFM that maps the magnetic field gradient on the sample surface. For magnetic imaging mode of an AFM for each scan line, two successive scans were performed. The topography was acquired in the main scan by standard tapping mode AFM, while for MFM imaging, the tip is subsequently retraced in lift mode at a certain tip-sample distance (lift height). Changing the lift height it is possible to follow the changes in the magnetic field, i.e. to acquire the magnetic field gradient. Accordingly, the chosen lift height affects the quality of MFM images, what was the aim of these investigations.

2. EXPERIMENTAL PROCEDURE

Co thin films on Si (100) substrate were prepared by e-beam evaporation at the TESLA facility (Bibic et al. 2002). The substrates were cleaned by means of standard procedure, rinsed in diluted HF and in deionized H_2O. Prior to deposition they were sputter-cleaned with a high-intensity 1,5 keV Ar ion beam. The pressure in the chamber during deposition was maintained 1×10^{-6} mbar, and the Co deposition rate at 0,5 nm/s. The IONAS implanter was used for ion irradiation. A sample area of 1×1 cm^2 was implanted homogeneously at a beam current of 2,5 μA/cm^2. The Co/Si layers were irradiated to (5, 10, 15) $\times$ 10^{15} ions/cm^2 with 250 keV Xe at 550 °C.

The imaging of the topography and magnetic domains was performed with scanning probe microscopy (SPM) Quadrex Multimode IIIe (Veeco Instruments), operated under ambient conditions. The topography was acquired in the main scan by standard tapping mode AFM using MESP tip. For MFM measurements, the tip is subsequently retraced in lift mode using lift height values of: 10, 20, 40, 60, 80, 100, 150, 200, 300, 400 and 1000 nm, with the aim to establish the optimum lift height range for the best image quality. The surface roughness average, the skewness and kurtosis were estimated in the dependence of the lift height, using the subprogram packages of the SPM.

3. RESULTS AND DISCUSSION

Characteristic AFM/MFM images of thin solid Co films are shown in Fig. 1. The image on the left side represents the topography of the surface and it was the same for all measurements for a given place on the surface. The image on the right side represents the magnetic field gradient which varied depending on the lift height. White areas on the image represent the repulsive forces between the tip and the sample, while dark areas represent the attractive forces.

From the estimation of kurtosis and skewness parameters we tried to find out an optimal range for the lift height. On Figure 2, the kurtosis vs. lift height is shown. In the range of the statistical error of measurements it can be seen from Fig. 2 that the symmetrical distribution of the magnetic field is obtained for images acquired for the lift heights ranging from 40 to 300 nm. A huge asymmetry obtained for the lift heights from 10 to 40 nm can be explained by the influence of the sample being close to the tip for MFM measurements (Naves and Andrade 1999). For lift heights set at

a) 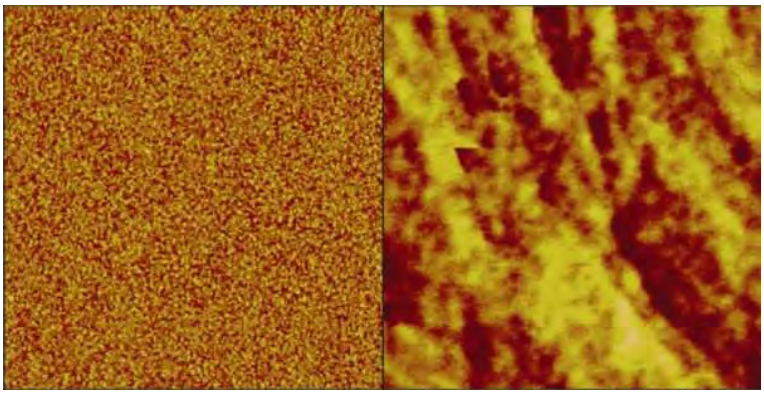 b)

Figure 1: SPM images ($5\mu \times 5\mu$) of 55 nm thick Co thin film: a) AFM image of surface topography; b) MFM image of the same area for the lift height of 60 nm.

300 nm and above, MFM images are in the domain of the noise and their adequate interpretation is not possible.

In order to discuss the anomalies of MFM images, the dependence of the skewness parameter as a function of the lift height is presented in Fig. 3. In the range of statistical error, the value of the skewness parameter of S_{sk}=0, have MFM images acquired for the lift heights from 40 to 100 nm. In the range from 100 to 300 nm, the anomalies of MFM images are found which could be a consequence of the decrease in the magnetic field intensity and consequently its equalization.

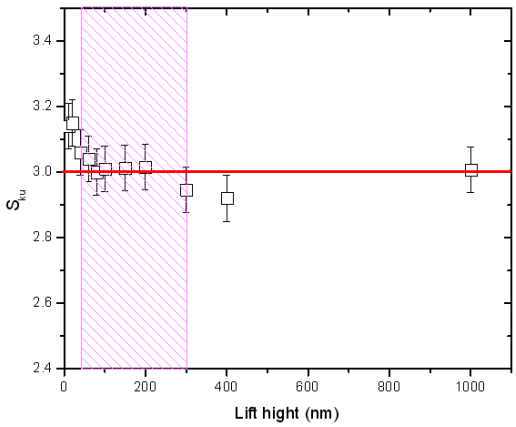

Figure 2: Kurtosis as a function of the lift height.

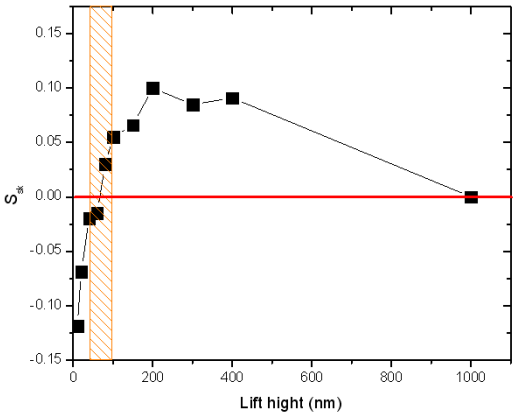

Figure 3: Skewness as a function of the lift height.

4. CONCLUSION

The obtained results have shown that surface texture analysis is very complex. There are many parameters which need to be involved. We have got values for R_{sk} and R_{ku} as a function of the lift height. The optimal ranges are estimated for each measurement.

References

***: 2007, Metro Pro Surface Texture Parameters, Zygo Corporation.
Bibic, N., Dhar, S., Lieb, K. P., Milosavljevic, M., Schaaf, P., Huang, Y.-L., Seibt, M., Homewood, K. P., McKinty, C.: 2002, *Surface and Coatings Technology*, **158**, 198.
Cohen, D. K.: 2002, Glossary of Surface Texture Parameters, Michigan Metrology, LLC.
Dong, W. P., Sullivan, P. J., Stout, K. J.: 1994, *Wear*, **178**, 29.
Hubert, A., Schafer, R.: 2000, Magnetic domains: the analysis of magnetic microstructures, Springer-Verlog Berlin Heidelberg New York.
Naves, B. R. A. and Andrade, M. S.: 1999, *Appl. Phys. Lett.*, **74**, 2090.

Publ. Astron. Obs. Belgrade No. 84 (2008), 201 - 204 *Contributed Paper*

MICROSTRUCTURAL CHANGES OF CHROMIUM-NITRIDE THIN FILMS INDUCED BY ARGON ION IMPLANTATION

M. NOVAKOVIĆ, M. POPOVIĆ, M. MILOSAVLJEVIĆ, D. PERUŠKO,
V. MILINOVIĆ, I. RADOVIĆ and N. BIBIĆ
VINČA Institute of Nuclear Sciences, Belgrade 11001, POBox 522, Serbia

Abstract. This paper presents a study of the structure and composition of Cr-N thin films as a function of deposition parameters and ion irradiation. Thin films were deposited by reactive ion sputtering on (100) Si substrates, to a thickness of 240-280 nm, at different nitrogen partial pressures. After deposition the samples were irradiated with 120 keV argon ions, to the fluences of 1×10^{15} and 1×10^{16} ions/cm^2. Structural characterization of the samples was performed by Rutherford backscattering spectrometry, x-ray diffraction and cross-sectional transmission electron microscopy. It was found that the film composition, Cr_2N or CrN, strongly depends on the nitrogen partial pressure during deposition. Ion irradiation induces local microstructural changes, formation of nanoparticles and defects.

1. INTRODUCTION

Chromium-nitride thin films were developed for many years as hard coatings, wear and corrosion protection materials (Nouveau et al. 2001, Wiklund et al. 1997, Komiya et al. 1997). Compared to TiN, the most widely used coating material, they exhibit close values of surface hardness, but about 1000 times better oxidation resistance (Vishnyakov 2006). In physical vapour deposition Cr-N films can grow in form of CrN or Cr_2N phases, the Cr_2N phase exhibiting a higher hardness. On the other hand, the CrN phase is also interesting due to its magnetic, optical and electronic properties. However, modern surface engineering involves application of ion beams in the processes such as ion implantation, plasma ion immersion, or ion beam assisted deposition. Ion beam modification of hard coating materials was found very efficient for improving their tribological properties (Sharkeev 2006).

In this study our main interest was to investigate the structure and composition of Cr-N films as a function of nitrogen partial pressure, and the effects of ion implantation on these structures. The layers were deposited by reactive ion sputtering on Si substrates and subsequently irradiated with 120 keV Ar ions. It was found that ion irradiation induces local rearrangements in the film structures.

2. EXPERIMENTAL PROCEDURE

Cr-N films were deposited by reactive ion sputtering in a Balzers Sputtron II system. We sputtered a 99.99% pure Cr target with argon ions in a nitrogen ambient. The base pressure in the chamber was in the low 10^{-6} mbar region, the Ar partial pressure 1×10^{-3} mbar, while the nitrogen partial pressure was set either at 2×10^{-4}, 3.5×10^{-4}, or 5×10^{-4} mbar. The substrates used were (100) Si wafers, held at room temperature (RT) during deposition. The Cr-N layers were grown at a rate of $\sim$ 10 nm/min, to a total thickness of 240-280 nm.

After deposition the samples were implanted with 120 keV Ar ions, to the fluences of 1×10^{15} and 1×10^{16} ions/cm^2. During irradiation the samples were held at room temperature, the ion beam was scanned uniformly over an area of 2×2 cm^2, and the beam current was kept at $\sim$ 1 μA/cm^2. Calculations by TRIM (Ziegler 1985) gave a projected ion range of $R_p \sim 70$ nm and straggle $\Delta R_p \sim 30$ nm, meaning that practically all implanted ions were stopped within the layers.

Structural characterization of the samples was performed with Rutherford backscattering spectroscopy (RBS), transmission electron microscopy (TEM) and x-ray diffraction analysis (XRD). For RBS we used 900 keV He^{++} ion beam, with a detector positioned at 165° backscattering angle, at the IONAS ion accelerator in Goettingen (Uhrmacher 1995). We took random spectra at normal incidence and analysed the data with the WiNDF code (Barradas 1997). Cross-sectional TEM analysis was done on a Philips EM 400 microscope. Micro diffraction (MD) technique was used to study the crystalline structure of the samples. XRD analysis was done at normal and grazing incidence, with Cu K_α emission, using a Bruker D8 Advance Diffractometer.

3. RESULTS AND DISCUSSION

Generally, the results of RBS analysis showed that the Cr-N layer stoichiometry strongly depends on the nitrogen partial pressure during deposition. For the nitrogen partial pressures of 2×10^{-4}, 3.5×10^{4} and 5×10^{-4} mbar, the layers contain $\sim$ 26 at %, $\sim$ 38 at % and $\sim$ 48 at % of N, respectively. All as-deposited layers contain 1-2 at % of argon, which is incorporated during the deposition process.

Fig. 1 (a-c) shows the extracted depth profiles obtained from experimental RBS spectra of the samples deposited at nitrogen partial pressure of 2×10^{-4} mbar (a), 3.5×10^{-4} mbar (b) and 5×10^{-4} mbar (c). It can be seen that the Cr and N profiles are nearly flat, the layers containing a fraction of Ar which is distributed from the surface to the interface with Si. In (c) the concentration ratio suggests a stoichiometric CrN phase. Indeed, XRD analysis showed the dominating Cr_2N peaks in the first two cases, while in the latter case we only see peaks corresponding to CrN. Ion implantation adds an extra up to 2 at % of Ar around the projected range. The RBS spectra remain essentially the same, except for a small increase in the yield arising from the implanted argon. This suggests that ion irradiation does not induce any redistribution of components or intermixing at the Cr-N/Si interface.

TEM analysis revealed that the as-deposited layers grow in form of a polycrystalline columnar structure, with very fine crystalline grains. The column width is of the order of a few tens of nm. After ion irradiation the structure remains polycrystalline, despite the high implanted fluences, which could induce amorphisation. An example of cross-sectional TEM analysis is illustrated in Fig. 2. In all cases we present micrographs

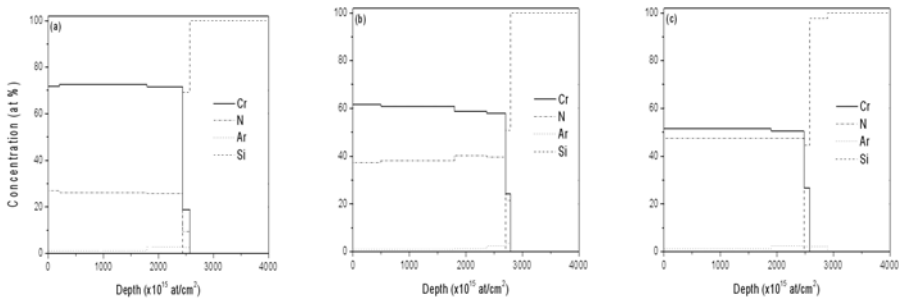

Figure 1: Extracted depth profiles from RBS analysis of as-deposited samples at nitrogen partial pressure of: (a) 2×10^{-4} mbar; (b) 3.5×10^{-4} mbar; (c) 5×10^{-4} mbar.

from the layers deposited at nitrogen partial pressure of 5×10^{4} mbar, when CrN is formed. Inset in the micrographs are the corresponding MD patterns taken from the layers using a beam spot that covers a sample area of $\sim$ 50 nm in diameter.

Bright field image in (a) is from an as-deposited sample, showing individual columns stretching to the surface, and the MD pattern indicates a very fine polycrystalline structure. Micrographs shown in (b) and (c) are from the sample implanted to 1×10^{15} ions/cm^2. Bright field image in (b) shows that the initial columns formed in as-deposited layers become broken after ion implantation. Besides that, the polycrystalline structure is retained, the MD pattern indicating slightly larger grains. Dark field image in (c) shows a presence of nano-particles of the same phase, which are either isolated or imbedded in larger grains.

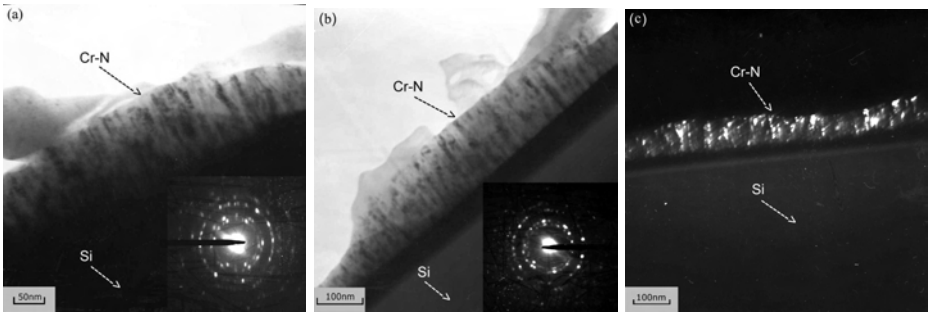

Figure 2: TEM analysis of samples deposited at nitrogen partial pressure of 5×10^{-4} mbar: (a) bright field image of as-deposited; (b) bright field image of implanted to 1×10^{15} Ar/cm^2; (c) dark field image of implanted to 1×10^{16} Ar/cm^2.

4. CONCLUSION

Composition and the phases grown in the investigated Cr-N films strongly depend on the nitrogen partial pressure during deposition. At the two lower pressures of 2×10^{-4} and 3.5×10^{4} mbar the grown phase is Cr_2N, while the highest pressure of 5×10^{-4} mbar yields the formation of stoichiometric CrN phase. The layers grow in form of a columnar structure. The column width is of the order of a few tens of nm.

Ion irradiation induces only local atomic rearrangements. The applied fluences were above the amorphisation level for the system, but the displaced Cr and N atomic species had sufficient mobility to recombine in a crystalline structure. The resulting effects are induced point defects in larger grains and nucleation of imbedded nanoparticles of the same phase.

Acknowledgments

This work was supported by the Ministry of Science and Environmental Protection of the Republic of Serbia (Project No. OI 141013).

References

Barradas, N. P., Jeynes, C., Webb, R. P.: 1997, *Applied Physics Letters*, **71**, 291.
Komiya, S., Ono, S., Umezu, N.: 1977, *Thin Solid Films*, **45**, 433.
Nouveau, C., Djouadi, M. A., Banakh, O., Sanjinés, R., Lévy, F.: 2001, *Thin Solid Films*, **398**, 490.
Sharkeev, Y. P., Bull, S. J., Perry, A. J., Klingenberg, M. L., Fortuna, S. V., Michler, M., Manory, R. R., Shulepov, I. A.: 2006, *Surface and Coatings Tehnology*, **200**, 5915.
Uhrmacher, M., Pampus, K., Bergmeister, F. J., Purschke, D. and Lieb, K.-P.: 1995, *Nuclear Instruments and Methods* B, **9**, 234.
Vishnyakov, V. M., Bachurin, V. I., Minnebaev, K. F., Valizadeh, R., Teer, D. G., Colligon, J. S., Vishnyakov, V. V., Yurasova, V. E.: 2006, *Thin Solid Films*, **497**, 189.
Wiklund, U., Bromark, M., Larsson, M., Hedenqvist, P., Hogmark, S.: 1997, *Surface and Coatings Tehnology*, **91**, 57.
Ziegler, J. F., Biersack, J. P., Littmark, U.: 1985, The Stopping and Range of Ions in Solids, Pergamon, New York.

Publ. Astron. Obs. Belgrade No. 84 (2008), 205 - 2008 *Contributed Paper*

ION BEAM MODIFICATION OF REACTIVELY SPUTTERED TiN THIN FILMS

M. POPOVIĆ, M. NOVAKOVIĆ, M. MILOSAVLJEVIĆ, D. PERUŠKO,
V. MILINOVIĆ, I. RADOVIĆ and N. BIBIĆ
VINČA Institute of Nuclear Sciences, Belgrade 11001, POBox 522, Serbia

Abstract. A study of ion beam modification of structural and electrical properties of TiN thin films is presented. The layers were deposited by reactive ion sputtering on (100) Si substrates to a thickness of $\sim$ 240 nm. After deposition the structures were implanted with argon ions at 120 keV, to the fluences from 1×10^{15} – 1×10^{16} ions/cm^2. Structural analysis of the samples was performed by cross-sectional transmission electron microscopy, x-ray diffraction and Rutherford backscattering spectrometry. It was found that the as-deposited layers have a columnar structure, individual columns stretching from the substrate to the surface and being a few tens of nanometers wide. Ion irradiation rearranges their crystalline structure, which remains polycrystalline, but the columns are broken, and nanocrystals of the same phase are formed.

1. INTRODUCTION

TiN thin films have been widely used due to their high hardness, high wear resistance, low electrical resistivity, good chemical stability (Chang et al. 2004, Ma et al. 2006). TiN layers are applied as hard and protective coatings for mechanical tools and wear parts, diffusion barriers in microelectronic industry, decorative coatings. In recant years, investigations have turned towards more complex nitride compounds, multi-layered films and also the modification of films by ion implantation (Lim et al. 2003, Oda et al. 1997). Ion irradiation is a powerful tool to modify a thin film structure by a series of collision cascades induced by the impact ions.

In this work we investigate the effects of microstructural changes in TiN films induced by ion implantation. TiN layers were deposited by reactive ion sputtering on (100) Si wafers and subsequently irradiated with 120 keV Ar ions. It was found that ion irradiation induces local micro-structural changes.

2. EXPERIMENTAL PROCEDURE

Titanium-nitride thin films have been prepared on (100) Si substrates by reactive ion sputtering in a Balzers Sputtron II system. Titanium target (99.9% purity) was sputtered with argon ions in a nitrogen ambient. The base pressure in the chamber was in the low 10^{-6} mbar region, partial pressure of argon was 1×10^{-3} mbar, and partial pressure of nitrogen was 3×10^{-4} mbar. During deposition the substrates were

held at room temperature (RT). We first deposited a ∼10 nm of pure Ti buffer layer, to increase adhesion to the substrate, which was followed by deposition of ∼230 nm TiN, at 8 nm/min. A total layer thickness of ∼240 nm was measured with a Taylor-Hobson profilometer, which gives an accuracy of ±2 nm in this range.

After deposition the samples were implanted with 120 keV Ar^+ ions, to the fluences of 1×10^{15} and 1×10^{16} ions/cm^2. During irradiation the samples were held at room temperature. Calculations by TRIM (Ziegler et al. 1985) gave a projected ion range of Rp ∼ 70 nm and straggle ΔRp ∼ 30 nm, meaning that practically all implanted ions were stopped within the layers. SUSPRE (Webb 1991) gave an estimate that the applied ion fluences were above the amorphisation threshold for the system.

Structural characterization of the samples was performed with Rutherford backscattering spectrometry (RBS), transmission electron microscopy (TEM) and x-ray diffraction analysis (XRD). For RBS analysis we used 900 keV He^{++} ion beam, with a detector positioned at 165° backscattering angle. We took random spectra at normal incidence and analysed the data with the Data Furnace code (Barradas et al 1997). Cross-sectional TEM analysis was done on a Philips EM 400 microscope, and we also used micro diffraction (MD) technique to study the crystalline structure. XRD analysis was done at grazing incidence of 3°, with Cu Kα emission, using a Bruker D8 Advance Diffractometer.

3. RESULTS AND DISCUSSION

Figure 1 (a-b) displays the RBS spectrum and corresponding calculated depth profiles for an as-deposited TiN layers. The experimental data could be fitted well by introducing Ti, N, Ar and Si in the Data Furnace structure file, as seen in (a). Here we also plotted separated elemental spectrum obtained from the fit. The analysis shows that argon is incorporated in the films during deposition. The extracted depth profiles (b) show a nearly uniform TiN layer stoichiometry, and 1-2 at % of Ar throughout the layer thickness. Towards the Si substrate we register an increased Ti yield, which corresponds to the thin buffer layer. RBS spectra taken from the implanted samples, are similar to the one given in Fig. 1. Ion implantation adds an extra up to 2 at % of Ar around the projected range for the higher fluence. The spectra remain essentially the same, except for a small increase in the yield that arises due to the implanted argon. RBS analysis suggests that ion irradiation does not induce any redistribution of components or intermixing at the layer/substrate interface.

TEM analysis revealed that the as-deposited layers grow in form of a polycrystalline columnar structure, with very fine crystalline grains. After ion irradiation the structure remains polycrystalline, despite the high implanted fluences, which could induce amorphisation. An example of cross-sectional TEM analysis is illustrated in Fig. 2.

The micrographs and the corresponding MD patterns were taken from an as-deposited layer (a), and from a layer implanted to 1×10^{16} ions/cm^2 (b). Bright field image in (a) shows individual columns that stretch from the substrate to the surface, and the MD pattern indicates a very fine polycrystalline structure. Micrograph in (b) shows that the polycrystalline structure of the layer is retained after ion implantation. However, the columns appear as partly broken or disconnected, and we observe randomly distributed sharp contrasts arising from nano-sized crystal grains. The corresponding MD pattern indicates a slightly finer grain structure. Compared

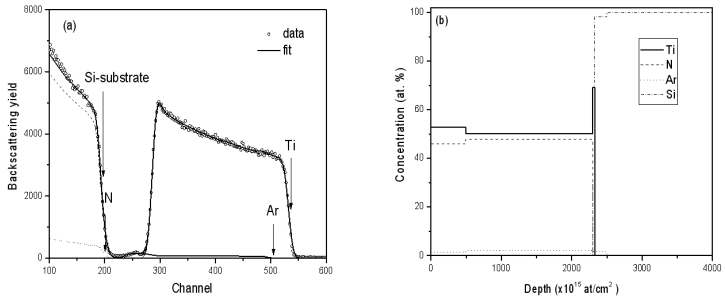

Figure 1: RBS analysis of an as-deposited sample: a) experimenta and fitted data, b) extracted depth profiles.

to the pattern shown in (a) we observe a larger number of smaller spots lying on the circles around the central spot, indicating a higher number of randomly oriented smaller grains.

The results of XRD analysis of as-deposited TiN sample, and after irradiation to 1×10^{15} and 1×10^{16} ions/cm^2, are shown in Fig. 3. We can observe a change of TiN diffraction line intensities after ion irradiation. After irradiation at the lower fluence the intensity of (111) line drops, while the intensity of (200) and (220) lines increases, suggesting a partial texturing of the layer. With further increase of the irradiation fluence the relative ratio of the diffraction line intensities remains roughly the same, but their height decreases, indicating that the mean grain size in the layers decreases.

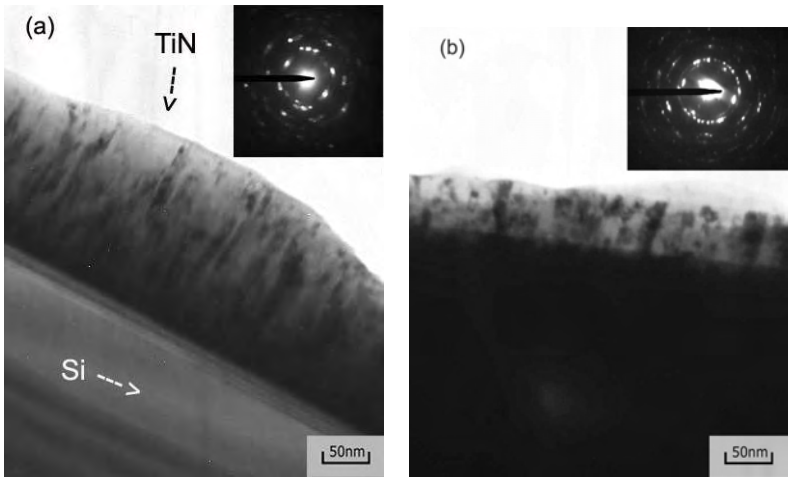

Figure 2: TEM analysis of samples: a) bright field image of as-deposited, b) bright field image of implanted to 1×10^{16} Ar/cm^2.

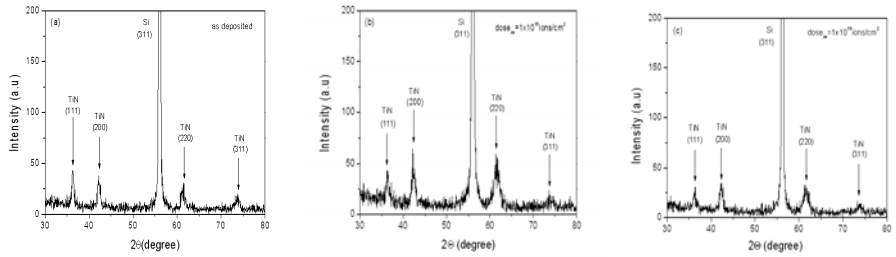

Figure 3: XRD analysis of TiN/Si samples: a) as-deposited, b) after ion irradiation to 1×10^{15} Ar/cm^2, c) after ion irradiation to 1×10^{16} Ar/cm^2.

4. CONCLUSION

We have studied the effects of Ar ion irradiation on the micro-structure of TiN films. The as-deposited layers have a columnar structure, with the mean column width of the order of a few tens of nm. Ion irradiation rearranges their crystalline structure, breaks up the columns, and induces growth of nanocrystals of the same phase.

Acknowledgements

This work was supported by the Ministry of Science and Environmental Protection of the Republic of Serbia (Project No OI 141013).

References

Barradas, N. P., Jeynes, C., Webb, R. P.: 1997, *Applied Physics Letters*, **71**, 291.
Chang, Y.-Y., Wang, D.-Y., Wu, W. T.: 2004, *Surface and Coatings Technology*, **177-178**, 441.
Lim, D.-C., Chen, G. C., Lee, S.-B., Boo, J.-H.: 2003, *Surface and Coatings Technology*, **163-164**, 318.
Ma, C.-H., Huang, J.-H., Chen, H.: 2006, *Surface and Coatings Technology*, **200**, 3868.
Oda, K., Nakayama, A., Ohara, H., Kitagawa, N., Nomura, T.: 1997, *Nuclear Instruments and Methods B*, **121**, 283.
Webb, R. P.: 1991, "Computer Codes and Simulation Background to Ion Implantation Distribution and Sputtering Programs", Appendix 3 from "practical Surface Analysis Vol. 3" eds. M. Seah and D. Briggs, Wiley 1991;
http://www.ee.surrey.ac.uk/SCRIBA/simulations/Suspre/.
Ziegler, J. F., Biersack, J. P., Littmark, U.: 1985, The Stopping and Range of Ions in Solids, Pergamon, New York.

Publ. Astron. Obs. Belgrade No. 84 (2008), 209 - 213 *Contributed Paper*

SPUTTERING OF Si(001) AND SiC(001) BY GRAZING ION BOMBARDMENT

A. A. ELMONOV[1], M. S. YUSUPOV[1], A. A. DZHURAKHALOV[1] and A. BOGAERTS[2]

[1] *Theoretical Dept., Arifov Institute of Electronics, F. Khodjaev Street 33, 100125 Tashkent, Uzbekistan*
E–mail: aelmonov@mail.ru

[2] *Department of Chemistry, University of Antwerp, Universiteitsplein 1, B-2610 Wilrijk-Antwerp, Belgium*
E–mail: annemie.bogaerts@ua.ac.be

Abstract. The peculiarities of sputtering processes at 0.5-5 keV Ne grazing ion bombardment of Si(001) and SiC(001) surfaces and their possible application for the surface modification have been studied by computer simulation. Sputtering yields in the primary knock-on recoil atoms regime versus the initial energy of incident ions (E_0 = 0.5-5 keV) and angle of incidence (ψ = 0-30°) counted from a target surface have been calculated. Comparative studies of layer-by-layer sputtering for Si(001) and SiC(001) surfaces versus the initial energy of incident ions as well as an effective sputtering and sputtering threshold are discussed.

1. INTRODUCTION

The sputtering process has been the subject of both scientific investigations for a long time and recent rapid developing micro- and nanotechnologies. Processes such as plasma etching and sputter deposition that involve ion bombardment at relatively low ($\sim$ 100 eV) ion energies are widely used in semiconductor processing (Labanda et al. 1997). However, using glancing-angle ion bombardment for surface modification rather than conventional near-normal incidence ions allows expanding the energy range up to $\sim$ 10 keV and has the advantages of reducing damage (such as crater formation) and preferentially removing surface asperities (Dzhurakhalov, 2004) leading to flat surfaces.

Si and SiC crystals have a great importance because of their use in semiconductor technologies. Especially, silicon carbide exhibits a large band gap, a higher breakdown field, a higher thermal conductivity, and a higher saturation velocity, compared to widely used silicon. Besides, SiC is a promising shielding material in nuclear fusion systems such as limiters in Tokamak devices, where the surface erosion is also important (Roth et al. 1976, Bischoff et al. 2001).

In (Kim et al. 2003) atomically clean and flat Si(100) surfaces suitable for nanoscale device fabrication were prepared by wet-chemical etching followed by 0.3–1.5 keV Ar ion sputtering. It was found that wet-chemical etching alone cannot produce a clean

and flat Si(100) surface which can be achieved by subsequent 300 eV Ar ion sputtering at room temperature followed by a 700 °C annealing.

Sputtering yields of crystalline silicon carbide and silicon have been experimentally determined and results have been compared with Monte Carlo simulations for Ne^+, Ar^+ and Xe^+ ion bombardment in the energy range of 0.5-5 keV under 60° sputtering with respect to the surface normal (Ecke et al. 2002). The simulation results depend strongly on the input parameters which are not well known especially for SiC. The TRIM simulation fits the experimental results very well.

The evolution of surface morphology during ion beam erosion of Si(111) at 500 eV Ar^+ ion bombardment (60° from normal, 0.75 mA/cm2 collimated beam current) was studied over a temperature range of 500-730 °C (Brown et al. 2004). Keeping ion flux, incident angle, and energy fixed, it was found that one-dimensional sputter ripples with wavevector oriented perpendicular to the projected ion beam direction form during sputtering at the lower end of the temperature range. For temperatures above approximately 690 °C, growth modes both parallel and perpendicular to the projected ion beam direction contribute to the surface morphological evolution.

Thus, recently sputtering and surface modifications of Si and SiC single crystals are widely studied although there are not sufficient data in the case of grazing incidence. In the present paper, grazing ion sputtering processes of Si(001) and SiC(001) surfaces at 0.5-5 keV Ne^+ bombardment have been studied by computer simulation.

2. COMPUTER SIMULATION TECHNIQUES

The theoretical investigation of atomic collision processes in crystals caused by ion irradiation is more and more done using computer simulation because real physical conditions (e.g. complicated interatomic interaction potential, surfaces, interfaces, defects) can be taken into account much easier than it is possible by using analytical methods (see e.g. Gtirtner et al. 1995).

The simulation used in our calculations to construct the trajectories of the ions or projectile scattered by target atoms is based on the binary collision approximation (see e.g. Parilis et al. 1993) with two main assumptions: (1) only binary collisions of ions with target atoms or between two target atoms are considered; and (2) the path which a projectile goes between collisions is represented by straight-line segments. For the description of the particle interactions the repulsive Ziegler-Biersack-Littmark potential (O'Connor et al. 1986) was used. The inelastic energy losses were regarded as local depending on the impact parameter and included into the scattering kinematics.

Sputtering has been simulated in the primary knock-on regime. Only the primary knock-on recoil atoms ejected from first, second and third layers have been considered. The presence of planar potential energy barrier on the surface was taken into account. The number of incident ions is $4x10^4$. Each new particle is incident on a reset, pure surface. The incident ions and the recoil atoms were followed throughout their slowing-down process until their energy falls below a predetermined energy: 25 eV was used for the incident ions, and the surface binding energy was used for the knock-on atoms. The calculations were performed on the crystals comprising up to 120 atomic layers. The initial energy of incident ions was varied from 0.5 to 5 keV, an angle of incidence ψ counted from target the surface was 0-30° and an azimuth angle of incidence ξ realized by rotating the target around its normal and counted from the $< 100 >$ direction was 0-180°.

3. RESULTS AND DISCUSSION

In Fig. 1a,b the angular dependences of the sputtering yield for Si(001) and SiC(001) surfaces are compared at three values of incident Ne^+ ion energy. Note, the angle of incidence is counted from the surface. It is seen that there is a threshold angle of sputtering in all dependences. At angles of incidence less than the threshold angle the incident ions can not penetrate into the crystal and can not eject target atoms. The threshold angle shifts to the lower values of angle of incidence with increasing the energy of incident ions. The same effect is seen for the main peak of the sputtering yield which increases drastically at first at not too low initial energies and afterwards decreases slowly with increasing angle of incidence. This decreasing is explained by penetration of incident ions to deeper layers at large angles. At low initial energies there is a plateau (shorter for Si and wider for SiC) near the threshold angle because of insufficient ion energy for both a long moving the ions within surface semichannels and their penetration to deeper layers. It is seen that the threshold angle is a bit smaller in the case of Si than for SiC. Besides, in general the sputtering yield is large in the case of SiC. These dependences allow choosing an angle of incidence for an effective sputtering at given initial energy.

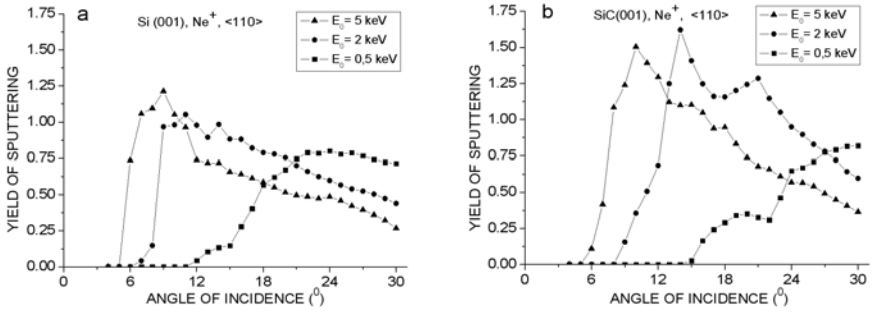

Figure 1: Sputtering yield of Si(001) (a) and SiC(001) (b) versus angle of incidence at Ne^+ ion bombardment.

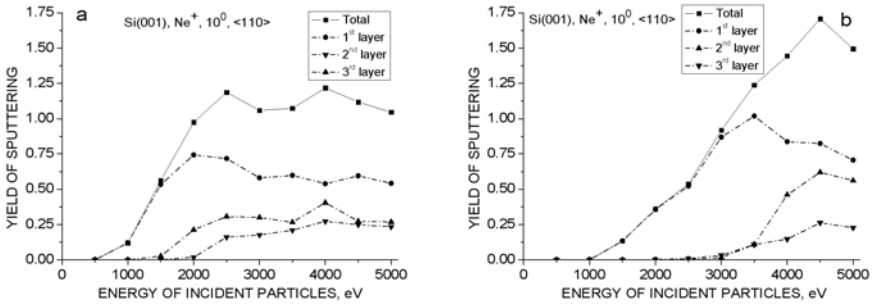

Figure 2: Sputtering yield of Si(001) (a) and SiC(001) (b) versus energy of incident Ne^+ ions at ψ=10°.

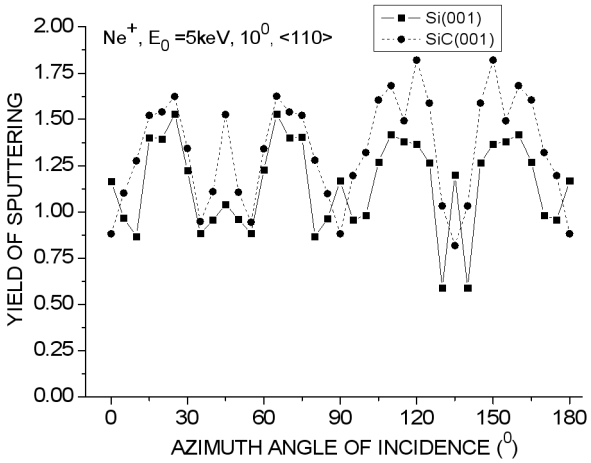

Figure 3: Sputtering yield of Si(001) and SiC(001) versus azimuth angle of incidence at E_0 =5 keV, ψ=10°.

In Fig. 2a,b the sputtering yields of Si(001) and SiC(001) surfaces subdivided into sputtering by the first three surface layers versus the energy of incident Ne^+ ions are shown at $\psi = 10°$. The threshold energy of sputtering is about 1 keV for these cases. There is more drastic increase of sputtering yield in the beginning of dependences for Si than for SiC. It is seen that the main contribution to the total sputtering comes from the sputtering of the first layer. Besides, in the energy range of 1-1.5 keV for Si and 1-3 keV for SiC, sputtering occurs only from the first layer. Further increasing the ion energy results in increasing the contribution from second and third layers. The contribution to sputtering from the third layer is larger than the one from the second layer as the atomic rows in the second layer lies directly under the one of the first layer in the $< 110 >$ direction. Two local maxima at 2.5 and 4 keV are observed in the total sputtering yield dependence in the case of Si. Sputtering from the first layer gives a basic contribution to the first maximum while the second maximum is formed by atoms ejected from the second and third layers. In the case of SiC the maximum of total dependence is formed by atoms ejected from the second layer. These results show that by choosing an angle and an energy of incidence one can produce layer-by-layer sputtering of Si(001) and SiC(001) surfaces.

In Fig. 3 the azimuthal angular dependences of the sputtering yield are compared for Si(001) and SiC(001) surfaces at 5 keV Ne^+ ion bombardment, ψ=10°. Main maxima and minima of dependences are observed in low crystallographic directions and near them. They are caused by the existence of original semichannels and channels in these directions. Thus, there is a good correlation between the sputtering yield dependences and crystallographic structures of studied crystals. From the comparison of the two curves it is seen that at some values of azimuth angle, instead of the peaks of sputtering yield of Si(001) the minima of sputtering yield of SiC(001) are observed. This difference is caused by differences of binding energies, lattice parameters and, of

course, compositions of these single crystals. In most range of the azimuth angle of incidence the sputtering yield for SiC is larger than the one for Si.

4. CONCLUSION

Sputtering yields of Si(001) and SiC(001) surfaces versus the initial energy of incident ions (E_0 = 0.5-5 keV), angle of incidence (ψ = 0-30°) and azimuth angle of incidence (ξ = 0-180°) have been calculated at Ne ion bombardment. It was shown that effective and layer-by-layer sputtering are possible near threshold angle and energy sputtering.

Parameters of single crystals (lattice parameter, binding energy and mass of atoms) influence significantly the angular and energy dependences of sputtering yield. In general, the sputtering yield of the SiC(001) surface is larger than the one of the Si(001) surface.

References

Bischoff, L., Teichert, J., Heera, V.: 2001, *Appl. Surf. Sci.*, **184**, 372.

Brown, A., George, H. B., Aziz, M. J., Erlebacher, J.: 2004, *Mat. Res. Soc. Symp. Proc.*, **792**, R7.8.1.

Dzhurakhalov, A. A.: 2004, *Nucl. Instr. and Meth. in Phys. Res.*, **B216**, 202.

Ecke, G., Kosiba, R., Kharlamov, V., Trushin, Yu., Pezoldt J.: 2002, *Nucl. Instr. and Meth. in Phys. Res.*, **B196**, 39.

Gtirtner, K., Stock, D., Weber, B., Betz, G., Hautala, M., Hobler, G., Hou, M., Sarite, S., Eckstein, W., Jimknez-Rodriguez, J. J., Perez-Martin, A. M. C., Andribet, E. P., Konoplev, V., Gras-Marti, A., Posselt, M., Shapiro, M. H., Tombrello, T. A., Urbassek, H. M., Hensel, H., Yamamura, Y., Takeuchi, W.: 1995, *Nucl. Instr. and Meth. in Phys. Res.*, **B102**, 183.

Kim, J. C., Ji, J.-Y., Kline, J.S., Tucker, J.R., Shen, T.-C.: 2003, *Appl. Surf. Sci.*, **220**, 293.

Labanda, J. G. C., Barnett, S. A.: Sep 1997, *J. Electronic Mater.*

O'Connor, D. J., Biersack, J. P.: 1986, *Nucl. Instr. and Meth. in Phys. Res.*, **B15**, 14.

Parilis, E. S., Kishinevsky, L. M., Turaev, N. Yu., Baklitzky, B. E., Umarov, F. F., Verlrger, V. Kh., Nizhnaya, S. L., Bitensky, I. S.: 1993, Atomic collisions on Solid Surfaces, North-Holland, Amsterdam.

Roth, J., Bohdansky, J., Poschenrieder, W., Sinha, M. K.: 1976, *J. Nucl. Mater.*, **63**, 222.

Publ. Astron. Obs. Belgrade No. 84 (2008), 215 - 218 *Contributed Paper*

A NEW TECHNIQUE OF SOLID MATERIAL SAMPLING FOR ANALYTICAL ATOMIC SPECTROMETRY WITH INDUCTIVELY COUPLED PLASMA

M. V. BELKOV, V. S. BURAKOV, V. V. KIRIS and S. N. RAIKOV
Stepanov Institute of Physics, 220072 Minsk, Belarus
E–mail: raikov@imaph.bas-net.by

Abstract. A new rapid method of direct spectrochemical analysis of solid-state materials is proposed on the basis of a tandem technique of pulsed laser ablation of a sample in deionised water with on-line transportation of a suspension of nanoparticles in analytical volume of inductively-coupled plasma of optical emission spectrometer. In result, all instrumentation and methodical advantages of the standard equipment in combination with calibration procedure by standard aqueous solutions are provided.

1. INTRODUCTION

Such widespread and well-known technique as optical emission spectroscopy with inductively coupled plasma (OES-ICP) has the routine application at the analysis of liquid samples. The simplest way of the analysis of solid-state materials is based on a direct dissolution of an analyzed sample or its fragment. Unfortunately, often this approach requires additional time and expenditures of labour, frequently significant, uses a sealed pressure vessels for holding strong mineral acids or alkalis at temperatures well above normal boiling points, does not allow carrying out microanalysis of analyzed samples.

For the analysis of solid and especially powder materials without their dissolution there are various variants of their direct input in analytical volume of ICP or preliminary evaporation in electrothermal atomizer with the subsequent transportation to analytical volume of ICP. OES with a sample atomization in ICP combined with preliminary laser ablation (LA) of a solid sample in a carrier gas (LA-ICP-OES) is at present the most conventional and suitable direct method for the elemental spectrochemical microanalysis of any solids with minimum or no sample preparation as well as of materials that are difficult to dissolve. Nevertheless, this high-sensitive technique is till now very limited by the availability of solid-state certificated reference materials with necessary matrixes and chemical elements.

There are successful attempts to realize really calibration-free laser-induced breakdown spectroscopy (LIBS) (see e.g. Burakov et al. 2007). However, it is true that the LIBS technique, having some important advantages, still suffers from relatively poor sensitivity with respect to more standard technique such as OES-ICP (see e.g.

Fichet et al. 2006). The detection limits of LIBS are about 3-4 orders of magnitude higher compared with those of OES-ICP even when double-pulse lasers are used in LIBS for sample ablation.

To replace calibration procedure with the help of the solid-state reference materials by the standard aqueous solutions spark ablation of conducting metallic samples in deionised water was offered originally for atomic absorption with thermal atomization (see e.g. Ghiglione et al. 1976), and subsequently for OES-ICP (see e.g. Aziz et al. 1984). However, such approach has a number of restrictions, therefore, in analytical practice it is not used except for not numerous research works.

We have realized the tandem technique of a direct laser sampling of any solid material in deionised water with on-line analysis of prepared by such way aqueous solution with the help of conventional OES-ICP. Such approach makes it possible to achieve a combination of all advantages of LA-ICP-OES with routine calibration by standard reference aqueous solutions usually available for any element of interest. On the other hand, laser ablation of a solid material in a liquid medium (see e.g. Iida et al. 1991) is at present a well established technique for nanoparticle production for various purposes. Generally speaking, the main problem in the described approach consists in revealing and discrimination of possible specific features of evaporation and atomization in ICP of such specific solutions (suspensions) containing nanoparticles in comparison with the real aqueous solutions.

2. EXPERIMENTAL

The instrumentation employed in our work is at present quite standard and maximally suitable for a routine practice (Fig. 1).

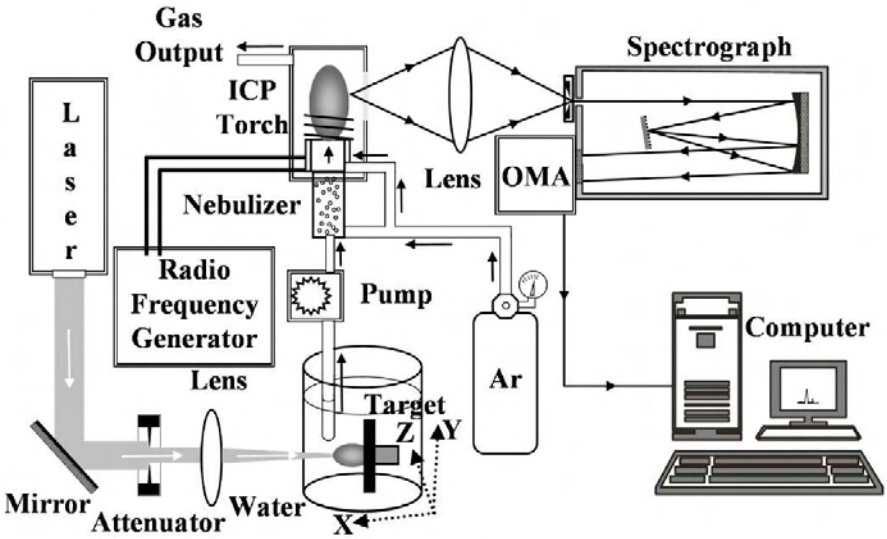

Figure 1: Schematic outline of OES-ICP with LA of a solid in a liquid.

The fundamental (1.06 μm) in the most cases or the second harmonic (0.53 μm) of a nanosecond Q-switched Nd:YAG laser (LS-2134 U, Lotis, Belarus) with a pulse duration of 6-8 ns (depending on wavelength and energy) and 10-Hz pulse repetition rate is employed for ablation of solids immersed in a cell with deionised water. The laser used is an improved version with variable reflectivity mirrors (VRM). This model provides high stability of the emitted radiation. The VRM resonator gives excellent harmonic conversion efficiency due to an increased spatial uniformity of the output beam, a low divergence and a short pulse duration. The laser beam, with an aperture of $\leq$ 6 mm and a beam divergence of $\leq$ 0.8 mrad, is sharply focused on the sample surface by a 50 mm focal length plano-convex quartz lens. The laser spot diameter on a target surface is about 50 μm. A sample is fixed at a X, Y, Z translation holder, which enables precise adjustment of focusing on sample surface. The laser pulse energy can be varied from 10 to 270 mJ with an energy stability of $\pm$ 3%. Thorough optimization of laser output parameters, mainly pulse power density on a target surface and a number of pulses (usually 50) were carried out at the microanalysis of bronze, glass and gold reference samples with known compositions. Comparatively small amounts of prepared aqueous suspensions (usually 10-15 cm^3) were on-line (to avoid possible nanoparticle agglomeration) analyzed by OES-ICP (IRIS Intrepid II, Thermo-Electron) in accordance with a conventional reliably fulfilled procedure of analysis of liquid samples and calibration by aqueous standards.

3. RESULTS AND DISCUSSION

Fig. 2 shows the TEM images (LEO 906E) of the trapped products of LA of a glass sample in a water.

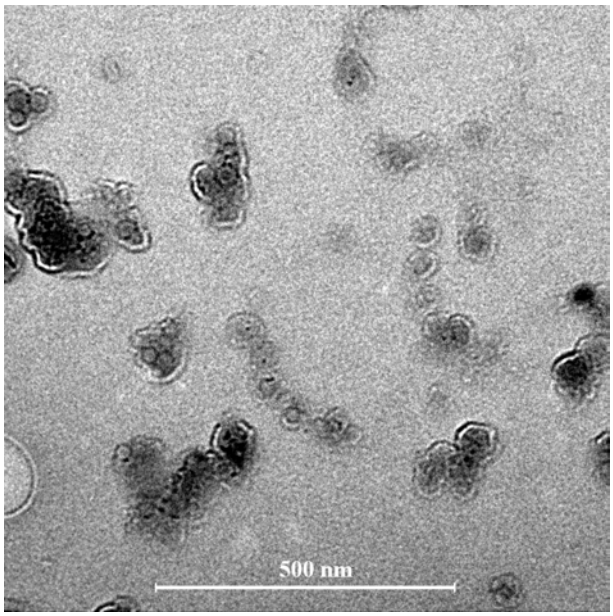

Figure 2: TEM photograph of nanoparticles produced by LA in deionised water.

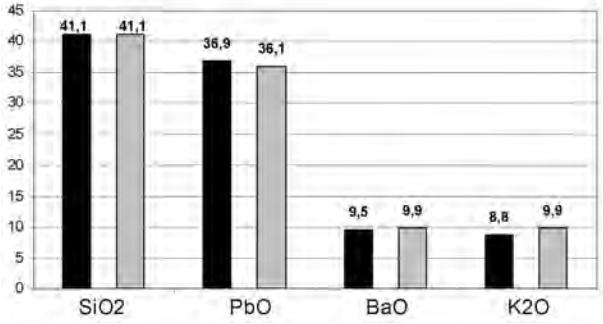

Figure 3: Composition of glass, % (black – reference data; grey – measured data).

As a whole, the satisfactory quantitative conformity of measured and reference data for all analyzed materials (bronze, glass and gold reference samples) has been received. Nevertheless, the further detailed optimization of ablation procedure, in particular, wavelengths of laser radiation, power density on a target surface, focusing conditions number of laser shots is necessary.

The results obtained have confirmed the suitability of the proposed approach and have proved its potential for the rapid, direct and sensitive microanalysis of any solid-state materials with minimum sample consumption and without solid-state certificated reference materials. All instrumentation and methodical advantages of the LA-ICP-OES standard equipment in combination with calibration procedure by standard aqueous solutions are provided.

In the practical case of impossibility to combine both techniques (LA and OES-ICP) in on-line apparatus it will be necessary to study and optimize the time delay between both procedures to discriminate influence of a possible nanoparticle agglomeration on the reproducibility of quantitative data or to take this phenomenon into account.

References

Aziz, A., Broekaert, J. A. C., Laqua, K., Leis, F.: 1984, *Spectrochim. Acta, Part B*, **39**, 1091.

Burakov, V. S., Raikov, S. N.: 2007, *Spectrochim. Acta, Part B*, **62**, 217.

Fichet, P., Tabarant, M., Salle, B., Gautier, C.: 2006, *Anal. Bioanal. Chem.*, **385**, 338.

Ghiglione, M., Eljuri, E., Cuevas, C.: 1976, *Appl. Spectrosc.*, **30**, 320.

Iida, Y., Tsuge, A., Uwamino, Y., Morikawa, H., Ishizuka, T.: 1991, *J. Anal. At. Spectrom.*, **6**, 541.

Publ. Astron. Obs. Belgrade No. 84 (2008), 219 - 222 *Contributed Paper*

LIGHT SCATTERING MEASUREMENT OF THE GAS BUBBLE DYNAMICS

V. LAZIĆ[1], S. JOVIĆEVIĆ[2], R. FANTONI[1], F. COLAO[1]
[1]*ENEA, FIS-LAS, V.E.Fermi 45. Frascati(RM), Italy*
E–mail: lazic@frascati.enea.it
[2]*Institute of Physics, 11080 Belgrade, P.O.Box 68, Serbia*
E–mail: jovicevic@phy.bg.ac.yu

Abstract. In order to optimize the LIBS signal from bulk waters, laser pulse energies were varied through changing of the QS trigger delays. It was noted that at mid pulse energies the LIBS signal had a tenfold enhancement. In order to explain such a phenomenon the dynamics of the gas bubble generated after the first laser pulse was studied through measurements of the HeNe laser light scattered on the bubble.

1. INTRODUCTION

One of the factors to take into consideration for double pulse LIBS applied on bulk liquids or immersed samples is the timing between the pulses. The maximum LIBS signal can be obtained if the second pulse hits the sample when the gas bubble produced by the first pulse reaches its expansion maximum, (Casavola et al. 2005).

Dynamic of the laser generated bubbles in liquids was mainly studied for laser medical applications (see Vogel et al. 1999 and therein cited papers) with the aim to avoid an excessive tissue damage, and also in the attempt to obtain efficient tissue ablation or high efficiency of the shock-wave generation (laser lithotripsy). The time evolution and maximum radius of the laser-induced bubble in a certain liquid are strongly dependent on the experimental conditions (see Vogel et al. 1999 and therein cited papers), such as laser wavelength, pulse duration and numerical aperture after the focusing lens.

One of the methods for studying the gas bubble dynamic is laser scattering, (Holt, Crum, 1990 and Lentz et al. 1995). The laser-induced bubbles have diameter in order of $0.010 - 1\ mm$ (Kennedy et al. 1970) and the scattering of light in the visible can be described by Mie's theory (Holt, Crum, 1990 and Kerker 1969).

The final scope of here described research was to improve the sensitivity of LIBS technique applied on bulk liquids, also intended to employ for sub-glacial lake exploration. To this aim, the influence of the laser energy, divided in two or more nanosecond pulses, on underwater plasma emission was studied. Dynamics of the lateral gas bubble expansion after the first laser pulse was measured by light scattering techniques and for different laser pulse energies.

2. EXPERIMENT

The underwater plasma was produced by a Q-Switched (QS) Nd:YAG laser operated at 1064 nm, with maximum pulse energy of about 300 mJ and with repetition rate of 10 Hz. The QS trigger was externally controlled, thus to have a possibility to extract also two laser pulses during single lamp flashing. In such case, the separation between two laser bursts was typically varied between $50 - 100$ μs, which together with the first trigger delay, determines the energy partition between the two pulses. The triggering scheme and examples of pulse energy partitions are reported in our recent papers (Lazic et al. 2005).

2. 1. SCATTERING MEASUREMENTS

The gas bubble produced by the first laser pulse was illuminated by a 35 mW HeNe laser. The scattered signal was measured at 90^o using the same collection optics as for LIBS measurements or at 20^o in forward direction where the light was collected with a plano-convex lens, (Fig. 1). In both cases the full angle aperture for the scattered light collection was larger than 15^o in order to minimize angle dependent signal ripples characteristic for Mie scattering (Holt, Crum, 1990, Lentz et al 1995, and Kerker 1969).

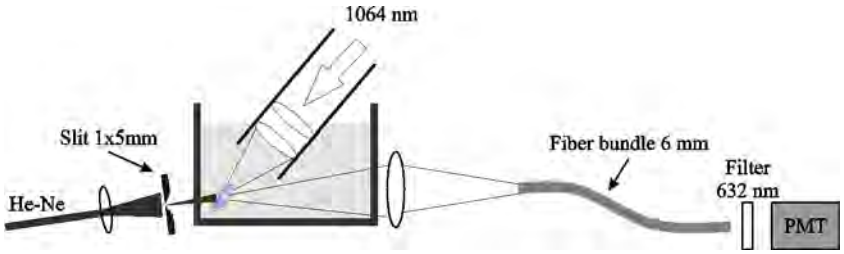

Figure 1: Experimental lay-out for forward scattering measurements.

The signal was brought to a photomultiplier (PMT) diameter fiber bundle. Between the fiber bundle exit and the PMT, an interferential filter centered at the HeNe laser emission was placed. The PMT used for the present experiment is a Hamamatsu R928. The high voltage power supply feeds a divider designed for high linearity; and the output anode is pre amplified and AC coupled with a Tektronix 2430A oscilloscope to record light transient. An additional gate circuit to electronically switch off the PMT gain during the time elapsing between consecutive laser shots was also used. Gated operation allowed us to use a CW laser, minimizing problems related with the high mean photon flux incident on the PMT cathode due to light scattering by hydrosols and particles suspended in water. However, this background scattering was always present and the PMT was operated at relatively low voltage (425 V) in order to avoid nonlinearities in its response.

Considering that the laser produced gas bubble might be elongated, in order to measure only its lateral expansion, a 1 mm high slit, with precisely adjustable vertical position, was placed in proximity to the optical window of the beaker wall. Position

of laser generated plasma and consequently the bubble center might depend on the laser pulse energy, (Kennedy et al. 1997). In order to keep the illumination constant across the bubble, a negative lens ($f = -50\ mm$) was placed before the slit, which horizontal width was restricted to 5 mm. The power distribution through the slit, scanned vertically in 3 mm range, was checked by a power-meter and resulted uniform within 5%. This range of the slit positions encloses both the bubble produced by low laser energy pulse (8 mJ) and the one produced at the maximum laser energy (300 mJ, single pulse).

The measurements of the bubble dynamics by the laser scattering technique were performed on tap water, whose standard impurities content was previously determined, (De Giacomo et al. 2005). In order to avoid disturbances from eventual nanoparticle formation, water in the beaker was exchanged each 30 minutes of the measurements. During water exchange, the focusing lens was always cleaned.

3. RESULTS AND DISCUSSION

In order to monitor only the lateral bubble expansion, which we consider more important for the LIBS signal after the arrival of the second laser pulse, the HeNe beam was sent through 1 mm high slit, moved with 1 mm step, and scattered signal was measured at different slit positions. At maximum laser energy here used (280 mJ) the signal could be observed for three slit positions (over 3 mm), while up to 170 mJ the signal is existent for only two slit positions. In all the cases, the same slit position gave the signal maximum and corresponding scattered light intensity as a function of time is depicted in Fig.2a.

The first, narrow peak, correspond to the laser pulse arrival, which produce the plasma continuum emission also in the spectral range transmitted by the interferential filter. In the same figure (2b), the scattering signal obtained without slit is also reported. Here, we could observe that the first bubble collapse occurs between 240 μs and 320 μs, followed by the first rebound. At the maximum energy, also the second and weak third rebounds were detected (Fig. 2b).

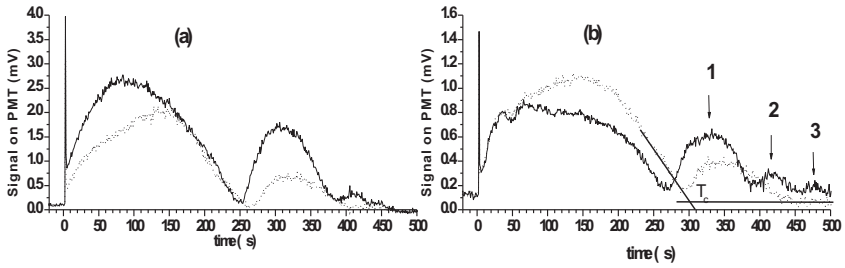

Figure 2: Signal from the light scattered at 90^o on the gas bubble produced by the laser with pulse energy 65 mJ (dots) and 280 mJ (solid): a) without slit; b) with slit; T_c is measured first collapse period at lower energy; 1-3 indicate the bubble rebounds at the higher laser energy.

The signal shape in presence of the slit is quite different from the one in the absence of the aperture. With the slit, the signal is more symmetrical, and the highest peak, as well as the longest first collapse period, is observed at a relatively low energy, thus indicating largest lateral bubble expansion.The intensity of the light scattered by the spherical bubble of radius R is proportional to R^2 for all scattering angles (Kerker 1969 and Barber, Putterman 1992). Consequently, the gas bubble diameter is proportional to the square root of the PMT voltage V (Barber, Putterman 1992). The maximum bubble radius achieved R_{max} is proportional to the first collapse period T_c through Rayleigh relation (Vogel et al. 1999). The first collapse period T_c was determined from the intersection of linearly fitted decaying signal on PMT and the final voltage level (see Fig. 2b) (Hubert et al. 1998). The maximum lateral bubble expansion corresponds to the laser energy of 65 mJ. Up to this energy, V_{max} value increases approximately linearly. After achieving the maximum, the gas bubble starts to elongate or to form in multiple sites as the breakdown threshold is reached also out of the focal volume. Therefore, a smaller part of the available optical energy is coupled to the mechanical energy (bubble expansion) in the focal point. The measured values of V_{max} and T_c are correlated with factor 0.91. The slightly different behaviour between these two parameters could be observed for the laser pulse energies between 65 mJ and 125 mJ, where probably an elongated bubble or multiple bubbles are formed inside the illuminated section, which corresponds to about 1.5 mm length along the laser axis.

From the results reported in this section, we might conclude that for the present focusing conditions, the optimal energy of the first laser pulse, used to prepare LIBS analyses by the second pulse, is about 65 mJ. Further increase of the first pulse energy leads to the LIBS signal deterioration due to the plasma elongation and reduced lateral bubble expansion.

References

Barber, B. P., Putterman, S. J.: 1992, *Phys. Rev. Letters*, **69**, 3839.
Casavola, A. et al.: 2005, *Spectrochim. Acta Part B*, **60**, 975.
De Giacomo, A. et al.: 2005, *Appl. Surf. Sci.*, **247**, 157.
Holt, R. G., Crum, L. A.: 1990, *Appl. Optics*, **29**, 4182.
Hubert, P. et al.: 1998, *Phys. Med. Biol.*, **43**, 3113.
Kennedy, P. K. et al.: 1997, *Prog. Quant. Electr.*, **21**, 155.
Kerker, M.: 1969, Academic Press, New York.
Lazic, V. et al.: 2005,*Spectrochim. Acta B*, **60**, 1002.
Lentz, W. J. et al.: 1995, *Appl. Opt.*, **34**, 2648.
Vogel, A. et al.: 1999, *Appl. Phys. B*, **68**, 271.

Publ. Astron. Obs. Belgrade No. 84 (2008), 223 - 226 *Contributed Paper*

FAST PHOTOGRAPHY OF PLASMA FORMED BY LASER ABLATION OF ALUMINUM

E. NEDANOVSKA[1,2], M. IVKOVIĆ[2]
[1]*Kodak European research, Cambridge, UK*
[2]*Institute of Physics, 11080 Belgrade, P.O.Box 68, Serbia*
E–mail: ivke@phy.bg.ac.yu

Abstract. In this paper we present results of the temporal and spatial analysis of laser induced plasma performed by use of ICCD fast photography. The plasma is formed by excimer laser ablation of aluminum target in vacuum, air or different pressures of argon and helium. It is shown how the plasma luminous intensity and duration depends on gas pressure. The obtained time dependence of wave propagation distance is also compared with predictions given by the blast wave and drag-force theory also.

1. INTRODUCTION

The study of plasmas obtained by laser ablation of different materials is of extreme importance in different areas of physics, starting from laser fusion to micro sampling for analytical investigations. Our attention is devoted to applications such as creation of nanocomposites by pulsed laser deposition or matrix assisted pulsed laser evaporation - MAPLE. In these processes the final product depends on properties of the laser (wavelength, energy density, pulse shape and duration, repetition rate, number of pulses), the target (material, rotation speed, angle etc.), the substrate (material, temperature, distance from target) and the surrounding atmosphere (air, vacuum or gas at different pressures) (Chrisey and Hubler 1994, Eason 2007). Among these properties, interaction with a background gas is probably the most important one, so here we demonstrate the use of ICCD fast photography for its study.

2. EXPERIMENT

Experimental setup is presented in Figure 1. The target was set in the center of the 30 cm diameter and 15 cm height, nonmagnetic stainless steel interaction chamber (1) that has eight equally spaced standard KF40 vacuum openings. The vacuum inside chamber ($\sim 10^{-6}$ mbar)was established through electromagnetic valve (2) by use of mechanical (4) and turbo molecular pump (3) and measured with Pirani (5) and ionization gauge (6). Argon or helium was introduced through a needle valve (7) and measured with MKS baratron gauge. As a radiation source an excimer, XeCl (308 nm) laser (8) with a maximum energy of 150 mJ, pulse duration 35 ns and

repetition rate of 50 Hz was used. The radiation was focused with a quartz lens (10) on the Al target under angle of 45 degree. In this way an energy density greater than 1 J/mm2 was obtained and plasma formed. The position of the target and ICCD camera (Andor DH734) (11) was adjusted using He-Ne laser (9). In order to obtain a more reliable data the target was mounted on a rotational vacuum feedthrough and rotated by use of a DC motor (12).

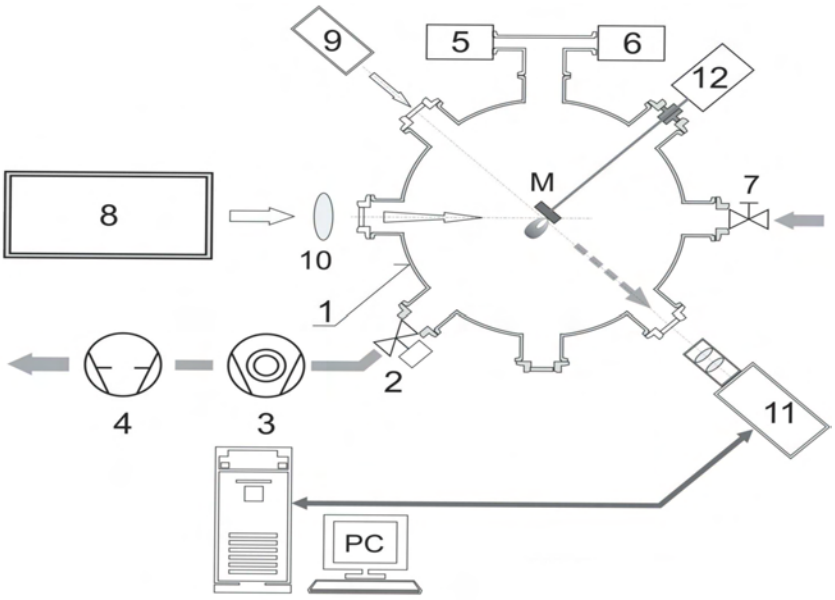

Figure 1: Experimental setup. (1) interaction chamber, (2) electromagnetic valve, (3) turbo molecular pump, (4) mechanical vacuum pump, (5) Piranni gauge, (6) ionization gauge, (7) needle valve, (8) excimer laser, (9) He-Ne laser, (10) quartz lens, (11) ICCD camera, (12) DC motor for target rotation.

3. RESULTS AND DISCUSSION

The ambient gas present during laser ablation scatters, attenuates and termalizes the plasma, which is clearly illustrated in Figure 2. as it can be seen that the luminous intensity decreases as the pressure increases. Also, it can be seen that the duration of the plasma formed in front of the target decreases as the gas pressure is increased.

The ambient gas also causes: a) sharpening of a plasma boundary, indicative for the shock front, b) slowing of the plasma relative to the propagation in vacuum, resulting in c) spatial confinement of the plasma, which can be seen in Figure 3. Also, from the Figure 3a (at 0 - 50 ns) it is visible that two (slow and fast) components of plasma appear. This effect was also detected earlier in laser ablated Al plasma by Tillack et al. 2003. The distance versus time, R = f (t), plots shows that from the linear dependence i.e. constant velocity in the first 50 ns, the plasma slow down. This behavior can be theoretically described by the:

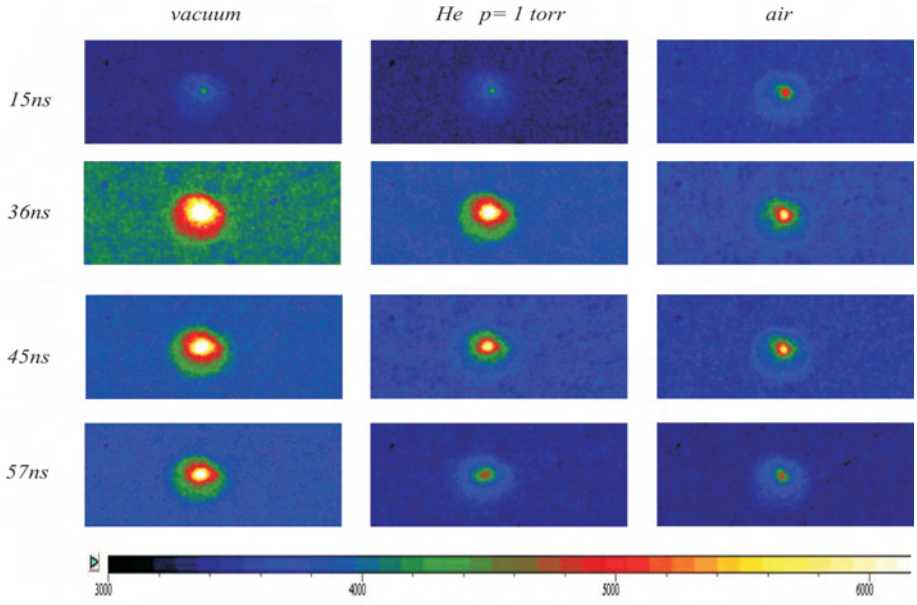

Figure 2: The fast photographs of Al plasma in different background gases.

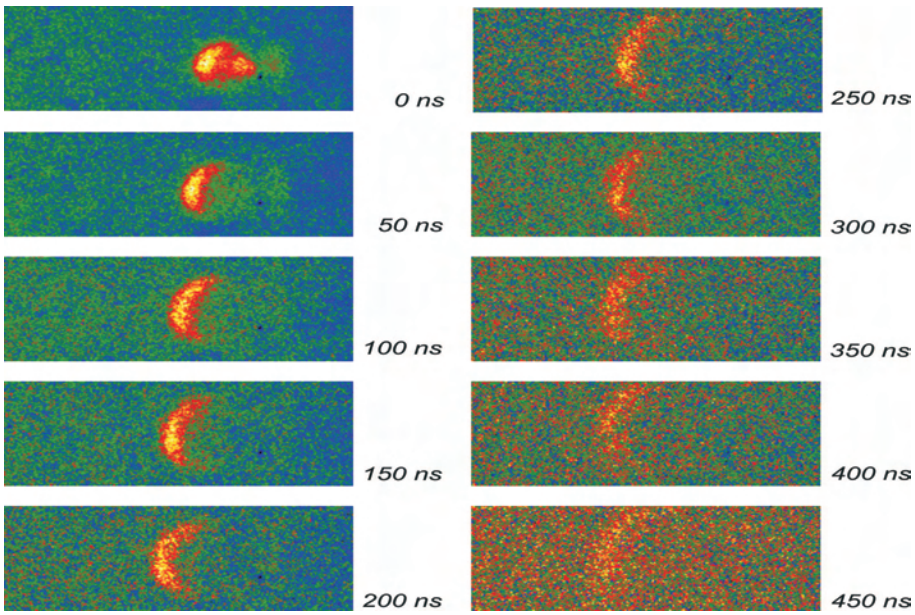

Figure 3: Aluminum ablation plasma evaluation in 0.3 mbar of Ar.

blast wave theory $R = \zeta_0 \, (E_0/\, \rho_0)^{0.2} \, t^{0.4}$ (Zeldovich, Raizer 1966) or
drag force theory $R = R_0(1 - \exp(\beta t))$ (Geohegan 1992).

Comparison of the experimental results of the $R = f(t)$ for Ar gas pressure of 0.3 and 3 Torr with both theories was presented in Figure 4.

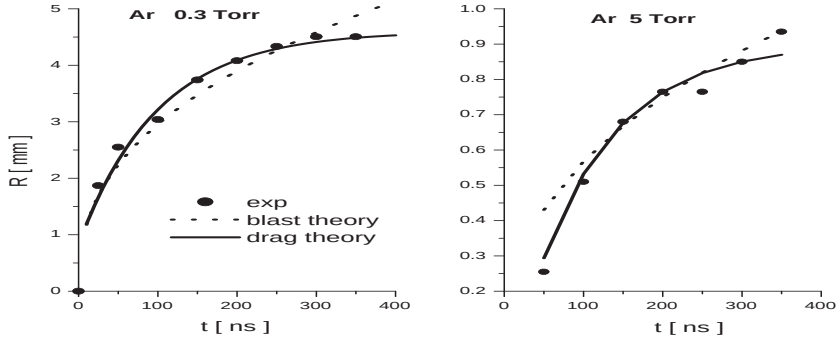

Figure 4: Comparison of ablation plasma propagation distance versus time in Ar at different pressures with a blast and drag theory.

As can be seen from Figure 4 due to the inclusion of viscosity the drag-force model better describes propagation of shock wave in the analyzed case.

Acknowledgement

This work is partially supported by Ministry of Science of Republic of Serbia under project 171032 and by Spanish Ministerio de Education y Ciencia under grants ENE2004-05038/FTN and ENE2007-63386/FTN.

References

Chrisey, D. B and Hubler, G. K.: 1994, Pulsed Laser Depositon of Thin Films, Wiley-Interscience publications, John Wiley & sons Inc.

Eason, R.: 2007, Pulsed Laser Deposition of Thin Films: Application-Led Growth of Functional Materials, Wiley-Intersience publications, John Wiley & sons Inc.

Geohegan, D. B.: 1992, in "Laser Ablation: Mechanisms and applications", (Miller J. C and Haglund R. F., eds) Springer-Verlag, Heidelberg, p. 28.

Tillack, M. S., Blair, D., Harilal, S. S.: 2002, UCSD-ENG-103.

Zeldovich, Y. B., Raizer, Y. P.: 1966, Physics of Shock Waves and High-Temperature Hydrodynamic Phenomena (Academic Press) p. 93.

Publ. Astron. Obs. Belgrade No. 84 (2008), 227 - 230 *Contributed Paper*

SURFACE MODIFICATIONS OF A Ti6AL4V IMPLANT/ALLOY BY A PICOSECOND Nd:YAG LASER

M. S. TRTICA[1*], B. GAKOVIĆ[1], B. RADAK[1], D. MARAVIĆ[1],
D. BATANI[2] and T. DESAI[2]

[1] *VINCA Institute of Nuclear Sciences, Belgrade, Serbia*
[*] *E–mail: etrtica@vin.bg.ac.yu*

[2] *Dipartimento di Fisica"G. Occhialini", Bicocca University, Italy*

Abstract. Interaction of an Nd:YAG laser, operating at 1064 or 532 nm, 40 ps pulse, with Ti6Al4V implant/alloy was studied. The energy absorbed from the laser is partially converted to thermal energy, which generates a series of effects, such as melting, vaporization of the molten material, shock waves, etc. The following changes were observed: (i) appearance of crater like form in the central zone of the irradiated area; (ii) resolidified droplets of the material in the surrounding outer zone, especially expressed at 1064 nm; and (iii) appearance of a periodic surface structures, also more prominent at 1064 nm. Generally, both laser wavelengths show potential of enhancing the roughness of the surface, particularly useful in implant applications, for better bio-integration. Laser interaction with the samples was accompanied by formation of plasma, which additionally helps obtaining a sterilizing effect.

1. INTRODUCTION

Laser surface modifications of materials are old almost as laser itself. Studies of titanium based alloys are of high importance. The Ti6Al4V is used in medicine, nuclear, and aero-space applications, etc. In medical applications this alloy is praised for its high bio-compatibility and bio-integration with the human body, see Long 1998, Trtica et al. 2006, Bereznai et al. 2003 and Guillemot et al. 2004. Generally, bio-integration is facilitated by surface roughness and sterile state Bereznai et al. 2003 and Guillemot et al. 2004.

Interaction of this alloy with a Nd:YAG laser beam pulsed in the picoseconds time domain has not been described in literature as that of the nanaosecond/microsecond domain. In the present paper, our emphasis is on studying the morphological effects of a picosecond laser emitting in the near-infrared (1064 nm) and the visible (532 nm) regions on a medical grade Ti6Al4V alloy.

2. EXPERIMENTAL

The samples were polycrystalline Ti6Al4V plates, face side polished, and the back was left as is. The face roughness was estimated by AFM at less than 100 nm. The laser was focused by a 12 cm focal length quartz lens, perpendicular to the surface,

in air. It is a Nd:YAG system, with a 40 ps pulse, see Gakovic et al. 2007, operated in TEM_{00} mode and *p*- polarization.

The samples where characterized before and after laser irradiation by X-ray diffractometry (XRD), optical microscopy (OM), scanning electron microscopy (SEM) with EDS, and atomic force microscopy (AFM) and profilometry.

3. RESULTS AND DISCUSSION

The alloy consisted mainly of the α-Ti phase, structurally polycrystalline. The laser induced morphological changes showed dependence on laser pulse energy density (LPED), pulse duration, peak power density, number of accumulated pulses, and laser wavelength.

The effects at 1064nm and 532 nm are presented in Figures 1 and 2. The LPEDs were 31.2 and 23.6 (1064 nm) and 25.9 Jcm^{-2} (532 nm).

3. 1. Nd:YAG LASER (1064 nm)

Morphology variations induced by 1064 nm, Figure 1, can be summarized as follows: (i) appearance of a crater in the central part of the irradiated area (Fig. 1B1,2 and C1,2); (ii) resolidified droplets of the molten material (Fig. 1B1 and C1); (iii) periodic surface structures (PSS) on the rim and wider periphery (Fig. 1C5, D5). Laser radiation was accompanied by appearance of the plasma in front of the target.

Generation of PSS is known on different materials, e.g. non-metals, metals, semiconductors, etc. following various kinds of mechanisms. Parallel ones are usually attributed to interferences of the incident laser light with scattered light on the surface, Le Harzic et al. 2005.

3. 2. Nd:YAG LASER (532 nm)

Surface feature induced by 532 nm, Figure 2, can be summarized as follows: (i) ablation of the target in the central zone (Fig. 2B1, C1, D1); (ii) appearance of wave-like periodic micro- and sub-micro structures, in near and further periphery, both concentric and parallel (Fig. 2 B1, C1, D1, D2); (iii) absence of defined crater structures. Irradiation was also accompanied by appearance of plasma in front of the target. The concentric periodic structures can be attributed to capillary waves, while the parallel ones are most probably surface/laser interferences, as in the case with 1064 nm.

Both Nd:YAG laser wavelengths induced damage on sample surface. Damage induced by 1064 nm was more severe than that induced by 532 nm. Craters made by 1064 nm were 100 times deeper than the damage made by 532 nm. Particles ejected by the laser appear within the first few picoseconds of the pulse, and it is possible that they had a more pronounced screening effect at 532 nm, thus preventing full laser power to reach the surface.

4. CONCLUSION

A study of morphological changes of Ti6Al4V implant/alloy surface induced by picosecond Nd:YAG laser, operating at 1064 nm and 532 nm, is presented. Much deeper craters were made by 1064 nm than by 532 nm, probably due to a screening effect at the shorter wavelength. Both concentric (with 542 nm) and parallel (with both

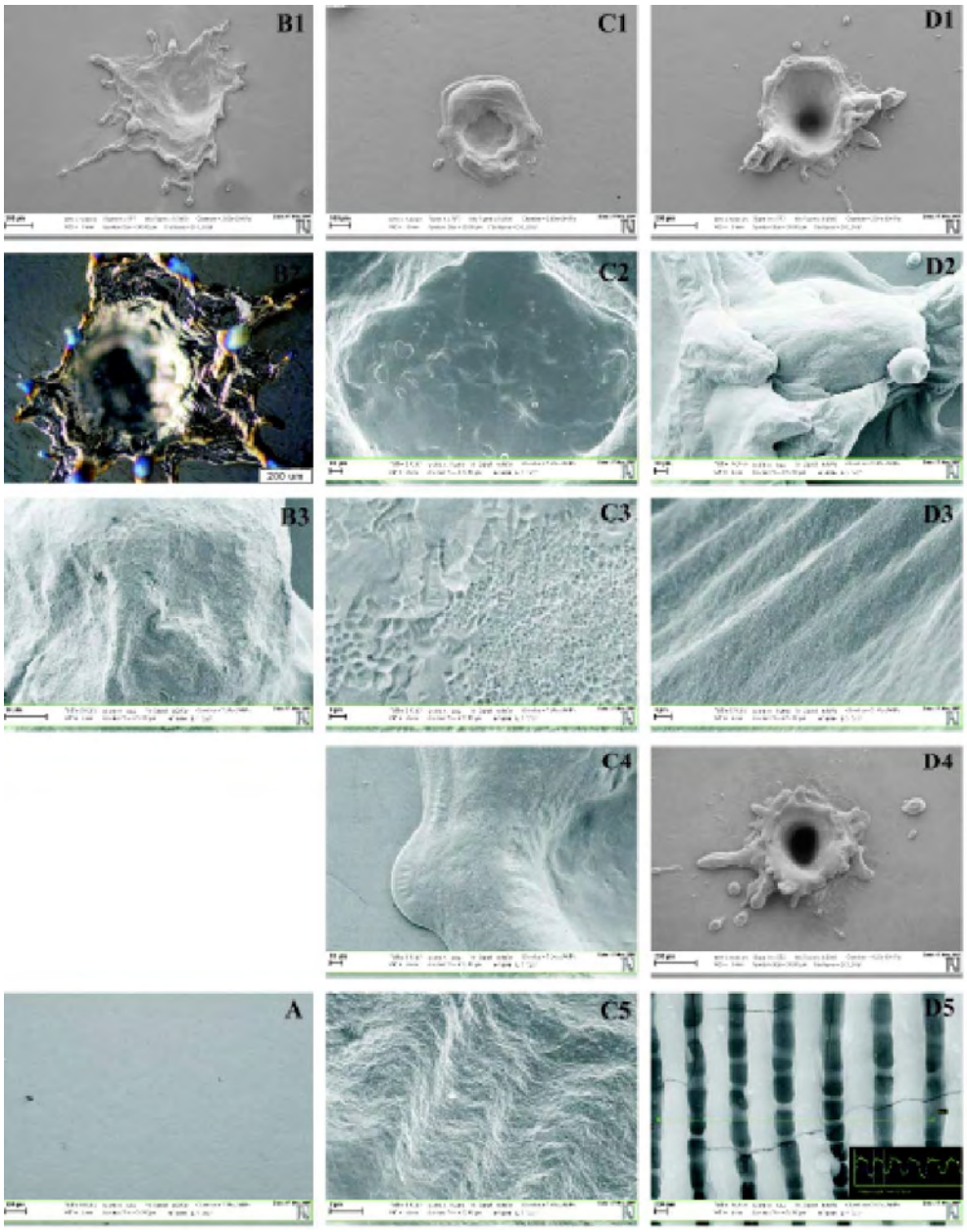

Figure 1: ps- Nd:YAG laser-induced Ti6Al4V implant morphology changes (λ=1064 nm). (A) Prior and, (B), (C) after 1 laser pulse (different LPED). (D) After 5 and 100 laser pulses. LPED = 31.2 (B) and 23.6 J/cm^2 (C) and (D).

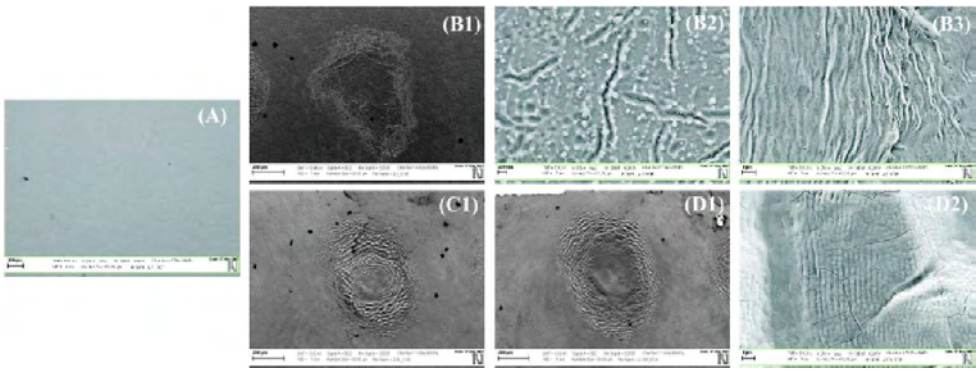

Figure 2: ps-Nd:YAG laser-induced Ti6Al4V implant morphology changes (λ=523 nm). (A) Prior to laser action; (B) 1 laser pulse, (C) and (D) after 50 laser pulses. LPED = 25.9 J/cm^2.

wavelengths) periodic surface structures were observed. Apparently, both laser wavelengths in 40 ps pulses can effectively enhance the Ti6Al4V implant/alloy roughness thus improving its bio-integration. Creation of damage at a Ti6Al4V surface is practically instantaneous, meaning that great implant surfaces can be processed in short times.

Acknowledgments

This research was sponsored by the Ministry of Science of the Republic Serbia, Contract No. 142065 and COST P-14 action. We would like to thank Dr Peter Panjan of the Jozef Stefan Institute, Slovenia, for valuable help and support.

References

Bauerle Dieter: 2003, Laser Processing and Chemistry (chapter 2), Berlin: Springer-Verlag.

Bereznai, M., Pelsoczi, I., Toth, Z., Turzo, K., Radnai, M., Bor, Z., Fazekas, A.: 2003, *Biomaterials*, **24** 4197.

Chichkov, B., Momma, C., Nolte, S., von Alvensleben, F., Tunnermann, A.: 1996, *Appl. Phys. A*, **63**, 109.

Gakovic, B., Trtica, M., Batani, D., Desai, T., Panjan, P., Vasiljevic-Radovic, D.: 2007, *Journal of Optics A: Pure and Applied Optics*, **9**, S76.

Guillemot, F., Prima, F., Tokarev, V., Belin, C., Porte-Durrieu, M., Gloriant, T., Baquey, C., Lazare, S.: 2004, *Appl. Phys. A*, **79**, 811.

Le Harzic, R., Schuck, H., Sauer, D., Anhut, T., Reimann, I., Konig, K.: 2005, *Optics Express*, **13**, 6651.

Long, M., Rack H.: 1998, *Biomaterials*, **19**, 1621.

Trtica, M., Gakovic, B., Batani, D., Desai, T., Panjan, P., Radak, B.: 2006, *Appl. Surf. Sciences*, **253,** 2551.

Publ. Astron. Obs. Belgrade No. 84 (2008), 231 - 235 *Contributed Paper*

SOME ASPECTS OF INCLUDING NON-ZERO INITIAL MOMENTA INTO IONIZATION OF ATOMS BY STRONG LOW-FREQUENCY LASER FIELDS

V. M. RISTIĆ, T. B. MILADINOVIĆ and M. M. RADULOVIĆ
Department of Physics, Faculty of Science, Kragujevac University, R. Domanovića 12, Kragujevac 34000, Serbia
E–mail: ristic@kg.ac.yu

Abstract. Including non-zero initial momenta for ejected electrons in strong infrared laser fields is further developed [compare Ristić et al. 2007]. It has been stressed that, apart from being natural, the including non-zero initial momenta enables one to go into deeper analysis of the process of tunnel ionization of atoms in strong laser fields (intensity up to 10^{16} W/cm^2). It is indicated that all electrons that could be ejected, under the circumstances, are ejected at field intensity $\sim 10^{13}$ W/cm^2, and that the effect of ionization after that is strongly diminished, which can be seen from the slope of the plates on Fig. 2. This, also, explains the saturation effect for the fields up to 10^{16} W/cm^2 (Ristić et al. 2006, Ristić and Stefanović 2007, Ristić et al. 1998, Milosevic et al. 2002), and probably this saturation goes on until the fields raising relativistic effects $\sim 10^{18}$ W/cm^2 (Milosevic et al. 2002). Opposite to what was believed earlier (Milosevic et al. 2002), that atomic field intensities could be raised to values over 10^{17}W/cm^2 only when more than 10 electrons are ejected from the atom, it is shown that, properly calculated, ionization of 9 electrons raises the atomic field intensity to $\sim 10^{18}$W/cm^2.

1. INTRODUCTION

There are several approaches to the problem of multiphoton ionization, and especially to the tunneling regime, when the low frequency lasers are involved (Ristić et al. 2006). But, to our opinion, the closest to the phenomenological picture which underlies theoretical model is the one that leans on assumptions based on the Keldysh approximation (Keldysh 1965). First, that the internal potential of atoms does not affect the energy of the final state of ejected electron, when it leaves the atom, because the electron is far enough from the nucleus (the short-range potential). Second, that the potential of the external field does not influence the initial energy of the electron (for this the external laser field should be smaller than the atomic field intensity $\sim 10^{16}$ W/cm^2). Thus the main effect of the external field was the speeding up of ionized electrons. The next step was to treat the Coulomb potential of the electromagnetic field as a perturbation of the final state energy, which was the essential in the ADK-theory (Ammosov et al. 1986). Yet, when constructing ADK-theory, the Coulomb interaction was not included into calculations of the turning point τsg

which, when revised, lead to the corrected ADK-theory, or cADK-theory (Ristić et al. 2006, Ristić and Stefanović 2007, Ristić et al. 2005, 1998, Milosevic et al. 2002). But it was always assumed that the ionized electrons are leaving the atom with zero initial momenta, which is not a natural assumption. In paper Ristić et al. (2007, see also references thereof) we were interested in how the non-zero initial momentum influences the transition probability of tunnel ionization. Now, using more precise expression for the momentum of ejected electrons (Bauer 2002), we are discussing results that emerged during this new research: the downshift of the probability maximum, its dependence on momenta of ejected electrons and above all the indicative result that gives one the insight into the process of tunnel ionization of atoms in the strong laser field (up to 10^{16} W/cm^2), see comment under Fig. 2.

2. CALCULATING NON-ZERO INITIAL MOMENTUM AND THE TRANSITION PROBABILITIES

Now we shall obtain the exact expression for the momentum that electron possesses when leaving the atom. In order to do this, we shall introduce parabolic coordinates $\xi = r+z$, $\eta = r-z$, $\phi = \mathrm{arctg}(y/x)$. Atomic unit system $e = \hbar = m_\mathrm{e} = 1$ will be used throughout this paper. So following (Bauer 2002), momentum of ejected electrons is given as

$$\mathrm{p}\,(\eta) = \frac{1}{2}\left(\sqrt{\mathrm{F}\eta - 1} + \frac{1}{\eta\sqrt{\mathrm{F}\eta - 1}} + ...\right) \quad \text{outside barrier } \eta > \frac{1}{\mathrm{F}}. \tag{1}$$

It is obvious that $\eta_\mathrm{L} = 1/F$ is a certain limit depending on field intensity (atomic unit system): $\eta_\mathrm{L} = 1/F[10^{12}] = 185.455$. We have chosen as the lowest field intensity of 10^{12} W/cm^2, at which we shall begin our evaluations of the transition rate for ejected electrons from potassium atoms in a strong field of a CO_2 – laser.

First we shall analyze the dependence of momenta of ejected electrons on the coordinate η. It can be seen from Fig. 1 that momentum of the ejected electrons is gaining in its strength as the intensity of the field is rising. Obviously the stronger the laser field is, the more energy is transferred to ejected electrons.

In (Ristić et al. 2006, Ristić and Stefanović 2007, Ristić et al. 2005) it was shown that the transition rate in cADK case is given by expression

$$W_\mathrm{cADK} = \left[\frac{4Z^3 e}{Fn^{*4}} \frac{1}{1 + \frac{2ZF}{(p^2+2E_i)^2} + \frac{Z^2F^2}{2E_i(p^2+2E_i)^3}}\right]^{2n*-1} \exp\left(-\frac{2Z^3}{3Fn^*}\right); \tag{2}$$

in Ristić et al. (2007) also was obtained the transition rate for cADK with the correction for the non-zero initial momenta

$$W_\mathrm{pcADK} = \left[\frac{4Z^3 e}{Fn^{*4}} \frac{1}{1 + \frac{2ZF}{(p^2+2E_i)^2} + \frac{Z^2F^2}{2E_i(p^2+2E_i)^3}}\right]^{2n^*-1} \exp\left(-\frac{2Z^3}{3Fn^*} - \frac{p^2\gamma^3}{3\omega}\right). \tag{3}$$

Thus the two transition rates, given by (2) and (3), when plotted together on a 3D graph for fields 10^{12}-10^{16} W/cm^2, and for η ranging from 185-585, arbitrary units for W, produce following drawing

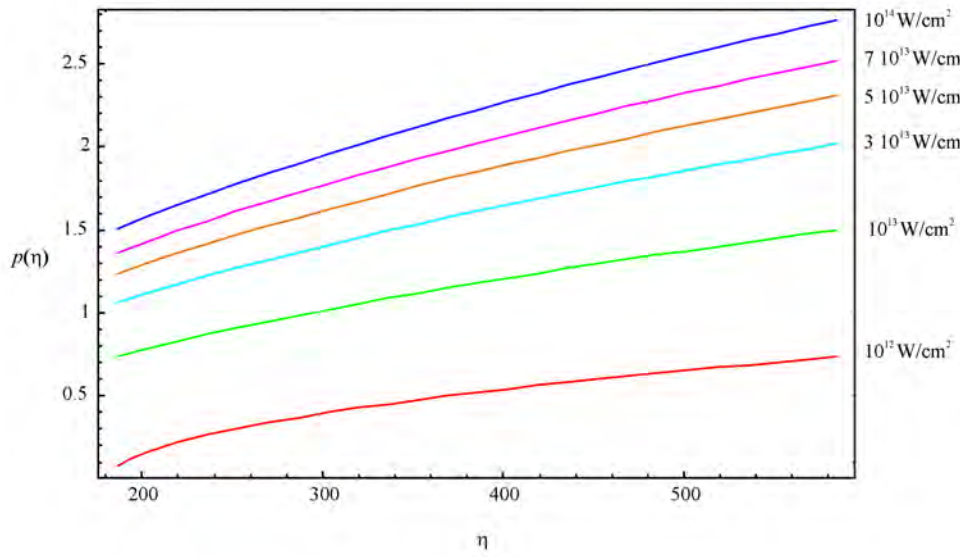

Figure 1: Momentum plotted against $\eta = 185 - 586$.

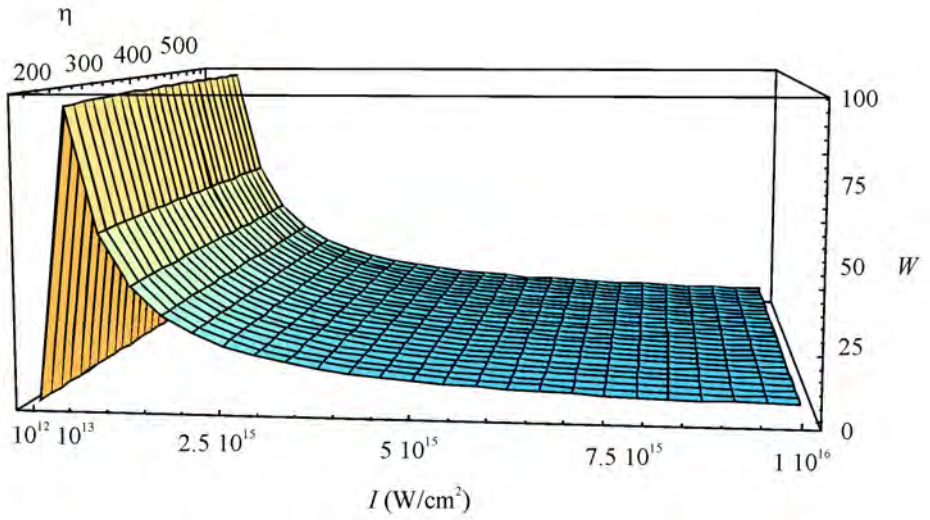

Figure 2: W_{cADK} and W_{pcADK} transition rates plotted together. The scale for the field intensities is not linear.

Fig. 2 gives us opportunity to understand better the phenomenology of the process of tunnel ionization. Notice that the scale on Fig. 2 for the field intensities is not linear.

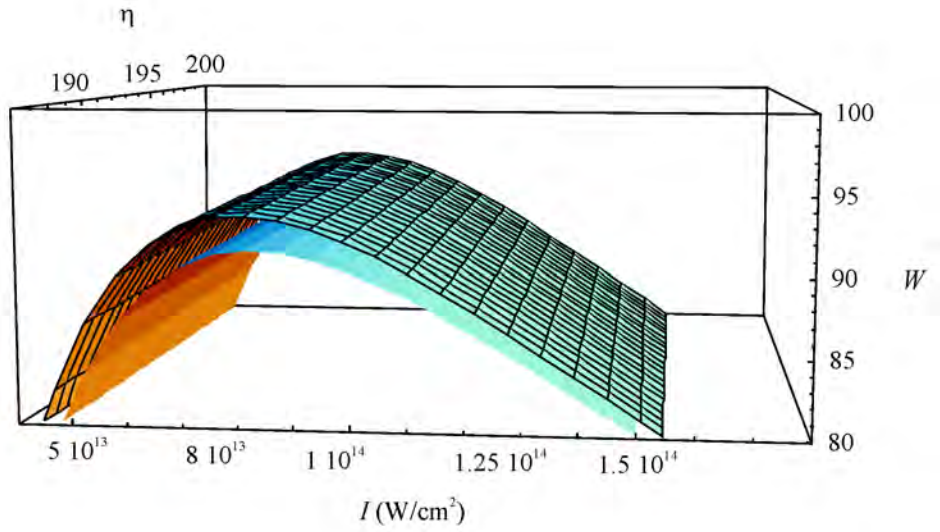

Figure 3: The peak of W_{cADK} and W_{pcADK} transition rates plotted together. Lower curved plate represents W_{pcADK}.

Fig. 3 is plotted for the same objects but in the range that shows only the peak of the graph on Fig. 2 and makes the differences obvious. So at the laser field intensity $\sim 10^{13} W/cm^2$, the transition rate has a maximum, which indicates that all electrons available are ejected. In the case of potassium, in the low frequency strong field of CO_2 laser, it is 1 valent electron assumingly the 8 electrons of the first closed shell, which makes 9 available electrons for ionization. with, i.e. for 10^{12}-10^{16}W/cm^2. Their depletion leads to freeing electrical charges of the atomic nuclei, making intensity of its electrical field of the order of magnitude 10^{18} W/cm^2. This enables us to use cADK-theory in the whole range of field intensities we are working

Close examination of Fig. 3 tells us that the transition rate in the W_{pcADK} case is a bit smaller then in the W_{cADK} case. This maximum was calculated to give values: $W^{\max}_{\text{cADK}} = 7,9 \cdot 10^{13}\text{W/cm}^2$, $W^{\max}_{pcADK} = 8,2 \cdot 10^{13}$ W/cm^2, and the differences of the two follow from the effect of transferring the energy of quanta from the laser beam to the momentum gain of ejected electrons.

It could be expected that this saturation goes further on, until the relativistic effects emerge at field intensities of $\sim 10^{18}$ W/cm^2 (Ristić et al. 1998).

3. FINAL REMARKS

We shall end this by reminding the reader of our analysis of Fig. 2, i.e. that at the laser field intensity $\sim 10^{13}$ W/cm^2, the transition rate has a maximum, which

indicates that the most of available electrons are ejected. In the case of potassium in the low frequency strong field of CO_2 laser, which we have chosen as typical case, there are 9 electrons that, after being depleted, are releasing the electrical charges of the atomic nuclei, thus resulting in electrical field of the order of magnitude 10^{18} W/cm^2, opposite to what was believed earlier, that atomic fields could be raised to values over 10^{17} W/cm^2 only when more than 10 electrons are ejected from the atom, so we can use cADK-theory for the whole range of field intensities we are working with, i.e. for 10^{12}-10^{16} W/cm^2).

As mentioned earlier, it was always assumed that the ionized electrons are leaving the atom with zero initial momenta. This assumption, being unnatural, has forced us to examine how the non-zero momentum influences the transition probability of tunnel ionization, and we are discussing results that emerged in this new research: the downshift of the probability maximum, its dependence on momenta of ejected electrons. Also, we discuss the saturation effect during ionization of potassium atoms by a low frequency field of CO_2 laser [see comment after Figs. 3 and 4].

Acknowledgements

This work was supported in part by the Ministry of Science and Ecology, Republic of Serbia (Project No. 141023).

References

Ammosov, V. M., Delone, N. B., Krainov, V. P.: 1986, *Sov. Phys. JETP*, **64**, 1191.
Bauer, D.: 2002, 1997, *Phys. Rev. A*, Vol. **55**, No. 3, 55; also Bauer, D.: 2002, Theory of laser-matter interaction, Max-Planck-Institute, Heidelberg, unpublished.
Keldysh, L. V.: 1965, *Sov. Phys. JETP*, **20**, 1307.
Landau, L. D., Lifshitz, E. M.: 1991, Quantum Mechanics: Non-Relativistic Theory, (3rd ed., Butterworth-Heinemann, London).
Milošević, N., Krainov, V. P. and Brabec, T.: 2002, *Phys. Rev. Lett.*, **89**, 193001-1.
Ristić, V. M., Miladinović, T. B. and Radulović, M. M.: 2007, *APP A*, **112/5**, 909.
Ristić, V. M., Radulović, M. M., Krainov, V. P.: 1998, *Laser Phys.*, **8**, 928.
Ristić, V. M., Radulović, M. M., Premović, T. S.: 2005, *Laser Phys. Lett.*, **2**, 314.
Ristić, V. M. and Stevanović, J. M.: 2007, *Laser Phys. Lett.*, **4**, 354.
Ristić, V. M., Stevanović, J. M., Radulović, M. M.: 2006, *Laser Phys. Lett.*, **3**, 298.

Publ. Astron. Obs. Belgrade No. 84 (2008), 237 - 240 *Contributed Paper*

DYNAMICS OF LIQUID METAL SURFACE UNDER THE ACTION OF XeCl-LASER PULSES

V. TARASENKO[2], F. LJUBCHENKO[1], A. PANCHENKO[2], A. TELMINOV[2] and A. FEDENEV[1]

[1] *Central Research Institute of Engineering of Russian Federation, Russia, 141070, Moscow region, Korolev, Pionerskaya st., 4*
E–mail: FedorNL@korolev-net.ru
E–mail: fedenev@kapella.gpi.ru

[2] *Institute of High Current Electronics, Russia, 634055, Tomsk, Academichesky av., 2/3*
E–mail: vft@loi.hcei.tsc.ru
E–mail: alexei@loi.hcei.tsc.ru

Abstract. Processes on surface of liquid metals under the action of XeCl-laser with pulsed energy of 50 mJ are studied. Relaxation time of the surface of melted Gallium and Wood and Gallium-Indium alloys is determined. Minimal relaxation time (about 4 ms) was found to be for Ga and Ga-In alloy. Qualitative description of the processes based on the assumption of capillary waves formation on the melted metal surface was suggested. Suggestion on the selection of liquid metal with minimal surface relaxation time was made based on the suggestion.

1. INTRODUCTION

At present laser-plasma thrusters (LPT) for correction of orbits of micro-satellites on the base of laser evaporation of different materials are intensively developed (see Phipps 2007). By present time first LPT prototypes are studied (see e.g. Phipps et al. 2004, Urech et al. 2004). Targets in the form of rotating metallic rod or moving tape covered with evaporating powder are used in these thrusters. Therewith operation time of such LPT is low due to fast destruction of the targets. Thereupon the use of liquid metals (LM) with low melting temperature should be very promising for great improving of the operating time and reliability of the LPT. In this case the target surface is recovered after a laser pulse due to surface tension forces without any mechanical system feeding evaporating target material into focal area. Relaxation time of the LM surface is important parameter defining maximal pulse repetition rate of the LPT.

It should be noticed that surface dynamics of LM after laser action is studied insufficiently. There is only one paper where relaxation time of surfaces of liquid Tin and Bismuth was measured to be 0,3-1 s after the action of ArF-laser (see Toth et al. 1999).

In this paper processes on a surface of different molten metals were studied using pulses of a XeCl-laser.

2. EXPERIMENTAL TECHNIQUE AND MEASUREMENT METHODS

LM drops were placed on a surface of a nickel plate at pressure p= 0,01-500 Torr. Gallium (melting temperature t_{melt} = 29,8 °C, density ρ = 5,904 g/cm^3), Gallium-Indium alloy (t_{melt} = 16 °C, ρ = 6,235 g/cm^3) and Wood alloy (t_{melt} = 65,5 °C, ρ = 9,72 g/cm^3) were used in experiments. The target temperature during experiments was constant. Radiation of a XeCl - laser with pulse energy of 50 mJ was focused on the target surface by means of a lens and a rotary mirror. The ablation area in the lens focus consisted of two overlapping quadrates with sizes d = 0,4×0,4 mm^2, the radiation power density was $\sim 1,5 \times 10^9$ W/cm^2. Processes on the target surface were monitored by a high-speed CCD-camera (SensisCam). The target surface was photographed through 100 μs with an exposure of 0,5 - 1 μs.

Waveforms of the laser pulse and radiation emission of the laser plasma in different spectral ranges were measured with a FEK – 22 vacuum photodiode. Electrical signals were recorded by a TDS-3034 digital oscilloscope.

3. EXPERIMENTAL RESULTS AND DISCUSSION

Characteristic waveforms of a laser pulse and light emission of laser plasma on surface of liquid and solid metal are shown in Figure 1. Intense peak of the laser radiation reflected from the metal surface was observed during several ns after onset of the laser pulse. This reflected signal sharply disappeared after beginning of the erosion plasma luminescence. Intensity of the reflected signal decreased when liquid surface was irradiated. Besides, replacement of solid surface by the liquid one reduces delay time of laser plasma luminescence onset near the metal surface by 2 - 3 ns. It means that threshold of ablation and plasma formation decreases for targets from liquid metal. Acceleration of the optical breakdown development on the liquid surface can be associated with decrease of reflection of incident laser energy and the lack of energy spent for heating of the metal surface to melting temperature. It was noticed in (see e.g. Götz et al. 1997, Zergioti et al. 1998) that the basic effect on the ablation threshold of liquid targets provides reduction of such thermal losses on target heating and heat conductivity into to the target deep because reflection from the metal surface was suggested to slightly dependent on its state. However, dense cloud of evaporated target material strongly absorbs incident and reflected UV-radiation (see Schittenhelm et al. 1996). In the case of liquid target this cloud is formed during shorter time, and absorption of the laser radiation begins earlier.

Surface of a drop of liquid gallium was recorded at different time moments after the laser pulse. Similarly to (see e.g. Toth et al. 1999, Hopp et al. 2000), changes on the liquid metal surface in our experiments began within 2 - 3 ns after the laser action. Two small cavities are visible on the LM surface by the moment. Their area corresponds to the laser focal spot size. The cavity dimensions vary slowly enough during approximately 0,1 ms. Then the cavities flow together, and fast growth of a hemispheric crater is observed during 0,6 ms. By the instant of 0,6 ms maximum size of the crater reached about 2-3 mm in diameter. Small ledges which have not time

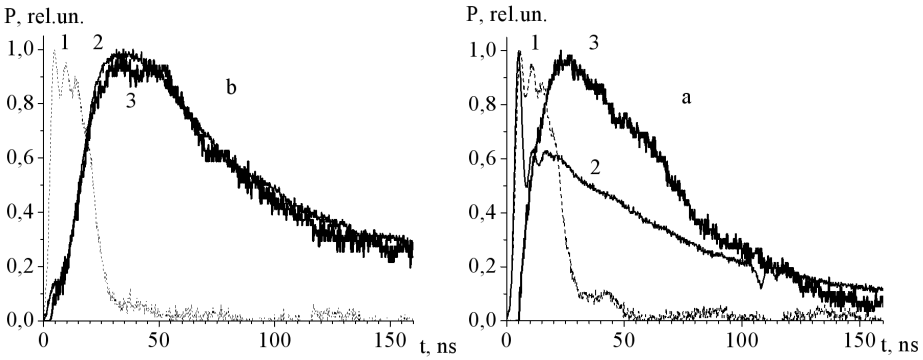

Figure 1: Waveforms of the laser pulse (1) and laser plasma emission pulses on surface of solid (a) and liquid (b) Wood alloy in spectral range 200 - 600 nm (2) and 340 - 600 nm (3) in Neon at p = 370 Torr.

to turn to drops are visible on the crater crest. Then liquid from the crater edges starts to flow downwards, forming a protuberance in the centre. This protuberance gradually grows and during 2 - 2,5 ms fills all crater. Then damped waves with small amplitude run several times on the drop surface. The surface is completely restored in time about 4 ms (see Figure 2). In the case of the Gallium-Indium alloy the recovery time increased approximately on 0,5 ms. Relaxation time increased with the liquid temperature, as well. Process of the surface relaxation of Wood alloy takes about 10 ms.

Relaxation time of the LM surface after the laser action can be qualitatively described in suggestion that surface capillary waves are formed on the liquid metal drop. Velocity of the capillary wave V_K can be written as (see Aleshkevich et al. 2001):

$$V_K = \sqrt{\frac{2\pi\sigma}{\rho\lambda} th\left(\frac{2\pi H}{\lambda}\right)}, \tag{1}$$

where λ is characteristic size of the perturbation on the liquid metal surface after the laser pulse, σ is surface tension and ρ is liquid density, th $(\pi H/\lambda)$ is hyperbolic tangent, H is depth of the liquid layer. It is easy to see, that the surface relaxation time is determined by a surface tension and density of the used molten metal. In the case of Gallium (σ = 0,705 N/m) the crater characteristic size is measured to be $\lambda \approx$ 2,5 mm (see Fig. 2), and propagation velocity of the capillary wave is V_K = 0,5 m/s. Accordingly, the surface relaxation time (about 5 ms) is in good agreement with experiment data. Density of Wood alloy is 1,5 times higher and its surface tension is two times lower than those for Gallium. Therefore propagation velocity of a capillary wave on the Wood alloy surface should decrease by a factor of 1,74, and the surface relaxation time increases in the same ratio. In our experiments, the relaxation time of the Wood alloy surface was approximately two times longer than that for Gallium.

Characteristic size of the surface crater strongly depends on the liquid viscosity (see Hopp et al. 2000). Therefore for minimization of the crater size it is necessary to use molten metals with maximal viscosity. Since viscosity sharply decreases at high temperature, the molten metal is necessary to maintain near the melting temperature.

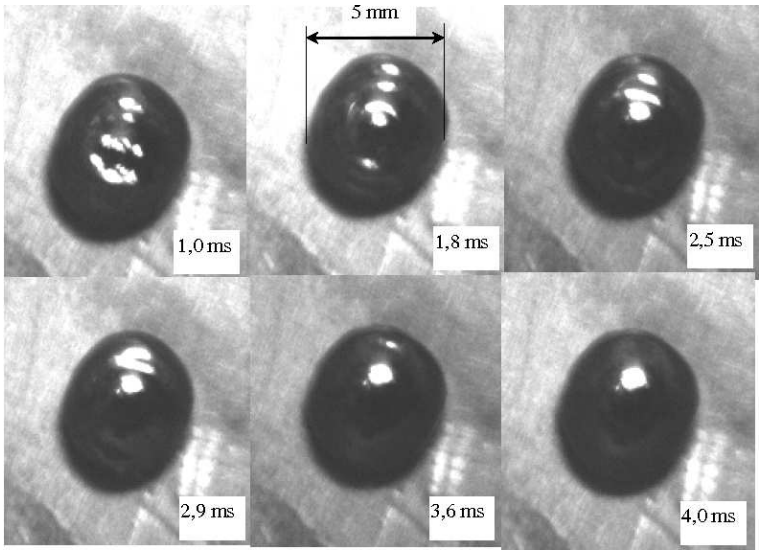

Figure 2: Dynamics of the liquid Gallium surface in the time interval 0 - 3,2 ms after the laser pulse. The exposure time is 1 μs, time interval after the laser pulse is written on each frame.

Basing on the above suggestion it is possible to form demands for selection of LM for LPT. The liquid metal should have high viscosity and maximal ratio σ/ρ. On the basis of this criteria Lithium is one of the best materials.

4. CONCLUSION

The processes on a surface of molten metals after the action of XeCl-laser with pulsed energy of 50 mJ were studied. Relaxation time of surface of some molten metals was measured. Minimal relaxation (about 4 ms) was measured to be for liquid Gallium and its alloy with Indium.

Qualitative description of the processes on the LM surface based on formation of the surface capillary waves is suggested. Demands for selection of LM for LPT are formulated.

References

Aleshkevich, V. A., Dedenko, L. G., Karavaev, V. A.: 2001, Oscillations and waves. Lectures. Physical faculty of the Moscow State University.

Götz, T., Stuke, M.: 1997, *Appl. Phys. A*, **64**, 539.

Hopp, B., Smausz, T., Wittmann, T., Ignácz, F.: 2000, *Appl. Phys. A*, **71**, 315.

Phipps, C. ed.: 2007, Laser Ablation and its Applications, Springer Series in Optical Sciences, V.129, Berlin/Heidelberg: Springer.

Phipps, C., Luke, J., Lipperta, T.: 2004, *Thin Solid Films*, **453-454**, 573.

Schittenhelm, H., Callies, G., Berger, P. and Hügel, H.: 1996, *J. Phys. D*, **29**, 1564.

Toth, Z., Hopp, B., Smausz, T., Kantor, Z., Ignacz, F., Szorenyi, T., Bor, Z.: 1999, *Appl. Surf. Sci.*, **138-139**, 130.

Urech, L., Hauer, M., Lippert, T. R., Phipps, C., Schmid, E., Wokaum, A.: 2004, *Proc. SPIE*, **5448**, 52.

Zergioti, I., Stuke, M.: 1998, *Appl. Phys. A*, **67**, 391.

Publ. Astron. Obs. Belgrade No. 84 (2008), 241 - 244 *Contributed Paper*

SIMULATION OF STREAKING EXPERIMENTS AT SURFACES

C. LEMELL[1], B. SOLLEDER[1], K. TŐKÉSI[2], and J. BURGDÖRFER[1]

[1] *Institute for Theoretical Physics, Vienna University of Technology, Wiedner Hauptstraße 8-10, A–1040 Vienna, Austria*
E–mail: lemell@concord.itp.tuwien.ac.at

[2] *Institute of Nuclear Research of the Hungarian Academy of Sciences, (ATOMKI), H–4001 Debrecen, P.O.Box 51, Hungary*

Abstract. Recently, surprisingly large run-time differences of electrons emitted in laser-metal interactions have been reported. In our work we aim at simulating this experiment starting with electron excitation by the XUV pump pulse, subsequent electron transport within the target material, and finally emission into and transport in vacuum under the influence of the NIR pump pulse. Our results can only partly explain the measured data.

1. INTRODUCTION

Gaining deeper understanding of electron dynamics in condensed-matter systems is an important step towards developments in the fields of, e.g., electronics or information processing. Applying the "streaking" technique originally developed for gas targets (Kienberger et al. 2004) to photoelectrons from metal surfaces, electron dynamics in solids (time scale for electronic motion ~ 1 as $= 10^{-18}$ s) could be observed in real time (Cavalieri et al. 2007). In their setup two collinear linearly polarized laser pulses (extreme ultraviolet (XUV) and near infrared (NIR)) were directed at a W(110) surface under a grazing angle of incidence. Electrons excited by the pump pulse were transported in the field of the probe pulse changing their energy as a function of emission time. Photoelectrons escaping the target surface were detected by a time-of-flight spectrometer with the detection direction normal to the surface (see Fig. 1).

On top of a strong background signal originating from above-threshold ionization two prominent features were observed in each of the streaking spectra: a low energy peak around 55 eV and a high energy peak at 85 eV. The former was attributed to electrons excited from 4f states of tungsten, the latter to electrons from the target conduction band (5d and 6s states). A run-time difference between the two groups of electrons of 110 ± 70 as was observed.

2. SIMULATION

Our simulation includes three main ingredients (Lemell et al. 2008): 1) the interaction of the XUV pulse with the target material, i.e., the excitation of target electrons to

continuum states; 2) A classical-trajectory Monte-Carlo simulation of the transport of excited electrons through the material (Solleder et al. 2007) and 3) the propagation of electrons which have escaped the surface to the detector in the streaking field.

In photoemission experiments with a Ne gas target, the photon energy of the pump pulse was measured to be 91 eV with a full width at half maximum (FWHM) of about 6 eV. Therefore, target electrons from only 4 states can be excited to energies in the measured energy range (above 30 eV): 6s, 5d, 4f, and 5p. The former two form the conduction band of tungsten and lead to a broad peak around 83 eV emission energy, the latter two to a peak with its centroid at 56 eV. The streaked energy shift of these two peaks has been analyzed in order to determine the run-time difference between these two groups of electrons (Cavalieri et al. 2007).

Electrons excited by the pump pulse are propagated through the target material subject to elastic and inelastic scattering events and to deflection of their trajectories in the electric field of the NIR probe pulse. Doubly differential and total elastic scattering cross sections have been calculated with the ELSEPA package (Salvat et al. 2005) using a muffin-tin potential for the crystal atoms. The energy dependent elastic mean free path was derived from the total cross sections. Computation of inelastic scattering was based on an extrapolation of optical data (i.e., the frequency dependent dielectric function at $q = 0$) to the $q - \omega$ plane (Powell 1974, Penn 1984). Energy loss in an inelastic scattering event can lead to the release of a secondary electrons whose trajectory is also followed in our simulation. Between subsequent scattering events the differential equation for electron transport in the time-dependent electric laser field was solved. To assess the influence of the crystal structure two different dispersion relations (DR) were employed: the free-particle DR $E = k^2/2$ and a DR derived from ab-initio calculations (Calvalieri et al. 2007) of group velocities along the surface normal.

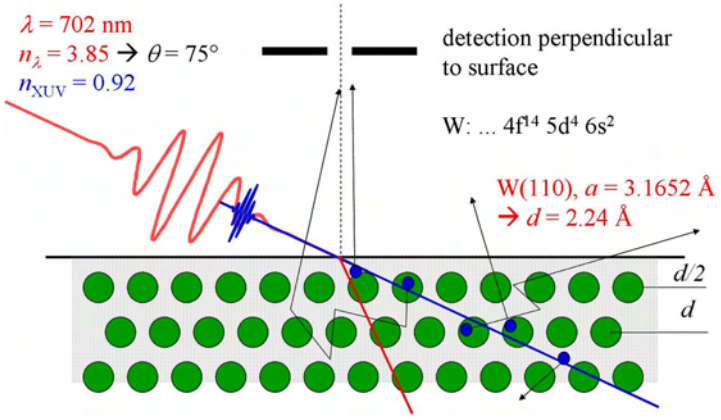

Figure 1: Schematic view of experimental setup: A 300 as XUV pulse hits the surface under a grazing angle of incidence ionizing target electrons. They are transported in the field of a 10 fs NIR pulse and detected by a TOF spectrometer mounted perpendicular to the surface.

Above the surface the electron is subject to the time-dependent streaking field $E(t)$ of the NIR laser pulse. It transfers a momentum of

$$\Delta p = \int_{t_{esc}}^{t_{end}} E(t)\, dt \tag{1}$$

to the electron where the integral is taken from the time of escape from the surface, t_{esc}, to the end of the laser pulse, t_{end}. Electrons with a final momentum perpendicular to the surface ($\theta \leq 5°$) are counted.

10^7 trajectories were started for each streaking spectrum, the time delay between pump and probe pulses was varied from -10 fs to 10 fs in 100 as steps.

3. RESULTS

Results presented in this section were calculated using the free-particle dispersion relation in our transport simulation.

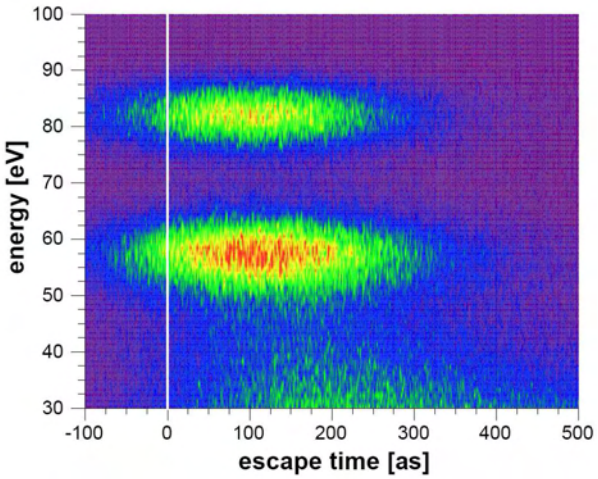

Figure 2: Energy vs. run time of electrons emitted from the surface.

In Fig. 2 the energies of electrons which have escaped the surface are plotted against their run time within the target where the zero point $t = 0$ is defined by the maximum of the envelope function of the pump laser field. Electrons with $t < 0$ have been released on the rising flank of the pulse with a duration (FWHM) of about 300 as. Two main features around 56 eV (4f and 5p electrons) and 82 eV (conduction band) can be seen. The escape time averaged over the peak regions is 159 as and 115 as for the low and high energy peaks, respectively. This difference in run time of our simulation lies at the lower limit of the experimental error bar. The present run-time difference can be accounted for by the following target properties: the inelastic mean free path (IMFP) of electrons with 56 and 83 eV emission energy is for both groups between 6 and 7 Å. Electrons which have not suffered any energy loss along their

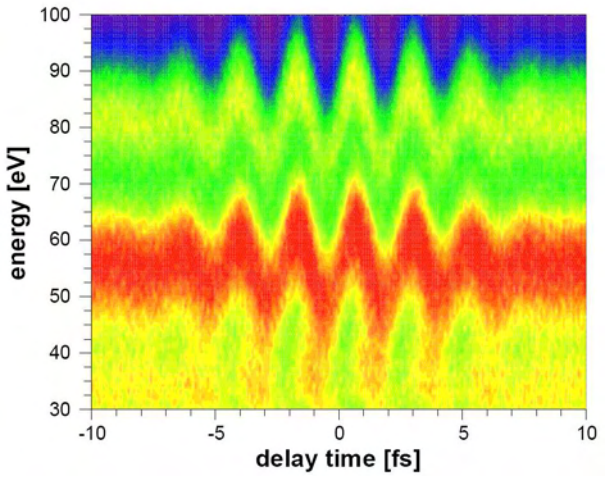

Figure 3: Streaking image for electrons detected in XUV-NIR laser-pulse surface interactions ($\theta_{esc} = 0 \pm 5°$).

trajectory in the target have traveled on the average a distance equal to the IMFP. This short traveling distance sets a lower limit for the run-time difference of only about 20 as. Scattering events increase this value to the observed 45 as. Using the crystal-structure DR the run-time difference is increased to about 80 as.

Fig. 3 shows the streaking image for the energy range from 30 – 100 eV. Momentum transfer due to the interaction with the probe laser field leads to the observed energy shift of the lines at 56 and 82 eV. We have found that influence of the streaking field on the trajectory does not change the observed run-time difference.

In conclusion, we have modeled a recent experiment by Cavalieri et al. who have succeeded in applying the streaking technique to solid-state targets. Our simulation includes excitation of target electrons, their transport through the metal, and, if they escape the target, streaking on their paths to the detector. Qualitative agreement (i.e., a run-time difference larger than derived from escape depths and electron velocities alone) with experiment is found, quantitative differences remain so far unexplained.

References

Cavalieri, A.L., Müller, N., Uphues, Th., Yakovlev, V.S., Baltuska, A., Horvath, B., Schmidt, B., Blümel, L., Holzwarth, R., Hendel, S., Drescher, M., Kleineberg, U., Echenique, P.M., Kienberger, R., Krausz, F., Heinzmann, U.: 2007, *Nature*, **449**, 1029.

Kienberger, R., Goulielmakis, E., Uiberacker, M., Baltuska, A., Yakovlev, V., Bammer, F., Scrinzi, A., Westerwalbesloh, Th., Kleineberg, U., Heinzmann, U., Drescher, M., Krausz, F.: 2004, *Nature*, **427**, 817; *ibid.* supplementary material.

Lemell, C., Solleder, B., Tökesi, K., Burgdörfer, B., Jakovlev, V.S., Cavalieri, A.L., Krausz, F.: 2008, *Phys. Rev. A*, in preparation.

Penn, D. R.: 1987, *Phys. Rev. B*, **35**, 482.

Powell, C. J.: 1974, *Surf. Sci.*, **44**, 29.

Salvat, F., Jablonski, A., Powell, C.: 2005, *Comp. Phys. Commun.*, **165**, 157.

Solleder, B., Lemell, C., Tökesi, K., Hatcher, N., Burgdörfer, J.: 2007, *Phys. Rev. B*, **76**, 075115.

Publ. Astron. Obs. Belgrade No. 84 (2008), 247 *Invited Lecture*

STOCHASTIC HEATING IN ASYMMETRIC CAPACITIVELY COUPLED RF DISCHARGES AND THE PSR EFFECT

J. SCHULZE[1], B. G. HEIL[1], D. LUGGENHÖLSCHER[1], R. P. BRINKMANN[2], and U. CZARENTZKI[1]

[1] *Institute for Plasma and Atomic Physics, Ruhr-University Bochum, 44780 Bochum, Germany*
E–mail: uwe.czarnetzki@ep5.rub.de.ac.cd.ef.uk

[2] *Institute for Theoretical Electrical Engineering, Ruhr-University Bochum, 44801 Bochum, Germany*

Abstract. Electron dynamics in asymmetric capacitively coupled radio frequency (RF) discharges is investigated experimentally and by developing basically simple models and simulations. The investigations focus on two closely related physical effects: Stochastic heating of electrons by the oscillating sheath in front of the electrode and the occurrence of high frequency oscillations of the current and the sheath in asymmetric discharges. Both effects become important only at low pressures. High frequency oscillations are caused by an effective series oscillator resulting from the sheath capacitance and the electron inertia in the plasma bulk, giving the effect its name: Plasma Series Resonance (PSR). The non-linear charge-voltage relation of the RF sheath is essential for the effect and makes asymmetric discharges quite distinct from symmetric discharges. The PSR effect leads to current and sheath oscillations at about one order of magnitude higher frequencies than the applied sinusoidal RF voltage, thus enhancing substantially stochastic heating. In the experiment a combination of various diagnostics is applied: Laser electric field measurements for the sheath, phase resolved optical emission spectroscopy for collisional excitation of atoms by energetic electrons, Langmuir probe measurements for the EEDF and electron density in the bulk, a SEERS sensor for current measurements and a high voltage probe for monitoring the applied RF voltage. Data from these diagnostics are correlated, compared, and further analyzed by analytical models and a hybrid fluid dynamic-kinetic simulation incorporating the Brinkmann sheath model. This integrated approach results in a unique insight into the underlying physics and provides a coherent picture of the discharge mechanism.

Funded by the DFG through SFB591 and GRK1051 and supported by Andor Technology.

Publ. Astron. Obs. Belgrade No. 84 (2008), 248 - 249 *Invited Lecture*

MICROPLASMAS AND MICRO-JETS

C. LAZZARONI[1], X. AUBERT[1], D. MARINOV[1], O. GUAITELLA[1], G. STANCU[2], S. WELZEL[2], A. PIPA[2], J. ROPCKE[2], N. SADEGHI[3], A. ROUSSEAU[1]

[1]*LPTP, Ecole Polytechnique, CNRS, Palaiseau, France*

[2]*INP, Greifswald, Germany*

[3]*INP-Greifswald, Greifswald, Allemagne*

Abstract. Microplasmas are now widely investigated, one of their advantages being to generate a plasma at relatively high pressure close to the Paschen minimum (Schoenbach et al. 1997). Here, the microplasma is generated in a microhollow cathode type configuration made of a hole drilled through a metal/dielectric/metal sandwich (Schoenbach et al. 1997). One of the electrodes acts as the cathode (K) and the other as the anode (A1). The hole diameter ranges from 100 to 400 μm and the pressure ranges from 50 to 500 Torr. When a second electrode (A2) is added, a large volume of plasma plume may be generated between A1 and A2, at a low electric field (1-20Td depending upon the gas) (Stark et al. 1999). A microhollow cathode type discharge operates in three different regimes depending on the plasma current: abnormal, self-pulsing and normal regime. The self-pulsing regime is achieved in the range of 1-100 kHz, in argon, helium, nitrogen and oxygen. The self-pulsing frequency is controlled by the microplasma device capacitance, the gas breakdown voltage, and the average discharge current (Rousseau et al. 2006, Aubert et al. 2007).

i) First, in pure argon, the radial dependence of atoms excitation mechanisms and of the electronic density is studied inside the micro-hole. Imaging of the emission from the microplasma is performed with a spatial resolution of few μm. The electron density is estimated from the Stark broadening of the H_β-line. The radial distribution of the emission intensities of an Ar atomic line and an Ar^+ ionic line are used for the excitation study. Ar and Ar^+ lines are excited in the cathode sheath edge by beam electrons accelerated within the sheath. These two excitations show the decay of the energy of electrons in negative glow. The Ar line presents also production of excited atoms by recombination of argon ions with electrons at the center of the micro-hole.Work is in progress to evaluate the contribution of the static electric field on the strak broadening

ii) Second, in oxygen containing mixture, a flowing micro-jet is generated: the reactor used is separated in 2 rooms by the MHC. Thus, the gas is constrained to flow only through the microhole and the quantity of treated gas is well known. The gas flow is supersonic in most operating conditions at the exit of the microhole; despite a very large injected power density (typically 10^4 W cm^{-3}), the gas heating does not exceed few hundreds of degrees, so that the plasma is non equilibrium. Different measurements are realized on the plume in pure O_2 and in Air. O_3 concentration has been measured by UV absorption spectroscopy; NO and NO_2 have been measured by tuneable diode laser absorption spectroscopy (TDLAS) in the infrared region (Röpcke et al. 2006). The production of NO and NO_2 in air mixture scales as universal function of the injected power, independently of the working regime (continuous or self-pulsing).

References

Aubert, X. et al.: 2007, *Plasma Sources Sci. Technol.*, **16**, 23.
Röpcke, J. et al.: 2006, *Plasma Sources Sci. Technol.*, **15**, S148.
Rousseau, A. et al.: 2006, *J. Phys. D.: Appl. Phys.*, **39**, 1619.
Schoenbach, K. H., et al.: 1997, *Plasma Sources Sci. Technol.*, **6**, 468.
Stark, R. H. et al.: 1999, *J. Appl. Phys.*, **85**, 2075.

Publ. Astron. Obs. Belgrade No. 84 (2008), 250 *Invited Lecture*

ATMOSPHERIC PRESSURE NON-THERMAL PLASMA: SOURCES AND APPLICATIONS

A. P. NAPARTOVICH
SRC RF TRINITI, Troitsk, Moscow region, Russia
E–mail: apn@triniti.ru

Abstract. Non-thermal plasma at atmospheric pressure is an inherently unstable object. Nature of discharge plasma instabilities and conditions for observation of uniform non-thermal plasma at atmospheric pressure in different environments will be discussed. Various discharge techniques have been developed, which could support uniform non-thermal plasma with parameters varied in a wide range. Time limitation by plasma instabilities can be overcome by shortening pulse length or by restriction of plasma plug residence time with a fast gas flow. Discharge instabilities leading to formation of filaments or sparks are provoked by a positive feedback between the electric field and plasma density, while the counteracting process is plasma and thermal diffusion. With gas pressure growth the size of plasma fluctuation, which could be stabilized by diffusion, diminishes. As a result, to have long lived uniform plasma one should miniaturize discharge.

There exist a number of active methods to organize negative feedback between the electric field and plasma density in order to suppress or, at least, delay the instability. Among them are ballast resistors in combination with electrode sectioning, reactive ballast, electronic feedback, and dielectric barrier across the electric current. The last methods are relevant for ac discharges. In the lecture an overview will be given of different discharge techniques scalable in pressure up to one atmosphere.

The interest in this topic is dictated by a potential economic benefit from numerous non-thermal plasma technologies. The spectrum of non-thermal plasma applications is continuously broadening. An incomplete list of known applications includes: plasma-assisted chemical vapor deposition, etching, polymerization, gas-phase synthesis, protective coating deposition, toxic and harmful gas decomposition, destruction of warfare agents, electromagnetic wave shielding, polymer surface modifications, gas laser excitation, odor control, plasma assisted combustion, and gas dynamic flow control. Many of these applications have been developed with low-pressure plasma. Atmospheric pressure non-thermal plasma technologies possess such advantages as simplicity of operation and relatively low cost of equipments. A variety of available discharge techniques provides non-thermal plasma at atmospheric pressure in various gases with parameters covering a wide range in power densities, reduced electric field strengths and current densities. Requirements to non-thermal plasma parameters and sorts of gas for various applications vary widely, too. For any specific application the most appropriate discharge type can be found. The spectrum of discharge devices already existing is surprisingly broad. The problem of a successful choice of a discharge type for a specific application will be discussed. A particular emphasis will be placed on the problem of plasma removal of toxic and harmful species from the gas flow.

Publ. Astron. Obs. Belgrade No. 84 (2008), 251 *Invited Lecture*

PHYSICAL AND PLASMACHEMICAL ASPECTS OF DIFFUSE COPLANAR BARRIER DISCHARGE AS A NOVEL ATMOSPHERIC-PRESSURE PLASMA SOURCE

M. ČERNÁK[1,2], D. KOVÁČIK[1], A. ZAHORANOVÁ[1] and J. RÁHEL[1,2]

[1] *Dept. of Experimental Physics, Comenius Univ., Mlynská dolina F2, 842 15 Bratislava, Slovakia*
E–mail: cernak@fmph.uniba.sk

[2] *Department of Physical Electronics, Masaryk University, Kotlářská 2, 611 37 Brno, Czech Republic*

Abstract. Collaborating Czech and Slovakian university teams have recently developed an innovative plasma source, the so-called Diffuse Coplanar Surface Barrier Discharge (DCSBD), which has the potential to move a step closer to the industry requirement for in-line treatment of low-added-value materials using a highly-nonequlibrium ambient air plasma (Šimor et al. 2002,

The idea is to generate a thin (on the order of 0.1 mm) layer of highly-nonequlibrium plasma with a high power density (up to 100 W/cm^3) in the immediate vicinity of the treated surface and bring it into a close contact with the treated surface. Comparing to atmospheric-pressure glow discharge, volume dielectric barrier discharge, and plasma jet plasmas, such a diffuse plasma layer is believed to provide substantial advantages in energy consumption, exposure time, and technical simplicity.

A brief outline of physical mechanism and basic properties of DCSBD will given using the results of emission spectroscopy, high-speed camera, and spatially resolved cross-correlation spectroscopy studies.

The presentation will review also a current state of the art in in-line plasma treatment of low-cost materials and opportunities for the use of the so-called Diffuse Coplanar Surface Dielectric Barrier Discharge (DCSBD). The results obtained on the ambient air plasma treatments of textile, paper, wood, and glass illustrate that DCSBD offers outstanding performance with extremely low energy consumption for large area, uniform surface modifications of materials under continuous process conditions.

References

Černák, M., Ráhel', J., Kováčik, D., Šimor, M., Brablec, A., Slavíček, P.: 2004, Contributions to *Plasma Physics*, **44**, 492.

Šimor, M., Rahel, J., Vojtek, P., Brablec, A., Černák, M.: 2002, *Appl. Phys. Lett.*, **81**, 2716.

Publ. Astron. Obs. Belgrade No. 84 (2008), 252 *Invited Lecture*

MEASUREMENT OF VOLTAGE AND CURRENT IN CONTINUOUS AND PULSED RF AND DC GLOW DISCHARGES

V. HOFFMANN[1], V. V. EFIMOVA[1], M. V. VORONOV[2], P. ŠMÍD[3],
E. B. M. STEERS[3], J. ECKERT[1]

[1]*Institut für Festkörper- und Werkstoffforschung Dresden, P.O.Box 270116,D-01171 Dresden*
E–mail: V.Hoffmann@ifw-dresden.de

[2]*AQura GmbH, P.O.Box 915-d115, Rodenbacher Chaussee 4,D-63457 Hanau-Wolfgang*
E–mail: VoronovMV@mail.ru

[3]*London Metropolitan University, 166-220 Holloway Road, London, N7 8DB, UK*
E–mail: p.smid@londonmet.ac.uk
E–mail: e.steers@londonmet.ac.uk

Abstract. Electrical measurements are an important tool for the characterisation of glow discharges and have proved to be useful for a variety of needs in fundamental studies and as control parameter. Therefore, extensive hardware developments and studies of I-U characteristics in continuous and pulsed, dc and rf modes have been made (Wilken et al. 2007) and will be presented together with new results.

In continuous dc mode, the I-U curves are non-linear and may be characterised by a threshold voltage U_0 and saturation current I_{max} (both cathode material and pressure dependent). On the other hand P-U curves are to a large extent linear and very similar in the continuous rf mode (Hoffmann et al. 1998). The ionic part of time resolved I-U curves of rf discharges however shows almost a linear behaviour and the capacitive component is small. No saturation current exists. This led to the assumption that gas heating is responsible for the non-linearity between U and I in continuous dc discharges. Consistent with this assumption, a dependence of the U-I curves of *pulsed* discharges on the duty cycle was found. The comparison of the curves with those at low duty cycle (cold) led to a rough estimation of the gas temperature.

Owing to the large changes of current in a very short time, the measurement of the electronic part of the U-I curve in rf mode is far more difficult. If conducting samples are analysed, this electronic part contains extra information. For *pulsed* rf discharges the hysteresis of electronic part increased with decreasing duty cycle (lower gas temperature). In a study of the effect of the addition of small amounts of H_2 to the Ar discharge gas similar changes in the electronic part of the U-I curve were observed whereas the ionic part was identical. Further investigation and cooperation with modelling groups is needed and planned to explain these results.

References

Hoffmann, V., Praessler, F., Wetzig, K.: 1998, in: C. Vogt, R. Wennrich, and G. Werner (Editors), Colloquium Analytische Atomspektroskopie, Universität Leipzig, 29-39.
Wilken, L., Hoffmann, V. and Wetzig, K.: 2007, *Spectrochim. Acta Part B*, **62**, 1085.

Publ. Astron. Obs. Belgrade No. 84 (2008), 253 *Topical Lecture*

ADVANCES IN OPTICAL DIAGNOSTICS OF ATMOSPHERIC PRESSURE DIELECTRIC BARRIER DISCHARGES

G. DILECCE, P. F. AMBRICO and S. DE BENEDICTIS
Istituto di Metodologie Inorganiche e dei Plasmi CNR, sede di Bari - Via Orabona 4, 70125 Bari, Italy
E–mail: giorgio.dilecce@ba.imip.cnr.it

Abstract. Dielectric barrier discharges at atmospheric pressure have recently received a growing interest because of their potentially advantageous use in a number of applicative fields, in both their main classes of "volume" and "surface" geometric arrangements. The possibility of obtaining a uniform, or glow, regime, in contrast to the usual filamentary one, has further enlarged their perspectives for surface treatments applications. From a diagnostic point of view, the high pressure regime adds problems relevant to an enhanced role of collision quenching, vibrational and rotational relaxation, while maintaining most of the demands of a highly non-equilibrium system for a detailed characterization of its degrees of freedom. In addition, filamentary DBDs are intrinsically pulsed systems, in which the electron impact excitation is confined in small space regions and very short time intervals, such that a prominent afterglow phase, both spatial and temporal, is present in the discharge volume, and kinetic processes involving long-lived species, chemi- luminescent reactions, recombinations (aided by the large pressure) can competitively come into play in the excitation of electronic states. We have applied our ensemble of diagnostic methods, based on time resolved emission and laser spectroscopy, to the investigation of elementary kinetics in DBDs. Here we present our last two years results that include: Optical-Optical Double Resonance (OODR)-LIF measurements of $N_2(A^3\Sigma_u^+)$ density, in a volume DBD that is of relevance in the debate upon the mechanisms for establishing the glow regime (Dilecce 2007); OODR-LIF and emission study on a Masuda type surface discharge (Ambrico 2008); measurement of $N_2(C^3\Pi_u, v)$ quenching and vibrational relaxation rate constants and its relevance to nitrogen Second Positive System emission diagnostics at atmospheric pressure (Dilecce 2006, 2007); kinetics of $CN(B^2\Sigma^+, v)$ formation and violet system emission in N_2-CH_4 discharges. The latter issue shows in addition a correlation between emissions and surface status (i.e. the presence of a deposit) that is a clear monitor of a gas surface interplay.

References

Ambrico, P. F., Simek, M., Dilecce, G. and De Benedictis, S.: 2008, *Plasma Chem. Plasma Proc.*, in press DOI: 10.1007/S11090-00P-9131-5.
Dilecce, G., Ambrico, P. F. and De Benedictis S.: 2007, *Plasma Sources Sci. Technol.*, **16**, 511.
Dilecce, G., Ambrico, P. F. and De Benedictis, S.: 2007, *Chem. Phys. Lett.*, **431**, 241.
Dilecce, G., Ambrico, P. F. and De Benedictis, S.: 2007, *Plasma Sources Sci. Technol.*, **16**, S45.

Publ. Astron. Obs. Belgrade No. 84 (2008), 254 *Topical Lecture*

PRESSURE-TEMPERATURE IONIZATION OF NONIDEAL PLASMAS

V. FORTOV

Institute for High Energy Density of RAS, Moscow, Russia
E–mail: fortov@ficp.ac.ru

Abstract. The physical properties of strongly coupled plasmas at high pressures and energy densities are analyzed in a broad region of parameters. The theoretical and experimental methods of non-ideal plasma investigations are discussed. Main attention is paid to the dynamical methods. Intense shock, rarefaction, and radiative waves in solid and porous samples, and electrical explosion were used for generation of high density plasmas at extremely high pressure. The pressure ionization plasma phenomena in hydrogen, helium, noble gases, iodine, silica, sulfur, H_2O, fullerenes and some metals are analyzed on the base of multiple shock wave experiments. The data obtained were described by the non-ideal plasma model taking into account increase of charge carrier number as a result of "temperature" and "pressure" ionization. In contrast to these experiments the multiple shock compression of solid Li, Ca and Na shows strong modification of electron plasma energy spectrum and as a result of that - dielectrization of these elements at megabars. The "plasma" phase transition phenomena are analyzed on the base of shock experiments and quantum Monte-Carlo simulations.

Publ. Astron. Obs. Belgrade No. 84 (2008), 255 *Topical Lecture*

SMART COATING TECHNOLOGY BY GAS TUNNEL TYPE PLASMA SPRAYING

A. KOBAYASHI

Joining and Welding Research Institute, Osaka University
11-1 Mihogaoka, Ibaraki, Osaka 567-0047, Japan
E–mail: kobayasi@jwri.osaka-u.ac.jp

Abstract. Nano-science & technology is one of the most important scientific fields, and the material processing using the nano-technology is now advanced towards more precise and controllable smart stage. Regarding thermal processing, an important key should be the the performance of the applied heat source. A plasma is fundamentally the most superior heat source, because of high temperature, high energy density, easy controllable, etc. Therefore more precious plasma system has been expected for smart thermal processing. The gas tunnel type plasma system developed by the author has high energy density and also high efficiency. The concept and the feature of this plasma system are explained and the applications to the various thermal processing are described in this report.

One practical application is plasma spraying of ceramics such as Al_2O_3 and ZrO_2. The characteristics of these ceramic coatings were superior to the conventional ones. The ZrO_2 composite coating has the possibility of the development of high functionally graded TBC (thermal barrier coating). Another application of gas tunnel type plasma is surface modification of metals. For example the TiN films were formed in a very short time of 5 s.

Now, advanced plasma application of spraying methods as a smart coating technology is expected to obtain the desired characteristics of ceramics such as corrosion resistance, thermal resistance, and wear resistance by reducing the porosity and increasing the coating density. One application of the smart coating technology is a formation of the metallic glass coating with high function, and another is Hydroxiapatite coating for bio-medical application. The formation process of those coatings and the coating characteristics were investigated in this study.

Publ. Astron. Obs. Belgrade No. 84 (2008), 256 - 257 *Topical Lecture*

EXCITATION AND IONISATION DYNAMICS IN HIGH-FREQUENCY PLASMAS

D. O'CONNELL

Centre for Plasma Physics, Queen's University Belfast, Northern Ireland
E–mail: deborah.oconnell@web.de

Abstract. Non-thermal low temperature plasmas are widely used for technological applications. Increased demands on plasma technology have resulted in the development of various discharge concepts based on different power coupling mechanisms. Despite this, power dissipation mechanisms in these discharges are not yet fully understood. Of particular interest are low pressure radio-frequency (rf) discharges.

The limited understanding of these discharges is predominantly due to the complexity of the underlying mechanisms and difficult diagnostic access to important parameters. Optical measurements are a powerful diagnostic tool offering high spatial and temporal resolution. Optical emission spectroscopy (OES) provides non-intrusive access, to the physics of the plasma, with comparatively simple experimental requirements. Improved advances in technology and modern diagnostics now allow deeper insight into fundamental mechanisms.

In low pressure rf discharges insight into the electron dynamics within the rf cycle can yield vital information. This requires high temporal resolution on a nano-second time scale. The optical emission from rf discharges exhibits temporal variations within the rf cycle. These variations are particularly strong, in for example capacitively coupled plasmas (CCPs), but also easily observable in inductively coupled plasmas (ICPs), and can be exploited for insight into power dissipation. Interesting kinetic and non-linear coupling effects are revealed in capacitive systems. The electron dynamics exhibits a complex spatio-temporal structure. Excitation and ionisation, and, therefore, plasma sustainment is dominated through directed energetic electrons created through the dynamics of the plasma boundary sheath.

In the relatively simple case of an asymmetric capacitively coupled rf plasma the complexity of the power dissipation is exposed and various mode transitions can be clearly observed and investigated. At higher pressure secondary electrons dominate the excitation and sustainment of the discharge. As the pressure decreases the discharge operates in so-called 'alpha-mode' where the sheath expansion is responsible for discharge sustainment. Decreasing the pressure towards the limit of operation (below 1 Pa) the discharge operates in a regime where kinetic effects dominate plasma sustainment. Wave particle interactions resulting from the flux of highly energetic electrons interacting with thermal bulk electrons give rise to a series of oscillations in the electron excitation phase space at the sheath edge. This instability is responsible for a significant energy deposit in the plasma when so-called 'ohmic heating' is no longer efficient. In addition to this an interesting electron acceleration mechanism occurs during the sheath collapse. The large sheath width, due to low plasma densities at the lower pressure, and electron inertia allows the build up of a local electric field accelerating electrons towards the electrode.

Multi-frequency plasmas, provide additional process control for technological applications, and through investigating the excitation dynamics in such discharges the limitations of functional separation is observed. Non-linear frequency coupling is observed in plasma boundary sheaths governed by two frequencies simultaneously. In an alpha-operated discharge the

sheath edge velocity governs the excitation and ionisation within the plasma, and it will be shown that this is determined by the time varying sheath width. The nature of the coupling effects strongly depends on the ratio of the applied voltages. Under technologically relevant conditions (low frequency voltage >> high frequency voltage) interesting phenomena depending on the phase relation of the voltages are also observed and will be discussed.

Publ. Astron. Obs. Belgrade No. 84 (2008), 258 *Topical Lecture*

EFFECTS OF TRACES OF MOLECULAR GASES (HYDROGEN, NITROGEN) IN GLOW DISCHARGES IN NOBLE GASES

E. B. M. STEERS[1], P. ŠMÍD[1] and V. HOFFMANN[2]

[1] *London Metropolitan University, 166-220 Holloway Road, London, N7 8DB, UK*
E–mail: e.steers@londonmet.ac.uk
E–mail: p.smid@londonmet.ac.uk

[2] *Leibniz Institute for Solid State and Materials Research Dresden, Helmholtzstraße 20, 01069 Dresden, Germany*
E–mail: V.Hoffmann@ifw-dresden.de

Abstract. The "Grimm" type of low pressure glow discharge source, introduced some forty years ago, has proved to be a versatile analytical source. A flat sample is used as the cathode and placed about 0.2mm away from the end of a hollow tubular anode leading to an obstructed discharge. When the source was first developed, it was used for the direct analysis of solid metallic samples by optical emission spectroscopy (OES), normally with argon as the plasma gas; it was soon found that, using suitable electrical parameters, the cathode material was sputtered uniformly from a circular crater of diameter equal to that of the tubular anode, so that the technique could be used for compositional depth profile analysis (CDPA). Over the years the capability and applications of the technique have steadily increased. The use of rf powered discharges now permits the analysis of non-conducting layers and samples; improved instrumental design now allows CDPA of ever thinner layers (e.g. resolution of layers 5 nm thick in multilayer stacks is possible). For the original bulk material application, pre-sputtering could be used to remove any surface contamination but for CDPA, analysis must start immediately the discharge is ignited, so that any surface contamination can introduce molecular gases into the plasma gas and have significant analytical consequences, especially for very thin layers; in addition, many types of samples now analysed contain molecular gases as components (either as occluded gas, or e.g. as a nitride or oxide), and this gas enters the discharge when the sample is sputtered. It is therefore important to investigate the effect of such foreign gases on the discharge, in particular on the spectral intensities and hence the analytical results.

The presentation will concentrate mainly on the effect of hydrogen in argon discharges, in the concentration range 0-2% v/v but other gas mixtures (e.g. Ar/N_2, Ne/H_2) will be considered for comparison. In general, the introduction of molecular gases can change the discharge impedance, alter the sputtering rate and crater profile and cause changes in the absolute and relative intensities of lines in both the atomic and ionic spectra of the sample element and the plasma gas.

The authors wish to acknowledge financial support from EC funded Analytical Glow Discharge Research Training Network GLADNET, contract no. MRTN-CT-2006-035459. P. Šmíd thanks the Deutsche Forschungsgemeinschaft (Ref 436 TSE 17/7/06) for support while carrying out experiments at IFW Dresden.

Publ. Astron. Obs. Belgrade No. 84 (2008), 259 - 260 *Topical Lecture*

SUPERSHORT AVALANCHE ELECTRON BEAMS AND X-RAY IN HIGH-PRESSURE NANOSECOND DISCHARGES

V. TARASENKO

Institute of High Current Electronics SB RAS, 634055, Tomsk, 2/3, Academichesky
E–mail: VFT@loi.hcei.tsc.ru

Abstract. Since 2003, an interest to investigation of e-beams generation in gas-filled diodes with high pressures has been rekindled. In 2005, the advanced recording methods of electron beams and the use of digital oscilloscopes with wide bandwidth provided the measurements of the beam current duration with time resolution of ∼100 ps. In this paper, the recent measurement results on duration and amplitude of a beam, generated at a nanosecond discharge in different gases have been summarized (Tarasenko et al. 2005, Baksht et al. 2007, Tarasenko et al. 2008). Voltage pulses ∼25, ∼150 and ∼250 kV in amplitude were applied to the gas gap with inhomogeneous electric field. It is presented that the current of supershort avalanche electrons beam (SAEB) recording through a area with a small diameter the pulse duration behind a foil from the gas diode with air at atmospheric pressure is no more than 90 ps. For recording, the pulse shape it is necessary to use a small-sized coaxial collector, loaded to a high-frequency cable, and the same collector is used for taking the charge density distribution over the foil surface in order to determine the SAEB amplitude. The electron distribution over the foil section should be compared with a per pulse distribution. In these experiments, we have compared the distributions obtained per pulse on a RF-3 and luminophore films, placed behind a foil. Besides that, intensity distribution of X-ray radiation at the gas diode output was recorded by using a multi-channel detection device based on microstrip arsenide-gallium detectors of ionizing radiation. An analysis of those data shows that at the beam current duration (FWHM) of ∼90 ps the beam current amplitude behind the 10-μm thickness Al-foil at atmospheric pressure of air is ∼50 A.

Discharge formation and SAEB generation in sulfur hexafluoride and xenon at pressure of 0.01-2.5 atm and helium of 10^{-4}-12 atm have been investigated. The beam of runaway electrons behind 45 μm Al-Be foil was observed at sulfur hexafluoride and xenon pressure up to 2 atm. It was found that the SAEB duration (FWHM) increased with sulfur hexafluoride pressure in the range 1-2 atm. Spectra of a diffuse and contracted discharges in sulfur hexafluoride are presented. Waveforms of the electrons beams generated in helium at pressure 10^{-4}-12 atm were registered. Therewith the electrons beam in helium at p = 12 atm was obtained for the first time. Complex dependence of the electrons beam current amplitude from helium pressure was obtained. Three peaks of the current were observed at pressure 0.01, ∼0.07 and ∼3 atm.

References

Baksht, K. Kh., Tarasenko, V. F., Lomaev, M. I., Rybka, D. V., Tkachev, A. N., and Yakovlenko, S. I.: 2007, Generation regimes for the runaway-electron beam in gas, *Laser Physics*, **17**, 1124.

Tarasenko, V. F., Rybka, D. V., Baksht, E. H., Kostyrya, I. D., Lomaev, M. I.: 2008, Generation and measurement of subnanosecond e-beams in gas-filled diodes, *Prib. Tech. Eksp.*, No. 2, 62.
Tarasenko, V. F., Shpak, V. G., Shunailov, S. A., Kostyrya, I. D.: 2005, Supershort electron beam from air filled diode at atmospheric pressure, *Laser and Particle Beams*, **23**, 545.

Publ. Astron. Obs. Belgrade No. 84 (2008), 261 *Progress Report*

SPECTROSCOPIC STUDY OF HYDROGEN ROTATIONAL, VIBRATIONAL AND TRANSLATIONAL TEMPERATURES IN A HOLLOW CATHODE GLOW DISCHARGE

G. Lj. MAJSTOROVIĆ

Military Academy, 11105 Belgrade, Generala Pavla Jurišića - Šturma 33, Serbia
E–mail: milosavm@ptt.yu

Abstract. Hydrogen hollow cathode glow discharges (HCGD) have been extensively used for study of fundamental discharge processes as well as for wide variety of applications. For instance, recently, this type of discharge was utilized for producing hydrogen by reforming natural gas (da Silva et al. 2006).

The translational or gas kinetic temperature in gas discharges is a parameter of utmost importance in the field of plasma chemistry while vibrationally excited neutral hydrogen molecules play significant role in the chemistry of weakly ionized hydrogen plasmas. This is why the modeling of cold, reactive hydrogen plasma includes rotational and vibrational energy of the hydrogen molecule. This is the reason why we study HC discharge parameters like rotational, translational and vibrational temperature.

Several diagnostic techniques are developed to determine gas kinetic temperature T_g like coherent anti-stokes Raman scattering (CARS), laser-induced fluorescence (LIF) and optical emission spectroscopy (OES). Here we selected OES. This diagnostic technique provides information about atom, molecule and ion density in excited and ground state, as well as rotational, vibrational, and gas temperature including the excitation temperature of certain group of excited levels. The technique is applied for measurements of the rotational T_{rot}, vibrational T_{vib} and determines translational temperatures in a hollow cathode glow discharge in hydrogen. The rotational temperature of excited electron energy levels is determined from the Boltzmann plot of intensities of rotational moleculelar hydrogen lines belonging to Fulcher-α diagonal bands. Following procedure described elsewhere (Astashkevich et al. 2006) the temperature of ground state rovibronic levels is evaluated. The constrains of rotational temperature are discussed in detail. The vibrational temperature is also determined, but from the relative intensities of the H_2 Fulcher-α diagonal bands. The dependence of these temperatures and their radial distribution within HC upon HC wall temperature was determined and discussed (Majstorović et al. 2007).

References

Astashkevich, S. A., Kaning, M., Kaning, E., Kokina, N. V., Lavrov, B. P., Ohl, A., Ropcke, J.: 1979, *J. Quant. Spectrosc. Radiat. Transfer*, **56**, 725.

da Silva, C. F., Ishikawa, T., Santos, S., Alves, Jr. C., Martinelli, A. E.: 2006, *International Journal of Hydrogen Energy*, **31**, 49.

Majstorović, G. Lj., Šišović, N. M., Konjević, N.: 2007, *Plasma Sources Sci. Technol.*, **16**, 750.

Publ. Astron. Obs. Belgrade No. 84 (2008), 262 *Progress Report*

MODELING OF A DIELECTRIC BARRIER DISCHARGE USED AS A FLOWING CHEMICAL REACTOR

D. PETROVIĆ[1,2], T. MARTENS[1], J. VAN DIJK[3], W. J. M. BROK[3], and A. BOGAERTS[1]

[1] *Research group PLASMANT, Dep. of Chemistry, University of Antwerp, Belgium*
E–mail: dragana.petrovic@ua.ac.be

[2] *Institute of Physics, University of Belgrade, Serbia*

[3] *Department of Applied Physics, Eindhoven University of Technology, The Netherlands*

Abstract. The non-thermal character of atmospheric pressure dielectric barrier discharges (DBDs) is one of their main advantages. The fact that they can operate at room temperature while the electrons are still highly energetic enables chemical reactions that thermodynamically would not occur at such low gas temperatures and it makes DBDs efficient plasma-chemical reactors.

Our aim is to develop and optimize a model for a dielectric barrier discharge used as a chemical reactor for gas treatment. In order to determine the optimum operating conditions, we have studied the influence of the gas flow rate, reactor geometry and applied voltage parameters on the discharge characteristics.

For this purpose, a two-dimensional time-dependent fluid model for an atmospheric pressure DBD, as a part of the PLASIMO code (see http://plasimo.phys.tue.nl), has been applied. It is based on the continuity and flux equations for each type of particles treated, the electron energy equation and the Poisson equation. The gas flow is incorporated in the conservation equations as a source term. The set of coupled partial differential equations is solved by the so-called modified strongly implicit method. The background gas flow is numerically treated separately, assuming in the model that there is no influence of the plasma on the flow. Indeed, the gas convection velocity is calculated using the commercial code FLUENT (see http://www.fluent.com) and it is used as input into the 2D fluid model. Details of the model can be found in e.g. Brok et al. 2003, Broks at al. 2005.

The numerical model has been applied to the atmospheric pressure DBD in helium with nitrogen impurities, in a cylindrical geometry. The plasma characteristics have been studied in terms of gas flow rate, applied voltage amplitude and frequency, and geometrical effects. The electric currents and the gap voltage as a function of time for a given applied potential have been obtained, as well as the number densities of plasma species.

References

Brok, W. J. M., van Dijk, J., Bowden, M. D., van der Mullen, J. J. A. M. and Kroesen G. M. W.: 2003, *J. Phys. D: Appl. Phys.*, **36**, 1967.

Broks, B. H. P., Brok, W. J. M., Remy, J., van der Mullen, J. J. A. M., Benidar, A., Biennier, L. and Salama F.: 2005, *Phys. Rev. E*, **71**, (3), 036409.

Publ. Astron. Obs. Belgrade No. 84 (2008), 263 *Progress Report*

DEVELOPMENT, DIAGNOSTIC AND APPLICATIONS OF RADIO-FREQUENCY PLASMA REACTOR

N. PUAČ

Institute of Physics, Pregrevica 118, Belgrade, Serbia
E–mail: nevena@phy.bg.ac.yu

Abstract. In many areas of the industry, plasma processing of materials is a vital technology. Nonequilibrium plasmas proved to be able to produce chemically reactive species at a low gas temperature while maintaining highly uniform reaction rates over relatively large areas (Makabe and Petrović 2006). At the same time nonequilibrium plasmas provide means for good and precise control of the properties of active particles that determine the surface modification. Plasma needle is one of the atmospheric pressure sources that can be used for treatment of the living matter which is highly sensitive when it comes to low pressure or high temperatures (above 40 C). Dependent on plasma conditions, several refined cell responses are induced in mammalian cells (Sladek et al. 2005). It appears that plasma treatment may find many biomedical applications. However, there are few data in the literature about plasma effects on plant cells and tissues. So far, only the effect of low pressure plasmas on seeds was investigated. It was shown that short duration pretreatments by non equilibrium low temperature air plasma were stimulative in light induced germination of Paulownia tomentosa seeds (Puač et al. 2005). As membranes of plants have different properties to those of animals and as they show a wide range of properties we have tried to survey some of the effects of typical plasma which is envisaged to be used in biotechnological applications on plant cells. In this paper we will make a comparison between two configurations of plasma needle that we have used in treatment of biological samples (Puač et al. 2006). Difference between these two configurations is in the additional copper ring that we have placed around glass tube at the tip of the needle. We will show some of the electrical characteristics of the plasma needle (with and without additional copper ring) and, also, plasma emission intensity obtained by using fast ICCD camera.

References

Makabe, T. and Petrović, Z. Lj.: 2006, Plasma Electronics, (Taylor and Francis: New York).

Puač, N., Petrović, Z. Lj., Živković, S., Giba, Z, Grubišić, D., Djordjević, A.: 2005, Plasma Processes and Polymers, (Berlin: Wiley-VCH), 193.

Puač, N., Petrović, Z. Lj., Malović, G., Djordjević, A., Živković, S., Giba, Z., Grubiić, D.: 2006, *J. Phys. D: Appl. Phys.*, **39**, 3514.

Sladek, R. E. J., Stoffels, E.: 2005, *J. Phys. D: Appl. Phys.*, **38**, 1716.

Publ. Astron. Obs. Belgrade No. 84 (2008), 265 - 268 *Contributed Paper*

BALMER ALPHA LINE SHAPE AND SURFACE MORPHOLOGY DURING DEPTH PROFILING ANALYSIS OF THIN FILM

V. STEFLEKOVA, J. JOVOVIĆ, N. M. ŠIŠOVIĆ and N. KONJEVIĆ
Faculty of Physics, University of Belgrade, 11001 Belgrade, P.O. Box 368, Serbia
E–mail: vsteflekova@ff.bg.ac.yu

Abstract. The results of the H_α line shape analysis during depth profiling of zinc thin layer at steel surface (commercial name of materials: galfan and galvanneal) are presented. Changes of the H_α line shape are detected during depth profiling of thin layer in Grimm discharge. An attempt is made to correlate the H_α line shape changes with surface morphology recorded with Atomic Force Microscope (AFM).

1. INTRODUCTION

The shape of Balmer alpha line emitted from a low-pressure gas discharge operated with inert gas-hydrogen mixture exhibits unusual multi component structure (see Gemišić et al. 2003, Šišović et al. 2005) The narrowest part of profile with the Doppler temperature not exceeding 1 eV, and of the middle part of the line profile, with the Doppler temperature less then 10 eV, are related to excited H* atoms generated in collisions of high- energy electron with H_2 molecule.

The profile of the hydrogen Balmer lines, recorded end-on from the Grimm discharge in H_2 and hydrogen-inert gases mixtures, are asymmetric. The explanation of the broadest part-asymmetric pedestal of the line profile comes from the sheath-collision model, see e.g. (Gemišić et al. 2003)and references therein. In this model ions H^+ and H_3^+ are accelerated in a high-voltage cathode sheath and produce fast H atoms in charge transfer/dissociation collisions with the matrix gasmolecular hydrogen. The fast H atoms are then excited and scattered in another collision. The same excitation process is occurring with H atoms backscattered from the cathode. In the Ar-H_2 discharge, the contribution of H^+ion is negligible in comparison with that of H_3^+ion.

The latter ion is fragmentized in collisions with matrix gas or at the cathode where generating H_f atoms of lower energy, and consequently lower energy excited atoms H^* are produced in collisions with matrix gas.

2. EXPERIMENTAL

The Grimm type discharge (anode diameter - 8 mm) is used. This discharge operates in a DC mode using a current stabilized power supply ($0 \div 2$ kV, $0 \div 100$ mA). The

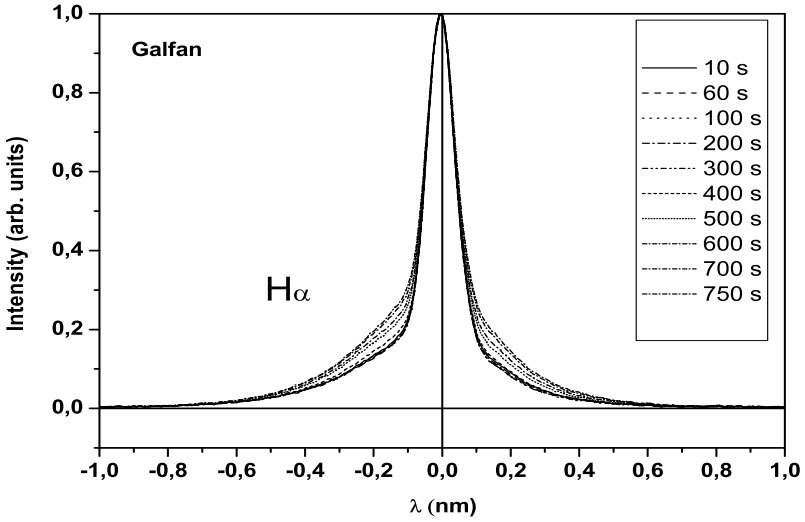

Figure 1: Galfan: The H_α profile versus time of depth profiling;current 42 mA, voltage 780 V and discharge pressure 4,4 mbar.

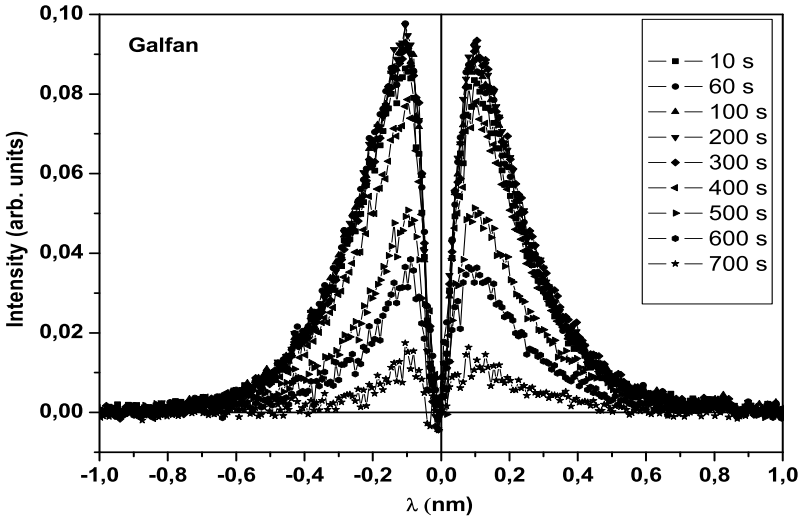

Figure 2: Galfan: Same as in Figure 1 but presented as difference between line profiles in different times of depth profiling.

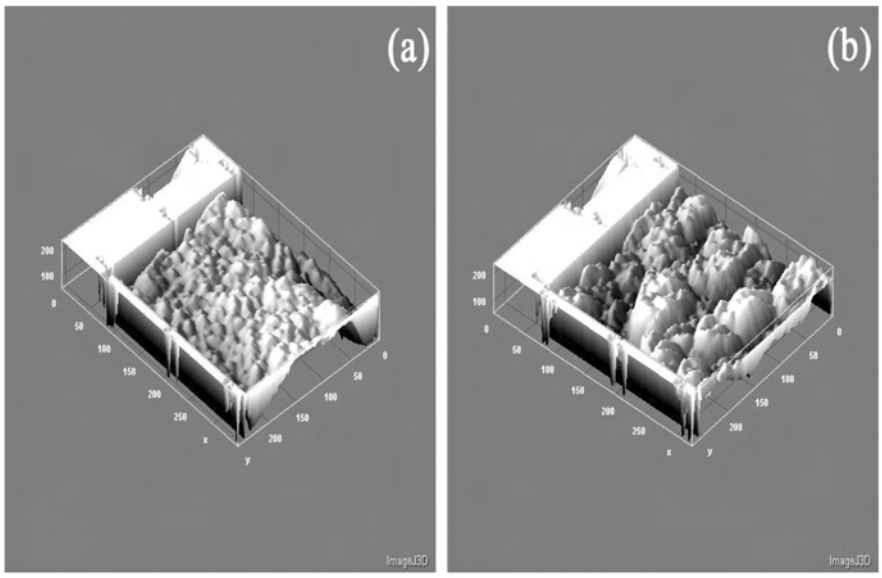

Figure 3: Galfan (i= 42 mA, U=780V, p= 4,4 mbar): (a) sputtering with Ar gas, (b) sputtering with Ar+0.5 %H_2 (AFM).

ballast resistor of 5 kΩ is placed in series with the discharge and DC power supply. During depth profiling current and voltage were kept constant. Since we used constant current power supply, small variations of voltage are corrected with adjustment of pressure (Bengtson et al. 2006). The discharge anode was grounded.

The double stage mechanical vacuum pump insured differential pump out of discharge source. The capacitive pressure gauge was used for pressure measurement in the Grimm source. In this experiment working gas was either pure Ar or gas mixture Ar +0.5 % H_2 vol.

The light along axis of Grimm lamp is focused by an achromat lens (75, 8 mm) onto the entrance slit of spectrometer. To record line spectra 2 m Carl Zeiss PGS-2 spectrometer and CCD detector (Toshiba 1304USB, 3648 channels) is used. The instrumental profile was Gaussian like having full half-width of 0.018 nm. Signals from CCD detector were A/D converted and processed by PC.

3. RESULTS AND DISCUSSION

The object of consideration was hydrogen Balmer alpha line. The shape of this line was recorded at different times of depth profiling and an example for Galfan is presented in Figure 1. Small differences of line shape during depth profiling are evident. In order to illustrate better these changes the difference between line shapes recorded at 10 second and several later times are presented in Figure 2. The AFM photos of thin layer surface for Galfan and Galvaneal are given in Figures 3 and 4, which show changes of the surface structure during depth profiling. Presently attempt

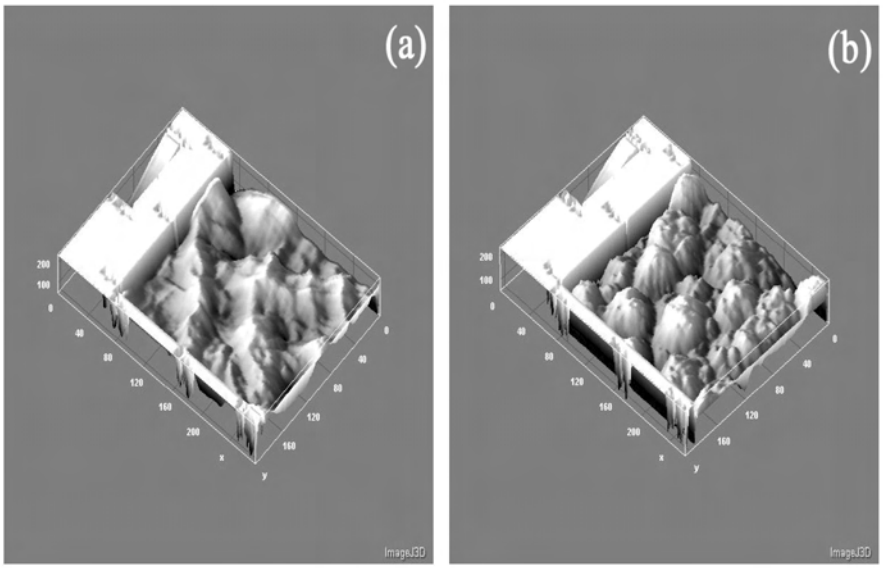

Figure 4: Galvanneal (I=42 mA, U=760V, p=4,4 mbar): (a) sputtering with Ar gas, (b) sputtering with Ar+0.5 % H_2 (AFM).

is beginning made to correlate line shapes, Figure 1 and 2 with surface structure of material, Figures 3 and 4.

Acknwoledgements

The authors thank to Dr. D. Vasilijvić - Radović for help with AFM samples analysis. This work is supported by the Ministry of Science of the Republic of Serbia (Project # 141032B) and EC (GLADNET, Project # 035459 and NANOLABFOR, Project # 026303).

References

Bengtson, A., Nelis, T.: 2006, *Analitical and Bioanalitical Chemistry*, **385**(3), 568.
Gemišić-Adamov, M. R., Obradović, B. M., Kuraica, M. M., Konjević, N.: 2003, *IEEE Trans. Plasma Sci.*, **31**, 444.
Šišović, N. M., Majstorović, G. Lj., Konjević, N.: 2005, *Eur. Phys. J. D*, **32**, 347.

Publ. Astron. Obs. Belgrade No. 84 (2008), 269 - 272 *Contributed Paper*

DOPPLER SPECTROSCOPY OF THE HYDROGEN BALMER BETA LINE IN A WATER VAPOUR HOLLOW CATHODE GLOW DISCHARGE

J. JOVOVIĆ, N. M. ŠIŠOVIĆ and N. KONJEVIĆ

Faculty of Physics, University of Belgrade, 11001 Belgrade, P.O. Box 368, Serbia
E–mail: jjovica@ff.bg.ac.yu

Abstract. The Doppler broadened H_β line profiles are recorded from a hollow cathode glow discharge (HCGD) operated with water vapour. The results revealed the existence of two components of the line profile, i.e. the narrow component and the broad one. The average kinetic energy (temperature) of excited hydrogen atoms in the center of the discharge are around 0.3 eV for the narrow component, and 3 eV for the broad one, respectively.The radial distribution shows slight monotonic increase of H^* temperature, from the center towards cathode wall.

1. INTRODUCTION

The electron impact disociative excitation of the H_α water vapor molecule was studied using Doppler profile measurements of the hydrogen Balmer alpha line shapes emitted in electron $\rightarrow H_2O$ molecule (Kouchi et al. 1979). The Doppler profiles consisted of two components, the narrow component and the broader one. This result indicates that there are two kinds of precursors leading to excited hydrogen atoms, H^*(n=3) contributing to the H_α emission. The average kinetic energies of H^*(n=3) are (0.4 $\pm$ 0.2) eV and (4 $\pm$ 1) eV for the narrow and broad component respectively. The authors analyzed numerous dissociation processes responsible for the production of the H_α emission (see Table 2 in Kouchi et al. 1979) and selected two responsible for narrow and broad component:

$$H_2O^{**}(\approx 18eV) \rightarrow H^*(n=3)(Ek=0.4eV) + OH(X^2\Pi)$$

$$H_2O^{***}(\approx 25-30eV) \rightarrow H^*(n=3)(Ek\approx 4eV) + (O(2p^4)H(n=1)$$

or

$$H_2O^{***}(\approx 25-30eV) \rightarrow H^*(n=3)(Ek\approx 4eV) + OH^*(B^2\Sigma^+)$$

The values in the parantheses after H_2O^{**} and H_2O^{***} are their internal energies, respectively. Since the first adiabatic ionization potential of H_2O is 12.6 eV, both H_2O^{**} and H_2O^{***} are superexcited states. The detailed study of $e \rightarrow H_2O$ interaction and the major processes responsible for the formation of excited hydrogen atoms

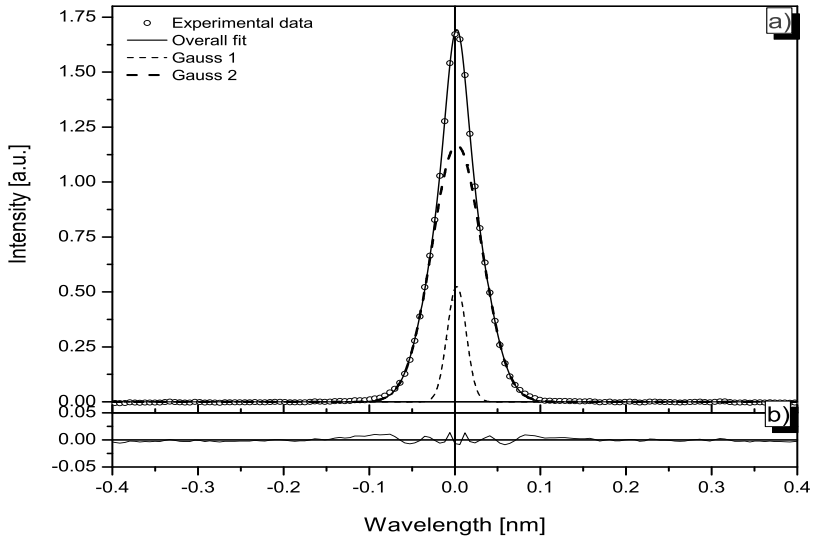

Figure 1: a) The typical H_β line profile recorded in a center of the hollow cathode glow discharge with a stainless steel cathode fitted with two Gaussians; b) residual plot.

from water, can be found elsewhere (see Kurawaki et al. 1983). Here, we report results of the hydrogen Balmer beta line shapes study in a stainless steel and copper hollow cathode glow discharge operated in water vapour.

2. EXPERIMENTAL

In experiments with water vapour we used the HCGD source with cylindrical stainless steel (SS) or copper (Cu) cathode and with two symmetrically positioned molybdenum anodes. The hollow cathode (HC) was 100 mm long with 6 mm internal diameter and 1 mm wall thickness. The construction details of the HCGD source are presented elsewhere (Šišović et al. 2005). The glassy container filled with bidistillated water was used as a water vapour generator. The spectral line shape recordings were realized with 2 m spectrometer (equipped with 651 g/mm reflection grating) having 0.74 nm/mm reciprocal dispersion in first diffraction order. The instrumental profile is Gaussian, with full half-width of approximately 0.018 nm. The discharge image, 1:1 magnification, was projected with an achromatic lens (focal length 75.8 mm), onto the entrance slit of the spectrometer. Signals from the CCD detector (3648 channels, pixel size 8 μm) are A/D converted, collected and processed by PC.

3. RESULTS AND DISCUSSION

The experiments were realized under the following discharge conditions: the pressure of 0.74 mbar, current 60 mA and voltage of 378 V and 327 V with SS and Cu hollow

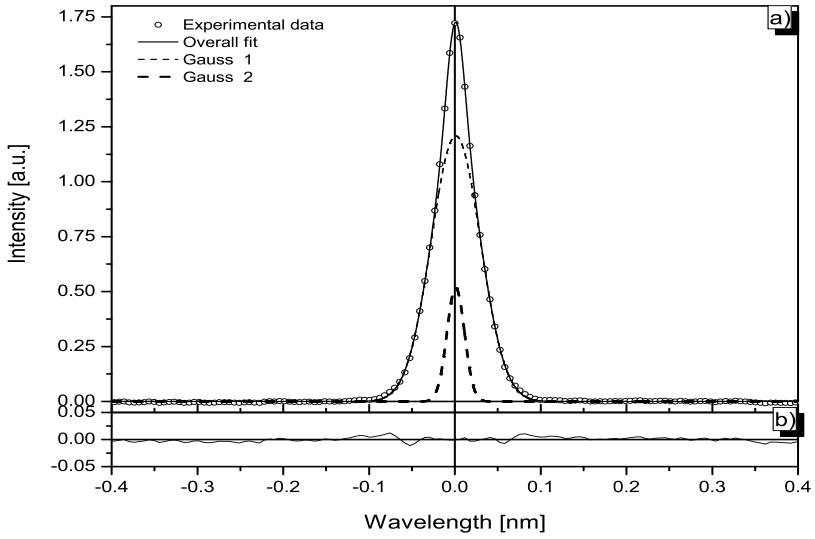

Figure 2: Same as Figure 1, but for Cu cathode. (a) Typical H_β line profile recorded in a center of the hollow cathode glow discharge with a copper cathode fitted with two Gaussians; b) residual plot.

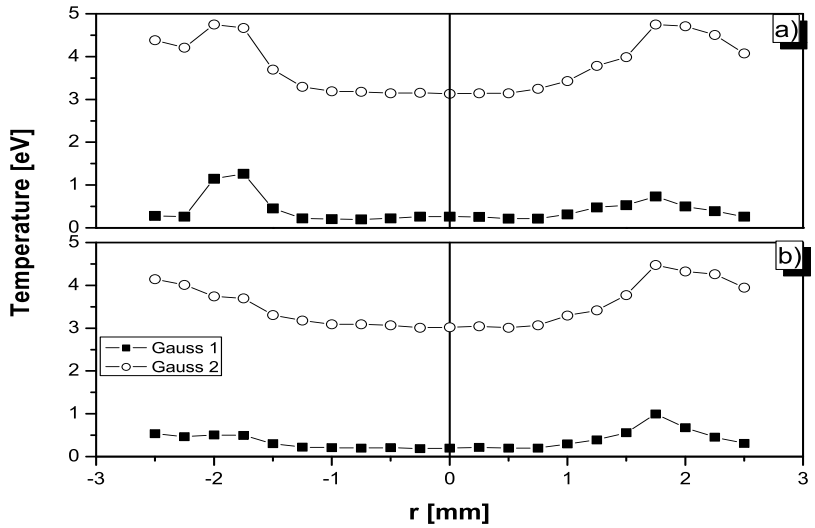

Figure 3: Temperature distribution of the H^* atoms derived from Gauss 1 and Gauss 2 component in a glow discharge with a) SS and b) Cu hollow cathode.

cathode, respectively. The typical H_β profile with SS and Cu cathode is presented in Fig. 1 and Fig. 2, respectively, together with best fit curve composed of two Gaussians. This result differs from earlier profiles with these two HC operated with hydrogen isotopes or hydrogen-inert gas mixtures where three Gaussians were needed (see Figs. 2-7 and Tables 1 and 2 in Šišović et al. 2005 and Šišović et al. 2007). This time largest width Gaussian related to anomalous Doppler broadening is missing. This is in agreement with the recent radio frequency (RF) excited experiment in water vapour flow (Mills et al. 2005). The full half-width of Gaussian components of the overall fit presented in Figure 1 are 0.026 nm and 0.068 nm, and 0.024 nm and 0.067 nm for those presented in Figure 2. Temperature of excited hydrogen atoms, derived from above values are 0.26 eV and 3.1 eV, and 0.2 eV and 3 eV for the discharge operated with SS and Cu cathode, respectively. The comparison of temperature radial distribution of H^* atoms originating from both excitation processes in HCGD for these two cathodes are presented in Figure 3. One should notice the linear increase in temperature from the center towards HC wall. Such behavior is a consequence of electric field radial distribution in HCGD, which is largest close to the HC wall (see Hirose and Masaki 1988). The maximum temperature value lies between 1.75 and 2 mm from the HC center and has the value in the range ($0.75 \div 1$ eV) for the first, and ($4 \div 4.5$ eV) for the second excitation process. The radial distributions in Figure 3 shows marginal difference in values in tendency of H^* atoms temperature change between SS and Cu HCGD.

Acknwoledgements

This work is supported by the Ministry of Science of the Republic of Serbia (Project # 141032B) and EC (FP-6 Project # 026303).

References

Hirose, C., Masaki T.: 1988, *Appl. Spectrosc.*, **5**, 42.
Kouchi, N., Ito, K., Hatano, Y.,Oda, N., Tsuboi, T.: 1979, *Chem. Phys.*, **36**, 239.
Kurawaki, J., Ueki, K.,Higo M., Ogawa, T.: 1983, *J. Chem. Phys.*, **78**, 3071.
Mills, R. L., Dhandapani B., Akhtar K.: 2008, *Int. J. Hydrogen Energy*, **33**, 802.
Šišović, N. M., Majstorović, G. Lj., Konjević, N.: 2005, *Eur. Phys. J. D*, **32**, 347.
Šišović, N. M., Majstorović G. Lj. and Konjević, N.: 2007, *Eur. Phys. J. D*, **41**, 143.

Publ. Astron. Obs. Belgrade No. 84 (2008), 273 - 275 *Contributed Paper*

Xe III SPECTRAL LINES WIDTH MEASUREMENTS

S. DJUROVIĆ[1], R. J. PELÁEZ[2], M. ĆIRIŠAN[1], J. A. APARICIO[2] and S. MAR[2]

[1] *Faculty of Sciences, Department of Physics, Trg Dositeja Obradovića 4, 21000 Novi Sad, Serbia*

[2] *Departamento de Fisica Teórica y Óptica, Facultad de Ciencias, Universidad de Valladolid, 47071 Valladolid, Spain*

Abstract. Stark halfwidths of 10 Xe III spectral lines have been measured and compared with experimental results by other authors, as well as with modified semiempirical calculations. The measurements were performed in a pulsed arc plasma.

1. INTRODUCTION

Investigation of ionized xenon spectra is of interest for many physics areas: laser physics, fusion diagnostics, spectroscopy, astrophysics etc. Stark parameters of spectral lines are usually used for plasma diagnostic purposes and also for testing the theoretical calculations. Stark width data are also very important for higher electron density plasmas, because in this regime Stark broadening is dominant in comparison with other broadening mechanisms. In this work, we examined ionized xenon lines, most of them belonging to the UV region. The Stark halfwidths of 10 Xe III spectral lines from 5d – 6p, 6s – 4f, 5d – 4f, 6s – 6p and 6p – 6d transition arrays were measured. Present results were compared with other experimental results (Konjević and Pittman 1987, Iriarte et al. 1997, Romeo et al. 1998). Comparison with modified semiempirical calculations based on (Dimitrijević and Konjević 1980) were also performed in some cases.

2. EXPERIMENTAL DATA AND DIAGNOSTICS

Experimental apparatus and diagnostic methods are described elsewhere (Mar et al. 2000, Djurović et al. 2006). Herein, only minimal details will be given. Excitation unit contains capacitor bank of 20 μF, charged up to 9.2 kV. The mixture of He-Xe at a pressure of $3.0 \cdot 10^3$ Pa continuously flows through the discharge lamp. Plasma electron density $(0.2 - 1.86) \cdot 10^{23}$ m^{-3} was determined by two-wavelength interferometrical method, with an error band lower than 10%. The electron temperature (17000 – 29000) K was determined by Boltzmann plot. Estimated error for temperature determination is lower than 15%.

3. RESULTS AND DISCUSSION

An example of recorded spectrum containing Xe III 376.585 nm and 377.253 nm lines is shown in Fig. 1. The spectra were fitted to a sum of Lorentzian functions (for spectral lines) and a linear function (for continuum emission).

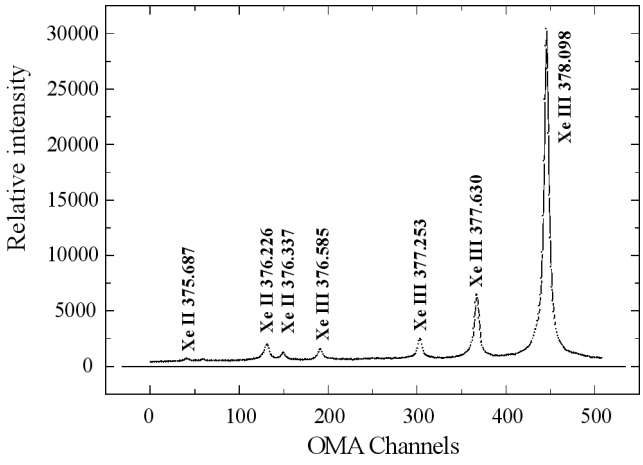

Figure 1: Example of one part of Xe spectrum and its fit.

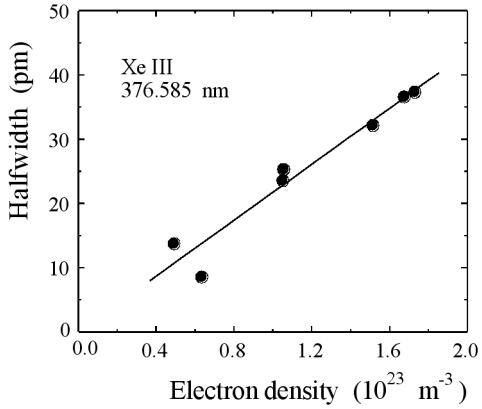

Figure 2: Example of line halfwidth vs. electron density and its linear fit.

The measured Stark halfwidth data are given in Table 1. In the two first columns, transitions and wavelengths of the lines are given. Next two columns present measured Stark halfwidths and comparison with calculations based on modified semiempirical formula (Dimitrijević and Konjević 1980) for the lines where all necessary data for the calculations were available. For semiempirical calculations jK-coupling scheme was used. The agreement is satisfactory.

Table 1: Experimental Stark halfwidths of Xe III lines (w_m) for T_e = 22000 K. Estimated accuracy is A (15-25%) and B (25-30%). The data are compared with modified semiempirical calculations (Dimitrijević and Konjević 1980, w_{th}) and with other experimental results (w) (1- Konjević and Pittman 1987, 2- Iriarte et al. 1997, Romeo et al. 1998). These data are given for corresponding electron temperatures. All data are normalized to the electron density of $N_e = 10^{23}$ m^{-3}.

Transitions	λ (nm)	w_m (pm)	Acc.	$\frac{w_m}{w_{th}}$	Other authors results		
					T (10^3K)	w (pm)	Ref.
(^{2}D^o)5d ^{3}F^o - (^{2}D^o)6p ^{3}F	308.353	15.36	B		29	32.09	3
(^{2}D^o)6s ^{3}D^o - (^{4}S^o)4f ^{5}F	360.702	16.95	B		27	16.40	1
					29	31.98	3
	360.946	17.23	A				
(^{2}P^0)5d ^{1}D^o - (^{4}S^o)4f ^{5}F	333.165	18.38	A		29	25.90	3
(^{2}P^o)5d ^{3}P^o - (^{2}D^o)6p ^{3}P	365.461	21.22	A		29	24.49	3
(^{2}D^o)6s ^{1}D^o - (^{2}D^o)6p ^{1}F	467.367	36.07	B	0.77	29	36.10	2
(^{2}P^o)6s ^{3}P^o - (^{2}P^o)6p ^{3}P	363.214	23.13	B	0.91	29	32.98	2
	376.585	23.85	B	0.86	29	37.26	2
(^{2}P^o)6s ^{1}P^o - (^{2}P^o)6p ^{1}P	377.253	24.46	A		29	39.80	2
(^{2}D^o)6p ^{3}P - (^{2}D^o)6d ^{3}P^o	328.791	41.14	B				

The estimated errors for Stark widths given in Table 1, might seem a bit high, but one should bear in mind that we have investigated low intensity lines. There is a very good agreement with Konjević and Pittman 1987 result. On the other hand, there is an obvious disagreement with the two other experimental results (Iriarte et al. 1997, Romeo et al. 1998). The reason of this discrepancy is discussed in (Peláez et al. 2006). Two results, for 360.946 nm and 328.791 nm, are new and there were no available data for comparison.

Stark width of Xe III 376.585 nm line as a function of electron density is plotted, as an example, in Fig. 2. It is obvious that there is a clear linear trend.

References

Dimitrijević, M. S., Konjević, N.: 1980, *J. Quant. Spectrosc. Radiat. Transfer*, **37**, 451.

Djurović, S., Peláez, R. J., Ćirišan, M., Aparicio, J. A., Mar, S.: 2006, *J. Phys. B*, **39**, 2901.

Iriarte, D., Romeo y Bidegain, M., Bertuccelli, G., Di Rocco, H. O.: 1997, *Physica Scripta*, **55**, 181.

Konjević, N., Pittman, T. L.: 1987, *J. Quant. Spectrosc. Radiat. Transfer*, **37**, 311.

Mar, S., Aparicio, J. A., de la Rosa, M. I. del Val, J. A., Gigosos, M. A., Perez, C.: 2000, *J. Phys. B*, **33**, 1169.

Peláez, R. J., Ćirišan, M., Djurović, S., Aparicio, J. A., Mar, S.: 2006, *J. Phys. B*, **39**, 5013.

Romeo y Bidegain, M., Iriarte, D., Bertuccelli, G., Di Rocco, H. O.: 1998, *Physica Scripta*, **57**, 495.

Publ. Astron. Obs. Belgrade No. 84 (2008), 277 - 279 *Contributed Paper*

STARK SHIFTS FOR SEVERAL Xe II UV LINES

M. ĆIRIŠAN[1], R. J. PELÁEZ[2], S. DJUROVIĆ[1], J. A. APARICIO[2] and S. MAR[2]

[1] *Faculty of Sciences, Department of Physics, Trg Dositeja Obradovića 4, 21000 Novi Sad, Serbia*

[2] *Departamento de Fisica Teórica y Óptica, Facultad de Ciencias, Universidad de Valladolid, 47071 Valladolid, Spain*

Abstract. In this paper, new results concerning Stark shifts of six Xe II spectral lines are presented. One of the experimental results is compared with modified semiempirical calculations. In this work, pulsed arc was used as a plasma source.

1. INTRODUCTION

Stark broadening and shift of Xe II UV spectral lines have been a subject of many experimental (Konjević et al. 1984, 1990, 2002 and References therein) and theoretical studies (Popović and Dimitrijević 1996, Di Rocco 1990). Examination of an ionized xenon spectrum is important for laser techniques, light sources, astrophysics etc. The results of Stark shift measurements for six Xe II spectral lines given in this paper, are reported here for the first time. Three of these lines belong to 6p – 6d and two to 6s – 7p transitions. These data can be used for diagnostic purposes, demonstration of regularities and similarities of the line shifts within the multiplets or transition arrays and for theory testing.

2. EXPERIMENTAL

Experimental apparatus and diagnostic methods are described elsewhere (Mar et al. 2000, Djurović et al. 2006). Herein, only minimal details will be given. Excitation unit contains capacitor bank of 20 μF, charged up to 9.2 kV. The mixture of He-Xe at a pressure of $3.0 \cdot 10^3$ Pa continuously flows through the discharge lamp. Plasma electron density $(0.2 - 1.86) \cdot 10^{23}$ m^{-3} was determined by two-wavelength interferometric method, with an error band lower than 10%. The electron temperature (17000 – 29000) K was determined by Boltzmann plot. Estimated error for temperature determination is lower than 15%. Spectra were recorded using a spectrometer equipped with an optical multichannel analyzer detector with 512 channels. Exposure times were usually 5 μs.

3. RESULTS AND DISCUSSION

An example of recorded spectrum containing Xe III 328.126 nm line is shown in Fig. 1. The spectra were fitted to a sum of Lorentzian functions (for spectral lines) and a linear function (for continuum emission).

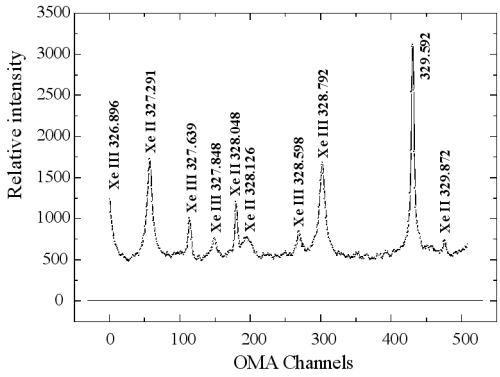

Figure 1: Example of one part of Xe spectrum and its fit.

The measured Stark shift data are given in Table 1. In the first two columns, configurations and Terms of the lines are given. Next two columns contain lines wavelengths and measured Stark shifts. All Stark shift data are new and presented here for the first time. Only one comparison with calculations based on modified semiempirical formula (Dimitrijević and Kršljanin 1986) was made. That was the only case where complete set of perturbing levels necessary for the calculations was available. For semiempirical calculations jK-coupling scheme was used. The agreement is satisfactory.

Table 1: Experimental Stark shifts of Xe II UV lines (d_m) for $T_e = 22000$ K. Estimated accuracy is about 30%. The result for 316.527 nm line is compared with modified semiempirical calculations (Dimitrijević and Kršljanin d_{th}). All data are normalized to electron density of $N_e = 10^{23}$ m^{-3}.

Configurations	Terms	λ (nm)	d_m (pm)	$\frac{d_m}{d_{th}}$
$5p^4$ (^{3}P$_0$) $6s$ – $5p^4$ (^{1}D$_2$) $6p$	$[0]_{1/2}$ - $[1]^\circ_{1/2}$	316.527	- 4.2	0.89
$5p^4$ (^{3}P$_2$) $6p$ – $5p^4$ (^{3}P$_0$) $6d$	$[1]^\circ_{1/2}$ - $[2]_{3/2}$	328.126	26.9	
$5p^4$ (^{1}D$_2$) $6s$ – $5p^4$ (^{3}P$_2$) $7p$	$[2]_{5/2}$ - $[1]^\circ_{3/2}$	337.392	-18.6	
$5p^4$ (^{1}D$_2$) $6s$ – $5p^4$ (^{3}P$_2$) $7p$	$[2]_{5/2}$ - $[3]^\circ_{7/2}$	331.348	-11.4	
$5p^4$ (^{3}P$_2$) $6p$ – $5p^4$ (^{3}P$_2$) $6d$	$[2]^\circ_{3/2}$ - $[3]_{5/2}$	366.170	53.5	
$5p^4$ (^{3}P$_2$) $6p$ – $5p^4$ (^{3}P$_1$) $6d$	$[1]^\circ_{3/2}$ - $[2]_{5/2}$	338.630	28.5	

The estimated errors for Stark shifts given in Table 1 might seem a bit high, but one should bear in mind that we have investigated very low intensity lines.

Stark shift of Xe II 328.126 nm line as a function of electron density is plotted, as an example, in Fig. 2. It is obvious that there is a clear linear trend.

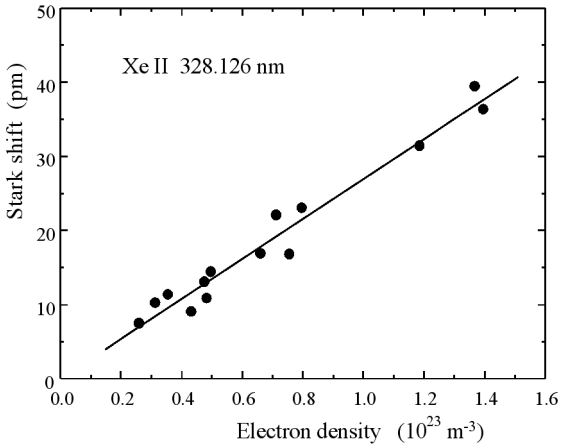

Figure 2: Example of Stark shift vs. electron density and its linear fit.

References

Di Rocco, H. O.: 1990, *Nuevo Cimento*, **12**, D, 1485.
Dimitrijević, M. S., Kršljanin, V.: 1986, *Astron. Astrophys.*, **165**, 269.
Djurović, S., Peláez, R. J., Ćirišan, M., Aparicio, J. A., Mar, S.: 2006, *J. Phys. B*, **39**, 2901.
Konjević, N., Dimitrijević, M. S., Wiese, W. L.: 1984, *J. Phys. Chem. Data*, **13**, 649.
Konjević, N., Wiese, W. L.: 1984, *J. Phys. Chem. Data*, **19**, 1307.
Konjević, N., Lesage, A., Fuhr, J. R., Wiese, W. L.: 1984, *J. Phys. Chem. Data*, **31**, 819.
Mar, S., Aparicio, J. A., de la Rosa, M. I. del Val, J. A., Gigosos, M. A., Perez, C.: 2000, *J. Phys. B*, **33**, 1169.
Popović, L. Č., Dimitrijević, M. S.: 1996, *Astron. Astrophys. Suppl. Ser.*, **116**, 359.

Publ. Astron. Obs. Belgrade No. 84 (2008), 281 - 284 *Contributed Paper*

USE OF THE VAN DER WAALS BROADENING OF ATOMIC ARGON LINES TO MEASURE THE GAS TEMPERATURE IN AN ATMOSPHERIC PRESSURE Ar-He SURFACE WAVE DISCHARGE

J. MUÑOZ[1], M. S. DIMITRIJEVIĆ[2], C. YUBERO[1] and M. D. CALZADA[1]

[1] *Grupo de Espectroscopía de Plasmas. Edificio A. Einstein (C-2), Campus de Rabanales. Universidad de Córdoba, 14071 Córdoba, Spain*
E–mail: fa1cazal@uco.es

[2] *Astronomical Observatory, Volgina 7, 11160 Belgrade, Serbia*

Abstract. The use of the van der Waals broadening to measure the gas temperature in an atmospheric pressure Ar-He surface-wave discharge is studied comparing the obtained results with those given by the OH radical and extended to He proportions up to 50%. Influence of the electron density through Stark broadening of the calculation of this parameter is found to be negligible. A good agreement is found between both techniques. Spectral line 603.2 nm is found to be the best choice for this purpose. An increase in the temperature from 1200 K to 2000 K is found when He is added to the discharge.

1. INTRODUCTION

A common characteristic of most of the technological applications of plasmas is that they are carried out with gas mixtures. When more than one kind of gas is present in the discharge, the complexity of experimental determination of plasma parameters by spectroscopic techniques increases as a consequence of the existence of different types of species in the discharge. Studying such influences is important for the application of diagnosis techniques in plasmas generated with gas mixtures. Usually, the gas temperature (T_g) is measured from the analysis of the rotational spectra of molecular species existing in the discharge, such as the OH species, N_2^+, CN or C_2. But sometimes, as is the case of the Ar-He microwave plasma studied herein, these species can not be properly detected. In such cases, T_g can be determined from the Doppler or the van der Waals broadenings of emitted atomic spectral lines, which are related to this parameter.

While theoretically any spectral line could be used for the determination of T_g from its van der Waals broadening (w_W), studies carried out by several authors (see J. Muñoz et al. (to be published) and references therein) have stated that only a few lines can be used for this purpose. On the other hand, the theory does not describe equally well the van der Waals broadening for each spectral line and for each kind of perturbers, and so investigations devoted to find out most convenient lines for this purpose are of interest.

A method to measure the gas temperature T_g from atomic lines whose Stark broadening is comparable with the van der Waals one was proposed by Yubero et al. (2007). Gas temperature was obtained from the origin ordinate corresponding to the Lorentzian width for zero electron density which could be considered approximately equal to van der Waals line width. The best argon atomic lines for the gas temperature T_g calculation in an argon microwave plasma at atmospheric pressure were found to be 603.2 nm, 549.6 nm and 522.1 nm. On the other hand, in the study of Christova et al. (2004) the Stark broadening of the 425.9 nm line was examined. By extrapolating the results of this work to their experimental conditions, Yubero et al. obtained that the van der Waals width value of the above mentioned line as about 90% of the total Lorentzian width and the gas temperature from the van der Waals broadening of this line was equal to 1380 K. Consequently, the use of $425.9, 603.2, 549.6$ and 522.1 nm lines to measure T_g in an Ar-He SWD has been considered in the present study.

In this work, the use of the van der Waals broadening of the atomic lines to determine the gas temperature in Ar-He plasmas, taking into account both argon and helium atoms as perturbers has been analyzed in an atmospheric pressure surface wave discharge with a setup similar to that described in the work of J. Muñoz et al. (2008). The values of the gas temperature inferred from this broadening have been compared with the ones obtained from the spectra emitted by the OH molecular species in the discharges.

2. GAS TEMPERATURE DETERMINATION

The Lorentzian width can be considered as the sum of the Stark and the van der Waals broadenings under our experimental conditions. The Stark broadening of these lines was estimated using the expression given by Griem (1964) for the electron density, calculated for different Ar-He mixtures from the H_β line using the data from Gigosos et al.(1996).

Table 1: Van der Waals and Lorentzian broadenings of the 603.2 atomic argon line for the different He concentration in the discharge

[He](%)	w_S (x 10^{-2} nm)	w_L (x 10^{-2} nm)
0	0.154	2.915
5	0.134	2.632
10	0.110	2.363
15	0.108	2.091
20	0.099	1.999
25	0.096	1.964
30	0.094	1.949

In Table 1, the values of the 603.2 nm Lorentzian width and the Stark broadening for the studied Ar-He mixtures are shown. One observes that w_S is one order lower than w_L. So, the assumption that w_L is mainly due to the van der Waals effect does not induce a significant error in the calculation of T_g. A similar result was obtained for

the 425.9 nm line. Following from Yubero et al. (2007), the van der Waals broadening of these two lines in the case of an Ar-He mixed gas discharge as can be written as:

$$w_W(425.9\,\mathrm{nm}) = \chi_{Ar}\frac{1.479}{T_g^{0.7}} + \chi_{He}\frac{1.059}{T_g^{0.7}} \tag{1}$$

$$w_W(603.2\,\mathrm{nm}) = \chi_{Ar}\frac{4.217}{T_g^{0.7}} + \chi_{He}\frac{3.019}{T_g^{0.7}} \tag{2}$$

Values of T_g obtained using the expressions above can be seen in Figure 1. There, T_g values have been compared with those ones obtained considering $\chi_{He} = 0$ and with the ones obtained from the OH molecular specie.

From these figures, it can be seen that the T_g values obtained from OH radical only experience a little variation when He is added in a 5% in the mixture and, from this percentage on, the temperature keeps almost constant at 1500 K. This can be due to a lack of sensitivity of the OH radical for temperatures above $1600 - 1800$ K.

A larger dispersion in T_g values obtained from the 425.9 nm line can be observed compared to those obtained from the 603.2 nm line. This is a consequence of its smaller Lorentzian width, which results in a higher error in the deconvolution process. Consequently, the 603.2 nm line should be considered more appropriate for the purpose of obtaining the gas temperature from its van der Waals broadening.

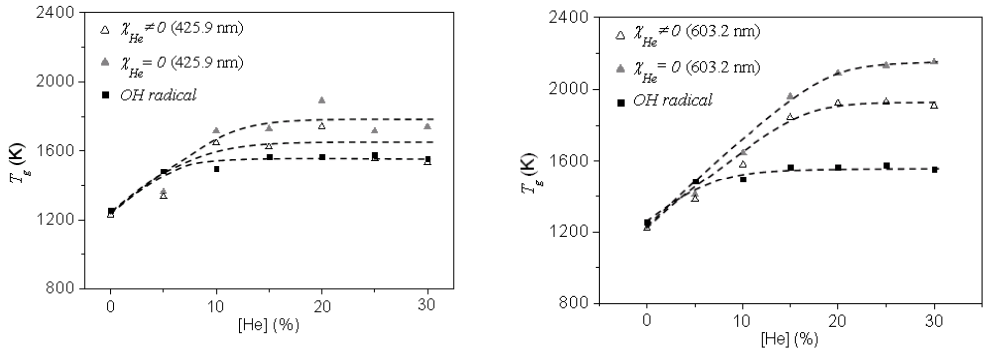

Figure 1: Gas temperature calculated using the $(0 - 0)$ 309 nm rovibrational band of the OH radical and 425.9 nm (left) and 603.2 nm (right) atomic argon lines taking into account (hollow triangle) and neglecting (full triangle) the contribution of He to the van der Waals broadening.

It is important to remark that, even while the larger difference in T_g temperatures obtained taking into account the influence of Helium in the van der Waals broadening in equations (1) and (2) is only about 300 K, the new term added to the equations in the case of gas mixtures shall not be rejected, specially for higher He proportions.

The measurement of T_g in a discharge generated with Ar-He mixtures for He percentages over 30% was carried out using the van der Waals broadening of the 603.2 nm atomic line, following the procedure proposed previously.

In order to verify the non-influence of the coolant used, the gas temperature were also calculated for the interval between 0% and 30% of He in the mixture. In Figure

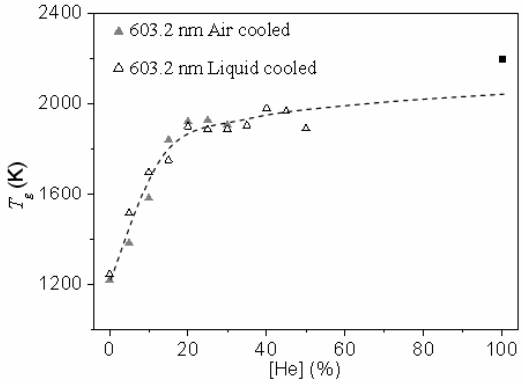

Figure 2: Gas temperature calculated using the van der Waals broadening of the 603.2 nm argon atomic line.

2, the T_g values obtained in this way are shown. It can be seen that the same values for this parameter are obtained in both cases, using air or dielectric liquid as coolant of the discharge tube. An extrapolation to 100% of He is shown too, the T_g value for a pure He discharge obtained in this way being approximately equal to 2200 K, which is in a good agreement with that obtained in Kabouzi et al. (2002).

Acknowledgements

This work was supported by the Ministry of Science and Technology (Spain) within the framework of the project no. ENE2005-00314, and by the Ministry of Science of Serbia through the project 146001.

References

Christova, M., Castaños–Martínez, E., Calzada, M. D., Kabouzi, Y., Luque, J. M. and Moisan, M.: 2004, *Appl. Spectrosc.*, **58**, 1032.

Gigosos, M. A., Cardeñoso, V.: 1996 *J. Phys. B: At. Mol. Opt. Phys.*, **29**, 4795.

Griem, H. R.: 1974, Spectral Line Broadening by Plasmas, Academic Press (London).

Kabouzi, Y., Calzada, M. D., Moisan, M., Tran, K. C. and Trassy, C.: 2002, *J. Appl. Phys.*, **91**, 1008.

Muñoz, J., Calzada, M. D. : 2008, *Journal of Physics D*, (accepted).

Muñoz, J., Dimitrijević, M. S., Yubero, C., Calzada, M. D.: to be published.

Yubero, C., Dimitrijević, M. S., García, M. C., Calzada, M. D.: 2007, *Spectrochim. Acta B*, **62**, 169.

Publ. Astron. Obs. Belgrade No. 84 (2008), 285 - 288 *Contributed Paper*

THE INFLUENCE OF THE SECONDARY ELECTRON EMISSION COEFFICIENT AND EFFECT OF THE GAS HEATING ON THE CALCULATED ELECTRICAL CHARACTERISTICS OF A GRIMM TYPE GLOW DISCHARGE CELL

A. DERZSI[1], Z. DONKÓ[1], A. BOGAERTS[2] and V. HOFFMANN[3]

[1] *Research Institute for Solid State Physics and Optics, Konkoly-Thege M. 29-33, H-1121 Budapest, Hungary*
E–mail: derzsi@sunserv.kfki.hu
E–mail: donko@sunserv.kfki.hu

[2] *Department of Chemistry, University of Antwerp, Universiteitsplein 1, B-2610 Wilrijk-Antwerp, Belgium*
E–mail: annemie.bogaerts@ua.ac.be

[3] *Institut für Festkörper- und Werkstoffforschung Dresden, Postfach 270116, D-01171 Dresden, Germany*
E–mail: V.Hoffmann@ifw-dresden.de

Abstract. Electron emission properties of cathode surfaces affect considerably the electrical characteristics of glow discharges. Using a heavy-particle hybrid model in 2 dimensions, we investigate the influence of the secondary electron emission coefficient γ on the calculated discharge characteristics for both 'clean' and 'dirty' cathode surface conditions, and assuming a constant γ parameter as well. The effect of the gas heating and the role of the heavy particles reflected from the cathode on this process is also studied.

1. INTRODUCTION

Modeling is a powerful method to gain a better understanding of the relevant plasma processes in gas discharges and of the behavior of different plasma species under various discharge configurations. Hybrid models – combining the particle simulation of fast plasma species with the fluid treatment of slow plasma particles (Boeuf and Pitchford 1991, Bogaerts et al. 1995) – have successfully been applied for the modeling of various low pressure dc discharges to obtain the potential distribution, the densities, energies and fluxes of the plasma species in a self-consistent way.

In order to reproduce the various discharge characteristics, a correct set of input data has to be specified in the modeling calculations. At this point, the secondary electron emission coefficient of the cathode is a relatively fuzzy parameter, and is often considered to be constant in the literature. Secondary electron emission yields, on the other hand, vary with the surface conditions and with the energy of particles bombarding the cathode (Phelps and Petrović 1999). Energy-dependent electron yield

data for the different plasma species can be used to calculate γ self-consistently (Donkó 2001). Electrical characteristics of the discharges are calculated here with such self-consistent γ values for 'clean' and 'dirty' surfaces (for definition of these conditions see (Phelps and Petrović 1999)), as well as with a constant value for γ. However, due to the heavy particle surface sputtering, we expect 'clean' cathode surfaces in Grimm type sources.

Studies of the (pulsed) discharge excitation on the electrical characteristics indicate the importance of gas heating, e.g. (Efimova et al. 2008). Here the effect of energy transferred to the background gas is studied for different voltage and pressure settings for dc discharges.

2. CELL GEOMETRY AND DESCRIPTION OF THE MODEL

In our study we consider a part of the Grimm type glow discharge cell (of the instrument Spectruma GDA 750) in the vicinity of the cathode, where all important plasma processes are expected to take place. The glow discharge cell considered in the simulations has a cylindrical symmetry, the length of the region investigated is 8 mm, the diameter of the cylindrical anode is 4 mm. We describe discharges in pure Ar gas and assume Cu as cathode material. The species considered in the model are the electrons, Ar^+ ions and fast Ar atoms. Fast electrons (if their energy is higher than the excitation threshold of Ar atoms) are simulated with Monte Carlo method, while the slow electrons are treated in a fluid model as well as the Ar^+ ions. The fast Ar atoms and Ar^+ ions in the cathode region are also followed in the Monte Carlo model. As the energy of these individual heavy particles bombarding the cathode is known, and their energy dependent electron emission yields can be found in the literature (see e.g. Phelps and Petrović 1999), the "apparent" secondary electron emission coefficient γ can be adjusted to the current conditions in each Monte Carlo cycle as explained in e.g. (Donkó 2001).

The temperature of the cathode is set to 330 K and the wall temperature is 300 K when gas heating is taken into account, otherwise the background gas temperature is fixed at 300 K. The energy transferred to the background argon gas results from the thermalization of fast heavy particles. The gas temperature distribution is obtained by solving the heat conductivity equation and is used to calculate the density distribution of the background gas atoms, according to the ideal gas law.

A detailed presentation of both the Monte Carlo and fluid models for 1 dimensional case is given in e.g. (Donkó 2001). A description of the heat conduction module and its coupling to the hybrid model can be found in (Bogaerts et al. 2000, Donkó 2001).

3. RESULTS AND DISCUSSION

Simulations have been performed in 2 dimensions for the simplified Grimm-type glow discharge cell geometry. As reported in (Bogaerts et al. 2001), for this type of cell geometry in case of operating conditions of 450-1200 Pa pressures and voltages 600-1000 V, the measured current ranges between 5 and 50 mA. In our study two different pressures (300 and 500 Pa) are considered and for each pressure the effect of the secondary electron emission coefficient and the gas heating is investigated at three voltage values (500, 700 and 900 V). The calculated secondary electron emission coefficient γ is in the range of 0.06-0.18 for 'dirty' cathode surfaces and it is equal

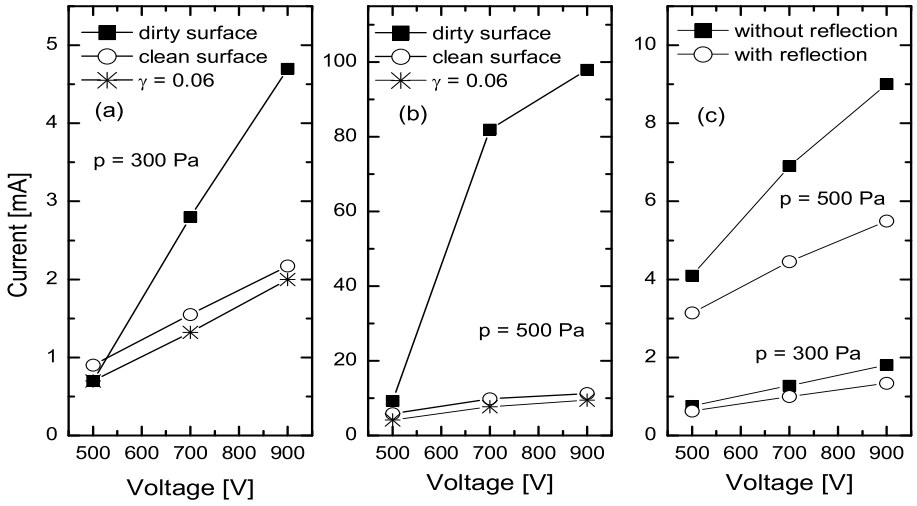

Figure 1: Currents obtained by using the self-consistently calculated γ for 'clean' and 'dirty' cathode surfaces and assuming (constant) $\gamma = 0.06$ for (a) 300 Pa and (b) 500 Pa. The effect of the gas heating is neglected in both cases. (c) Currents obtained with gas heating calculations: the effect of the reflection of heavy particles from the 'clean' copper cathode surface.

to ≈0.07 for 'clean' copper cathode at all conditions under study (Figure 1(a)-(c)). These values of γ are in accordance with the simulation results of (Bogaerts and Gijbels 2002). As a consequence of neglecting the effect of the gas heating on the background gas density and through this on the collision processes in the discharge, considerably higher current values have been obtained compared to the expected ones for both pressures investigated (Figure 1(a) and (b)). Taking into account the gas heating process in the calculations, the currents approximate the experimental values. A decrease with 15-40 % of the currents has been calculated as the effect of heavy particle reflection from the cathode surface. The results of gas heating calculations are plotted in Figure 1(c). Several characteristics of the discharge calculated for $p = 500$ Pa pressure and $V = 700$ V voltage operating conditions are presented in Figure 2. Here we have assumed a 'clean' copper cathode surface and considered the effect of the gas heating in the model. Reflection of fast heavy particles from the cathode is taken into account. In Figure 2(a) the two-dimensional distribution of ion density is plotted indicating maximum value inside the negative glow, with values around $3{\times}10^{13}$ cm^{-3}. Figure 2(b) shows the potential distibution and reveals the formation of the sheath & negative glow stucture. A plasma potential of ≈ 9 V (above the anode potential) is formed in the negative glow. The power input per unit volume is displayed in Figure 2(c). The energy transferred to the background argon gas is mainly concentrated within a narrow region close to the cathode. Consequently, a major increase of the gas temperature can be observed in this part of the cell as it visible in Figure 2(d).

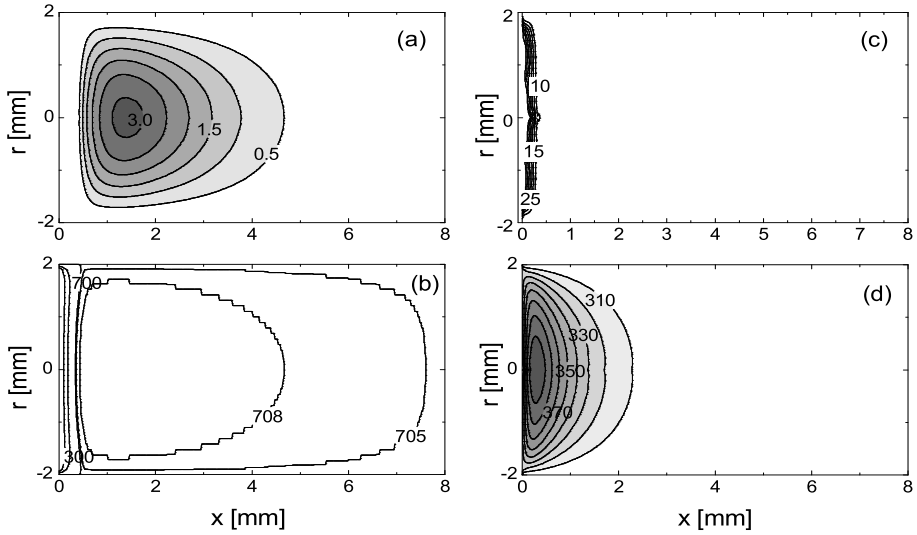

Figure 2: Results of the two-dimensional hybrid model coupled with gas heating calculation for 'clean' Cu cathode surface, at $p = 500$ Pa, $V_{\mathrm{anode}} = 700$ and $V_{\mathrm{cathode}} = 0$ V. The cathode is situated at the $x = 0$ plane. (a) Density distribution of argon ions. The labels on contour lines give the density in units of 10^{13} cm^{-3}. (b) Potential distribution (in Volts). (c) Distribution of the power input into the background gas. Values are in units of Wcm^{-3}. (d) Gas temperature profile (in Kelvins).

4. CONCLUSIONS

Our simulations have certified the relevance of the correct choice of the used secondary electron emission coefficient in the model and have confirmed the importance of the gas heating in order to obtain realistic results for the calculated electrical characteristics of the Grimm type discharge cell.

Acknowledgements

This work has been supported by the MRTN-CT-035459 GLADNET project.

References

Boeuf, J. P., Pitchford, L. C.: 1991, *IEEE Trans. Plasma Sci.*, **19**, 286.
Bogaerts, A., Gijbels, R., Goedheer, W. J.: 1995, *J. Appl. Phys.*, **78**, 2233.
Bogaerts, A., Gijbels, R., Serikov, V. V.: 2000, *J. Appl. Phys.*, **87**, 8334.
Bogaerts, A., Wilken, L., Hoffmann, V., Gijbels, R., Wetzig, K.: 2001, *Spectrochimica Acta Part B*, **56**, 551.
Bogaerts, A., Gijbels, R.: 2002, *Plasma Sources Sci. Technol.*, **11**, 27.
Donkó, Z.: 2001, *Phys. Rev. E*, **64**, 026401.
Efimova, V. V., Voronov, M. V., Hoffmann, V., Eckert, J.: 2008, *publ. Astron. Obs. Belgrade*, **84**, 369.
Phelps, A. V., Petrović Z. Lj.: 1999, *Plasma Sources Sci. Technol.*, **8**, R21.

Publ. Astron. Obs. Belgrade No. 84 (2008), 289 - 292 *Contributed Paper*

FLUCTUATIONS AND CORRELATIONS OF THE FORMATIVE AND STATISTICAL TIME DELAY IN NEON

V. Lj. MARKOVIĆ, S. N. STAMENKOVIĆ and S. R. GOCIĆ

Department of Physics, University of Niš, P.O. BOX 224, 18001 Niš, Serbia
E–mail: vidosav@pmf.ni.ac.yu.

Abstract. In this paper the fluctuations and correlations of the formative t_f and statistical time delay t_s in neon studied by electrical breakdown time delay measurements are presented. The Gaussian distribution for the formative time delay, as well as Gaussian, Gauss-exponential and exponential distribution for the statistical time delay were obtained experimentally. By fitting their dependencies on the afterglow period by simple analytical models, the correlations of the formative and statistical time delay were found. Linear correlation coefficient is $\rho \approx 1$ at high electron yields and $\rho \approx 0$ at low electron yields. Thus, the formative and statistical time delay are correlated at high electron yields during charged particle decay and therefore not independent.

1. INTRODUCTION

In a recent paper (Marković et al. 2006) two new distributions of the statistical time delay of electrical breakdown in nitrogen were reported. It was shown that a distribution of the statistical time delay changes from an exponential distribution at low electron yields (i.e. rates of electron production) to Gauss-exponential and Gaussian distribution at high electron yields due to the influence of residual ionization. In paper by Marković et al. (2007a) the distribution of the formative time delay is experimentally obtained and fitted by Gaussian density distribution. Besides that, the metastable and charged particle decay in neon afterglow was studied by the breakdown time delay measurements and the memory effect in neon was explained (Marković et al. 2007b). The metastable hypothesis as an explanation of the memory effect (the long time variation of the electrical breakdown time delay on the relaxation time $\overline{t_d}(\tau)$, Bošan (1978), Bošan et al. (1986), Maluckov et al. (2004)), completely failed to explain the afterglow kinetics in neon.

2. EXPERIMENTAL DETAILS

The breakdown time delay measurements were carried out on a gas tube made of borosilicate glass (8245, Shottt technical glass) with volume of $V \approx 300\,cm^3$ and gold-plated copper cathode, with the diameter $D = 0.6\,cm$ and the interelectrode distance $d = 0.6cm$. The tube was filled with research purity neon at the pressure of $13.3\,mbar$ (Matheson Co. with a nitrogen impurity below $1\,ppm$). Prior to measurements, the

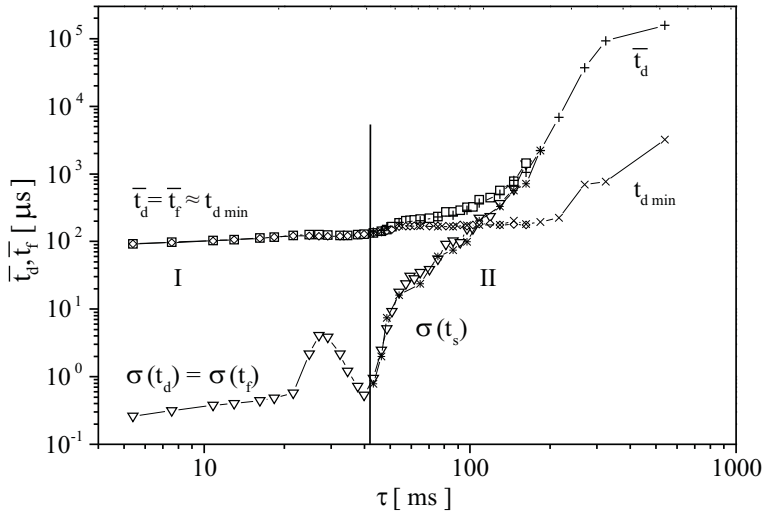

Figure 1: The memory curve, the formative and statistical time delay and their standard deviations in neon as a function of the afterglow period.

cathode surface was conditioned by running a glow discharge and several thousands breakdowns. The static breakdown voltage was $U_s = 271\,V$ DC. The time delay measurements were carried out by applying step pulses, at glow current $I_g = 0.1\,mA$, glow time $t_g = 1\,s$, working voltage $U_w = 320V$ and at different afterglow periods τ . More details about the experimental procedure, measuring system and tube preparation can be found in Marković et al (2006,2007a).

3. RESULTS AND DISCUSSION

The time that elapses from the moment of applying of voltage greater than the static breakdown voltage U_s to the breakdown occurrence is denoted as the breakdown time delay t_d. It consists of the statistical t_s and formative time delay t_f, i.e. $t_d = t_s + t_f$ (Morgan 1978), where t_s is the time from the application of voltage to the appearance of a free electrons initiating breakdown and t_f is the time from this moment to the collapse of the applied voltage and occurrence of a self sustained current (Morgan 1978). The breakdown time delay dependence on the afterglow period $\overline{t_d}(\tau)$ (the memory curve, Bošan, 1978), as well as the formative and statistical time delay and their standard deviations $\sigma(t_f)$ and $\sigma(t_s)$, respectively, are shown in Fig. 1, and will be discussed on the basis of simple analytical models.

According to Kasner 1968 and Philbrick et al 1969, the molecular neon ions Ne_2^+ are dominant during the glow under given conditions. Their number density decay in the afterglow (the region I in Fig. 1) can be described by equation $dn_i/dt = -\nu\, n_i - \beta\, n_i^2$, whose solution is:

$$n_i = \frac{n_{i0}\, exp\,(-\nu\tau)}{1 + (\beta\, n_{i0}/\nu)\,[1 - exp\,(-\nu\tau)]}. \qquad (1)$$

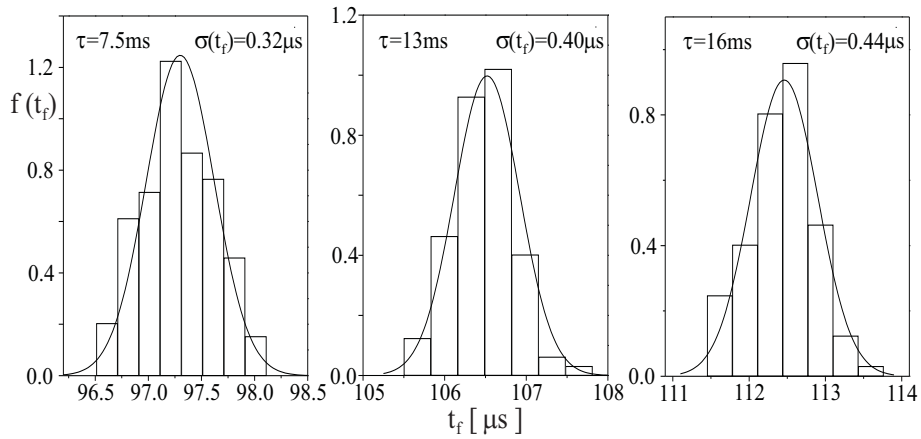

Figure 2: The density distribution functions of the formative time delay (region I).

Here, n_{i0} represents the initial number density of Ne_2^+, β is the electron-ion dissociative recombination coefficient and $\nu = D/\Lambda^2 + k_{cn}[N_2]$ is the first order decay frequency including diffusion and conversion to N_2^+ ions (reaction $Ne_2^+ + N_2 \rightarrow N_2^+ + 2Ne$). When the first order loss processes are predominant $\nu \gg \beta\, n_{i0}$, the exponential decay is obtained:

$$n_i = n_{i0}\, e^{-\nu\, \tau} \tag{2}$$

On the other side, the formative time can be expressed by (Marković et al. 2007a):

$$\overline{t_f} = \frac{q}{q-1}\frac{d}{w_i} \ln \frac{1 + (q-1)(n_{it}/n_i)}{q}, \tag{3}$$

where n_{it} is the ion number density in the Townsend's dark discharge before the collapse of applied voltage (Marković et al, 2008), n_i is the initial ion number density for the formative time, $q = \gamma\,[exp\,(\alpha\, d) - 1]$, α and γ are the primary and secondary ionization coefficients and w_i is the ion drift velocity. Inserting the exponential decay (2) into (3), it follows that the formative time is proportional to the afterglow period $\overline{t_f} \propto \tau$ (the region I in Fig. 1). Thus, the formative time delay in the ionic region (I) increases when the afterglow period (τ) increases, contrary to results in Maluckov et al (2004,2006) where the ionic region is flat.

In this case, the experimental density distribution functions of the formative time delay are obtained providing that $t_s << t_f$ and $\sigma\ (t_s) << \sigma\ (t_f)$, which can be fulfilled by measurements at high level of residual ionization in the region (I) in Fig. 1 (Marković et al. 2007a). The experimental density distribution functions of the formative time are fitted by Gaussian distributions and shown in Fig. 2, accompanied by their standard deviations. The standard deviation of the formative time delay increases with the afterglow period faster than the formative time delay (Figs. 1,2).

In the region II of the memory curve, the electrical breakdown time delay distributions are dominated by the fluctuations of the statistical time delay. According to Marković et al (2006), the three characteristic distributions of the statistical time delay are obtained when the afterglow period increases (the electron yield decreases):

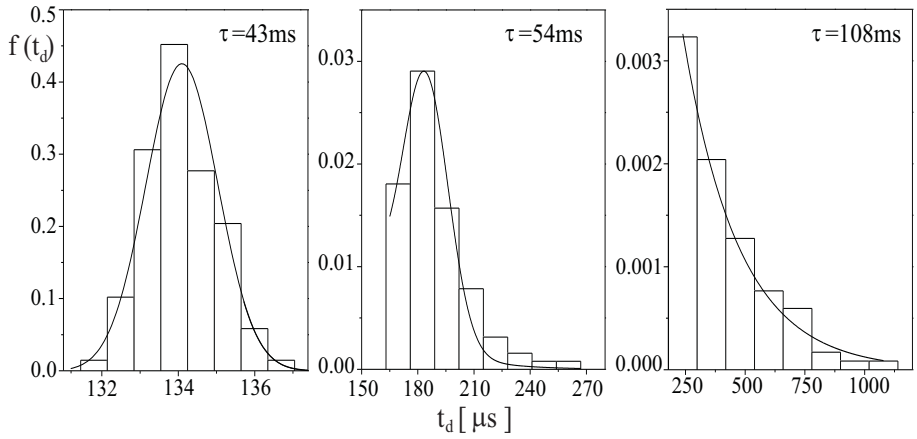

Figure 3: The three characteristic distributions of the statistical time delay (Gaussian, Gauss-exponential and exponential) in the region (II) of Fig. 1.

Gaussian, Gauss-exponential and exponential (Fig. 3). The corresponding effective electron yields are as follows : $Y_{eff} \equiv Y\,P \gtrsim 10^6\,s^{-1}$, $10^6\,s^{-1} \gtrsim Y_{eff} \gtrsim 10^4\,s^{-1}$ and $Y_{eff} \lesssim 10^4\,s^{-1}$, respectively. According to Marković et al. (2008), the linear correlation coefficient is $\rho \approx 1$ at high electron yields $Y_{eff} \gtrsim 10^{11}\,s^{-1}$ (t_s and t_f distributions are Gaussians) and decreases to $\rho \approx 0$ at low electron yields $Y_{eff} \lesssim 10^4\,s^{-1}$ (t_s distribution is exponential and t_f Gaussian). In other words, the distributions are independent if $t_s \gtrsim t_f$, which is equivalent to $Y_{eff} \lesssim 10^4\,s^{-1}$ (Figs. 1,3). Thus, the formative and statistical time delay are correlated at electron yields $Y_{eff} \gtrsim 10^4\,s^{-1}$ and therefore not independent, contrary to claims in Maluckov et al (2004,2006). It is clear that t_f follows t_s and the output from t_s is the input for t_f; therefore, the higher particle transfer means the higher degree of correlation and vice versa.

References

Bošan, Dj. A.: 1978, *Proc. 5th Int. Conf. Gas Discharges, Liverpool, UK*, 273.
Bošan, Dj. A., Radović, M. K., Krmpotić, Dj.: 1986, *J. Phys. D: Appl. Phys.*, **19**, 2343.
Kasner, W. H.: 1968, *Physical Review*, **167**, 148.
Maluckov, Č. A., Karamarković, J. P. , Radović M. K. and Pejović M. M.: 2004, *Physics of Plasmas*, **11**, 5328.
Maluckov, Č. A. , Karamarković, J. P. , Radović M. K. and Pejović M. M.: 2006, *Physics of Plasmas*, **13**, 083502.
Marković, V. Lj. , Gocić, S. R., Stamenković, S. N.: 2006, *J. Phys. D*, **39**, 3317.
Marković, V. Lj., Stamenković, S. N., Gocić, S. R. and Djurić, S. M.: 2007a, *Eur. Phys. J: Appl. Phys.*, **38**, 73.
Marković, V. Lj., Gocić, S. R. , Stamenković, S. N. and Petrović, Z. Lj.: 2007b, *Physics of Plasmas*, **14**, 103504.
Marković, V. Lj., Stamenković, S. N. and Gocić, S. R.: 2008, to be published.
Morgan, C. G.: 1978, Irradiation and Time Lags, in Electrical Breakdown of Gases, eds. J. M. Meek & J. D. Craggs, Chichester: John Wiley & Sons.
Philbrick, J., Mehr, F. J., Biondi, M. A.: 1969, *Physical Review*, **181**, 271.

Publ. Astron. Obs. Belgrade No. 84 (2008), 293 - 296 *Contributed Paper*

MEMORY EFFECT IN AIR IN THE PRESENCE OF VACUUM BREAKDOWN MECHANISM

E. N. ŽIVANOVIĆ and M. M. PEJOVIĆ
Faculty of Electronic Engineering, University of Niš, Serbia
E–mail: emilija@elfak.ni.ac.yu
E–mail: pejovic@elfak.ni.ac.yu

Abstract. Investigation of memory effects in air at 0.7 mbar pressure in the presence of vacuum electrical breakdown mechanism has been performed in this paper. The memory effect has been followed using the time delay method.

1. INTRODUCTION

Low-pressure nonequilibrium plasmas of air and $N_2 - O_2$ mixtures are currently attracting the attention of many scientific groups due to their relevance in different fields, from the study of the Earth's ionosphere to the reactivity in the boundaries of hypersonic vehicles or the sterilization of surgical equipment (de Benedictis et al. 1996, Castillo et al. 2004). During the electrical breakdown and discharge in air, positive and negative ions, vibrationally excited molecules and electronic excited atoms and molecules, as well as atoms in ground state are created. It is shown (Pejović et al. 2002) on the basis of the secondary emission of electrons due to the bombardment of the cathode surface with positive ions and some neutral active particles that their presence in afterglow can be followed by the electrical breakdown time delay measurements as a function of afterglow period (memory curve).

2. EXPERIMENT

The time delay t_d measurements have been performed on air-filled cylindrical glass tube with inner radius $R = 2.5\,cm$ and tube length $L = 22\,cm$, connected with two cylindrical iron electrodes with spherical surface facing (10 mm radius) each other and $d = 0.1$ mm gap length between them. Before evacuation the air has been residence in the tube at atmospheric pressure. The air evacuation was performed by mechanical pump until 0.7 mbar pressure. The static breakdown voltage was estimated using the discredized dynamic method (Pejović 2005) and its value was 545 V. The breakdown voltage and time delay were measured at room temperature by electronic systems shown in paper Pejović 2005.

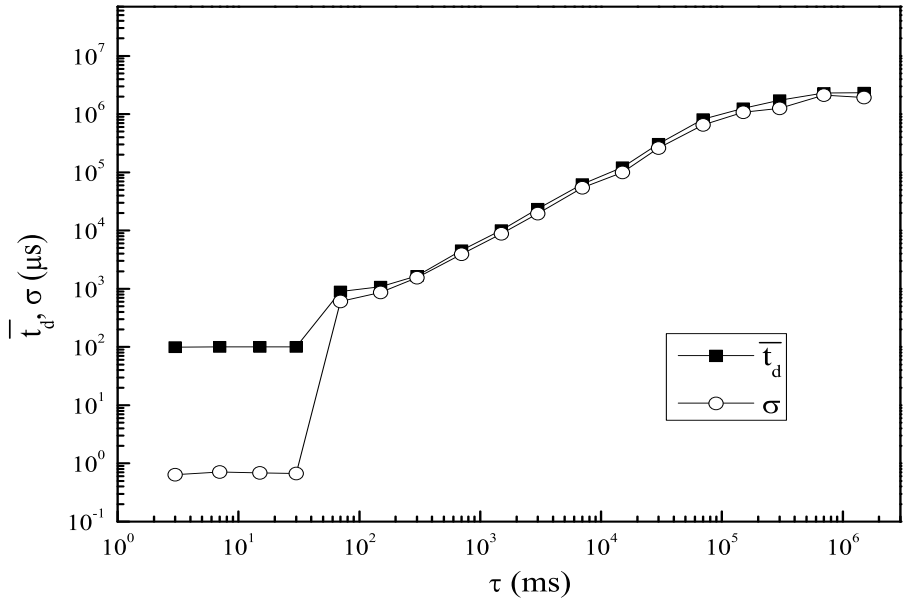

Figure 1: Dependences of the mean value of time delay $\overline{t_d}$ and standard deviation σ on the afterglow period τ.

3. RESULTS AND DISCUSSION

Vacuum breakdown mechanism (VEB) occurs when the breakdown initiation and self-sustenance are origin of electrodes and it appears when the ratio of electron mean free path $\overline{\lambda}_e$ to interelectrode gap d is greater then unity (Osmokrović et al. 2007). This type of breakdown is initiated either by electron emission or by microparticles when the primary and secondary effects are electrodes effects. Beyond the gas electrical breakdown (GEB) appears when $\overline{\lambda}_e/d < 1$. In this case for low pressures the initiation of breakdown is caused by positive ions or neutral active particles which in the collision with cathode emitting electrons which formed the avalanche in gas (Townsend mechanism). In order to determinate which of mechanism is dominate in our experimental conditions, it can estimate value of electron mean free path using the formula $\overline{\lambda}_e = 4\sqrt{2}\,\overline{\lambda}_g$ (von Engel 1965), where $\overline{\lambda}_g$ is the mean free path of air molecules. The calculation shows that $\overline{\lambda}_e \approx 0.6$ mm for air at 0.7 mbar pressure. Also, it indicates that for distance $d = 0.1$ mm the electrical breakdown is aided by vacuum electrical breakdown mechanism initiating of electrons from the cathode. This type of mechanism is probably a consequence of cold electron emission from the cathode microspikes, which is a quantum mechanical effect (Pejović et al. 2008). In this case the presence of high local electric field in the vicinity of microspikes with extremely small radii of curvature leads to decrease of potential barrier for cold electron emission.

The dependences the mean values of time delay $\overline{t_d}$ ($\overline{t_d}$ is the mean value of 100 t_d for every τ value) and the standard deviation σ v.s. afterglow period τ for overvolatge

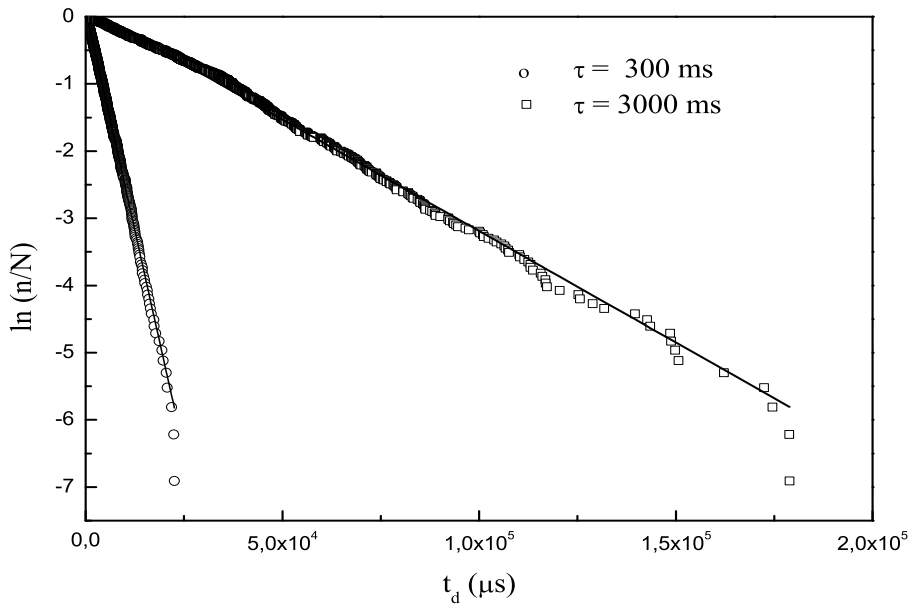

Figure 2: Laue distribution of time delay for afterglow periods of 300 and 3000 ms.

of 50 % are shown in Figure 1. As can be seen from this figure, in time interval of afterglow period from $3-30\,ms$, the curves have plateaus and $\overline{t_d}$ and σ slightly depend on τ. In this interval, σ is less then $\overline{t_d}$ for two order of magnitude. In τ interval from $3\,ms$ to $30\,ms$ low values of σ indicate that $\overline{t_d} \approx t_f$ (t_f is the formative time), i.e., statistical time delay is $\overline{t_s} << t_f$ and $\sigma = \overline{t_s}$ (Llewellyn-Jones et al. 1953). This indicates that the secondary emission of electrons is dominantly induces by positive ions formed in afterglow by reactions (Kossyi et al. 1992):

$$N_2(A) + N_2(a') \rightarrow N_4^+ + e \tag{1}$$

$$N_2(a') + N_2(a') \rightarrow N_4^+ + e \tag{2}$$

$$O + N(^2P) \rightarrow NO^+ + e. \tag{3}$$

The ions, due to their high drift velocity, reach the cathode almost immediately after the application of the voltage on the tube. As τ increases, the concentration of $N_2(A), N_2(a')$ metastable molecules and $N(^2P)$ metastable atoms decrease and the probability of reaction (1)-(3) also decreases. For $\tau > 30\,ms$ the influence of positive ions on breakdown initiation is insignificant. Beyond the nitrogen is at most presence gas in the air, it can be suppose that $N(^4S)$ atoms are responsible for this process for $\tau > 30\,ms$ and its recombination on the electrode can release the secondary electrons from the cathode (Pejović et al. 2004). During this τ period (Fig. 1) σ and $\overline{t_d}$ have the same order of magnitude. Than, the formative time can be neglected, and $\overline{t_d} \approx \sigma = \overline{t_s} = \frac{1}{YP}$ (Meek et al. 1978), where Y is electron yield in electrode gap caused by neutral active species and P is the probability of one electron caused

breakdown. Due to the fact that the breakdown probability caused by $N(^4S)$ atoms existence is considerably smaller than one caused by both ions and neutral active states, $\overline{t_d}$ rapidly increases. For given voltage on the electrodes, $P = const.$, while Y is directly proportional to concentration of neutral active species in gas. When τ increases, the concentration of these particles in afterglow decreases and $\overline{t_d}$ increases.

Our assumption that for $\tau > 30\,ms$, $t_f << t_s$ and $t_d \approx t_s$ is in accordance with the Laue distributions of t_d shown in Fig. 2 which relate to the statistical time delay. Laue distributions have been obtained for 1000 data of t_d for afterglow periods of 300 and 3000 ms and overvoltage of 50%. The insignificant variance of experimental points from straight lines indicates the validity of Laue distribution.

For $\tau > 7 \times 10^6\,ms$ memory curve $\overline{t_d} = f(\tau)$ (Fig. 1) reaches the saturation and it is a consequence of the significant decrease of neutral active species concentration in afterglow. In this case the dominant role in breakdown initiation have a cosmic rays which flux has insignificant changed. Memory curve shown in Fig. 1 reaches the saturation faster then in the case when the tube was filled by nitrogen under the same experimental conditions. It can be concluded comparing this memory curve with memory curve for nitrogen (Pejović et al. 2004). This is a consequence of efficient lost of $N(^4S)$ atoms by oxygen atoms formed in air during discharge as well as oxygen molecules. The two most important reactions which lead to lost of $N(^4S)$ atoms are (Kossyi et al. 1992):

$$N(^4S) + O_2 \rightarrow NO + O \tag{4}$$

$$N(^4S) + O + O_2 \rightarrow NO + O_2. \tag{5}$$

Also, the saturation of memory curve is faster because of addition electron yield initiated by VEB mechanism presences in our experiment.

4. CONCLUSION

On the basis of memory curve the contribution of positive ions, neutral active particles and cosmic rays on the breakdown initiation has been separated in air at 0.7 mbar pressure. The analysis has shown that the breakdown initiation also aided by the vacuum breakdown mechanism.

References

Castillo, M., Herrero, V. J., Mendez, I., Tanarro, I.: 2004, *Plasma Sources Sci.Technol.*, **13**, 343.

de Benedictis, S., Dilecce, G.: 1996, *J. Phys. III*, **6**, 1189.

Kossyi, I. A., Kostinsky, A. Yu., Mateveyev, A. A., Silakov, V. P.: 1992, *Plasma Sources Sci. Technol.*, **1**, 207.

Llewellyn-Jones, E., de la Perrelle, E. T.: 1953, *Proc. R. Soc. London, Ser. A*, **216**, 267.

Meek, J. M., Craggs, J. D.: 1978, Electrical Breakdown of Gases (New York: Wiley).

Osmokrović, P., Vujisić, M., Stanković, K., Vasić, A., Lončar, B.: 2007, *Plasma Sources Sci. Technol.*, **16**, 643.

Pejović, M. M.: 2005, *Rev. Sci. Instr.*, **76**, 015102.

Pejović, M. M., Pejović, M. M.: 2008, *Appl. Phys. Lett.*, **92**, 011507.

Pejović, M. M., Ristić, G. S., Karamarković, J. P.: 2002, *J. Phys. D: Appl. Phys.*, **35**, R91.

Pejović, M. M., Živanović, E. N., Pejović, M. M.: 2004, *J. Phys. D: Appl. Phys.*, **37**, 200.

von Engel, A.: 1965, Ionized Gases (Clarendon, Oxford).

Publ. Astron. Obs. Belgrade No. 84 (2008), 297 - 300 *Contributed Paper*

DYNAMIC OPTOGALVANIC KRYPTON AND NEON SPECTRA FOR 428-451nm RANGE IN HOLLOW CATHODE DISCHARGE

R. DJULGEROVA[1], V. MIHAILOV[1], J. KOPERSKI[2], M. RUSZCZAK[2],
T. DOHNALIK[2] and Z. Lj. PETROVIĆ[3]

[1] *Institute of Solid State Physics of Bulgarian Academy of Sciences, 1784 Sofia, Bulgaria*
E–mail: renna@issp.bas.bg

[2] *Institute of Physics of Jagellonian University, 30-059 Krakow, Poland*

[3] *Institute of Physics of Academy of Sciences of Serbia, 11080 Belgrade, Serbia*

Abstract. Dynamic optogalvanic Kr and Ne spectra in 428-451nm range are recorded in Kr and Ne hollow cathode lamps for calibration purposes.

1. INTRODUCTION

Some of the most widely used optogalvanic spectroscopy applications include wavelength calibration and frequency and power laser stabilization. The development of tunable lasers, capable nowadays of generating in various spectral ranges, requires the availability of new relevant optogalvanic spectra. The optogalvanic effect is a change in plasma conductivity caused by resonant light absorbed by different discharges (Foote 1925, Barbieri 1990). The combination of the optogalvanic effect with the hollow cathode glow discharge turns out to be very useful due to the availability of a great number of commercial hollow cathode lamps emitting rich and stable spectra of different materials. The dynamic optogalvanic signals (DOGS) represent plasma reaction after absorption of a short (∼ns) laser pulse. Compared with the stationary type optogalvanic signal, the DOGS is characterized not only by its amplitude and sign, but also by its time dependence shape and peculiarities. For this reason, the DOGSs can be used in many cases as explicit markers for the purposes of wavelength calibration, plasma diagnostics, etc.

In this work a great number of Kr and Ne DOGSs in 428-451nm range have been registered in Kr and Ne hollow cathode lamps. No data have been found for Kr optogalvanic spectra so far in the optogalvanic spectroscopy literature, except for reports of registrations of few particular signals. For example, the optogalvanic signal of Kr corresponding to 826.32nm transition has been recorded for comparison purposes when an AlGaAs diode laser has been frequency stabilized to an U I transition using optogalvanic effect in hollow cathode discharge (David 1990). For the aims of plasma diagnostics the shape of the three Kr DOGSs (556.2nm, 557.0nm, 567.2nm) related to its metastable levels, have been used recently (Piracha 2007). Neon DOGSs registered

in Ne hollow cathode lamp for the above mentioned range are published (Bezlepkin 1988, Reddy 1991) but their time dependences are not shown and there are no data for the DOGSs amplitude (Reddy 1991).

2. EXPERIMENTAL SET-UP

The hollow cathodes have the shape of 10mm and 15mm long cylinders with diameters of 3mm and 6mm for the Kr and Ne hollow cathode lamps, respectively. Spectrally pure Kr and Ne are used as working gases at the pressure of about 4Torr. The discharge current (i) is changed from 1mA to 12.4mA. The hollow cathode discharge is illuminated by a pulsed (5ns, 10Hz frequency) dye laser (Sopra LCR1 pumped by Nd:YAG laser), tuned to the 428-451nm wavelength range. The laser power is varied within the range of 1.2 - 2.6mW. The incident laser beam passes along the cathode axis and illuminates both the hollow cathode plasma and the cathode bottom. The DOGSs of the Kr and Ne optical transitions are recorded as function of i using a two-channel digital real-time oscilloscope (Le Croy 9361) and processed by a computer.

3. EXPERIMENTAL RESULTS AND DISCUSSION

A great number of dynamic optogalvanic signals relevant to many Kr atomic optical transitions between $5s$ low levels and highly excited $6p$, $8p$ and $5f$ levels, situated very close to the Kr ionization potential, are registered in the 428-451nm range. The Kr DOG spectrum is demonstrated in Table 1 and a typical dynamic optogalvanic signal shape is shown in Fig. 1.

Dynamic optogalvanic signals relevant to many Ne atomic optical transitions between $3p$ low levels and different highly excited ns and nd levels situated very close to the Ne ionization potential are presented in Table 2 and a typical dynamic optogalvanic signal shape is shown in Fig. 2.

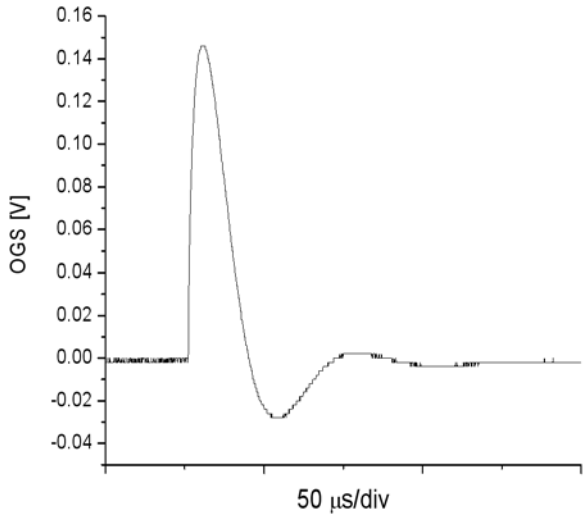

Figure 1: Dynamic optogalvanic signal corresponding to Kr I 439.99nm optical transition at 10mA discharge current and 2mW laser power.

The rich optogalvanic Kr and Ne spectra with high amplitudes obtained here is due to the very important advantage of the hollow cathode plasma, namely, the dense population of the higher energy atomic levels. The main reason is the special shape of the electron energy distribution function, having a large plateau of higher energy electrons.

The dynamic optogalvanic signals have sinusoidal shape (Figs. 1 and 2). As signal amplitude value of the DOGS is taken the first component. This component is interpreted as a result of the impedance decrease in the discharge. In our case it is due to the increased population of the upper levels, which can be much easier ionised by low energy electrons than the origin levels. The next part of the DOGS reveals the relaxation behaviour of the disturbed plasma. It depends not only on the characteristics of the two levels coupled in the transition, but also on the discharge conditions, tube design and parameters of the electrical circuit.

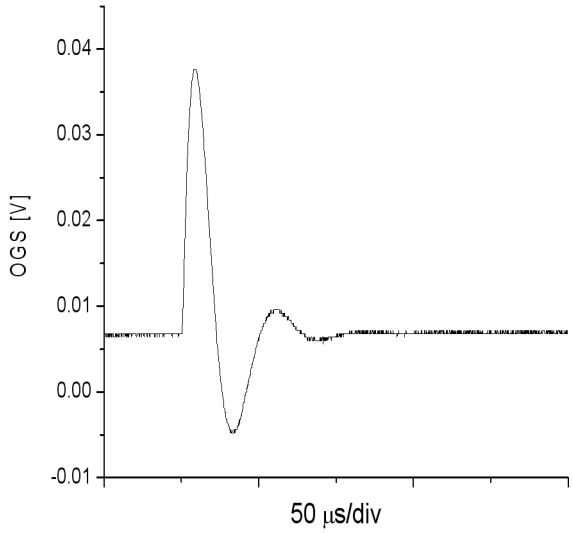

Figure 2: Dynamic optogalvanic signal corresponding to Ne I 436.35nm optical transition at 8mA discharge current and 1.2mW laser power.

Table 1: Krypton dynamic optogalvanic spectrum registered in the 428-451nm range at 10mA discharge current and 2mW laser power

Wavelength [nm]	OGS [mV]	Wavelength [nm]	OGS [mV]
427.396	100	439.996	200
428.296	50	441.036	100
428.648	120	441.239	20
430.048	140	441.688	65
430.244	60	441.876	100
431.855	100	442.519	130
431.957	160	445.391	70
435.135	110	446.369	60
436.264	80	450.235	40
437.612	70		

Table 2: Neon dynamic optogalvanic spectrum registered in the 428-451nm range at 8mA discharge current and 1.2mW laser power

Wavelength [nm]	OGS [mV]	Wavelength [nm]	OGS [mV]
427.927	4	441.356	4
428.324	4	441.681	8
430.324	5	442.252	15
430.625	4	442.480	15
431.469	8	442.540	10
431.600	6	442.775	4
432.726	5	443.251	10
433.412	4	443.372	20
434.335	4	444.154	5
434.603	7	444.497	8
435.791	5	445.298	7
436.352	23	445.556	4
437.215	5	446.017	15
437.525	6	446.652	4
438.122	10	446.565	8
439.555	10	446.681	12
440.278	5	447.565	5
440.364	5	448.319	5
440.962	5	448.809	7
441.228	5	450.018	2

4. CONCLUSION

Krypton and Neon dynamic optogalvanic spectra are registered in the 428-451nm range for Kr and Ne hollow cathode lamps. DOGS amplitude values and time shapes are obtained. Since there were no Kr optogalvanic spectra found in the literature, the one registered in this work compensates for this omission. The Ne optogalvanic spectra registered extends the Ne DOGS atlas.

These results can be used for calibration purposes and for Kr and Ne plasma modeling in hollow cathode discharge.

Acknowledgement

Support for this work is gratefully acknowledged by the joint research project between the Institute of Solid State Physics of Bulgarian Academy of Sciences, the Institute of Physics of Jagiellonian University, and the Institute of Physics of Academy of Sciences of Serbia based on the scientific cooperation between Bulgarian Academy of Sciences, Polish Academy of Sciences and Academy of Sciences of Serbia.

References

Barbieri, B., Beverini, N., Sasso A.: 1990, *Rev. Modern Phys.*, **62**, 603.
Bezlepkin, A. I., Velikozkii, V. L., Cromskii, D. G., Mnuskii, V. C., Trishchuk, B. F., Homjak, A. C.: 1988, *Appl. Spectr.* (Russ.), **48**, 253.
David, E., Gane, J-M.: 1990, *Applied Optics*, **29**, 4489.
Foote, P., Mohler, F.: 1925, *Phys. Rev.*, **26**, 195.
Piracha, N. K., Nesbet, K., Moteu, S., Moeler, P.: 2007, *Contrib. Plasma Phys.*, **47**, 435.
Reddy, B. R., Venkateswarlu, P.: 1991, *Opt. Comm.*, **85**, 491.

Publ. Astron. Obs. Belgrade No. 84 (2008), 301 - 304 *Contributed Paper*

DETERMINATION OF PLASMA ELECTRON DENSITY BY MICROWAVE RESONANCE PROBE

D. POPOVIĆ, J. VUČETIĆ and V. MILOSAVLJEVIĆ†

Faculty of Physics, University of Belgrade, P.O.B. 368, Belgrade, Serbia
E–mail: †vladimir@ff.bg.ac.rs

Abstract. The time-dependent spatial electron density distribution in a constricted, pulsed plasma source is measured using a floating microwave hairpin resonance probe and an extrapolation method is used for determining the peak in electron density from the experimental data. Using these techniques a detailed characterization of the spatio–temporal evolution of the electron density, outside the constricted region above the anode of the pulsed plasma source is presented.

1. INTRODUCTION

It is desirable to develop/demonstrate a remote plasma diagnostic to prevent possible affects on constricted plasma column/channel which could be caused by placing a probe there and to remove interference with the application of other diagnostics like laser interferometric measurement, absorption spectroscopy or self–absorption measurement (doubling optical path by putting reflecting mirror). To realize the remote diagnostic, a hairpin probe is introduced to the discharge tube volume (extended pocket) outside of the constricted channel and opposite to the electrode. The electron density is found to fall sharply with the distance from the constructed channel. By modeling the electron density in time and space we develop the method to calculate electron density in the constricted channel from our remote diagnostics.

In the paper Milosavljević et al. (2007), the hairpin technique is used only along the axis of the constricted channel and in conjunction with OES. Interpretation of the results was based on the knowledge of the peak density. In this paper, we further consolidate the curve–fitting technique to interpret approximate values of the peak density evolution in the direction perpendicular to the constricted channel of the discharge tube without using OES measurement. Our main motivation in the present work is to (1) measure the electron density along the direction perpendicular to the constricted channel, (2) validate the robustness of the extrapolation technique, (3) verify the electron density projected by measurements perpendicular to the constricted channel to measurement made along the constricted channel, (4) to establish using hairpin as a remote probe to determine the time–window when the OES technique are useful for the study of plasma density along the constricted channel of discharge tube.

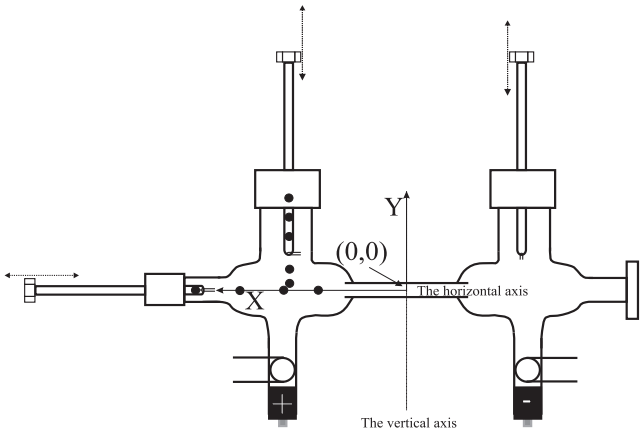

Figure 1: Diagram of the plasma source. The positions where the electron density has been measured are denoted with black circles on the Anode-side extended pocket.

2. EXPERIMENTAL SETUP & DIAGNOSTICS TECHNIQUES

The modified version of the linear, low pressure, pulsed arc (Djeniže et al. 1992,1998; Milosavljević et al. 2003) is used as the plasma source. A pulsed discharge was driven in a pyrex tube of 5 mm inner diameter and effective plasma length of 72 mm Figure 1. The tube has an end–on quartz window. The working gas is helium–argon mixture (He(28%)+Ar(72%)) at 130 Pa filling pressure in flowing regime. A main capacitor of 14 μF is charged to 1.8 kV, yielding 15.8 J dissipation energy. To facilitate introduction of the probes into the plasma source, we have change our original glass tube (see Fig. 1 in Djeniže et al. 1998) providing three ports; Two on the top of the expanded glass tube sections, and one on the side aligned with the constricted channel. The second quartz window remains for the observation of spectral line shapes by spectrometers. The main dimensions of the tube have not been changed. More details about experimental set–up is presented in Milosavljević et al. (2007).

The principle of the microwave hairpin resonance probe is based on measuring the plasma dielectric constant, ε_p, using a microwave resonant structure Karkari & Ellingboe (2006). The hairpin consists of a 1/4 wavelength parallel transmission line with one end short–circuited and the other end open, with the plasma as the dielectric medium of the transmission line. When the resonator is immersed in plasma it's self–resonant frequency shifts from the characteristic resonance frequency in vacuum.

The electron density is directly obtained from the shift in the characteristic resonance frequency according to the formulae Karkari & Ellingboe (2006), Milosavljević et al. (2007).

$$N_e/10^{10}cm^{-3} = \frac{(f_r/GHz)^2 - (f_o/GHz)^2}{0.81}. \quad (1)$$

Where f_r and f_o are the resonance frequencies in plasma and in vacuum. For all hairpin measurement the alignment of the probe tip itself is parallel to the constricted channel.

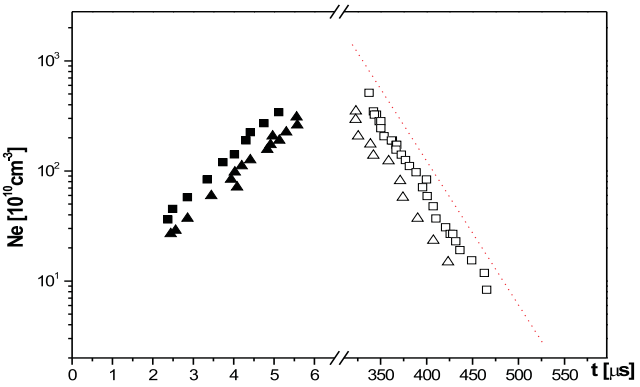

Figure 2: Measurement of the electron density at two position close to each other, from the top port: x=48mm, y=4 mm (square) and from the side port: x=50mm, y=0mm (△). Full and empty symbols represents creation and decay phase, respectively. The dotted line represent extrapolated curve for position x=48 mm and y=0 mm.

3. RESULTS AND DISCUSSION

Electron density is measured during the creation and decay of the plasma by floating hairpin probe. We have performed hairpin measurements in vertical axis at y=4, 10, 35, 43 and 50 mm from the constricted channel, and for all 5 y–position the x is 48mm, 13mm from the end of the narrow part of the tube. Previous measurements along the horizontal axis at x=45, 50, 58, and 67 mm, has been presented in Milosavljević et al. (2007).

In the Figure 2 are presented electron densities measured around coordinate (48,0) (this point is in the constricted channel). This coordinates is relevant because of two hairpin measurement which have been done very close to each other, i.e. along horizontal and vertical axis. These two hairpin measurement are done at the position (48,4) and (50,0) for the probe introduced from the top and from the side port, respectively. The hairpin position from the top port (48,4) is the closest one from all 5 measured, to the constricted channel. The features show a characteristic rise in electron density in the creation phase and comparatively slower decay in density in the decay phase measured by the both probe, i.e. for the axial and perpendicular probe. The data in the Figure 2 shows very similar trends and that is expected, since the probe tip from the side port is a straight and from the top port is perpendicular to the probe itself, i.e. both probe tips have same orientation in respect to the constricted channel. Thus, verification of the hairpin data taken along two direction, perpendicular to each other, is done by comparing the result of electron density direct measured along axial port with electron density gotten by extrapolation technique, from the top port hairpin measurement.

The extrapolated curves for experimental data collected at (48,4) and (50,0), as well extrapolated curve at (48,0) presented in Figure 2 pass very close to independed determinate electron density by OES Milosavljević et al. (2007). This also gives a possibility of using hairpin probe for estimate of electron density at a constricted

channel, even in case the measuring of electron density in the constricted channel is not possible due to construction limitation of plasma chamber, like other diagnostics already applied (Interferometry, OES, ...) or a lack of port at the chamber. So, hairpin probe can be use as remote sensor for electron density measurement.

Extrapolation technique used in this work is different one from previously used in Milosavljević et al. (2007), because we introduce a possibility that free parameters in previous work constants are changed along y–axis.

4. CONCLUSION

We have applied a floating microwave hairpin resonance probe, yielding the spatially–temporal resolved electron density during both the breakdown phase and the decay phase of the plasma. The hairpin probe data is collected for vertical position, i.e. perpendicular position to the constricted channel.

The extrapolation technique, was used to obtain an approximate value of the peak electron density for the axial probe measurement, is changed to be more robustness one by introducing a fitting over y–coordinate and excluding the constraint that the peak density must matches with the peak in discharge current recorded by Rogowskii coil.

In the paper we present also the possibility of extracting the information related to electron density in the constricted channel, even when the measurement of electron density in the constricted channel is not possible due to construction limitation of plasma chamber by using so–called remote hairpin probe. This become possible after we change the extrapolation technique. This is done by setting the value for y position to zero. The same analyze help us to validate data around coordinate (48,0) in constricted channel. The results shows consistent agreement of the measured density using the axial and the perpendicular probe at (48,0).

Comparison the data taken at almost same point in the discharge tube, from the side port (x=50mm; y=0mm) and from the top port (x=48mm; y=4mm) we demonstrated the position of probe tip in respect to the probe itself is not so critical. Therefore the results shows consistent agreement of the measured density using the axial and the perpendicular probe around the (48,0) point.

Acknowledgments

This work is a part of the project "Nonlinear dynamical phenomena in photorefractive media, liquid crystals, plasmas and left–handed materials (OI141031)" supported by the Ministry of Science and Environment Protection of the Republic of Serbia. Authors are grateful to Dr. S. Karkari for help.

References

Djeniže, S., Milosavljević, V., Srećković, A.: 1998, *J. Quant. Spect. Rad. Transfer*, **59**, 71.
Djeniže, S., Srećković, A., Labat, J.: 1992, *Astron. Astrophys.*, **253**, 632.
Karkari, S., Ellingboe, A. R.: 2006, *Appl. Phys. Lett.*, **88**, 101501.
Milosavljević, V., Djeniže, S., Dimitrijević, M. S.: 2003, *Phys. Rev. E*, **68**, 016402.
Milosavljević, V., Karkari, S., Ellingboe, A. R.: 2007, *Plas. Sour. Sci. Technol.*, **16**, 304.

Publ. Astron. Obs. Belgrade No. 84 (2008), 305 - 308 *Contributed Paper*

THE TEMPERATURE DETERMINATION OF THE ATMOSPHERIC ARGON PLASMA JET

S. DJUROVIĆ, Z. MIJATOVIĆ, M. ĆIRIŠAN, B. VUJIČIĆ, R. KOBILAROV and T. GAJO

Department of Physics, Faculty of Sciences,
Trg Dositeja Obradovića 4, 21000 Novi Sad, Serbia
E–mail: djurovic@uns.ns.ac.yu

Abstract. In this paper we report the results of plasma jet temperature determination from the Stark shift of Ar I 415.86 nm spectral line. For the plasma jet formation modified wall stabilized electric arc was used.

1. INTRODUCTION

In this experiment modified wall stabilized electric arc as a plasma source was used. This kind of arc works in DC regime with typical current of few tens of amps, usually less than 100 A. High arc current can be realized in pulses, using power from AC network and these currents can reach values up to 1000 A or more. Increase of arc current increases also plasma electron density and temperature. In order to form pulsed plasma jet in free space, outside of the plasma column, high current pulses was applied to the wall stabilized arc and added to DC current. For this purpose one of stabilized arc ends was opened. This is illustrated in Fig. 1.

The electric circuit was described earlier (Djurovic et al. 2004, Ćirišan et al. 2006). Here will be given only short description. Wall stabilized arc in DC regime is supplied from current stabilized electrical source with the current stability of 0.3 %. Maximum current which can be reached is 30 A. This current provides plasma electron temperature between 10000 and 11000 K and electron density of few times 1016 cm-3 (Djurović et al. 1997, 2002). Higher values of these plasma parameters demand higher discharge current. One way to do this economically is to apply high current pulses superposed to the DC current. This can be done using civil AC network of 220 V in combination with appropriate electronic circuit. In combination with appropriate resistor it provides current pulses lasting 8 ms, with the peak current of 170 A. Every 16th of 50 Hz cycle is used to produce high current pulse. So, repetition rate of the high current pulses is 3.12 Hz. This repetition rate is low enough not to affect temperature of the arc walls which were water cooled in usual manner. The pulsed current was measured by means of Rogowski coil, and monitored by digital oscilloscope.

In this paper we report the results of plasma jet temperature determination from the Stark shift of Ar I 415.86 nm spectral line.

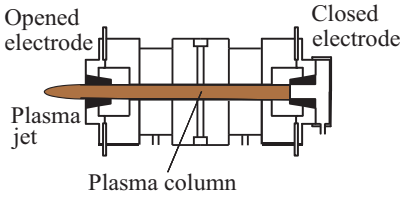

Figure 1: Illustration of plasma jet formed in free space.

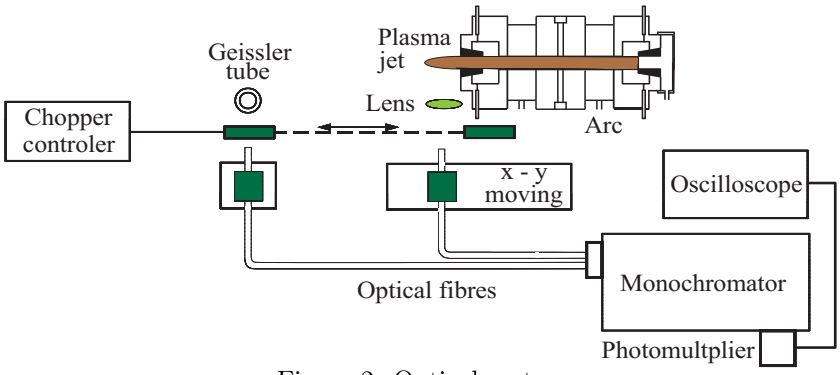

Figure 2: Optical system.

2. OPTICAL ASSEMBLY FOR PULSED PLASMA JET OBSERVATION

In order to record optical emission from plasma jet, optical system shown in Fig. 2 was assembled. It enables recording of spatially resolved integral intensity of the plasma jet radiation. X-Y moving system provides recordings of integral optical emission at different positions. Optical signals are led to the digitizing oscilloscope through the optical fibre monochromator and photomultiplier.

An example of time resolved recorded optical signal is given in Fig. 3. In the figure one can see pulsation in the optical intensity. It is consequence of the pressure pulsation inside of the stabilized arc after the current pules was applied.

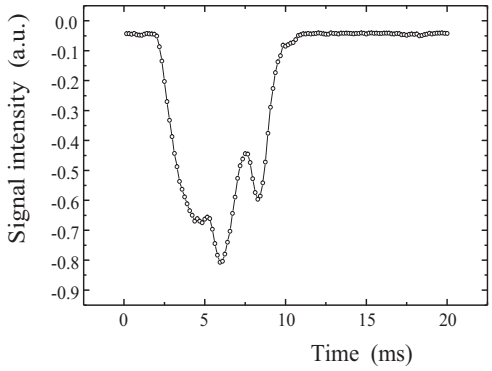

Figure 3: Time resolved optical signal.

3. THE TEMPERATURE DETERMINATION

The temperatures at different times of the plasma jet decay were determined from the measured dependence of Ar I 415.86 nm line shift on the temperature (Djurović et al. 2002, Popenoe and Shumaker 1965) (Fig. 4).

A low pressure argon Geissler tube is used as a reference source of unshifted argon spectral line. For the shift measurements, the light from both plasma jet and reference source is directed onto the entrance slit of the monochromator by optical fibers (see Fig. 2). In this way by using a chopper, light from the reference source or from plasma jet can be detected alternatively by the photomultiplier placed at the exit slit of the monochromator. Both signals are recorded at each wavelength step along the investigated wavelength interval.

An example of recorded Ar I 415.86 nm spectral line from the plasma jet and reference source is shown in Fig. 5. This profile corresponds to the time of maximal emissivity and it was recorded at the position on the jet axis close to the exit hole of the arc.

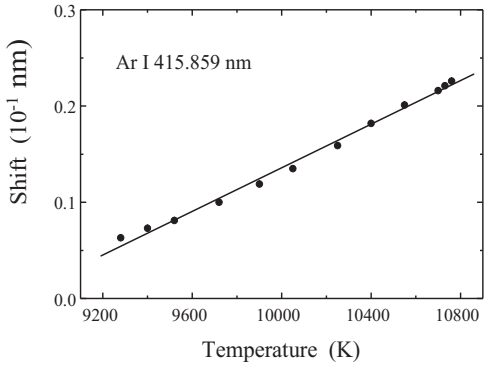

Figure 4: Dependance of the shift of 415.86 nm line on the temperature (Djurović et al. 2002, Popenoe and Shumaker 1965).

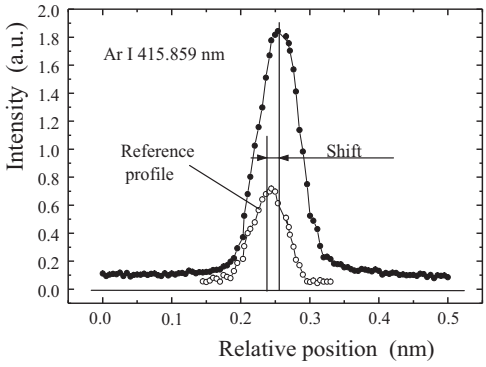

Figure 5: An example of the recorded profiles from plasma jet and reference source.

Combining the results of measured shifts with graph in Fig. 4, the temperatures of plasma jet for various times of plasma decay were obtained. This is presented in Fig. 6. The values on the horizontal axis correspond to the time measured from the beginning of the plasma jet formation.

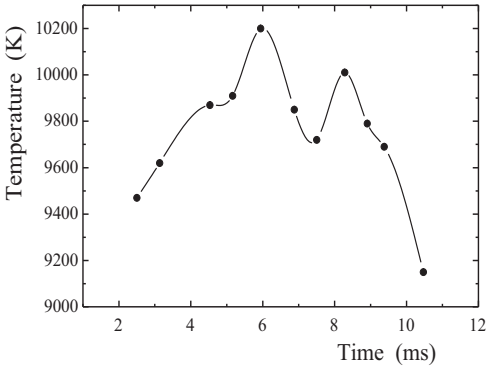

Figure 6: Temporal dependence of the plasma jet temperature.

As it can be seen from Fig. 6, the maximuma of the temperature are at 6 and 8.3 ms after plasma jet formation. This corresponds to the maximum of the plasma emissivity (see Fig. 3). At 6 ms plasma temperature reaches 10200 K, while in the later times it falls to 9000 K.

Acknowledgements

This work is supported by the Ministry of Science, Republic of Serbia, under contract No. 141024.

References

Ćirišan, M., Djurović, S., Mijatović, M., Vujičić, B. and Kobilarov, R.: 2006, *J. Res. Phys.*, **30**, 95.

Djurović, S., Mijatović, Z., Ćirišan, M., Vujičić, B. and Kobilarov, R.: 2004, *Contributed paper of 22nd SPIG*, Ed. Lj. Hadievski, p. 333.

Djurović, S., Mijatović, Z., Kobilarov, R. and Konjević, N.: 1997, *J. Quant. Spectrosc. Radiat. Transfer*, **57**, 695.

Djurović, S., Nikolić, D., Mijatović, Z., Kobilarov R. and Konjević, N.: 2002, *Plasma Sources Sci. Technol.*, **11**, 95.

Popenoe, C. H. and Shumaker J. B. Jr.: 1965. *J. Res. NBS, Phys. Chem.*, **69A**, 495.

Publ. Astron. Obs. Belgrade No. 84 (2008), 309 - 312 *Contributed Paper*

SPECTROSCOPIC STUDY OF HIGH ENERGY EXCITED HYDROGEN ATOMS IN A HOLLOW CATHODE GLOW DISCHARGE

N. M. ŠIŠOVIĆ[1], G. Lj. MAJSTOROVIĆ[2] and N. KONJEVIĆ[1]

[1] *Faculty of Physics, University of Belgrade, 11001 Belgrade, P.O. Box 368, Serbia*
E–mail: nikolas@ff.bg.ac.yu

[2] *Military Academy, 11105 Belgrade, Pavla Jurišića - Šturma 33, Serbia*

Abstract. Presented results are concerned with the shape of Balmer alpha line emitted from a low pressure DC glow discharge with aluminum (Al) and copper (Cu) hollow cathode (HC) in pure hydrogen and in Ar-H_2 gas mixture. The analysis indicates that the line profile represents a convolution of Gaussian profiles resulting from different collision excitation processes.

1. INTRODUCTION

Recently recorded Balmer line shapes along the axis of a hollow cathode discharge and side-on to the Grimm discharge are found to be symmetric in H_2 and in hydrogen-inert gas mixtures (Šišović et al. 2005, Cvetanović et al. 2005). These profiles exhibit multicomponent behaviour that can be analyzed with great precision by fitting with several Gaussians.

The narrowest part of profile with the Doppler temperature not exceeding 1 eV, and middle part of line profile, with Doppler temperature smaller then 10 eV, are related to excited H* atoms generated in collision of high-energy electrons with H_2 molecules (see e.g. Majstorović et al. 2007 and references therein). The pedestal of line profile is anomalously broad, indicating the presence of energetic H* atoms, having energies larger than hundred eV, see Fig. 1.

The explanation of the phenomena of anomalous Doppler broadening (ADB) of hydrogen Balmer lines is based on a sheath-collision model (Petrović et al. 1992, Radovanov et al. 1995, Gemišić-Adamov et al. 2003). According to this model, the anomalously broaden part of hydrogen line profile is related to the hydrogen atomic and molecular ions (H^+, H_2^+ and H_3^+) present in discharge under the typical discharge conditions. In the cathode sheath region the accelerated ions exchange electric charge with hydrogen molecules and, as a result, fast neutrals and slow ions appear:

$$(H^+)_f + (H_2)_s \rightarrow H_f^* + (H_2^+)_s$$

$$(H_2^+)_f + (H_2)_s \rightarrow H_f^* + H_f + (H_2^+)_s$$

$$(H_3^+)_f + (H_2)_s \rightarrow H_f^* + (H_2)_f + (H_2^+)_s$$

where f and s denote fast and slow particles, respectively. It is shown that the particles (H^+, H_2^+ and H_3^+, H_2 and H) having energies of the order of magnitude of 10^2 eV are back scattered from metals in the form of fast hydrogen atoms H (Eckstein et al. 1976). The number and the energy of back-scattered atoms depend upon the material, while their spatial distribution follows cosine law.

The main sources of fast excited hydrogen atoms are H^+ and H_3^+ ions (exhibit an asymmetrical charge-exchange reaction in collisions with H_2), which are, as a consequence of relatively low cross-sections for collisions, efficiently accelerated towards cathode. On their way to cathode, some of these ions collide with the matrix gas H_2, producing fast exited neutrals H^*. The rest of accelerated ions reach the cathode where they neutralize, or neutralize and fragmentize. The back-reflected particles from the cathode are fast H atoms directed back to discharge. After collisions of these fast H atoms with H_2 and/or with other discharge constituents, fast excited hydrogen atoms H^*, are produced also. Thus, the fast excited hydrogen atoms moving towards and from the cathode are detected in different discharges by means of Doppler spectroscopy of Balmer lines.

In argon-hydrogen mixtures, the ADB Balmer line profile looks different from those in pure hydrogen isotopes (see Šišović et al. 2007 and the references therein). The line shape with strong line wings, see below, Fig. 2, is the result of dominant role of H_3^+ ion that is efficiently produced in Ar-H_2 mixture. The excited H atoms after fragmentation of H_3^+ ion in collision with H_2 or back-scattered H atoms from cathode have smaller energy (total ion energy is shared between three particles) than in the case of H^+.

The aim of this work is to study the H_α line shape in aluminum (Al)and copper (Cu) HC glow discharge operated in H_2 and Ar-H_2 gas mixture. Special attention will be devoted to the correlation between line shape and cathode material.

2. EXPERIMENTAL

In this experiment, the H_α line shapes were observed in aluminum and copper hollow cathode discharges operated in pure hydrogen and in inert gas-hydrogen mixture (Ar + 0.8% vol. H_2) at a pressure of 2 mbar. The HC tubes were 100 mm long with 6 mm internal diameter. The discharge source is described elsewhere (Šišović et al. 2005). Here, we shall mention only few important details relevant to the optical setup for line shape recordings. The light along the axis of hollow cathode glow discharge is focused by an achromat quartz lens onto the entrance slit of spectrometer (2 m focal length; reciprocal dispersion 0.74 nm/mm in the first order with a 651 grooves/mm reflection grating). Spectral line shape measurements are performed with an instrumental profile having Gaussian shape with 0.018 nm full half-width. Signals from CCD detector (3648 pixels, 8 μm) are collected and processed by PC. During the discharge operation, cathode was air cooled while HC wall temperature is controlled with a K-type thermocouple.

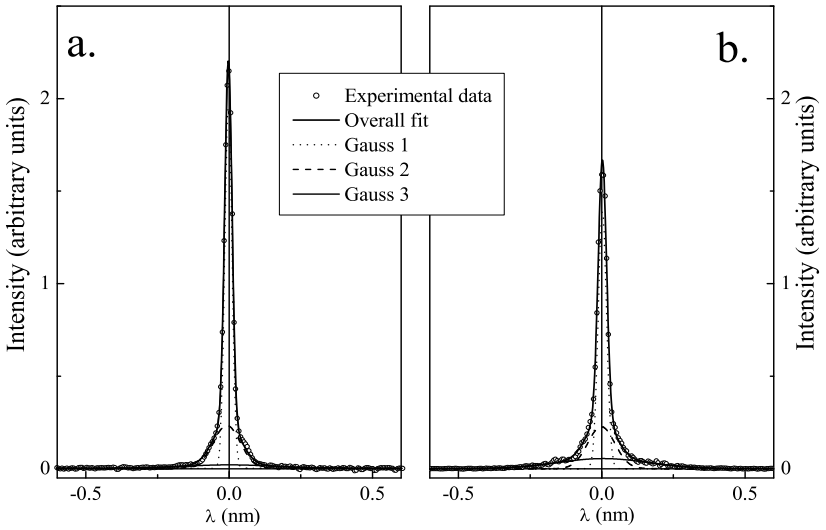

Figure 1: The H_α line profiles recorded in the center of an hollow cathode glow discharge in H_2 and their best fits: (a) Aluminum, U=385V; I=90 mA and p=2mbar; and (b) Copper, U=405V; I=90 mA and p=2 mbar.

3. RESULTS AND DISCUSSION

Typical examples of the H_α line shape recording from the central region of aluminum and copper HC operated with hydrogen in low-voltage glow discharge regime are given in Fig. 1. For the fitting of experimental profiles three Gaussian (Gauss 1, 2 and 3) are successfully used in most cases. Here, it should be noticed that an exception occurs when the extremely large contribution of the ADB part masks the middle component. An illustrative example is the shape of H_α line recorded from the copper HC discharge in Ar-H_2 mixture, see Fig. 2b.

The results for energies of fast excited hydrogen atoms derived from the width of Gauss 3, about 56eV, prove that the anomalous H_α line broadening is present in both discharges under studied experimental conditions. The Gauss 3 contribution to the profile is considerably lower for aluminum (7.7%) than for copper (18.0%) HC. This difference can be explained qualitatively by lower number reflection coefficient R_N of H^+ ions on aluminum (Tabata et al. 1983).

In the HC experiment with Ar-H_2 gas mixture, this difference is detected as well (46.9% and 29 eV for Al versus 95.1% and 44 eV for Cu). Here, it should be pointed out that the reflection coefficients of H and H^+ are of marginal importance in Ar-H_2 gas mixture where the dominant interacting ion with cathode is H_3^+. Unfortunately, the reflection coefficients of H_3^+ from polycrystalline metals are not available.

The results in Figures 1 and 2 indicate that the concentration and energy of fast excited hydrogen atoms depend upon cathode material through its back scattering coefficient.

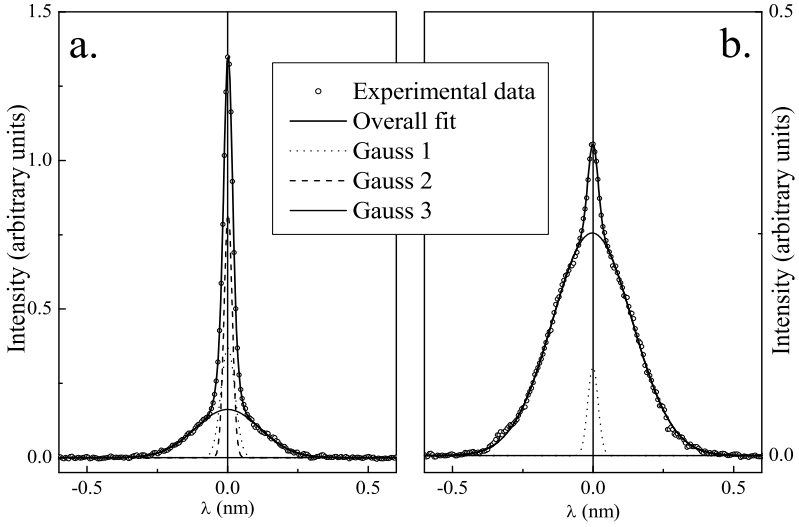

Figure 2: The H_α line profiles recorded in the center of an hollow cathode glow discharge in H_2 and their best fits: (a) Aluminum, U=324V; I=90 mA and p=2 mbar; and (b) Copper, U=326V; I=90 mA and p=2mbar.

The surface composition like the presence of metalic hydrades at cathode surface is of importance also (Šišović et al. 2007).

Acknwoledgements

This work is supported by the Ministry of Science of the Republic of Serbia (Project 141032B).

References

Cvetanović, N., Kuraica, M. M., Konjević, N.: 2005, *J. Appl. Phys.*, **97**, 033302.
Eckstein, W., Matschke, F. E. P., Verbeek, H.: 1976, *J. Nucl. Mater.*, **63**, 199.
Gemišić-Adamov, M. R., Obradović, B. M., Kuraica M. M., Konjević N.: 2003, *IEEE Trans. Plasma Sci.*, **31**, 444.
Majstorović, G. Lj., Šišović, N. M., Konjević, N.: 2007, *Phys. Plasmas*, **14**, 043504.
Petrović, Z. Lj., Jelenković, B. M., Phelps, A. V.: 1992, *Phys. Rev. Lett.*, **68**, 325.
Radovanov, S. B., Dzierzega, K., Roberts, J. R., Olthoff, J. K.: 1995, *Appl. Phys. Lett.*, **66**, 2637.
Šišović, N. M., Majstorović, G. Lj., Konjević, N.: 2005, *Eur. Phys. J. D*, **32**, 347.
Šišović, N. M., Majstorović, G. Lj., Konjević, N.: 2007, *Eur. Phys. J. D*, **41**, 143.
Tabata, T., Ito, R., Itikawa, Y., Itoh, N., Morita, K.: 1983, *At. Data Nucl. Data Tables*, **28**, 493.

Publ. Astron. Obs. Belgrade No. 84 (2008), 313 - 316 *Contributed Paper*

DETERMINATION OF PLASMA SPACE POTENTIAL FROM A LANGMUIR PROBE BY TIKHONOV'S REGULARIZATION METHOD

S. MIJOVIĆ[1], M. VUČELJIĆ[1], I. VOJVODIĆ[1], R. SCHRITTWIESER[2], M. MALJKOV[3], D. G. DIMITRIU[4], C. IONITA[5]

[1] *Faculty of Sciences and Mathematics, Podgorica, Montenegro*
E–mail: slavom@rc.pmf.cg.ac.yu

[2] *Institute for Ion Physics and Applied Physics, Leopold-Franzens University of Innsbruck, Technikerstr. 25, A-6020 Innsbruck, Austria*

[3] *University of Saransk, Serova 3,Saransk, Russia*

[4] *Department of Plasma Physics, Faculty of Physics, "Al. I. Cuza" University of Iasi, 11 Carol I Blvd., RO-700506 Iasi, Romania*

[5] *Institute for Ion Physics and Applied Physics, University of Innsbruck, Technikerstr. 25, A-6020 Innsbruck, Austria*

Abstract. An analysis of the accurateness of determining the plasma space potential from the probe current-voltage characteristics have been performed to improve the accurateness of the consequently determining plasma parameters from it. The problem is analyzed as an inverse and ill-posed one. Tikhonov's regularization method was introduced to solve such problem. It was shown that the accurate determination of the plasma potential is the most important for low temperature plasma $< 1eV$. The method was checked in argon plasma created in the double plasma machine. The satisfactory results were obtained.

1. INTRODUCTION

One of the most important and frequently used plasma diagnostic techniques is the Langmuir probe method. This method, which was first introduced by Langmuir more than eighty years ago, allows to provide the most important characteristics such as electron density n , space potentials V_s , average electron energies $< \varepsilon >$(temperatures T_e), electrical fields E, electron energy distribution function (EEDF), drift velocities etc. Knowing these parameters gives a possibility to determine a series of other important characteristics-rates of many non-elastic processes, populations of excited levels of an atom or ion, coefficients of mobility and diffusions and others. One should note that nowadays, namely probe methods produced a great number of quantitative data of plasma characteristics. The main advantage of electrical probes to greatness other methods, is their possibility to measure local values of plasma characteristics. Thus, a great attention is constantly given to developing and accuracy of the probe methods. The starting point in the processing of a probe current-voltage characteristic (CVC)

is always determination of the plasma space potentials. The consequently determined plasma parameters highly depend on the accurateness of the determination of the space potential. In this work an analysis of determination of the plasma potential from the CVC is done, considering the problem as an ill-posed one (Tikhonov and Goncharski 1987).

2. METHOD

The fundamental plasma parameters can be determined by placing a small conducting probe into the plasma and observing the current to the probe as a function of the difference between the probe and the plasma space potentials. The plasma space potential is just the potential difference of the plasma volume with respect to the vessel wall (anode). The simplicity of equipment and experiment constitute the advantages of the probe method. The disadvantages lie in complexities of the theory used to extract plasma characteristics from probe measurement data. There is only a limited range of conditions under which the theory is only moderately complicated and does not lead to a considerable probability of obtaining erroneous results and faulty interpretation (Raizer 1987). As it is shown in (Kagan 1970), the electron component of the probe current is given as,

$$i_e = (2e\pi n_e/m^2)S \int_{eV}^{\infty} (\varepsilon - eV)\ f_0(\varepsilon)\ d\varepsilon \tag{1}$$

where are n_e- electron density; e, m- elementary charge and mass of an electron respectively; ε- electron energy; V- a retard potential applied on the probe; S the surface area of the probe, and $f_0(\varepsilon)$- electron energy distribution functions in the unperturbed plasma. With the distribution function known, any quantity characterizing electron gas can in principle be calculated. Twice differentiating the eq. 1, with respect to the probe potentials V gives

$$d^2 i_e/dV^2 = (2e^3 n_e \pi/m^2) S f_0(eV) \tag{2}$$

This method, first employed by Druyvesteyn in 1930 (Druyvesteyn 1930), is still used nowadays, with certain improvements. Because of the function $i_e(V)$ is measured with some errors,its direct double differentiation involves considerably errors.For this reason, $d^2 i_e/dV^2$ has to be found by indirect means. Let us analize than, not the eq.2 but eq.1. The given inverse problem is a typical example of so-called ill-posed problem (Tikhonov and Goncharski 1987). The basic characteristic of such problems is its nonstability of the solution in respect to the perturbation of the input information. In our case small errors in the given curve $i_e(V)$ can result in arbitrarily great errors of the asked EEDF $f_0(eV)$.

A. N. Tikhonov found a possibility for obtaining a stable approximate solution $f_0(\varepsilon)$ knowing minimum *a priori* information of the asked solution.

3. RESULTS

Some typical results of our analyses are shown in the Figures below. In order to check applicability of the Tikhonov's method several model tasks were introduced. At the Fig. 1., are shown results obtained in such way: a hypothetical electron component

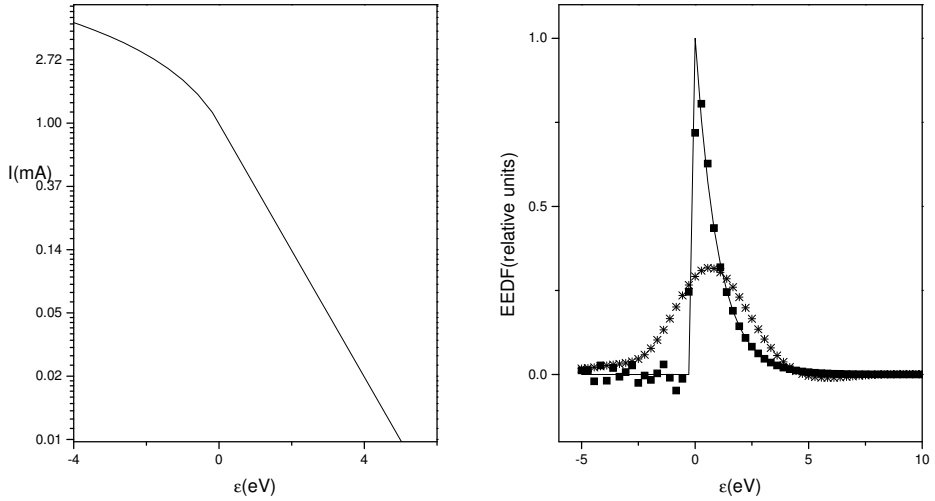

(a) (b)

Figure 1: (a) Model probe CVC ; (b) The exact EEDF (solid line); EEDF obtained by the regularization, the simulated absolute maximum errors 0.1% (square); the simulated maximum errors 5% (star).

of a CVC was simulated by solving the direct problem described by eq. 1, in an assumption that EEDF $f_0(\varepsilon)$, is Maxwell's with the electron temperature $T_e = 1eV$. Then, artificial random noises were added to the CVC in order to simulate an experimental CVC. Finally, the inverse problem, i.e., finding $f_0(\varepsilon)$, was solved using Tikhonov's procedure. Only *a priory* information was an estimation (in this case known) of the experimental errors. From the Fig. 1., one can estimate the powerfulness of the method. Extracting information from real experimentally obtained CVCs using Tikhonov's regularization method is shown in Fig. 2. The experimentally CVC were obtained in the double plasma machine in Institute of Ion Physics in Innsbruck.The extracted EEDF from the CVC of the probe is shown in Fig. 3, supposing the experimental errors to be 0.4 %.

4. DISCUSSIONS AND CONCLUSIONS

From the Fig. 1b) one can see the severe dependence of obtaining the plasma potential and EEDF versus the experimental errors. At the knee of the probe CVC (given on semi-logarithmic scale), d^2i/dV^2 reverses its sign and this fact rather facilitates the determination of the bend point of the CVC and of the plasma potential. It is clear from the Fig. 1, that one can not pretend to obtain the plasma potential in better accuracy than 0.5 V , even in very quiescent plasmas. Such deviation is the most important if the plasma temperatures are less than 1 V , due to the great relative error. The situation is more complex when applying this method to the real experimentally probe CVC due to influences of many other factors.

From the Fig. 2 it is clear that EEDF is not Maxwell's one (the CVC on semi-logarithmic scale is not a line) and our method discovered two groups of electrons (see the Fig. 3) like as in (Sternovsky and Robertson 2004). Furthermore the second derivative of the CVC is still reverses sign at (or near) the plasma potential. Thus, it was found that Tikhonov's regularization procedure could be a reasonable effective method to estimate the plasma potentials and EEDF from a probe CVC.

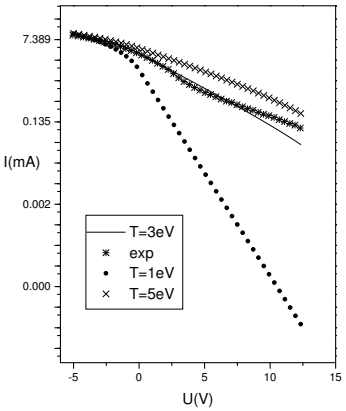

Figure 2: The experimental probe characteristic (*); model probe characteristic for different temperatures.

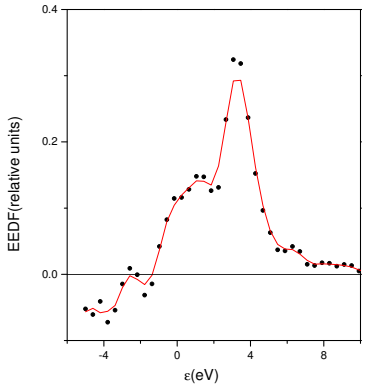

Figure 3: EEDF obtained by regularization method from the experimental CVC.

References

Druyvesteyn, M. J.: 1930, *Z. Phys.*, **64**, 917.
Kagan, Yu. M.: 1970, Raspredelenie elektronov po skorostyam v polozhitel'nom stolbe razryada, Nauka, Lenjingrad, str. 201-223,
Raizer, Y. P.: 1987, Fizika gazovogo razryada, Nauka, Moscow.
Sternovsky, Z. and Robertson, S.: 2004, *Phys.Plasmas*, **11**, 3610.
Tikhonov, A. N. and Goncharski, A, V.: 1987, Ill-posed Problems, Moscow University Press, Moscow.

Publ. Astron. Obs. Belgrade No. 84 (2008), 317 - 320 *Contributed Paper*

ELECTRIC FIELD MEASUREMENT IN THE CATHODE FALL REGION OF A DIELECTRIC BARRIER DISCHARGE IN HELIUM

B. M. OBRADOVIĆ, S. S. IVKOVIĆ, I. P. DOJČINOVIĆ, M. M. KURAICA and J. PURIĆ

Faculty of Physics, University of Belgrade, P.O.Box 368, 11000, Belgrade, Serbia
E–mail: obrat@ff.bg.ac.yu

Abstract. Dielectric barrier discharges in helium is investigated by temporally and spatially resolved optical emission spectroscopy. Focus of our investigation was He I 447.15 nm line which can be used in electric field measurements. At maximum discharge current the spatial line intensity distribution and the electric field distribution are characteristic for the cathode fall region. Estimated electric field strength distribution is in agreement with theoretical calculation. Temporal evolution of He I 447.15 nm line during the breakdown is also studied.

1. INTRODUCTION

The barrier discharge is one of the plasma sources at high pressure widely applied in thin film deposition, surface modification, and plasma chemistry. It is a low frequency alternating current (AC) discharge in a narrow gap between two electrodes of sufficiently large area covered by a dielectric barrier. Various configurations of electrodes are used in the barrier discharge; the plane configuration is most simple and suitable for an experimental investigation and a theoretical description. At certain conditions this discharge is homogeneous in the plane of electrodes. The homogeneous barrier discharge is very attractive for the applications in plasma technologies, especially in surface treatment. It has become the object of the intensive experimental and theoretical investigations, see e.g. Massines et al. 1998, Golubovskii et al. 2003, Navrátil et al. 2006. The homogeneous barrier discharge in helium is characterized by the narrow current pulses of large (tens of milliampere) amplitude; there is only one pulse per half-cycle of the external voltage. In this mode of the discharge, the spatial structure containing the cathode fall, Faraday dark space, and positive column, develops in the phase of maximal current, see Massines et al. 1998. This circumstance allowed referring to this mode of discharge as the atmospheric pressure glow discharge. In this work we studied development of a barrier discharge in helium and measured electric field strength nearby the cathode.

2. EXPERIMENT

The discharge was generated in a parallel plane discharge configuration consisting of two metal electrodes (50 × 50mm) both covered by a 0.65 mm thick alumina layer (105 × 105 mm). The electrodes were fixed by two space holders made of glass ensuring a constant discharge gap of 2 mm. The discharge cell was placed in a vacuum chamber that was evacuated down to 10^{-3} mbar first and then filled with helium (purity

99.996 %) at 200 mbar pressure. The gas was directly injected into the discharge volume with a flow rate of 2 l/min. The discharge was driven by a pulse voltage of frequency 5 kHz. The applied voltage and the discharge current were measured by Tektronics TDS 3032 (300 MHz bandwidth, 2 GSamples/s) digital oscilloscope. The applied voltage was measured via a 1000:1 voltage probe; the current was monitored by measuring the voltage across a 50 Ω resistor connected in series with the discharge cell. For time resolved emission measurements, projection optics are used to image the whole electrode gap region onto the entrance slit of a 1m spectrometer and detected using an intensified charge coupled detector (ICCD). ICCD is triggered with a time delayed pulse generated initially by the power supply. Recorded images consist of 50 accumulations each made of 50000 gates per exposure. The gate duration was 80 ns.

3. RESULTS AND DISCUSSION

Typical current and voltage oscillogram of DBD in pure helium during a single cycle is shown in Fig. 1. The current is characterized by one pulse per cycle with the amplitude of 60 mA and the rise time 0.3 μs. At first the current pulse has quick decrease ($\sim$ 1 μs) followed by a slower decrease ($\sim$ 10 μs). The applied voltage has one negative pulse during the cycle. The voltage oscillations is due imperfection of power supply. Before the breakdown i.e. before the current peak starts to rise, the applied voltage reached values of 0.5 kV. In Fig. 1b an enlarged view of the current oscillogram is shown and the time interval in which the discharge is spectroscopicaly investigated is marked.

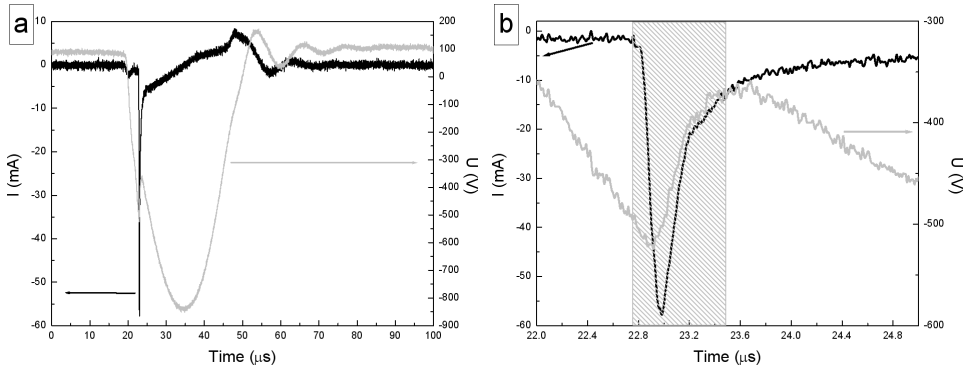

Figure 1: a) Applied voltage and discharge current variation during one cycle. Pressure 200 mbar.

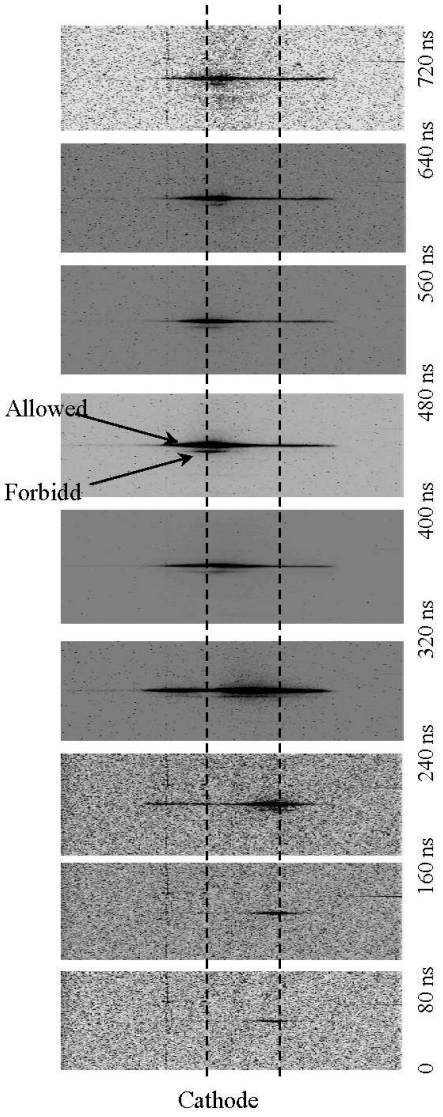

Figure 2: Spatial and temporal evolution of the He I 447.15 nm.

Figure 2 shows the evolution of He I 447.15 nm line in the time interval marked on Fig. 1b. In our earlier papers, see Kuraica and Konjević 1997, Kuraica et al. 1997, we used Stark splitting and shifting of the He I 447.15 nm line and its forbidden component in order to measure electric field strength in the cathode fall region of an analytical glow discharge. Time evolution and space distribution of the He I 447.15 nm line can give information about evolution of the electric field in the DBD during the breakdown. In Fig. 2 can be observe the characteristic phases of the breakdown, see

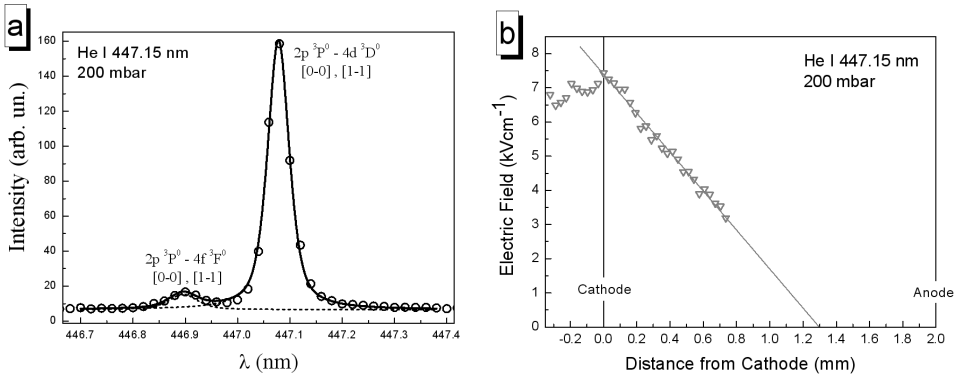

Figure 3: a) Typical π polarized spectra of He 447.1 nm allowed and its forbidden component.

Golubovskii et al. 2003. At t $<$ 160 ns the maximum of the ionization rate is nearby the anode. In this phase, the electric field is weakly disturbed by spatial charge, and the electron density increases from the cathode to the anode exponentially. Further, an ionization wave appears nearby the anode which can be observed by higher intensity of the He I 447.15 nm line nearby the anode. The ionization wave moves towards the cathode at 160 $<$ t $<$ 400 ns. In this phase, the field nearby the cathode begins to grow. As the ionization wave reaches the cathode (t $\sim$ 400 ns), the spatial profile of the electric field changes abruptly. The structure of the discharge becomes similar to that of an ordinary glow discharge, containing a cathode fall, observable by the large intensity of the He I 447.15 nm line forbidden component in a narrow region near the cathode.

Following the method that demonstrated Kuraica and Konjević 1997, the electric field strength, in the time of maximal current, is determined using Stark splitting of He I 447.15 nm line polarized in electric field direction (π polarized). An example of a typical π polarized spectra of He I 447.15 nm allowed and its forbidden component, recorded in the DBD in helium is shown in Fig. 3a. Both components of the line are fitted with pseudo-Voight profiles (sum of Gauss and Lorentz profiles) in order to estimate peak-to-peak distance according to which the electric field is determined. Spatial distribution of the measured electric field strength in the vicinity of the cathode is presented in Fig. 3b. Negative values for the distance from the cathode is consequence of light reflection from the alumina layer and has no physical meaning. The electric field values and its spatial distribution is comparable with the theoretical calculation see e.g. Massines et al. 1998, Golubovskii et al. 2003, that are made for 1000 mbar pressure.

References

Golubovskii, Yu. B., Maiorov, V. A., Behnke, J., Behnke, J. F.: 2003, *J. Phys. D*, **36**, 39.
Kuraica, M. M., Konjević, N.: 1997, *Appl. Phys. Lett.*, **70**, 1521.
Kuraica, M. M., Konjević, N., Videnović, I. R.: 1997, *Spectrochim. Acta B*, **52**, 745.
Massines, F., Rabehi, A., Decomps, P., Ben Gadri, R., Segur, P., Mayoux, C.: 1998, *J. Appl. Phys.*, **83**, 2950.
Navrátil, Z., Brandenburg, R., Trunec, D., Brablec, A., St'ahel, P., Wagner, H-E., Kopecký, Z.: 2006, *Plasma Sources Sci. Technol.*, **15**, 8.

Publ. Astron. Obs. Belgrade No. 84 (2008), 321 - 324 *Contributed Paper*

DETERMINATION OF NITROGEN DENSITY IN DIRECT CURRENT (dc) GLOW DISCHARGES

D. POPOVIĆ[1], V. MILOSAVLJEVIĆ[2] and S. DANIELS[3]

[1] *Faculty of Physics, University of Belgrade, P.O.B. 368, Belgrade, Serbia*
E–mail: dusan@ff.bg.ac.rs

[2] *Faculty of Physics, University of Belgrade, P.O.B. 368, Belgrade, Serbia*
NCPST, School of Physics, Dublin City University, Dublin 9, Ireland
E–mail: vladimir@ff.bg.ac.rs

[3] *NCPST, School of Electronic Engineering, Dublin City University, Dublin 9, Ireland*
E–mail: daniels@eeng.dcu.ie

Abstract. Measurement of atomic and molecular nitrogen in an oxygen–nitrogen dc plasma has been presented. This is achieved by monitoring the intensities of the atomic nitrogen spectral line at 821.6 nm and the molecular nitrogen bandhead at 337.1 nm, relative to the atomic oxygen spectral line at 844.7 nm. Oxygen is the one of most frequently used gases for surface chemical treatment, including deposition and etching and therefore the ability to measure and control the process and chemical composition of the process is essential.

To validite the oxygen actimometry method for N_2–$x$$O_2$ (where x varies from zero to one) dc plasmas, threshold tests have been performed with Ar actinometry.

1. INTRODUCTION

Nitrogen plays an important role in the synthesis of nitrides owing to its high chemical reactivity. Therefore information regarding the concentration of active species in a nitrogen discharge is essential for the better control of plasma reactions and plasma–surface interactions.

Most plasma diagnostic techniques are either electrical or optical in nature. Among the electrical techniques, the most widely used method is the Langmuir probe because of its easy implementation. However, experimental problems such as contamination of the probe tip and complexities in the theory to interpret the measurements can often lead to erroneous results. Additionally, most modern commercial reactors that use reactive plasmas as processing reagents are not amenable to probes, which are invasive by nature and risk introducing undesirable process shifts. Optical actinometry provides a non–intrusive means of studying a reactive plasma. In this diagnostic technique a small amount (1–2%) of a rare gas is added to the reactive plasma and this serves as the actinometer. The concentration of the actinometer is kept constant and the optical emission derived from it is used to determine the excitation efficiency of the plasma when the discharge parameters are changed. This 'actinometry' method works well when the relative energy dependence of the electron impact excitation of

the rare gas matches that of the emitting species of interest. However, the use of a trace gas as an actinometer in an industrial setting can be problematic, as the requirement for an additional gas line would be outweighed by cost considerations. Also, a rare trace gas dilutes the chemically reactant gases and for many plasma processes this is unwanted. Therefore, the ability to use non–trace gas (like oxygen in our experiment) as the actinometric gas would negate the requirement for additional trace gases and therefore allow this technique to be applied in a manufacturing process. It must be stated, however, that the validity of actinometry is somewhat controversial and the criteria for the utilization of the technique and its limits of validity must be verified in each case (Popović et al. 2007). It is because of this cautionary note that extensive validation measurements have been performed on our system which uses oxygen as the actinometry gas. The validation procedure uses the actinometric technique itself as trace amounts of Ar gas have been added to the N_2–O_2 discharge to confirm the applicability of the technique for a range of N_2–O_2 discharges. The validity of using the non–trace gas as the actinometer should be manifested as an agreement between the oxygen and argon actinometry data under a range of plasma conditions. Once this validation procedure is complete, we no longer use trace gas Ar in the process and can revert back to actinometry measurements using the buffer gas (Milosavljević et al. 2007) of the process (oxygen).

2. EXPERIMENT

A dc discharge is produced in a Pyrex tube of 5 mm inner diameter and effective plasma length of 72 mm.

The discharge tube is evacuated using a rotary vane pump which gives a base pressure of 2 Pa. The working pressures from 50 Pa to 266 Pa are achieved using a gate valve positioned above the rotary pump. Gas flow into the chamber is controlled via mass flow controllers which precisely determine gas content in the discharge tube. The nitrogen and oxygen flow rate is varied up to 200 sccm. The power supply used was a Keithley Model 248 High Voltage Supply with the maximum voltage of 5kV

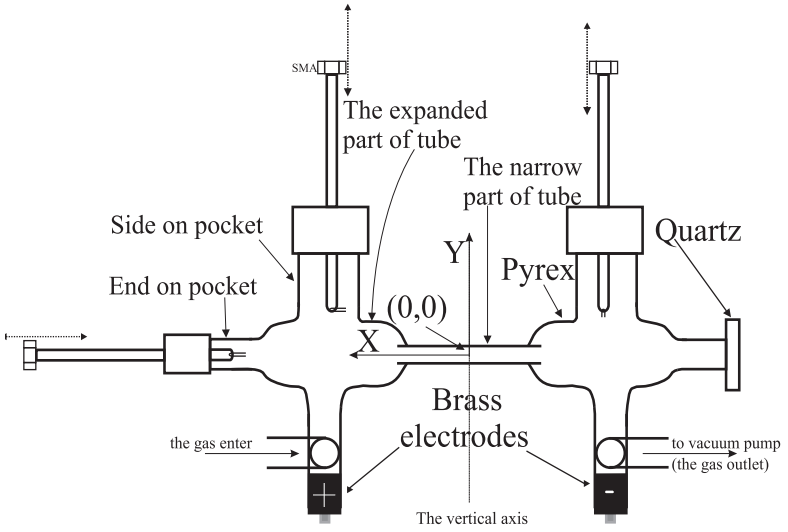

Figure 1: Plasma source with ports for the probes.

and discharge current of 5 mA. For the purposes of this experimental work the maximum voltage is 2.2kV. In fact the large parameter space required of this work meant that a Design of Experiment (DOE) had to be implemented i.e. DC voltage: 700–2200 V, N_2 gas flow rate (4–200 sccm), O_2 gas flow rate: (2–200 sccm) and chamber pressure: 50–266 Pa. The application of this DOE reduced the number of experimental runs to 36. The creation of DOE table is done by The Statistical Discovery software^{TM}, JMP IN^{TM}.

The experimental setup with associated diagnostics is present in Popović et al. (2007).

3. RESULTS AND DISCUSSION

The actinometry atomic oxygen spectral lines are: the 777 nm spectral line from the 3s–3p transition originating from the $^5S^o$–^5P multiplet and the 845 nm spectral line from 3s–3p transition originating from the $^3S^o$–^3P. In the N_2–O_2 mixture only the 845 nm line was used for actinometry since the 777 nm line is embedded in the first positive system of nitrogen molecules. The O I 844.476 nm is also a good choice, since the electron excitation of the ground state of O–atoms is a dominant process (Ricard 1996).

The density of atomic nitrogen is determinated by measuring the emission of the spectral line at 821.634 nm from 3s–3p transition and $^4P_{5/2}$–$^4P^o_{5/2}$ multiplet. While, the density of molecular nitrogen is determinated by the measurement of emission from a second positive system, i.e. 337.1 nm transition $C^3\Pi_u$,v'=0 → $B^3\Pi_g$,v"=0. Transition from second positive system are usually used for this purpose because they are mainly populated by direct electronic excitation from the ground state of N_2, and the excitation energy is close to that of excited nitrogen atom.

As is well known the actinometer should not disturb the discharge but oxygen is, in fact, part of the plasma chemistry used in these experiments. Therefore, argon was required to be employed as an actinometer in trace amounts (about 4% of the total pressure) in order to determine the threshold for actinometry by oxygen in these plasmas. It is essential that as little argon as possible be introduced into the nitrogen–oxygen plasma, only enough to be able to record the argon actinometry line. Argon is commonly chosen as an actinometer, and the 750 nm Ar I spectral line from the 4s–4p transition originating from the $^2[1/2,\ 3/2]^o$–$^2[1/2]$ multiplet is very popular because it is not sensitive to two step excitation. However, for the same reasons as in the case of oxygen actinometry line 777.4 nm, the emission of argon 750.4 nm spectral line is disturbed by the emission of nitrogen. However, this problem can be overcome by using another atomic argon actinometry line 811.531 nm. This line belongs to 4s–4p transition and $^2[3/2]^o_2$–$^2[5/2]_3$ multiplet.

Figure 2 shows a selection of the actinometry results obtained from oxygen and argon as the percentage of oxygen in the nitrogen–oxygen plasma is increased from 0 to 100%.

This plot reveals that in the plasma operating conditions used here, oxygen can be used as an actinometer when the concentration of oxygen in the plasma is not higher then 28%, the DC voltage is less than 1.1 kV and the total pressure is less than 120 Pa. To operate successfully over the full range of dc voltage used in this experiment, pressure and flows, oxygen can only be used as the actinometer if its concentration in the nitrogen–oyxgen plasma is less than 15%.

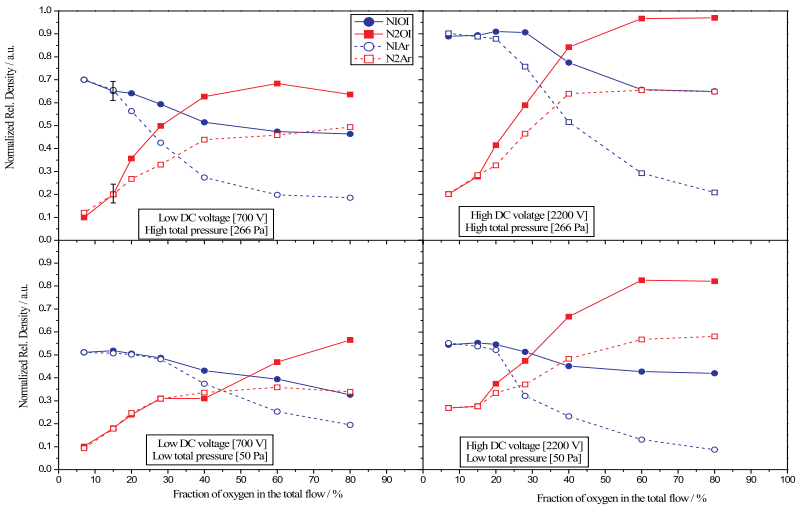

Figure 2: Actinometry results by oxygen (full lines) and by argon (broken line). NIOI and N2OI represent densities of atomic nitrogen and molecular nitrogen, respective, determinate by oxygen as actinometer. NIAr and N2Ar represent densities of atomic nitrogen and molecular nitrogen, respective, determinate by argon as actinometer. The error bar include reproducibility of the measurement.

4. CONCLUSION

We have presented a technique using optical emission spectroscopy for the measurement of nitrogen density in a nitrogen–oxygen DC glow discharge.

The validity of using the non-trace gas (oxygen) as the actinometer was determined by a set of actinometric measurements with argon gas used in trace amounts.

Acknowledgments

This work is a part of the project "Nonlinear dynamical phenomena in photorefractive media, liquid crystals, plasmas and left–handed materials (OI141031)" supported by the Ministry of Science and Environment Protection of the Republic of Serbia.

References

Milosavljević, V., Faulkner, R., Hopkins, M. B.: 2007, *Optical Express*, **15/21**, 13913.
Popović, D., Milosavljević, V., Daniels, S.: 2007, *J. Appl. Phys.*, **102**, 013303.
Ricard, A.: 1996, Reactive Plasmas–SFV Edition, p. 116.

Publ. Astron. Obs. Belgrade No. 84 (2008), 325 - 329 *Contributed Paper*

THE EFFECT OF HYDROGEN ON THE SPATIAL INTENSITY DISTRIBUTION OF IRON LINES IN ANALYTICAL GLOW DISCHARGES

P. ŠMÍD[1], E. B. M. STEERS[1] and V. HOFFMANN[2]

[1]*London Metropolitan University, 166-220 Holloway Road, London, N7 8DB, UK*
E–mail: p.smid@londonmet.ac.uk
E–mail: e.steers@londonmet.ac.uk

[2]*Leibniz Institute for Solid State and Materials Research Dresden, Helmholtzstraße 20, 01069 Dresden, Germany*
E–mail: V.Hoffmann@ifw-dresden.de

Abstract. Analytical glow discharges running in pure Ar are commonly used for direct solid analysis and depth profiling. The analytical results can be very significantly affected by molecular gases (H_2, N_2 and O_2) which are very often present in the discharge for various reasons. One approach to understanding of the processes involved when a small amount of H_2 is present in the discharge is to investigate the spatial intensity distribution of emission lines and the effect of H_2 on this distribution. Different processes take place in different parts of the discharge volume and affect thus different lines in various ways. The aim of this study was to investigate the effect of H_2 on spatial intensity distribution of different Fe and Zn emission lines but only Fe results are discussed in this paper.

1. INTRODUCTION

Analytical glow discharges (GD) in the so-called Grimm-type configuration have been used for direct solid sample analysis and for depth profile analysis of coated materials for several decades (Jakubowski et al. 2007). Elements present in the sample (the cathode of the GD source) are sputtered, excited and ionised in the discharge and information about the elemental composition of the sample is obtained either by an optical emission spectrometer (GD-OES) or by a mass spectrometer (GD-MS).

One of the areas of great importance is the effect of molecular gases (H_2, N_2 and O_2) on the characteristics of the analytical glow discharge (Martín et al. 2007, and references cited therein). These gases can be present in the discharge due to contamination of the gas, source and/or sample or as a constituent in the sample. The presence of a very small amount of molecular gas, in particular H_2, affects the electrical characteristics of the discharge, the sputtering rate of samples and the intensities of emission lines sample and working gas atoms and ions. Such changes have a serious impact on analytical results. Therefore, it is necessary to study the discharge processes involved in order to interpret the analytical results correctly.

It has been shown recently that ionic emission lines of the sample with the total excitation energy[1] close 13.6 eV can be selectively excited in the Ar-H_2 discharge by an asymmetric charge transfer (ACT) reaction between the metallic atom and hydrogen ion (Steers et al. 2006). Furthermore, it has been observed that those Fe II lines which are in pure Ar excited by ACT with Ar ions are suppressed in the intensity in the presence of H_2. Very recently, it has been also shown that some Fe atomic lines with the excitation energy close to 5.3 eV can be also selectively excited in the presence of hydrogen (Šmíd et al. 2008). In the standard configuration, the GD source is viewed 'end-on' and the light emitted from the end of the source is imaged on the entrance slit of the spectrometer. This means that an integrated intensity from the whole discharge volume is recorded. However, different discharge processes take place in different distances from the cathode; therefore, it is very useful to view the source 'side-on' and to study the spatial intensity distribution of sample emission lines.

In this paper, results obtained in the experiments with a modified Grimm-type glow discharge source for 'side-on' observations will be presented. Emission spectra in different distances from the cathode were recorded using Fe and Zn as a cathode material and mixtures of Ar with various H_2 concentrations were used as working gas; only the results on Fe emission lines are shown and discussed here.

2. EXPERIMENTAL

For the study of the spatial intensity distribution of emission line, a modified Grimm-type GD source was used; the anode tube has a longitudinal slot which can be observed via two viewing ports in a block inserted between the cathode plate and the anode body. The inner diameter of the anode tube is 8 mm. The gas was introduced into the source via a mixing unit consisting of a set mass flow controllers (5 ml/min, 50 ml/min and 500 ml/min, Bronkhorst) – which allowed mixing of pure argon with a premixed mixture of Ar with 2% v/v of H_2. The source was powered by a dc power supply (MCN 350-2000, FuG) and run in the mode with constant voltage and constant current – 700 V & 10 or 20 mA. Pure Fe and pure Zn were used as cathode materials.

Optical emission spectra were studied using an Echelle spectrometer with CCD detection (ESA 3000, LLA Instruments GmbH). This spectrometer can record spectra in the spectral range between 200 and 1000 nm with resolution 5 pm at 200 nm and 27 pm at 600 nm. An ICCD (intensified charge-coupled device) camera was used as a detector. The image of the slit of the anode tube was focused with an achromatic lens on the entrance connector of an optical fibre. The lens and the optical fibre were firmly connected together and mounted on a stage whose position could be adjusted using a micrometer screw to view different positions along the anode slot. The spectra were always recorded in 12 positions from the cathode, the step was 0.5 mm close to the cathode (up to 4 mm from the cathode) and 1 mm further away (up to 7 mm from the cathode).

[1]The total excitation is a sum of the excitation energy of the ion and the ionisation energy.

3. RESULTS

3. 1. Fe I LINES

The axial distribution of intensities of Fe I lines is shown in Figure 1 (a) for selected lines and the discharge in pure argon at 700 V and 20 mA, the overall pressure was 4.0 mbar. The selection of the lines was made to cover the whole range of the excitation energies found in the spectra. The intensities were normalised to the maximum intensity of the corresponding line in the plot.

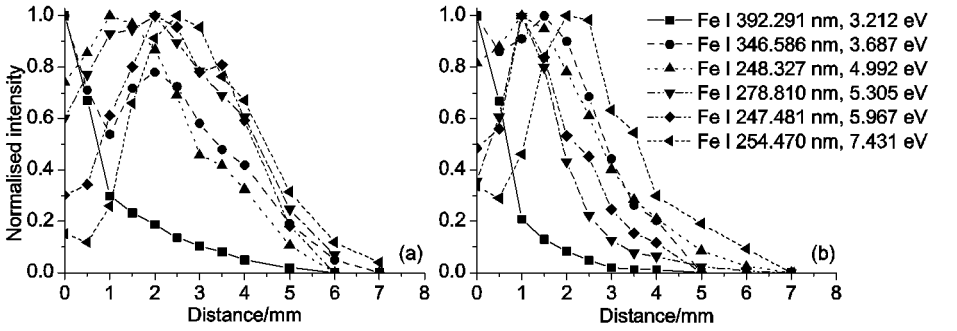

Figure 1: Axial intensity distribution of Fe I lines; (a) pure Ar, (b) Ar+0.3% v/v H_2, the discharge conditions 700 V & 20 mA.

It is apparent that lines coming from different excitation energies show different intensity distribution. The line with the lowest excitation energy (Fe I 392.291 nm, 3.212 eV) has its maximum near to the cathode after which the intensity monotonically decreases. In the intensity distribution of the next two lines (Fe I 370.556 nm, 3.397 eV and Fe I 346.586 nm, 3.687 eV), the maximum intensity is still at the cathode but a second local maximum is developing approx. 2 mm from the cathode. The maximum intensity of the line with even higher excitation energy (Fe I 381.296 nm, 4.209 eV) is no longer at the cathode but approx. 1–2 mm from the cathode. The same is true for the next two lines (Fe I 248.327 nm, 4.992 eV and Fe I 278.810 nm, 5.305 eV). The intensity distribution of the last two lines shown in this plot (Fe I 247.481 nm, 5.967 eV and Fe I 254.470 nm, 7.431 eV) is different in that the intensity at the cathode is relatively lower than for the other lines and the maximum intensity is furthest away form the cathode (approx. 2.5 mm) compared to the other lines in this plot.

The different axial intensity distributions of various lines are most probably linked with different excitation processes involved in the population of the energy levels of the iron atoms. It has been reported (Bogaerts et al. 2000) that in the glow discharge atomic emission lines can be excited by two main excitation processes depending on the distance from the cathode: heavy particle excitation (fast argon ions and fast argon neutrals) and electron impact excitation. The first process appears mainly close to the cathode where heavy particles have enough energy whereas the latter process can only take place in the negative glow because there are few electrons present in the cathode dark space. Clearly, individual emission lines investigated have different

sensitivity to these two excitation processes. The lines with lower excitation energy can be easily excited by heavy particles (higher intensity near the cathode) whereas the lines with higher excitation energy can be excited mainly by collisions with electrons (higher intensity in the negative glow). The relative importance of these two processes gradually changes as the excitation energy increases.

In Figure 1 (b), the axial intensity distributions of the same set of lines in the same format are shown for Ar+0.3% v/v H_2 in the discharge at 700 V and 20 mA, the overall pressure was 4.7 mbar (compared to 4.0 mbar in case of pure Ar). The most obvious difference between the intensity distributions in pure Ar and in Ar+0.3% v/v H_2 is an overall shift of the intensity maxima closer to the cathode. Also, the peaks of the intensity distributions of the lines which have their intensity maxima further away from the cathode seem to be narrowed down in the presence of hydrogen. Furthermore, when the axial intensity distributions of the line selectively excited in the presence of hydrogen (Fe I 278.810 nm, 5.305 eV) were compared for pure Ar and Ar+0.3% v/v H_2, it turned out that the maximum enhancement of this line was observed in the region between the cathode and 2 mm away from the cathode.

3. 2. Fe II LINES

Axial intensity distribution (normalised as in the Fe I case) of Fe II lines is shown in Figure 2 (a) and (b) for the discharge in pure Ar and in Ar+0.3% v/v H_2, respectively. The discharge conditions were the same as those used for Fe I lines in the previous part.

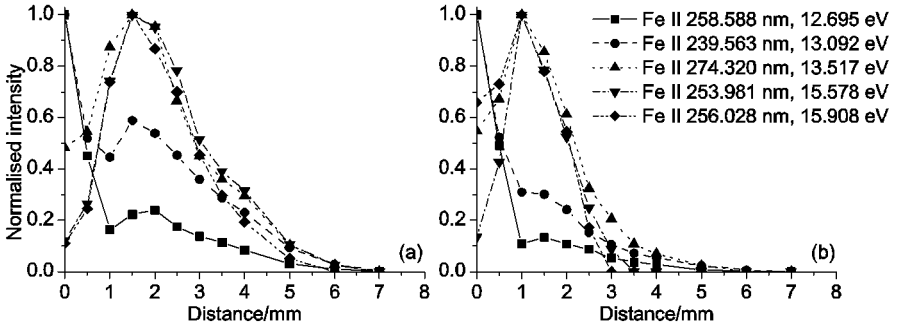

Figure 2: Axial intensity distribution of Fe II lines; (a) pure Ar, (b) Ar+0.3% v/v H_2, the discharge conditions 700 V & 20 mA.

One can see in Figure 2 (a) a similar pattern to that observed in the case of Fe I lines, but the intensity drop at distances of 5-7 mm is more marked. The lines with relatively low excitation energy (Fe II 258.588 nm and 239.563 nm) have their intensity maximum near the cathode with a second peak at about 1–2 mm away from the cathode. For the other lines, the proportion between the intensities of the two peaks in the intensity distributions is changing in favour of the second peak further away from the cathode and the relative intensity of the lines near the cathode decreases with the increasing excitation energy. This again suggests that the relative importance of different excitation processes (heavy particle excitation and electron

impact excitation) changes with the excitation energy in similar way as in the case of Fe I lines.

When H_2 is present in the discharge (Figure 2 (b)), all axial intensity distributions are shifted closer to the cathode. Furthermore, the last three Fe II lines in the plot are in pure Ar discharge excited by ACT with Ar ions. It has been shown that hydrogen suppresses this reaction significantly (Steers et al. 2006). If the intensity distributions are plotted in arbitrary units, it can be shown that in Ar-H_2 discharge the intensities of these lines are dramatically reduced and this reduction mainly occurs between 1.5 and 2.0 mm from the cathode.

4. CONCLUSION

The study of the axial intensity distribution of iron emission lines in the analytical glow discharge showed that the relative importance of different excitation processes differs depending on the excitation energy of the lines involved. The lines with relatively low excitation energies (up to 3.7 eV) can be easily excited by collisions with heavy particles (maximum intensity close to the cathode) whereas the lines with higher excitation energy are predominantly excited by collisions with electrons (the maximum intensity further away from the cathode). It has been also shown that the intensity distribution of the lines is shifted closer to the cathode in the presence of H_2. A similar pattern has been observed for zinc emission lines.

Acknowledgements

The authors would like to acknowledge financial support from EC funded Research Training Network GLADNET, contract no. MRTN-CT-2006-035459. P. Šmíd thanks the Deutsche Forschungsgemeinschaft for funding of the experiments carried out at IFW Dresden (436 TSE 17/7/06).

References

Bogaerts, A., Donko, Z., Kutasi, K., Bano, G., Pinhao, N. and Pinheirod, M.: 2000, *Spectrochim. Acta, Part B*, **55**, 1465.

Jakubowski, N., Dorka, R., Steers, E. B. M. and Tempez, A.: 2007, *J. Anal. At. Spectrom.*, **22**, 722.

Martín, A., Menéndez, A., Pereiro, R., Bordel, N. and Sanz-Medel, A.: 2007, *Anal. Bioanal. Chem.*, **388**, 1573.

Steers, E. B. M., Šmíd, P. and Weiss, Z.: 2006, *Spectrochim. Acta, B*, **61**, 414.

Šmíd, P., Steers, E. B. M., Weiss, Z., Pickering, J. and Hoffmann, V.: 2008, *J. Anal. At. Spectrom.*, submitted.

Publ. Astron. Obs. Belgrade No. 84 (2008), 331 - 334 *Contributed Paper*

ELECTRICAL PROPERTIES AND SPATIOTEMPORAL PROFILES OF THE LOW PRESSURE HOLLOW CATHODE DISCHARGE

N. ŠKORO[1], D. MARIĆ[1], G. MALOVIĆ[1], Z. Lj. PETROVIĆ[1],
V. MIHAILOV[2] and R. DJULGEROVA[2]

[1] *Institute of Physics Belgrade, Pregrevica 118, 11080 Zemun, Belgrade, Serbia*
E–mail: nskoro@phy.bg.ac.yu

[2] *Institute of Solid State Physics of Bulgarian Academy of Sciences, 1784 Sofia, Bulgaria*
E–mail: renna@issp.bas.bg

Abstract. We report measurements of electrical properties and spatial emission profiles of hollow cathode discharge, both for steady state and transient phases during formation of the discharge. A commercial hollow cathode tube normally applied as a spectral source has been studied. Our aim was to relate discharge anatomy to the voltage-current characteristics in a wide range of the discharge currents. It was particularly interesting to track down in time formation of the discharge structure, which is typical for hollow cathode effect.

1. INTRODUCTION

Ever increasing number of hollow cathode applications invokes continuous research of these discharges with complex geometry discharge. Apart from long-standing spectroscopic applications (e.g. Caroli 1983), many more have been introduced recently including newly developed micro size devices (Becker et al. 2006, Djulgerova et al. 2004).

The most important feature of these devices is the hollow cathode effect, manifesting itself trough a large increase in the current density and discharge light intensity accompanied by a drop of the sustaining voltage (e.g Pillow 1981). It can occur for certain discharge conditions in a given discharge geometry. During appearance of the effect, negative glow regions facing opposed cathode surfaces overlap. If one compares hollow cathode and parallel plate glow discharges, lower operating voltages for the same current density can be detected (Baguer et al. 2002, Eichhorn et al. 1993). Discharge is running more efficiently due to the fast electrons and ions, confined inside the cathode hole (Arslanbekov et al. 1998).

2. EXPERIMENTAL SETUP

We used a commercial hollow cathode Hilger and Watts lamp connected to the power circuitry and detection system. Lamp is a glass tube filled by Ne ($p = 3.5$ Torr) and sealed. The lamp has connections for cylindrical Mn hollow cathode with bottom

and a ring shaped anode. Cathode hole is 3 mm in diameter and 15 mm long. Our power circuitry is able to impose a current pulse of desired length while running a low current DC discharge. This technique allows us to avoid long breakdown delay times and it enables us to follow formation of the discharge (e.g. Marić et al. 2002). Spatial profiles are recorded in the visible range of spectra using an ICCD camera (Andor, iStar DH720-18U-03). Recording of voltage and current signals as well as camera gating are synchronized with the current pulse

3. RESULTS AND DISCUSSION

3. 1. STEADY-STATE MEASUREMENTS

In Fig. 1, VI characteristic and current dependence of the peak emission intensity inside the cathode cavity are shown. The discharge voltage is presented as the difference between the operating (V) and the breakdown (V_b) voltage. Fig. 2 shows 2D images of selected radial emission profiles (labels (a)–(f) correspond to those in Fig. 1). In the range of low currents, the discharge dominantly operates outside the cathode cavity (Figs. 2(a) and (b)) and it resembles discharge in parallel-plane geometry (Marić et al. 2002). The gap in descending part of VI characteristic corresponds to region of free-running oscillations. Further increase in current leads to the changes of the discharge regime. Now it operates mainly intra-cavity becoming more constricted and intense in the center (Fig. 2(c), (d), (e)). With a large increase in current density followed by voltage decrease, discharge switches to a more efficient regime typical for hollow cathode effect. Further rise in current is accompanied by the discharge expansion within the cavity and emission increment. This kind of behavior is typical for normal glow in parallel plate geometry. At even higher currents, the voltage current slope becomes positive, as in an abnormal glow mode. Almost entire cathode cavity is covered by the discharge (Fig. 2(f)).

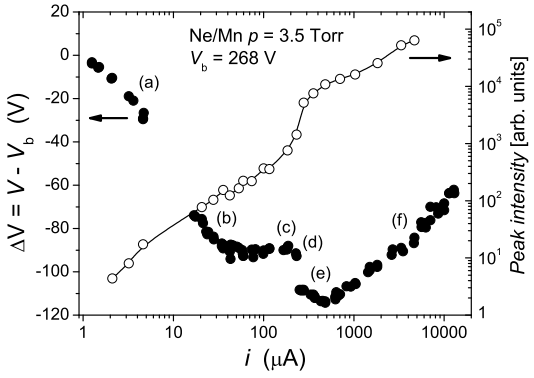

Figure 1: Discharge voltage (solid symbols) and peak emission intensity (open symbols) plotted against discharge current. Labels (a)-(f) correspond to spatial profiles in Fig. 2.

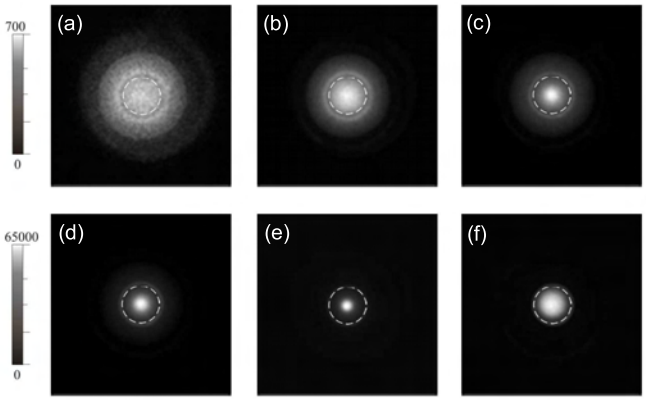

Figure 2: Radial profiles of the emission for different discharge currents: (a) $i = 3.2\ \mu$A, (b) $i = 28\ \mu$A, (c) $i = 184\ \mu$A, (d) $i = 231\ \mu$A, (e) $i = 278\mu$A, (f) $i = 4690\ \mu$A. White lines mark cathode cavity edge.

3. 2. TIME RESOLVED MEASUREMENTS

We were able to obtain temporally resolved discharge profiles by using fast ICCD camera synchronized with the power circuit. It can provide perceptible images even for short exposition and low light intensities. In that way discharge profile formation could be traced from the beginning of the current pulse, through the transient behavior and to the steady state. Measurements for several different modes of the discharge were made. Here we show formation of the hollow-cathode regime of discharge. We were able to follow transition from parallel-plate-like discharge to the regime of discharge with distinct hollow-cathode effect developed, within the single pulse. This corresponds to the gradual change of discharge regime from the point labelled by (d) to the point (e) in VI characteristic (Fig 1). Discharge voltage and current waveforms are shown in Fig 3. Transient part at the beginning of the pulse is magnified in Fig 3(a) in order to show rapid changes in waveform intensity (amplitude). Labels 1–8 in Fig 3 correspond to spatial images in Fig 4. In the beginning of the pulse, both discharge voltage and current experience steep rise. At the same time, 2D images show that discharge becomes radially inhomogeneous moving from the cathode edge into the cavity. Profile intensity increment follows current signal peeking at current maximum. Further changes in voltage and current are mirrored only through profile intensity variations while discharge stays inside the cathode. At the moment when current runs though the minimum, local maximum voltage is achieved with minor changes in the profile intensity. Discharge briefly sets at one current and then slips to another mode accompanied by a slight current increase and significant voltage decrease. Major increase in emission intensity is noticeable.

In summary, we have shown that hollow cathode discharge can be represented as a combination of discharges between parallel plates and inside the cavity. We were able to relate electrical properties to spatial structure of the discharge.

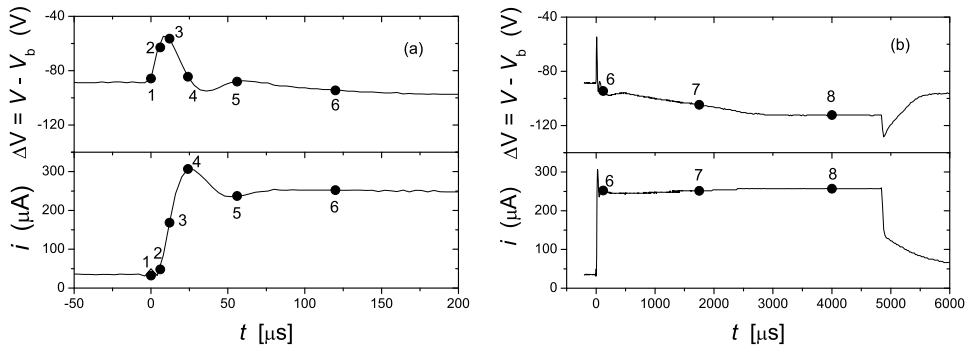

Figure 3: Voltage and current signals after the application of the voltage pulse: (a) beginning of the pulse zoomed in, (b) the whole pulse.

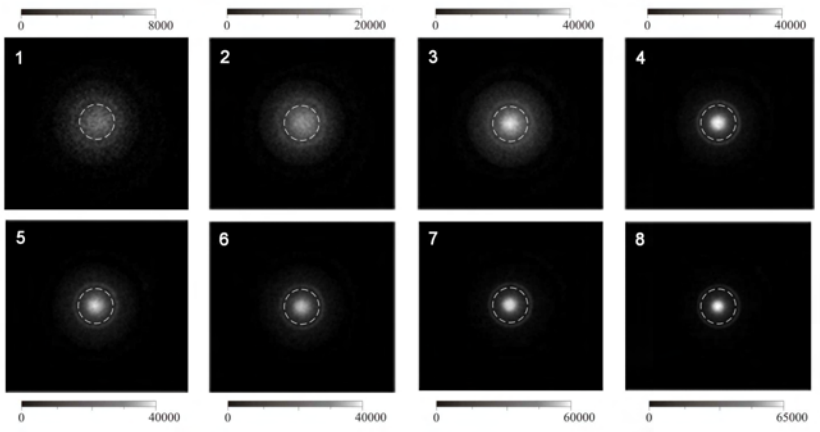

Figure 4: Axial emission profiles that correspond to labels 1-8 in Fig. 3.

References

Arslanbekov, R. R., Kudryavtsev, A. A., Tobin, R. C.: 1998, *Plasma Sources Sci. Technol.*, **7**, 310.

Baguer, N., Bogaerts, A., Gijbels, R.: 2002, *Spectrochimica Acta B*, **57**, 311.

Becker, K. H., Schoenbach, K. H., Eden, J. G.: 2006, *J. Phys. D: Appl. Phys.*, **39**, R55.

Caroli, S.: 1983, *Prog. Analyt. Atom. Spectosc.*, **6**, 253.

Djulgerova, R. B., Popova, L. I., Mihailov, V. I., Beshkov, G. D., Szytula, A., Gondek, L., Petrović, Z. Lj.: 2004, *Spectrochimica Acta B*, **59**, 905.

Eichhorn, H., Schoenbach, K. H., Tessnow, T.: 1993 *Appl. Phys. Lett.*, **63**, 2481.

Marić, D., Kutasi, K., Malović, G., Donko, Z., Petrović, Z. Lj.: 2002, *Eur. Phys. J. D*, **21**, 73.

Pillow, M. E.: 1981, *Spectrochim. Acta B*, **36**, 821.

Publ. Astron. Obs. Belgrade No. 84 (2008), 335 - 338 *Contributed Paper*

ARGON DYNAMIC OPTOGALVANIC SPECTRUM IN HOLLOW CATHODE DISCHARGE

V. MIHAILOV[1], R. DJULGEROVA[1], J. KOPERSKI[2], M. RUSZCZAK[2],
T. DOHNALIK[2] and Z. Lj. PETROVIĆ[3]

[1]*Institute of Solid State Physics of Bulgarian Academy of Sciences, 1784 Sofia, Bulgaria*
E–mail: valentin@issp.bas.bg

[2]*Institute of Physics of Jagellonian University, 30-059 Krakow, Poland*

[3]*Institute of Physics of Academy of Sciences of Serbia, 11080 Belgrade, Serbia*

Abstract. Argon dynamic optogalvanic spectrum in 450-471nm range is recorded in hollow cathode discharge. Qualitative interpretation of the signals shape is discussed.

1. INTRODUCTION

The optogalvanic effect represents the plasma conductivity change as a result of resonant light absorption (Barbieri 1990). The population of the levels belonging to the illuminated optical transition is changed by the absorption of the resonant quanta. This disturbs the ionization rate which causes variations in the discharge tube impedance. The optogalvanic technique has been most widely used for wavelength calibration of the spectra and for frequency and power stabilization of the lasers. Recently the dynamic optogalvanic signals are applied for obtaining of some plasma parameters by fitting the modeled dynamic signals with the experimentally registered signals.

The hollow cathode lamps turned out to be favorable optogalvanic detectors due to their rich spectra which include the emitted spectral lines from highly excited levels of both the working gas and the sputtered atoms of the cathode materials. The buffer gases in the hollow cathode lamps become advantageous by providing simultaneous calibration spectra. The use of dynamic optogalvanic signals turns out to be extremely interesting since these signals are described not only by their amplitude and sign (as the stationary optogalvanic signals are), but also by their positive and negative time components. They could also contain additional components originating from the sputtered material, damped oscillations, etc.

In this work, Ar dynamic optogalvanic spectrum in 450-471nm region is being registered in a hollow cathode discharge for the purpose of wavelength calibration applications. Ar dynamic optogalvanic spectra in this range are recorded in (Gusev 1987) and (Reddy 1990). In the first paper the Ar spectrum is not measured in hollow cathode discharge. In the second it is measured in hollow cathode discharge but the optogalvanic signal amplitudes are not shown.

2. EXPERIMENTAL

The hollow cathode with 3mm diameter and 8mm length represents an Al cylinder without a bottom. The optimal Ar pressure is 6Torr. The 0.1mm laser light beam illuminates the hollow cathode discharge along its axis and is centered in the negative glow region. The pulse dye laser (Sopra LCR1 pumped by the third harmonics of Nd:YAG laser Power Lite 700) has 5ns temporal width, 10Hz frequency and 80μJ pulse energy. The light is tuned to the 450-470nm spectral range. The dynamic optogalvanic signals are recorded using a two-channel digital real-time oscilloscope (Le Croy 9361) and are then processed by a computer.

3. RESULTS AND DISCUTION

Dynamic optogalvanic signals relevant to Ar atomic optical transitions in 450-471nm spectral range are registered as function of the discharge current (i). The Ar optogalvanic spectrum is demonstrated in Table 1.

Table 1: Ar dynamic optogalvanic spectrum registered in 450-471nm range

Wavelength [nm]	Configurations	Terms	OGS [mV]
451.07	$3s^23p^5(^2\mathrm{P}^\circ_{1/2})4s$–$3s^23p^5(^2\mathrm{P}^\circ_{3/2})5p$	$^2[^1/_2]$ - $^2[^1/_2]$	25
452.23	$3s^23p^5(^2\mathrm{P}^\circ_{1/2})4s$ - $3s^23p^5(^2\mathrm{P}^\circ_{3/2})5p$	$^2[^1/_2]$ - $^2[^1/_2]$	35
454.47	$3s^23p^5(^2\mathrm{P}^\circ_{3/2})4p$– $3s^23p^5(^2\mathrm{P}^\circ_{3/2})11d$	$^2[^1/_2]$ - $^2[^1/_2]$	18
455.43	$3s^23p^5(^2\mathrm{P}^\circ_{3/2})4p$–$3s^23p^5(^2\mathrm{P}^\circ_{1/2})7d$	$^2[^1/_2]$ - $^2[^3/_2]$	20
458.49	$3s^23p^5(^2\mathrm{P}^\circ_{3/2})4p$– $3s^23p^5(^2\mathrm{P}^\circ_{3/2})10d$	$^2[^1/_2]$ - $^2[^3/_2]$	20
458.66	$3s^23p^5(^2\mathrm{P}^\circ_{3/2})4p$– $3s^23p^5(^2\mathrm{P}^\circ_{3/2})10d$	$^2[^1/_2]$ - $^2[^1/_2]$	15
458.72	$3s^23p^5(^2\mathrm{P}^\circ_{3/2})4p$ -$3s^23p^5(^2\mathrm{P}^\circ_{3/2})10d$	$^2[^1/_2]$ - $^2[^1/_2]$	22
458.93	$3s^23p^5(^2\mathrm{P}^\circ_{1/2})4s$–$3s^23p^5(^2\mathrm{P}^\circ_{3/2})5p$	$^2[^1/_2]$ - $^2[^3/_2]$	20
459.61	$3s^23p^5(^2\mathrm{P}^\circ_{1/2})4s$–$3s^23p^5(^2\mathrm{P}^\circ_{3/2})5p$	$^2[^1/_2]$ - $^2[^3/_2]$	40
462.84	$3s^23p^5(^2\mathrm{P}^\circ_{1/2})4s$– $3s^23p^5(^2\mathrm{P}^\circ_{3/2})5p$	$^2[^1/_2]$ - $^2[^5/_2]$	12
464.21	$3s^23p^5(^2\mathrm{P}^\circ_{3/2})4p$ -$3s^23p^5(^2\mathrm{P}^\circ_{3/2})9d$	$^2[^1/_2]$ - $^2[^3/_2]$	10
464.75	$3s^23p^5(^2\mathrm{P}^\circ_{3/2})4p$– $3s^23p^5(^2\mathrm{P}^\circ_{3/2})9d$	$^2[^1/_2]$ - $^2[^1/_2]$	10
470.23	$3s^23p^5(^2\mathrm{P}^\circ_{1/2})4s$–$3s^23p^5(^2\mathrm{P}^\circ_{3/2})5p$	$^2[^1/_2]$ - $^2[^1/_2]$	15

The dynamic optogalvanic signals with maximum amplitude correspond to the 452.23nm (Fig.1) and 459.61 optical transitions. The shapes and time dependences of the other DOGSs registered are similar, so they differ only in their amplitudes. This could be explained by taking into account that their upper levels are very close. The first component of the signal can be understood as a decrease of the impedance in the discharge due to the increased population of the upper levels which can be much easier ionized. The next part of the DOGS reveals the relaxation behavior of the disturbed plasma. It is seen in Fig. 1 that the DOGS amplitudes increase and their width decrease at growing values of the discharge current.

The dynamic optogalvanic signal corresponding to the 451.07nm transition is the only one whose first component is negative (Fig. 2). The qualitative understanding of this signal shape could be associated with the extremely long time (10^{-2}s) of the

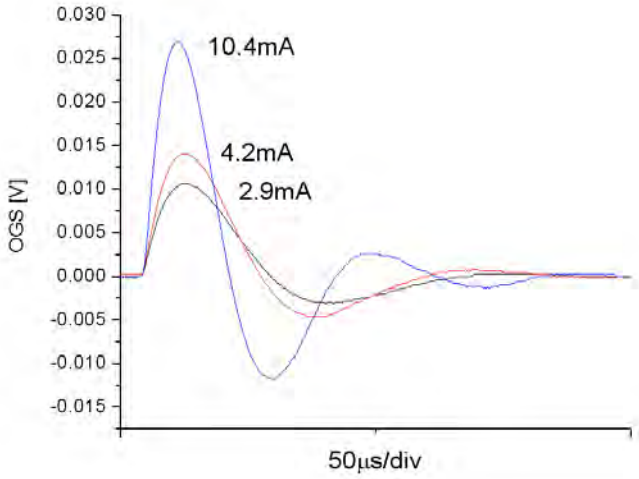

Figure 1: Dynamic optogalvanic signal corresponding to Ar I 452.23nm optical transition as function of the discharge current.

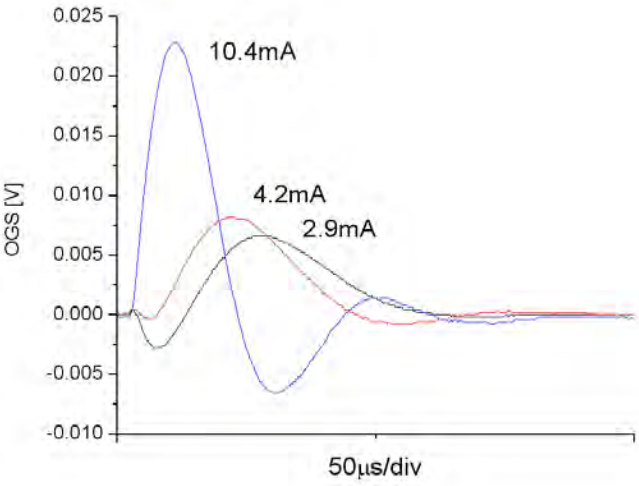

Figure 2: Dynamic optogalvanic signal corresponding to the Ar I 451.07nm optical transition as function of the discharge current.

lower energetic level of this transition. This lower state obviously plays a significant role in the ionization in the hollow cathode plasma especially at lower discharge current values. In this case, the depopulation of this long living level resulting in the decreased ionization could not be compensated by the increased ionization from the higher level of the transition. The amplitude of this component decreases with the discharge current and it is transformed into positive component at i > 5mA. The interpretation of this result is complicated. This could be related to the increased particle concentration in the hollow cathode plasma at higher discharge current values followed by higher frequencies of particle interactions. It means that in this case the contribution of the ionization from the other excited levels becomes crucial.

4. CONCLUSION

The Ar dynamic optogalvanic spectrum recorded in 450-471nm spectral range enriches the atlas of the Ar optogalvanic markers useful for wavelength calibration. The dynamic optogalvanic signal related to the 451.07nm is the only signal starting with a negative component in the spectral region of interest. The results obtained could be also applied in hollow cathode plasma modeling.

Acknowlegement

Support for this work is gratefully acknowledged by the joint research project between the Institute of Solid State Physics of Bulgarian Academy of Sciences (Sofia, Bulgaria), the Institute of Physics (Belgrade, Serbia) and the Institute of Physics of Jagiellonian University (Krakow, Poland), based on the scientific cooperation between the Bulgarian Academy of Sciences, the Academy of Sciences of Serbia and the Polish Academy of Sciences.

References

Barbieri, B., Beverini, N., Sasso, A.: 1990, *Rev. Modern Phys.*, **62**, 603.
Reddy, B. R, Venkateswarlu, George, M. C.: 1990, *Optics Communications*, **75**, 267.
Gusev, V. M., Kompanec, O. N.: 1987, *Quant. Electr.* (Russ.), **14**, 2379.

Publ. Astron. Obs. Belgrade No. 84 (2008), 339 - 340 *Contributed Paper*

IFLUENCE OF OUTER ELECTRODE MATERIAL ON OZONE PRODUCTION IN COAXIAL NEGATIVE CORONA DISCHARGE FED BY OXYGEN

J. ORSZAGH[1,2], J. D. SKALNY[1,2], N. J. MASON[2]

[1] *Department of Experimental Physics, Comenius University, Mlynská dolina F-2, 842 48 Bratislava, Slovakia*

[2] *Department of Physics and Astronomy, The Open University, Walton Hall, MK7 6AA, Milton Keynes, United Kingdom*

Abstract. The "electric odour", observed by Van Marum when oxygen was passing trough electric spark in 1785, has been later (1839), identified by Ch. F. Schönbeim as a new chemical compound named ozone (Stolarski 1999). Almost from those times ozone is widely used chemical compound.

The effect of outer electrode material on the ozone production in negative corona discharge have been studied. Two electrodes with the same dimensions were used in the experiment. One was made of stainless steel other one of brass. First the outer electrode was mechanically cleaned to remove the layer of oxides. The reactor have been filled by pure oxygen and closed. Then the measurement (1 hour measurement of discharge current at the constant voltage and time dependence of ozone concentration in the reactor) was repeated 5 times without cleaning the surface to see the ageing effects. Especially the influence of electrode oxidation on ozone concentration was studied. The experiments have been carried out at atmospheric pressure and ambient temperature. The ozone concentration was measured by UV spectroscopy method directly in the discharge reactor.

As one can expect the brass surface was oxidizing faster. After five measurements the electrode surface was covered by layer of greenish oxides. On the other hand the steel electrode surface had no visible oxides layer. The oxidation of the outer electrode had little systematic effect on the ozone concentration but in case of brass electrode the results were scattered in the range from 8000 ppm to 15000 ppm of ozone. It seems that the more oxides are created on the surface the less ozone is produced or the faster the ozone decomposition processes are (see Fig. 1). On the other hand in case of stainless steel electrode the ozone concentrations were comparable in all 5 measurements. Overall ozone concentration was higher in steel electrode.

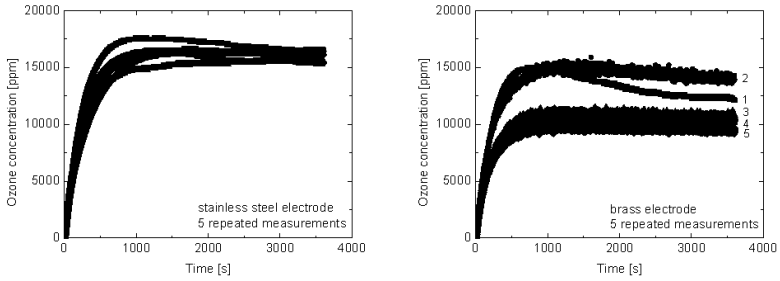

Figure 1: Time dependence of ozone concentration.

Acknowledgments

This research project was partially supported by Slovak Grant Agency VEGA1/1267/04, UK/400/2008, ESF projects COST CM0601 the UK Royal Society for a Joint International project and the Leverhulme Trust for a Visiting Professorship.

References

Stolarski, R. S.: 1999, Proceedings of International Ozone Symposium, Basel, Switzerland, 41.

Publ. Astron. Obs. Belgrade No. 84 (2008), 341 - 342 *Contributed Paper*

POSITIVE CORONA DISCHARGE IN N_2+CH_4 MIXTURE AT ATMOSPHERIC PRESSURE

G. HORVÁTH[1,2], J. D. SKALNÝ[1,2], N. J. MASON[2], M. ZAHORAN[1], J. ORSZÁGH[1,2]

[1] *Comenius University, FMFI Mlynska dolina F2, 84248 Bratislava, Slovakia*

[2] *Open University, Department of Physics and Astronomy, Milton Keynes, United Kingdom*

Abstract. Titan is considered as one of the few places in Solar system, where atmospheric and surface conditions could have produced organic molecules as precursors of higher hydrocarbons, nitriles or amino acids. Most of laboratory simulations of Titan's atmosphere were carried out at lower pressures presenting stratospheric conditions but there is poor knowledge about simulated reactions of Titan's troposphere. In our work an experimental investigation of products in positive coaxial corona discharge fed by mixture of N_2 and CH_4 with ratio of N_2:CH_4=98:2 in stationary regime has been made using UV spectroscopy. The measurements have been carried out at pressure of 1 bar and ambient temperature. The discharge reactor used for the treatment of the gas mixture consisted of a brass cylinder with diameter of 16 mm and length of 70 mm. A stainless steel and tungsten wires of diameter of 0.125 mm was centred inside the metal cylinder and was connected to the high voltage power supply. Coaxial corona discharge was generated by a Glassman high voltage power supply. The mixing ratio of methane and nitrogen was regulated by a MKS flow controllers. The reactor was placed in a Shimadzu VUV spectrometer for the in-situ measurements of absorbance of synthesized compounds. The measurements were focused on the UV analysis of time evolution of C_2H_2 and C_2H_4 concentrations and EMS study of deposited compounds on discharge electrodes (Figure 1). After a certain time a yellow- orange layer was formed on the active discharge electrode causing sparks and forming a dense rose-like spots on the covered electrode surface (Figure 2).

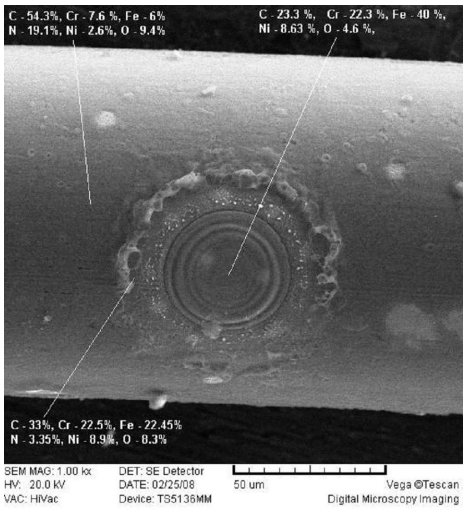

Figure 1: EMS study of electrode surface.

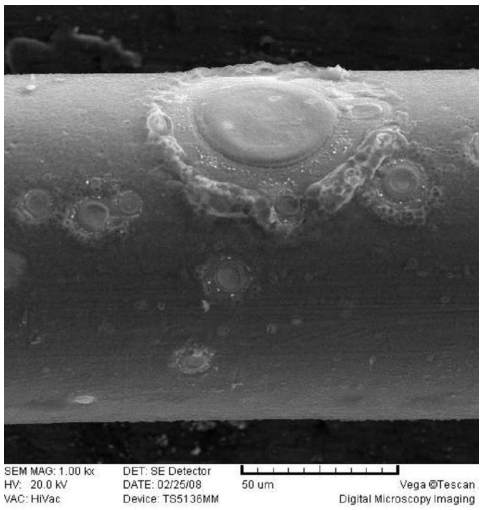

Figure 2: EMS picture of a treated electrode.

Acknowledgments

This research project was partially supported by Slovak Grant Agency VEGA1/1267/04, UK/400/2008, ESF projects COST CM0601 the UK Royal Society for a Joint International project and the Leverhulme Trust for a Visiting Professorship.

Publ. Astron. Obs. Belgrade No. 84 (2008), 343 - 346 *Contributed Paper*

MICRO DISCHARGES: BREAKDOWN, VOLT-AMPERE CHARACTERISTICS AND EMISSION PROFILES

N. ŠKORO[1], D. MARIĆ[1], G. MALOVIĆ[1], I. STEFANOVIĆ[1,2] and Z. Lj. PETROVIĆ[1]

[1] *Institute of Physics Belgrade, Pregrevica 118, 11080 Zemun, Belgrade, Serbia*
E–mail: nskoro@phy.bg.ac.yu

[2] *Institute for Experimental Physics II, Ruhr-University Bochum, D-44780 Bochum, Germany*
E–mail: ilija.stefanovic@rub.de

Abstract. We give preliminary results on breakdown and low current limit of volt ampere characteristics of simple parallel plate discharges at standard and micro discharge conditions. Experiments with micro discharges are reported attempting to establish maintenance of E/N, pd and j/p^2 scalings at small dimensions. Paschen curves and Volt-Ampere characteristics are presented and compared to those of the standard size discharges.

1. INTRODUCTION

Scope of non-equilibrium plasmas was extended recently to include micro discharges - discharges with characteristic dimensions from a few micrometers to several mm. Applications such as UV and visible light sources, sources for thin film treatment, etching, and deposition (Eden and Park 2005, Mohan Sankaran and Giapis 2003) are connected to applications in biological and environmental areas (Becker et al. 2005, Becker et al. 2006). Attractiveness of micro discharges is due to a possibility to realize non-equilibrium conditions and minimum breakdown voltages at atmospheric pressure.

The breakdown of pd scaling is essential in deciding whether one may proceed by extrapolating discharges with standard properties (centimeters and Torrs) to micro discharges, atmospheric pressure discharges and high frequency discharges. Recently we have analyzed the E/N, pd and j/p^2 scaling of low pressure discharges close to the minimum and to the left of the minimum of the Paschen curve (Marić et al. 2003). Our aim here is to extrapolate those studies to sub-millimeter discharges at high pressures. While most micro discharges are realized in complex geometries similar to hollow cathode geometries where inhomogeneous field localizes production of charges and thereby stabilized the discharge, we pursue parallel plate geometry which is more prone to oscillations and instabilities but the results are easier to interpret.

2. EXPERIMENTAL PROCEDURE

The discharge is realized in a simple, parallel plate geometry, with distance between electrodes $d = 0.5$ mm and electrode diameter $D = 2$ mm. Discharge chamber has a stainless steel cathode and transparent anode with conductive ITO (Indium tin oxide) film so radial profiles can be recorded. Before measurement, device was pumped down to low pressure (10^{-6} Torr) but no further electrode preparation was done. Electrical circuit and detection system are the same as in our cm size experiment (e.g. Marić et al. 2003). Measurements were performed in pure Ar.

3. RESULTS AND DISCUSSION

In Fig. 1 we show Paschen curves (breakdown voltage (V_b) vs. pressure x electrode distance (pd)) for micro and cm size discharges. We have shown that the standard shape of the Paschen curve is maintained at $d = 500\mu$m. It is important to emphasize that measurements in the left branch of the Paschen curve are particulary sensitive under these conditions. Mean free path of the electrons is of the μm scale and special care has to be taken to avoid long path breakdown.

Fig. 1 shows that breakdown voltages are somewhat lower in the case of micro discharges. The discrepancy is more pronounced in the left branch of Paschen curve – lower pd i.e. higher E/N. For these conditions, processes at the cathode surface are dominant in secondary electron production (Phelps and Petrović 1999). Different conditions at the cathode surface could lead to discrepancy between the two sets of results. Another issue that could be important here is that electrode gap/electrode diameter (d/D) ratio is smaller than that of the standard size discharge. Thus, loss of charged particles due to diffusion is more pronounced and can lead to an increase of the breakdown voltage (Lisovskiy et al. 2000). Both effects are more pronounced at correspondingly lower pressures.

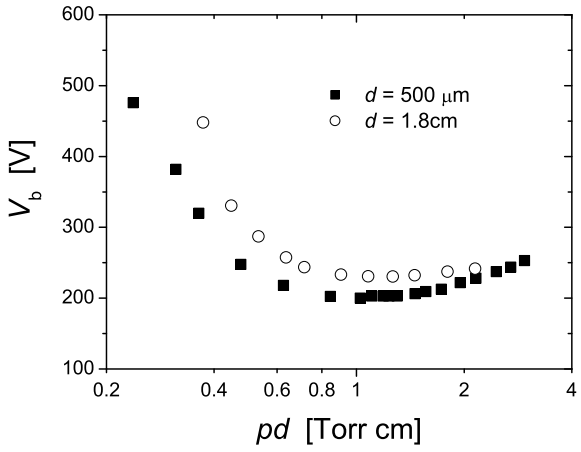

Figure 1: Comparison between Paschen curve for micro discharge (solid symbols) and standard size discharge (open symbols) in argon. In both cases, cathode is made of stainless steel.

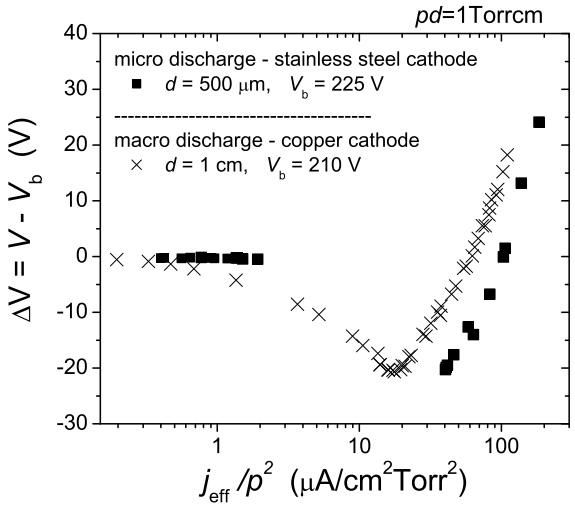

Figure 2: Discharge voltage vs. scaling parameter $j_{\rm eff}/p^2$ for $d = 500\mu$m (stainless steel cahtode) and for $d = 1$ cm (copper cathode) (Marić et al. 2003). Voltage is given as a difference between discharge (V) and breakdown voltage ($V_{\rm b}$).

In Fig. 2 normalized voltage-current (VI) characteristic for 1 Torrcm is shown. Measurements with micro dimensions are taken with cathode made of stainless steel. However, results for macro dimensions shown here are taken for copper cathode. Voltage is given as a function on standard scaling parameter j/p^2. Current is here normalized with "effective discharge area", not the electrode area, to produce "effective current density" ($j_{\rm eff}$). Effective discharge area is estimated from emission profiles recorded by ICCD camera (Fig. 3). In our recent paper (Škoro et al. 2008), we have shown that effective discharge area is critical parameter for a proper determination of scaling parameter j/p^2.

Our measurements covered a wide range of discharge currents – from low-current (Townsend) to abnormal glow discharge. A gap that may be observed in the descending part of the VI characteristics corresponds to free oscillations interval. Comparison shows that agreement between the two sets of the results is reasonably good, considering that measurements are taken with different cathode materials and that the dimensions of those discharges differ by an order of magnitude. In the range of low currents, slope of the VI characteristics is notably smaller in micro discharge and the voltage is higher. On the other hand, in the range of the high currents, micro discharge voltage is somewhat higher than in the centimeter case. It is not clear whether those discrepancies are due to violation of scaling laws or due to different cathode materials. Further measurements in cm size discharges with stainless steel cathode will certainly clarify these results.

Selected radial emission profiles for micro-discharges are shown in Fig. 3. Emission profiles exhibit typical behavior for different regimes of nonequilibrium DC discharges. Profile of emission for the lowest current shown here is multiplied by 50 for better visibility of the graph. In this range of currents, emission profile is typical for Townsend

regime of the discharge - the discharge is diffuse and the shape of the profile may be fitted by the Bessel function. Emission profile at $i = 407$ μA is significantly constricted and it gradually widens up with the increase of the discharge current, which is typical for a normal glow discharge. Finally, at the transition of the discharge to the abnormal glow mode, the discharge occupies the entire electrode diameter.

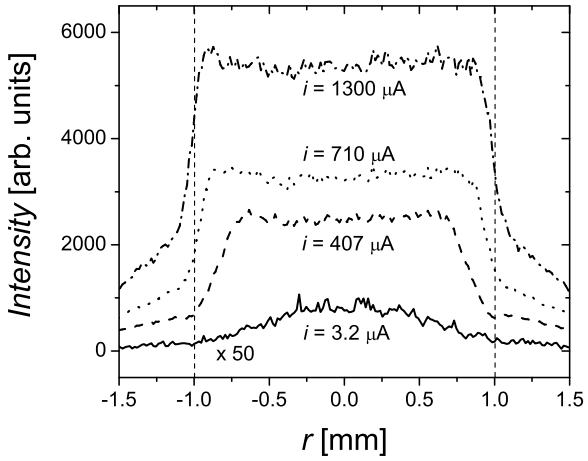

Figure 3: Radial emission profiles for micro discharge at: $i = 3.2$ μA ($j/p^2 = 0.56$ μA/cm^{2}Torr^2), $i = 407$ μA ($j/p^2 = 41.7$ μA/cm^{2}Torr^2), $i = 709$ μA ($j/p^2 = 58.3$ μA/cm^{2}Torr^2) and $i = 1300$ μA ($j/p^2 = 107$ μA/cm^{2}Torr^2).

4. SUMMARY

We have presented some of the results of measurements for sub-millimeter parallel plate DC micro discharges and compared them with the results from the cm size discharges for the same *pd*. These results are necessary for understanding of scaling laws in micro discharges. As the measurements are taken in very simple geometry and in a wide range of discharge currents, they also provide s basis for modelling.

References

Becker, K. H., Koutsospyros, A., Yin, S.-M., Christodoulatos, C., Abramzon, N, Joaquin, J. C., Brelles-Mari, G.: 2005, *Plasma Phys. Control. Fusion*, **47**, B513.

Becker, K. H., Schoenbach, K. H., Eden, J. G.: 2006, *J. Phys. D: Appl. Phys.*, **39**, R55.

Eden, J. G., Park, S.-J.: 2005, *Plasma Phys. Control. Fusion*, **47**, B83.

Lisovskiy, V. A., Yakovin, S. D., Yegorenkov, V. D.: *J. Phys. D: Appl. Phys.*, **33**, 2722.

Marić, D., Hartmann, P., Malović, G., Donko, Z., Petrović, Z. Lj.: 2003, *J. Phys. D: Appl. Phys.*, **36**, 2639.

Mohan Sankaran, R., Giapis, K. P.: 2003, *J. Phys. D: Appl. Phys.*, **36**, 2914.

Phelps, A. V., Petrović, Z. Lj.: 1999, *Plasma Sources Sci. Technol.*, **8**, R21.

Škoro, N., Marić, D., Petrović, Z. Lj.: 2008, *IEEE Trans. Plasma Phys.*, doi:10.1109/TPS.2008.917952.

Publ. Astron. Obs. Belgrade No. 84 (2008), 347 - 350 *Contributed Paper*

FORMATION OF ION-ION PLASMAS BY ELECTRON MAGNETIC FILTERING: 2D FLUID SIMULATION

A. MEIGE[1], G. J. M. HAGELAAR[2] and P. CHABERT[1]
[1] *LPTP, Ecole Polytechnique, Palaiseau Cedex 91128, France*
E–mail: albert.meige@polytechnique.edu
[2] *Laplace, Universit Paul Sabatier, Toulouse, France*

Abstract. A two-dimensional magnetized plasma fluid simulation is developed to investigate the electron magnetic filtering in an electronegative plasma and the formation of an ion-ion plasma (electron-free plasma). The model uses the three first moments of the Boltzmann equation, namely the continuity equation, the conservation of momentum approximated by the drift-diffusion equation and an energy equation for the electrons. The various reaction rates, mobility and diffusion constants (accounting for the presence of an axial magnetic field) are calculated from experimental cross-sections by using a Boltzmann solver. Preliminary results and applications to space plasma propulsion are presented.

1. FLUID MODEL

For every species s of the plasma, the time evolution of the density is described by the continuity equation

$$\frac{\partial n_s}{\partial t} + \boldsymbol{\nabla} \cdot \boldsymbol{\Gamma}_s = S_s, \tag{1}$$

where n_s is the density, $\boldsymbol{\Gamma}_s$ is the flux and S_s is the net source term (creation and loss) of the considered species s (electron, ion or neutral particle). The particle flux $\boldsymbol{\nabla} \cdot \boldsymbol{\Gamma}_s$ is given by the momentum balance

$$m_s n_s \left[\frac{\partial \boldsymbol{u_s}}{\partial t} + (\boldsymbol{u_s} \cdot \boldsymbol{\nabla}) \boldsymbol{u_s} \right] = q_s n_s (\boldsymbol{E} + \boldsymbol{u_s} \times \boldsymbol{B}) - \boldsymbol{\nabla} P_s + \boldsymbol{f_s}\big|_{\boldsymbol{c}}, \tag{2}$$

where m_s, $\boldsymbol{u_s}$ and $\boldsymbol{\nabla} P_s$ are the mass, the average velocity and the kinetic pressure gradient of the species s, respectively, while $\boldsymbol{E}$, $\boldsymbol{B}$ and $\boldsymbol{f_s}\big|_{\boldsymbol{c}}$ are the electric field, the magnetic field and the rate of momentum transfer due to collisions with other species. The left hand side of the momentum equation ("inertial" terms) is neglected so that equation 2 can be approximated by the drift-diffusion equation

$$\boldsymbol{\Gamma}_s = \mathrm{sgn}(q_s) \mu_s \boldsymbol{E} n_s - D_s \boldsymbol{\nabla} n_s, \tag{3}$$

where $\mathrm{sgn}(q_s)$ indicates the sign of the charge of the considered species. The coefficients μ_s and D_s are the transport coefficients (mobility and diffusion coefficients) and are respectively given by $\mu_{s,\parallel} = |q_s|/(m_s \nu_s)$ and $D_{s,\parallel} = k_B T_s/(m_s \nu_s)$ along the

magnetic field lines and by $\mu_{s,\perp} = \mu_{s,\parallel}/(1+\Omega^2)$ and $D_{s,\perp} = D_{s,\parallel}/(1+\Omega^2)$ across the lines, where $\Omega = |q_s|B/(m_s\nu_s)$.

In equation 3, $\boldsymbol{f_s}\big|_{\boldsymbol{c}}$ was taken equal to $m_s n_s \nu_s \boldsymbol{u_s}$ and isothermal conditions were assumed ($\boldsymbol{\nabla} P_s = k_B T_s \boldsymbol{\nabla} n_s$). The first term of equation 3 represents the flux due to the electric field (drift), while the second term represents the flux due to the density gradient (diffusion). Equation 3, that is derived from a local balance between the forces and the collisional momentum loss, holds rather well for conditions where the mean free path is small with respect to the plasma dimensions and gradient lengths.

The reaction rates and the transport coefficients are supposed to be functions of the reduced electric field (E/N) for heavy species and functions of the electron mean energy $\bar{\varepsilon}$ for electrons. The electron mean energy, $\bar{\varepsilon}$, which is obtained by solving the continuity equation for the electron energy

$$\frac{\partial n_\varepsilon}{\partial t} + \boldsymbol{\nabla} \cdot \boldsymbol{\Gamma}_\varepsilon = -e\boldsymbol{E} \cdot \boldsymbol{\Gamma}_e - L + H, \tag{4}$$

where the first term of the right-hand side is the Ohm heating, the second term is the power lost in the various collision processes and the last term represents inductive heating. On the left-hand side, n_ε is the electron density energy and the electron mean energy is then given by $\bar{\varepsilon} = n_\varepsilon/n_e$. The energy flux $\boldsymbol{\Gamma}_\varepsilon$ can be approximate by an expression similar to equation 3.

The transport equations are coupled to Poisson's equation to determined the electric field which depends on the space charge density, ρ

$$\boldsymbol{\nabla} \cdot (\epsilon \boldsymbol{E}) = -\nabla \cdot (\epsilon \boldsymbol{\nabla} \Phi) = \rho, \tag{5}$$

where Φ is the potential, and ρ is given by

$$\rho = \sum_s q_s n_s. \tag{6}$$

The equations above are implemented for a two-dimensional system in cylindrical coordinates. Any geometry with various materials (electrode, dielectric etc.) can be simulated. A chemistry module allows an unlimited number of species and reactions to be taken into account.

2. PRELIMINARY RESULTS

For the preliminary results presented below, an oxygen plasma in a 5 cm long and 20 cm diameter grounded cylinder was simulated. The various species O_2, O, O_2^+, O^- and 14 reactions between them were taken into account (momentum transfer, dissociative attachment, dissociation, ionization, electron impact detachment, dissociative recombination, mutual neutralization etc.). The magnetic field is uniform and parallel to the system revolution axis. The inductive power was 250 W with a heating profile maximum on the axis of the cylinder and exponentially decaying from the center of the discharge. Finally, the neutral pressure was 10 mTorr. In the following we investigate the effect of the magnetic field strength on the structure of the plasma.

Figure 1(a) shows the various radial steady-state charged species densities for a position $x = 2.5$ cm when the magnetic field is completely switched off. In this situation, we can observe the usual stratification of electronegative plasmas, where

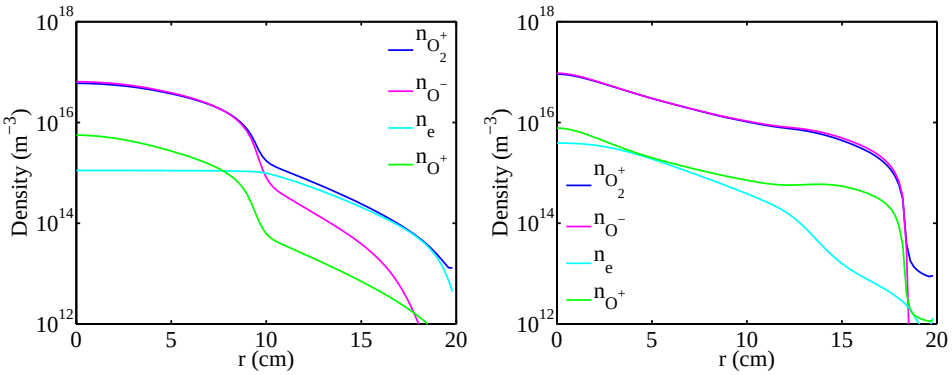

Figure 1: Density of the charged species along the radius r in the middle of the discharge (for$x = 2.5$ cm).

the core of the discharge is essentially electronegative (the two dominant species are the positive ions and the negative ions), while the periphery of the plasma is essentially electropositive (the two dominant species are positive ions and electrons). This is a well known result and it is attributed to the fact that negative ions are electrostatically confined in the core of the discharge by the ambipolar electric field of the plasma and the electrons are the only negative species being able to reach the walls.

Figure 1(b) shows the various radial steady-state charged densities for a position $x = 2.5$ cm when the magnetic field is fixed to 100 G. In this situation, the plasma remains highly electronegative along the whole radius (the dominant species are positive and negative ions and the electron density is at least an order of magnitude lower). This completely different situation is due to the fact that the mobility of the electrons is much smaller across the magnetic field lines than along them. As a result, electrons are confined in the region where they are mostly created i.e. in the center of the discharge (where they are the hottest).

Figure 2 shows the radial electronegativity (or negative ion fraction) $\alpha = n_-/n_e$ as a function of r for a position $x = 2.5$ cm. The blue and pink lines correspond to $B = 0$ and $B = 100$ G, respectively. This figure confirms what was just mentioned: for low or null magnetic field, the plasma presents a usual stratified structure with an electronegative core (α large) and an electropositive periphery (α almost null), while for a sufficiently large magnetic field strength, the plasma appears to be electronegative along the whole radius. In addition, for $r > 12$ cm the negative ion density becomes several orders of magnitude larger than that of the electrons, hence forming an ion-ion plasma at the periphery of the discharge.

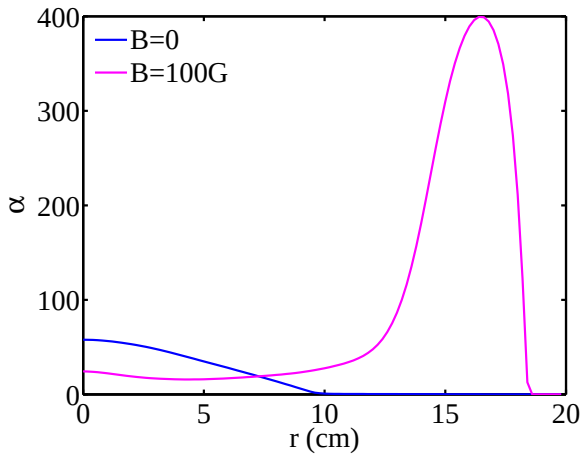

Figure 2: Negative ion fraction $\alpha = n_-/n_e$ along the radius r in the middle of the discharge (for $x = 2.5$ cm), for $B = 0$ (thick line) and $B = 100$ G (thin line).

3. CONCLUSION

We have developed a two-dimentional fluid simulation of a magnetized oxygen plasma. The preliminary results have shown the possibility to create an ion- ion (electron-free) plasma at the periphery of the discharge, hence confirming our earlier experimental results.

Publ. Astron. Obs. Belgrade No. 84 (2008), 351 - 354 *Contributed Paper*

MODELING OF A FLOWING Ar-O_2 MICROWAVE DISCHARGE AND POST-DISCHARGE

K. KUTASI[1,2], V. GUERRA[1], P. A. SÁ[1,3] and J. LOUREIRO[1]

[1] *Instituto de Plasmas e Fusão Nuclear, Instituto Superior Técnico, 1049-001 Lisboa, Portugal*

[2] *Research Institute for Solid State Physics and Optics, Hungarian Academy of Sciences, POB 49, H-1525 Budapest, Hungary*
E–mail: kutasi@sunserv.kfki.hu

[3] *Departamento de Eng.Fízica, Faculdade de Engenharia da Universidade do Porto, 4200-465 Porto, Portugal*

Abstract. A flowing Ar-O_2 microwave discharge and its afterglow have been investigated by means of a 1-D kinetic and a 3-D hydrodynamic model, respectively. The evolution of the densities of species created in the discharge have been determined along the early afterglow present in the connecting tube between the discharge region and reactor, as well as in the late afterglow developed in a large reactor.

1. INTRODUCTION

Ar-O_2 plasmas are widely used in material processing and biomedical applications, e.g. the post-discharge of Ar-O_2 has been successfully used as oxidizing media in deposition of oxide films (Belmonte et al. 1997), and the inactivation of bacterial spores have been achieved in the flowing afterglow of an Ar-O_2 microwave discharge (Moreau et al. 2000). In pure Ar post-discharges the main sterilizing agents are believed to be the VUV photons (105-107 nm) emitted by the Ar atoms in the resonant states, whereas in Ar-O_2 mixture the VUV photons and O atoms. The aim of this work is to follow by modeling the evolution of the densities of active species produced by a flowing Ar-O_2 microwave discharge, from the discharge region to the late-afterglow present in a large volume reactor, thus contributing to the understanding of the elementary processes occurring in these systems, in particular those responsible for plasma sterilization.

2. MODELING

Figure 1 shows the post-discharge system set-up used in our investigations, similar to the one used in (Pintassilgo et al. 2007). The discharge is generated in a 0.8 cm diameter silica tube, which is connected with a 2.6 cm diameter tube to a $60\times30\times28$ cm^3 reactor made of aluminum. The gas inlet and outlet are symmetrically positioned in the middle of the left side and bottom walls, respectively.

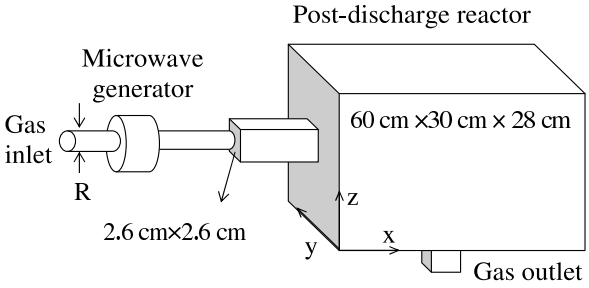

Figure 1: The post-discharge system set-up.

The system is described with two different models valid for the discharge and early afterglow region, and for the late afterglow present in the large reactor, respectively. The species densities in the discharge region are calculated by solving the homogeneous electron Boltzmann equation, coupled together with the rate balance equations describing the creation and destruction of $Ar(^1S_0, {}^3P_2, {}^3P_1, {}^3P_0, {}^1P_1)$, $O_2(X^3\Sigma_g^-,v)$, $O_2(a^1\Delta_g, b^1\Sigma_g^+)$, $O(^3P)$, O_3, Ar^+, O_2^+, O^+, O^-, under the assumption of a quasi-neutral discharge. The concentrations obtained for the steady-state discharge are used as initial values to the early afterglow taking place in the tube connecting the discharge to the main reactor, where the same system of equations is solved in time under zero electric filed. The evolution of the species densities in the post-discharge reactor are followed with a 3-D hydrodynamic model (Kutasi et al. 2007), where only the neutral active species are considered.

3. RESULTS AND DISCUSSION

The discharge results have been obtained at f=2.45 GHz, p=400 Pa, T_g=1000 K, in a 99%Ar-1%O_2 mixture with electron density n_e=3.74×10^{11} cm^{-3}, which is the critical value for surface-wave propagation. In the early afterglow the gas temperature is assumed to be 500 K. The gas flow rate is 500 sccm, while the flight time of species in the connecting tube between the discharge and reactor is assumed to be 10^{-4}s.

Figure 2 shows the time evolution of several species in the early-afterglow. As it is clearly seen, the Ar(4s) states are quickly depleted. As a matter of fact, they are very effectively quenched by O atoms in Ar(4s)+O→ $Ar(^1S_0)$+O process and O_2 molecules through the Ar(4s)+O_2→ $Ar(^1S_0)$+O+O reaction. Another relevant point is that O_2 is strongly dissociated, both by electron impact with O_2(X,a,b) and by Ar(4s) atoms. The latter contributes about 15% to the total dissociation rate.

The results of the hydrodynamic model show that the Ar metastable and resonant states become totally depopulated in the vicinity of the reactor's entrance. These results suggest that, contrary to the earlier suppositions (Moreau et al. 2000), the Ar resonant states cannot contribute to the VUV/UV emission in the reactor. Figure 3 shows the relative density distribution of O atoms in the central (y = 15 cm) x-z vertical plane of the reactor (the gas enters the reactor in the z = 12-14.6 cm region). According to this, the O atoms density decreases from the entrance towards the walls about one order of magnitude. The loss of O atoms in the reactor is due to their surface recombination, the loss probability for the aluminum surface has

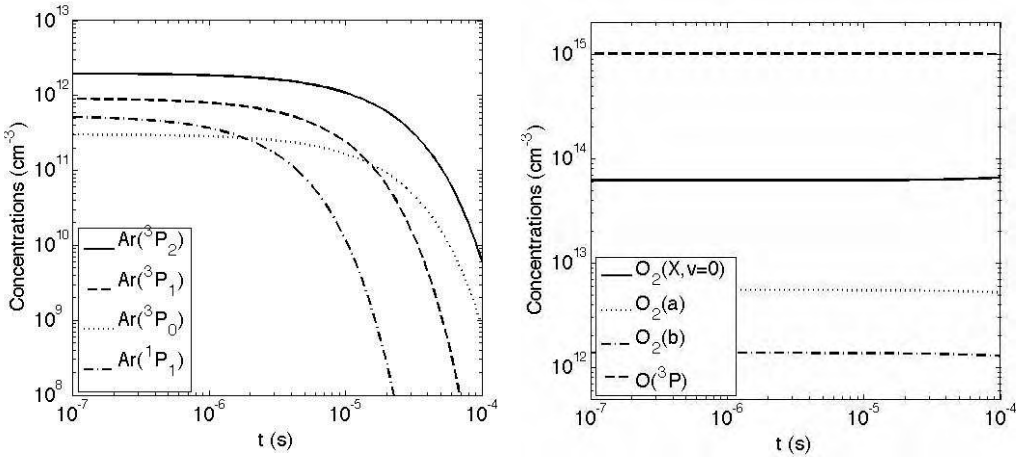

Figure 2: Time evolution of heavy-particles along the early afterglow.

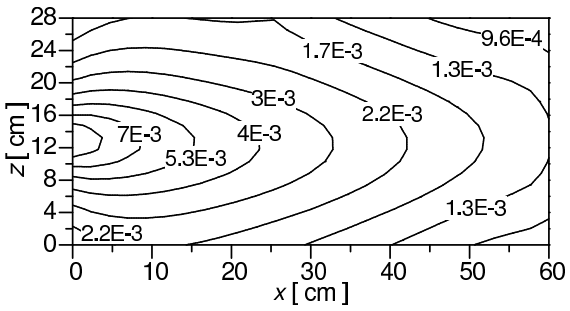

Figure 3: The relative density of O atoms in the reactor for x-z vertical plane at y= 15 cm.

been chosen γ_O=1.7×10^{-3} (Wickramanayaka et al. 1991). A more homogeneous density distribution, which is more favorable for applications, can be achieved in Pyrex reactors, where the atomic recombination on the surface is less efficient.

Figure 4 shows the relative density distribution of O_2(a) and O_2(b) in the central (y = 15 cm) x-z vertical plane of the reactor. The density of O_2(a) decreases about one order of magnitude in the reactor from the entrance to the walls, while the O_2(b) density two orders of magnitude. In case of O_2(a), similarly to the O(^{3}P) atoms, the losses are mainly due to the surface recombination, while in the case of O_2(b) besides the surface recombination the quenching by O(^{3}P) has also a great contribution. The surface loss probabilities of O_2(a) and O_2(b) have been taken $\gamma_{O2(a,b)}$=1×10^{-3} from (Sharpless et al. 1989).

The evolution of the species for different discharge conditions, especially gas mixture composition, which influence the dissociation degree of the O_2 molecules and also the quenching of radiative Ar states, are investigated and will be presented at the meeting. The influence on the UV radiation of N_2 impurities, which can be present in the system, will be discussed as well.

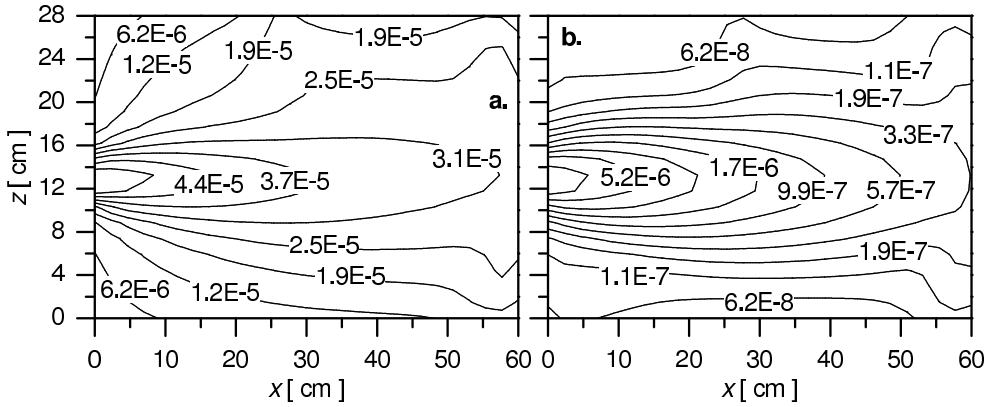

Figure 4: The relative density of a) O_2(a) and b) O_2(b) molecules in the reactor for x-z vertical plane at y= 15 cm.

Acknowledgments

This work has been supported by the Portuguese Science Foundation FCT through the post-doc fellowship of KK and Hungarian Science Foundation OTKA through project F-67556.

References

Belmonte, T. et al.: 1997, *Surf. Coat. Technol.*, **97**, 642.
Kutasi, K., Loureiro, J.: 2007 *J. Phys. D: Appl. Phys.*, **40**, 5612.
Moreau, S. et al.: 2000 *J. Appl. Phys.*, **88**, 1166.
Pintassilgo, C. D., Kutasi, K., Loureiro, J.: 2007 *Plasma Sources Sci. and Technol.*, **16**, S115.
Sharpless, R. L. and Slanger T. G.: 1989 *J. Chem. Phys.*, **91**, 7947.
Wickramanayaka, S., Meikle, S., Kobayashi, T., Hosokawa, N., Hanataka, Y.: 1991 *J Vac. Sci. Technol A*, **9**, 2999.

Publ. Astron. Obs. Belgrade No. 84 (2008), 355 - 358 *Contributed Paper*

ON A SELF-SUSTAINED OSCILLATING MODE FOR OPERATION OF A GLOW DISCHARGE

D. ZHECHEV and V. STEFLEKOVA

Institute of Solid State Physics, Bulgarian Academy of Sciences,
72 Tzarigradsko Chaussee Blvd., BG-1784 Sofia, Bulgaria
E–mail: spectron@issp.bas.bg

Abstract. A self-sustained oscillating mode for operation of a hollow cathode discharge (HCD) is analyzed based on a equivalent glow discharge RCL scheme. The oscillation takes place under i-V operating point of positive differential resistance and its frequency ($\approx$ kHz) depends on the discharge current value. The oscillation arising is found to require reasonable date values characterizing glow discharge plasma in general.

1. INTRODUCTION

Numerous glow discharge (GD) applications are based on its stable mode for operation. From another point of view, the gaseous plasma in a GD is known as a typical nonlinear dynamical "open system" with a large number of degrees of freedom. Within these frames a GD modification, i.e. hollow cathode discharge (HCD) should possess one more additional degree of freedom due to the specific Penning ionization (Dimova et al. 2004) of sputtered atoms. There are very little accessible data on this process. To date the instabilities observed are closely related to the i-V- region of negative differential resistance $(\partial U/\partial i)<0$ and a qualitative analysis is done in ref. (Zhechev et. al. 1998). In some experiments (Jung et. al. 1999) self-sustained instabilities in a HCD are observed under operating point of $(\partial U/\partial i)>0$.

In this work the origins of the self-sustained oscillating mode for operation under operating point of $(\partial U/\partial i)>0$ is studied within the frames of both space structure of a HCD and equivalent GD scheme.

2. EXPERIMENTAL

The stability of a HCD dc operation is studied at absence of any external perturbation. A standard HCD experimental set-up is used. Time-dependent change in the impedance of the discharge is detected by measuring the voltage ΔU(t) across the 50 Ω resistor R_m. The R_mC constant is low enough to allow one to resolve the shape structure of ΔU(t). The signal was sampled by the oscilloscopes LP142 and C-108. A home made HCD modification where the cathode consists of two parallel nets (20 x 20 x 20 mm) (Figure 1) is used. Here the space structure of HCD is related to various i-V operating points.

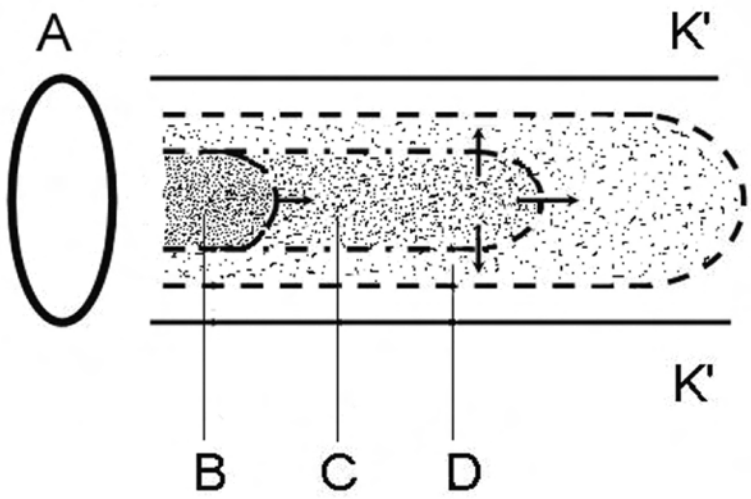

Figure 1: Macro-structure of HCD plasma bulk under p_{Ar}=0.15 Torr. **B** - initial NG under [253÷ 267] V; **C** - development of NG along the axis under [267÷ 305] V; **D** - enlargement of **C** - structure. (The conditional board lines are given by dotted ones).

3. RESULTS AND DISCUSSION

3.1. Some periodic self-sustained instabilities of various character were observed on i-V branches of both negative and positive dynamic resistance. Self-sustained oscillating mode for operation was observed under the initial i-V region of the i-V curve, where $(\partial U/\partial i) > 0$. The oscillations were localized to arise in the plasma layer **B** near the anode (Figure 1). Here a discontinuous transition of the operating voltage, i.e. 255 V - 263 V - 267 V takes place. The frequency of the oscillation is of the order of a few tens kHz and varies under these voltages. Further, the oscillating mode disappears under the voltage region 267 V - 300 V - **C** - mode. Here plasma fills up the HC cavity fractionally.

3.2. Obviously, under above points of $(\partial U/\partial i) > 0$ the discharge transforms the energy of the feed continuous discharge current into oscillating one. The transformation occurs in the anode plasma layer (APL) **B** of the NG (Figure 1). This process may be ascribed on both external inductance L (due to cables and ballast resistor, e.g. $\approx 10^{-4} \div 10^{-5}$ H) and HCD capacitance. The transformation may be analyzed qualitatively within the frames of the glow discharge equivalent electrical scheme (Figure 2)(Miniature Lamp Department, 1966).

We analyze whether a small deviation vs. the selected working point (i_0, V_0) can rise in amplitude spontaneously. Generally, the discharge current i in APL may be expressed as:

$$i = j_a V_a + C_a[dV_a/dt] + V_a[dC_a/dt) \tag{1}$$

where j_a is the plasma active conductivity, V_a voltage drop in APL. Let η is a small

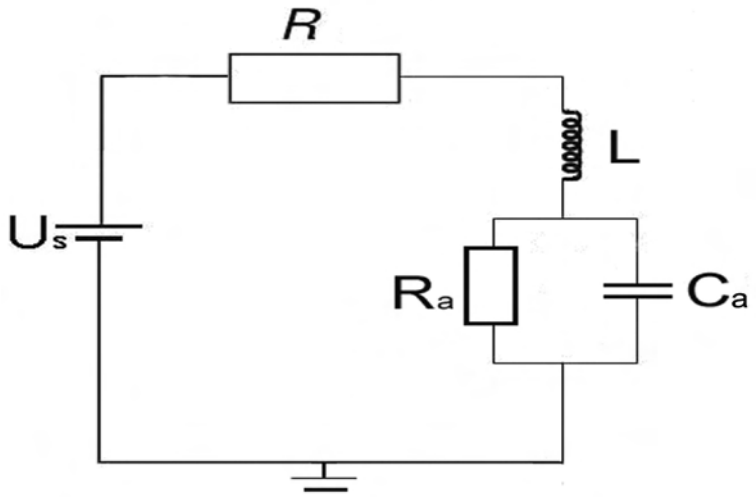

Figure 2: Equivalent scheme of a HCD: U_s - power supply, L - inductance, R - resistance of both ballast resistor and plasma bulk out of APL, R_a - APL active resistance, C_a - capacitance resistance of APL.

deviation of the continuous discharge current i_0 . Then

$$i = i_0 + \eta \tag{2}$$

and

$$V_a = V_0 + [dV_a/di]\eta = V_0 + r_{din}\eta \tag{3}$$

where r_{din} is the slope of the dynamical resistance in vicinity of (i_0, V_0). Two more equations are valid:

$$L[di/dt] + Ri + V_a = U_s \tag{4}$$

$$L[d\eta/dt] + R\eta + r_{dyn}\eta = 0 \tag{5}$$

On the other hand (Ginzburg et. al. 1967) the conductivity j_a may be taken as

$$j_a = K\omega_0\nu_{eff}[4\pi[(\omega_i\omega_e/\omega)^2 + {\nu_{eff}}^2]]^{-1} = A[B(i_0^4 + C)]^{-1}$$

where

$$A = K{\omega_0}^2\nu_{eff}$$

$$C = \nu_{eff}^2 B^{-1}$$

$$B = 64\pi^4 e^4 (c^8 r^4 M^2 m^2 \omega^2)^{-1}$$

and $\omega_{i,e}$ is Larmor's frequency of either ions (*i)* or electrons, ν_{eff} - frequency of pulse transferring collisions *electron* (mass m) → *heavy particle* (mass M), K - coefficient related to the discharge geometry.

The substitution of Eqs (2) and Eqs (3) in Eqs (1) and Eqs (4) and the relation $i_0(A,\ B,\ C)$ give the standard equation of the type

$$a(\partial\eta/\partial t)^2 + b(\partial\eta/\partial t) + d = 0$$

where the coefficients a, b and d represent functions of the above signification A, B, C, L, R, V_0, η, i_0 and of value D, characterizing the plasma dielectric property. In particular, $d = B\eta\ i_0(C - Di_0^2)$. The positive solution of the interest $\partial\eta/\partial$t> 0 takes place at $d < 0$. It means $i_0 > (C/D)^{1/2}$. Reasonable values of both circuit and HCD plasma answer the requirements of this inequality. A rod - like anode used in some commercially available HCD lamps has been taken in this consideration.

4. CONCLUSIONS

Self-sustained oscillating instabilities are found to arise under i-V region of both negative resistance $(\partial U/\partial i) < 0$ (frequency of Hz) and positive resistance $(\partial U/\partial i) > 0$. At $(\partial U/\partial i) > 0$ the instability takes place in two cases: under i-V point close to the critical low one (kHz) and under i-V point close enough to the inflection point. Here period-doubling is observed as a transition to chaos-like state. The self-sustained instabilities correlate with the plasma structure development. The oscillating mode for operation at $(\partial U/\partial i) > 0$ is found to arise under combination of reasonable parameters of a HCD plasma.

References

Dimova, E., Petrov, G., Blagoev, K.: 2004, Conference, SPIE, Smolian, Bulgaria, **5449**, 350-353.

Ginzburg, V. L.: 1967, Propagation of EM waves in plasma, Moskva, Nauka.

Jung, E.: 1999, *Opt. Commun.*, **156**, 149.

Miniature Lamp Department: 1967, General Electric Glow Lamp Manuel (General Electic, Nela Park, East Cleveland, OH), 7.

Mihailova, D., Groyeva, M., Bogaerts, A., Gijbels, R. and Sabotinov, N.: 2003, *VACUUM*, **5226**, 49.

Zhechev, D. and Atanassova, S.: 1998, *Opt. Commun.*, **156**, 400.

Publ. Astron. Obs. Belgrade No. 84 (2008), 359 - 360 *Contributed Paper*

MICROSECOND PULSED GLOW DISCHARGE SOURCE IN "ELEMENT GD" AND "VG 9000" MASS-SPECTROMETERS

M. VORONOV, Th. HOFMANN, C. VENZAGO

AQura GmbH, P.O. Box 915-d115, Rodenbacher Chaussee 4, D-63457, Hanau-Wolfgang
E–mail: VoronovMV@mail.ru

Abstract. Microsecond pulsed glow discharge (PGD) may consume several kW of instantaneous power that may lead to a significant increase of a sample atoms excitation and ionization efficiency. Improvement of analytical characteristics of a glow discharge source using pulsed mode of power supply is demonstrated earlier for different optical and mass spectral methods (Drobyshev, Turkin 1981, Bengtson et al. 2000, Huang et al. 1991, Hang et al. 1996, 1994, Farnsworth, Walters 1982), including fast flow ion source (Voronov, Hoffmann 2007). However, practical use of microsecond PGD is limited to scientific investigations.

In this work the microsecond PGD is applied to existing commercial mass-spectrometers "Element GD" and "VG 9000" to develop a system, which can be used in commercial routine analysis. Investigations are focused on possibilities of analysis with microsecond PGD and in comparison of PGD in fast flow source ("Element GD") and usual Grimm type source ("VG 9000"). Detection limits in DC and PGD modes are investigated and compared.

The secondary discharge in Grimm type fast flow source was discovered in (Voronov, Hoffmann 2007), and it certainly exists in "Element GD" instrument. However, practical application of the secondary discharge for improvement of analytical properties of the instrument is not clear. To answer this question, dynamics of ions extracted from the discharge pulses is measured using earlier developed method (Voronov, Hoffmann 2007) (see the fig.). Based on the measured ion dynamics and results of the PGD numerical simulation, influence of the secondary discharge in "Element GD" instrument is discussed.

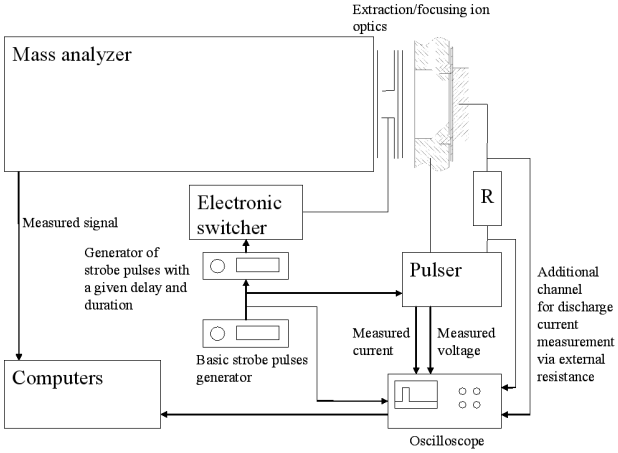

References

Bengtson, A., Yang, C., Harrison, W. W.: 2000, *JAAS*, **15**, 1279.
Drobyshev, A. I., Turkin, Y.I.: 1981, *Spectrochimica Acta*, **36B**, 1153.
Farnsworth, P. B., Walters, J. P.: 1982, *Anal. Chem.*, **54**, 885.
Hang, W., Walden, W. O. and Harrison, W. W.: 1996, *Anal. Chem.*, **68**, 1148.
Hang, W., Yang, P. Y., Wang, C. L., Su, Y. X., Huang, B. L.: 1994, *Rapid commun. Mass Spectrom.*, **8**, 590.
Huang, B., Yang, P., Lin, Y., Wang, X., Yuan, D.: 1991, *Fenxi Huaxue*, **19**, 259.
Voronov, M., Hoffmann, V.: 2007, *JAAS*, **22**, 1184.

Publ. Astron. Obs. Belgrade No. 84 (2008), 361 - 364 *Contributed Paper*

SELF-SUSTAINED UNSTABLE MODES FOR OPERATION OF GLOW DISCHARGE. AN APPLICATION

V. STEFLEKOVA[1], D. SLAVOV[2], D. ZHECHEV[1] and G. TODOROV[2]

[1] *Institute of Solid State Physics, Bulgarian Academy of Sciences, 72 Tzarigradsko Chaussee Blvd., BG-1784 Sofia, Bulgaria*

[2] *Institute of Electronics, Bulgarian Academy of Sciences, 72 Tzarigradsko Chaussee Blvd., BG-1784 Sofia, Bulgaria*

E–mail: spectron@issp.bas.bg

Abstract. Two self-sustained unstable modes for operation dependent on the operating i-V point are observed in a hollow cathode discharge (HCD). They manifest themselves as either galvanic oscillation or pulsation. The instabilities take place under i-V sections of both positive and negative differential resistance. The frequency f of the instabilities is found depending on the current discharge value i. The function $f(i)$ is a precondition some deviations of the both gas pressure and purity fixed to be noticed.

1. INTRODUCTION

Glow discharge (GD) is known as a medium of certain important and only possible applications (Marcus et al. 1993). As a rule, the stability of the selected mode for operation is a necessity vs. above field. A GD modification, e.g. hollow cathode discharge (HCD) is known as a stable light - and sputtered atoms source enlarging some of these applications (Caroli et al. 1993). However, from another point of view the plasma in a GD is known as a typical nonlinear dynamical '' open system'' with a large number of degrees of freedom. Within these frames a HCD should possess one more additional degree of freedom due to the intensive atomization of the cathode surface. Some new HCD application fields revealed instabilities vs. both induced and spontaneous Δi-ΔV deviations (Lee et al. 1987 and Zhechev et al. 1998). The instabilities are observed under i-V branch of $(\partial U/\partial i) < 0$. The latter arises due to Penning ionization (Dimova et al. 2004 and Dimova et al. 2003).

In this study two self-sustained unstable modes for operation of a HCD are analyzed vs. the operating i-V point. The self-sustained instabilities are analyzed as an indicator of Δp - and ΔP deviations of both pressure p and purity P of the gas medium.

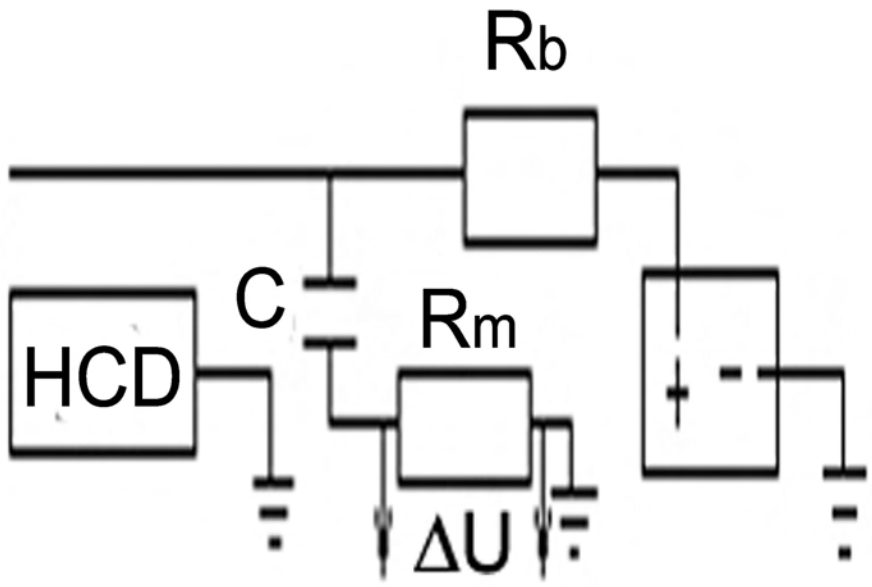

Figure 1: Experimental scheme: R_b - ballast resistor (11 kΩ), C (0.47μF) - decoupling condenser, R_m - measuring resistor.

2. EXPERIMENTAL

The stability of a HCD dc operation is studied at absence of any external perturbation. Figure 1 contains a schematic drawing of the standard experimental set-up. Time - dependent change in the impedance of the discharge was determined by measuring the voltage $\Delta U(t)$ across the 50 Ω resistor R_m. A trademarked HCD modifications, i.e. trademarked lamp Ne/Ca/Ba ("Cathodeon Inc") was used.

Both regions of negative dynamic resistance $\partial U/\partial i < 0$ and great slope variety of some HCD i-V curves (Zhechev et al. 1998) drew our attention to i-V operating points of different $\partial U/\partial i$ values.

3. RESULTS AND DISCUSSION

3.1. Generally, self-sustained oscillating components were observed under some operating i-V points on overlapping i-V parts of both $\partial U/\partial i < 0$ and $\partial U/\partial i > 0$ (Figure 2) and under operating i-V point close enough to the critical low one. At the beginning a self - sustained oscillating voltage component (18 Hz, $\sim$ 7 V) was detected under operating points of $\partial U/\partial i < 0$ (Figure 3). Both frequency f and shape of oscillation change within the discharge current values of (1.5 - 1.9) mA. Earlier, self-sustained oscillations were observed in (Lee et al. 1987). The oscillation negative peaks were observed to extinguish the discharge and HCD passes into a twinkling mode for operation of the same frequency. Self-sustained instabylity of pulsing type and frequency (50kHz) was observed for the first time. It takes place at $i \in [3.0 \div 6.8]$mA where $\partial U/\partial i > 0$.

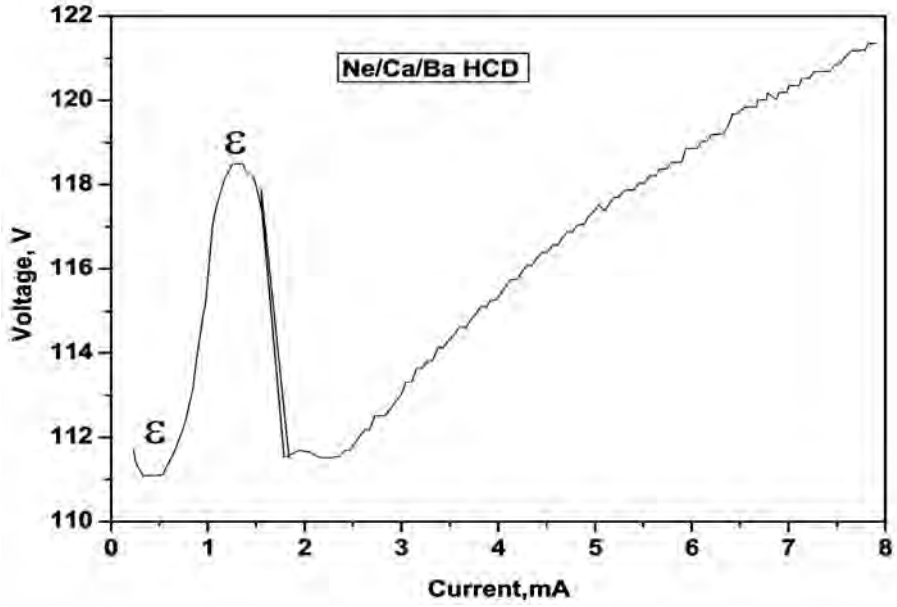

Figure 2: A section of i-V- curve of HCD lamp ("Cathodeon Inc").

Both oscillation-and pulsation frequencies depend strongly on their i-value.

The genesis of the observed instabilities may be analyzed formally within the frames of an equivalent HCD circuit.

Both self-sustained oscillations and light-induced conductivty are precondition for OG optogalvanic transfer of instability within the sections of a segmented GD including that used as a laser medium (Mihailova et al. 2003). This opportunity was checked.

3.2. Generally, the methods for monitoring of either gas pressure p or purity P are based on some simple *measurable effect* dependent on the value of p and P. Earlier the shape of the optogalvanic signal was discussed as a sensitive indicator of changing p and P (Zhechev et al. 2003). The sensitivity of both oscillation - and pulsation frequency f vs. current discharge value, i is a precondition any deviation Δp or ΔP to be noticed by using the function $f(i)$. Indeed, either of Δp or ΔP stimulates change in the gas medium effective potential of ionization, i. e. $\Delta i(\Delta p)$. The latter influences the self-sustained oscillation frequency f.

Obviously, the sensitivity $\Delta f(\Delta p)$is a function of the operating i-V point. The steeper the i-V sections the higher sensitivity $\Delta f(\Delta p)$.

4. CONCLUSIONS

Two self-sustained unstable modes for operation of a HCD are observed. The low frequency oscillations (of tens Hz) take place under i-V operating points of negative dynamic resistance. The disharge passes into a twinkling mode for operation of the same frequency. Pulsations of tens kHz frequency arise under i-V operating points of

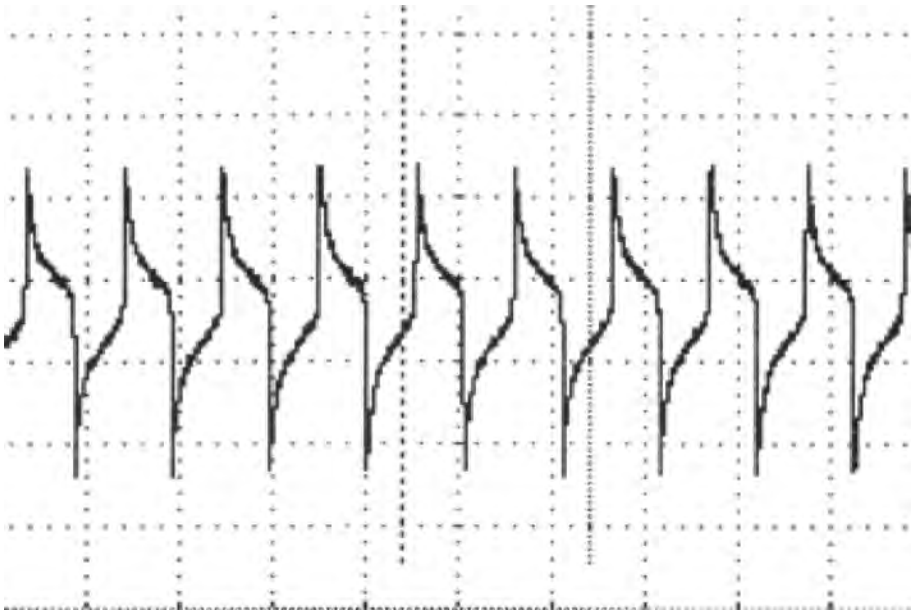

Figure 3: Oscillations under $i = 1{,}5$ mA, $\partial U/\partial i < 0$.

positive dynamic resistance. The frequency of the self-sustained unstable modes for operation depends on the discharge current value. This function is a precondition for gas pressure and purity monitoring.

References

Caroli, S. and Senofonte, O.: 1993, Hollow Cathode Discharges. In: Glow Discharge Spectroscopies; Marcus, R., Ed.; Plenum Press: New York, 1-14.

Dimova, E., Petrov, G. and Blagoev, K.: 2004, *VACCUM*, **76**, 405.

Dimova, E., Petrov, G. and Blagoev, K.: Proceedings of the ILLA'2003 Conference, Smolian, Bulgaria, SPIE 2004, **5449**, 350.

Lee, S., Rothe, E. and Reck, G.: 1987, *J. Appl. Phys.*, **61**, 109.

Marcus, R.: 1993, Introduction. In: Glow Discharge Spectroscopies; Marcus, R., Ed.; Plenum Press: New Yourk, 1-14.

Mihailova, D., Grozeva, M., Bogaerts, A., Gijbels, R. and Sabotinov, N.: 2003, In: Proc. SPIE XII ISQE Varna, **5226**, 49-53.

Zhechev, D. and Atanassova, S.: 1998, *Opt. Commun.*, **156**, 400.

Zhechev, D. and Parvanova, N.: 2003, *Opto-Electronics Review*, **11** (1), 31.

Publ. Astron. Obs. Belgrade No. 84 (2008), 365 - 368 *Contributed Paper*

APPLICATION OF RELATIVE SENSITIVITY FACTORS FOR INVESTIGATION OF PROCESSES IN PULSED GLOW DISCHARGE PLASMA WITH TOFMS ION DETECTION

A. KRAVCHENKO, A. GANEEV, S. POTAPOV, R. TJUKALTZEV, A. ZLOTOROWICZ

Chemical Faculty, Saint Petersburg State University,
Universitetsky pr., 26, Petrodvoretz, St. Petersburg, Russia, 198504
E–mail: anchen_88@mail.ru

Abstract. Relative sensitivity factors (RSF's) for different matrices (copper, steel, nickel, lead, silicon) in pulse-GD MS are determined. The possibilities of time-of-flight mass spectrometry with pulse glow discharge ionization in semi-quantitative analysis without using of standards samples are discussed. Dispersal of RSF's is appreciably low in comparison with RSF dispersal for DC discharge. Different types of correlation between RSF of the element and its ionization potential were obtained. According to this fact assumptions about different plasma processes in glow discharges were made.

1. LOW TEMPERATURE PLASMAS

1. 1. PLASMA APPLICATIONS AND DEVICES

It is known that sensitivities for different elements in Glow Discharges (GD) are to lesser degree depend on matrix than ones for spark, laser ablation and ICP MS. This feature connects with two factors – sputtering rates for the elements in GD are equal and differences of rates of ionization (it is determined in high degree by nonselective Penning process) aren't very high. Relative Sensitive Factor (RSF) is used for description of matrix influence on measured concentrations:

$$RSF(x/y)_z = \frac{I_x \cdot C_y}{I_y \cdot C_x}, \tag{1}$$

where I_x and I_y – intensities of determined element and element used as internal standard (main component of the sample), C_y and C_x – appropriate concentrations. RSF describes dependence of sensitivity of element X from matrix Z.

Due to that processes of atomization and ionization in glow discharge are divided in space and in time, the disorder of sensitivities for different elements is not so great. This case the analysis possible without strict conformity of a standard and analyzed samples. Besides at values of RSF close to unit, carrying out the semi-quantitative analysis without use of the standard is possible.

There are numerous measurements RSF for various elements and matrixes at ionization in the glow discharge. Values RSF of elements for the given matrix at ionization in the glow discharge make sizes of one order, as against again secondary ionic and laser sources where distinction can achieve three orders. Besides spread in values of RSF in GD MS doesn't exceed 30% for one element in different matrix. These features make GD by attractive source for sample ionization, therefore many investigations carried out in this field. However all of this works relate to DC and RF discharges, while RSF for pulsed discharges don't investigate practically. Taking into account that processes in afterglow play primary role in pulsed discharges, which can essentially differ from the processes in DC or RF discharges, than one can expect of rather another situation with RSF.

Experiments were carried out on TOFMS with pulsed ionization in combined hollow cathode. The cathode consisted of flat sample and cathode wall produced from pure Aluminum (99.9999%). The sample press oneself to the wall. This technique allowing analyze as conductive as semiconductive and dielectric samples. RSF were measured for different samples – Copper, Nickel, Lead, Steel and Silicon (see Table 1).

RSF for the most part of the elements close to 1 (moderate differences can be explained by the differences of cross sections of Penning ionization for different elements) while distinction is appreciable greater for few elements. The distinction can be connects with selective process (for example asymmetric charge transfer). However this dispersal is appreciably low in comparison with RSF dispersal for DC discharge. Apparently efficiency of different selective processes of ionization (for example asymmetric charge transfer) in afterglow is appreciably lower than efficiency of Penning ionization, while in DC or RF discharge selective processes of ionization play significant role.

For two matrices in the case of pulsed GD (cooper and silicon) influence of ionization potential on RSF was investigated (see Figure 1). Also such investigations were made for the DC GD using experimental data from literature (see Figure 2).

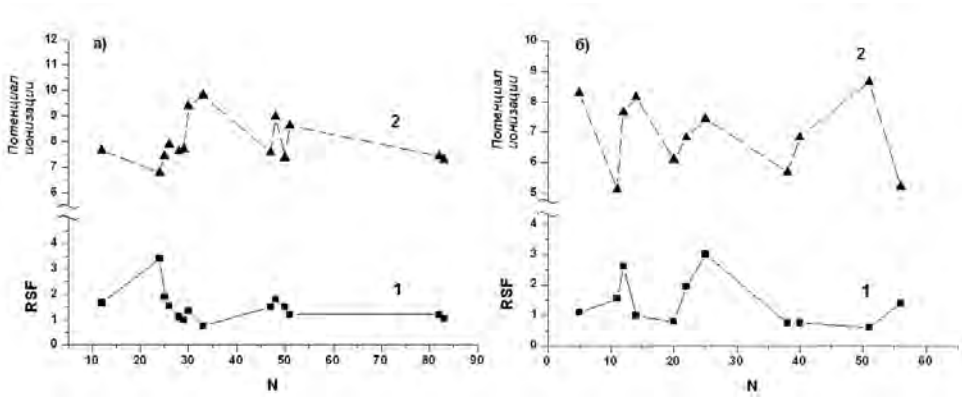

Figure 1: Correlation between RSF (1) of an element and its ionization potential (2). Pulsed GD. a) – cooper matrix b) – silicon matrix.

In the case of DC GD slight positive correlation between RSF of an element and its ionization potential was found. Meanwhile for pulsed GD there was no such correlation. Correlation coefficients are presented in Table 2. These facts confirm our previous assumption that in pulsed GD Penning ionization is dominating ionization process, while in DC GD selective processes such asymmetric charge transfer play significant role.

Table 1: Determined relative sensitivity factors

Sample	Element RSF	
Copper	Mg	1.65
	Cr	3.4
	Mn	1.9
	Fe	1.55
	Ni	1.1
	Zn	1.35
	As	0.76
	Ag	1.5
	Cd	1.8
	Sb	1.2
	Sn	1.50
	Pb	1.2
	Bi	1.05
	Cu	1.0
Nickel	Ag	2,10
	Pt	1,45
	Pd	2,30
	Rh	2,0
	Ni	1,0
Lead	Ag	2.1
	Se	0.65
	Te	0.65
	Sb	1.45
	Pb	1,0
Steel	Cr	1.4
	Mn	1,2
	Ni	1.5
	Fe	1.0
Silicon	Sr	0.75
	Mn	3.0
	Ti	1.95
	Ca	0.80
	Mg	2.6
	Ba	1.4
	Na	1.55
	B	1.1
	Zr	0.75
	Sb	0.6
	Si	1.0

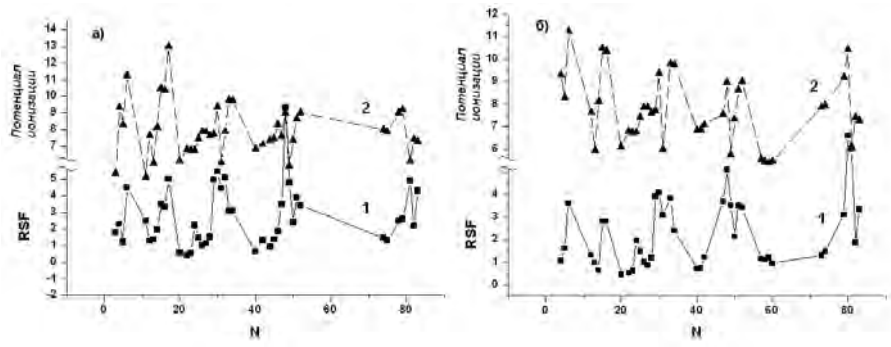

Figure 2: Correlation between RSF (1) of an element and its ionization potential (2). DC GD. Steel matrix.a) – Bogaerts and Gijbels 1996 b) – Saka and Inoue 2000

Table 2: Correlation coefficients
* - different literature sources were used for DC GD.

Matrix. Discharge type.	r
Cooper. Pulsed GD	-0,45
Silicon. Pulsed GD	0,03
Steal. DC GD [1]*	0,35
Steal. DC GD [2]*	0,52

Indeed according to computer simulation results for used pulsed GD concentration of argon ions in the discharge cell decreases sharply after pulse, whereas concentration of argon metastables decreases in significantly lesser degree. Such situation determines dominate role of Penning ionization mechanism and nearly absence of asymmetric charge transfer from argon ions for pulsed GD.

For cooper matrix in pulsed GD was found slightly negative correlation between RSF of an element and its ionization potential. Possible explanation of this fact is the presence of asymmetric charge transfer with cooper ions. Cooper has high sputtering coefficient and its ionization potential is close to many sample elements ionization potentials, consequently such process is very probable. If our assumption is correct, it is very promising, because varying operating conditions one can influence on RSFs.

References

Adams, F., Adriaens, A., Bogaerts, A.: 2002, *Analytica Chimica Acta*, **456**, 63.
Adams, F. and Vertes, A.: 1990, *Fresenius J Anal Chem*, **337**, 638.
Bogaerts, A. and Gijbels, R.: 1996, *J. Anal. At. Spectrom.*, **11**, 841.
King, F. L., Teng, J. and Steiner, R. E.: 1995, *J. of Mass Spectrometry*, **30**, 1061.
Raparthi, S., Arunachalam, J., Das, N., Srirama Murthy, A. M.: 2005, *Talanta*, **65**, 1270.
Saka, T. and Inoue, M.: 2000, *Analytical sciences*, **16**, 653.
Vieth, W. and Huneke, J. C.: 1991, *Spectrochim Acta B*, **46**, 137.

Publ. Astron. Obs. Belgrade No. 84 (2008), 369 - 373 *Contributed Paper*

ELECTRICAL PROPERTIES OF PULSED GLOW DISCHARGE

Two new aspects

V. V. EFIMOVA[1], M. V. VORONOV[2], V. HOFFMANN[1], J. ECKERT[1]

[1] *Leibniz-Institut für Festkörper- und Werkstoffforschung Dresden, P.O.Box 270116, D-01171 Dresden*
E–mail: V.Efimova@ifw-dresden.de

[2] *AQura GmbH, P.O.Box 915-d115, Rodenbacher Chaussee 4, D-63457 Hanau-Wolfgang*
E–mail: VoronovMV@mail.ru

Abstract. At the application of pulsed glow discharge (PGD) a transient power of several kW can be reached. This leads to a significant increase of the excitation and ionization efficiency of the sputtered sample atoms. Moreover, with pulsed mode temporally resolved optical emission spectrometry (OES) and mass spectrometry (MS) deliver additional information about the chemical bonds (Harrison 1998, Bengtson et al. 2000, Hang et al. 1996, Klingler et al. 1990, Lewis et al. 2001, Jackson and King 2003).

However, the practical application of pulsed glow discharge (PGD) requires an understanding of the processes taking place in the pulsed system. There are some publications, where attention was paid on the voltage current characteristics and the current signal shape of PGD (King and Pan 1993, Lewis et al. 2003). Nevertheless more attention should be paid on the electrical properties of the PGD. In this work the shapes of current, voltage and emission intensity signals, obtained with two different pulse generators are compared.

For better understanding of processes, taking place in the discharge the knowledge of the gas temperature is very important. Several authors have mentioned that heating of the cathode leads to changes of the voltage current curve, mainly a decrease of the current at the same voltage. This can be explained by a lower gas density at the same pressure but at higher temperatures (Chenlong et al. 1999, Tian and Chu 2001, Kasik et al. 2002). This phenomenon gives an approach to estimate the gas temperature of the plasma.

1. INVESTIGATION OF VOLTAGE CURRENT AND EMISSION INTENSITY SHAPES

1. 1. EXPERIMENTAL

For direct current (dc) and pulsed dc measurements an 8-mm Grimm type source from "Spectruma" with floating anode was used.

Two power supplies with significant difference in the electronic circuits were compared. "RUP3-3a" unlike the "IRCO M3kS-20N" has an additional high voltage switch, which discharges the load after the termination of the pulse.

1. 2. VOLTAGE AND CURRENT SIGNAL SHAPES

The voltage and current signal shapes during the pulse were compared for a generator with and without second switch ("RUP3-3a" and "IRCO M3kS-20N"). It is apparent that differences in the electronic circuit lead to differences in the current and voltage signal behaviour (Fig. 1).

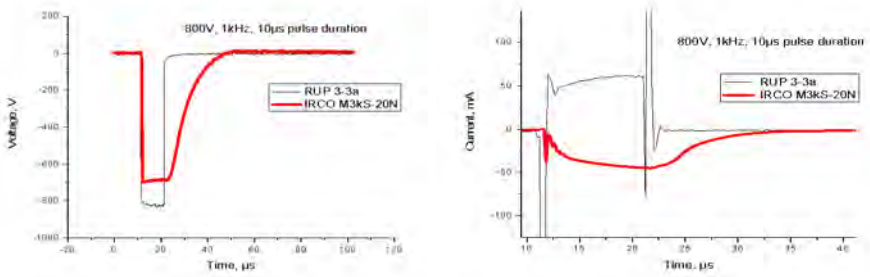

Figure 1: Voltage and current shapes during the pulse (the current of RUP3-3a is inverted for better presentation).

During the pulse at "RUP3-3a" first switch is on and second is off. To terminate the pulse the first switch is turned off, but at the same moment the second is turned on and discharges the residual load charge. Therefore there are no voltage and current signals after the termination of the pulse.

In the case of "IRCO M3kS-20N" the capacity of the pulsed system caused residual current after the pulse termination. Therefore the voltage and current signal disappears gradually and means that the plasma still exists.

1. 3. LIGHT EMISSION SIGNAL SHAPES

The light emission of Ar I (696,54 nm) during the pulse time was measured. The emission from the GD cell was delivered through an optical fiber to the monochromator "SPEX 270M" from Jobin Yvon. The signal from the monochromator "SPEX 270M" was directed to the high speed low-noise current preamplifier "SR 570" from Stanford Research and then to the oscilloscope. In Fig. 2 the emission using "RUP3-3a" and "IRCO M3kS-20N" is compared. It was observed that the behaviour of current and light signals is similar. When the "RUP 3-3a" generator is used, the second switch discharges the cell after the pulse termination. This leads to the sharp fall of current and emission signal. In case of "IRCO M3kS-20N" power supply the residual charge in the system is not discharged after the end of the pulse. This means that the plasma doesn't disappear after pulse termination and still emits light.

It was found out that with decreasing voltage the light emission shapes are changing. Mainly, the maximum of intensity is moving to the end of the pulse (Fig. 2(b)).

The emission shapes from Fig. 2(b) are products of averaged signals from 32 pulses. If no averaging is used and the emission of one pulse is recorded, one will see the following picture (Fig. 3).

In the case of the generator without second switch ("IRCO M3kS-20N") the maximum of intensity appears after pulse termination, in contrast to "RUP 3-3a", where the second switch removes all signals after the pulse.

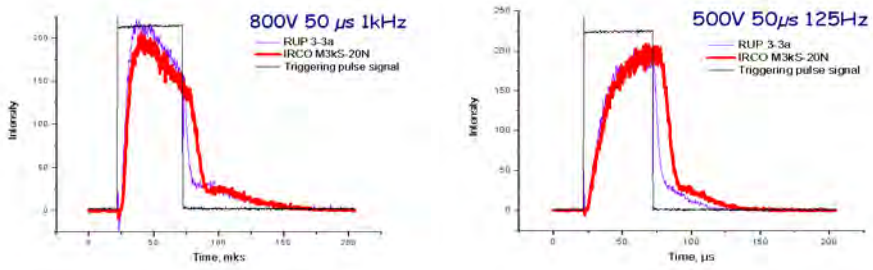

(a) (b)

Figure 2: Emission intensity signal shapes under normal (a) and low (b) conditions.

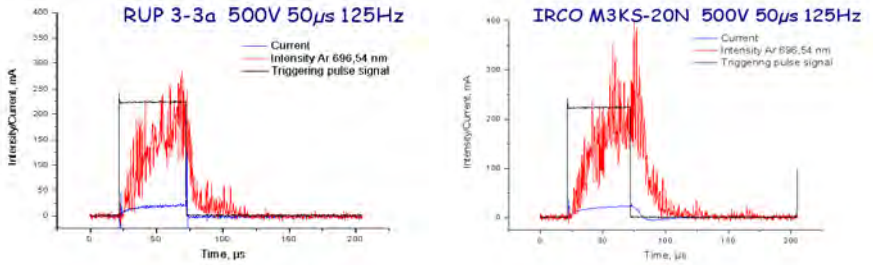

Figure 3: Emission intensity shapes of single pulses measured under low discharge conditions.

2. VOLTAGE CURRENT CHARACTERISTICS AS A THERMOMETER

Electrical current in the dc and radio frequency (rf) mode was measured as function of the discharge voltage under different pressures. In dc and rf pulsed mode the influence of repetition frequency and pulse duration was additionally investigated. The current signals were averaged during the first 10 μs (for the dc pulsed mode) and the last 1 μs (for the rf pulsed mode).

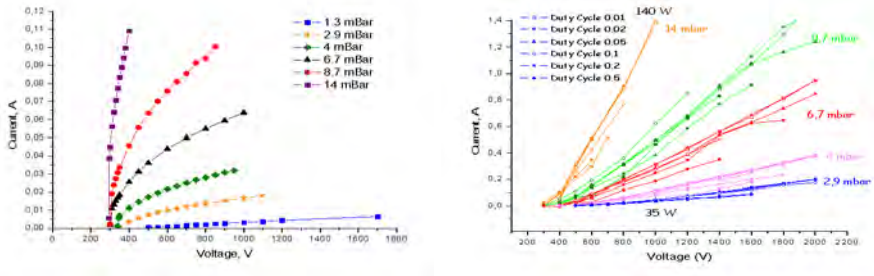

(a) (b)

Figure 4: Voltage current characteristics of the (a) dc and (b) pulsed dc discharges.

For rf and pulsed rf measurements a special free-standing Grimm-type source with 4 mm anode and a free-running rf generator (Forschungstechnik IFW 3,37 MHz) was used. The instantaneous current and voltage signals were measured by integrated current and voltage probes (unique measurement system, developed at IFW Dresden) (Wilken et al 2003).

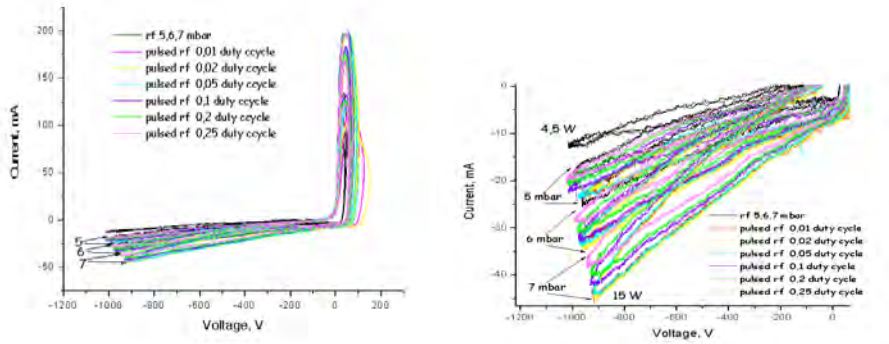

(a) (b)

Figure 5: Voltage current characteristics of the rf and pulsed rf discharges.

Changing of the current amplitude with the duty cycle can be explained by the influence of discharge power on the temperature of the gas. When the duty cycle increases the mean power consumption increases too, what leads to a heating of the plasma. In this work it was assumed that the different temperature of gas and thus different discharge gas concentrations are the main reason for the observed changes of the V-I characteristics. Processes like different secondary emission yield at the sample surface caused by temperature changes of the sample or changing concentration of the sputtered material in the plasma are considered as less important. Mainly, under constant pressure according to the thermodynamic law p=nkT an increase of the gas temperature leads to the decrease of Ar atom concentration and therefore of the current.

This phenomenon gives an approach to the discharge temperature estimation. Each V-I curve with the same slope is characterised by a certain Ar atom concentration. Two V-I plots with the same slope can correspond to the low temperature and low pressure and to the high temperature and high pressure, but the Ar atom concentration is equal. Mainly, $p_{high}/T_{high}=p_{low}/T_{low}$, from witch T_{high} can be calculated.

The V-I curves, measured under 0,01 duty cycle were assumed to correspond to the room temperature. For these curves, the dependence of the V-I slope on the pressure was plotted. By interpolating of the plot the pressures (p_{high}), which correspond to the higher temperatures (higher duty cycles) were determined. At the end, the T_{high} values were calculated (see tables).

It was observed, that the gas temperature does not depend on the pressure in limits of accuracy of the measured data, so only the average temperature as function of duty cycle is presented in the tables. It is apparent from the Figs 4 and 5, that the power which is introduced into the plasma for the dc pulsed mode in the first 10 μs is one order of magnitude higher than for the rf pulsed mode at the end of the pulse. Hence the temperature values for the dc pulsed mode are higher than for the rf pulsed ones.

Duty Cycle **dc** pulsed	Temperature °C
0,01	20
0,02	36
0,05	55
0,1	74
0,2	116
0,5	149
dc f(U,p)	350

Duty Cycle **rf** pulsed	Temperature °C
0,01	20
0,02	19
0,05	20
0,1	25
0,2	33
0,25	44
rf	123

At this moment, the estimation of the dc discharge temperature is complicated, because the V-I curves are not linear due to the heating effect. It is questionable to select one slope of such curve. Therefore, the temperature for the dc mode in the table was given as dependent on voltage and pressure.

3. CONCLUSIONS

1. Shapes of current, voltage and emission intensity signals, obtained with two different pulse generators are compared. At research of the pulsed discharge, particularly of the afterglow it is very important to pay attention on the electronic circuit of the pulsed generator.

2. At the variation of voltage, pressure and duty cycle in the given range, the duty cycle has the main influence on the voltage current characteristics. The temperature of the plasma was estimated from these curves, but further investigation and comparison with model calculations are necessary.

References

Bengtson, A., Yang, C., Harrison, W. W.: 2000, *JAAS*, **15**, 1279.
Chenlong, Y. et al.: 1999, *Anal. Chem.*, **71**, 5328.
Cris L. Lewis, et al.: 2001, *Spectrochim. Acta B*, **56**, 487.
Cris L. Lewis et al.: 2003, *JAAS*, **18**, 527.
Hang, W., Walden, W. O., Harrison, W. W.: 1996, *Anal. Chem.*, **68**, 1148.
Harrison, W. W.: 1998, *JAAS*, **13**, 1051.
Jackson, G. P., King, F. L.: 2003, *Spectrochim. Acta B*, **58**, 1417.
Kasik, M., Michellon, C. and Pitchford, L. C.: 2002, *J. Anal. At. Spectrom.*, **17**, 1398.
King, F. L., Pan, C.: 1993, *Anal. Chem.*, **65**, 735.
Klingler, J. A., Savickas, P. J., Harrison, W. W.: 1990, *Amer. Soc. Mass Spectrom*, **1**, 138.
Tian, X. B., Paul K. Chu: 2001, *J. Phys. D: Appl. Phys.*, **34**, 354.
Wilken, L., Hoffmann, V., Uhlemann, H.-J., Siegel, H. and Wetzig, K.: 2003, *J. Anal. At. Spectrom.*, **18**, 646.

Publ. Astron. Obs. Belgrade No. 84 (2008), 375 - 377 *Contributed Paper*

BREAKDOWN PHENOMENA IN RADIO-FREQUENCY HELIUM MICRODISCHARGES

M. RADMILOVIĆ-RADJENOVIĆ, B. RADJENOVIĆ and A. NINA
Institute of Physics, P.O. Box 57, 11080 Belgrade, Serbia
E–mail: marija@phy.bg.ac.yu

Abstract. In this paper, the Kihara equation has been applied in order to determine the breakdown voltage in helium rf microdischarges. It was found that the Kihara equation, with modified moleculer constants, describes the breakdown process well even for gaps of the order of a few millimeters. A good agreement between numerical solutions of the Kihara equation and the available experimental data reveals that the breakdown voltages depend on the *pd* product and vary substantially with changes in rf frequencies.

1. INTRODUCTION

Capacitively coupled rf discharges are attracting an increased attention due to their wide applications in many technological processes such as plasma etching for semiconductor materials (Flamm et al. 1983, Moreu 1988), thin film deposition (Catherine and Couderc 1986, Yalamanchi and Thutupalli 1988) and plasma cleaning (Raizer et al. 1995).

The majority of plasma processing, so far, is done at low pressures. Atmospheric pressure plasmas, however, can provide a critical advantage over the widely used low pressure plasmas since the cost of the material processing could be reduced substantially (Park et al. 2001). In this paper, we have investigated the applicability of the Kihara equation (Kihara 1952) in describing rf discharges in microgaps.

2. KINETIC THEORY OF THE RF BREAKDOWN

During rf discharges, the gas breakdown mechanism in low frequency alternating electric fields is essentially the same as for dc fields, i.e. it is controlled by secondary electron emission due to ion impact (Phelps and Petrović 1999, Radmilović-Radjenović and Lee 2005). At sufficiently high frequencies, however, ions are not capable to respond to the ac field and electrons are "trapped" in an oscillatory motion within the inter-electrode gap. In that case, the electron loss is dominated by diffusion and a significant reduction of the breakdown voltage is observed as compared to the dc case (Radmilović-Radjenović and Lee 2005).

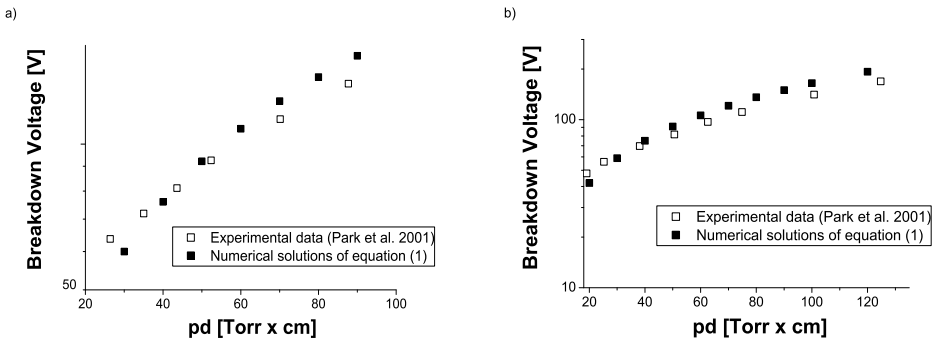

Figure 1: Breakdown voltage as a function of *pd* product in helium discharges at 13.56 MHz and gap size of: a) 0.18 cm and b) 0.25 cm.

In studying the rf breakdown it is customary to use the Kihara equation (Kihara 1952]) that describes conditions for the rf gas breakdown:

$$\mathrm{e}^{\frac{B_0 p}{2E}} = A_1 pd\Big(1 - \frac{E/B_0 p}{C_2 d/\lambda}\Big), \tag{1}$$

where $E = E_{rf}/\sqrt{2}$ is the effective rf field, p is the gas pressure, d is the electrode spacing, λ is the vacuum wave length of the rf field and finally, A_1, B_0 and C_2 are molecular constants (Kihara 1952, Lisovsky and Yegorenkov 1994).

3. RESULTS

Comparison between numerical solutions of the equation (1) (solid symbols) and measurements (open symbols) carried out by Park and his co-workers (Park et al. 2001) is shown In Fig. 1. For both gap sizes, a satisfactory agreement between theoretical and experimental results were achieved by using modified values for molecular constants $A_1 = 28$ and $B_0 = 18$.

As can be observed from Fig. 2, the breakdown voltage decreases with increasing rf frequency. For pure helium at the pressure of 600 Torr and the gap size of 0.16 cm numerical solutions of the equation (1) including modified molecular constants (solid symbols) provide a good agreement with the experimental data (Park et al. 2001) (open symbols).

4. CONCLUSIONS

This paper displays theoretical studies of the breakdown voltage in rf helium discharges. The obtained numerical solutions and their good agreement with the experimental results confirm that in the case of rf discharges at 13.56 MHz and the gap spacings of a few millimeters, breakdown voltage depends on the *pd* product and is mostly independent on the gap size. At the same time, in studying the effect of frequency variation in a high-frequency helium discharges we have also obtained satisfactory agreement between numerical results and experimental data. As expected,

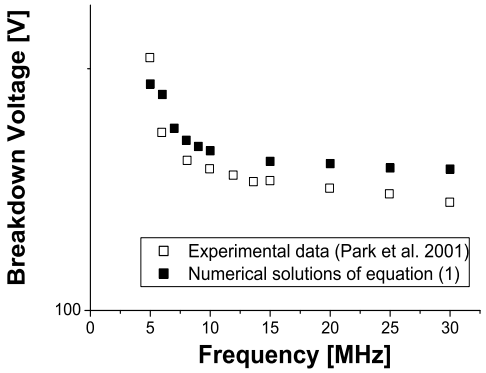

Figure 2: Breakdown voltage versus rf frequency in pure helium. Results were obtained for a gap spacing of 0.16 cm and a gas pressure of 600 Torr, varying the frequency from 5 MHz to 30 MHz.

the breakdown voltage decreases with increasing the frequency as in the case of large scale systems. The next step in our work will be investigation of the applicability of the Kihara equation for the micrometer gaps.

The present work has been performed under MNZŽS 141025 project.

References

Catherine, Y., Couderc, P.: 1986, *Thin Solid Films*, **144**, 265.
Flamm, D. L., Donnelly, V. M., Ibbotson, D. E.: 1983, *J. Vac. Sci. Technol. B*, **1**, 23.
Kihara, T.: 1952, *Rev. Modern Phys.*, **24**, 45.
Lisovsky, V., Yegorenkov, V. D.: 1994, *J. Phys. D: Appl. Phys.*, **27**, 2340.
Moreu, W. M.: 1988, Semiconductor Litography: Principles, Practices and Materials, Plenum, New York.
Park, J., Henins, I., Herrmann, H. W., Selwyn, G. S.: 2001, *Journal of Applied Physics*, **89**, 15.
Phelps, A. V., Petrović, Z. Lj.: 1999, *Plasma Sources Sci. Technol.*, **8**, R21.
Radmilović-Radjenović, M., Lee, J. K.: 2005, *Phys. Plasmas*, **12**, 063501.
Radmilović-Radjenović, M., Lee, J. K., Iza, F., Park., G. Y.: 2005, *Journal of Physics D: Applied Physics*, **38**, 950.
Raizer, Yu. P., Schneider, M. N., Yatsenko, N. A.: 1995, Radio-Frequency Capacitive Discharges, CRC, New York.
Yalamanchi, R. S., Thutupalli, G. K. M.: 1988, *Thin Solid Films*, **164**,

Publ. Astron. Obs. Belgrade No. 84 (2008), 379 - 382 *Contributed Paper*

THE EFFECT OF THE ION-ENHANCED FIELD EMISSION ON THE WATER VAPORS IN MICROGAPS

M. RADMILOVIĆ-RADJENOVIĆ and B. RADJENOVIĆ

Institute of Physics, P.O. Box 57, 11080 Belgrade, Serbia
E–mail: marija@phy.bg.ac.yu

Abstract. In this paper, the departure of the breakdown voltage from the Pachen's law at extremely small electrode separations is theoretically studied. In the standard DC breakdown criteria the enhancement of the secondary emission coefficient has been included. The obtained expression has been applied for determination of the breakdown voltage in water vapors in microgaps. The results of this research can be applied in the construction of compact pulse power generators for bioelectric applications.

1. INTRODUCTION

Micro discharges can be regarded as a new class of plasmas that allow formation of non-equilibrium plasmas at atmospheric pressures (Korolev and Mesyats 1998, Radmilović-Radjenović and Radjenović 2007). The fact that microdischarges operate under conditions where boundary effects dominate indicates the importance of establishing scaling laws in a such small gaps.

We were motivated by the fact that the electrical breakdown in microgaps occurs at voltages far below the pure Paschen curve minimum and that the modified Paschen curve should be used instead for micron and sub-micron gaps (Torres and Dhariwal 1999). Electrons from the field emission are one of the possible reasons why the breakdown and sparks occur in a vacuum, which of course is not possible if one only considers the Townsend avalanche mechanisms for the gas phase and the surface ionization that are normally used to generate the Paschen curve (Radmilović-Radjenović et al. 2005). In this paper, we have fitted numerical solutions in order to estimate the dependence of the breakdown voltage on the gap size and on the pressure in water vapors in microgaps.

2. ION-ENHANCED FIELD EMISSION

Failures from the Paschen curve are expected when the secondary emission process is governed by the ion-enhanced field emissions rather than ion impact. The effective yield of electrons per ion defined as the ratio of the field-emission electron current density to the incoming positive-ion current density at the breakdown is given by the

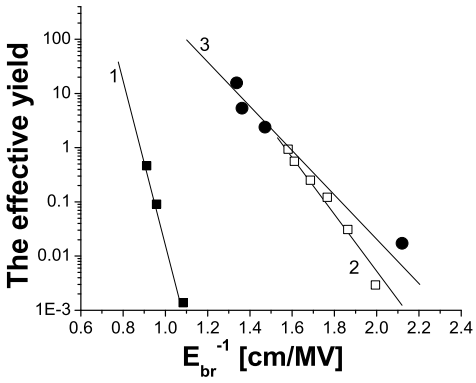

Figure 1: The effective yield versus the inverted breakdown electric field (E_{br}) for three different cathode materials: 1) stainless steel, 2) conventional steel and 3) aluminium.

expression (Boyle and Kisliuk 1955):

$$\gamma = Ke^{-D/E}. \tag{1}$$

As can be seen from Fig. 1, the equation (1) fits the experimental data (Boyle and Kisliuk 1955) well. At the same time, from the slopes of the straight lines shown in Fig. 1 the constant D was found to be equal to 26, 11 and 9.3 MV/cm for stainless steel, conventional steel and aluminium, respectively.

2. 1. SEMI-EMPIRICAL FORMULA

Putting the expression for the yield (1) and for the ionization coefficient:

$$\frac{\alpha}{p} = A\mathbf{e}^{-Bpd/V}, \tag{2}$$

in the expression for the DC breakdown criteria:

$$\gamma\left(\mathbf{e}^{\alpha d} - 1\right) = 1, \tag{3}$$

the transcendental equation can be obtained (Radmilović-Radjenović and Radjenović 2008):

$$K\mathbf{e}^{-Dd/V}\left(\mathbf{e}^{Apd\mathbf{e}^{-Bpd/V}} - 1\right) = 1, \tag{4}$$

Fitting numerical solutions of the equation (4), leads to the expressions for the breakdown voltage as a function of the gap size d and the pressure p, separately.

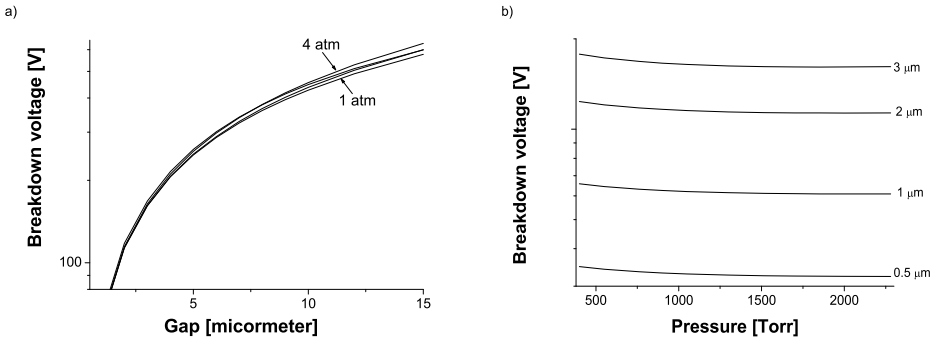

Figure 2: Dependence of the breakdown voltage in water vapors on: a) gap spacing with varying the pressure form 1 atm to 4 atm and b) pressure for gaps from 0.5 μm to 3 μm.

Table 1: Fitting coefficient for the expression (5), for the gas pressure from 1 atm to 4 atm.

Pressure [atm]	a	b	c
1	-26.122	90.012	0.719
2	-20.662	82.597	0.733
3	-14.906	76.304	0.772
4	-11.456	73.16	0.804

3. RESULTS

The obtained numerical solutions of the equation (4) for the breakdown voltage against the gap size are shown in Fig. 2a and are fitted by simple expression:

$$V = a + b * d^c, \tag{5}$$

where values of the fitting coefficients a, b and c, for the gas pressure from 1 atm to 4 atm, are given in Table 1.

The variation of the breakdown voltage with the pressure (see Fig. 2b) has been achieved by fitting based on the expression:

$$V = m * p^n, \tag{6}$$

with fitting coefficients m and n, for the gap spacing from 0.5 μm to 3 μm, listed in Table 2.

In Figure 1 we have shown results obtained by using the semi-empirical expressions (5) and (6), for the breakdown voltage. The fall of the breakdown voltage for gaps less than 5 μm is observed in Figure 1a. On the other hand, Figure 1b demonstrate weak dependence of the breakdown voltage on the pressure.

Table 2: Fitting coefficient for the expression (6), for the gap spacing from 0.5 μm to 3 μm.

Gap [μm]	m	n
0.5	45.094	-0.0442
1	85.898	-0.0456
2	166.531	-0.052
3	247.582	0.0574

4. CONCLUSIONS

The results in this paper clearly show that incorporation of the field emissions leads to deviations from the well-known Paschen curve in small gap sizes. This reduction in the breakdown voltage becomes significant for the gaps smaller than $5\mu m$ m and may be attributed to the onset of appreciable field emissions. The fitting coefficients for semi-empirical expressions that describes the modified Paschen curve for water vapors including field emission effects in microgaps has been purposed. The results of our studies should be useful for determining minimum ignition voltages in microplasma sources as well as the maximum safe operating voltage and critical dimensions in other microdevices.

The present work has been performed under MNZŽS 141025 project.

References

Boyle, W. S., Kisliuk, P.: 1955, *Phys. Review*, **97**, 255.
Korolev, Yu. D., Mesyats, G. A.: 1998, *Physics of pulsed breakdown in gases*, URO-PRESS.
Radmilović-Radjenović, M., Lee, J. K., Iza, F., Park., G. Y.: 2005, *Journal of Physics D: Applied Physics*, **38**, 950.
Radmilović-Radjenović, M., Radjenović, B.: 2007, *Contribution to Plasma Physics*, **47**, 165.
Radmilović-Radjenović, M., Radjenović, B.: 2008, *Plasma Sources Science and Technology*, **17**, 024005.
Torres, J. M., Dhariwal, R. S.: 1999, *Nanotechnology*, **10**, 102.

Publ. Astron. Obs. Belgrade No. 84 (2008), 383 - 386 *Contributed Paper*

THEORETICAL STUDY OF THE THE BREAKDOWN MECHANISM IN BENZOL MICRODSICHARGES

M. RADMILOVIĆ-RADJENOVIĆ and B. RADJENOVIĆ
Institute of Physics, P.O. Box 57, 11080 Belgrade, Serbia
E–mail: marija@phy.bg.ac.yu
E–mail: bradjeno@phy.bg.ac.yu

Abstract. In this paper, the role of the field emission in the deviation of the breakdown voltage from that predicted by Paschen's law has been studied. The expressions for the dependence of the breakdown voltage on the gap spacing and the pressure, separately, in DC microdsicharges in benzol have been derived. Semi-empirical expressions are based on the fitting of numerical solutions of the equation that describes the DC breakdown criteria in microgaps.

1. INTRODUCTION

Localized plasma processing may be required on integrated circuits for different purposes and therefore, studies of micro and nanoscale plasmas are of a great interest (Ito et al. 2001, Tachibana et al. 2005, Chen et al. 2006). Making the gap small is the easiest way to obtain a big force, which is restricted by the electric field of breakdown (Boyle and Kisliuk 1955, Torres and Dhariwal 1999, Radmilović-Radjenović et al. 2005). It is necessary to be aware of the breakdown voltage in microgaps. When changing the size of plasmas there are scaling laws that are helpful in determining the operating parameters of various sizes of plasmas.

In large scale systems, the experimentally observed Paschen law has been successfully explained by the Townsend theory (Paschen 1889).The Paschen's law is based on the observation that, over a large range of pressures and electrode separations, the probability of the ionization per collision in the gas and the probability of the production of electrons by ions by a secondary process are both dependent on the average kinetic energy of the electrons and ions and therefore on the reduced electric field E/N (Loeb 1939). The Townsend mechanism by which successive ionizations of gas molecules induce the gas breakdown describes the process satisfactorily at large separations (Meek and Craggs 1953). The significant parameter is pd, the product of the gap distance and the pressure. Typically, the Townsend's mechanism (and by extension Paschen's law) applies at pd products less than $1000\,\mathrm{Torr}\cdot\mathrm{cm}$, or gaps around a centimeter at one atmosphere (Radmilović-Radjenović and Radjenović 2006).

The mechanism of the electrical breakdown is, however, completely different in microgaps (Radmilović-Radjenović et al. 2005, Radmilović-Radjenović and Radjenović

2007). A rapid fall of the breakdown voltage with decreasing the gap size may be attributed to the onset of the ion-enhanced field emission in microgaps. Violations of the similarity law take place for the left hand branch, for such *pd* values where the electron mean free path is comparable with the gap. This regime can be determined from the condition:

$$d/\lambda_0 = \sigma n_0 pd \leq 1, \tag{1}$$

where λ_0 is the mean free path of the electron, σ is the effective cross section for the collisions of electrons with neutrals and n_0 is the gas density at a unit pressure (Radmilović-Radjenović and Radjenović 2008). When the electron mean free path is comparable with the electrode separation the electrical breakdown is based on the cathode-induced breakdown model.

In this paper, the expressions for the DC breakdown criteria including the ion-enhanced secondary emission coefficient (Radmilović-Radjenović and Radjenović 2008) has been applied to benzol in order to determine the breakdown voltage versus the gap spacing and the pressure, respectively.

2. SEMI-EMPIRICAL FORMULA

It was shown that the DC breakdown criteria:

$$\gamma\left(\mathbf{e}^{\alpha d} - 1\right) = 1, \tag{2}$$

combined with the expression for the yield:

$$\gamma = K\mathbf{e}^{-D/E}, \tag{3}$$

and for the ionization coefficient:

$$\frac{\alpha}{p} = A\mathbf{e}^{-Bpd/V}, \tag{4}$$

leads to the transcendental equation (Radmilović-Radjenović and Radjenović 2008):

$$K\mathbf{e}^{-Dd/V}\left(\mathbf{e}^{Apd\mathbf{e}^{-Bpd/V}} - 1\right) = 1, \tag{5}$$

which has to be solved numerically. In the equation (5), K and D are labels for the material and gas dependent constants, respectively, while A and B are numerical constants which values can be found elsewhere (Raizer 1991, Korolev and Mesyats 1998). Numerical solutions of the equation (5), result in expressions for the breakdown voltage as a function of the gap size d and the pressure p, separately.

3. RESULTS

For the gas pressure in the range from 1 atm to 5 atm, the obtained numerical solution of the equation (5) for the breakdown voltage are fitted by simple analytical expression:

$$V = a + b * d^c, \tag{6}$$

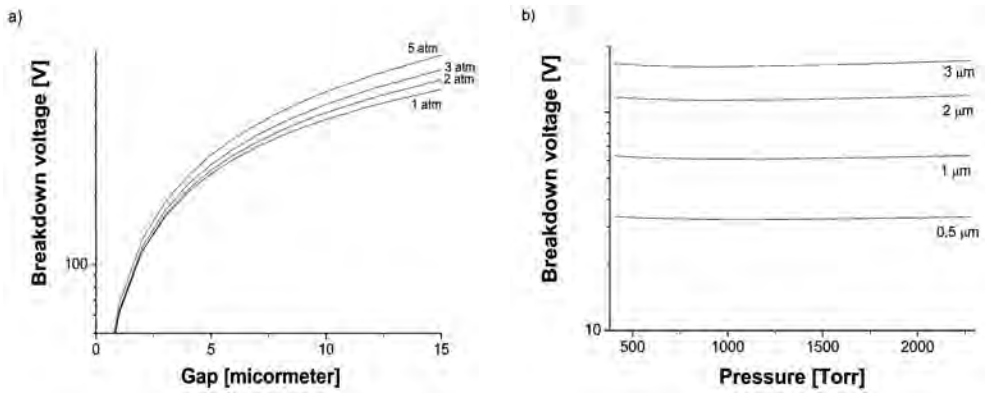

Figure 1: Breakdown voltage as a function of: a) gap spacing with varying pressure form 1 atm to 5 atm and b) pressure for gaps from 0.5 μm to 3 μm.

Table 1: Fitting coefficient for the expression (6).

Pressure [atm]	a	b	c
1	0.00	68.757	0.795
2	0.00	66.222	0.841
3	-6.578	70.134	0.859
5	0.00	68.63	0.918

where values of the fitting coefficients a, b and c, for various pressures are given in Table 1.

In similar way, for the gap spacing from 0.5 μm to 3 μm, the pressure dependence of the breakdown voltage has been fitted by using a simple functional form:

$$V = m * p^n, \tag{7}$$

with fitting coefficients m and n given in Table 2.

In Fig. 1 we have shown results obtained by using the semi-empirical expressions (6) and (7), for the breakdown voltage. The fall of the breakdown voltage for gaps less than 5 μm is observed in Fig. 1a. On the other hand, Fig. 1b demonstrate weak dependence of the breakdown voltage on the pressure.

Table 2: Fitting coefficient for the expression (7).

Gap [μm]	m	n
0.5	33.131	-0.00143
1	60.726	0.00278
2	107.125	0.01114
3	144.954	0.01917

4. CONCLUSIONS

This paper displays theoretical studies of the breakdown voltage in microgaps. Departures from the large scale similarity laws are expected with the onset of field emission on such small gaps. Failure of the Paschen law observed in microgaps indicates that Townsend mechanism is not sufficient to explain the breakdown at small gaps. The semi-empirical expressions based on the fit of the numerical solutions of the breakdown criteria including field emission effects in microgaps has been suggested. The results presented here should be useful for determining minimum ignition voltages in microplasma sources as well as the maximum safe operating voltage and critical dimensions in other microdevices.

The present work has been performed under MNZŽS 141025 project.

References

Boyle, W. S., Kisliuk, P.: 1955, *Phys. Review*, **97**, 255.
Chen, C. H., Yeh, J. A., Wang, P. J.: 2006, *J. Micromech. Microeng.*, vol16, 1366.
Ito, T., Izaki, T., Terashima, K.: 2001, *Thin Solid Films*, **386**, 300.
Korolev, Yu. D., Mesyats, G. A.: 1998, *Physics of pulsed breakdown in gases*, URO-PRESS.
Loeb, L. B.: 1939, Fundamental Processes of Electrical Dishcarges in Gases, J. Wiley and Sons, Inc., New York.
Meek, J. M., Craggs, J. D.: 1953, Electrical breakdown of gases, Oxford Unversity Press.
Paschen, F.: 1889, *Wied. Ann.*, **37**, 69.
Radmilović-Radjenović, M., Lee, J. K., Iza, F., Park., G. Y.: 2005, *Journal of Physics D: Applied Physics*, **38**, 950.
Radmilović-Radjenović, M., Radjenović, B.: 2006, *Plasma Sources Science and Technology*, **15**, 1.
Radmilović-Radjenović, M., Radjenović, B.: 2007, *Plasma Sources Science and Technology*, **16**, 337.
Radmilović-Radjenović, M., Radjenović, B.: 2008, *Plasma Sources Science and Technology*, **17**, 024005.
Raizer, Yu. P.: 1991, Gas Discharge Physics, Springer, Berlin.
Tachibana, K., Kishimoto, Y., Kawai, S., Sakaguchi, T., Sakai, O.: 2005, *Plasma Physics Control. Fusion*, **47**, A167.
Torres, J. M., Dhariwal, R. S.: 1999, *Nanotechnology*, **10**, 102.

Publ. Astron. Obs. Belgrade No. 84 (2008), 387 - 390 *Contributed Paper*

THE EFFECT OF THE LOW FREQUENCY VOLTAGE ON THE CHARACTERISTICS OF THE CAPACITIVELY COUPLED DUAL FREQUENCY RF DISCHARGES

A. BOJAROV, M. RADMILOVIĆ-RADJENOVIĆ and Z. Lj. PETROVIĆ
Institute of Physics, P.O. Box 57, 11080 Belgarde, Serbia
E–mail: marija@phy.bg.ac.yu

Abstract. In this paper, a Particle-in-cell Monte Carlo collision (PIC/MCC) modeling of dual frequency (DF) asymmetric capacitively coupled plasma (CCP) sources has been performed. In particular, the following configuration has been modelled: 27/2 MHz system with an electrode separation of 2cm and the gas pressure of 45 mTorr. The characteristics of dual-frequency argon discharge are studied for a wide range of low-frequency voltages.

1. INTRODUCTION

In practical application of the capacitively coupled plasmas (CCP) involves utilization of multiple-frequencies to control the plasma parameters (Goto et al. 1992, Kitajima et al. 2000, Robiche et al. 2003, Wakayama and Nanbu 2003, Kim and Lee 2004). In a typical dual-frequency discharge, the plasma density, and hence the ion flux at the plasma boundary are proportional the current density, which is controlled by the higher frequency, while the ion energy at the boundary depends mainly on the bias voltage, and this is mainly controlled by the lower frequency. In this paper, plasma discharge characteristics with various conditions in dual frequency capacitively coupled plasma (DF-CCP) are studied by a modified electrostatic 1d3v PIC/MCC code (xpdc1) (Lee et al. 2004, Verboncouer 2005). It is found that the low frequency voltage affects both the plasma density and the potential, while on the other hand, the kinetic energy of particles weakly depends on the variation of the low- frequency voltage (Donko and Petrović 2006, Turner and Chabert 2006).

2. SIMULATION CONDITIONS

PIC modeling techniques have been well documented in previous publications (Birdsall 1991, Verboncouer et al. 1993) so only a brief description of the code will be given here. In PIC simulations, the so-called "superparticles" move in the discharge space through an artificial grid on a time step basis. Only charged particles are simulated. At the beginning of the simulation, superparticles are distributed in the simulation domain and a self-consistent potential distribution is determined based on the superparticles positions and the externally applied voltage. This is done by weighting the

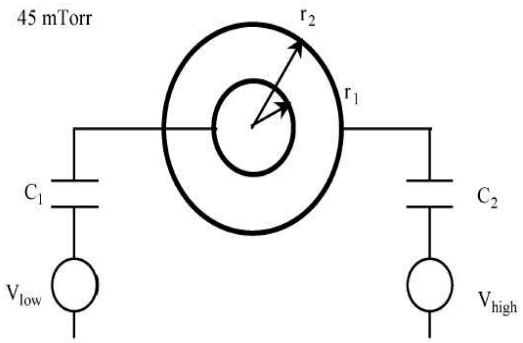

Figure 1: Schematic diagram of DF-CCP (27MHz/2MHz), $V_{hf} = 400\,V$, with the gap spacing of 2 cm and the gas pressure of 45 Torr. V_{lf} is varied in the range $(50 - 200\,V)$.

particles to the grid points and solving Poisson's equation. The simulation proceeds by calculating the electric field and weighting it to the particle positions. The force exerted by the electric field is then computed and particle velocities and positions are updated. The null-collision method introduced by Vahedi (Vahedi and Surendra 1995) is used to account for the collisional processes.

In this paper, Particle-in-cell simulations have been used to study the nature of dual frequency plasma discharges. The schematic diagram of the cylindrical DF-CCP source is shown in Figure 1. The discharge is maintained in a chamber between two electrodes separated by the gap of 2 cm. The inner electrode is capacitively coupled to power supply operating at low frequency of 2 MHz, while the upper electrode is powered by the high-frequency source at a conventional frequency of 13.56 MHz and a constant voltage of 400 V (amplitude).

3. RESULTS

The influence of the low frequency voltage on the time average value of the plasma density is shown in Figure 2a. The increase of the low-frequency voltage results in decreasing of the plasma density. At the same time, profiles are shifted toward the outer electrode as the low-frequency voltage increases.

The ion energy distribution function (IEDF) for a single frequency (SF) CCP (solid line) and DF-CCP (dash-doted line) are shown in Figure 2b. In the arrangement when only the high frequency source is applied (solid line), the ion transit time across the sheath is much longer as compared to the period of the operating frequency. Most ions traverse sheath and experience the time averaged sheath voltage causing the main peak, while ion-neutral collisions cause small peaks. The shape of IEDF loses its single-peak structure and this structure is destroyed. The total range of ion energies does not correspond to the mean potential drop at the electrodes. As the low frequency voltage is increased, the maximal ion bombardment energy increases and broader ion energy spectrum is obtained.

Figure 3a demonstrates the principle of controlling the substrate self-bias voltage by varying the low frequency voltage with fixing the high frequency voltage. As the

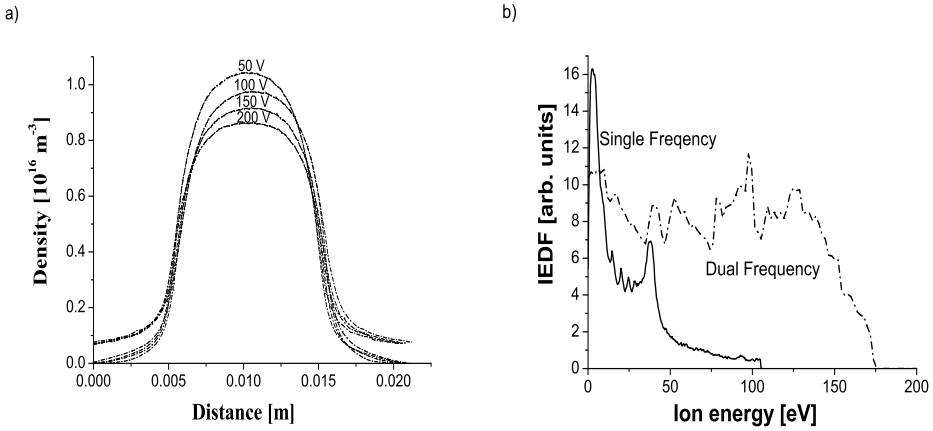

Figure 2: Effect of low-frequency voltage on: a) time average density and b) the ion energy distribution function (IEDF) at the inner electrode. DF-CCP (27MHz/2MHz), $V_{hf} = 400\,V$.

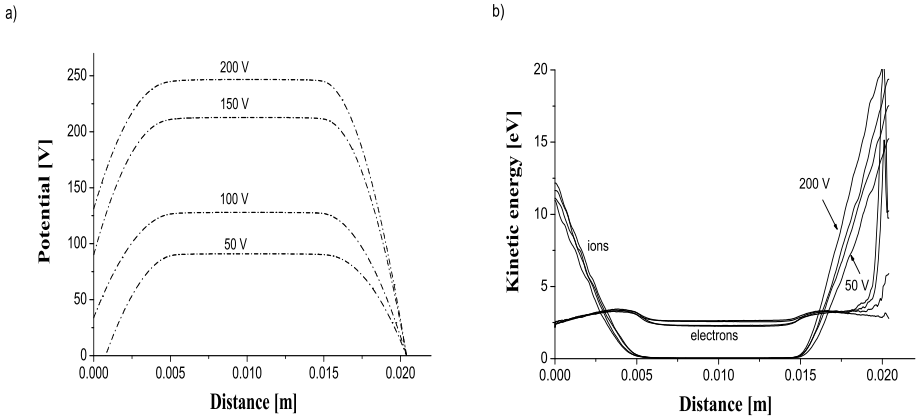

Figure 3: Changes of time-average: a) potential profile and b) kinetic energy, with the variation of the V_{lf} from 50 V to 200 V in DF-CCP (27MHz/2MHz) with a fixed $V_{hf} = 400\,V$.

low frequency voltage is increased, plasma potential is almost constant but the self-bias is increased.

As can be seen from Figure 3b, the kinetic energy of electron in the balk region is higher than the ion energy. On the other hand, in the sheath region, the ions gain a large energy that slightly depends on the low frequency voltage. The decrease of the plasma density at low frequencies is related to the increase in the plasma sheath width and therefore to the increase of the energy absorbed by ions in the sheath region.

The present work has been performed under MNZŽS 141025 project.

References

Birdsall, C. K.: 1991, *IEEE Trans. Plasm. Sci.*, **19**, 65.
Donko, Z., Petrović, Z. Lj.: 2006, *Japn. J. of Applied Physics*, 45, 8151.
Goto, H. H., Lowe, H. D., Ohmi, T.: 1992, *J. Vac. Sci. Technol. A*, **10**, 3048.
Kim, H. C., Lee, J. K.: 2004, *Phys. Rev. Lett.*, **93**, 085003.
Kitajima, T., Takeo, Y., Petrović, Z. Lj., Mkabe, T.: 2000, *Appl. Phys. Lett.*, **77**, 489.
Lee, J. K., Babaeva, N. Yu., Kim, H. C., Manuilenko, O. V.: 2004, *IEEE Trans. on Plasma Science*, **32**, 47.
Robiche, J., Boyle, P. C., Turner, M. M., Ellingboe, A. R.: 2003, *J. Phys. D: Appl. Phys.*, **36**, 1810.
Turner, M. M., Chabert, P.: 2006, *Phys. Rev. Lett.*, **96**, 205001.
Verboncouer, J. P.: 2005, *Plasma Physics Control. Fusion*, **47**, A231.
Vahedi, V., Surendra, M.: 1995, *Comp. Phys. Commun.*, **87**, 179.
Verboncoeur, J. P. et al.: 1993, *J.Comp.Phys.*, **104**, 321.
Wakayama, G., Nanbu, K.: 2003, *IEEE Trans. on Plasma Science*, **31**, 638.

Publ. Astron. Obs. Belgrade No. 84 (2008), 391 - 395 *Contributed Paper*

DEGRADATION OF AQUEOUS PHENOL SOLUTIONS BY COAXIAL DBD REACTOR

B. P. DOJČINOVIĆ[1], D. MANOJLOVIĆ[2], G. M. ROGLIĆ[2], B. M. OBRADOVIĆ[3*], M. M. KURAICA[3] and J. PURIĆ[3]

[a] *Center of Chemistry, Institute of Chemistry, Technology and Metallurgy, Belgrade, Studentski trg 12-16, 11000, Serbia*

[b] *Faculty of Chemistry, University of Belgrade, Belgrade, P.O. Box 158, 11000, Serbia*

[c] *Faculty of Physics University of Belgrade, Belgrade, P.O.Box 368, 1100, Serbia*
E–mail: obrat@ff.bg.ac.yu

Abstract. Solutions of 2-chlorophenol, 4-chlorophenol and 2,6-dichlorophenol in bidistilled and water from the river Danube were treated in plasma reactor. In this reactor, based on coaxial dielectric barrier discharge at atmospheric pressure, plasma is formed over a thin layer of treated water. After one pass through the reactor, starting chlorophenols concentration of 20 mg/l was diminished up to 95%. Kinetics of the chlorophenols degradation was monitored by High Pressure Liquid Chromatography method (HPLC).

1. INTRODUCTION

Chlorophenols are important intermediers during synthesis of pesticides, herbicides and dyes. Also, they have arisen in the chlorination process of water with high organic carbon concentration. The chlorophenols are very toxic materials for humans and animals. They are even more toxic than phenols. The chlorophenols are most often found in natural and waste waters. In this paper we have given the demonstration of degradation efficiency for 2-chlorophenol, 4-chlorophenol and 2,6-dichlorophenol by plasma reactor based on a coaxial dielectric barrier discharge (DBD), see Kuraica et al. 2004, Manojlovi et al. 2006. DBD plasma reactor was used for direct water ozonation, see Gottschalk et al. 2000, Tajima et al. 2001. The chlorophenols degradation dynamics were tested in synthetic waters, see Andreozzi et al. 1999, Benitez et al. 2000, in bidistilled water and water from the river Danube, taken near Belgrade. These waters were used as matrix waters. The coaxial DBD as a plasma reactor system operates in the air at atmospheric pressure. In the reactor one of the dielectric layers is the flowing water. This reactor is very efficient because the plasma that is formed abovewater has, except ozone, also UV radiation and radicals (e.g. OH·), excited atoms (e.g. O·) and molecules, electrons and ions. Existence of so many reactive species in plasma and in water is the reason why electrical discharges that have plasma in direct contact with water solutions are very interesting for many researches. There are several discharges in which plasma is formed above water, like

corona above water, see e.g. Grabowski et al. 2006, Lukes et al. 2005, or DBD above water, see Bubnov et al. 2006.

2. EXPERIMENTAL SETUP

A schematic diagram of experimental setup is shown in Fig. 1. Water flows up through a vertical hollow cylindrical electrode (diameter 21.5 mm) and flows down making a thin dielectric film over the electrode. Discharge is generated in air within 4 mm gap between the dielectric and the water layer by applying voltage up to 20 kV, as shown in Fig. 1. Plasma produced in coaxial DBD reactor is typical for silent (filamentary) discharges and consists of numerous micro discharges (filaments). Ozone generated in this discharge sustained in the gap between outer glass barrier electrode (diameter 30 mm; thickness 1.5 mm) and flowing water layer as inner barrier electrode of coaxial DBD reactor. High voltage at 50 Hz is applied between the inner, grounded stainless steel electrode and outer metal electrode 40 cm in length. To increase the water flow through the reactor (∼150 ml/min) three coaxial DBD units are connected parallel, as shown in Fig. 1. The process of chlorophenols degradation was tested with several synthetic samples prepared by dissolving of analytical grade 2-chlorophenol, 4-chlorophenol and 2,6-dichlorophenol in bidistilled water and water from Danube, with chemical oxygen demand (COD) between 92 and 105 mg O2/l, and pH from 6.2 to 6.5. Amount of 5 l of synthetic water (20 mg/l corresponding phenol concentration) was prepared per sample, and it was instantly treated with DBD. The concentration of dissolved and residual ozone was determined by standard methods, see e.g. Eaton et al. 1995, (for dissolved ozone the iodometric method and for residual ozone the indigo colorimetric method). Residual ozone concentration was determined by photometer (PC 22, LOVIBOND), and original reagents indigo- trisulfonate in pills were used. The chlorophenol concentration was determined by chromatographic method by HPLC (Agilent1100 Series), under these conditions: colon LiChrospher 100 RP-18 (250 × 4 mm, 5 μm) Agilent Technologies; UV detector; A (H_2O) and B (MeCN) solutions; sample volume 50 ml at 280 nm wavelength. The chlorophenol concentration has been determined before plasma treatment, and after the plasma treatment, every 5 min for the first 20 min; after 1 h, and after 24 h. During the monitoring of degradation process, synthetic samples were kept in well closed vessels with no gas exchange with atmosphere. The increase of 2,6-dichlorophenol degradation is obtained with another passing of the sample trough the DBD plasma reactor (recirculation after 1 h).

3. EXPERIMENTAL RESULTS AND DISCUSION

Change of the concentrations of 2-chlorophenol in bidistilled water and real water samples from Danube with time is presented in Fig. 2a. The concentration of 2-chlorophenol decreases significantly during ozonation, and then decreases slowly. In bidistilled water after 24 h, concentration of 2-chlorophenol is 0.01 mg/l, i.e. degradation of 2-chlorophenol is 99.95%. Corresponding results for Danube water are 1.05 mg/l with degradation of 94.8%. Change of the concentrations of 4-chlorophenol in bidistilled water and Danube water with time is represented in Fig. 2b. From Fig. 2b one can see a significant decrease of 4-chlorophenol concentration in bidistilled water during DBD treatment and after 5 min. During further time degradation, concen-

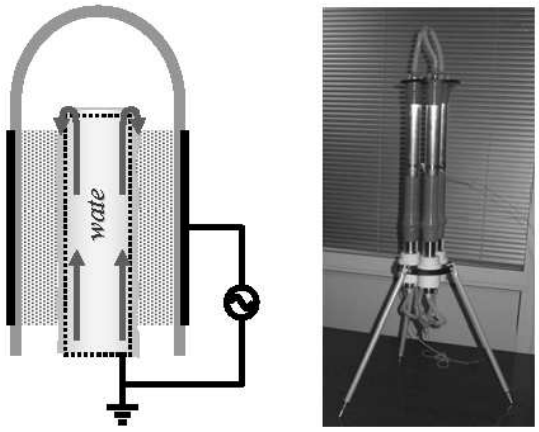

Figure 1: Schematic picture of coaxial DBD and photo of three parallel connected DBDs.

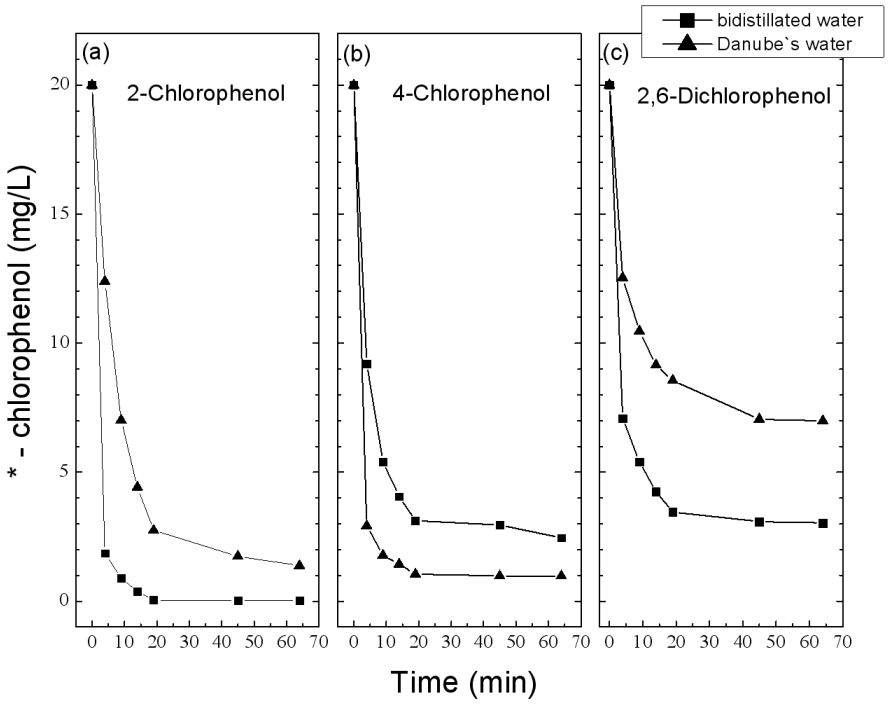

Figure 2: Change of the concentrations of (a) 2-chlorophenol, (b) 4-chlorophenol, and (c) 2,6-dichlorophenol in bidistilled water and Danube water with time degradation.

tration change is relatively small. The percentage of removed 4-chlorophenol after 24 h for bidistilled water is 96%, and for Danube water 89.8%. Change of the concentrations of 2,6-dichlorophenol in bidistilled water and Danube water with time is represented in Fig. 2c. The percentage of removed 2,6-dichlorophenol after 24 h for bidistilled water is 85%, and for Danube water 74.6%. With recirculation after 1 h, 2,6-dichlorophenol is removed for bidistilled water for 93.8%, and for Danube water 90.2%. With the recirculation, better results are obtained. These results can be explained by higher stability of 2,6-dichlorophenol for reaction with OH radical, i.e. smaller number of places for possible reactions according to previously published results, see Tang et al. 1996.

The 2,6-dichlorophenol is more resistant towards ozone compared to 2-chlorophenol and 4-chlorophenol. The percentage of phenol removal from Danube water was considerably lower than the corresponding value for bidistilled water. Lower removal of chlorophenols from sample prepared with Danube water could be explained by protective effect of fulvic and humic acids which also reacted with ozone. During the experiments, although the total oxidation capability was high, residual ozone concentration was low. Therefore, we have assumed that active species was hydroxyl radical (OH·), which is in accordance with previously published results obtained when non-thermal plasma was in contact with water solutions, see Lukes et al. 2005. The DBD plasma reactor construction enabled synergetic effect for advanced oxidation process: simultaneous exposition of water layer to ionized gas and to UV emission from the electric discharge, see Legrini et al, 1993. UV light induces homolyses of O_3 and subsequent production of OH·, radicals by the reaction of O· with water, see Glaze et al. 1987. Small concentration of residual ozone, and large concentration of, so called "dissolved ozone", could be explained in this way. The proposed mechanism of reactions of hydroxyl radical with chlorophenol was previously described, see e.g. Lukes et al. 2003, Long et al. 2007. The chlorophenols undergo two types of reactions. One is chlorine substitution and other is hydroxylation in ortho or para positions. Reaction of substitution is much slower and this is possible explanation for less efficient degradation of 2,6-dichlorophenol. The obtained quinoness undergo further degradation through dicarboxylic acids resulting finally in carbon dioxide production.

4. CONCLUSION

The coaxial DBD with flowing water as one of the dielectric layers has been used as the plasma reactor for treatment of water with high content of chlorophenols. In the experiments performed at laboratory level, with 2-chlorophenol, 4-chlorophenol and 2,6-dichlorophenol dissolved in bidistilled water, after 24 h, 99.95%, 96.0% and 85.0% of chlorophenols were removed, respectively. Corresponding values for Danube water were significantly smaller: 94.8%, 89.8% and 74.6%. With recirculation after 1 h, 2,6-dichlorophenol was removed 93.8% and 90.2% in bidistilled and Danube water, respectively.

References

Andreozzi, R., Marotta, R.: 1999, *J. Hazard Mater.*, **B69**, 303.
Benitez, F. J., Beltra'n-Heredia, J., Acero, J. L., Rubio, F. J.: 2000, *J. Hazard Mater.*, **B79**, 271.

Bubnov, A. G., Burova, E. Yu,, Grinevich, V. I., Rybkin, V. V., Kim, J-K., Choi, H-S.: 2006, *Plasma Chem. Plasma Proc.*, **26**, 19.

Eaton, A. D., Clesceri, L. C., Greenberg, A. E., Franson, M. A. H. eds.: 1995, Standard methods for the examination of water and wastewater, methods 2–41, 2–42 (dissolved ozone) iodometric method; method 4–104 (ozone residual) indigo colorimetric method. Washington: American Public Health Association.

Glaze, W. H., Kang, J. W., Chapin, D. H.: 1987, *Ozone Sci. Eng.*, **9**, 335.

Gottschalk, C., Libra, J. A., Saupe, A.: 2000, Ozonization of drinking water and of wastewater. 1st ed. New York: Wiley & Sons.

Grabowski, L. R,, Veldhuizen, E. M., Pemen, A. J. M., Rutgers, W. R.: 2006, *Plasma Chem. Plasma Proc.*, **26**, 3.

Kuraica, M. M., Obradović, B. M., Manojlović, D., Ostojić, D. R.: Purić, J.: 2004, *Vacuum*, **73**, 705.

Legrini, O., Oliveros, E., Braun, A. M.: 1993, *Chem. Rev.*, **93**, 671.

Long, H. X., Hua, Z. M., Cheng, L. L.: 2007, *J Hazard Mater.*, **141**, 475.

Lukes, P., Clupek, M., Babicky, V., Sunka, P., Winterova, G., Janda, V.: 2003, *Acta Phys. Slov.*, **53**, 423.

Lukes, P., Locke, B. R.: 2005, *J. Phys. D: Appl Phys*, **38**, 4074.

Manojlović, D., Ostojić, D. R., Obradović, B. M., Kuraica, M. M., Krsmanović, V. D., Purić, J.: 2006, *Desalination*, **213**, 116.

Tajima, R., Ehara, Y., Kishida, H., Ito, T.: 2001, *Proceedings of the Hakone VII*, Greifswald, Germany, **2**, 412.

Tang, W. Z., Huang, C. P.: 1996, *Chemosphere*, **33**, 1621.

Publ. Astron. Obs. Belgrade No. 84 (2008), 397 - 400 *Contributed Paper*

MASS SPECTROMETRY OF A PLASMA NEEDLE WITH AN EXTERNAL GROUNDED COPPER RING

S. LAZOVIĆ, N. PUAČ, G. MALOVIĆ and Z. Lj. PETROVIĆ
Institute of Physics, Pregrevica 118, Belgrade, Serbia
E–mail: lazovic@phy.bg.ac.yu

Abstract. Plasma needle is 13.56MHz RF discharge that operates in a mixture of ambient air and helium. This type of plasma source is used in treatment of plant tissue, microsurgery, disinfection of dental cavities and wounds. In this paper we used the configuration with an additional, grounded copper ring placed near the tip of the needle. Larger volume of plasma and lower plasma ignition powers are provided by adding the ring. Hiden HPR60 mass analyzer was used to obtain the mass spectra and determine the yields of N,O and NO radicals in the plasma.

1. INTRODUCTION

Advantage of atmospheric non-equilibrium plasmas is that it is possible to treat samples that are sensitive to low pressures and plasma can easily be put in contact with samples that need to be treated. A variety of applications have already been demonstrated, e.g., in semiconductor technology, art restoration and treatment of living plant tissue (Puač at.al., 2006). Because of its mild plasma and geometry, plasma needle is especially convenient for medical applications. Non contact disinfection of dental cavities and wounds and minimum-destructive precise treatment and removal of diseased tissue can be done by the plasma needle (Stoffels et.al., 2006). Treatment can be done with better than 0.1 mm accuracy (resolution).

Plasma parameters such as power given to the plasma, helium flow rate, distance between the tip of the needle and the treated sample have to be optimized so that necrosis of cells would be avoided. The exact mechanisms of plasma-cell interactions have not been fully understood yet. Radicals generated by plasma itself may play a very important role in such interactions. Measurements of the concentration of nitric oxide provided by plasma is also very important because it plays major role in many processes in the organism. Mass spectrometry was done to provide better insight into plasma-cell interactions. While similar work of Stoffels et.al (Stoffels et.al, 2006). has been done on the seemingly identical system in their papers they had to use somewhat larger dimensions and flow because pumping of the mass analyzer perturbed and even turned off the discharge.

Our measurements were performed on a standard size plasma needle that we originally used for the treatment of plant cells. After some efforts we were able to make

plasma needle operate in conditions similar to the ones used during the treatments of biological samples. Power transmitted to the plasma was less then 1 % of the power given by RF power supply. However, we had to increase the gas flow from several 100 sccm to more than 1000 sccm. Our goal was to make the mass analyzer work under conditions similar to those one used in plasma treatments which would not greatly affect the discharge itself. Application of a higher flow rate would only reduce the density of detected radicals.

2. EXPERIMENTAL SET UP

The needle consist of a central tungsten wire (0.5 mm in diameter) placed inside a ceramic tube with slightly larger diameter and both placed inside the glass tube 6 mm in diameter. Helium flows between ceramic and glass tube with typical flow rate of few hundred standard cubic centimeters per minute. In our configuration, additional grounded copper ring is added around the glass tube and close to the tip of the needle. This kind of configuration provides a larger volume of plasma and lower plasma ignition powers in addition to operation less dependent on the exact position of the target. The central wire represents the powered electrode and the grounded electrode is the treated sample. Experiments were performed using the ambient air at atmospheric pressure and room temperature. The flow rate of helium was varied from 1 slm to 3 slm.

Hiden HPR 60 MBMS system which incorporates a Hiden EQP mass/energy analyzer is used. Hiden EQP consists of two parts: pumping part that has three different pumping stages and which makes it possible to work on atmospheric pressures and the detector part witch itself works on low pressures. Plasma needle is placed in such a way that the tip of the wire electrode is positioned against the orifice of the analyzer system at the variable distance of several millimeters. Species created in the discharge are sampled using a triple stage differentially pumped molecular beam inlet system which consists of three orifices of different diameter. The sampling orifices are carefully aligned to produce a molecular beam which minimizes the collisions of the sampled particles with each other and with surfaces.

3. RESULTS AND DISCUSSION

Our measurements were done in Residual Gas Analysis mode. Stable plasmas could be obtained in air-helium atmospheres containing down to 10 % of helium. Data were collected for different values of plasma parameters such as power, various distances between the needle and the spectrometer and flow rate. When presenting the results we have used yields of specific masses instead of counts per second obtained directly from the detector. Yield was calculated as percentage of a certain signal in the total signal in order to cancel out the fluctuations:

$$Y = \frac{Y^i_{mass}}{\Sigma_i Y^i_{mass}}[\%] \tag{1}$$

where Y^i_{mass} is specific positive ion (like N^+, O^+, etc.) and this was divided by sum of all recorded masses (1-100 amu). Besides the expected helium peak we can see intense peaks of numerous molecules. It is impossible to distinguish N_2O^+ from CO_2^+ as both

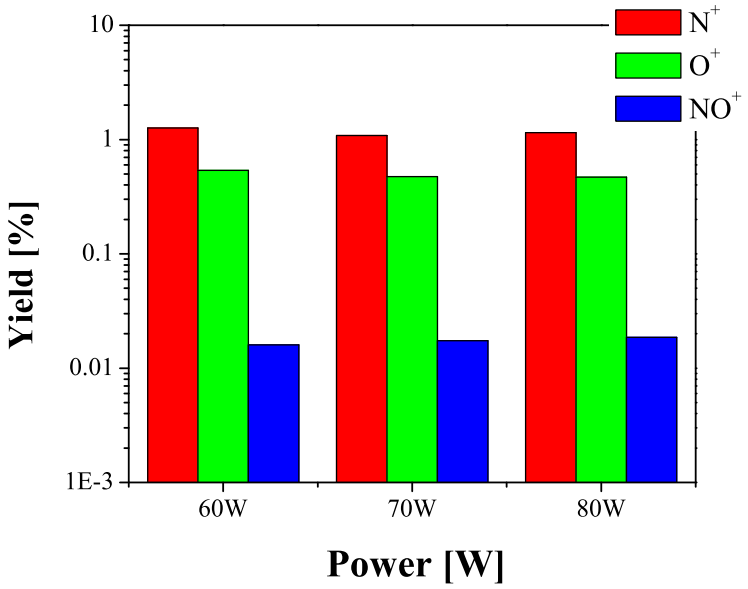

Figure 1: Yields for N, O and NO radicals as a function of power given by the RF source for distance of 1mm and helium flow of 1 slm.

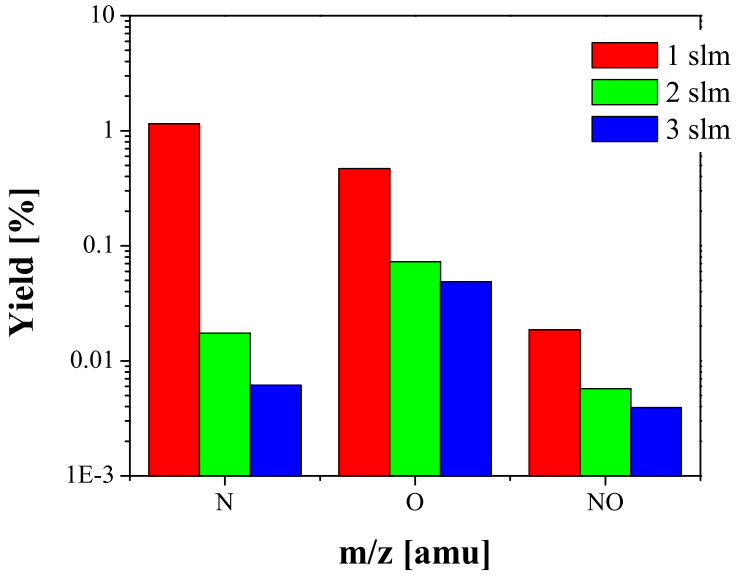

Figure 2: Yields for N, O and NO radicals as a function of helium flow rate for the distance of 1mm and power of 80W.

have the mass of 44 amu. Another problem is that pumping speed of different species such as He and N_2 may be quite different so relative intensities may be unreliable and a more thorough callibration is required.

The yields for N^+, O^+ and NO^+ ions for three different powers can be seen in Fig 1. Signal of NO^+ increases with the increase of the power while signals of the atomic ions decrease. With the increase of the flow rate of the feeding gas (He) from 1 standard liter per minute to 3 slm one can observe a decrease in yields for all three ions (Fig 2). This may be explained by dilution of the atmospheric gases by the buffer gas which is supported by the increased yield of helium. Thus we have to use smaller flow rates of helium in order to gain more active species. During our previous work on the treatments of plant cells the flow rate of helium was around 100 sccm so we can assume that even a larger amount of active species was created as long as the electron temperatures are not reduced by molecular species.

4. CONCLUSION

Mass spectrometry of plasma generated by plasma needle with additional grounded copper ring was done using Hiden HPR 60 mass spectrum analyzer. Concentrations of N, O, NO were determined as well as their dependence from RF power and helium flow rate. Plasma mode transition was observed for higher values of power transmitted to plasma. Concentrations of NO_2 and O_3 were also measured. Plasma needle was operated in such configuration and conditions that are convenient for both spectrometry and treatment of samples.

References

Puač, N., Petrović, Z. Lj., Malović, G., Djordjević, A., Živković, S., Giba, Z., Grubišić, D.: 2006, *Journal of Physics D: Applied Physics*, **39**, 3514.

Stoffels, E., Aranda-Gonzalvo, Y., Whitmore, T. D., Seymour, D. L., Rees, J. A.: 2006, *Plasma Sources Sci. Technol.*, **15**, 501.

Stoffels, E., Kieft, I. E., Sladek, R. E. J., van den Bedem, L. J. M., van der Laan, E. P., Steinbuch, M.: 2006, *Plasma Sources Sci. Technol.*, **15**, S169.

Publ. Astron. Obs. Belgrade No. 84 (2008), 401 - 404 *Contributed Paper*

MASS SPECTROMETRY OF DIFFUSE COPLANAR SURFACE BARRIER DISCHARGE

S. LAZOVIĆ[1], N. PUAČ[1], N. RADIĆ[2], T. HODER[2], G. MALOVIĆ[1], J. RAHEL[2], M. CERNAK[2] and Z. Lj. PETROVIĆ[1]

[1] *Institute of Physics, Pregrevica 118, Belgrade, Serbia*
E–mail: lazovic@phy.bg.ac.yu

[2] *Dept. of Physical Electronics, Masaryk University, Kotlarska 2, 61137 Brno, Czech Republic*

Abstract. In this paper we present some of the results obtained in non-equilibrium low-temperature diffuse coplanar surface barrier discharge by using Molecular Beam Mass Spectrometer. In order to understand the process of treatment by this type of plasma, knowledge of the composition of plasma, i.e. of the active species, is needed. In this work we present mass spectrometric studies on chemical products and active species in the plasma generated by the DCSBD at atmospheric pressure in the ambient air. Neutral chemistry and nitric oxide production are discussed.

1. INTRODUCTION

In many areas of industry, plasma processing of materials is a vital technology. Nonequilibrium plasmas have proved to be capable of producing chemically reactive species at low gas temperature while maintaining highly uniform reaction rates over relatively large areas. Their action is versatile, the effects include changing of surface properties (wettability, dyeability etc.), surface activation to improve germination, adhesion of coatings, etching and many more (Puač et al. 2006, Radetić et al. 2007).

Mass spectrometry is a popular method to analyse chemical composition of gases and plasmas. The results are particularly relevant for surface treatment, because the mass spectrometer samples the species which arrive at and potentially interact with the surface. Mass spectrometry of radical species is well established in low-pressure discharges (Sugai et al. 1992), but its applications to atmospheric plasmas are relatively new (Stoffels et al. 2006, Aranda-Gonzalvo et al. 2006).

In this work attention is given to atomic nitrogen and oxygen and to nitrogen monoxide (NO). We will present mass spectrometric studies on gas conversion in the plasma generated by the diffuse coplanar surface barrier discharge. Neutral chemistry and nitric oxide production are discussed.

2. EXPERIMENT

Coplanar barrier discharge - DCSBD (diffuse coplanar surface barrier discharge) was developed to provide functionality of a non-equilibrium low-temperature plasma at atmospheric pressure in ambient air. The DCSBD electrodes, consisting of 15 pairs of silver strip electrodes embedded 0.5 mm below the surface of 96% Al_2O_3 ceramics, was energized by 14 kHz sinusoidal voltage, supplied by HV generator LIFETECH VF700. The mutual distance of the 200 mm long and 2 mm wide silver strip electrodes was 1 mm.

The MBMS(Molecular Beam Mass Spectrometer) system incorporates a Hiden EQP mass/ energy analyzer. Species created in the discharge are sampled using a triple stage differentially pumped molecular beam inlet system. The mass spectrometer can be operated in two different modes: the SIMS mode to extract positive ions and record their energy spectra or in the RGA mode to detect neutrals. In order to detect neutrals the mass spectrometer is equipped with an internal electron source with variable electron energy, which allows ionization of species (positive RGA). Since our main interest are radicals created in the plasma we have used RGA mode in all our measurements.

The surface of the discharge created by DCSBD was positioned against the orifice of a HIDEN EQP mass/energy analyzer system at the distance of 5 mm. Experiments were performed using the ambient air of the laboratory at atmospheric pressure and ambient temperature. Measurements by the mass-energy analyser were performed for two different powers of 300 and 400 W.

3. RESULTS AND DISCUSSION

When presenting the results we have used 'yields' of specific masses instead of counts per second obtained directly from the detector. Yield was calculated as percentage of a certain signal in the total signal summed over a range of masses in order to cancel out the fluctuations:

$$Y = \frac{Y^i_{mass}}{\Sigma_i Y^i_{mass}}[\%] \tag{1}$$

where Y_i is the count of specific positive ion (like N+, O+, etc.) and this was divided by sum of all recorded masses (1-100 amu).

In Fig. 1 mass spectra for the power of 400 W is shown. We can see that $N_2{}^+$ and $O_2{}^+$ have the largest yields followed by H_2O^+, N^+ and O^+. One should bear in mind that, N_2O^+ has mass of 44 amu, which coincides with the persistent $CO_2{}^+$ peak and this causes some problems in the analysis of the recorded spectra.

Main radical species of our interest are N^+, O^+ and NO^+ and in Fig. 2 their yields are shown for two different powers (300 and 400 W). The distance between the electrodes and the mass analyser was 5 mm.

As we can see, in case when applied power was 300 W, yields for N^+ and O^+ are somewhat smaller then in the case when applied power was 400 W. On the other hand, yields for NO^+ decrease with the increase of the applied power.

This behavior can be explained by reaction kinetics in the discharge. In case of nitrogen monoxide (NO) one of the possible reactions is forming NO by dissociation of N_2 and O_2 and then by three-body recombination $N + O + M \rightarrow NO + M$. The

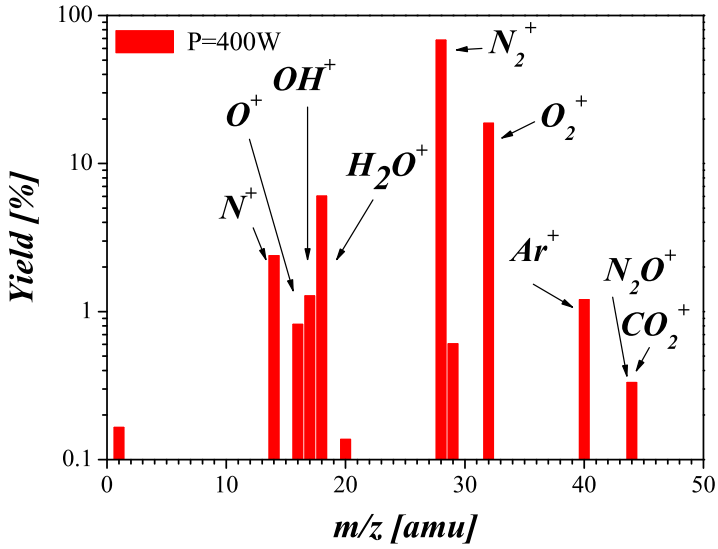

Figure 1: Mass to charge spectra for power of 400 W. Distance from the electrode from the mass analyzer was 5 mm.

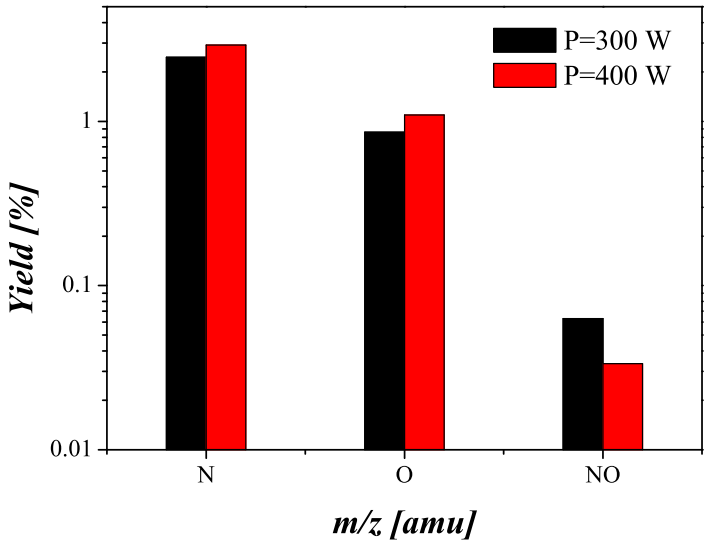

Figure 2: Yields for three different radicals are shown. Distance from the electrode to the mass analyzer was 5 mm and applied powers were 300 and 400 W.

recombination rate at close to the ambient temperature for this reaction is about $10^{-45}m^6s^{-1}$ (http://kinetics.nist.gov). Another possibility is the reaction $N + O_2 \rightarrow NO + O$ which has rate coefficient about $10^{-21}m^3s^{-1}$ at 400 K (Hewson et al. 1999).

Nitric oxide plays an important role in various treatments involving living tissues and organisms and its concentration should be significant in order for the treatment to be successful. On the other hand, nitrogen oxide (NO_2) and ozone (O_3) are quite toxic and its concentrations should be minimized. In our DCSBD discharge concentration of NO_2 and O_3 are very small and this makes this discharge eligible for different types of treatments in ambient air without worrying about pollution.

4. CONCLUSION

We have made mass spectrometry measurements of the diffuse coplanar surface barrier discharge by using HIDEN HPR60 mass spectrum analyzer. DCSBD works in ambient air at atmospheric pressure. Main radicals of our interest were N^+, O^+ and NO^+ since nitric oxide plays important role in various treatments. Significant amount of NO radical is created in plasma and we can say that atmospheric plasma can be an efficient source of nitric oxide. In addition, concentrations of toxic NO_2 and O_3 are very small so this type of discharge may be safe to be used for treatment of living tissues.

References

Aranda-Gonzalvo, Y., Whitmore, T. D., Rees, J. A., Seymour, D. L., Stoffels, E.: 2006, *J. Vac. Sci. Technol. A*, **24**, 550.

Hewson, J. C., Williams, F. A.: 1999, *Combust. Flame*, **117**, 441.

Puač, N., Petrović, Z. Lj., Malović, G., Djordjević, A., Živković, S., Giba, Z., Grubišić, D.: 2006, *Journal of Physics D: Applied Physics*, **39**, 3514.

Radetić, M., Radojević, D., Ilić, V., Jocić, D., Povrenović, D., Potkonjak, B., Puač, N., Jovančić, P.: 2007, *J. Serb. Chem. Soc.*, **72** (6) 605.

Stoffels, E., Aranda-Gonzalvo, Y., Whitmore, T. D., Seymour, D. L., Rees, J. A.: 2006, *Plasma Sources Sci. Technol.*, **15**, 501.

Sugai, H. and Toyoda, H.: 1992, *J. Vac. Sci. Technol. A*, **10**, 1193.

Publ. Astron. Obs. Belgrade No. 84 (2008), 405 *Contributed Paper*

MODELING OF NON-THERMAL PLASMA IN FLAMMABLE GAS MIXTURES

A. P. NAPARTOVICH[1], I. V. KOCHETOV[1], S. B. LEONOV[2]
[1]*SRC RF TRINITI, Troitsk, Moscow region, Russia*
E–mail: apn@triniti.ru

[2]*Joint Institute for High Temperature Russian Academy of Science, Moscow, Russia*

Abstract. An idea of using plasma-assisted methods of fuel ignition is based on non-equilibrium generation of chemically active species that speed up the combustion process. It is believed that gain in energy consumed for combustion acceleration by plasmas is due to the non-equilibrium nature of discharge plasma, which allows radicals to be produced in an above-equilibrium amount. Evidently, the size of the effect is strongly dependent on the initial temperature, pressure, and composition of the mixture. Of particular interest is comparison between thermal ignition of a fuel-air mixture and non-thermal plasma initiation of the combustion. Mechanisms of thermal ignition in various fuel-air mixtures have been studied for years, and a number of different mechanisms are known providing an agreement with experiments at various conditions. The problem is – how to conform thermal chemistry approach to essentially non-equilibrium plasma description. The electric discharge produces much above-equilibrium amounts of chemically active species: atoms, radicals and ions. The point is that despite excess concentrations of a number of species, total concentration of these species is far below concentrations of the initial gas mixture. Therefore, rate coefficients for reactions of these discharge produced species with other gas mixture components are well known quantities controlled by the translational temperature, which can be calculated from the energy balance equation taking into account numerous processes initiated by plasma.

A numerical model was developed combining traditional approach of thermal combustion chemistry with advanced description of the plasma kinetics based on solution of electron Boltzmann equation. This approach allows us to describe self-consistently strongly non-equilibrium electric discharge in chemically unstable (ignited) gas. Equations of pseudo-one-dimensional gas dynamics were solved in parallel with a system of thermal chemistry equations, kinetic equations for charged particles (electrons, positive and negative ions), and with the electric circuit equation. The electric circuit comprises power supply, ballast resistor connected in series with the discharge and capacity. Rate coefficients for electron-assisted reactions were calculated from solving the two-term spherical harmonic expansion of the Boltzmann equation. Such an approach allows us to describe influence of thermal chemistry reactions (burning) on the discharge characteristics.

Results of comparison between the discharge and thermal ignition effects for mixtures of hydrogen or ethylene with dry air will be reported. Effects of acceleration of ignition by discharge plasma will be analyzed. In particular, the role of singlet oxygen produced effectively in the discharge in ignition speeding up will be discussed.

Publ. Astron. Obs. Belgrade No. 84 (2008), 407 - 410 *Contributed Paper*

LOW-PRESSURE RF PLASMA AND CORONA DECOLOURISATION OF INDIGO DYED DENIM FABRICS

M. RADETIĆ[1], N. PUAČ[2], P. JOVANČIĆ[1], Z. ŠAPONJIĆ[3] and Z. Lj. PETROVIĆ[2]

[1] *Textile Engineering Department, Faculty of Technology and Metallurgy, University of Belgrade, Karnegijeva 4, 11120 Belgrade, Serbia*
E–mail: maja@tmf.bg.ac.yu

[2] *Institute of Physics-Belgrade, Pregrevica 118, 11080 Zemun, Serbia*

[3] *Vinča Instute of Nuclear Sciences, PO BOX 522, 11001 Belgrade, Serbia*

Abstract. This study was aimed to investigate the influence of low-pressure RF plasma (gas, treatment time and power) and atmospheric pressure corona (number of passages and power) parameters on decolourisation of indigo dyed denim fabrics. CIEL*a*b* colourimetric system was used for determination of colour difference between untreated and differently plasma treated denim fabrics. The morphology of plasma treated fibres was assessed by SEM analysis. The results showed that decolourisation was highly affected by plasma parameters and desired "worn look" effects could be designed by adequate control of plasma processing.

1. INTRODUCTION

The popularity of the "worn look" of denim products lasts more than two decades. Originally, this effect was achieved by abrasive action of pumice stones on the garment surface. This process was replaced by more efficient enzymatic stonewashing i.e. biostoning . Recent reports indicated that "worn look" can be provided by DC plasma and corona treatments (see e.g. Ghoranneviss et al. 2006, Nourbakhsh Alizadeh et al. 2006). In this study the influence of RF low-pressure plasma (LPP) and corona (COR) parameters on the decolourisation of indigo dyed denim fabrics was considered.

2. EXPERIMENTAL

The experiments were performed on indigo dyed 100% cotton denim fabric (twill, 377 g m^{-2}).

Glow-discharge treatment of denim fabric was carried out in a low-pressure capacitively-coupled RF-induced (13.56 MHz) argon and air plasmas. The power applied to the CCP reactor was 100, 200 and 300 W, treatment times were 5, 10 and 15 min while the pressure was maintained at the constant level of 0.27 mbar. Corona treatment of denim fabric was carried out at atmospheric pressure by using a commercial device Vetaphone CP-Lab MK II. Samples were placed on the electrode roll covered with silicon coating, rotating at the minimum speed set to 4 m/min. The distance between

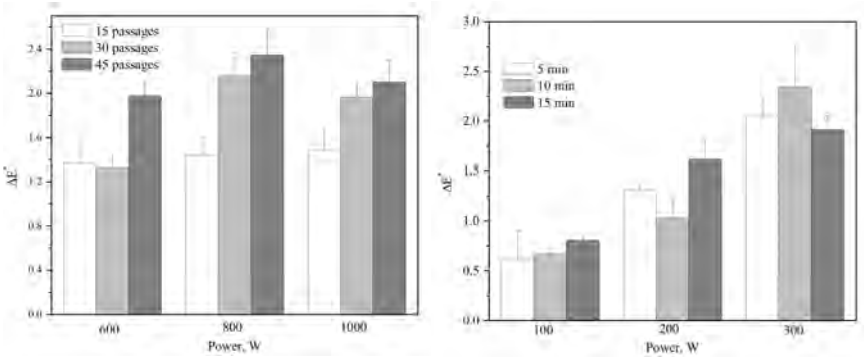

a) b)

Figure 1: Colour difference (ΔE^*) after a) COR treatment and b) LPP treatment of denim.

electrodes was 2 mm. The effect of power (600, 800 and 1000 W) and the number of passages (15, 30 and 45) on the fabric properties were assessed.

CIEL*a*b* colourimetric system was used for determination of colour difference between LPP/COR treated and untreated samples. L*, a* and b* colour coordinates (D65/10°) of samples were determined by using a Datacolor SF300. Colour difference (ΔE^*) is expressed as:

$$\Delta E^* = \sqrt{(\Delta a^*)^2 + (\Delta b^*)^2 + (\Delta L^*)^2} \tag{1}$$

where:

ΔL^*- the colour lightness difference between treated and untreated samples; Δa^* - red/green difference between treated and untreated samples; Δb^* - yellow/blue difference between treated and untreated samples.

Fibre topography was assessed by scanning electron microscope JEOL JSM 6460 LV. Prior to the analysis, the samples were coated with a thin layer of gold

3. RESULTS AND DISCUSSION

Colour change of denim fabrics after COR and LPP treatments was expressed via colour (Fig. 1), lightness, red/green and yellow/blue (Table 1) differences. Fig. 1a revealed that prolongation of the treatment time (i.e. increase in the number of passages) caused considerable increase in ΔE^* between COR treated and untreated samples independently of the applied power. ΔE^* was only slightly affected by the increase of power during shorter treatments (15 passages). However, the influence of power was more pronounced in the case of 30 and 45 passages. COR treatment increased the lightness of fabric regardless of power and number of passages, indirectly indicating the removal of indigo dye from the surface of the denim fabric. The results on Δa^* showed that all COR treated samples were greener in comparison with untreated samples. The higher the power, the greener the fabrics. COR treatment induced an increase in fabric yellowness, which was more pronounced at more severe treatment conditions.

Table 1: ΔL^*, Δa^* and Δb^* of COR and argon LPP treated denim. P-power, N-Number of passages, t-time in minutes.

Corona treated denim					LPP treated denim				
P (W)	N	ΔL^*	Δa^*	Δb^*	P (W)	t	ΔL^*	Δa^*	Δb^*
600	15	1.19	-0.17	0.69	100	5	0.68	-0.07	-0.14
	30	1.02	0.07	0.83		10	1.47	-0.17	-0.26
	45	1.62	-0.14	1.12		15	0.71	-0.19	-0.02
800	15	1.15	-0.17	0.84	200	5	1.18	-0.38	-0.42
	30	1.83	0.03	1.13		10	1.01	-0.15	0.14
	45	1.99	-0.18	1.23		15	1.39	-0.53	0.53
1000	15	1.19	-0.18	0.86	300	5	1.47	-0.55	1.59
	30	1.67	0.04	1.02		10	1.83	-0.55	1.30
	45	1.73	-0.15	1.18		15	1.67	-0.43	0.72

Argon LPP treatment induced ΔE^*, which is highly affected by power (Fig. 1). On the contrary, the influence of prolongation of the treatment time was less prominent. Similar trend can be noticed for the lightness difference (Table 1). Argon LPP treatments brought about remarkable decrease in Δa^*, showing that denim became greener particularly after the treatments at higher powers. Similarly, the higher the power, the higher the yellowness .

Air LPP treatment of denim was studied only for the most severe treatment conditions (15 min, 300 W). ΔE^* between air LPP treated and untreated denim was 2.02, ΔL^* 1.37, Δa^* 0.59 and Δb^* 1.31. The comparison of these results with the results obtained with argon LPP under the same treatment conditions indicates that the ΔE^* was almost the same. However, argon LPP treated denim demonstrated higher lightness by about 20%. Yellowness of air LPP treated denim was almost doubled.

The results pointed out that both LPP and corona treatments caused the increase in yellowness. Ghoranneviss et al. reported that no yellowness occurred after treatment of denim in argon low-current d.c. glow-discharge (see e.g. Ghoranneviss et al. 2006), whereas corona treatment induced the appearance of yellowness (see e.g. Nourbakhsh Alizadeh et al. 2006). The results presented in Table 1 revealed that increase in yellowness was considerably more dominant after corona treatments independently on treatment conditions. Additionally, air LPP treatment led to the highest increase in yellowness. Increased yellowness is suggested to be due to possible oxidation of indigo dyes on the denim fabric surface.

SEM images of untreated, COR treated, argon and air LPP treated fibres are shown in Fig. 2a, 2b, 2c and 2d, respectively. Obviously, COR treatment induced the formation of fine striations that are running parallel to the fibre axis. Fig. 2c revealed significant changes in topography of argon LPP treated fibres. The fibre surface became rougher due to existence of numerous pits. Additionally, parts of the fibres are lifting apart from the fibres. Morphological changes were the most prominent in the case of air LPP treated fibres. The formation of numerous widened pits, holes and striations unhomogeniously scattered over the fibre surface is noticeable. Such topography induced by plasma can be attributed to fibre ablation, which occurred as

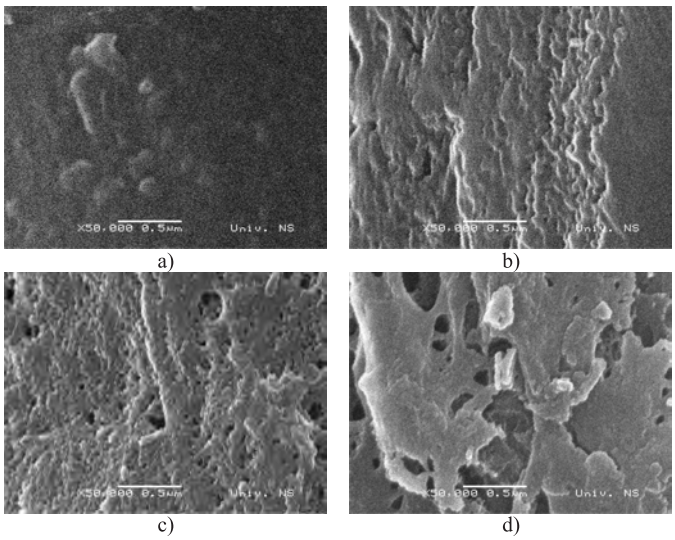

Figure 2: SEM images of a) untreated; b) corona treated (1000 W, 45 passages); c) argon LPP treated (300 W, 15 min) and air LPP treated (300 W, 15 min) fibres.

a consequence of a severe bombardment of fibre surface by energetic particles and by reactive particles generated by the plasma and its sheath. SEM images are in good correlation with the results related to breaking strength of fabrics.

4. CONCLUSIONS

Low-pressure plasma and corona treatments can be a viable alternative to conventional biostoning for obtaining "worn out" look of indigo dyed denim fabric. In addition to satisfactory colour change effects, the main advantages of these treatments are the lack of water consumption and a shorter duration. However, avoiding an increase in yellowness requires a further research.

Acknowledgments

We gratefully acknowledge the support from Ministry of Science of the Republic of Serbia for Eureka projects NANOVISION E! 4043 and BIOPOLS E! 3456. We gratefully acknowledge M. Bokorov (University of Novi Sad, Serbia) for providing SEM measurements.

References

Ghoranneviss, M., Bahareh, M., Shahidi, S., Anvari, A., Rashidi, A.: 2006, *Plasma Process. Polym.*, **3**, 316.

Nourbakhsh Alizadeh, S., Yazdanshenas, M.E., Ghoranneviss, M., Mazaheri, F.M., Rashidi, A.: 2006, *Proc. 3rd Int. Textile, Clothing & Design Conf.*, Dubrovnik, Croatia, 303.

Publ. Astron. Obs. Belgrade No. 84 (2008), 411 - 414 *Contributed Paper*

THE ANTIFUNGAL ACTIVITY OF CORONA TREATED POLYAMIDE AND POLYESTER FABRICS LOADED WITH SILVER NANOPARTICLES

Z. ŠAPONJIĆ[1], V. ILIĆ[2], V. VODNIK[1], D. MIHAILOVIĆ[2], P. JOVANČIĆ[2], J. NEDELJKOVIĆ[1] and M. RADETIĆ[2]

[1] *Vinča Instute of Nuclear Sciences, PO BOX 522, 11001 Belgrade, Serbia*
E–mail: saponjic@vin.bg.ac.yu

[2] *Textile Engineering Department, Faculty of Technology and Metallurgy, University of Belgrade, Serbia*
E–mail: maja@tmf.bg.ac.yu

Abstract. This study is aimed to highlight the possibility of using the corona treatment for fiber surface activation that can facilitate the loading of silver nanoparticles from colloids onto the polyester and polyamide fabrics and thus enhance their antifungal activity against *Candida albicans*. Additionally, the laundering durability of achieved effects was studied. Corona activated polyamide and polyester fabrics loaded with silver nanoparticles showed better antifungal properties compared to untreated fabrics. The positive effect of corona treatment became even more prominent after 5 washing cycles, especially for polyester fabrics.

1. INTRODUCTION

The interests for the manufacturing of sportswear, medical and protective textiles with antimicrobial properties increased in the last several years. Different textile materials loaded with silver nanoparticles (NPs) as antimicrobial agents can provide desirable antimicrobial efficiency (see e.g. Pohle et al. 2001, Yuranova et al. 2006). However, the most of these materials are based on synthetic fibers, which are often highly hydrophobic. Higher accessibility of hydrophobic fibers to various chemical species can be obtained by plasma functionalization and plasma etching. Therefore, improved loading of silver NPs from colloids and enhanced interaction between hydrophilic silver NPs and hydrophobic fabrics can be achieved by appropriate plasma treatment.

In this study, we discuss the possibility of using the corona treatment for fiber surface activation, which can facilitate the loading of silver NPs from colloids onto the polyester (PES) and polyamide (PA) fabrics and thus, improve their antifungal activity against *Candida albicans*. Additionally, the laundering durability of obtained antifungal effects was examined.

2. EXPERIMENTAL

The experiments were performed on desized and bleached polyester (PES, 165 g/m^2) and polyamide (PA, 150, g/m^2) fabrics, which were cleaned as described elsewhere (see e.g. Radetic et al.).

Corona treatment of fabrics was carried out at atmospheric pressure using a commercial device Vetaphone CP-Lab MK II. Fabrics were placed on the electrode roll covered with silicon coating, rotating at the minimum speed of 4 m/min. The distance between electrodes was 2 mm. The power was 900 W and the number of passages was set to 30.

$AgNO_3$ and $NaBH_4$ were used for the synthesis of colloid of silver NPs (50 ppm) as described elsewhere (see e.g. Radetic et al.). One gram of fabric was immersed in 65 mL of colloid of silver NPs for 5 min and dried at room temperature. After 5 min of curing at 100 °C, the samples were rinsed twice (5 min) with deionized water and dried at room temperature. The whole procedure was repeated twice on each fabric.

Fiber morphology was observed by scanning electron microscope (SEM) JEOL JSM 6460 LV.

The contact angle of water in air on the surface of fabrics was measured by Krüss tensiometer K12.

The antifungal properties of fabrics were quantitatively evaluated using a *Candida albicans*. 70 mL of sterile potassium hydrogen phosphate buffer solution (pH 7.2) was inoculated with 0.7 mL of a fungal inoculum. One gram of sterile fabric cut into small pieces was put in the flask and shaked for 1 h. 1 mL aliquots from the flask were diluted with phosphate buffer and 0.1 mL of the solution was placed onto a tryptone soy agar (Torlak, Serbia). After 24 h of incubation at 37 °C, the zero time and one hour counts of viable fungi were made. The percentage of fungi reduction (R, %) was calculated in accordance to equation:

$$R = \frac{C_0 - C}{C_0} \tag{1}$$

where C_0 is the number of fungi colonies on the control fabric (untreated fabric without Ag) and C is the number of fungi colonies on the fabric loaded with silver NPs. Laundering durability of antifungal effects was determined after five cycles of washing (see e.g. Radetic et al.).

3. RESULTS AND DISCUSSION

In order to improve the interaction between hydrophilic colloidal silver NPs and hydrophobic fibers, corona treatment of PA and PES fabrics was performed. Contact angles of untreated PES and PA fabrics were 89° and 83°, respectively. However, contact angles decreased to 56° for PES fabric and to 76° for PA fabric after corona treatment, demonstrating that the fibers became more hydrophilic due to the oxidation of the fiber surface and the formation of new polar functional groups.

In addition to changes in wettability of fibers, corona treatment induced the changes in surface morphology, which were assessed by SEM. SEM images of untreated and corona treated PES and PA fibers are shown in Fig. 1. It is evident that both, untreated PES and PA (Fig. 1a and 1b) fibers have smooth surfaces. The ripple-like structure of submicrometer-size was developed on the surface of corona treated PES

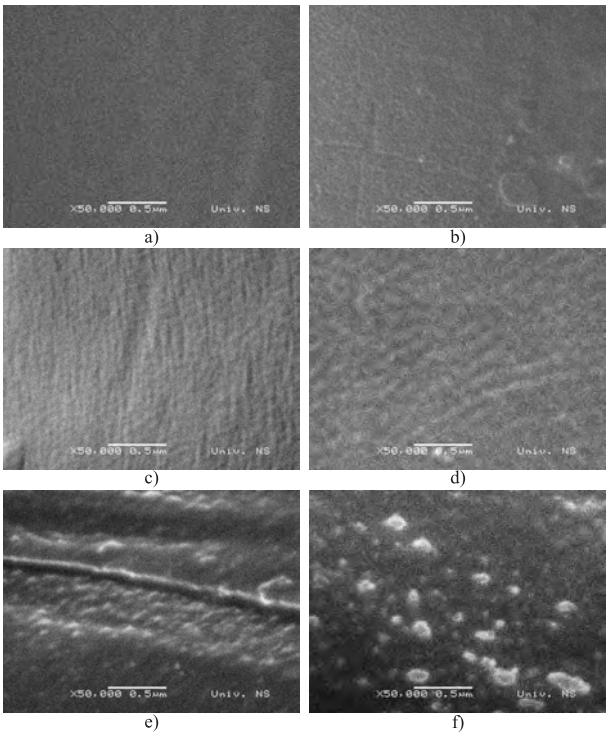

Figure 1: SEM images of a) untreated PES; b) untreated PA; c) corona treated PES; d) corona treated PA; e) corona treated PES loaded with silver NPs and f) corona treated PA loaded with silver NPs.

and PA fibers (Fig. 1c and 1d). Corona treatment increased the fiber surface area and the surface roughness. Corona induced morphological changes that can be attributed to fiber etching, which occurred as a consequence of a severe bombardment of fiber surface by particles generated by the plasma.

SEM technique was also used for analysis of fibers loaded with silver NPs from colloids. Deposition of silver NPs (Fig. 1e and 1f) led to a formation of granular structure on the surface of corona treated PES and PA fabrics.

To evaluate the antifungal activity of PA and PES fabrics loaded with silver NPs from colloids, tests with *Candida albicans* were accomplished. Fungal reduction of untreated (UPA and UPES) and corona treated (CPA and CPES) fabrics loaded with silver NPs before and after 5 washing cycles is presented in Table 1. Fungal reduction of UPES fabrics was higher by 3.9% compared to UPA fabrics. Apparently, corona treatment considerably contributed to increase in antifungal efficiency of both fabrics. The positive effect of corona treatment was more pronounced in the case of PA fabrics. Antifungal efficiency of corona treated fabrics after 5 washing cycles was remarkably higher in comparison with untreated fabrics. Silver loaded PES fabrics showed considerably better laundering durability than PA fabrics. Obtained results are in good correlation with our previous study on bacterial reduction for *Escherichia coli* and *Staphylococcus aureus* (see e.g. Radetic et al.).

Table 1: Antifungal efficiency of PES and PA fabrics loaded with silver NPs. C_i - Initial number of fungal colonies, C_{f1}-Number of fungal colonies on the fabric (before washing), C_{f2}- Number of fungal colonies on the fabric (after washing)

Sample	C_i	C_{f1}	R, %	C_{f2}	R, %
Control PES		$6.3\ 10^4$		$6.3\ 10^4$	
UPES+Ag		$1.9\ 10^3$	97	$9.0\ 10^3$	85.7
CPES+Ag	$4.2\ 10^5$	$5.6\ 10^2$	99.1	$2.1\ 10^3$	96.7
Control PA		$1.9\ 10^5$		$1.9\ 10^5$	
UPA+Ag		$1.3\ 10^4$	93.2	$8.4\ 10^4$	55.8
CPA+Ag		$1.6\ 10^2$	99.9	$6.7\ 10^4$	64.7

4. CONCLUSIONS

Deposition of silver NPs from colloids provided excellent antifungal effect for *Candida albicans* to PA and PES fabrics. Untreated PES fabrics loaded with silver NPs showed better antifungal efficiency than PA fabrics. Corona treatment positively affected the antifungal efficiency especially of PA fabrics loaded with silver NPs. The contribution of corona treatment to improvement of antifungal efficiency of both fabrics became even more prominent after 5 washing cycles. The antifungal effect of silver loaded PES fabrics which were corona pretreated was slightly altered after washing, indicating the excellent laundering durability.

Acknowledgments

We gratefully acknowledge the support from Ministry of Science of the Republic of Serbia for Eureka projects NANOVISION E! 4043 and BIOPOLS E! 3456. We gratefully acknowledge M. Bokorov (University of Novi Sad, Serbia) for providing SEM measurements.

References

Pohle, D., Damm, C., Neuhof, J., Roesch, A., Muenstedt, H.: 2001, *Polym. Polym. Compos.*, **15**, 357.

Radetić, M., Ilić, V., Vodnik, V., Dimitrijević, S., Jovančić, P, Šaponjić, Z., Nedeljković, J.: *Polym. Advan. Technol.*, in press

Yuranova, T., Rincon, A. G., Pulgarin, C., Laub, D., Xantopoulos, N., Mathieu, H. J., Kiwi, J. J.: 2006, *Photochem. Photobiol. A*, **181**, 363.

Publ. Astron. Obs. Belgrade No. 84 (2008), 415 - 419 *Contributed Paper*

HIGH POWER UV AND VUV PULSED EXCILAMPS

V. TARASENKO, M. EROFEEV, M. LOMAEV, D. RYBKA
Institute of High Current Electronics SB RAS, 634055, Tomsk, 2/3, Academichesky
E–mail: VFT@loi.hcei.tsc.ru

Abstract. Emission characteristics of a nanosecond discharge in inert gases and its halogenides without preionization of the gap from an auxiliary source have been investigated. A volume discharge, initiated by an avalanche electron beam (VDIAEB) was realized at pressures up to 12 atm. In xenon at pressure of 1.2 atm, the energy of spontaneous radiation in the full solid angle was $\sim$ 45 mJ/cm^3, and the FWHM of a radiation pulse was $\sim$ 110 ns. The spontaneous radiation power rise in xenon was observed at pressures up to 12 atm. Pulsed radiant exitance of inert gases halogenides excited by VDIAEB was $\sim$ 4.5 kW/cm^2 at efficiency up to 5.5 %.

1. INTRODUCTION

Today the sources of spontaneous radiation developed on the basis of nonequilibrium emission of excimer molecules in UV and VUV spectrum – excilamps attract attention of many researchers and find wide application in various fields of research and engineering (Gellert and Kogelschatz 1991, Lomaev et al. 2003, 2006, Zhu et al. 2007). Most often, electrodeless barrier or capacitive discharges are used for excitation of excilamps (Gellert and Kogelschatz 1991, Lomaev et al. 2003, 2006). In this case it is possible to reach at pulse repetition rate of excitation $\sim$ tens-hundreds kHz the radiant power of $\sim$ 100 W and greater with the radiant flux about 100 mW/cm^2. However, in a number of applications there is a need to have a spontaneous UV or VUV radiation with the greater pulse power. For that one could use the volume pulse high current discharges in inert gases at high pressures, and inert gas mixtures with halogens.

This paper reports on the pulse sources of spontaneous UV and VUV radiation with the power up to 8 MW, developed on the basis of volume pulse high-current discharges at high specific power of excitation ($\sim$100 MW/cm^3) and pressures (up to 12 atm) in inert gases and its halogenides excited by high voltage generators of nanosecond pulses.

2. THE EXPERIMENTAL SET-UPS AND TECHNIQUES

In the experiments we used three set-ups. First set-up, forming a volume discharge without preionization, included a primary capacitive store, a pulse transformer, a coaxial line with a wave impedance of 10 Ω, a peaking discharger and gas diode. This

developed set-up presents by itself a source of optical pumping with emitting area of a radiator of greater than 20 cm^2. The duration of a generator voltage pulse at a matched load is $\sim$ 50 ns. For study of discharge in inert gas halogenides (XeCl, KrCl, XeBr and KrBr) we used discharge chamber shown on Fig. 1 (set-up #2). Inner diameter was 36 mm. The discharge ignited between plane brass anode 1 (which was connected with ground through current shunt 3) and tube cathode 2, which was made from steel foil. The distance between electrodes was 5-12 mm. High voltage pulse with leading front width of $\sim$0.5 ns had amplitude $\sim$150 kV and $\sim$1.5 ns FWHM applied from RADAN-150 to cathode through isolator 5. A voltage pulse in case of RADAN-220 generator had a leading front width $\sim$0.5 ns, amplitude $\sim$220 kV and $\sim$2 ns FWHM. Pulse repetition rate was 1 Hz. For registration of the voltage on discharge gap we used capacitive voltage divider 6. FEK-22 SPU photocathode and Tektronix TDS-6604 (6 GHz, 20 Gs/s) were used for light registration. Radiation spectrum registered by StellarNet EPP2000-C25 spectrometer and vacuum monochromator VM-502.

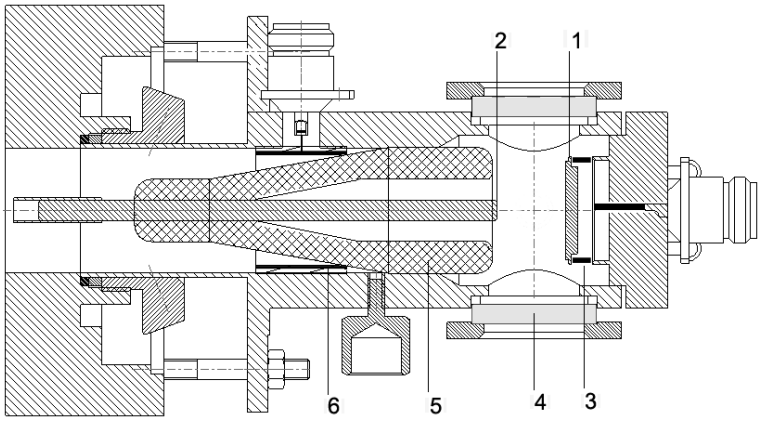

Figure 1: Discharge chamber. 1 – anode, 2 – cathode, 3 – current shunt, 4 – quartz window, 5 – insulator, 6 – capacitive divider of voltage.

3. RESULTS AND DISCUSSION

3.1. *Volume discharge in inert gases.* The discharge shape in Xe obtained on set-up #1 was like a truncated cone with a base on the anode. The diameter of the emitting area of the near-cathode discharge plasma was $\sim$ 6 cm, and $\sim$ 8 cm near the grid anode; the interelectrode distance was 4.5 cm. The maximum radiating power on Xe_2^* dimmers at 140-200 nm to the full spatial angle was obtained at the pressure of Xe of 760 Torr amounting $\sim$8 MW. The radiation pulse FWHM was of no greater than $\sim$100 ns, and the radiant exitance at excitation pulse duration of tens ns was $\sim 2\times10^4$ W/cm^2. The investigations shows that the Xe dimers radiant power obtained on set-up #1 increases with the pressure growth of Xe until the value of 1 atm.

The characteristics of radiant emittance of the volume high-current discharge plasma in inert gases at pressure greater than 1 atm was investigated by using a RADAN-220

generator (Zagulov et al. 1989) with the voltage pulse amplitude of 220 kV and pulse duration at a matched load of $\sim$ 2 ns. The width of the pulse leading edge was $\sim$0.5 ns. A flat anode and a cathode with a small-curvature radius provided the electric field gain in the near-cathode region. Interelectrode distance ranged as 4 - 16 mm. The most homogeneous discharge was obtained in the high-pressure He. Fig. 2 shows an image of such a discharge. The subnanosecond electron beam of fast electrons was registered in He at the pressure of 12 atm. The beam current pulse duration at a half-height was no greater than 100 ps.

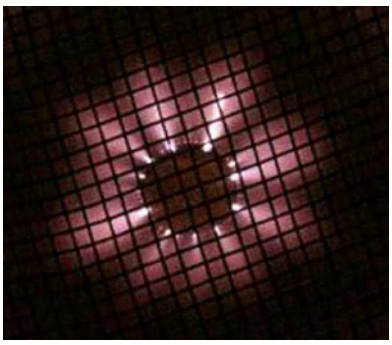

Figure 2: A photograph of a discharge in He at the pressure of 12 atm.

At Xe pressures greater than 3-4 atm there were observed the discharge contraction channels. At the same time, the high-power radiation of Xe dimer band was recorded at the pressures less than 12 atm. The duration $\tau_{1/2}$ at FWHM and power P of VUV radiation pulse as functions of Xe pressure are presented on Fig. 3. It is seen, that the value of P increases at pressures up to 12 atm meanwhile radiation energy decreasing. The maximal value of $P \sim 1$ MW and the shortest $\tau_{1/2} \sim 8$ ns was obtained at pressure 12 atm.

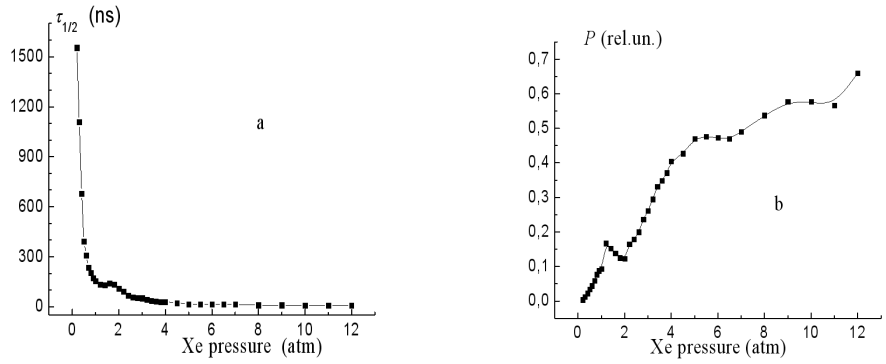

Figure 3: The duration (a) and power (b) of VUV radiation of Xe dimers vs Xe pressure.

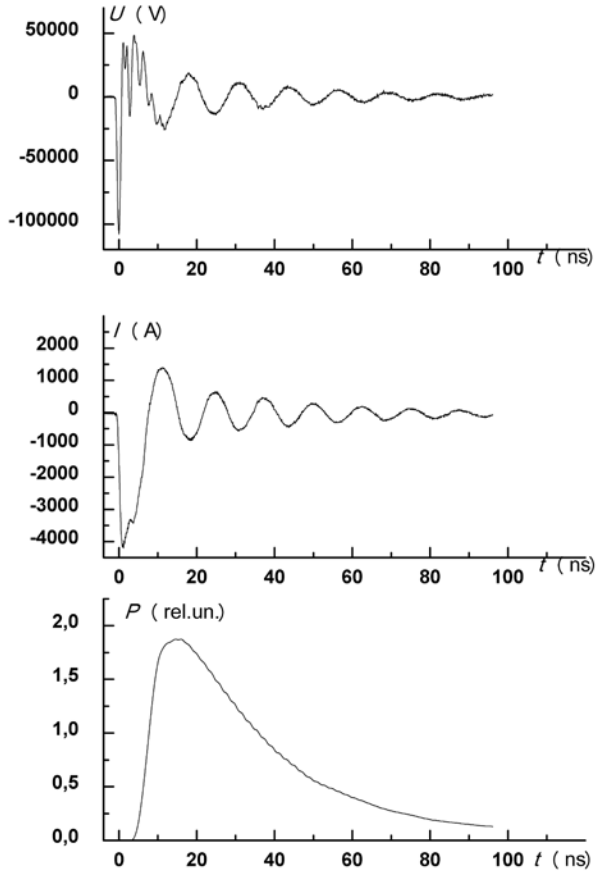

Figure 4: Typical oscilloscope traces of voltage pulse, discharge current and light pulse of volume discharge in Xe/Br_2=50/1 working mixture at 500 Torr.

3.2 *Radiation of inert gas halogenides.* Investigations of radiation of inert gas halogenides excited by high voltage generator RADAN-150 (set-up #2) was carried out in the operating mixtures pressure range of 60–750 Torr at various inert gas/halogen. Peak power of volume discharge radiation increases with increasing gap between electrodes. At low pressure (60–120 Torr) and discharge gap of 12 mm discharge had diffuse radiated cone-like form. With increasing of pressure discharge obtained form of the diffuse canal with diameter ∼3 mm which contracted at the pressure of 500 Torr and than became in a spark. Increasing of halogen concentration in an operating mixture leads to the discharge contration at lower pressures and to the decreasing of radiant power. The optimal values of working pressures for the working gas mixtures Kr/Cl_2, Xe/Cl_2, Xe/Br_2 are 500 Torr at the ratio inert gas/halogen = 50/1. For Kr/Br_2 the working pressure was 750 Torr at Kr/Br_2 = 100:1. The highest pulsed power densities of $KrCl^*$, $XeCl^*$, $XeBr^*$, and $KrBr^*$ molecules radiation were 3.7 kW/cm^2, 3.1 kW/cm^2, 4.5 kW/cm^2, and 2.1 kW/cm^2 at the efficiencies 5%, 4.8%, 5.5%, and 4%, respectively. At this conditions input energy to discharge plasma was ∼1 J.

Oscillograms of voltage pulse, discharge current and light pulse of volume discharge in Xe/Br_2=50/1 working mixture at 500 Torr are shown in Fig. 4. Pulse of the current was recorded at the front of the voltage pulse and had short delay (< 1 ns) relative to the voltage pulse. There was no prebreakdown peak at the voltage pulse which amplitude usually higher than voltage of quasi-steady phase of volume discharge with intense preionization. Similar oscillograms was obtained in (Kostyrya 2004) where such mode of discharge has been named volume discharge initiated by an avalanche electron beam (VDIAEB).

Pulse duration of volume discharge radiation in inert gas halogenides was 30-40 ns at FWHM. The radiation spectra of pulse XeCl-, KrCl-, XeBr-excilamps consist of narrow intensive bands of B–X transitions and weak-intensive bands of D–A and C–A transitions. The radiation spectrum of the pulse KrBr-excilamp consists of bands of B–X transitions of KrBr* (206 nm) and Br^*_2 (289 nm) molecules, and bands of C–A (222 nm) and B–A (228 nm) transitions of KrBr* molecule. The ratios of band intensities of transitions of KrBr* and Br^*_2 molecules change depending on the content of Br_2 in a working mixture – the more Br_2 portion, the less intensive bands of B–X, C–A and B–A transitions of KrBr* molecule are.

4. CONCLUSION

A volume discharge in helium, initiated by an avalanche electron beam, was realized at pressures up to 12 atm. In xenon with pulser RADAN-220 at pressure of 1.2 atm, the energy of spontaneous radiation in the full solid angle was ~ 45 mJ/cm^3, and the FWHM of a radiation pulse was ~ 110 ns. The power of $\sim$1 MW /cm^3 at duration of ~ 8 ns of Xe dimer radiation was obtained at pressure of 12 atm. The maximum radiant power on Xe^*_2 dimmers to the full spatial angle was obtained with set-up #1 was $\sim$8 MW. In this report the opportunity of generation of volume pulsed discharges in inert gas halogenides without preionization is also shown. The highest pulsed power densities of KrCl*, XeCl*, XeBr*, and KrBr* molecules radiation were 3.7 kW/cm^2, 3.1 kW/cm^2, 4.5 kW/cm^2, and 2.1 kW/cm^2 at the efficiencies 5%, 4.8%, 5.5%, and 4%, respectively. In the optimal conditions, radiation pulse duration at a half-height was 30 – 40 ns. The radiation spectra of KrCl-, XeCl-, XeBr-excilamps possessing the high-pulsed power density consist of the narrow intensive bands of several nm at a half-height of B–X transitions of the respective molecules.

References

Alekseev, S., Gubanov, V., Kostyrya, I., Orlovskii, V., Tarasenko, V.: 2004, *Quant. El.*, **34**, 11 1007.

Babich, L., Looeko, T. and Tarasova, L.: 1977, *Prib. Tekh. Éksp.*, **1**, 203.

Gellert, B. and Kogelschatz, U.: 1991, *Appl. Phys. B*, **52**, 14.

Kostyrya, I., Skakun, V., Tarasenko, V., Fedenev, A.: 2004, *Tech. Phys.*, **49**, 987.

Lomaev, M., Skakun, V., Sosnin, E., Tarasenko, V., Erofeev, M.: 2003, *Usp. Fiz. Nauk.*, **173**, 2 201.

Lomaev, M., Sosnin, E., Tarasenko, V., Shitz, D., Skakun, V., Erofeev, M.: 2006, *Prib. Tech. Eksp.*, **5**, 5.

Zagulov, F., Kotov, A., Shpak, V., Yurike, Ya., Yalandin, M.: 1989, *Prib. Tech. Eksp.*, **2**, 146.

Zhu, W., Takano, N., Schoenbach, K., Guru, D., McLaren, J.: 2007, *J. Phys. D: Appl. Phys.*, **40**, 3896.

Publ. Astron. Obs. Belgrade No. 84 (2008), 421 - 425 *Contributed Paper*

ELECTRON-BEAM PLASMA SYSTEMS IN INDUSTRIAL AND AEROSPACE APPLICATIONS

M. N. VASILIEV, A. H. MAHIR

Moscow Institute of Physics and Technology, Dolgoprudny, Moscow region, 141700 Russia
E–mail: csl@mipt.mail.ru

Abstract. Compact multipurpose experimental complex for the study of Aerosol Electron Beam Plasma generation and applications is described. The advantages and novel functional abilities of the experimental complex are demonstrated in comparison with the prototypes. Examples of new facilities for both physical and technological experiments are given. Perspectives of further setup modernization, in particular, the development of the beam-plasma unit for experiments on board the air- and spacecrafts are considered.

1. INTRODUCTION

The Electron–beam plasma (EBP) is generated by injecting the electron beam (EB) into a dense medium that could be atomic and molecular gases, vapors of organic and non-organic substances, gas-vapor mixtures. Practically there are no restrictions as to the chemical composition of the plasma-generating medium and the ratio of its components, and the pressure range in the plasma generating zone can be quite wide –from $\sim 10^{-2}$ Torr up to atmospheric and the plasma bulk does not contract even at high pressures. The EBP composition is complex: molecules, atoms, ions and radicals in the ground and excited states, and electrons of the degrading EP and secondary plasma electrons. At moderate gas pressure (P_m lower than 10^2 Torr) the EBP is strongly non-equilibrium and chemically active even at low (about 300 K and lower) temperatures. To generate the EBP of aerosols the dispersed particles as solid powders or liquid drops are added into the plasma bulk in a particular way. Since the EBP can be injected into both still gases and gas streams (sub- or supersonic) the dispersion of the injected condensed phase can be produced via the pneumatic spraying of the liquid jet (sheet) or solid particles by a preliminary formed EBP flow (Mahir et al. 2004). Still plasma formations containing the condensed dispersed phase are formed by means of the mechanical spraying of the liquids and powders throughout the EBP cloud. In addition, gas discharges of various kinds (for example: spark, barrier, high frequency), can be initiated in both still and moving plasma aerosols. This fact, as it is given bellow, is extremely important for the applications of the EBP.

Activities to develop the beam-plasma systems based on the EBP of aerosols and dust plasma, studies of generation, properties and applications of this plasma have been carried on in MIPT for a long time. A complete modernization of the exper-

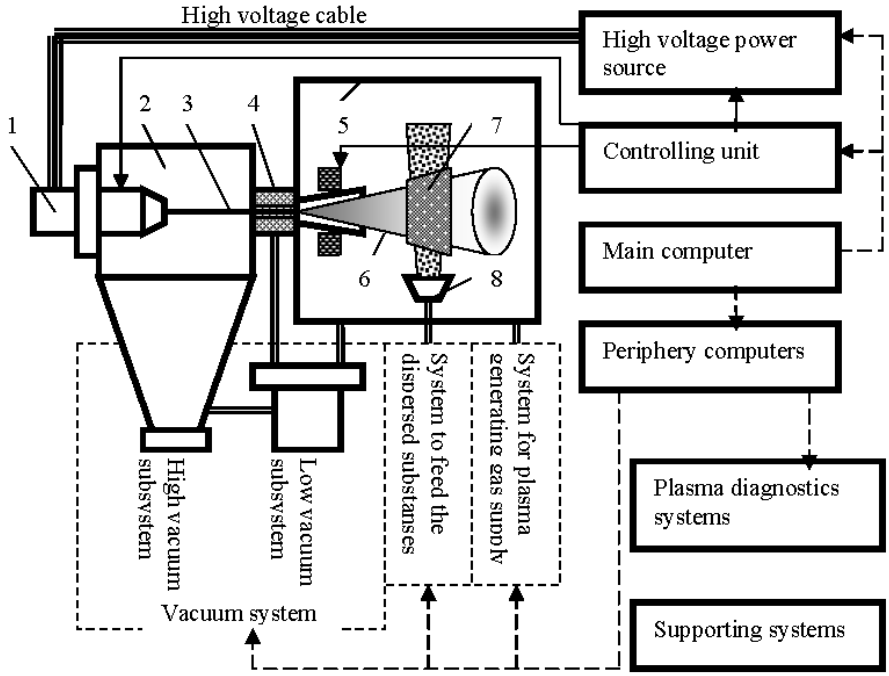

Figure 1: The scheme of the experimental complex EBPG-3.

imental facilities of the MIPT Training & research complex "Beam plasma systems and technologies" at the Department of the aero physics and space research has been made recently. The present paper considers new potential of the complex and the first results, obtained with the new experimental equipment.

2. GENERATORS THE AEROSOL EBP

Fig. 1 presents the scheme of the aerosol EBP generator for physical and technological experiments. The generator is a complicated system consisting of the following subsystems:

- The injector of the EB (electron gun 1 with controlling electrode to adjust the EB current value) equipped with the electrostatic and electromagnetic lenses to form the beam 3 in the high vacuum chamber 2 and to position the beam at the inlet of the injecting unit 4 (see bellow);
- The high voltage source generating the accelerating voltage to feed the electron gun; it is connected to the gun with a high voltage cable;
- The beam control unit to vary and monitor the operation performance of the electron injector and high voltage source and to maintain specific operating regimes of the EBP generator, for example: pulsed-intermittent regime, modulation or the EP scanning regimes and so on;

- The injection window 4 to transport the EP out of the high vacuum chamber, with the gun in it, into the working chamber 5 where the EBP cloud 6 or plasma flow is generated;
- The vacuum system responsible for maintaining the required rarefaction in the high vacuum chamber, the injection window operation, and preliminary evacuation of the working chamber;
- The plasma generating gas supply system that adjusts and maintains required gas pressure in the working chamber (or fractional pressures of the mixture components if a gas mixture of given composition is used as plasma generating medium);
- The system to supply the dispersed substances into the reaction chamber;
- The internal equipment of the working chamber containing elements and units to deflect or scan the beam injected into the working chamber, nozzles to form beam plasma jets, proper dispersing devices 8 to form aerosol particles cloud (flows)[1], electrode systems to initiate and sustain combustion of the additional gas discharges and other elements;
- The system to control the unit as an integral complex on the basis of a local network of a few computers that obtain the data from the sensors which record the working parameters of all subsystems of the complex and give the commands to executive elements of the subsystems;
- The supporting systems to ensure the reliability of the complex (cooling system, radiation protection, emergency cut off in case of hazard threat and some other supporting systems);
- Plasma diagnostics systems (they are not considered in this paper);

Characteristics of the compact generator of EBP aerosols (EBPG-3) as compared to the previously used complex EBPG-2 are given in table 1. This table shows that the modernizations have improved the performance and characteristics of the EBP generator, while the weight and size have been reduced more than tenfold. The radical change of weight and size was made thanks to complete modification of the high voltage source and the beam control unit. The onboard aerosol plasma generator (EBPG-4) with the weight less than 50 kg and the same power 6,0 kW is under development now to prepare experiments in space flights.

[1]It is in this zone of the working chamber 5, where the dispersed phase particles flow is inside the beam plasma cloud (flow) 6, that the formation of the aerosol EBP 7 takes place.

Table 1: Operation performances of the compact generator of the EBP of aerosols (EBPG-4) in comparison with the prototype (EBPG-2).

Characteristics	**EBPG-3**	**EBPG-2 (prototype, (Mahir et al. 2004))**
Accelerating voltage, kV	20-50	25-30
Power, kW	6,0	6,0
Minimal diameter of the EB, mm	0,8	1,0
Gas pressure, Torr	10^{-2}-$2{\cdot}10^{2}$	10^{-2}-10^{2}
System to maintain the gas pressure	Automatic	Manual
Plasma generator operating modes	Continuous, pulsed with the count of the pulse number, scanning.	Continuous, pulsed pulse without the count of the number, scanning.
Pulse frequency	0-1000	0-200
Generators to control the scanning of the EBP cloud	Located inside the main controlling unit.	External, manually controlled.
Modes of the EBP cloud scanning	Linear in x and$y$ raster, directions, rectangular circular scanning.	Linear in x and$y$ directions.
Mass, kg	≈ 100	≈ 2000

3. PHYSICAL AND TECHNOLOGICAL EXPERIMENTS WITH THE EBP OF AEROSOLS

The research teams of the Training & research complex "Beam plasma systems and technologies" continue the experiments in the following fields of the aerosol EBP generation and applications.

- Fundamental study of the EB propagation in aerosols:
  - The EB scattering and absorption in aerosols;
  - Spectral and energetic characteristics of the aerosol radiation stimulated by the EB propagating through it;
  - The abnormally high charging of the aerosol particles caused by the EB, the electrostatic fly-out of the aerosol cloud;
  - The formation of the dust-plasma structures in plasma traps by means of the condensation of organic and inorganic substances preliminary evaporated by the EB, the control of the dust-plasma structure properties by means of the EB action (Fortov et al. 2007).

- Production of powder semi-products for compound materials, including nano-materials, with unique physical-chemical properties and performance:
  - Low-temperature plasma-assisted synthesis and plasma-assisted deposition of functional layers (nitride, carbide, oxide, boron-containing, and others) on surfaces of dispersed powder particles;

  - Production of ultra-dispersed powders by condensing vapors of various substances (for example polymers, carbon) in plasma traps.

- Medical and biological applications of the aerosol EBP (Vasilieva 2007):
  - Production of effective agents for novel drugs by means of the beam-plasma treatment of native and artificially synthesized peptides, amino acids, and polysaccharides;
  - Beam-plasma technologies of nano-complexes formation for the addressed drugs delivering to organs of the human and animal organisms.
- Aerospace technologies, experiments on board the aircrafts and space vehicles, experiments in the terrestrial outer space:
  - Physical and technological experiments with the aerosol EBP under low gravity conditions;
  - Air pre-ionization in the intakes of ramjets;
  - Plasma generation in the vicinity and far from aircraft surface;
  - Plasma-assisted combustion of propellants.

In the latter case the supersonic flow of the air-fuel mixture is preliminary activated by the EBP and then ignited by the additional spark discharge, i.e. hybrid plasma, rather than simple gas-discharge or electron-beam plasmas, is generated in the ignition zone. Gas discharges of other types (especially RF-discharges) are successfully used in combination with the EBP to modify various dispersed materials, for example preliminary ground carbon, ceramics, natural biopolymers.

Acknowledgments

This study was supported in part by the Russian Foundation of Fundamental Research, grant 06-08-01569a.

References

Fortov, V. E., Vaulina, O. S., Petrov, O. F., Vasiliev, M. N. et al.: 2007, *Phys. Rev. E*, **75**, 026403, 1.

Mahir, A. H., Lysenko, S. L., Vasiliev, M. N.: 2004, Contributed papers of the 22-nd Summer School and Int. Conf. On the Ionized Gases, August 23-27, National Park Tara, Serbia and Montenegro, 473.

Vasilieva, T.: 2007, Peptide Science, ed. Saburo Aimoto and Sin Ono, Japanese Peptide Society, 35.

Publ. Astron. Obs. Belgrade No. 84 (2008), 427 - 430 *Contributed Paper*

THE APPLICATION OF THE ELECTRON-BEAM PLASMA FOR THE PRODUCTION OF NOVEL EFFECTIVE PLATELET AGGREGATION INHIBITORS

T. VASILIEVA[1], D. CHUHCHIN[2]

[1] *Moscow Institute of Physics and Technology, Institutsky per., 9, 141700 Dolgoprudny, Moscow region, Russia*
E–mail: protein7@rambler.ru

[2] *Arkhangelsk State Technical University, nab. Severnoy Dviny, 17, 163002 Arkhangelsk, Russia*
E–mail: dimatsch@mail.ru

Abstract. The modification of the artificially synthesized derivative of the natural amino acid alanine with pirozolidine cycle in its structure, the blood protein fibrin-monomer, and heterocyclic compounds (6-R-1,3,4-thiadiazine-2- amines) by the electron-beam plasma (EBP) was studied experimentally. All studied substances were effectively and controllably modified due to non- equilibrium plasmachemical processes in the EBP. The technique involved is likely to be useful to produce compounds with new pharmacological activities (for instance, to produce the effective platelet aggregation antagonists).

1. INTRODUCTION

Low-temperature strongly non-equilibrium plasma generated by means of the electron beam (EB) was used for the materials modification to engineer active agents for new drugs. The study objective was to produce agents inhibiting the platelet aggregation activity using EBP-assisted processes of the biomolecules modification. The modification of the artificially synthesized derivative of the natural amino acid alanine with pirozolidine cycle in its structure, the blood protein fibrin-monomer (FM), and heterocyclic compounds (6-R-1,3,4- thiadiazine-2-amines) by the EBP was studied experimentally. The substances were treated in the EBP of helium (He-EBP) or water vapor (H_2O-EBP). Our previous studies showed the combination of plasma-chemical processes, the fast electrons bombardment, and X-ray irradiation to be responsible for the modification of the original biomaterials but the effects appearing due to the plasmachemical modification predominate. The modification usually appears as a formation of new macromolecules, the structure and molecular mass of these macromolecules differing from those of the original ones (Vasilieva 2007). As a result the products can exhibit absolutely new and unique bio-properties. In our study the conventional techniques of the IR-spectroscopy, NMR-spectroscopy, ion-exchange chromatography, exclusion chromatography were used to characterize macromolecules

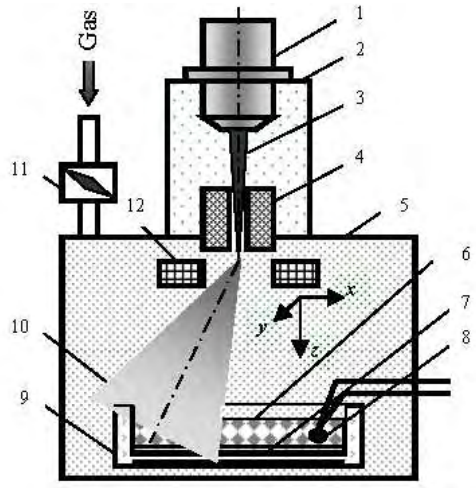

Figure 1: Scheme of the Electron-Beam Plasmachemical Reactor

modification, and the human platelet aggregation *in vitro* was measured to demonstrate the bioactivity of the products obtained, adenosine diphosphoric acid ADP (final concentration 1×10^{-5} M) being used as an aggregation agent. All effects were studied as functions of the plasma treatment conditions.

2. TREATMENT PROCEDURE

Fig. 1 illustrates a way of the substances powder treatment. The focused electron beam (EB) 3 generated by the electron-beam gun 1 which is located in the high vacuum chamber 2 is injected into the working chamber 5 filled with the plasma-generating gas (helium or water vapor) through the injection window (IW) 4. In passing through the gas the EB is scattered in elastic collisions and the energy of fast electrons gradually diminishes during various inelastic interactions with the medium (ionization, excitation, dissociation). As a result the plasma cloud 10 is generated. In general, all plasma parameters are functions of x, y, and z coordinates (z is the axis of the EB injection). Special electromagnetic scanning system 12 is placed inside the working chamber near the IW. The system is able to deflect the EB in x and y directions: being fed with sinusoidal or saw-tooth voltages the system controls the spatial distribution of the plasma particles over the plasma bulk. The working chamber is preliminary evacuated to pressure $\sim10^{-3}$ kPa and then filled with the plasma-generating gas through the feeder 11. The powder of the substance to be treated partially fills the glass container 9. Thin plate 7 made of piezoelectric ceramics is placed on the container bottom. Being fed with alternative current voltage the plate vibrates, throws up the powder particles and forms the mixing layer 6 of the treated material. The miniature thermo-sensor 8 is inserted into the container to monitor the material temperature T_s during the treatment.

3. THE PRODUCTION OF PLATELET AGGREGATION INHIBITORS BY THE EBP-TREATMENT

The treated alanine derivative became partially water-soluble even at room temperature whereas the untreated compound was not dissolvable in distilled water either cold or heated up to 90 °C. The water-soluble products of the treated alanine derivative reduced the aggregation degree down to ≈ 30 % and suppressed the platelet aggregation by ≈ 45 % more effectively than the untreated substances. The effect of the treatment duration on their anti-aggregation activity increased as the treatment prolonged, the anti-aggregation activity rising sharply at $90 < \tau < 180$ s (Table 1).

Table 1: The effect of the plasma modification in the EBP of water vapor on the anti-aggregation activity of the alanine derivative (*in vitro*): the aggregation degree as a function of the treatment duration τ and temperature of the substance T_s under the treatment procedure

ADP	ADP + untreated amino acid	ADP + treated amino acid				
		$\tau = 45$s, $T_s = 38$ °C	$\tau = 90$s, $T_s = 38$ °C	$\tau = 180$s, $T_s = 38$ °C	$\tau = 180$s, $T_s = 55$ °C	$\tau = 300$s, $T_s = 55$ °C
56±2%	46±2%	41±3%	41±3%	34±3%	32±3%	31±3%

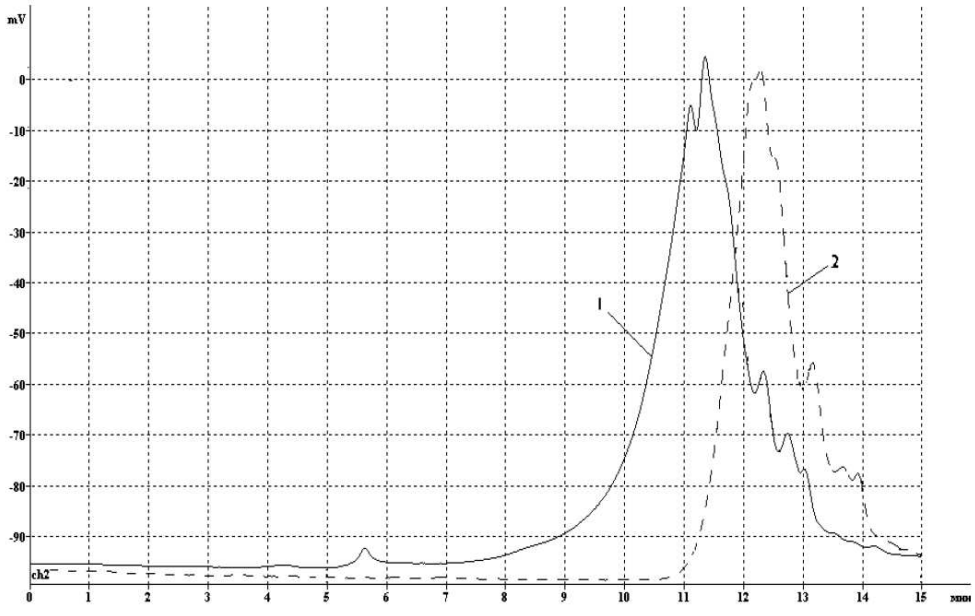

Figure 2: The chromatograms of the FM treated in the EBP of helium (1), water vapor (2).

The EBR-treatment was found to cause the partial destruction of peptide –CO-NH-bounds in the primary FM structure and the oxidation of disulfide bounds stabilizing tertiary peptides structure. All changes were more significant after the treatment in the H_2O-EBP in comparison with the treatment in the He-EBP. The EBP-treatment reduced the amount of some amino acids forming the primary protein structure. The percentage of lysine, threonine, cystine, tyrosine and phenylalanine was found to reduce significantly (down to 2 times with respect to the native FM). The reduction of other amino acids was not so sharp (only 1.3-1.5 times with respect to the native FM. The EBP-modified products did not exhibit the specific antigenic properties of original FM and did not react with specific antibodies, while the native substance gave specific precipitation line. The water-soluble products of the FM modification decreased the platelet aggregation up to $\approx$ 33-35 % *in vitro* at concentrations 1×10^{-5}-1 mg/ml, treatment in the plasma of water vapor being more effective than that in the plasma of helium. The peak corresponding to the elution time 12.3 min was observed at the exclusion chromatograms of the FM modified both in the H_2O- and He-EBP. It is this peptide that is likely to inhibit the platelet aggregation (Fig. 2).

The modification of 6-R-1,3,4-thiadiazine-2-amines in the H_2O-EPB resulted in their solubility increase as well. The plasma treatment increases the antiaggregating activity of the substance involved up to twofold with respect to that of the untreated substance. The NMR-spectroscopic analysis showed the sample of 6-R-1,3,4-thiadiazine-2-amines after the EBP-treatment to contain new products in $\approx$ 6% concentration.

Thus, fine powders of some natural substances dispersed in the EBP cloud can be effectively and controllably modified due to non-equilibrium plasmachemical processes in the EBP. The technique involved is likely to be useful to produce compounds with new pharmacological activities (for instance, to produce the effective platelet aggregation antagonists). The electron-beam plasmachemical reactors with the aerosol reaction volume seem to be competitive with technologies conventionally used in pharmaceutical industry.

Supported by the Russian Foundation of Fundamental Investigations, grant 06-08-01569_a; U.S. Civilian Research & Development Foundation; grant of President of Russian Federation for young scientists (MK-2635.2008.2).

References

Vasilieva, T.: 2007, *European Bioperspectives*, 30 May-1 June, Cologne, Germany, 487.

Publ. Astron. Obs. Belgrade No. 84 (2008), 431 - 434 *Contributed Paper*

PULSED DISCHARGE IN COMBINED HOLLOW CATHODE AS SOURCE FOR ANALYTICAL GD TOFMS. DYNAMIC DISCRIMINATION OF CLUSTERS AND DISCHARGE GAS IONS IN AFTERGLOW

A. GANEEV[1], S. POTAPOV[2], A. KRAVCHENKO[3],
R. TJUKALTZEV[2], A. ZLOTOROWICZ[4]

[1]*Faculty of Chemistry, St. Petersburg State University, Russia*
E–mail: ganeev@lumex.ru

[2]*Saint Petersburg State University, Russia*

[3]*St. Petersburg State University, Chemical Faculty, Russia*

[4]*GLADNET, Faculty of Chemistry, St. Petersburg State University, Russia*

Abstract. Some dynamic processes in pulsed discharge in combined hollow cathode used as source for analytical GD TOFMS are considered. The effect of the addition of hydrogen to glow discharge coupled to a time of flight mass spectrometer has been studied. Addition of hydrogen has shown the increase intensities of sample components and decrease intensities of discharge gas components. Reactions describing processes at presence of hydrogen are considered. Influence of pressure on discharge gas and dynamic of clusters transportation on intensities of clusters components was investigated for some types of clusters. Dynamic discrimination has allowed to increases number of determined elements due to essential reduction of interferences.

1. LOW TEMPERATURE PLASMAS

1. 1. PLASMA APPLICATIONS AND DEVICES

Some types of glow discharge are used as sources coupled with mass-spectrometry for solid, bulk samples analysis and thin-layer determinations. These sources work with direct current (DC), magnetron, radiofrequency (RF) and pulsed discharges. High sputtering and ionization efficiency for pulsed discharge increase sensitivity, asymmetric origin of analyte and discharge gas ions allowing reduce background gas contribution, perturbation of chemical system, followed by different relaxation effects – for example dissociation and recombination of different molecular ions in afterglow, selective reactions between molecular ions and Hydrogen etc. These effects can be used in analytical GD TOFMS system for effective background discrimination. Besides pulsed glow discharge reduce average of discharge power and cathode temperature under high pulsed power. Pulsed discharge in combined hollow cathode (CHC) (see

Ganeev et al. 2007) has a side benefit (compare with Grimm pulsed discharge) – it allowing analyse, as RF discharge, dielectric and semi-conducting samples.

In the glow discharges some types of clusters are generated in afterglow and consequently well known problem of occurrence interferences in clusters and sample components. For pulsed discharge intensities of some clusters can be decreased in high degree by optimization of two parameters - pressure and repelling pulse delay τ_d. Influence of pressure on discharge gas and dynamic of clusters transportation on intensities of clusters components was investigated for three types of clusters: Hydroxyls, MOH^+, MOH_2^+ ($SiOH^+$, $CuOH^+$, $CuOH_2^+$, etc.); symmetric ionic molecules of matrix element: $MiMj^+$ ($^{63}Cu^{63}Cu^+$, $^{63}Cu^{65}Cu^+$, $^{65}Cu^{65}Cu^+$, $^{28}Si_2^+$) and Argides: MAr^+ ($SiAr^+$, $NiAr^+$, $CuAr^+$).

In experiment CHC TOFMS system (Lumas-30) was used. It was found that as the pressure as repelling pulse delay increasing decreases relative intensities of first two types of clusters in high degree. This effect can be explained by clusters dissociation in collisions with neutrals in afterglow. Let's note that the effect of clusters temporal discrimination is feebly marked for argides. Probably dissociation energies for argides is appreciable higher than the energies for others types of clusters. Besides clusters dissociation, ion-electron recombination can play essential part in decreasing of relative clusters intensities when repelling pulse delay and pressure increases.

2. EFFECT OF HYDROGEN ON MASS SPECTRA

It was shown that hydrogen (1-20%) in direct current GD significantly decreases intensity of such spectra components as Ar^+, H_2O^+, H_3O^+, ArH^+ and increases intensity of Cu^+ in 6 times (see Saito, 1997). The increasing of sample elements intensities under the same conditions was reported in the same paper. Various effects connected with nonconductive sample ions sensitivities were reported for RF GD source (see Tanaka, et al. 1996).

In this work the experiments with a gas mixture containing hydrogen in pulsed discharge in hollow cathode are described. The copper standard 9410 was used. It is found that intensities for Sb^+, Ag^+, Cu^+ are not appreciably changed, in contrast to the results reported in (see Tanaka, 1996). More significant changes can be noted for Al (its intensity decreases approximately in 2 times) and Pb (its intensity increases in 1.5 times). At the same time intensities of gas components (Ar^+, OH^+, H_2O^+, H_3O^+, ArH^+) were reduced in many times (20-100) in the presence of hydrogen, that is consistent with (see R.S.Mason et al. 1997). These changes are illustrated in Fig. 1 where spectra of copper standard sample N 9410 without Hydrogen (Fig. 1a) and with 0.5% Hydrogen (Fig. 1b) are presented. It can be seen from the figure that the presence of hydrogen appreciably decreases intensity of gas components in mass spectrum (Ar decrease in 10^4 times, ArH – in 10^3 times, OH, OH_2 – in 10^2 times). It significantly reduces an interference of gas components and sample elements, especially for light elements.

However in the presence of relatively high hydrogen concentration (5-15%) miscellaneous clusters were observed in spectra, for example, $CuArH^+$, $CuAlH^+$, $CuOH_2^+$, $CuOH_3^+$, $Al_2O_3H^+$ and others. Although theirs intensities were lower than basic spectra components on 5-6 degrees, their presence significantly decreases analytical performance of the mass-spectrometer. As a result in further experiments the gas mixture with relatively low hydrogen concentration (0.3%) was used. In this case

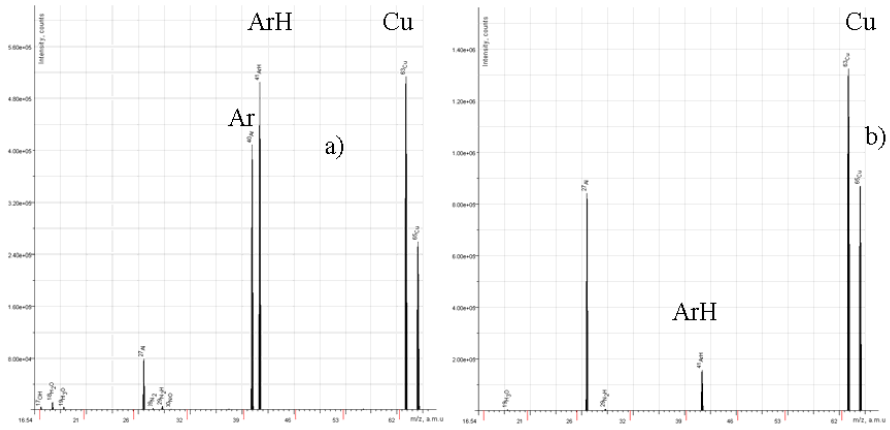

Figure 1:

a significant suppress of gas components is observed and at the same time hydride clusters are practically absent.

Mechanism of hydrogen influence on mass-spectrum components is not clear until now. Attempts to explain this phenomenon were undertaken in (see Newmann et al. 2004). Increase of metastable Ar atoms due to quenching of higher resonant levels by H_2 is suggested in (see Mason 1997), Rydberg Ar atoms production mechanism leading to interactions with H_2 is considered in (see Newmann et al. 2004). Apparently the suggested explanation are valid only for direct current glow discharge (namely this discharge type was used in these works). At the same time increase intensities of sample components and decrease intensities of gas components are more universal phenomena because they are observed in radiofrequency discharge (see Tanaka et al. 1996) and in our case in pulsed glow discharge.

It's necessary to note that addition of Hydrogen in discharge gas in pulsed discharge leads to occurrence in a spectrum of such components as H_4^+ and even H_5^+ (see Fig. 2). Presence of these a component follows from the equations for the basic reactions in glow discharge at presence of hydrogen.

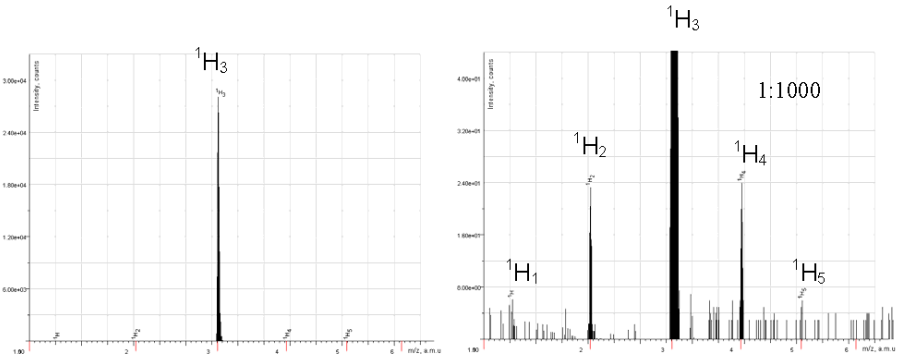

Figure 2:

These reactions are presented below:

$$\begin{gathered} Ar^+ + H_2 - ArH^+ + H \\ ArH^+ + H_2 - Ar + H_3^+ \\ OH^+ + H_2 - OH_2^+ + H \\ OH_2^+ + H_2 - OH_3^+ + H \\ H_2^+ + H_2 - -H_3^+ + H \\ H_3^+ + H_2 - -H_4^+ + H \\ H_4^+ + H_2 - -H_5^+ + H \\ COH^+ + H_2 - COH_2^+ + H \\ Cu + OH + - CuAr^+ + e \\ Cu + Ar^* - CuAr^+ + e \\ ArH^+ + e - -Ar + H + e \end{gathered} \tag{1}$$

$$\begin{gathered} CuAr^+ + H_2 - CuArH^+ + H \\ CuArH^+ + H_2 - - CuArH_2^+ + H \end{gathered} \tag{2}$$

These processes rapidly increase Ar^+ and other atom's ions recombination rate because cross-sections of molecules recombination are much higher than cross-sections of atoms recombination, even if we assume three-body, radiative or other atoms direct recombination mechanisms. We suggest that these processes also significantly increase recombination rates of molecular and atom gas components like Ar, OH, OH_2, CO, CO_2, N_2, etc in afterglow. Increase in intensities of metals ions in presence of in presence of hydrogen may be explained by increase of metastable Ar and H atoms owing to process (1) and thus by increase of Penning ionization rate. Penning ionization is a nonselective process but it can ionize only atoms or molecules that have ionization energy less than Ar or H excitation energy. This condition is valid for the large majority of metals. Other gas compounds in the discharge (molecules) have higher ionization energy (10-13 eV). Hence only intensities for several metals are (slightly) increased which is proved by our measurements. It is significant that metals ions can not take part in reactions (1) because ionization energies of majority of metals (6 – 9 eV) are less than the first excitation potential of hydrogen (10.2 eV). In this case a potential barrier of 3-6 eV prevents reactions (1). Therefore presence of hydrogen in the discharge does not reduce the intensities of sample components.

Dynamic discrimination allowing determines some element in different types of samples despite the presence of interference. For example spectra of cleared and metallurgical Silicon are shown on Fig. 3. As one can see ^{40}Ca in metallurgical Silicon does not interfere with ^{40}Ar because intensity of ^{40}Ar is very low.

References

Ganeev, A., Kuzmenkov, M., Ljubimtzev, V., Potapov, C., Drobishev, A., Potemin, S., Voronov, M.: 2007, *Journ. Of Analytical Chemistry*, (Rus), **62**, 444.

Mason, R. S., Miller, P. D. and Mortimer, I. P.: 1997, *Phys. Rev. E*, **55**, 7462.

Newmann, K., Mason, R. S., Williams, D. R., Mortinar, I. P.: 2004, *J. Anal. At. Spectrom.*, **19**, 1192.

Saito, M.: 1997, *Anal. Chim. Acta*, **355**, 129.

Tanaka, T., Matsuno, M., Woo, J.-C. and Kawagachi, H.: 1996, *Anal. Sci.*, **12**, 591.

Publ. Astron. Obs. Belgrade No. 84 (2008), 437 *Invited Lecture*

PRESENT STATUS AND PROSPECTS OF FIREX PROJECT

K. MIMA

Institute of Laser Engineering, Osaka Univ.,
2-6 Yamada-oka, Suita, Osaka 565-0871 Japan
E–mail: azechi@ile.osaka-u.ac.jp

Abstract. The goal of the first phase of Fast Ignition Realization EXperiment (FIREX) project (FIREX-I) is to demonstrate ignition temperature of 5-10 keV, followed by the second phase to demonstrate ignition and burn. Since starting FIREX-I project, plasma physics study in ILE has been devoted to increase the coupling efficiency and to improve compression performance.

The heating efficiency can be increased by the following two ways. 1) A previous experiments indicate that the coupling of heating laser to imploded plasmas increases with coating a low-density. foam used in the experiment, low-Z plastic foam is desired for efficient electron transport. (Lei et al. 2006). 2) Electrons generated in the inner surface of the double cone will return by sheathe potential generated between two cones. A 2-D PIC simulation indicates that hot electron confinement is improved by a factor of 1.7 (Nakamura et al. 2007). Further optimization of cone geometry by 2-D simulation will be presented in the workshop.

The implosion performance can be improved by three ways. 1) Low-Z plastic layer coating on the outer surface of the cone: The 2D hydro-simulation PINOCO predicts that the target areal density increases by a factor of 2. 2) Br doped plastic layer on a fuel pellet may significantly moderate the Rayleigh-Taylor instability (Fujioka et al. 2004), making implosion more stable. 3) Reducing vapor gas pressure in a pellet is necessary to suppress strength of a jet that will destroy the cone tip. (Stephens et al. 2005).

As for the cryogenic target fabrication, R&D of fabricating foam cryogenic cine shell target are under development by the joint group between Osaka Univ. and NIFS.

The amplifier system of the heating laser LFEX is completed in March 2008. The amplification test has demonstrated laser energy of 3 kJ/beam at 3nm bandwidth. The equivalent 12 kJ in 4 beams meets the specification of LFEX. The large tiled gratings for pulse compressor are completed and installed. The short pulse laser will be delivered on a target in September, 2008. The fully integrated fast ignition experiments is scheduled on February 2009 until the end of 2010. If subsequent FIREX-II will start as proposed, the ignition and burn will be demonstrated in parallel to that at NIF and LMJ, providing a scientific database of both central and fast ignition.

References

Fujioka, S., Azechi, H. et al.: 2004, *Phys. Rev. Lett.*, **92**, 195001.
Lei, A. L., Tanaka, K. A. et al.: 2006, *Phys. Rev. Lett.*, **96**, 255006.
Nakamura, T., Sakagami, H., Johzaki, T., Nagatomo H. and Mima, K.: 2007, *Phys. Plasmas*, **14**, 103105.
Stephens, R. et al.: 2005, *Phys. Plasmas*, **12**, 056312.

Publ. Astron. Obs. Belgrade No. 84 (2008), 438 *Invited Lecture*

COLLISIONLESS KELVIN - HELMHOLTZ INSTABILITY AND VORTEX INDUCED RECONNECTION IN THE EXTERNAL REGION OF THE EARTH MAGNETOTAIL

F. PEGORARO, M. FAGANELLO and F. CALIFANO
Dipartimento di Fisica Universita' di Pisa, Italy
E–mail: pegoraro@df.unipi.it

Abstract. In plasma configurations, such as those produced by the onset of the Kelvin-Helmholtz instability in a plasma with a velocity shear, qualitatively different magnetic structures are produced depending on how fast the reconnection process develops and competes with the pairing process of the vortices produced by the Kelvin-Helmholtz instability.

In a magnetized plasma streaming with a nonuniform velocity, the Kelvin-Helmholtz (K-H) instability plays a major role in mixing different plasma regions and in stretching the magnetic field lines leading to the formation of layers with a sheared magnetic field where magnetic field line reconnection can take place. A relevant example is provided by the formation of a mixing layer between the Earth's magnetosphere and the solar wind at low latitudes during northward periods. In the considered configuration, in the presence of a magnetic field nearly perpendicular to the plane defined by the velocity field and its inhomogeneity direction, velocity shear drives a K-H instability which advects and distorts the magnetic field configuration. If the Alfvén velocity associated to the in-plane magnetic field is sufficiently weak with respect to the variation of the fluid velocity in the plasma, the K-H instability generates fully rolled-up vortices which advect the magnetic field lines into a complex configuration, causing the formation of current layers along the inversion curves of the in-plane magnetic field component. Pairing of the vortices generated by the K-H instability is a well know phenomenon in 2-D hydrodynamics Here we investigate the development of magnetic reconnection during the vortex pairing process and show that completely different magnetic structures are produced depending on how fast the reconnection process develops on the time scale set by the pairing process.

References

Faganello, M. et al.: 2008, *Phys. Rev. Lett.*, **100**, 015001.

Publ. Astron. Obs. Belgrade No. 84 (2008), 439 *Invited Lecture*

SIMULATION SCIENCE FOR FUSION PLASMAS

M. M. ŠKORIĆ and S. SUDO
National Institute for Fusion Science,
Graduate University for Advanced Studies,
Toki-shi, 509-5292, Japan
E–mail: skoric.milos@nifs.ac.jp

Abstract. The world fusion effort has recently entered a new age with the construction of ITER in Cadarache, France, which will be the first magnetic confinement fusion plasma experiment dominated by the self-heating of fusion reactions. In order to operate and control burning plasmas and future demo fusion reactors, an advanced ability for comprehensive computer simulations that are fully verified and validated against experimental data will be necessary. The ultimate goal is to develop the capability to predict reliably the behavior of plasmas in toroidal magnetic confinement devices on all relevant time and space scales. In addition to developing a sophisticated integrated simulation codes, directed advanced research in fusion physics, applied mathematics and computer science is envisaged.

In this talk we review the basic strategy and main research efforts at the Department of Simulation Science of the National Institute for Fusion Science (NIFS)- which is the Inter University Institute and the coordinating Center of Excellence for academic fusion research in Japan. We overview a simulation research at NIFS, in particular relation to experiments in the Large Helical Device (LHD), the worlds largest superconducting heliotron device, as a National Users facility (see Motojima et al. 2003). Our main goal is understanding and systemizing the rich hierarchy of physical mechanisms in fusion plasmas, supported by exploring a basic science of complexity of plasma as a highly nonlinear, non-equilibrium, open system. The aim is to establish a simulation science as a new interdisciplinary field by fostering collaborative research in utilizing the large-scale supercomputer simulators. A concept of the hierarchy-renormalized simulation modelling will be invoked en route toward the LHD numerical test reactor. Finally, a perspective role is given on the ITER Broad Approach program at Rokkasho Center, as an integrated part of ITER and Development of Fusion Energy Agreement.

References

Motojima, O. et al.: 2003, *Nuclear Fusion*, **43**, 1674.

Publ. Astron. Obs. Belgrade No. 84 (2008), 440 *Invited Lecture*

MULTI-LAYER PHOTOIONIZATION MODELS OF THE NUCLEAR AND CIRCUMNUCLEAR REGION OF TYPE 2 AGN

P. RAFANELLI, S. CIROI, F. DI MILLE, L. VAONA
Department of Astronomy, University of Padova, Italy
E–mail: stefano.ciroi@unipad.it

Abstract. We present an overview of the physical conditions occurring in the nuclear and circumnuclear regions of nearby Active Galactic Nuclei of type 2 ($z<0.1$) and the results of simulation, using multicomponent photoionization models. The comparison of calculated with observed line ratios, measured in the spectra of a sample of around 1300 type 2 active galaxies, is critically discussed.

Publ. Astron. Obs. Belgrade No. 84 (2008), 441 *Topical Lecture*

SPECTROSCOPY METHODS APPLIED TO THE RESEARCH IN PLASMAS AT ATMOSPHERIC PRESSURE

M. D. CALZADA

Grupo de Espectroscopía de Plasmas. Edificio A. Einstein (C-2), Campus de Rabanales. Universidad de Córdoba, 14071 Córdoba, Spain
E–mail: fa1cazal@uco.es

Abstract. Plasmas operated at atmospheric pressure are being the object of an increased attention due to their potential and current use in various applications such as excitation source for elemental analysis, purification of noble gases and more recently hydrogen production and sterilization of medical instruments.

In order to ensure that the technological applications of plasmas are carried out with a maximum of efficiency it is necessary to know the ability of the discharge to induce the desired microscopic processes. This ability depends on the densities of different plasma species such as electron density and both atoms and molecules at excited levels together with the energy available in the discharge. This energy is fundamentally in form of the kinetic energy of electrons (electron temperature) and heavy particles like atoms and ions (gas temperature).

Passive spectroscopy techniques can be used to measure the densities and temperatures in plasma. Moreover, these techniques also allow us to know and control the processes that take place in the plasmas during their applications in specific fields. These techniques are based on the analysis of the radiation emitted by the own plasma. So, the use of passive spectroscopy does not perturb the internal kinetics of the discharge when the observation and control of plasma application are being carried out. Therefore, an important part of the effort in experimental and theoretical research in plasmas is devoted for devising, developing and proving spectroscopy methods for the purpose mentioned above.

New methods have been recently developed in order to measure the electron density (see e.g. Yubero et al. 2005, Yubero et al. 2006) and gas temperature (see e.g. Yubero et al. 2007) of plasmas at atmospheric pressure which can be considered as a complement to the classical methods (see e.g. Calzada et al. 1996, Luque et al. 2003). An example of the use of the spectroscopy to know the processes that take place in plasmas corresponds to the study of the capacity of a surface wave discharge to dissociate the alcohols molecules for obtaining hydrogen (see e.g. Jiménez at al. 2008).

References

Calzada, M. D., Moisan, M., Gamero, A., Sola, A.: 1996, *J. Appl. Phys.*, **80**, 46.
Jiménez, M., Yubero, C., Calzada, M. D.: 2008, *J. Phys. D: Appl. Phys.* (in press).
Luque, J. M., Yubero, C., Calzada, M. D.: 2003, *J. Phys. B: At. Mol. Opt. Phys.*, **36**, 1573.
Yubero, C., Calzada, M. D., García, M. C.: 2005, *J. Phys. Soc. Jpn.*, **74**, 2249.
Yubero, C., Dimitrijević, M. S., García, M. C., Calzada, M. D.: 2007, *Spectrochim. Acta B*, **62**, 169.
Yubero, C., García, M. C., Calzada, M. D.: 2006, *Spectrochim. Acta B*, **61**, 540.

Publ. Astron. Obs. Belgrade No. 84 (2008), 442 *Progress Report*

PROCESSES WITH NEUTRAL HYDROGEN AND DEUTERIUM MOLECULES RELEVANT TO EDGE PLASMA IN TOKAMAKS

I. ČADEŽ, S. MARKELJ, Z. RUPNIK, P. PELICON
Institute Jožef Stefan, Jamova cesta 39, 1000 Ljubljana, Slovenia
E–mail: Iztok.Cadez@ijs.si

Abstract. Detailed understanding and characterization of plasma-wall interaction and edge plasma in present tokamaks and future fusion reactors is becoming more and more important due to the ITER project. Involved processes determine the physical and chemical sputtering of the wall material, fuel retention in exposed material, edge plasma properties, disruption phenomena etc. Neutral hydrogen atoms and molecules are present in the edge plasma. They are continuously generated by ion recombination on the wall of the fusion reactor and on the other plasma facing components and subsequently reemitted in the plasma. Neutral molecules are especially important for plasma detachment in tokamak divertors. The interaction of excited neutral molecules with the walls and their importance for the edge plasma is still not well understood since there are not many experimental studies of relevant processes. Moreover, spectroscopic results from tokamak edge plasma are dominated by processes involving ions and electrons, so that direct evidence of the influence of neutrals is difficult to extract. Direct correlation of the observed phenomena to the processes with neutrals is mainly possible by numerical simulations.

We have constructed a set-up for vibrational spectroscopy of hydrogen molecules (H_2 and D_2) that is based on the properties of the dissociative electron attachment in hydrogen in order to facilitate dedicated experimental studies of relevant processes with hydrogen molecules. For the same purpose we also developed a technique for in-situ hydrogen depth profiling on the samples exposed to the controlled hydrogen atmosphere. This is done by Ion Beam Analytical (IBA) method ERDA (Elastic Recoil Detection Analysis), utilizing 4.2 MeV probing beam of $^7Li^{2+}$ ions. A short description of experimental techniques and results on chemical erosion of graphite layers, production of vibrationally excited hydrogen molecules on tungsten and isotope exchange on tungsten are to be presented in this report.

Publ. Astron. Obs. Belgrade No. 84 (2008), 443 *Progress Report*

KINEMATICAL PARAMETERS IN THE CORONAL AND POST-CORONAL REGIONS OF THE Oe STARS

A. ANTONIOU[1], E. DANEZIS[1], E. LYRATZI [1,2], D. NIKOLAIDIS[1],
L. Č. POPOVIĆ[3] and M. S. DIMITRIJEVIĆ[3]

[1] *University of Athens, School of Physics, Department of Astrophysics, Astronomy and Mechanics, Panepistimiopolis, Zografos 157 84, Athens - Greece*
E–mails: ananton@phys.uoa.gr, edanezis@phys.uoa.gr, elyratzi@phys.uoa.gr, mail@nikolaidis.info

[2] *Eugenides Foundation, 387 Sygrou Av., 17564, Athens, Greece*

[3] *Astronomical Observatory of Belgrade, Volgina 7, 11160 Belgrade, Serbia*
E–mails: lpopovic@aob.bg.ac.yu, mdimitrijevic@aob.bg.ac.yu

Abstract. In this progress report we present the main results of our research. Using a new model we studied the kinematical parameters such as the random velocities of the ions, which create the spectral lines of the C IV, N IV and N V in the spectra of 20 O_e stars, as well as the rotational and radial velocities of the regions, where the above ions are created. We calculated the values of the above parameters and we present the relations between them as well as the variation of them as a function of the spectral subtype. We present the random velocities of the ions for each one of the C IV, N IV and N V regions as a function of the photospheric rotational velocities. Finally, we propose an explanation for the large widths that we observe in the studied spectral lines, as these widths can not be explained as large rotational or random velocities.

Publ. Astron. Obs. Belgrade No. 84 (2008), 444 *Progress Report*

VARIABILITY OF GRB LIGHT CURVE: SHOCK WAVE MODEL MODIFICATION

S. SIMIĆ[1] and L. Č. POPOVIĆ[2]

[1]*Faculty of Science, Department of Physics, Radoja Domanovića 12, 34000 Kragujevac, Serbia*
E–mail: ssimic@kg.ac.yu

[2]*Astronomical observatory, Volgina 7, 11000 Beograd, Serbia*

Abstract. The main topic of our investigation is a mysterious phenomena of gamma ray bursts. If someone analyze the observation of these events, its emerge that most interesting data are among the gamma phase, during the first couple of seconds. In this stage a central engine generates high intensity and high energy radiation, observed in the form of pulses in the light curve. If we could understood the main physical processes in this phase, we could put some constraints for the model which try to explain the core of this phenomena, deeply hidden from observation by high optical thickness of surrounding material.

Observation of the GRB light curve can be easily done with the help of modern satellites, so the data of this kind are vastly dispersed. We try to analyze them and to explain in details physical process which create the light curve pulses. Our research is based on the broadly accepted scenario of a gamma phase in GRBs, which predicts that GRB core generates highly relativistic mater in some amount of time. This mater form a shock waves of different velocities, due to highly differential motions. The shock waves can interact with each others, and in that moment radiation significaly increases, creating the observed pulses in the GRB light curve. We develop a phenomenological model based on the model developed by Huang and coauthors, to explain evolution of shock wave expanding from some distance. In it, we implemented the ability to simulate collision between an incoming shock and density barrier. We also propose that density barrier is created by the material ejected from the core and spread around by the shocks. As a result of simulation we can get synthesized pulses, and by comparing them with the observational data we can acquire values of basic parameters used in our model.

Publ. Astron. Obs. Belgrade No. 84 (2008), 445 *Progress Report*

γ-RADIATION FROM THE GALACTIC CENTER: DARK MATTER ANNIHILATION OR MORE CONSERVATIVE ASTROPHYSICAL MODELS?

A. F. ZAKHAROV

State Scientific Center – Institute of Theoretical and Experimental Physics, Moscow, Russia
Bogoliubov Laboratory of Theoretical Physics, Joint Institute for Nuclear Research, Dubna
E–mail: zakharov@itep.ru

Abstract. The existence of dark matter (DM) at scales of few pc down to $\simeq 10^{-5}$ pc around the centers of galaxies and in particular in the Galactic Center region has been considered in the literature. Under the assumption that such a DM clump, principally constituted by non-baryonic matter (like WIMPs) does exist at the center of our galaxy, the study of the γ-ray emission from the Galactic Center region allows us to constrain both the mass and the size of this DM sphere. Further constraints on the DM distribution parameters may be derived by observations of bright infrared stars around the Galactic Center. Hall and Gondolo (2006) used estimates of the enclosed mass obtained in various ways and tabulated by Ghez et al. (2003, 2005). Moreover, if a DM cusp does exist around the Galactic Center it could modify the trajectories of stars moving around it in a sensible way depending on the DM mass distribution. Here, we discuss the constraints that can be obtained with the orbit analysis of stars (as S2 and S16) moving inside the DM concentration with present and next generations of large telescopes. In particular, consideration of the S2 star apoastron shift may allow improving limits on the DM mass and size.

Publ. Astron. Obs. Belgrade No. 84 (2008), 446 *Progress Report*

CONFINEMENT AND ANISOTROPY OF ULTRAHIGH-ENERGY COSMIC RAYS IN ISOTROPIC PLASMA WAVE TURBULENCE

M. VUKČEVIĆ

Faculty of Natural Sciences and Mathematics, University of Montenegro, Montenegro

Abstract. The mean free path and anisotropy of galactic cosmic rays is calculated in weak plasma wave turbulence that is isotropically distributed with respect to the ordered uniform magnetic field.

The modifications on the value of the Hillas energy, above which cosmic rays are not confined to the Galaxy, are calculated. The original determination of the Hillas limit has been based on the case of slab turbulence where only parallel propagating plasma waves are allowed.

We use quasilinear cosmic ray Fokker-Planck coefficients to calculate the mean free path and the anisotropy in isotropic plasma wave tuurbulence.

In isotropic plasma wave turbulence the Hillas limit is enhanced by about four orders of magnitude to Ec = 2.03 · 104An1/2 e (Lmax/1 pc) resulting from the dominating influence of transit-time damping interactions that obliquely propagating magnetosonic waves undergo with cosmic rays.

Below the energy Ec the cosmic ray mean free path and the anisotropy exhibit the well known E1/3 energy dependence for relevant undamped waves. In case of damped waves, the cosmic ray mean free path and the anisotropy do not depend on energy. At energies higher than Ec both transport parameters steepen to a E3-dependence for undamped and damped waves. This implies that cosmic rays even with ultrahigh energies of several tens of EeV can be rapidly pitch-angle scattered by interstellar plasma turbulence, and are thus confined to the Galaxy.

Publ. Astron. Obs. Belgrade No. 84 (2008), 447 - 450 *Contributed Paper*

BLOBS IN THE TOKAMAK SCRAPE-OFF LAYER

D. JOVANOVIĆ[1], P. K. SHUKLA[2] and F. PEGORARO[3]

[1]*Institute of Physics, P. O. Box 57, 11001 Belgrade, Serbia*
E–mail: djovanov@phy.bg.ac.yu

[2]*Institut für Theoretische Physik IV, Ruhr–Universität Bochum, D-44780 Bochum, Germany*
E–mail: ps@tp4.rub.de

[3]*Dipartimento di Fisica Universitá di Pisa, largo Pontecorvo 3, 56127 Pisa, Italy*
E–mail: pegoraro@df.unipi.it

Abstract. A three-dimensional model for the warm-ion turbulence at the tokamak edge plasma and in the scrape-off layer is proposed. It is based on the nonlinear interchange mode, coupled with the nonlinear resistive drift mode, in the presence of the magnetic curvature drive, the density inhomogeneity, the electron dynamics along the open magnetic field lines, and the electron-ion and electron-neutral collisions. Numerical solutions indicate the collapse of the blob in the lateral direction, followed by a clockwise rotation and radial propagation. The symmetry breaking, caused both by the parallel resistivity and the finite ion temperature, introduces a poloidal component in the plasma blob propagation, while the overall stability properties and the speed are not affected qualitatively.

The transport in the scrape-off layer is mostly intermittent, due to the coherent filamentary plasma structures, or "blobs". They are elongated along the magnetic field and small (cm-sized) in the perpendicular direction, propagating radially with a velocity in the thermal range. They are usually an order of magnitude, or more, denser and hotter than the surrounding plasma. Blobs and SOL turbulence are usually studied within the interchange paradigm, see the recent review (Krasheninnikov et al., 2008). We include the effects of parallel electron dynamics and finite ion temperature, using the standard hydrodynamic equations of continuity and momentum, in a purely electrostatic regime. The collision frequency is below the ion gyrofrequency, and the electron and ion dynamics are expressed in the drift aproximation. The equations are further simplified for a weakly inhomogeneous tokamak magnetic field, $\vec{B} = B_0(1 - x/R)[\vec{e}_z + (x/L_s)\vec{e}_y - (z/R)\vec{e}_x]$ where the coordinates x, y, and z correspond to the radial, poloidal and toroidal distances. We consider electrons to be isothermal, and alow for finite ion temperature, $T_i \leq T_e$. Finally, we assume a weak variation along the magnetic field, $\nabla_\parallel \ll \nabla_\perp$, which allows us to neglect the nonlinear convection along the magnetic field. Neglecting the polarization and finite Larmor radius effects, the electron continuity equation, can be written as

$$\left[\frac{\partial}{\partial t} + \frac{1}{B_0}\left(\vec{e}_z \times \nabla\right)\cdot\nabla\right] n + \frac{\gamma_{e,i}\, n^2}{\Omega_e B_0}\,\frac{T_e+T_i}{e}\,\nabla_\perp^2 \ln n$$
$$-\frac{\gamma_{e,n}^{(sc)}\, n n_n}{\Omega_e B_0}\,\nabla_\perp^2\left(\phi - \frac{T_e}{e}\,\ln n\right) + \nabla_\parallel\left(n v_{e\parallel}\right) = \gamma_{e,n}^{(ion)}\, n n_n, \qquad (1)$$

where we used $n_e = n_i \equiv n$, and we neglected the gradients of temperature, electron-ion and electron-neutral collision frequencies across the SOL. $\gamma_{\alpha,n}^{(sc)} n_n$ is the effective frequency of the scattering collisions between the particle species α and the neutrals. The particle source term $\gamma_{e,n}^{(ion)} n_e n_n$ comes from the electron impact ionization of the neutrals. $\gamma_{e,i}\, n_e$ is the electron-ion collision frequency.

Subtracting the ion- and electron continuity equations, we obtain the ion vorticity equation which in the Boussinesq approximation (we neglect the terms $\nabla_\perp n_\alpha$ compared to $n_\alpha \nabla_\perp$) takes the form

$$-\tfrac{T_e+T_i}{eB_0}\left(\tfrac{1}{L_s}\tfrac{\partial}{\partial z} - \tfrac{2}{R}\tfrac{\partial}{\partial y}\right) n_i + \nabla_\parallel \left[n\left(v_{i_\parallel} - v_{e_\parallel}\right)\right]$$
$$+\tfrac{n}{\Omega_i B_0}\nabla_\perp \cdot \left\{\left[\tfrac{\partial}{\partial t} + \tfrac{1}{B_0}\left(\vec{e}_z \times \nabla\phi\right)\nabla - \eta_i \nabla_\perp^2 + \gamma_{i,n}^{(sc)}\, n_n\right] \nabla_\perp \left(\phi + \tfrac{T_i}{e}\ln n\right)\right\} = 0. \quad (2)$$

For the description of the parallel dynamics, we average the parallel momentum equations along the magnetic field. We seek an elongated, quasi 2-D solution that is tilted by the angle θ relative to the toroidal axis (z axis), and whose projection on the tokamak cross-section (x, y plane) makes the angle ϑ with the radius (x axis), for which we may write $\nabla_\parallel = \partial/\partial z' + \tan\theta\ \vec{p}_\perp(x) \cdot \nabla_\perp$, where $\vec{p}_\perp(x) = \vec{e}_x \cos\vartheta + \vec{e}_y(x/L_s + \sin\vartheta)$. Neglecting the electron inertia, after the multiplication of the parallel electron momentum equation by $\nabla_\parallel$ and integration along the z axis from the wall ($z = 0$) to $z = L_\parallel$, where the average parallel velocity is equal to zero, we have

$$v_{e_\parallel}(0) = \frac{e/m_e}{\gamma_{e,i}\, n + \gamma_{e,n}^{(sc)}\, n_n}\left[\left(\frac{\partial}{\partial z'} + 2\,\tan^2\theta\ \vec{p}_\perp \cdot \nabla_\perp\right)\left(\phi - \frac{T_e}{e}\ln n\right) - \gamma_{e,i}\, n\, v_{i_\parallel}\right]_{L_\parallel}^{0}. \quad (3)$$

The electron velocity at the plasma-wall interface is determined from kinetic considerations. When the magnetic field is perpendicular to the the wall, we have

$$v_{e_\parallel}(z=0) = n\, c_s\, \exp\left\{(e/T_e)\left[\phi_0 - \phi(z=0)\right]\right\}, \quad (4)$$

where c_s is the acoustic velocity, $c_s = [(T_e + T_i)/m_i]^{\frac{1}{2}}$ and ϕ_0 is the unperturbed plasma potential $\phi_0 = \phi^{wall} + (T_e/e)\ \ln\{[T_e/(T_e+T_i)](m_i/m_e\sqrt{2\pi})\}$. The ion velocity at the plasma-sheath boundary is found by the integration of the 1-D ion momentum equation, since the sheath thickness is typically much smaller than the perpendicular scale of turbulence. The sheath is a thin (Debye sized) layer, that is created at the plasma-conducting wall interface, due to the different rates of escape of the electrons and ions. When the magnetic field is perpendicular to the wall, we have $v_{i_\parallel} = c_s$. Then, approximating the z-averaged flows by their local values, the divergence of the parallel flows in Eqs. (1) and (2) can be written as

$$\nabla_\parallel v_{e_\parallel} = \frac{c_s}{L_\parallel}\ \exp\left[-\frac{e\tilde{\phi}(z=0)}{T_e}\right] + \frac{(e/m_e)\ \tan^2\theta}{\gamma_{e,i}\, n + \gamma_{e,n}^{(sc)}\, n_n}\left(\vec{p}_\perp \cdot \nabla_\perp\right)\vec{p}_\perp \cdot \nabla_\perp\left(\phi - \frac{T_e}{e}\ln n\right), \quad (5)$$

and $\nabla_\parallel v_{i_\parallel} = c_s/L_\parallel$, where $\tilde{\phi} = \phi - \phi_0$ is the variation of the potential at a given point from the background plasma potential ϕ_0. In the rest of the text, for simplicity, tilde will be omitted. Now, using above equations and appropriate normalizations, we can rewrite our basic Eqs. (1) and (2) in a dimensionless form as

$$\left[\frac{\partial}{\partial t} + \left(\vec{e}_z \times \nabla\phi\right)\cdot\nabla\right] n - D\nabla_\perp^2 n = -\sigma n, \quad (6)$$

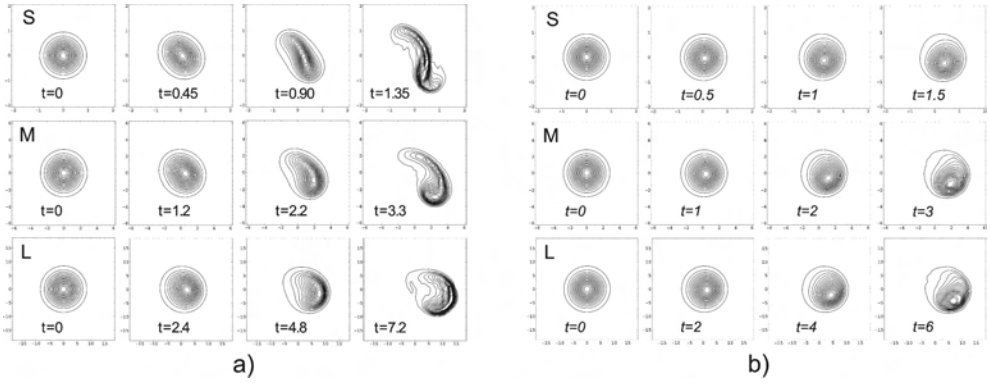

Figure 1: a) The effect of the parallel electron dynamics. **Collisional** regime, with cold ions and negligible perpendicular collisional effects. The parameters are $\chi_{2_\parallel} = 1$, $\vartheta = 0$, $D = 10^{-3}$, $\chi_0 = 2 \times 10^{-3}$, $\chi_{2_\perp} = \chi_4 = \gamma = \sigma = \tau = 0$. b) The effect of the finite ion temperature in the **inertial** regime. We used $D = 10^{-3}$, $\chi_0 = 2 \times 10^{-3}$, $\chi_{2_\perp} = \chi_{2_\parallel} = \chi_4 = \gamma = \sigma = 0$, while $\tau = 1, 3$ and 12 for the S, M, and L structures.

$$\left[\tfrac{\partial}{\partial t} + (\vec{e}_z \times \nabla\phi)\cdot\nabla\right]\nabla_\perp^2\,(\phi + \tau\, n) - \tfrac{\partial n}{\partial y} + \tau\left(\vec{e}_z \times \nabla\tfrac{\partial\phi}{\partial x_i}\right)\cdot\nabla\tfrac{\partial n}{\partial x_i}$$
$$= \chi_0\,\phi\,(z=0) + \chi_{2_\parallel}\,(\vec{p}_\perp\cdot\nabla_\perp)^2\,n + \left(\chi_{2_\perp}\nabla_\perp^2 - \chi_4\,\nabla_\perp^4\right)(\phi + \tau n)\,. \qquad (7)$$

The expressions for $\sigma, D, \chi_0, \chi_2, \chi_4$, and τ depend on our choice of the normalizations, i.e. on the appropriate scaling laws. We can distinguish four different orderings with respect to the intensities of various dissipation mechanisms, to the blob's temporal and spatial scales, and to the amplitude of electrostatic potential.

Inertial regime is realized when all dissipations can be neglected and, with the accuracy to leading order, we have $\chi_0 = \chi_{2_\parallel} = \chi_{2_\perp} = \chi_4 = \sigma = D = 0$.

In the **sheath resistivity** regime the dominant dissipation mechanism is the current loss to the wall, when we have $\chi_0 = 1$, $\chi_{2_\parallel} = \chi_{2_\perp} = \chi_4 = \sigma = 0$, $\tau = \tau_i\,(\nu_{sink}^3\Omega_i/\nu_{_{RT}}^4)^{\frac{1}{5}}$, $D = [(D_{e,i} + D_{e,n})/\rho_s^2](\nu_{sink}^3/\nu_{_{RT}}^4\Omega_i^4)^{\frac{1}{5}}$. Here we introduced the notations $\rho_s = (1/\Omega_i)(T_e/m_i)^{\frac{1}{2}}$, $\tau_i = T_i/T_e$, $\nu_{src} = \gamma_{e,n}^{(ion)}\,n_n$, $\nu_{i,n} = \gamma_{i,n}^{(sc)}\,n_n$, $\nu_{_{RT}} = 2\Omega_i(1+\tau_i)(\rho_s/R)$, $\nu_\parallel = |\Omega_e|\,\Omega_i\,\tan^2\theta/(\gamma_{e,i}\,n + \gamma_{e,n}^{(sc)}\,n_n)$, $\nu_{sink} = c_s/L_\parallel$, $D_{e,n} = (m_e/m_i)\rho_s^2\,\gamma_{e,n}^{(sc)}\,n_n$, $D_{e,i} = (m_e/m_i)(1+\tau_i)\rho_s^2\,\gamma_{e,i}\,n$.

Collisional regime is realized if the electron-ion and ion-neutral collisions are the dominant dissipation mechanisms, when we have $\chi_{2_\parallel} = 1$, $\chi_{2_\perp} = (\nu_{i,n}/\nu_{_{RT}})(\nu_\parallel/\Omega_i)^{\frac{1}{2}}$, $\chi_0 = \chi_4 = 0$, $\sigma = (\nu_\parallel/\Omega_i)^{\frac{1}{2}}(\nu_{sink} - \nu_{src})/\nu_{_{RT}}$, $\tau = \tau_i\,\nu_{_{RT}}\Omega_i^{\frac{1}{2}}/\nu_\parallel^{\frac{3}{2}}$, and $D = \nu_{_{RT}}\,(D_{e,i} + D_{e,n})/(\rho_s^2\nu_\parallel^{\frac{3}{2}}\Omega_i^{\frac{1}{2}})$.

Viscosity regime corresponds to $\chi_4 = 1$, $\chi_0 = \chi_{2_\parallel} = \chi_{2_\perp} = \sigma = 0$, $\tau = \tau_i\,\rho_s^2\Omega_i/\eta_i$, and $D = (D_{e,i} + D_{e,n})/\eta_i$.

Equations (6) and (7) are numerically solved in all above regimes. We used the method of lines, with a finite difference discretization of the spatial variables x and y, with 32×32 points. We set to zero the plasma source and sink, as well as the collision frequency with the neutrals. The initial condition was adopted as $\phi\,(t=0) = 0$, and

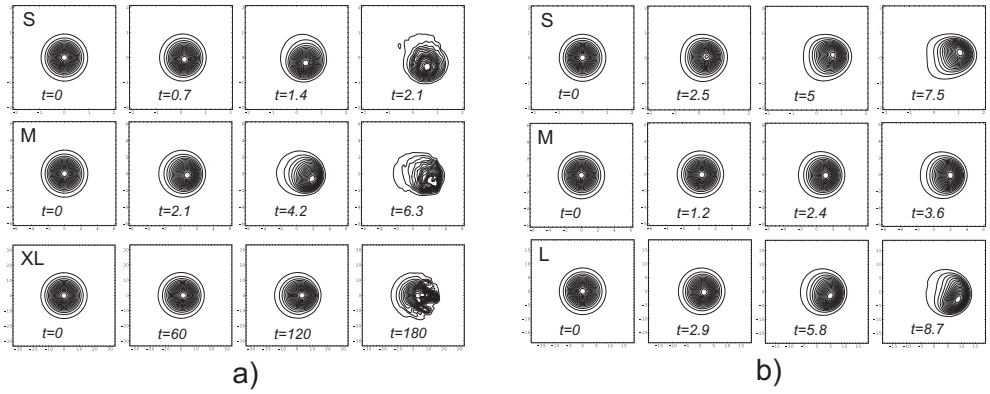

Figure 2: a) The effect of the finite ion temperature in the **sheath connected** regime, in the vicinity of the wall of the vessel. We used $D = 10^{-3}$, $\chi_0 = 1$, $\chi_{2_\perp} = \chi_{2_\parallel} = \chi_4 = \gamma = \sigma = 0$, with $\tau = 1, 5$ and 5 for the S, M, and XL structures. b) The effect of the ion temperature in the **sheath connected** regime. We used $D = 10^{-3}$, $\chi_4 = 1$, $\chi_2 = \chi_{2_\perp} = \chi_{2_\parallel} = \gamma = \sigma = 0$, while $\tau = 2, 5$, and 12 for the S, M, and L structures.

$n_i\,(t=0) = n_{i_{SOL}} + n_{i_{max}} \exp\left[-(x^2+y^2)/L_\perp^2\right]$, which corresponds to a Gaussian blob, injected at $t = 0$, into a background SOL plasma whose density is $n_{i_{SOL}}$. We studied four characteristic blob sizes, labelled as S (Small, $L_\perp = 0.5$), M (Medium, $L_\perp = 1.5$), L (Large, $L_\perp = 4.5$), and XL (eXtra Large, $L_\perp = 8.5$). The peak blob density was taken five times larger than the background plasma density, $n_{i_{max}} = 5\, n_{i_{SOL}}$. The coupling with nonlinear drift modes introduces a fundamentally different behavior compared to its 2-D counterparts (Jovanović et al., 2007). Due to the presence of the resistive drift drive,the collapse of the oblique blobs in the lateral direction is followed by a clockwise rotation and radial propagation, see Fig. 1 a). The finite ion temperature effects in the *inertial*, *sheath connected* and *viscous regime*, are shown in Figs. 1 a), 2 a) and 2 b), respectively. The symmetry breaking introduces a poloidal component in the blob velocity, while its overall stability properties and the speed are not affected qualitatively.

References

Jovanović, D., de Angelis, U., Fedele, R. and Pegoraro, F.: 2007, *Phys. Plas.*, **14**, 3704.
Krasheninnikov, S. I., D'Ippolito, D. A. and Myra, J. R.: 2008, *J. Plasma Phys.*, **74**, published online, doi: 10.1017/S0022377807006940.

Publ. Astron. Obs. Belgrade No. 84 (2008), 451 - 454 *Contributed Paper*

A REVIEW ON THE EFFECT OF FINITE TARGET THICKNESS IN ABLATIVE RAYLEIGH TAYLOR-INSTABILITY

Á. DE ANDREA GONZÁLEZ

Departamento de Física. Escuela Politécnica Superior.
Universidad Carlos III de Madrid. Av. Universidad 30. 28911 Leganés (Madrid), Spain
E–mail: aandrea@fis.uc3m.es

Abstract. We consider the ablative Rayleigh-Taylor instability at a steady ablation front of a finite thickness target. In the present work a more accurate prediction is obtained based on the sharp boundary model (SBM). One the advantages of the simple model here presented is that offers the possibility of analyzing the effect of finite target thickness, which is stabilizing for long-wavelength modes. On the other hand, it shows that the cut-off wave number k_c is independent of target thickness.

1. INTRODUCTION

In Inertial Confinement Fusion (ICF), a cold target material is accelerated by a hot, low density plasma (Lindl 1995). The surface (front ablation) between the heavy and light materials is Rayleigh-Taylor (RT) unstable similar to the interface between two fluids of constant densities ρ_2 and ρ_1 subject to a gravitational field $\vec{g}$ pointing toward the lighter fluid ρ_1 (Rayleigh 1883, Taylor 1950). The Rayleigh–Taylor instability (RTI) in ICF is one of the principal physical processes inhibiting the achievement of inertial fusion. In this work, the linear stability analysis of accelerated ICF targets is carried out including the finite thickness effect.

2. LINEAR STABILITY ANALYSIS

In This section, we study the RTI in a finite thickness target. We consider the following planar configuration: the heavier target material of constant density ρ_2 (heavy-fluid region, $-d < y < 0$) is accelerated against the lighter blow-off plasma of constant density ρ_1 (blow-off region, $y > 0$). The acceleration $\vec{g}$ is pointing in the y direction $\vec{g} = g\ \vec{u}_y$. In order to determine the growth rate of unstable perturbations, one needs to solve the hydrodynamic equations describing mass, momentum and energy conservation. We use one-fluid equations in the frame moving with the unperturbed ablation front (Piriz et al. 1997):

$$\frac{\partial \rho}{\partial t} + \vec{\nabla} \cdot (\rho \vec{v}) = 0$$
$$\rho \frac{\partial \vec{v}}{\partial t} + \rho \left(\vec{v} \cdot \vec{\nabla} \right) \vec{v} = -\vec{\nabla} p + \rho \vec{g}$$
$$\frac{\partial}{\partial t} \left[\rho \left(\frac{v^2}{2} + \varepsilon \right) + \vec{\nabla} \cdot \left[\rho \, \vec{v} \left(\frac{v^2}{2} + \frac{5}{3} \varepsilon \right) + \vec{Q} \right] \right] = \rho \vec{v} \cdot \vec{g}$$
$$\vec{Q} = -\kappa_D \vec{\nabla} \varepsilon$$

Where we have assumed that the fluid is an ideal gas and ρ, $\vec{v}$, and ε are, respectively, the density, the velocity, and the specific internal energy of the fluid. Moreover, $p = (2/3)\,\rho\varepsilon$ is the fluid pressure, Q is the energy flux corresponding to a diffusive process of transport, and $\kappa_D = \chi \varepsilon^n$ is the thermal conductivity, where for electronic heat conduction in laser fusion n=5/2. The stability of such an equilibrium is investigated by imposing a small perturbation of the interface between the two fluids in the following form: $\psi = \psi_o + \delta\psi$, where ψ_o is the unperturbed value and $\delta\psi << \psi_o$ is a small perturbation $\delta\psi \prec \exp(\gamma t + qy + ikx))$; q represents the longitudinal wave number and γ is the instability growth rate.

2. 1. RESULTS AND DISCUSSION

The growth rate of the ablative RT can be calculated using a sharp boundary model (SBM). We perform a first-order perturbation expansion on the above equations. After a tedious but simple algebra (see e.g. Piriz et al. 1997), we obtain the following dispersion relation that includes the effect of finite shell in terms of the density jump r_D

$$\gamma^2 + \frac{k v_2 \left[3 + \coth(kd) \right]}{r_D + \coth(kd)} \gamma + kg \left(\frac{k \; {v_2}^2}{g \; r_D} - A_T \right) \left[\frac{1 + r_D}{r_D + \coth(kd)} \right] = 0$$

Where v_2 is the fluid speed ahead the front (ablation speed) and A_T is the Atwood number: $A_T = \frac{1 - r_D}{1 + r_D}$

The former equation can be easily solved for obtaining the instability growth rate:

$$\gamma = \sqrt{\left\{ \frac{k v_2}{2} \left[\frac{3 + \coth(kd)}{r_D + \coth(kd)} \right] \right\}^2 - kg \left(\frac{k \; {v_2}^2}{g \; r_D} - A_T \right) \left[\frac{1 + r_D}{r_D + \coth(kd)} \right]} - \frac{k v_2}{2} \left[\frac{3 + \coth(kd)}{r_D + \coth(kd)} \right]$$

We can also find the following analytical expression for the cut-off wave number k_c:

$$\frac{k_c {v_2}^2}{g} = \frac{(1 - r_D)\, r_D}{1 + r_D}$$

This one is exactly the result obtained for the semi-infinite target model: the cut-off wave number is invariant to target thickness.

It may be interesting, from a qualitative point of view, taking the limit $kd >> 1$, where, $\coth(kd) \to 1$. Our model reduces to semi-infinite target one, and the relation dispersion from Piriz is recovered:

$$\gamma = \sqrt{\left(\frac{2kv_2}{r_D+1}\right)^2 - kg\left(\frac{k\ {v_2}^2}{g\ r_D} - A_T\right)} - \frac{2kv_2}{r_D+1}$$

By introducing a simple corona model based on diffusive process of energy transport, the parameter r_D as a function of the Froude number results (Piriz et al. 1997, Betti et al. 1996):

$r_D = \left(\frac{4\alpha}{5F_r}\right)^{\frac{2}{5}}$, where α is the dimensionless parameter $\alpha = \frac{k\ {v_2}^2}{g}$. We can plot the dispersion relations which are shown in figures 1-2, for Fr=5. The solid lines plotted are the results that would be obtained with our model (finite thickness target); dashed lines are the results from Piriz model (semi-infinite target). The dimensionless parameter kd is varied as indicated in the figures for kd=1 and kd=2. The solid line (figure 1) show a considerable reduction of the growth rate due to finite thickness for long-wavelength perturbations. Also notice that the cut-off wave number is the same in both models. Therefore, the finite thickness does not affect the cut-off wave number.

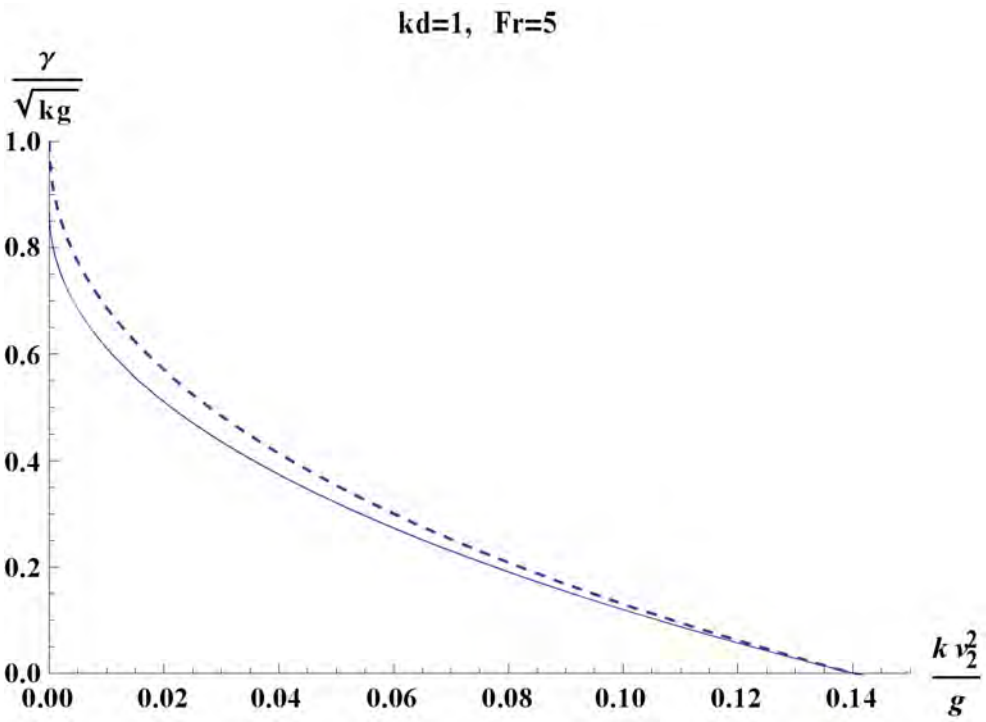

Figure 1: Dimensionless normalized growth rate versus dimensionless normalized wave number. Dashed line corresponds to the Piriz's results; solid line corresponds to our model. Finite-thickness corrections are most important for long-wavelength perturbations.

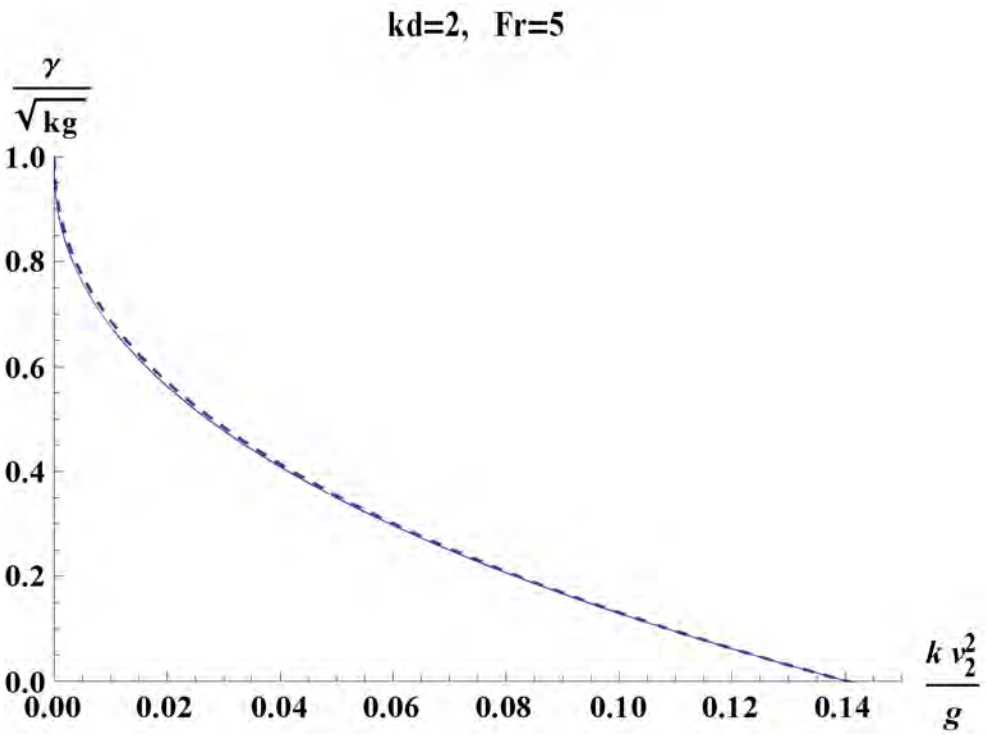

Figure 2: Dimensionless normalized growth rate versus dimensionless normalized wave number. Dashed line corresponds to the Piriz's results; solid line corresponds to our model. For kd$\geq$ 2 and Froude number Fr=5 there is an excellent agreement with semi-infinite target model.

References

Betti, R., Goncharov, V., Mc-Crory, R., Sorotokin, P., Verdon, C.: 1996, *Phys. Plasmas*, **3**, 1402.
Lindl, J.: 1995, *Phys. Plasmas*, **2**, 3933.
Lord Rayleigh: 1883, *Proc. London Math. Soc.*, **14**, 170.
Piriz, A. Sanz, J. Ibáñez, L.: 1997, *Physics Plasmas*, **4** (4), 1117.
Taylor, G.: 1950, *Proc. Soc. London A*, **201**, 192.

Publ. Astron. Obs. Belgrade No. 84 (2008), 455 - 458 *Contributed Paper*

A STUDY OF AX Mon (HD 45910) KINEMATICAL PARAMETERS OF THE Fe II DENSITY REGIONS

A. ANTONIOU[1], E. DANEZIS[1], E. LYRATZI[1,2], L. Č. POPOVIĆ[3], M. S. DIMITRIJEVIĆ[3], E. THEODOSSIOU[1] and D. STATHOPOULOS[1]

[1] *University of Athens, School of Physics, Department of Astrophysics, Astronomy and Mechanics, Panepistimiopolis, Zografos 157 84, Athens - Greece*
E–mails: ananton@phys.uoa.gr, edanezis@phys.uoa.gr, elyratzi@phys.uoa.gr, mail@nikolaidis.info

[2] *Eugenides Foundation, 387 Sygrou Av., 17564, Athens, Greece*

[3] *Astronomical Observatory of Belgrade, Volgina 7, 11160 Belgrade, Serbia*
E–mails: lpopovic@aob.bg.ac.yu, mdimitrijevic@aob.bg.ac.yu

Abstract. The UV spectrum of AX Mon (HD 45910) presents a series of complex structure spectral lines, that present SACs or DACs. In this paper, using the GR model, we study the complex profile of Fe II spectral lines and we calculate the relation of some physical parameters with the excitation potential.

1. INTRODUCTION

Fleming (1898) was the first that noted that AX Mon (HD 45910=BD+5°, 1267=SAO 13974, a=6^h 27^m 52^s, δ=+5°, 54′,1 (1950), V=6,59-6,88 mag) had bright hydrogen lines. Merrill (1923) and Plaskett (1923) noted a variability of the spectrum. The most pronounced changes discovered in photographic studies were the occasional appearance of a shell spectrum of ionized metals and variable hydrogen lines with one or more components.

Merrill (1952) discovered the binary nature of AX Mon. He derived an orbit for the late-type star with a period of 232 days. Cowley (1964) concluded that the system consists of a rapidly rotating B3nn star and a somewhat fainter K0 giant and that the rotational velocity of the early-type star is 345 km/s.

Danezis et al. (1991) studied a series of Fe II lines with classical method and indicated the existence of three satellite components with radial velocities of -75, -260 and +10 km/s. These values did not present any variation with the excitation potential.

In this paper we study a series of Fe II lines with GR model (Danezis et al. 2007), in order to verify the results found by Danezis et al. (1991), as well as the accuracy of GR model. Additionally, we present the radial, rotational and random velocities, the FWHM and the absorbed energy of a group of Fe II lines, as a function of their excitation potential between 0.08 and 4.75 eV.

Table 1: The λ_{lab} of the Fe II spectral lines and the respective excitation potential

λ_{lab} (Å)	Excitation Potential (eV)
1558.542	0.35
1646.187	1.07
1673.462	1.96
1679.388	2.02
1720.042	1.72
1731.038	2.27
1880.976	2.57
2237.577	4.75
2445.559	2.69
2607.086	0.08
2767.500	3.23
2858.340	3.75

2. OBSERVATIONAL DATA

In Table 1 we present the studied Fe II spectral lines, taken with IUE, and the respective excitation potential.

3. RESULTS AND DISCUSSION

In Figure 1, we give as an example the fit of the λ 2607.086 Å Fe II spectral line. We can see that the observed complex structure can be explained with SACs phenomenon.

In Figure 2 we present the variation of the radial velocities of the studied group of Fe II lines as a function of the excitation potential (left). As we can see the radial velocities stay nearly constant as a function of I.P. We detected three levels of radial velocities. The first level has values about -260 km/s (circle), the second one has values about -125 km/s (open square) and the third one has values about -18 km/s (triangle). We compare our results with the results found by Danezis et al. (1991) (right). As we can see the results are almost the same. This fact verifies the previous results, as well as the accuracy of GR model. Specifically, we verify the number of satellite components, their radial velocities, and the relation between the radial velocities of the Fe II lines with their excitation potential.

In Figure 3 we present the variation of the rotational and the random velocities of the studied group of Fe II lines as a function of the excitation potential. As the radial velocities, the random velocities stay also nearly constant as a function of I.P. The values of the rotational velocities (left) for all SACs are between 20 and 60 km/s. We detected three levels of the random velocities of the ions (right). The first level has values about 115 km/s (open circle), the second one about 70 km/s (square) and the third one about 35 km/s (triangle).

In Figure 4 we present the variation of the Full Width at Half Maximum (FWHM in Å) of the studied group of Fe II lines as a function of the excitation potential. We also detected three levels of values of the FWHM. The first level has values about 2 Å, the second one about 1.3 Å and the third one about 0.6 Å.

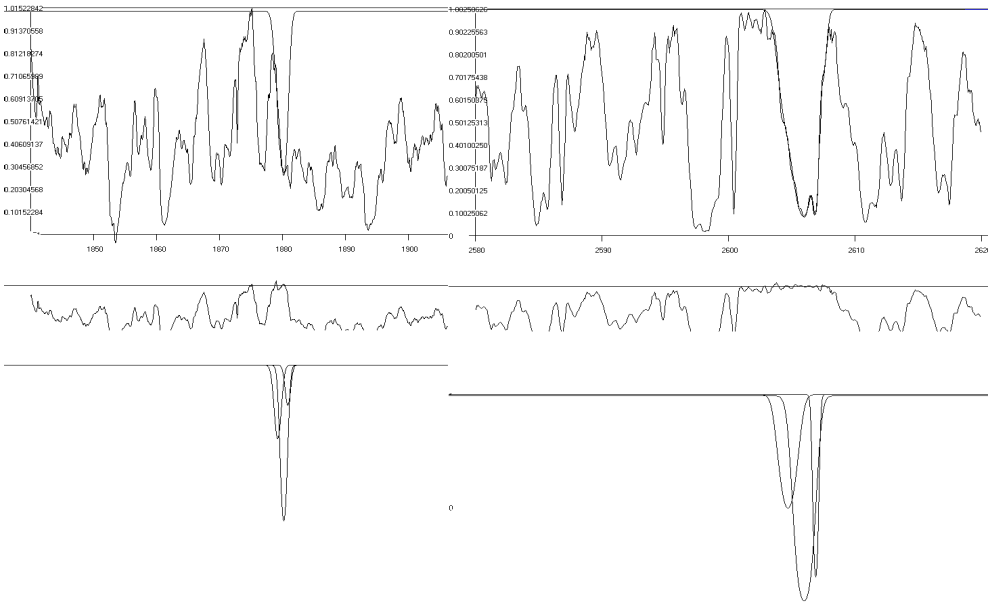

Figure 1: Best fit of the λ 1880.976 Å (left) and λ 2607.086 Å Fe II (right) spectral line. We can explain the complex structure of these lines as a DACs or SACs phenomenon. Below the fit one can see the analysis (GR model) of the observed profile to its SACs.

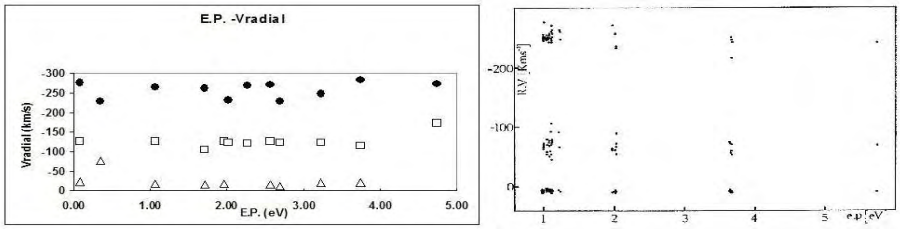

Figure 2: Radial velocities of the studied group of Fe II spectral line as a function of the excitation potential (E.P.) that result from this study (left), compared with the results deriving from the study of Danezis et al. (1991) (right).

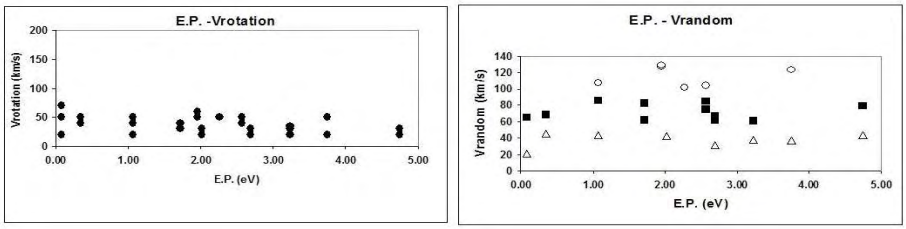

Figure 3: Rotational (left) and random (right) velocities of the studied group of Fe II spectral line as a function of the excitation potential (E.P.).

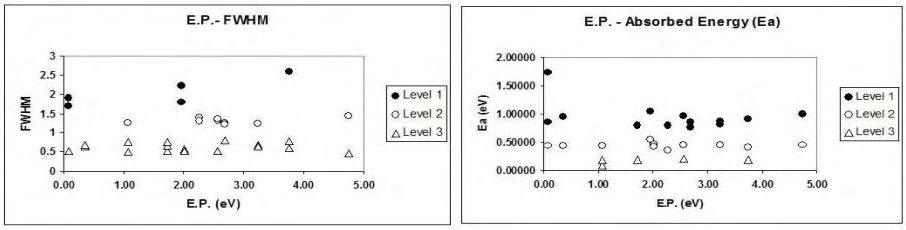

Figure 4: Full Width at Half Maximum (FWHM) and Absorbed Energy (Ea in eV) of the studied group of Fe II spectral line as a function of the excitation potential (E.P.).

Finally, in Figure 5 we present the variation of the absorbed energy (Ea in eV) of the studied group of Fe II lines as a function of the excitation potential. Also here we found three levels of absorbed energy. The first level has values about 1 eV, the second one about 0.4 eV and the third one about 0.14 eV.

Acknowledgments

This research project is progressing at the University of Athens, Department of Astrophysics, Astronomy and Mechanics, under the financial support of the Special Account for Research Grants, which we thank very much. This work also was supported by Ministry of Science of Serbia, through the projects "Influence of collisional processes on astrophysical plasma line shapes" and "Astrophysical spectroscopy of extragalactic objects".

References

Cowley, A. P.: 1964, *Astrophys. J.*, **139**, 817.
Danezis, E., Theodossiou, E., Laskarides, P.: 1991, *Astrophys. Sp. Sc.*, **179**, 111.
Danezis, E., Nikolaidis, D., Lyratzi, E., Popović, L. Č., Dimitrijević, M. S., Antoniou, A., Theodossiou, E.: 2007, *PASJ*, **59**, 827.
Fleming, W. P.: 1898, *Harvard College Obs.*, No **32**.
Merrill, P. W.: 1923, *PASP*, **35**, 303.
Merrill, P. W.: 1952, *Astrophys. J.*, **115**, 145.
Plaskett, J. S.: 1923, *PASP*, **35**, 145.

Publ. Astron. Obs. Belgrade No. 84 (2008), 459 - 462 *Contributed Paper*

THE MONOCEROS RADIO LOOP: TEMPERATURE AND BRIGHTNESS

V. BORKA-JOVANOVIĆ[1] and D. UROŠEVIĆ[2]

[1] *Laboratory of Physics (010), Vinča Institute of Nuclear Sciences, P. O. Box 522, 11001 Belgrade, Serbia*
E–mail: vborka@vin.bg.ac.yu

[2] *Department of Astronomy, Faculty of Mathematics, University of Belgrade, Studentski trg 16, 11000 Belgrade, Serbia*

Abstract. In this article we estimated the average brightness temperatures and surface brightnesses of Monoceros radio loop at 1420, 820 and 408 MHz. It is possible to make new estimation for distance to this loop using new derived brightnesses.

1. INTRODUCTION

It is well known that some radio spurs can be joined into small circles. The set of spurs which form the same small circle is called a loop. The Monoceros filamentary loop nebula, the shell source of radio emission, was suggested to be a supernova remnant (SNR) by Davies 1963 on the basis of 237 MHz observations. The Monoceros loop was suspected already by Davies 1963 to be a SNR, while Gebel & Shore 1972 developed this idea into a more detailed study. It was considered as an object similar to major loops when Spoelstra 1973 included it in his study of galactic loops as supernova remnants expanding in the local galactic magnetic field.

Graham et al. 1982 found that the constellation of Monoceros is remarkably rich in extended Galactic radio sources. Large parts of it have been mapped in the radio continuum over a wide range of frequencies. Monoceros Nebula can be found in a catalog of Galactic SNRs with number G205+0.5 (Green 2004, 2006).

The aim of this paper is to calculate the average brightness temperatures and surface brightnesses of the Monoceros radio loop at 1420, 820 and 408 MHz and to study how these results are getting along with previous result (Urošević & Milogradov-Turin 1998; Milogradov-Turin & Urošević 1996) and with current theories of supernova remnant evolution. These theories predict that SNRs are non-thermal sources which are spreading inside of the hot and low density bubbles made by former supernova explosions or by strong stellar winds (see Salter 1983, McKee & Ostriker 1977 and references therein).

2. ANALYSIS

2. 1. DATA

The radio continuum surveys at 1420 MHz (Reich & Reich 1986), 820 MHz (Berkhuijsen 1972) and 408 MHz (Haslam et al. 1982) are used as the basic source of data in this paper. The data were obtained from the 1420-MHz Stockert survey (Reich & Reich 1986), the 820-MHz Dwingeloo survey (Berkhuijsen 1972) and the 408-MHz all-sky survey (Haslam et al. 1982). The angular resolutions are $35'$, $1°.2$ and $0°.85$, respectively. The effective sensitivities are about 50 mK T_b (T_b is for an average brightness temperature) at 1420 MHz, 0.20 K at 820 MHz and about 1.0 K at 408 MHz. These data are available on MPIfR's Survey Sampler ("Max-Planck-Institut für Radioastronomie", Bonn). This is an online service (http://www.mpifr-bonn.mpg.de/survey.html), which allows users to pick a region of the sky and obtain images at a number of wavelengths.

2. 2. METHOD

The area of Monoceros loop is enclosed with brightness temperature contours (see Figure 1). These contour lines correspond to the minimum and maximum brightness temperatures which define its borders. A more complete description of method of calculation is given in Borka (2007) and Borka et al. (2008). The Galactic longitude and latitude intervals for spurs belonging to Monoceros loop are the following: l = [210°,200°], b = [-6°,5°].

3. RESULTS AND CONCLUSIONS

For deriving temperatures over the Monoceros loop, the areas used for the individual spurs were not defined with respect to their best-fit circles, but they were obtained from the radio continuum maps. The areas over which an average brightness temperature is determined at each of the three frequencies are taken to be as similar as possible within the limits of measurement accuracy. However, some differences between these areas still remain and we think that the major causes of differing borders between the three frequencies are small random and systematic errors in the calibrated data. The surface brightnesses of SNRs must be above the sensitivity limit of the observations and must be clearly distinguishable from the Galactic background emission (Green 1991). Therefore, the data from the fainter parts of the loops (which are very low - surface - brightness SNRs) are not taken into account because it is very difficult to resolve them from the background. On the other hand, this would significantly reduce brightnesses of entire loop and there is a general trend that fainter SNRs tend to be larger (Green 2005). For evaluation brightness temperatures over the spurs we had to take into account background radiation (Webster 1974). Borders enclosing the spurs are defined to restrict the spur and its background. For the method of calculation see Borka (2007).

The loops are SNRs which material is spreading inside of bubbles of low density, which are made by former SNR explosions or by strong stellar winds (Salter 1983; McKee & Ostriker 1977 and references therein). Shell type supernova remnants are believed to be particle accelerator to energy up to a few hundred TeV, and it is shown that Monoceros loop is a good candidate for acceleration of particles (Fiasson et al. 2007).

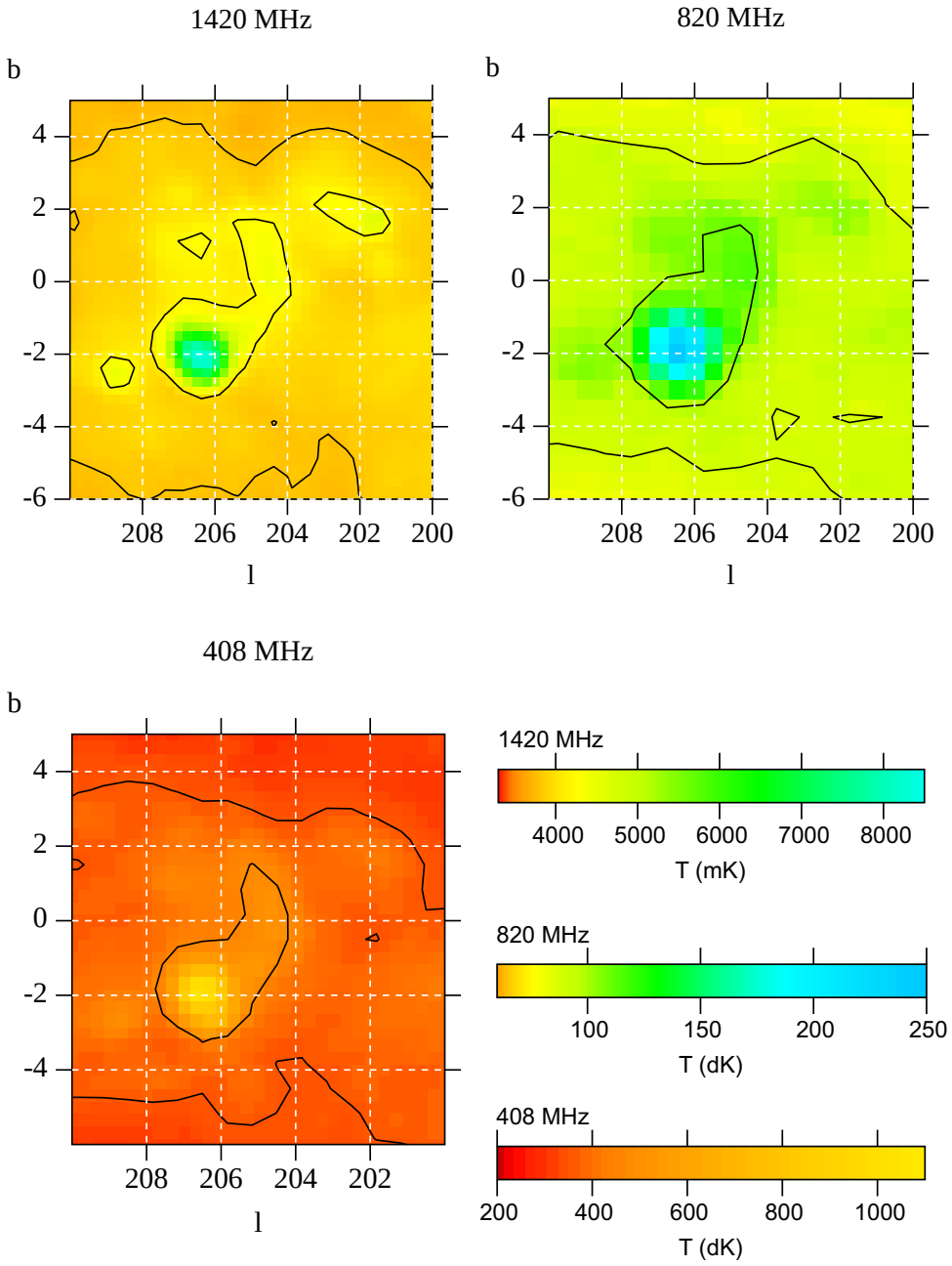

Figure 1: The area of Monoceros loop at 1420, 820 and 408 MHz, showing contours of brightness temperature. The two contours plotted represent the temperatures T_{min} and T_{max} in K, as given in Table 1. This radio loop has position: l = [210°,200°]; b = [-6°,5°].

Table 1: Temperatures and brightnesses of Monoceros radio loop at 1420, 820 and 408 MHz.

frequency (MHz)	temperature limits T_{min}, T_{max} (K)	temperature (K)	brightness (10^{-22} W/(m^2 Hz Sr))
1420	3.8, 4.2	0.18 ± 0.05	1.09 ± 0.30
820	8.8, 10.7	0.90 ± 0.20	1.85 ± 0.40
408	36, 47	5.15 ± 1.0	2.63 ± 0.50

In this paper we calculated the brightness temperatures and surface brightnesses of the Monoceros radio loop at 1420, 820 and 408 MHz. For 820 and 408 MHz frequencies it is the first time that the brightness temperature of Monoceros loop is calculated from the experimental data, and for frequency of 1420 MHz we sample it in much more points (more than 1 000 points) then in previous papers (95 points) (Urošević & Milogradov-Turin 1998, Milogradov-Turin & Urošević 1996) and they are derived using different method. The temperature of this radio loop at 1420 MHz is in good agreement with the result for temperature from papers (Urošević & Milogradov-Turin 1998). For the distance, mean optical velocity suggests 0.8 kpc, and low frequency radio absorption suggests 1.6 kpc (Graham et al. 1982, Green 2006). With new derived brightnesses, it is possible to calculate new diameters and distances to this loop at the three frequencies: 1420, 820 and 408 MHz and then do estimate some average distance. Our analysis indicates that Monoceros radio loop emission is in good agreement with current theories of supernova remnant evolution.

References

Berkhuijsen, E. M.: 1972, *A&AS*, **5**, 263.
Berkhuijsen, E. M.: 1973, *A&A*, **24**, 143.
Borka, V.: 2007, *MNRAS*, **376**, 634.
Borka, V., Milogradov-Turin, J., Urošević, D.: 2008, *Astron. Nachr.*, **329**, 397.
Davies, R. D.: 1963, *Observatory*, **83**, 172.
Fiasson, A., Hinton, J. A., Gallant, Y., Marcowith, A., Reimer, O., Rowell, G. (for the H. E. S. S. Collaboration): 2007, *arXiv: astro-ph/0709.2550.*
Gebel, W. L., Shore, S. N.: 1972, *Ap. J.*, **172**, L9.
Graham, D. A., Haslam, C. G. T., Salter, C. J., Wilson, W. E.: 1982, *A&A*, **109**, 145.
Green, D. A.: 1991, *PASP*, **103**, 209.
Green, D. A. : 2004, *Bull. Astron. Soc. India*, **32**, 335.
Green, D. A.: 2005, *Mem. S.A.It*, **76**, 534.
Green, D. A.: 2006, A Catalogue of Galactic Supernova Remnants (2006 April version), Cavendish Laboratory, Cambridge, UK.
Haslam, C. G. T., Salter, C. J., Stoffel, H., Wilson, W. E.: 1982, *A&AS*, **47**, 1.
McKee, C. F., Ostriker, J. P.: 1977, *ApJ*, **218**, 148.
Milogradov-Turin, J., Urošević, D.: 1996, *Publ. Astron. Obs. Belgrade*, **54**, 47.
Quigley, M. J. S., Haslam, C. G. T.: 1965, *Nat*, **208**, 741.
Reich, P., Reich, W.: 1986, *A&AS*, **63**, 205.
Salter, C. J.: 1983, *Bull. Astron. Soc. India*, **11**, 1.
Spoelstra, T. A. Th.: 1973, *A&A*, **24**, 149.
Urošević, D., Milogradov-Turin, J.: 1998, *Serb. Astron. J.*, **157**, 35.
Webster, A. S.: 1974, *MNRAS*, **166**, 355.

Publ. Astron. Obs. Belgrade No. 84 (2008), 463 - 466 *Contributed Paper*

THE VERY BROAD LINES IN THE UV SPECTRA OF HOT EMISSION STARS - A POSSIBLE EXPLANATION

E. DANEZIS[1], E. LYRATZI[1,2], L. Č. POPOVIĆ[3],
A. ANTONIOU[1] and M. S. DIMITRIJEVIĆ[3]

[1] *University of Athens, Faculty of Physics Department of Astrophysics, Astronomy and Mechanics, Panepistimioupoli, Zograhou 157 84, Athens, Greece*
E–mails: edanezis@phys.uoa.gr, elyratzi@phys.uoa.gr, ananton@phys.uoa.gr

[2] *Eugenides Foundation, 387 Sygrou Av., 17564, Athens, Greece*

[3] *Astronomical Observatory of Belgrade, Volgina 7, 11160 Belgrade, Serbia*
E–mails: lpopovic@aob.bg.ac.yu, mdimitrijevic@aob.bg.ac.yu

Abstract. In some cases, the UV spectral lines of hot emission stars and quasars have very large widths that can not be explained as the consequence of rotational or random velocities. In this paper we present a new idea to explain this phenomenon.

1. INTRODUCTION

In the UV spectra of some hot emission stars and quasars (Andrillat & Fehrenbach 1982, Andrillat 1983, Marlborough 1969, Poeckert & Marlborough 1979, Doazan 1970, Antoniou et al. 2008) we can detect very broad absorption or emission lines that we can not explain as rotational or random velocities of the density layers that construct these lines.

In the case of emission lines, Marlborough (1969) and Poeckert & Marlborough (1979) tried to justify the large width of the Hα line wings, with their model, according to which the envelope is rotating and expanding. They showed that the photon scattering due to electrons is able to produce significant wing broadening, meaning that a large number of photons may be scattered from the center of the emission line towards the wings. Also, Doazan (1970) suggested that the rotation of the regions that create the Hα line is not able to explain the whole observed width and there should be an additional way of acceleration. This means that the observed width is due to the combination of these two movements. She concluded that since these movements affect the width of Hβ and Hγ, we should accept that such regions exist also in the surface of the star. This means that a similar phenomenon could happen in the C IV regions.

Moreover, Doazan (1970) observed that in many Be stellar spectra the rotational velocity which corresponds to the width of the Hα emission line, is larger than the velocity which is due to the stellar rotation ($V\sin i$), when $V\sin i$ is smaller than 350 km/s. She suggested that if we accept that the only reason of the emission line

broadening is the rotation, then we should also accept that the emission layers rotate more quickly than the central star and that in many cases their rotational velocity is larger than the critical velocity. Finally, she proposed that the large width of the Hα, Hβ and Hγ emission lines is due to the movement of matter that lies in regions away from the central star. She concludes that since these movements affect the width of Hβ and Hγ, we should accept that such regions exist also in the surface of the star. However, the rotation of these regions is not able to explain the whole observed width and there should be an additional way of acceleration. This means that the observed width is due to the combination of these two movements.

In this paper we propose a new idea in order to explain the large absorption broadening, based on the theory of SACs phenomenon (see also Antoniou 2008).

2. DISCUSSION

In Figure 1 we present the analysis of SACs that construct the Hα line in the spectrum of HD 57815 (Lyratzi et al. 2005). We can detect very large absorption components with widths that can not be explained as random velocities (V_{rand}) of the ions or rotational velocity (V_{rot}) of the region that produces the spectral line. This means that if we consider V_{rot} or V_{rand} as main reasons of the line broadening, we calculate too large values for them, that are not physically accepted.

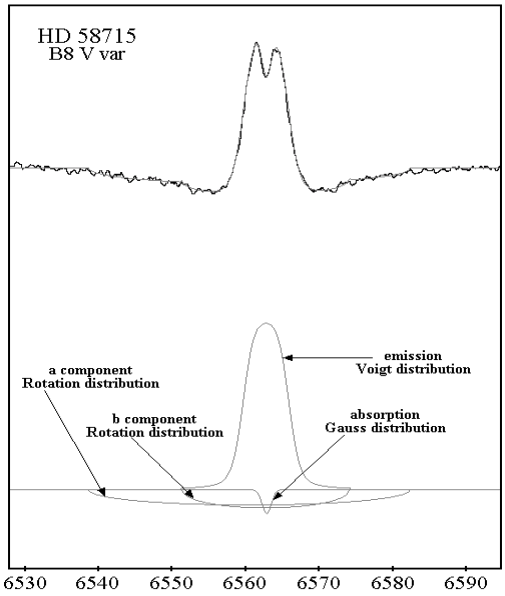

Figure 1: Very broad absorption lines of Hα in the spectrum of HD 57815. Below the fit one can see the analysis (GR model) of the observed profile to its SACs. Some of the SACs present widths which can not be interpreted as rotational or random velocities.

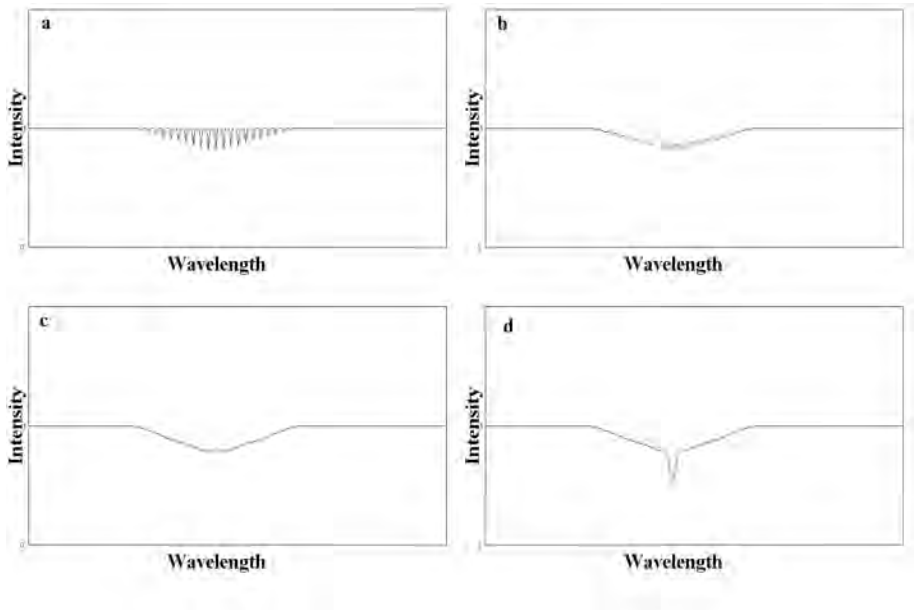

Figure 2: In (a) to (c) one can see how a sequence of lines could produce an apparent very broad absorption spectral line as an effect of SACs phenomenon. This means that when the width of each of the narrow lines is increasing (from a to c), the final observed feature looks like a single very broad absorption spectral line. In (d) one can see a combination of the apparent very broad absorption spectral line with a classical absorption line.

In Figure 2 we explain how a sequence of lines could produce an apparent very broad spectral line as an effect of SACs phenomenon.

In order to explain this very large width we propose that around a central density region that produces the main absorption lines (that may have the form of spiral streams and which have accepted values of rotational and random velocities), we can detect micro-turbulent movements, which produce narrow absorption components with different shifts. These narrow lines create a sequence of lines, on the left and on the right of the main components. The density of these lines and their widths, which are added, give us the sense of line broadening (SACs phenomenon, see Lyratzi & Danezis 2004, Danezis et al. 2007). As a result, what we measure as very broad absorption line, is the composition of the narrow absorption lines that are created by micro-turbulent effects. If this hypothesis is correct, the calculated width gives only the maximum value of the radial velocities of these very narrow components. Their appearance depends on the inclination of the rotational axis of the stellar disk.

Acknowledgments

This research project is progressing at the University of Athens, Department of Astrophysics, Astronomy and Mechanics, under the financial support of the Special

Account for Research Grants, which we thank very much. This work also was supported by Ministry of Science of Serbia, through the projects "Influence of collisional processes on astrophysical plasma line shapes" and "Astrophysical spectroscopy of extragalactic objects".

References

Andrillat, Y. & Fehrenbach, Ch.: 1982, *Astron. Astrophys. Suppl.*, **48**, 93.
Andrillat, Y.: 1983, *Astron. Astrophys. Suppl.*, **53**, 319.
Antoniou, A., Danezis, E., Lyratzi, E., Popović, L. Č., Dimitrijević, M. S.: 2008 *PASJ*, submited.
Danezis, E., Nikolaidis, D., Lyratzi, E., Popović, L. Č., Dimitrijević, M. S., Antoniou, A., Theodossiou, E.: 2007, *PASJ*, **59**, 827.
Doazan, V.: 1970, *Astron. Astrophys.*, **8**, 148.
Marlborough, J. M.: 1969, *Astrophys. J.*, **156**, 135.
Lyratzi, E. & Danezis E.: 2004, *AIP Conference Proceedings*, **740**, 458.
Lyratzi, E., Danezis, E., Nikolaidis, D., Popović, L. Č., Dimitrijević, M. S., Theodossiou E., Antoniou, A.: 2005, *MSAIS*, **7**, 114.
Poeckert, R., Marlborough, J. M.: 1979, *Astrophys. J.*, **233**, 259.

Publ. Astron. Obs. Belgrade No. 84 (2008), 467 - 470 *Contributed Paper*

MODELING OF VARIATIONS IN X-RAY EMISSION FROM ACCRETION DISKS OF ACTIVE GALAXIES

P. JOVANOVIĆ and L. Č. POPOVIĆ
Astronomical Observatory, Volgina 7, 11160 Belgrade 74, Serbia
E–mail: pjovanovic@aob.bg.ac.yu

Abstract. The observed profiles of the Fe Kα line in case of some Active Galactic Nuclei (AGN) show certain variations. In this paper we propose a model of disk emissivity variability to explain the observed Fe Kα line profiles. The disk emission was analyzed using the ray-tracing method in Kerr metric, assuming a modification of the power-law emissivity which allows us to include perturbations in disk emission. When the emissivity law is modified in such way, we find that the corresponding variations in disk emission can explain the observed Fe Kα line profiles if the line is emitted from the innermost part of the accretion disk.

1. INTRODUCTION

The most prominent feature in 3-10 keV X-ray reflection spectrum of approximately 30% of type 1 AGN is the broad Fe Kα line at 6.4 keV. The observed profiles of the Fe Kα line in case of some AGN show certain variations. For example, a narrow component of the Fe Kα line in NGC 3516 is seen to vary systematically in energy and flux at time intervals of 25 ksec (Iwasawa et al. 2004), and also in Mrk 766 (Miller et al. 2006; Turner et al. 2006), possibly in a periodic manner (Fabian, 2006). On the other hand, in the best objects where a very broad Fe Kα line is seen (e.g. MCG-6-30-15 and NGC 4051) amplitude of the line variations are considerably less than expected despite large variations in the continuum (Fabian & Vaughan, 2003; Ponti et al. 2006; Fabian, 2006).

To model the observed variability in the Fe Kα line profiles and intensities, here we consider the perturbations in the accretion disk emissivity, which is analyzed using ray-tracing method in Kerr metric (see Popović et al. 2003 and references therein).

2. A MODEL OF DISK PERTURBING REGION

Surface emissivity of the disk is usually assumed to vary with radius as a power law (e.g. Popović et al. 2003): $\varepsilon(r) = \varepsilon_0 \cdot r^q$, where ε_0 is an emissivity constant and q – emissivity index. Total observed flux is then given by (see e.g. Popović et al. 2006):

$$F_{obs}(E_{obs}) = \int\limits_{image} \varepsilon(r) \cdot g^4 \delta(E_{obs} - gE_0) d\Xi, \qquad (1)$$

where g is the energy shift due to the relativistic effects: $g = \dfrac{\nu_{obs}}{\nu_{em}}$ and the rest energy of the Fe Kα line is: $E_0^{FeK\alpha} = 6.4$ keV. $d\Xi$ is the solid angle subtended by the disk in the observer's sky.

In this paper we propose a modification of the power-law disk emissivity in order to explain the observed profiles. Here, the following emissivity law of the disk is assumed:

$$\varepsilon_1(x_p, y_p) = \varepsilon(r(x_p, y_p)) \cdot \left(1 + \varepsilon_p \cdot e^{-\left(\left(\frac{x - x_p}{w_x} \right)^2 + \left(\frac{y - y_p}{w_y} \right)^2 \right)} \right), \tag{2}$$

where where $\varepsilon_1(x_p, y_p)$ is the modified disk emissivity at the given position (x_p, y_p) of perturbing region (in gravitational radii R_g), $\varepsilon(r(x_p, y_p))$ is the power-law disk emissivity at the same position, ε_p is emissivity of perturbing region and (w_x, w_y) are its widths (also in R_g). Under assumption that perturbation is moving by speed of light c, one can calculate time $t_p\,[s]$ that corresponds to current position (x_p, y_p) using the following expression:

$$t_p\,[s] = \frac{r(x_p, y_p)\,[R_g]}{c\,[m \cdot s^{-1}]} = \frac{r_{x,y} \cdot GM_{BH}}{c^3}, \tag{3}$$

where $r_{x,y} = \dfrac{r\,(x_p, y_p)}{R_g}$, G is Newton's gravitational constant and M_{BH} is the mass of central black hole.

3. RESULTS AND DISCUSSION

For numerical simulations in case of the above disk perturbing model, we adopted the following parameters: disk inclination $i = 35^o$, inner and outer radii of the disk $R_{in} = R_{ms}$ and $R_{out} = 30\ R_g$ (where R_{ms} is the radius of marginally stable orbit), emissivity constant $\varepsilon_0 = 1$, emissivity index $q = -2.5$ and the emissivity of perturbing region $\varepsilon_p = 5$. We made simulations for different positions of perturbing region along x-axis (i.e. for $y_p = 0$) between $x_p = 8$ and 26 R_g in both, positive and negative directions. At the same time, the widths of perturbing region $w_x = w_y$ were varied between 1 and 10 R_g. The corresponding times t_p are calculated for black hole mass $M_{BH} = 1 \times 10^9 M_\odot$.

The obtained results for two different positions of perturbing region are presented in left panels of Figs. 1 and 2, and the corresponding perturbed and unperturbed profiles of the Fe Kα line are given in the right panels of the same Figs. As one can see from these Figs, the perturbing model affects the line flux in only one of "red" (Fig. 1) or "blue" (Fig. 2) spectral bands, while the other one stays nearly constant, as well as the line core. In the first case perturbation moves along positive direction of x-axis (receding side of the disk), while in the second case it moves along negative direction of x-axis (approaching side of the disk). It is even more obvious if we analyze the corresponding simulated light curves which are presented in Fig. 3. From this figure it can be seen that in the first case, displacement of perturbing region results in variations of only "red" light curve (0.1 – 6.1 keV), while in the second case, it affects only the "blue" one (6.7 – 12.8 keV), and these variations are then reflected in

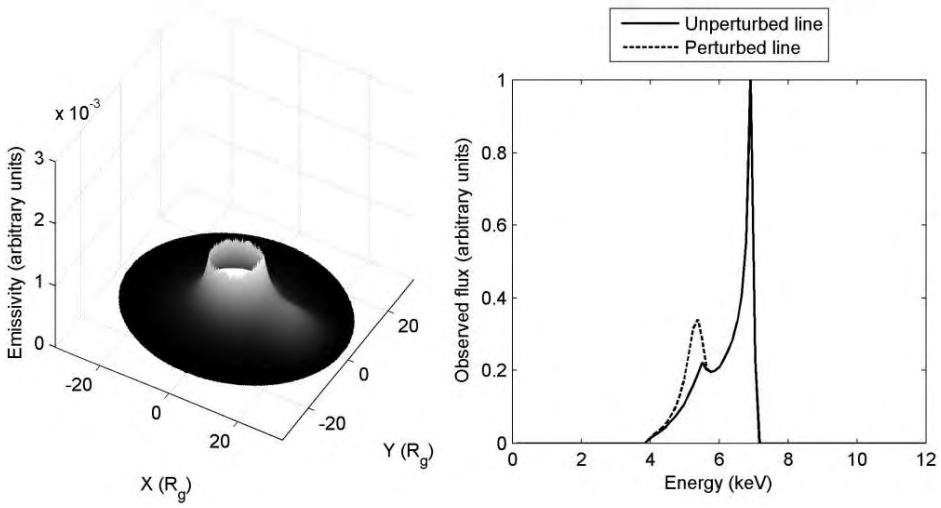

Figure 1: *Left:* shape of perturbed emissivity of an accretion disk in Schwarzschild metric for the following parameters of perturbing region: $x_p = 20\ R_g$, $y_p = 0$ and $w_x = w_y = 7\ R_g$. The values of the remaining parameters are given in §3. *Right:* the corresponding perturbed (dashed line) and unperturbed (solid line) Fe Kα line profiles.

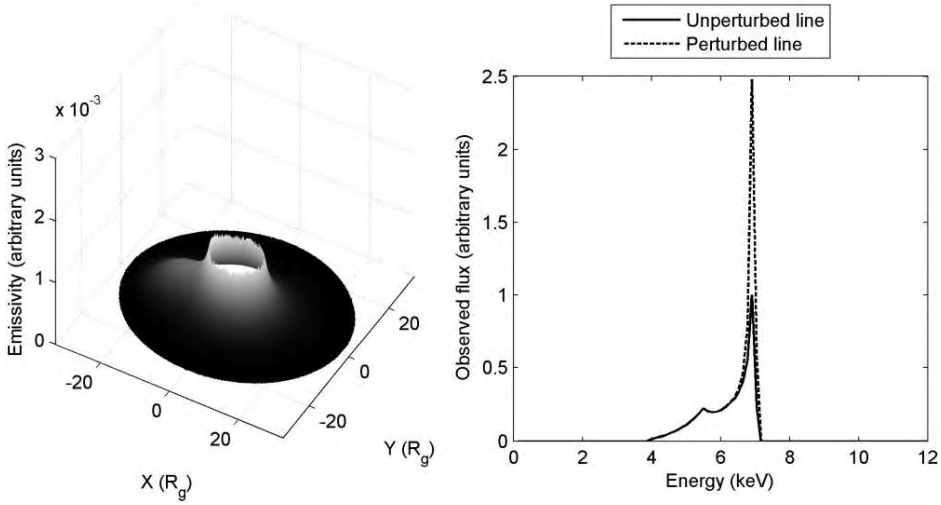

Figure 2: The same as in Fig. 1, but for the following position of perturbing region: $x_p = -20\ R_g$ and $y_p = 0$.

total line flux in 0.1 – 12.8 keV energy band. In both cases the "core" light curve (6.1 – 6.7 keV) stays almost constant. Thus, this model could satisfactorily explain the observed variations of the Fe Kα line flux. Besides, we are able to obtain the realistic durations of disk emissivity perturbations when we assume central supermassive black hole with mass $M_{BH} = 1 \times 10^9 M_\odot$.

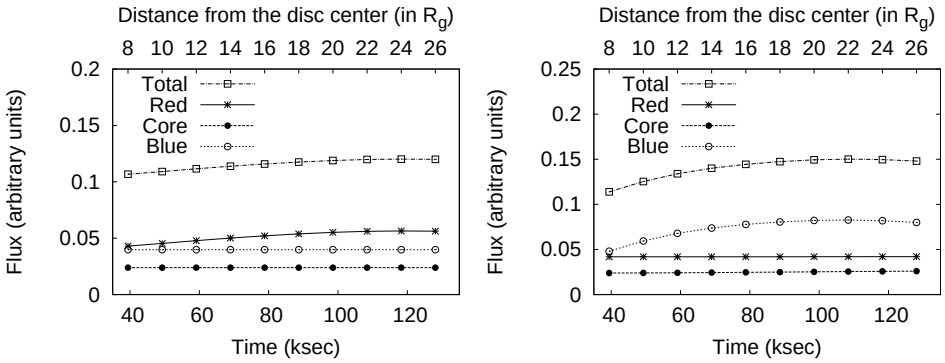

Figure 3: The simulated light curves in case of displacements of perturbing region along the positive (left panel) and negative (right panel) directions of x-axis. Light curves correspond to the following spectral bands: total flux (black) to 0.1 – 12.8 keV, "red" to 0.1 – 6.1 keV, "core" to 6.1 – 6.7 keV and " blue" to 6.7 – 12.8 keV.

4. CONCLUSIONS

Perturbations of accretion disk emissivity were analyzed using numerical simulations based on a ray-tracing method in Kerr metric from wich we can conclude the following:

(i) observed variations of the Fe Kα line flux could be caused by perturbations in the disk emissivity
(ii) a model of disk perturbing region was developed
(iii) this model affects the line flux in only one of "red" or "blue" spectral bands, while the other one stays nearly constant, as well as the line core. Thus it results in variations of only one of the "red" or "blue" light curves, and therefore, this model could satisfactorily explain the observed variations of the Fe Kα line flux
(iv) there are only small differences between the Fe Kα line flux variability in Schwarzschild and Kerr metrics for both models
(v) realistic durations of disk emissivity perturbations in both analyzed models were obtained for central black hole mass $M_{BH} = 1 \times 10^9 M_\odot$

Acknowledgements

This work has been supported by the Ministry of Science of Republic of Serbia through the project "Astrophysical Spectroscopy of Extragalactic Objects" (146002).

References

Fabian, A. C.: 2006, *AN*, **327**, 943.
Fabian, A. C., Vaughan, S.: 2003, *MNRAS*, **340**, L28.
Iwasawa, K., Miniutti, G., Fabian, A. C.: 2004, *MNRAS*, **355**, 1073.
Miller, L., Turner, T. J., Reeves, J. N., George, I. M., Porquet, D., Nandra, K., Dovciak, M.: 2006, *A&A*, **453**, L13.
Ponti, G., Miniutti, G., Cappi, M., Maraschi, L., Fabian, A. C., Iwasawa, K.: 2006, *MNRAS*, **368**, 903.
Popović, L. Č., Mediavilla, E. G., Jovanović, P., Muñoz, J. A. : 2003, *A&A*, **398**, 975.
Popović, L. Č., Jovanović, P., Mediavilla, E.G., Zakharov, A. F., Abajas, C., Muñoz, J. A. & Chartas, G.: 2006, *ApJ*, **637**, 620.
Turner, T. J., Miller, L. J., George, I. M., Reeves, J. N.: 2006, *A&A*, **445**, 59.

Publ. Astron. Obs. Belgrade No. 84 (2008), 471 - 474 *Contributed Paper*

THE BLR STRUCTURE OF NGC4151 - POSSIBLE OUTFLOW MODEL

A. KOVAČEVIĆ[1], A. I. SHAPOVALOVA[2], L. Č. POPOVIĆ[3], A. N. BURENKOV[4] and V. CHAVUSHYAN[5]

[1]*Faculty of Mathematics, Studentski trg 16, Belgrade, Serbia*

[2]*Special Astrophysical Observatory, Russia*

[3]*Astronomical Observatory, Volgina 7, Belgrade, Serbia*

[4]*Special Astrophysical Observatory of the Russian AS, Nizhnij Arkhyz, Karachaevo-Cherkesia 369167, Russia*

[5]*Instituto Nacional de Astrofísica, Óptica y Electrónica, Apartado Postal 51, CP 72000, Puebla, Pue. México, México*

Abstract. Using the 2D CCF of the Hα line of NGC 4151, we analyzed the BLR structure in this active galaxy. We found that the line wings have different response to the continuum variation that line core. This type of variation indicates an outflow model for the BLR of NGC 4151.

1. INTRODUCTION

In the central regions of active galactic nuclei (AGN) the broad emission lines (with widths more than 1000 km/s) are originated. The region where these lines are formed is so called the Broad Line Region (BLR). The BLR is assumed to be photoionized by the continuum from the accretion disk.

From the response of the BLR emission (observed in the broad lines) to the continuum variation can be used to obtain required geometrical characteristics of the BLR by constructing the velocity-delay diagrams of emission lines.

The quality of obtained results depend on homogeneousness of data set, the level of signal to noise ratio,variability of flux of an active galaxy,the length of time spans covered by observations and its sampling rate.

Velocity-delay maps were obtained by many authors (Kolatschny & Dietrich 1996, 1997; Done & Krolik 1996, Kolatshny & Bischoff 2002). However, the most of results are preliminary due to low quality of observations (low signal to noise ratio, short time spans covered by observations, sampling rate is higher than 1 day, nonhomogeneous distribution of observations, etc.).

Here we present and discuss the velocity delay map of the $H\alpha$ line in NGC4151. The aim of this paper is discuss the BLR structure of NGC 4151.

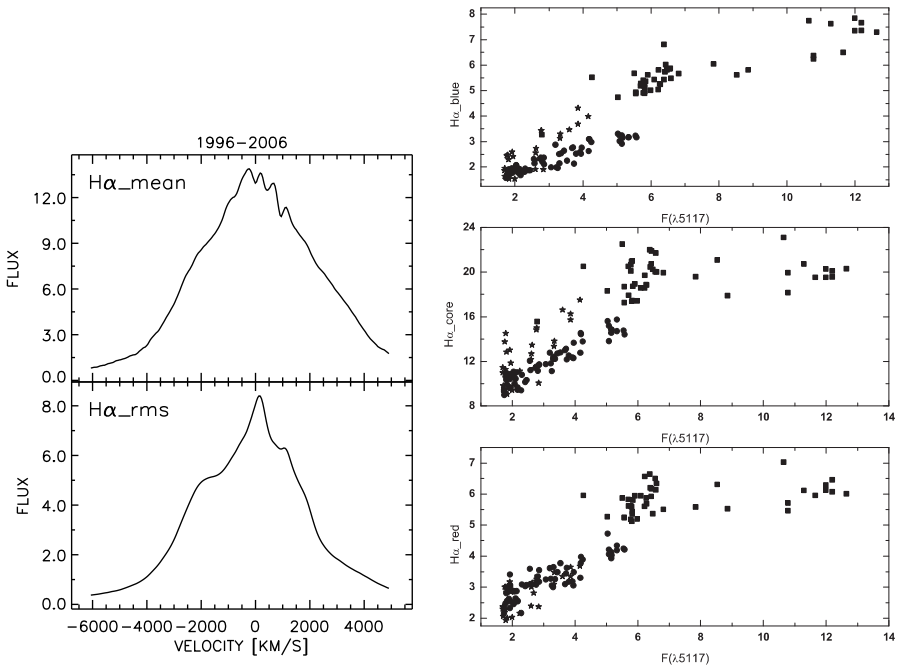

Figure 1: *Left:* The averaged and rms profiles of the broad $H\alpha$ for whole monitoring period 1996–2006; *Right*: he wings and core fluxes as a function of the continuum flux (at $\lambda = 5117$ Å) for $H\alpha$. Shapovalova et al. (2008).

2. OBSERVATIONS AND DATA ANALYSIS

We chose NGC 4151 as our target because it was subject of many monitoring campaigns as well as many authors obtain different response delays in emission lines with respect to changes in continuum (see Shapovalova et al, 2008, hereafter Paper I).

The observations and procedure of data reduction in more details is described in the Paper I and here will not be repeated. The data-set of the Hα line has 141 spectra observed between 1996 and 2006. The spectra cover wavelength range from 4000 Å to 7500 Å with resolution R=4.5-15 Å. In the most cases it was yielded S/N >50 in the continuum. The averaged $H\alpha$ profile and rms is present in Fig. 1 (left).

3. RESULTS AND DISCUSSION

In Paper I it was found that an excess line emission with the respect to a pure photoionization model during whole monitoring period. Light curves of the $H\alpha$ line core as well as $H\alpha$ line wing segments in function of the optical continuum ($\lambda = 5117$ Å) are shown in Fig. 2 (right). As it is shown, the flux in the wings and core of the line express a very similar flow during the whole period. Based on the similarity of line profiles, we found three characteristic profiles during the period 1996-2006. In the first period (1996-1999, JD=(2450094.466-2451515.583), where the $H\alpha$ line was very intense, a red asymmetry and a shoulder in the blue wing were present. In the

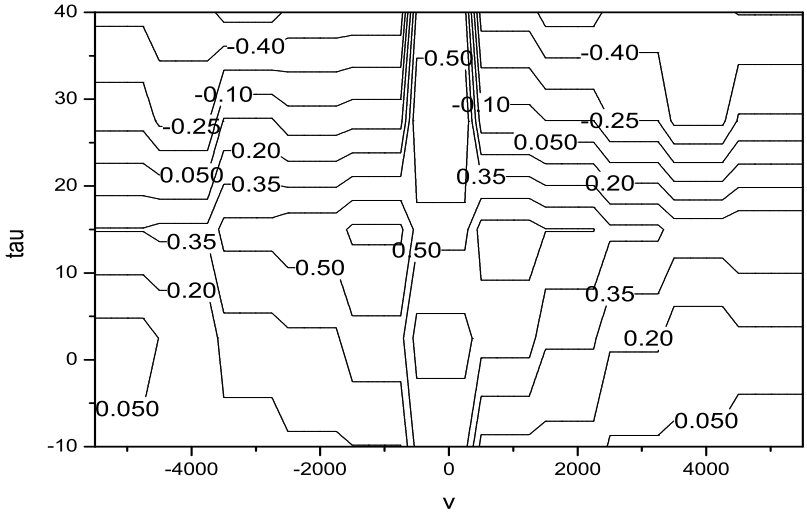

Figure 2: The 2-D CCF(τ, v) shows the correlation of the $H\alpha$ line profile with core variations as a function of velocity and time delay.

second period (2000-2001, JD=2451552.607-2452238.000), the $H\alpha$ was weaker and the shoulder in the blue wing is smaller and a shoulder in the red part is present. From 2002 to 2006 (third period, JD=2452299.374-2453846.403), the line showed a blue asymmetry, and a shoulder in the red part was dominant in the line profiles.

As a description of the $H\alpha$ line vs. continuum variation, the CCF analysis was carried out for the full data set which covers the whole monitoring period from 1996 to 2006 and the three periods mentioned above. The time lags for $H\alpha$ in the whole period are 5 days, but they were different in the three subperiods. In the first and in the third period, the time lags were much smaller (from 0.6 to 1.1 days) than in the second period (11 and 21 days).

In Paper I we found that the BLR is very complex so we generated the light curves from various $H\alpha$ velocity segments ($\Delta v = 1000$ km s^{-1}).

Also, we computed cross-correlation functions (CCF) of all $H\alpha$ line segment light curves with the (6573-6595) Å core light curve (for CCF calculation details see Paper I). The light curve of the outer wings segments (for whole monitoring period) show the same time delay 5 days.

Having in mind this, we derived from the cross-correlation functions a delay map of the $H\alpha$ line segments ($\Delta v = 1000$ kms^{-1}) for the first subperiod which is shown in Fig. 2. This 2-D CCF shows some clear trends. The outer red and blue $H\alpha$ line wings respond almost symmetrically to core variations with a delay of about 5 days only. Towards the line center the delay is getting systematically shorter until up to about 0 days at the line center.

The 2-D CCF(τ, v) has similar mathematical characteristics as a 2-D response function (Welsh 2001). Our observed velocity-delay map for core vs line follows some patterns predicted by model calculations for continuum vs line (Perez et al. 1992;

Welsh & Horne 1991; O'Brien et al. 1994). For example, both $H\alpha$ line wings show the largest delay (around 15 days) with respect to the core ($\sim$ 0 days) and react nearly simultaneously (it is specific for radial inflow or outflow motions models).

As it can be seen, short delays are observed at the center which is in contrary to the spherical BLR models with chaotic virial velocity field or randomly oriented Keplerian orbits. On the other hand, a Keplerian disk BLR model cannot describe exactly the observed velocity-delay pattern, since in this model we expect the faster response of both line wings compared to the center.

A slightly faster and stronger response of the red line wing vs the blue wing, as seen in Fig. 2, follows the disk-wind model of the BLR of Chiang & Murray (1996).

The correlation of the red [+500; +2000] kms^{-1} wing with the core is about 9% stronger than that of the blue wing [−2000; −500] kms^{-1} (Fig. 2). The blue wing (v = [−4000; −3000] kms^{-1}) lags the red wing (v = [+3000; +4000] kms^{-1}) by 2 days.

4. CONCLUSION

We performed 2D-CCF analysis of the $H\alpha$ vs. continuum variation, in order to investigate the BLR strucutre in NGC4151. We found that different lags for line wings and core corresponds to the outflow model for the BLR of NGC 4151.

Acknowledgements

This work has been supported by the Ministry of Science of Republic of Serbia through the project "Astrophysical Spectroscopy of Extragalactic Objects" (146002).

References

Chiang, J., Murray, N.: 1996, *Astrophys. J.*, **466**, 704.
Done, C., Krolik, J. H.: 1996, *Astrophys. J.*, **463**, 144.
Kollatschny, W., Bischoff, K.: 2002, *Astron. Astrophys.*, **386**, L19.
Kollatschny, W., Dietrich, M.: 1996,*Astron. Astrophys.*, **314**, 43.
Kollatschny, W., Dietrich, M.: 1997, *Astron. Astrophys.*, **323**, 5.
O'Brien, P. T., Goad, M. R., Gondhalekar, P. M.: 1994, *MNRAS*, **268**, 845.
Perez, E., Robinson, A., de la Fuente, L.: 1992, *MNRAS*, **256**, 103.
Shapovalova, A., Popović, L. Č., Suzy, C. et al.: 2008, *Astron. Astrophys.*, **486**, 99.
Welsh, W. F.: 2001, *Probing the Physics of AGN, eds. B. M. Peterson, R. W. Pogge,R. S. Polidan, et al.*, ASP Conf. Ser., **224**, 123.
Welsh, W. F., Horne, K.: 1991,*Astrophys. J.*, **379**, 586.

Publ. Astron. Obs. Belgrade No. 84 (2008), 475 - 478 *Contributed Paper*

RELATIONS AMONG EMISSION LINES AND CONTINUUM LUMINOSITY IN ACTIVE GALACTIC NUCLEI

J. KOVAČEVIĆ, L. Č. POPOVIĆ and M. S. DIMITRIJEVIĆ
Astronomical Observatory, Volgina 7, 11160 Belgrade, Serbia
E–mail: jkovacevic@aob.bg.ac.yu

Abstract. We have investigated the line-continuum relations by using an AGN SDSS sample. For the first time we have considered $H\alpha$ and [N II] emission lines in the line-continuum analysis. Also, in order to find more details, we decomposed complex profiles of Balmer lines ($H\alpha$ and $H\beta$) on three components (NLR, ILR and BLR) which are coming from different line emission regions and we examine line components-continuum relations. Numerous Fe II lines ($\lambda\lambda$ 4450-5350 Å) are separated in the three groups (^4F, ^6S and ^4G), according to atomic properties of their transitions, and each Fe II line group is compared separately with continuum luminosity. Indications of Baldwin effect are found for the [O III], [N II] and NLR component of $H\beta$, but trends of inverse Baldwin effect are observed for the Fe II ^6S line group, $H\beta$ BLR, $H\alpha$ ILR and specially for the $H\alpha$ BLR component. Different trends in line-continuum relations required further investigations, to explain their physical background.

1. INTRODUCTION

Investigation of emission lines and continuum luminosity relations may help in understanding AGN structure and physics. In 1977. Baldwin discovered an anticorrelation between equivalent width (EW) of C IV λ1549 Å line and the continuum luminosity L_λ1450 Å (Baldwin 1977). Later, it is detected that majority of emission lines in the UV and V spectral range, and also some lines from the X range are showing the Baldwin effect, i.e. their equivalent width decreases with increase of continuum luminosity. Dietrich et al. (2002) have found Baldwin Effect in almost all lines from O VI λ1034 Å to [O III] λ5007 Å. Only a few lines from considered range, show no correlation or they are showing weak inverse Baldwin Effect (N V λ1240 Å, $H\beta$, $H\gamma$ and Fe II optical lines). Baldwin Effect could be described by function: $EW_{line} \sim L_\lambda^\alpha$, $\alpha < 0$, where EW_{line} is the line equivalent width, L_λ is continuum luminosity for given λ and α is index of the slope. It is noticed that different lines are showing different slopes in the EW versus L diagram. Higher ionization lines usually have steeper slopes than low ionization lines.

The physical explanation of Baldwin effect is still an open question. It is proposed that the continuum shape is luminosity-dependent, i.e. that the UV and X spectra are softer in more luminous AGNs. This results in weaker ionization and heating of emission gas around central engine which cause decreasing of line equivalent widths (Netzer et al. 1992, Korista et al. 1998).

It is also proposed that Baldwin Effect may be driven by an increase of metallicities in more luminous AGNs (Korista et al. 1998). Very interesting question is whether the Baldwin Effect is caused by some stronger, more fundamental relation among equivalent widths and another AGN property, which correlates with AGN luminosity, such as: redshift, the Eddington ratio (L/L_{Edd}) or black hole mass M_{BH}. Baskin & Laor (2004) have found that EW (C IV) better correlate with L/L_{Edd}, then with continuum luminosity, which is also confirmed from other authors using different lines (Warner et al. 2004).

It is observed that Baldwin Effect is connected with group of correlations "Eigenvector 1" (E1), identified by Boroson & Green (1992) in optical AGN spectra. The proposed physical causes which lie under E1 correlations are the same as those proposed for Baldwin Effect (L/L_{Edd}, M_{BH} or inclination angle), which make connection between this two phenomena.

The importance of Baldwin Effect is that it could be used as cosmological standard candle and it could help in studying metal abundances (Korista et al. 1998) as evolution and physics of AGNs.

2. THE SAMPLE AND ANALYSIS

We selected 79 AGN spectra from the Date Release Four (DR4) of the SDSS Database. Our sample is chosen by criteria of high signal to noise ($S/N > 30$), and $z < 0.7$. Spectra are corrected for Galactic reddening and continuum emission is substracted by DIPSO software.

We considered two spectral ranges: $\lambda\lambda$ 4400-5500 Å (Fe II lines, [O III] $\lambda\lambda$4959, 5007 Å, $H\beta$, He II λ4686 Å) and $\lambda\lambda$ 6400-6800 Å ($H\alpha$ and [N II] $\lambda\lambda$6548, 6583 Å) (Fig. 1). We assume that emission lines arise in two or more emission regions, so we fit their profiles with sum of Gaussian functions. Shifts, widths and intensities of Gaussian functions are reflecting physical conditions of emission regions where those components arise. $H\alpha$ and $H\beta$ are decomposed with three Gaussians, which represent emission from BLR (Broad Line Region), ILR (Intermediate Line Region) and NLR (Narrow Line Region).

Parameters of shift and width of the [O III], [N II] and NLR components of $H\beta$ and $H\alpha$, have the same value for a particular AGNs spectrum, because all those lines originate from the same Narrow Line Region. Optical Fe II lines were fited with template calculated by using of the 29 strongest Fe II lines within the $\lambda\lambda$ 4450-5350 Å, and they are separated into three line groups according to the lower level of transition: $3d^6$ ($^3F2$) $4s$ $^4\mathbf{F}$, $3d^5 4s^2$ $^6\mathbf{S}$ and $3d^6$ (^3G) $4s$ $^4\mathbf{G}$ (in further text ^4F, ^6S and ^4G groups of lines). Detailed description of fitting procedure and Fe II calculated template is given in Kovačević et al. (2008).

3. PRELIMINARY RESULTS

We analyzed the relations of equivalent widths (EW) of considered lines and continuum luminosity (λ5100 Å). For the first time we considered $H\alpha$ and [N II] emission lines in the line-continuum analysis. In order to find more details, we analyzed the relations of the line components (NLR, ILR and BLR of $H\alpha$ and $H\beta$) and continuum. EW Fe II lines-continuum relation is examined by comparing continuum luminosity with three Fe II line groups (^4F, ^6S and ^4G). In this way, we connected Fe II atomic

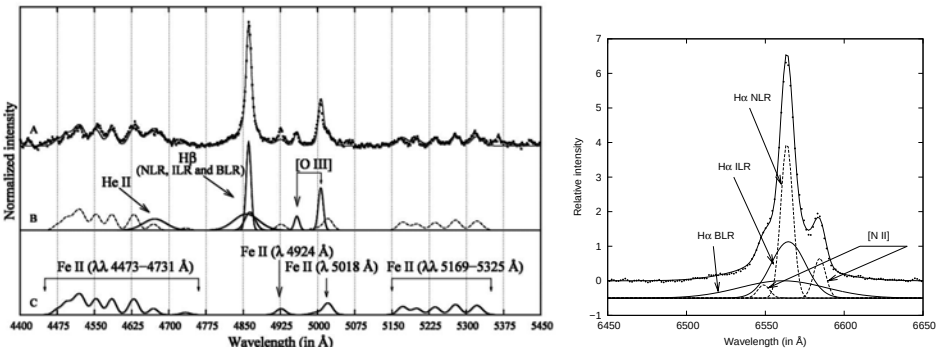

Figure 1: Example of fit of Mrk 493 in the $\lambda\lambda$ 4400-5500 Å range (Fe II lines, [OIII], $H\beta$, He II) (left) and in $\lambda\lambda$ 6400-6800 Å range ($H\alpha$ and [N II]) (right). Lines are decomposed on Gaussians and Fe II lines were fited with calculated template.

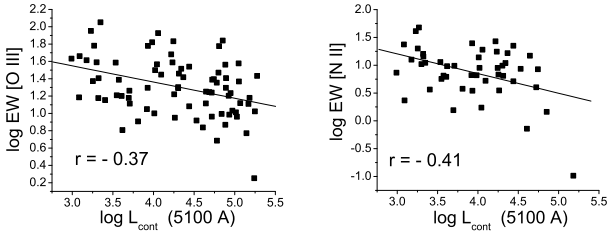

Figure 2: Correlation among continuum luminosity (λ5100 Å) and EW [O III] lines (left) and EW N II (right). Significant negative trend is present (Baldwin effect).

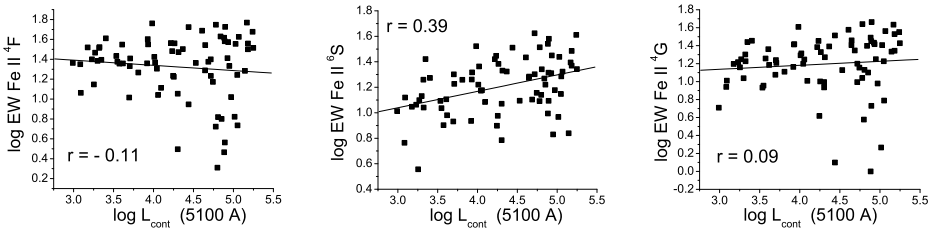

Figure 3: Relation among continuum luminosity (λ5100 Å) and EW $^{4}\mathbf{F}$, $^{6}\mathbf{S}$ and $^{4}\mathbf{G}$ line groups (up) and total EW Fe II (down). The correlation is not observed, but weak positive trend is present only in the case of $^{6}\mathbf{S}$ group.

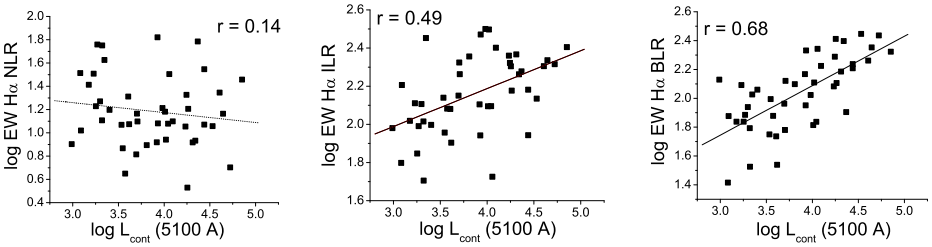

Figure 4: Correlation among continuum luminosity (λ5100 Å) and EW $H\alpha$ NLR (left), ILR (middle) and BLR (right) components. Significant positive trend is observed in the case of EW $H\alpha$ ILR and strong correlation in the case of EW $H\alpha$ BLR.

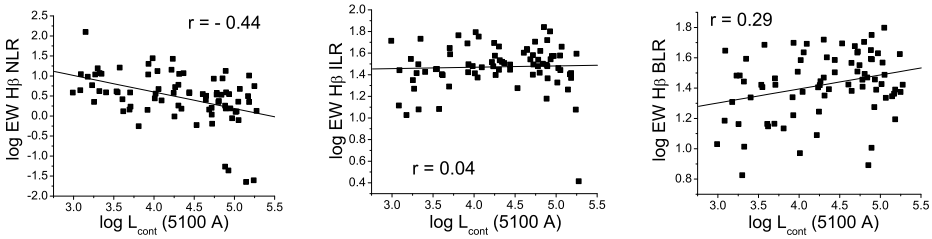

Figure 5: Correlation among continuum luminosity (λ5100 Å) and EW $H\beta$ NLR (left), ILR (middle) and BLR (right) components. Significant negative trend is observed in the case of EW $H\beta$ NLR and weak positive trend in case of EW $H\beta$ BLR.

structure with physical properties of AGN, which brings more information about the Fe II emission region.

Baldwin effect is noticed for the [O III] (the coefficient of correlation r=-0.37) and [N II] (r=-0.41) lines (Fig. 2), as significant negative trends. There is no correlation among log EW Fe II $^{\mathbf{4}}\mathbf{F}$, $^{\mathbf{6}}\mathbf{S}$, $^{\mathbf{4}}\mathbf{G}$ and log L_{cont} (Fig. 3), only weak positive trend is noticed in the case of log EW FeII $^{\mathbf{6}}\mathbf{S}$ (0.29). This difference may originate in diverse multiplicity of Fe II line groups (M=6 for $^{\mathbf{6}}\mathbf{S}$ and M=4 for $^{\mathbf{4}}\mathbf{F}$ and $^{\mathbf{4}}\mathbf{G}$). Trends of Balmer lines vs. continuum luminosity are shown in Fig. 4 and Fig. 5. BLR and ILR components of $H\alpha$ and BLR $H\beta$ are showing indications of inverse Baldwin Effect, which is specially strong in the case of the BLR $H\alpha$ (0.68). Contrary, the NLR $H\beta$ is showing Baldwin Effect (-0.44). No trends are noticed in case of the NLR $H\alpha$ and ILR $H\beta$.

For explanation of those different trends and correlations and finding their physical cause, more detailed analysis is required, and it will be presented in future work.

Acknowledgment

This work is a part of the project (146002): "Astrophysical Spectroscopy of Extragalactic Objects" and (146001) "Influence of collisional processes on astrophysical plasma spectra", supported by Serbian Ministry of Science.

References

Baldwin, J.A.: 1977, *ApJ*, **214**, 679.
Baskin, A. & Laor, A.: 2004, *MNRAS*, **350**, L31.
Boroson, T. A. & Green, R. F.: 1992, *Astrophys. J. Suppl. Series*, **80**, 109.
Dietrich, M., Hamann, F., Shields, J. C., Constantin, A.,Vestergaard, M., Chaffee, F., Foltz, C. B., Junkkarinen, V. T.: 2002, *ApJ*, **581**, 912.
Korista, K., Baldwin, J. & Ferland, G.: 1998, *ApJ*, **507**, 24.
Kovačević, J., Popović, L. Č., Dimitrijević, M. S.: 2008, to be submitted to *MNRAS*.
Netzer, H., Laor, A. & Gondhalekar, P. M.: 1992, *MNRAS*, **254**, 15.
Warner, C., Hamann, F. & Dietrich, M.: 2004, *ApJ*, **608**, 136.

Publ. Astron. Obs. Belgrade No. 84 (2008), 479 - 482 *Contributed paper*

ELECTRIC AND QUANTUM EFFECTS IN SELF GRAVITATING STATIC PLASMA CONFIGURATIONS

A. LALOVIĆ and V. M. ČADEŽ
Astronomical Observatory Belgrade, Volgina 7, 11160 Belgrade, Serbia
E–mails: alalovic@aob.bg.ac.yu, vcadez@aob.bg.ac.yu

Abstract. We derive dimensionless numbers that define relative significance of electrostatic, gravitational and quantum forces in self gravitating astrophysical plasmas and show that quantum effects have practically no influence on static configurations of self gravitating plasmas. The inclusion of quantum forces, which can be frequently found in the literature in recent years, is therefore not justified for realistic astrophysical conditions. Moreover, our estimates show that inclusion of quantum effects into the hydrodynamic treatment of plasma is essentially meaningless.

1. INTRODUCTION

Self gravitating multicomponent plasma configurations are commonly found in nature on various characteristic scales of physical quantities (Verhest 2000). Among problems of interest in this field that are frequently dealt with in literature are properties of quasi-static distributions of charged and massive particle components of plasmas subject to particle electrostatic and gravitational interactions (Verhest 2000, Mayer 2005, Chavanis 2002). In recent years, also the contribution of quantum forces is included into studies of various hydrostatic equilibrium states and their perturbations resulting into varieties of plasma modes and possible instabilities (Sahu et al 2007, Shukla et al. 2006).

In this paper, we introduce dimensionless numbers into equations for a hydrostatic equilibrium of a two component electron-ion (e-i) self gravitating quantum plasma, which determine the significance of electrostatic and quantum effect terms in a broad domain of characteristic plasma parameters. Such an analysis is necessary in particular in those cases when quantum effects are added (Sahu et al. 2007) in standard approaches of finding static plasma configurations, and studies of waves and instabilities.

2. HYDROSTATIC EQUILIBRIUM

The considered plasma is assumed a perfect polytropic two component gas with a pressure-density relation for electrons and ions given by $p_{e,i} \sim n_{e,i}^{\kappa}$.

The hydrostatic equilibrium of a two component e-i self gravitating quantum plasma is now described by the following set of equations (Sahu et al 2007, Shukla et al. 2006):

1. Balance of forces for the electron and ion component respectively:

$$\begin{aligned} Z_i e\nabla\phi + m_i\nabla\psi + \frac{1}{n_i}\nabla p_i - \frac{\hbar^2}{2m_i}\nabla\left[\frac{\nabla^2\sqrt{n_i}}{\sqrt{n_i}}\right] = 0, \\ e\nabla\phi - m_e\nabla\psi - \frac{1}{n_e}\nabla p_e + \frac{\hbar^2}{2m_e}\nabla\left[\frac{\nabla^2\sqrt{n_e}}{\sqrt{n_e}}\right] = 0. \end{aligned} \tag{1}$$

2. Poisson's equations for the electrostatic and gravitational potentials:

$$\nabla^2\phi = \frac{4\pi e}{\epsilon_0}(n_e - Z_i n_i), \qquad \nabla^2\psi = 4\pi G(m_i n_i + m_e n_e). \tag{2}$$

3. Polytropic electron and ion components:

$$\frac{p_i}{p_{i0}} = \left(\frac{n_i}{n_{i0}}\right)^{\kappa_i}, \qquad \frac{p_e}{p_{e0}} = \left(\frac{n_e}{n_{e0}}\right)^{\kappa_e} \tag{3}$$

where: $p_{0e,0i} = n_{0e,0i}kT_{e,i}$ with $p_{0e,0i}, n_{0e,0i}$=const and k=1.38x10^{-23}kg m^{2}s$^{-2}K^{-1}$ is the Boltzmann constant.

In what follows, we shall take $T_e = T_i$ and $Z_i = 1$ meaning we are dealing with an electron-proton plasma.

3. SCALING AND DIMENSIONLESS NUMBERS

Equations Eq. (1)-(3) can be cast in a dimensionless form by introducing typical scaling quantities r_0, T_0, and n_0 for the length, temperature and particle number densities respectively.

In this case, Eq. (1)-(3) can be written as:

$$\begin{aligned} &K_Q\frac{m_i}{m_e}\tilde{\nabla}^2\left[\frac{\tilde{\nabla}^2\sqrt{n_i}}{\sqrt{n_i}}\right] - \kappa\tilde{n}_i^{\kappa-2}\tilde{\nabla}^2\tilde{n}_i - \kappa(\kappa-2)\tilde{n}_i^{\kappa-3}(\tilde{\nabla}\tilde{n}_i)^2 \\ &\quad -K_E(\tilde{n}_e - \tilde{n}_i) - K_G(\frac{m_i}{m_e}\tilde{n}_i + \tilde{n}_e) = 0, \\ &K_Q\tilde{\nabla}^2\left[\frac{\tilde{\nabla}^2\sqrt{n_e}}{\sqrt{n_e}}\right] - \kappa\tilde{n}_e^{\kappa-2}\tilde{\nabla}^2\tilde{n}_e - \kappa(\kappa-2)\tilde{n}_e^{\kappa-3}(\tilde{\nabla}\tilde{n}_e)^2 \\ &\quad +K_E(\tilde{n}_e - \tilde{n}_i) - K_G(\tilde{n}_i + \frac{m_e}{m_i}\tilde{n}_e) = 0. \end{aligned} \tag{4}$$

where tilde designates the corresponding dimensionless quantities:

$$\tilde{n}_{e,i} \equiv \frac{n_{e,i}}{n_0} \quad \text{and} \quad \tilde{\nabla} \equiv r_0\nabla.$$

The introduced dimensionless numbers in Eq. (4) are defined as:

$$\begin{aligned} K_Q &\equiv \frac{1}{2}\frac{\hbar^2}{m_e kT r_0^2} = \frac{1}{2}\frac{\lambda\!\!\!^{-2}}{r_0^2}, \\ K_G &\equiv 4\pi\frac{Gm_i m_e n_{i0}}{kT}r_0^2 = 4\pi\frac{r_0^2}{\lambda_G^2}, \\ K_E &\equiv 4\pi\frac{n_{i0}e^2 r_0^2}{\epsilon_0 kT} = 4\pi\frac{r_0^2}{\lambda_D^2}. \end{aligned} \tag{5}$$

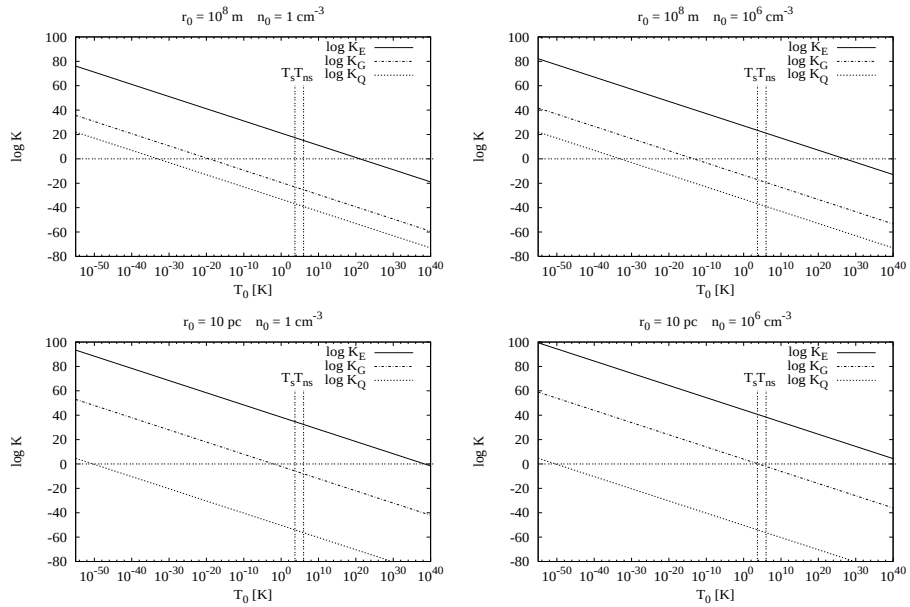

Figure 1: Temperature dependence of dimensionless numbers for two characteristic densities $n_0 = (1, 10^6)$ cm^{-3} and for r_0=10^{8}m, and $n_0 = (1, 10^6)$ cm^{-3} and for r_0=10 pc are shown in the upper i.e. lower two plots respectively. As a reference, two temperatures T_{ns} and T_s related to a neutron star and the Sun are indicated in the plots.

where: $\lambda\!\!\!^{-}$ and λ_D are the electron de Broglie and Debye length respectively while λ_G is a sort of gravitational equivalent to the Debye length. It sets a typical distance at which kinetic energy of thermal motions matches the gravitational potential energy of particles.

4. CONCLUSIONS

The obtained characteristic dimensionless numbers Eq. (5) depend on scaling parameters r_0 and n_0, and also on temperature T as shown in Figs. 1 and 2.

Domains where $K_E \gg 1$ indicate strong electrostatic forces and practically no local charge separation as can be concluded from Eq. (4). Namely, if $K_E \to \infty$ then $|\tilde{n}_e - \tilde{n}_i| \to 0$ which further makes the product $K_E(\tilde{n}_e - \tilde{n}_i)$ finite and of the same order of magnitude as the remaining leading terms in Eq. (4).

Large K_G indicates strong gravitational effects resulting in a pronounced plasma density stratification while the number K_Q measures the contribution of quantum effects in the plasma. As seen in Figs. 1 and 2, this number is extremely small for physical conditions relevant to realistic astrophysical systems. Inclusion of quantum effects into processes typical for astrophysical plasmas is therefore of purely academic significance and it induces no new phenomena to those already widely investigated in classical plasmas. In addition, one can easily see from Figs. 1 and 2 that $\lambda\!\!\!^{-2} \ll \lambda_D^2$

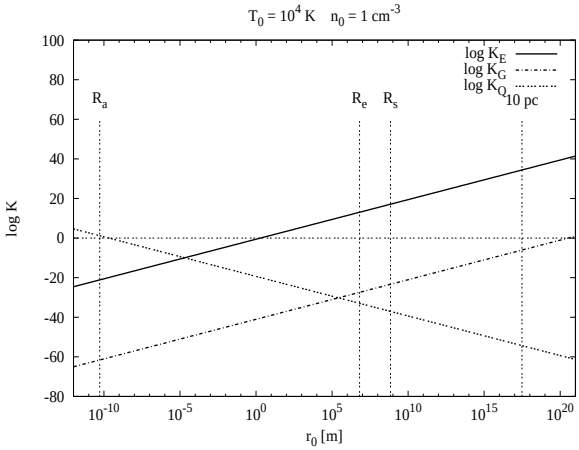

Figure 2: Dimensionless numbers as a function of the typical length r_0 for T_0=10^4K and n_0=1cm. As a reference several characteristic sizes are indicated in the plot: radii of an atom (R_a), Earth (R_E), Sun (R_S) and 10 pc a size typical of an HII region.

which clearly violates the very implicit assumption of a fluid description of plasmas as frequently found in the literature on quantum plasmas.

References

Chavanis, P. H.: 2002, *Astron.Astrophys.*, **386**, 732.
Mayer, L., Wadsley, J., Quinn, T., Stadel, J.: 2005, *Mon. Not. R. Astron. Soc*, **363**, 641.
Sahu, B., Roychoudhury, R.: 2007, *Physics of Plasmas*, **14**, 072310.
Shukla, P. K., Stenflo, L.: 2006, *Phys. Lett. A*, **355**, 378.
Verhest, F.: 2000, Waves in Dusty Space Plasmas, Kluwer Ac. Publ. Dordrecht/Boston/London.

Publ. Astron. Obs. Belgrade No. 84 (2008), 483 - 486 *Contributed Paper*

DACs AND SACs PHENOMENA IN THE C IV EMITTING REGIONS OF QSOs

E. LYRATZI[1,2], E. DANEZIS[1], L. Č. POPOVIĆ[3],
M. S. DIMITRIJEVIĆ[3] and A. ANTONIOU[1]

[1] *University of Athens, Faculty of Physics Department of Astrophysics, Astronomy and Mechanics, Panepistimioupoli, Zographou 157 84, Athens, Greece*
E–mails: elyratzi@phys.uoa.gr, edanezis@phys.uoa.gr, ananton@phys.uoa.gr

[2] *Eugenides Foundation, 387 Sygrou Av., 17564, Athens, Greece*

[3] *Astronomical Observatory of Belgrade, Volgina 7, 11160 Belgrade, Serbia*
E–mails: lpopovic@aob.bg.ac.yu, mdimitrijevic@aob.bg.ac.yu

Abstract. In this paper we study the C IV resonance lines in the UV spectra of 5 Broad Absorption Line Quasars (BAL QSOs). We found that the Broad Absorption Lines (BALs) that we analyzed in the spectra of some BAL QSOs, are created by a number of Satellite Absorption Components (SACs). We calculated the kinematical parameters such as the apparent rotational (V_{rot}) and radial (V_{rad}) velocities of the regions where the studied lines are created and the random velocities (V_{rand}) of the C IV ions. We also calculated the Full Width at Half Maximum (FWHM) and the column density (CD).

1. INTRODUCTION

In the spectra of Broad Absorption Line Quasars (BAL QSOs) we observe complex profiles of Broad Absorption Lines (BALs), mainly in the case of high ionization ions (e.g. C IV, Si IV, N V). Danezis et al. (2006, 2008) indicated that these complex profiles result from the fact that the BALs are composed of a number of Satellite Absorption Components (SACs). In this paper we test the idea of SACs in quasars' spectra, proposed by Danezis et al. (2006, 2008), using the GR model (Danezis et al. 2007).

Here we investigate the physical properties of Broad Absorption Line Regions (BALRs), where the C IV resonance lines ($\lambda\lambda$ 1548.187, 1550.772 Å) are created, in the case of five quasars. With this model one can accurately fit the observed complex profiles of both emission and absorption spectral lines. Generally, with this model we can calculate the apparent rotational and radial velocities, the random velocities of the ions, as well as the Full Width at Half Maximum (FWHM), the column density of the independent density regions of matter which produce the main and the satellite components of the studied spectral lines and the respective absorbed or emitted energy. We are able to explain the observed peculiar profiles of the BALs using the DACs/SACs theory, i.e. the complex profiles of the BALs are composed

by a number of DACs or SACs which are created in different regions (Danezis et al. 2006, 2008).

2. OBSERVATIONAL DATA AND METHOD OF ANALYSIS

The observational data are taken with HST and are shown in Table 1. The studied spectra have resolution between 1.2 and 3.2 Å.

In order to study the C IV regions of the above BAL QSOs, we used the model proposed by Danezis et al. (2007).

3. RESULTS AND DISCUSSION

In Figure 1 one can see the best fit of the C IV resonance lines in the spectra of PG 0946+301 (left) and PG 1700+518 (right). In the case of PG 1700+518 the complex profile of the observed C IV Broad Absorption Line (BAL) is composed by a number of Satellite Absorption Components (SACs). However, in the case of PG 0946+301 the complex profile of the C IV BAL is composed by two discrete groups of SACs. This means that we also observe the DACs phenomenon.

We point out that the C IV doublet of PG 0946+301 is one of the very few lines that present clearly the DACs phenomenon, in the case of quasars.

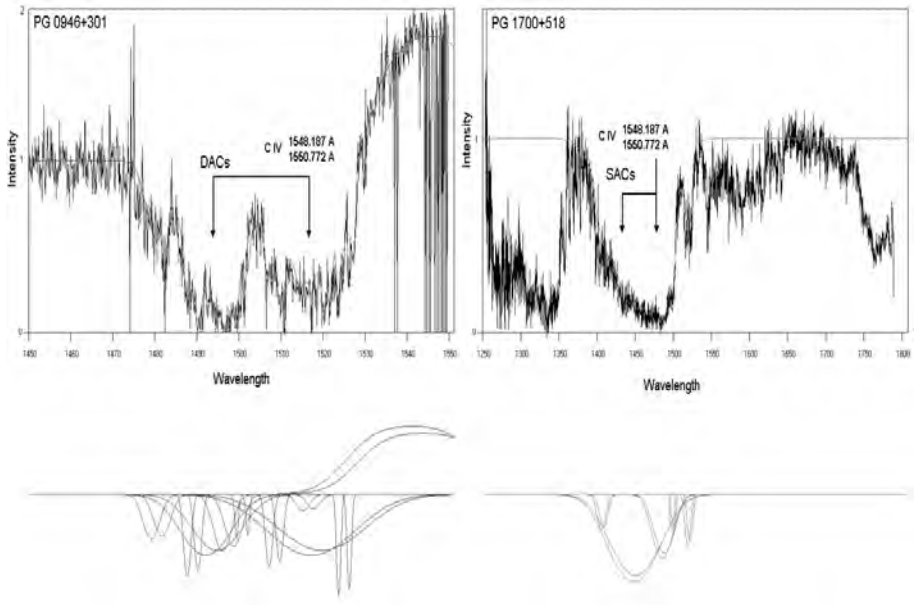

Figure 1: Best fit of the C IV resonance lines in the spectra of PG 0946+301 (left) and PG 1700+518 (right). We can explain the complex structure of these lines as a DACs or SACs phenomenon, respectively. Below the fit one can see the analysis of the observed profile to its DACs/SACs.

Table 1: Observational Data

Name	Z	Obs. Date	Ins./grat.
PG 0946+301	1.216	Feb 16, 1992	FOS/G400,G570
PG 1700+518	0.292	Sep 12, 2000	STIS/G430L,G750L
3C 351	0.371940	Oct 22,1991	FOS/G190H
H 1413+1143	2.551	Jun 23, 1993, Dec 23,1994	FOS/G400H,G570H
PG1254+047	1.024	Feb 17,1993	FOS/G160L,G270H

Table 2: Random (V_{rand}), Rotational (V_{rot}), Radial (V_{rad}) velocities (in km/s) of all the C IV SACs (a to e) of the studied quasars spectra.

Object	SAC	V_{rand} (km/s)	V_{rad} (km/s)	V_{rot} (km/s)
PG0946+301	a	615	-5998	3000
	b	615	-10835	1800
	c	228	-10061	600
PG1700+518	a	5699	-19348	6500
	b	2280	-12092	3000
	c	1140	-27474	1000
	d	456	-5611	1000
	e	114	-9674	800
3C351	a	39	-1722	270
H1413+1143	a	2280	-5224	3600
PG1254+047	a	1596	-5804	1000

Table 3: Full Width at Half Maximum (FWHM) (in km/s) and Column Density (CD) (in cm^{-2}) of all the C IV SACs (a to e) of the studied quasars spectra.

Object	SAC	FWHM	CD (cm^{-2})	
		(km/s)	λ 1548.187 Å	λ 1550.772 Å
PG0946+301	a	5058	$5.84 \cdot 10^{10}$	$5.36 \cdot 10^{10}$
	b	3025	$3.60 \cdot 10^{10}$	$3.30 \cdot 10^{10}$
	c	1010	$1.00 \cdot 10^{10}$	$9.17 \cdot 10^{9}$
PG1700+518	a	15134	$2.39 \cdot 10^{11}$	$2.20 \cdot 10^{11}$
	b	6271	$7.23 \cdot 10^{10}$	$6.61 \cdot 10^{10}$
	c	2624	$1.69 \cdot 10^{10}$	$1.53 \cdot 10^{10}$
	d	1738	$1.53 \cdot 10^{10}$	$1.40 \cdot 10^{10}$
	e	1316	$7.58 \cdot 10^{9}$	$6.90 \cdot 10^{9}$
3C351	a	602	$7.27 \cdot 10^{9}$	$6.73 \cdot 10^{9}$
H1413+1143	a	7245	$1.19 \cdot 10^{11}$	$1.10 \cdot 10^{11}$
PG1254+047	a	3491	$1.73 \cdot 10^{10}$	$1.57 \cdot 10^{10}$

By applying the model proposed by Danezis et al. (2007) (GR model), we calculated the kinematical parameters such as the apparent rotational (V_{rot}) and radial (V_{rad}) velocities of the regions where the studied lines are created and the random velocities (V_{rand}) of the C IV ions. The calculated values are presented in Table 2. We also calculated the Full Width at Half Maximum (FWHM) and the column density (CD) (see Table 3). As one can see in Table 2, the C IV complex profiles are created by a number of SACs.

In some cases we observe that the calculated values of the random and/or the rotational velocities are too large (see Table 2), indicating that the region of origin of the components is close to the massive black hole. Such large rotational and random velocities are expected near the massive black hole, in difference with the large widths observed in stellar spectra (see Antoniou et al. 2008).

Acknowledgments

This research project is progressing at the University of Athens, Department of Astrophysics, Astronomy and Mechanics, under the financial support of the Special Account for Research Grants, which we thank very much. This work also was supported by Ministry of Science of Serbia, through the projects "Influence of collisional processes on astrophysical plasma line shapes" and "Astrophysical spectroscopy of extragalactic objects".

References

Antoniou, A., Danezis, E., Lyratzi, E., Popović, L. Č., Dimitrijević, M. S.: 2008, *PASJ*, submited.

Danezis, E., Lyratzi, E., Popović, L. Č., Dimitrijević, M. S., Antoniou, A.: 2008, "Similarity between DACs/SACs phenomena in hot emission stars and quasars absorption lines", in *Proceedings of 19th ICSLS, Valladolid, Spain.*

Danezis, E., Nikolaidis, D., Lyratzi, E., Popović, L. Č., Dimitrijević, M. S., Antoniou, A., Theodossiou, E. : 2007, *PASJ*, **59**, 827.

Danezis, E., Popović, L. Č., Lyratzi E., Dimitrijević, M. S.: 2006, *AIP Conference Proceedings*, **876**, 373.

Publ. Astron. Obs. Belgrade No. 84 (2008), 487 - 490 *Contributed Paper*

STARK BROADENING OF Sn III LINES IN A TYPE STELLAR ATMOSPHERES

Z. SIMIĆ[1], M. S. DIMITRIJEVIĆ[1], A. KOVAČEVIĆ[2] and M. DAČIĆ[1]

[1] *Astronomical Observatory, Volgina 7, 11160 Belgrade, Serbia*
E–mail: zsimic@aob.bg.ac.yu

[2] *Department of Astronomy, Faculty for Mathematics, Studentski Trg 16, 11000 Belgrade, Serbia*

Abstract. Here we present Stark broadening parameters for Sn III 6s $^1S_0 - 6p\ ^1P^o_1$ spectral line obtained by using semiclassical perturbation approach and Stark widths for this transition obtained by using modified semiempirical approach. Results obtained have been compared with available experimental data and used for the consideration of the influence of the Stark broadening effect in A type stellar atmospheres.

1. INTRODUCTION

With the development of new space tehniques, the quality and quantity of spectroscopic data for trace elements as tin has increased. Spectral lines of neutral tin are present in the spectra of A type stars, for example γ Equ (Adelman et al. 1979). Also, a Sn II spectral line is observed in Przybylski's star by Cowley et al. (2000).

For the considered Sn III 6s $^1S_0 - 6p\ ^1P^o_1$ spectral line, Kieft et al. (2004) measured Stark width and they also, obtained the first theoretical result by using semiempirical (Griem, 1968) approach.

Here we present Stark broadening parameters for Sn III 6s $^1S_0 - 6p\ ^1P^o_1$ as a function of temperature, obtained by using semiclassical perturbation (Sahal-Bréchot, 1969ab) approach and Stark widths for this transition as a function of temperature, obtained by using modified semiempirical (Dimitrijević & Konjević, 1980) approach.

2. RESULTS AND DISCUSSION

For Sn III spectral line Stark broadening parameters, the full semiclassical perturbation approach (Sahal−Bréchot, 1969ab) has been applied. A summary of the formalism for ionized emitters is given in Dimitrijević et al. (1991) and Dimitrijević & Sahal - Bréchot, (1996). Also, for Sn III spectral line Stark width, modified semiempirical approach (Dimitrijević & Konjević, 1980) has been applied. The needed energy levels have been taken from Moore (1971). The oscillator strengths have been calculated by using the method of Bates & Damgaard, (1949), and the tables of Oertel & Shomo (1968). For higher levels, the method of Van Regemorter et al. (1979) has been used.

Our results for Sn III line are shown in Tables 1 and 2. We also specify a parameter C (Dimitrijević & Sahal−Bréchot 1984) which gives an estimate for the maximum perturber density for which the line may be treated as isolated, when it is divided by the corresponding full width at half maximum.

One can see from Table 3, a good agreement with experimental value of both our results for Stark width for Sn III 6s $^1S_0 - 6p\ ^1P^o_1$ obtained by using semiclassical and modified semiempirical approach. Obviously, this ratio is better for our values than for semiempirical one obtained by Kieft et al. (2004) using Griem (1968) method, not applicable for multiply charged ions (see Dimitrijević & Konjević, 1980).

Table 1: Electron- and proton-impact broadening parameters for Sn III 5226.2 Å obtained by using semiclassical perturbation approach for perturber density of 10^{17}cm^{-3} and temperatures from 10000 up to 150000 K.

Transition	T(K)	W_{e-}(Å)	d_{e-}(Å)	W_{p+}(Å)	d_{p+}(Å)
	10000	1.39	-0.149	0.391E-01	-0.207E-01
Sn III	20000	1.05	-0.987E-01	0.615E-01	-0.339E-01
6s $^1S_0 - 6p\ ^1P^o_1$	30000	0.907	-0.886E-01	0.758E-01	-0.426E-01
5226.2 Å	50000	0.788	-0.900E-01	0.869E-01	-0.513E-01
C= 0.24E+21	100000	0.676	-0.846E-01	0.102	-0.619E-01
	150000	0.626	-0.788E-01	0.111	-0.686E-01

Table 2: Stark widths for Sn III 5226.2 Å obtained by using modified semiempirical approach for perturber density of 10^{17}cm^{-3} and temperatures from 2500 up to 50000 K.

Transition	T(K)	W(Å)
	2500	2.217
	5000	1.567
6s $^1S_0 - 6p\ ^1P^o_1$	10000	1.108
5226.2Å	20000	0.784
	30000	0.640
	50000	0.514

Table 3: Comparison between W_m-experimental Stark width with theoretical: W_{se}-semiempirical, W_{sc}-semiclassical and W_{mse}-modified semiempirical.

Transition	W_m(Å)	Rel. error	$\frac{W_m}{W_{se}}$	$\frac{W_m}{W_{sc}}$	$\frac{W_m}{W_{mse}}$
Sn III					
6s $^1S_0 - 6p\ ^1P^o_1$	1.22	50%	1.70	0.92	1.15
5226.2 Å					

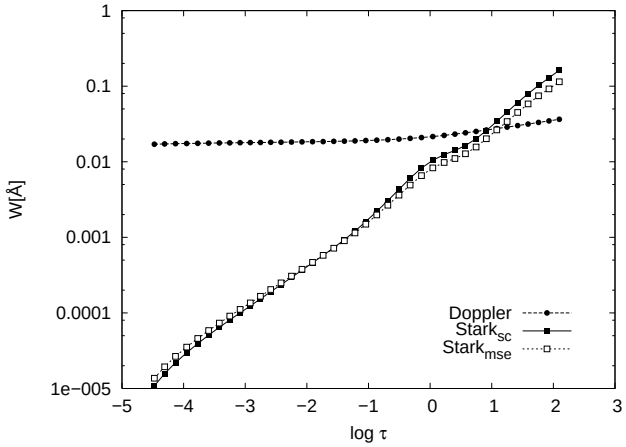

Figure 1: Thermal Doppler and Stark widths (sc-semiclassical, mse-modified semiempirical) for Sn III 6s $^1\mathrm{S}_0 - 6\mathrm{p}\ ^1\mathrm{P}^{\mathrm{o}}_1$ line as functions of optical depth for an A type star ($\mathrm{T_{eff}} = 10000$ K, $\log\, g = 4.5$).

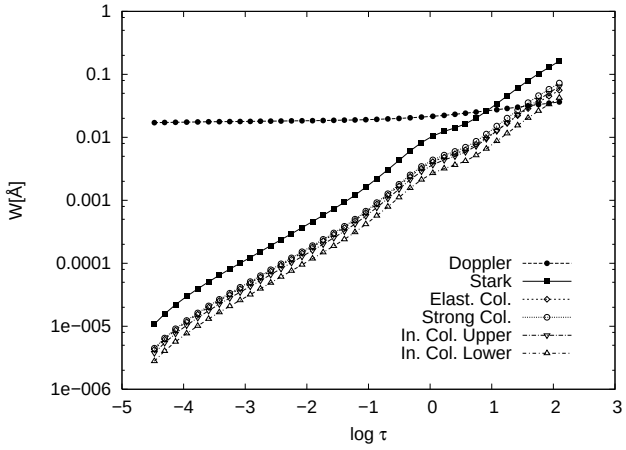

Figure 2: Thermal Doppler, Stark and contributions of different collision processes to the total Stark width of Sn III 6s $^1\mathrm{S}_0 - 6\mathrm{p}\ ^1\mathrm{P}^{\mathrm{o}}_1$ line as functions of optical depth for an A type star ($\mathrm{T_{eff}} = 10000$ K, $\log\, g = 4.5$).

In order to see the influence of Stark broadening mechanism for Sn III spectral line in stellar plasma conditions, we have calculated Stark widths for a Kurucz's (1979) A type star ($T_{\rm eff} = 10000$ K, $\log g = 4.5$) atmosphere model and compared them with Doppler ones. Obtained results in function of the Rosseland optical depth are presented in Fig. 1. One can see, that exist photospheric layers where Doppler and Stark widths are comparable and even where the Stark width is dominant and must be taken into account. Also, in Fig. 2, for the same atmosphere model, we presented Stark widths and contributions of different collision processes to the total Stark width in comparison with Doppler one. In this case, elastic and strong collisions and inelastic collision from upper levels have a similar contribution to the full Stark width as well as the similar behaviour with temperature.

References

Adelman, J., Bidelman, P., Pyper, M.: 1979, *ApJ SS*, **40**, 371.
Bates, D.R., Damgaard, A.: 1949, *Phyl. Trans. Roy. Soc.*, **A242**, 101.
Cowley, C. R., Ryabchikova, T., Kupka, F., Bord, D. J., Mathys, G., Bidelman, W. P.: 2000, *MNRAS*, **317**, 299.
Dimitrijević, M. S., Konjević, N.: 1980, *JQSRT*, **24**, 451.
Dimitrijević, M. S., Sahal-Bréchot, S.: 1984, *JQSRT*, **31**, 301.
Dimitrijević, M. S., Sahal-Bréchot, S.: 1996, *Physica Scripta*, **54**, 50.
Dimitrijević, M. S., Sahal-Bréchot, S., Bomier, V.: 1991, *A&AS*, **89**, 581.
Griem, H.R.: 1968, *Phys. Rev.*, **165**, 258.
Kieft, E. R., van der Mullen, J. J. A. M., Kroesen, G. M. W., Banine, V., Koshelev, K. N.: 2004, *Physical Review*, **E 70**, 066402.
Kurucz, R. L.: 1979, *ApJS*, **40**, 1.
Moore, C. E.: 1971, *Atomic Energy Levels*, **Vol. III**, NSRDS-NBS.
Oertel, G. K., Shomo, L. P.: 1968, *ApJS*, **16**, 175.
Sahal-Bréchot, S.: 1969a, *A&A*, **1**, 91.
Sahal-Bréchot, S.: 1969b, *A&A*, **2**, 322.
van Regemorter, H., Hoang Binh D., Prud′homme, M.: 1979, *J. Phys.*, **B12**, 1053.

Publ. Astron. Obs. Belgrade No. 84 (2008), 491 - 494 *Contributed Paper*

LINE PROFILE VARIABILITY DUE TO PERTURBATIONS IN AGN ACCRETION DISK EMISSIVITY

M. STALEVSKI, P. JOVANOVIĆ and L. Č. POPOVIĆ
Astronomical Observatory, Volgina 7, 11160 Belgrade, Serbia
E–mail: mstalevski@aob.bg.ac.yu

Abstract. In this paper we analyzed the observed variability of the broad double-peaked spectral lines of some Active Galactic Nuclei (AGN). We assumed that such lines originate from outer part of an accretion disk around massive black hole of AGN, and that line variability is caused by perturbations in the disk emissivity. The disk emissivity was studied using numerical simulations based on relativistic ray-tracing method, assuming a modification of power-law emissivity which allows us to introduce the perturbations in form of the bright spots. Our results show that this model of disk emissivity perturbations can satisfactorily reproduce the observed line variability.

1. INTRODUCTION

Broad, double-peaked emission lines provide dynamical evidence for presence of an accretion disk feeding a supermassive black hole in the center of AGN. Such line profiles are found in less than 5% of these objects (Gezari et al. 2007; Eracleous & Halpern 1994, 2003). Variability of disk emission is observed in the line profiles (see e.g. Shapovalova et al. 2001) on timescales from months to years (Flohic & Eracleous 2008; Gezari et al. 2007), and this variability does not appear to be correlated to changes in the continuum flux, so it likely traces changes in the accretion disk structure. Shapovalova et al (2001) found that sometimes, the observed Hβ line profiles have prominent asymmetric wings, while at other times, they have profiles with weak, almost symmetrical wings. Also, they found that in some periods "blue" wing of Hβ was brighter than the "red" one. Our goal is to model perturbations in an accretion disk emissivity which can produce the observed variations in the Hβ line profiles.

2. MODELING OF DISK EMISSIVITY PERTURBATIONS

Many processes in the accretion disk may lead to perturbations in its emissivity, such as self gravity, disk-star collisions and baroclinic vorticity (Flohic & Eracleous 2008). For emissivity perturbing region we used bright spot model given by Jovanović & Popović (2008). We modeled emission from outer part of accretion disk in optical spectral band. In this case, there is no significant difference between Kerr and Schwarzschild metrics.

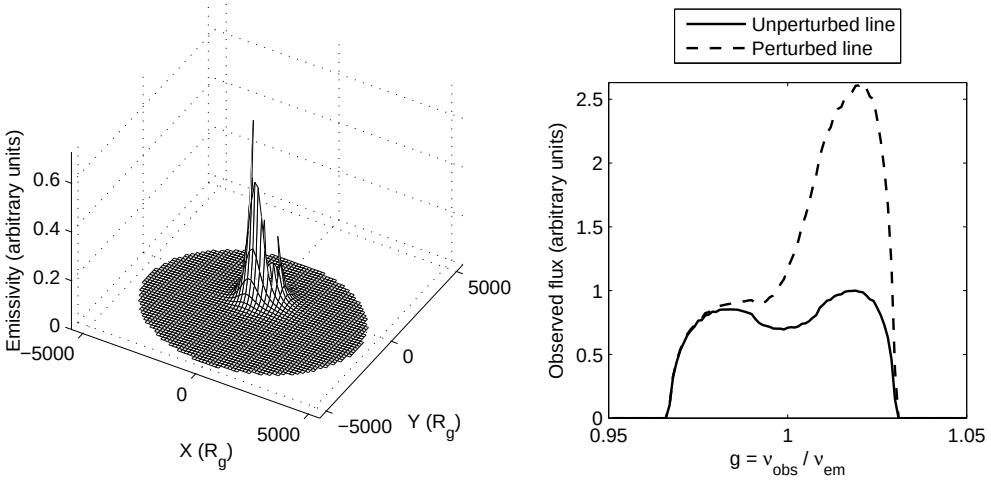

Figure 1: *Left*: Shape of perturbed emissivity of an accretion disk for the following parameters of perturbing region: $x_p = y_p = -550\ R_g$ and $w_x = w_y = 500\ R_g$. The values of the remaining parameters are given in §2. *Right:* The corresponding perturbed (dashed line) and unperturbed (solid line) Hβ line profiles.

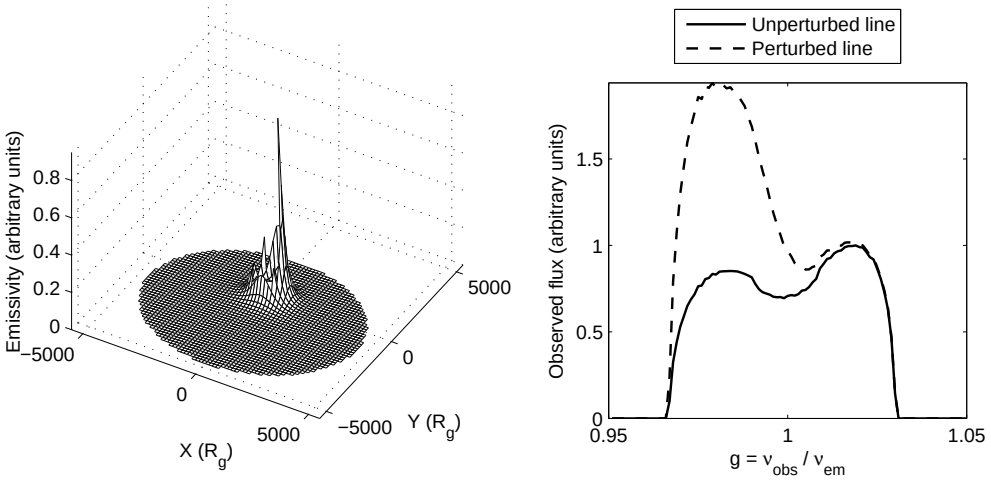

Figure 2: The same as in Fig. 1, but for the following position of perturbing region: $x_p = y_p = 550\ R_g$.

For numerical simulations in case of this disk perturbing model, the following parameters were used: disk inclination $i = 45°$, inner and outer radii of the disk $R_{in} = 500\ R_g$ and $R_{out} = 5000\ R_g$, emissivity constant $\varepsilon_0 = 1$, emissivity index $q = -3.5$ and the emissivity of perturbing region $\varepsilon_p = 5$. The widths of perturbing region are $w_x = w_y = 500\ R_g$. We performed simulations for different positions of perturbing region along $y = x$ direction, where x_p and y_p take values between 500

and 2500 R_g and between -500 and -2500 R_g. Radial distances are measured in units of gravitational radius, $R_g = GM/c^2$, where G is Newton gravitational constant, M is the mass of central black hole and c is the speed of light. Obtained results show that for adopted parameters the emissivity perturbations become insignificant outside 2500 R_g. Observed wavelength is given by $\lambda = \lambda_0/g$, where $\lambda_0 = 4861.32$ Å is transition wavelength of the Hβ line and g is energy shift due to relativistic effects which in our case, takes values between 0.95 and 1.05.

3. RESULTS AND DISCUSSION

The obtained results for two different positions of perturbing region are presented on left panels of Figs. 1. and 2, and the corresponding perturbed and unperturbed profiles of the Hβ line are given in the right panels of the same Figs. As one can see from these Figs, the perturbing model has greater influence on one of the Hβ line wings, the "blue" one in Fig. 1, or the "red" one in Fig. 2. The first case corresponds to the approaching side of the disk, while the second one corresponds to the receding side of the disk.

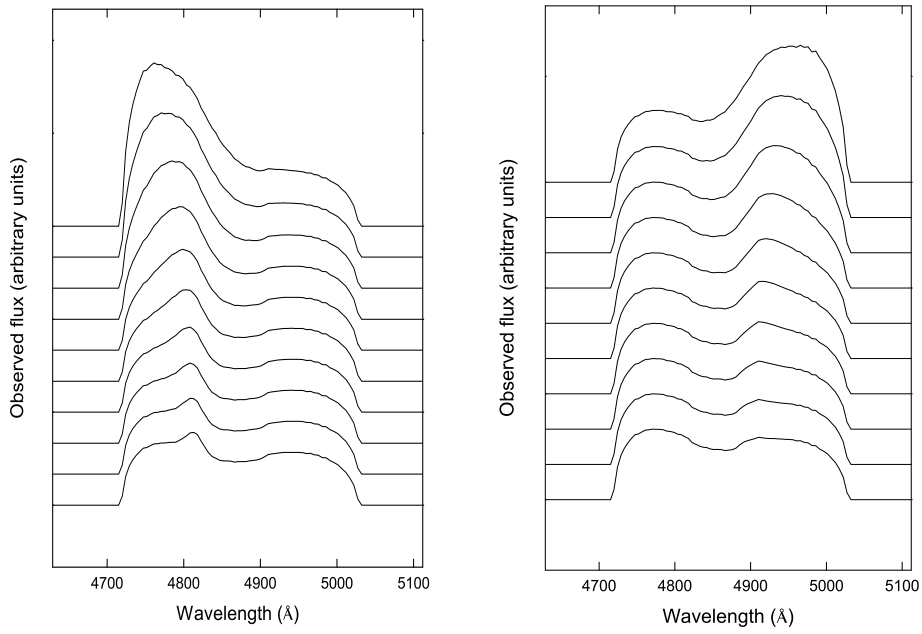

Figure 3: Variations of perturbed Hβ line profile for different positions of the perturbing region (bright spot) along the $y = x$ direction. Left panel corresponds to the positions of perturbing region on approaching side of the disk, while the right panel corresponds to the receding side of the disk. In both cases, the positions of perturbing region are varied from the inner radius towards its outer radius.

Fig. 3. shows variations of the perturbed Hβ line profiles for different positions of the perturbing region along the $y = x$ direction. For certain positions of perturbing region we obtained almost symmetrical wings (see middle profiles on the right panel of Fig. 3). In other cases either the "blue" wing is brighter than the "red" one (see top profiles in the left panel of Fig. 3) or the "red" peak is stronger than the "blue" one (see the top profiles in the right panel of Fig. 3). This is in a good agreement with the observed profiles of Hβ line in the case of 3C 390.3 (see e.g. Fig. 8. in Shapovalova et al. 2001) where the similar variations were detected.

4. CONCLUSIONS

In this paper we performed numerical simulations in order to study the variability of the Hβ spectral line due to emissivity perturbations. From these simulations we can conclude the following:

1. Observed variations of the Hβ line could be caused by perturbations in the disk emissivity.

2. Depending on the position of the perturbing region, it has greater influence on one of the Hβ line wings than on the other one.

3. Using the bright spot model for perturbation region we were able to reproduce the observed variations of the Hβ line profile in the case of some AGN such as 3C 390.3.

Acknowledgements

This work has been supported by the Ministry of Science of Republic of Serbia through the project "Astrophysical Spectroscopy of Extragalactic Objects" (146002).

References

Eracleous, M., Halpern, J. P.: 1994, *Astrophys. J. Suppl. Series*, **90**, 30.
Eracleous, M., Halpern, J. P.: 2003, *Astrophys. J. Suppl. Series*, **599**, 886.
Flohic, H. M. L. G., Eracleous, M.: 2008, *astro-ph 0806.0163v*
Gezari, S., Halpern, J. P., Eracleous, M.: 2007, *Astrophys. J. Suppl. Series*, **169**, 167.
Jovanović, P., Popović, L. Č.: 2008, *Publ. Astron. Obs. Belgrade*, **84**, 467.
Shapovalova, A. I., Burenkov1, A. N., Carrasco, L., Chavushyan, V. H., Doroshenko, V. T., Dumont, A. M., Lyuty, V. M., Valdés, J. R., Vlasuyk1, V. V., Bochkarev, N. G., Collin, S., Legrand, F., Mikhailov1, V. P., Spiridonova1, O. I., Kurtanidze, O. and Nikolashvili, M. G.: 2001, *Astron. Astrophys.*, **376**, 775.

Publ. Astron. Obs. Belgrade No. 84 (2008), 495 - 498 *Contributed Paper*

TRANSMITTANCE OF GRAVITO-ACOUSTIC WAVES IN NON-MAGNETIZED STRATIFIED PLASMA

V. M. ČADEŽ[1] and G. JOVANOVIĆ[2]

[1] *Astronomical Observatory Belgrade, Volgina 7, 11160 Belgrade, Serbia*
E–mail: vcadez@aob.bg.ac.yu

[2] *University of Montenegro, Natural-Science Faculty,*
POB 211, 81000 Podgorica, Montenegro
E–mail: gocaj@dell.pmf.cg.ac.yu

Abstract. We study transmittance properties of gravito-acoustic modes at a horizontal interface separating two isothermal regions of a gravitationally stratified non-magnetized plasma. Possible applications to the boundary between the solar interior and the corona are discussed.

1. INTRODUCTION

Observations and measurements of solar global oscillations have been carried out with high precision for decades (see Christensen-Dalsgaard 1989) within the framework of helioseismology studies, aiming to enlighten the internal structure of the Sun. The standard mathematical procedures in that field are based on solving eigen value problems for various models of solar interior and atmosphere (Goedbloed et al. 2004 and references therein). In this paper, we consider a driven problem in which wave modes propagate in a two region model of the system solar interior and solar atmosphere, the corona. The two different regions assumed quasi-isothermal and without magnetic fields are separated by a boundary z=0 where the considered gravito-acoustic waves suffer reflection and refraction. Taking physical parameters with values typical for a simplified two-region configuration of the solar photosphere and corona we analyze the conditions for gravito-acoustic waves to cross and totally reflect from the boundary z=0.

2. BASIC EQUATIONS

We start from the standard set of hydrodynamic equations describing the dynamics of adiabatic processes in a fully ionized hydrogen plasma in presence of gravity with constant acceleration:

$$\begin{aligned} &\frac{\partial\rho}{\partial t} + \nabla\cdot(\rho\vec{v}) \;=\; 0, \qquad \rho\frac{\partial\vec{v}}{\partial t} + \rho\vec{v}\cdot\nabla\vec{v} \;=\; -\nabla p + \rho\vec{g}, \\ &\frac{\partial p}{\partial t} + \vec{v}\cdot\nabla p \;=\; \gamma\frac{p}{\rho}\left(\frac{\partial\rho}{\partial t} + \vec{v}\cdot\nabla\rho\right). \end{aligned} \tag{1}$$

The above equations are linearized with respect to the initial basic state quantities Ψ_0 assuming small adiabatic perturbations $\Psi_1(x,y,z,t)$ that are harmonic in time t and in coordinates x and y, whose amplitudes $\hat{\Psi}_1$ satisfy the condition $|\hat{\Psi}_1| \ll |\Psi_0|$ and depend on the vertical coordinate z:

$$\Psi_1(x,y,z,t) \;=\; \hat{\Psi}_1(k_x,k_y,\omega;z)\mathrm{e}^{-i\omega t+i(k_x x+k_y y)}. \tag{2}$$

The unperturbed gas is initially in hydrostatic equilibrium and assumed to be stepwise isothermal T_0 =const, i.e. with constant speed of sound V_s in two regions separated by the boundary z=0. The basic state is thus described by:

$$\frac{d}{dz}\ln\rho_0 \;=\; -\frac{\gamma g}{V_s^2} \tag{3}$$

with $V_s^2 = \gamma \mathrm{R}\mathrm{T}_0$, γ=$\mathrm{c}_p/\mathrm{c}_v$ being the ratio of specific heats; R=$\mathrm{R}_0/\overline{M}$ where R_0=8.3145 $\mathrm{JK}^{-1}\mathrm{mol}^{-1}$ is the universal gas constant and $\overline{M} = 0.5\mathrm{kg\ mol}^{-1}$ is the mean particle molar mass of the considered e-p plasma.

Eq. (3) now yields:

$$\rho_0 \;=\; \rho_0(0)\mathrm{e}^{-z/H} \quad \text{where:} \quad H = \frac{V_s^2}{\gamma g}, \tag{4}$$

while the linearized Eqs. (1) with perturbations given by Eq. (2) reduce to:

$$\begin{aligned} V_s^2\omega^2\rho_0(z)\frac{d\xi_1}{dz} &= g\omega^2\rho_0(z)\xi_1 - (\omega^2 - k_p V_s^2)p_1, \\ V_s^2\frac{dp_1}{dz} &= V_s^2\rho_0(z)(\omega^2 - \omega_{BV}^2)\xi_1 - gp_1, \end{aligned} \tag{5}$$

with $\rho_0(z)$ given by Eq. (4). Here, ξ_1 is defined by $v_{1z} = -i\omega\xi_1$, and:

$$k_p^2 \equiv k_x^2 + k_y^2, \qquad \omega_{BV}^2 \equiv (\gamma-1)\frac{g^2}{V_s^2},$$

designate squares of the perpendicular wave-number and the Brunt-Väisäläa frequency respectively.

Eqs. (5) can further be transformed to a system of equations with constant coefficients if expressions:

$$\exp(-z/2h)\xi_1 \quad \text{and} \quad \exp(z/2H)p_1$$

are introduced as new unknowns. This finally yields the dispersion relation:

$$k_p^2 = \frac{\omega^2 - \omega_{co}^2 - V_s^2 k_z^2}{\omega^2 - \omega_{BV}^2} \quad \frac{\omega^2}{V_s^2} \tag{6}$$

where $\omega_{co}^2 \equiv \gamma^2 g^2/(4V_s^2)$ is the acoustic wave cut-off frequency squared.

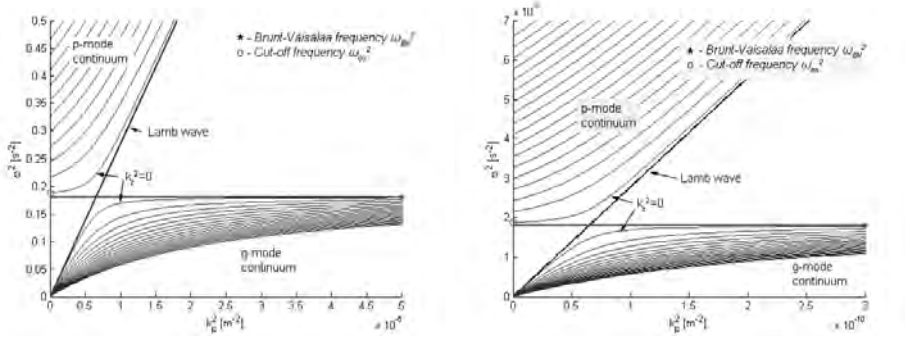

Figure 1: Dispersion curves for the region $z < 0$ (left) and region $z > 0$ (right) i.e. the photosphere and corona repsectively. Two sets of curves are related to acoustic p-modes and gravity g-modes with k_z^2=n$\times 10^{-11}$m^{-2} and k_z^2=n$\times 10^{-11}$m^{-2} (n=0,1,2...) in the left and right plot respectively.

3. RESULTS AND CONCLUSIONS

Figure 1 shows dispersion curves for the region 1 ($z < 0$) simulating the solar photosphere with temperature $T_1 = 10^4$K , and for the region 2 ($z > 0$) simulating the corona with temperature $T_2 = 10^6$K. Gravitational acceleration g is assumed constant within the domains of studied harmonic perturbations and we take g=274ms^{-2} as it is on the Solar surface. Two discrete sets of (ω^2-k_p^2) curves are related to acoustic p-modes and gravity g-modes for k_z^2=n$\times 10^{-11}$m^{-2} and k_z^2=n$\times 10^{-11}$m^{-2} with n=0,1,2...

Figure 2 is a combination of two plots in Figure 1 showing domains of wave propagation where $k_z^2 > 0$ and wave evanescence where $k_z^2 < 0$ in both regions i.e. in the photosphere and corona. Three distinct ranges of the wave period τ and corresponding horizontal wavelength λ_p are noticeable in this figure:

1. Waves with periods $\tau > 200$s are transmitted through the boundary z=0 in both directions if their wavelength λ_p remains below certain value. Waves with larger λ_p are totally reflected in the corona, i.e. they do not enter the photosphere where they become evanescent. Further increase of λ_p results into evanescent waves in the corona too. Since waves become evanescent in both regions, this may indicate a possibility of surface modes at z=0.

2. For wave periods τ between 20s and 200s the waves can not be transmitted through the boundary z=0 as they are evanescent in one or in both regions depending on λ_p.

3. Waves with $\tau < 20$s are evanescent in both regions if λ_p is sufficiently small, then, at larger λ_p, they propagate only in the photosphere and are totally reflected from the boundary z=0. At even larger λ_p, these waves propagate in both regions, i.e. they are transmitted through z=0 between the photosphere and corona in both directions.

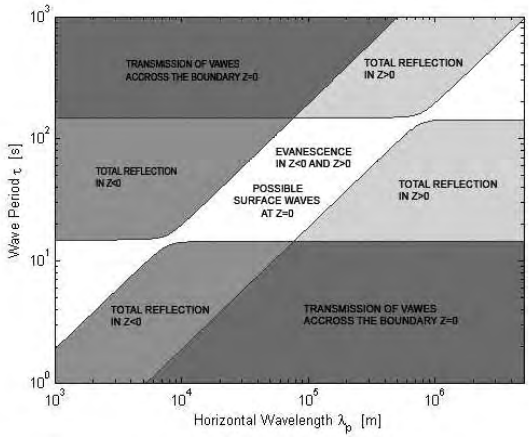

Figure 2: Domains of the bulk wave transmission, total reflection and total evanescence in the considered two region model.

As a conclusion, waves in the corona with sufficiently long, as well as those with short time periods can originate in the photosphere. An analogous statement holds for the wavelength intervals. For example, waves with the period τ=1000 s (≈15.7 min) can be transmitted through z=0 if $\lambda_p < 400$km.

In addition, we conclude that surface modes are possible at $z = 0$ for perturbations with $k_z^2 < 0$ in both regions around the boundary, i.e. in the photosphere and corona.

References

Christensen-Dalsgaard, J.: 1989, Stellar Oscillations (Aarhus, Lecture Notes, Astronomisk Institut, Aarhus Universitet.

Goedbloed, H., Poeds, S.: 2004, Principles of Magnetohydrodynamics,Cambridge University Press, Cambridge, UK.

Publ. Astron. Obs. Belgrade No. 84 (2008), 499 - 502 *Contributed Paper*

RELATIVISTIC COMPRESSION OF A LASER PULSE REFLECTED FROM A MOVING PLASMA

M. M. ŠKORIĆ[1], B. V. STANIĆ[2], Lj. HADŽIEVSKI[2] and Lj. NIKOLIĆ[3]
[1] *National Institute for Fusion Science, Toki-shi 509-5292, Japan*
E–mail: skoric.milos@nifs.ac.jp
[2] *Vinča Institute of Nuclear Sciences, POB 522, Belgrade 11001, Serbia*
[3] *ECERF, University of Alberta, Edmonton AB T6G 2V4, Canada*

Abstract. The reflection of an obliquely incident electromagnetic pulse from a moving plasma half-space is studied. Using the Lorentz transformations, covariance of Maxwell's equations and principle of phase invariance to transform between the rest frame and the moving frame, analytical formula for the linear reflected waveform shows temporal compression and pulse amplification at relativistic velocities of interest for generation of ultra-short laser optical pulses.

1. INTRODUCTION

A transient reflection and transmission of an obliquely incident EM pulse at the steady (non-moving) plasma-vacuum interface has been solved analytically in a closed form by Chabris and Bolle 1971, and Stanić and Škorić 1973ab. Recently, generation of ultra-short (attosecond range - 10^{-18}s) light and relativistic particle bunches gained importance in various applications (see Mourou et al. 2006). Here, we revisit a general problem of a linear reflection of a time-dependent EM (laser) pulse from a plasma half-space moving at the relativistic velocity, see, Stanić and Škorić 1974.

1. 1. FORMULATION

A time-dependent electromagnetic plane wave pulse is incident at the moving cold plasma-vacuum interface. The incident angle is θ_i and the plane of incidence is Oxz, as shown in figure 1. The incident electric field (S- polarization) of the EM pulse in the time domain, by inverse Fourier transformation, is

$$\begin{aligned} E_{yi} &= (1/2\pi)\int_{-\infty}^{+\infty} E_0 \exp\left[j\left(\omega_i t - \mathbf{k}_i\mathbf{r}\right)\right] d\omega_i \\ &\equiv E_0\delta\left(t - (x/c)\sin\theta_i + (z/c)\cos\theta_i\right), \end{aligned} \tag{1}$$

where $\delta(t)$ is the Dirac's function and ω_i and $\mathbf{k}_i$ are the angular frequency and the wavenumber vector in the observer's rest frame K, respectively. The uniform plasma half-space is moving with the velocity $\mathbf{v}$, where in two special cases: a) $\mathbf{v} = \mathbf{e}_x v$ and b) $\mathbf{v} = \mathbf{e}_z v$. The rest frame of the moving plasma is K'.

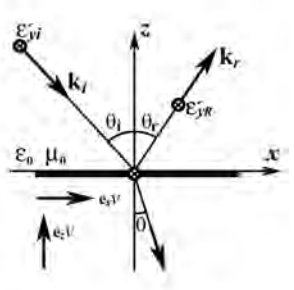

Figure 1: Geometry of the problem.

2. ANALYTICAL THEORY

Making use of the Lorentz transformations, covariance of Maxwell's equations and the principle of phase invariance, to transform between the rest (laboratory) frame and the moving frame (see e.g. Papas 1965, Ch. 7); the incident electric field in the moving frame K', can be represented as

$$\begin{aligned} E_{yi}^{'} &= (1/2\pi)\int_{-\infty}^{+\infty}\gamma\left(1-\mathbf{k}_i\mathbf{v}/\omega_i\right)E_0\exp\left[j\left(\omega_i t-\mathbf{k}_i\mathbf{r}\right)\right]d\omega_i = \\ &= (1/2\pi)\int_{-\infty}^{+\infty}\gamma\left(1+\mathbf{k}_i'\mathbf{v}/\omega_i'\right)E_0'\exp\left[j\left(\omega_i' t'-\mathbf{k}_i'\mathbf{r}'\right)\right]d\omega_i', \end{aligned} \tag{2}$$

with physical quantites with the "prime" superscript corresponding to the moving frame K', and where

$$\omega_i' = \gamma\left(1-\mathbf{k}_i\mathbf{v}/\omega_i\right)\omega_i, \quad \gamma = \left(1-v^2/c^2\right)^{-1/2} = \left(1-\beta^2\right)^{-1/2}, \tag{3}$$

$$\mathbf{k}_i^{'} = \mathbf{k}_i - \gamma\omega_i\mathbf{v}/c^2 + (\gamma-1)\left(\mathbf{k}_i\mathbf{v}\right)\mathbf{v}/v^2, \quad \text{and} \tag{4}$$

$$E_0' = \gamma\left(1-\mathbf{k}_i\mathbf{v}/\omega_i\right)E_0, \quad E_{01}' = \gamma\left(1+\mathbf{k}_i'\mathbf{v}/\omega_i'\right)E_0'. \tag{5}$$

With the $\exp\left(j\omega_i^{'}t^{'}\right)$ time dependence suppressed, the incident electric field in the frequency domain in the moving frame is given by

$$\mathcal{E}_{yi}^{'} = E_{01}'\exp\left(-j\mathbf{k}_i^{'}\mathbf{r}^{'}\right), \tag{6}$$

and the frequency domain expression for the reflected field is simply

$$\mathcal{E}_{yR}^{'} = \frac{1-N^{'}}{1+N'}E_{01}'\exp\left(-j\mathbf{k}_r^{'}\mathbf{r}^{'}\right), \tag{7}$$

where, the well-known index of refraction for cold plasma at rest in K', is

$$N' = \left|1-\left(\omega_p^{'}/\omega'\cos\theta_i^{'}\right)^2\right|^{1/2}, \quad \omega_i' = \omega_r' = \omega_t' \equiv \omega'.$$

The vacuum dispersion relation $\omega_{i,r}^{(\prime)} = k_{i,r}^{(\prime)} c$, is valid in K and K' frame.

Using again the Lorentz transformations, covariance of Maxwell's equations and the principle of phase invariance to transform back from the moving frame K' to the laboratory frame K, the time domain reflected field becomes

$$\begin{aligned} E_{yR} &= (1/2\pi) \int_{-\infty}^{+\infty} \gamma \left(1 + \mathbf{k}_r' \mathbf{v}/\omega_i'\right) \mathcal{E}_{yR}^{'} \exp\left(j\omega^{'} t^{'}\right) d\omega^{'} \\ &= \gamma \left(1 + \mathbf{k}_r' \mathbf{v}/\omega_i'\right) E_{yR}^{'}. \end{aligned} \tag{8}$$

The expression for $E_{yR}^{'}$ found by the standard method of contour integration as

$$E_{yR}^{'} = -\left(2E_0'/\tau^{'}\right) J_2\left(a^{'}\tau^{'}\right) U\left(\tau^{'}\right), \tag{9}$$

where

$$\tau^{'} = t^{'} - \mathbf{k}_r^{'}\mathbf{r}^{'}/\omega^{'}, \quad a^{'} = \omega_p^{'}/\cos\theta_i^{'}, \quad \text{and } U\left(\tau^{'}\right), \tag{10}$$

is the Heaviside unit step function, while $J_2(x)$ is the Bessel's function of the first kind of second order. We note that (9) is the Green's function solution, while a linear solution to another incident pulse profile is found by a convolution integration.

Further, we discuss two cases of the moving plasma half-space:

- a) $\mathbf{v} = \mathbf{e}_x v$

The reflected field is identical to non-moving plasma case; as normally incident wave does not "see" plasma motion in x-direction.

- b) $\mathbf{v} = \mathbf{e}_z v$

$$E_{yR} = -\left(2E_0\alpha_0/\xi\right) J_2\left(\alpha_1\xi\right) U\left(\xi\right), \tag{11}$$

where

$$\alpha_0 = \gamma^2\left(1 + 2\beta\cos\theta_i + \beta^2\right), \quad \alpha_1 = \left|\omega_p/\gamma\left(\beta + \cos\theta_i\right)\right|, \tag{12}$$

and

$$\xi = \alpha_0 t - (x/c)\sin\theta_i - (z/c)\,\gamma^2\left|\left(1+\beta^2\right)\cos\theta_i + 2\beta\right|. \tag{13}$$

3. RESULTS AND DISCUSSION

It is clear that the plasma motion modifies both the amplitude and the oscillatory phase of the reflected field (11); with a departure from the classical Snell's law ($\theta_i \neq \theta_r$). More precisely, (13) gives: $\tan\theta_r = \sin\theta_i/\gamma^2\left|\left(1+\beta^2\right)\cos\theta_i + 2\beta\right|$, which for large $\beta > 0$, predicts $\theta_r < \theta_i$, i.e. the reflection angle close to normal incidence. We note that earlier authors, Rattan et al 1973, erroneously performed inverse Fourier transform over the incident ω_i; instead of integrating over the reflected frequency. The reflected waveforms for E_{yR}, as function of time and the plasma velocity $v\,(\mathbf{v} = \mathbf{e}_z v)$ for normal incidence ($\theta_i = 0$), are plotted in figure 2a. The time delays in terms of the inverse plasma frequency of the maximum positive and negative reflected amplitude, as a function of plasma velocity β, are shown in figure 2b. Large compression and

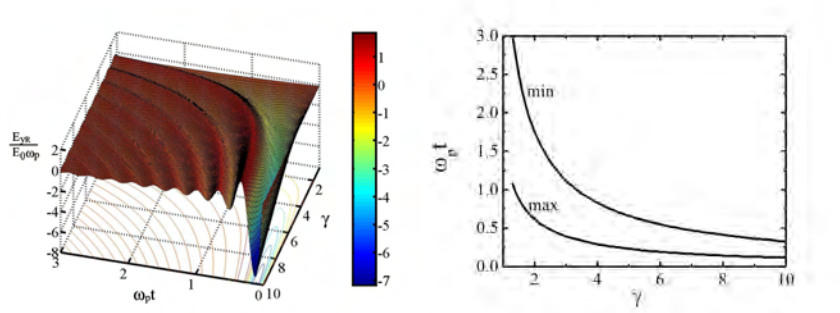

Figure 2: (a) Reflected EM field in time as a function of the plasma velocity γ. (b) Time period of the first and second peak in the reflected wave versus plasma velocity.

amplification of the reflected pulse (factor $\sim 2\gamma$) at highly relativistic plasma motion reveals a remarkable feature and some potential of this linear mechanism for ultra-short (attosecond) pulse generation by low intensity high-rep-rate femtosecond laser pulses scattering at counter-propagating relativistic electron beams, see e.g. Nikolić et al. 2008. For example, a short green laser light pulse ($\lambda \sim 0.5$ microns) reflected from 5MeV electrons ($\gamma \sim 10$) at critical density gives a main reflected pulse width of around 60 attoseconds; basically given by the relativistically upshifted plasma frequency which can be high in solid density plasmas.

Acknowledgments

The work was supported by the Ministry of Science of Serbia, Project No. 141034.

References

Chabris, D. B., Bolle, D. M.: 1971, *Radio Science*, **6**, 1143.
Mourou, G. A., Tajima, T., Bulanov, S. V.: 2006, *Rev. Mod. Phys.*, **78**, 309.
Nikolić, Lj., Škorić, M. M., Ishiguro, S., Sakagami, H., Vidal, F., Johnston, T. W.: 2008, *J. Phys: Conference Series*, **112**, 022086.
Papas, C. H.: 1965, Theory of Electromagnetic Wave Propagation, Mc Graw Hill, New York.
Ratan, I., Gautama, G. D.: 1973, *J. Phys. D: Appl. Phys.*, **6**, L85.
Stanić, B. V., Škorić, M. M.: 1973, *J. Phys. D: Appl. Phys.*, **7**, L137.
Stanić, B. V., Škorić, M. M.: 1973, *Electronics Lett.*, **9**, 583.
Stanić, B. V., Škorić, M. M.: 1974, *Proc. of* 7^{th} *SPIG Conf.*, Rovinj, Yugoslavia, p. 221.

Publ. Astron. Obs. Belgrade No. 84 (2008), 503 - 506 *Contributed Paper*

MAGNETIC FIELD GENERATION AT ION ACOUSTIC TIME SCALE

J. VRANJES[1,2], H. SALEEM[3] and S. POEDTS[1]

[1] *Center for Plasma Astrophysics, and Leuven Math. Modeling and Comp. Science Center, Celestijnenlaan 200B, 3001 Leuven, Belgium*

[2] *Faculté des Sciences Appliquées, Avenue F.D. Roosevelt 50, 1050 Bruxelles, Belgium*

[3] *Theoretical Plasma Physics Division, PINSTECH, P.O. Nilore, Islamabad, Pakistan*

Abstract. Ion acoustic wave in an inhomogeneous plasma naturally couples with a transverse electromagnetic perturbations. Due to this coupling the ion acoustic mode becomes electromagnetic. There appears a lower frequency cut off of the ion acoustic wave, the wave becomes dispersive and backward.

1. INTRODUCTION

The model of electron-magnetohydrodynamics (EMHD) includes electron perturbations on a background of immobile ions. Usually, the displacement current in the Ampère law is neglected in this model, implying $(\omega/k)^2 \ll c^2$, where ω and k denote the wave parameters, and c denotes the speed of light. Moreover, in a plasma containing only electrons and static ions, the perturbations are usually assumed to be incompressible. This is formally seen by substituting the Ampère's law (without the displacement current $\mu_0\varepsilon_0\partial\vec{E}/\partial t$) into the electron continuity equation. The mentioned assumption of static ions implies electron perturbations that take place at spatial scales at which the ions, due to their much larger inertia, are not able to react, i.e., much below the ion skin depth $\lambda_i \equiv c/\omega_{pi}$, where ω_{pi} is the ion plasma frequency. This may formally be checked by making the ratio $|n_i\vec{v}_i|/|n_e\vec{v}_e|$, and by further using the ion momentum equation and the Ampère law to express the ion and electron velocities, and by applying the operator $\nabla\times$ onto the resulting expression in the numerator and denominator separately. This yields

$$\left|\frac{\omega_{pi}^2}{\omega c^2}\frac{\nabla\times\vec{E}}{\nabla\times(\nabla\times\vec{B})}\right| = \frac{1}{\lambda_i^2 k^2} \ll 1.$$

In the presence of an equilibrium density gradient, using the EMHD set of equations together with an electron energy (temperature) equation, such perturbations describe the generation of magnetic field in plasmas with sharp discontinuities (the magnetic surface waves) Jones (1983), Yu and Stenflo (1985), or in weakly inhomogeneous plasmas Nycander et al. (1987). The magnetic field is generated due to the baroclinic

vector $\nabla n_0 \times \nabla T_{e1}$ (where T_{e1} is the electron temperature perturbation). This mechanism was first suggested by Stamper and Tidman (1973), and is essentially an electron dynamics effect.

In the present work we give an alternative approach to the problem of the generation of magnetic field in plasmas. We shall show that when the ion perturbations are taken into account (implying compressible perturbations), there appears a coupling between the ion acoustic and electromagnetic perturbations. The coupling is entirely due to the presence of small equilibrium density and temperature gradients. Note that here both equilibrium gradients enter into the mode description only in order to have a properly satisfied equilibrium. This means that the two gradient vectors are antiparallel.

2. DERIVATIONS AND RESULTS

To demonstrate the coupling we use a simple model with a minimum number of equations forming a closed set. We start from the wave equation for the perturbed EM field:

$$k^2\vec{E}_1 - \vec{k}(\vec{k}\cdot\vec{E}_1) - \frac{\omega^2}{c^2}\vec{E}_1 - \frac{i\omega}{c^2\varepsilon_0}\vec{j} = 0. \tag{1}$$

Here, the perturbations are assumed to be of the form $\sim f(x)\exp(-i\omega t + ikz)$. In addition, we assume that the equilibrium plasma has small density and temperature gradients along the x-axis. Therefore, a weak x-dependence of the wave amplitude is considered along with the local approximation implying $|\partial/\partial x| \ll |k| = 2\pi/|\lambda_z|$. The perturbations are assumed to be isothermal (contrary to the usual EMHD theory) and the ions are assumed to be cold. Having the density and temperature gradients along the x-axis, we choose perturbations propagating in any perpendicular, e.g., z-direction. The properties of the medium enter Eq. (1) through the current $\vec{j} = en_0(x)(\vec{v}_{i1} - \vec{v}_{e1})$.

The electron dynamics must include the momentum and continuity equations while the ions are completely described by $m_i n_0 \partial\vec{v}_{i1}/\partial t = en_0\vec{E}_1$. A static plasma equilibrium without macroscopic electromagnetic field is satisfied by

$$\frac{1}{T_0}\frac{dT_0}{dx} = -\frac{1}{n_0}\frac{dn_0}{dx}. \tag{2}$$

The electron velocity is given by

$$\vec{v}_{e1} = -\frac{ie}{m_e\omega}\vec{E}_1 + \frac{iev_{Te}^2}{\omega m_e\omega_0^2}\nabla(\nabla\cdot\vec{E}_1) + \frac{iev_{Te}^2}{\omega m_e\omega_0^4}(\nabla\cdot\vec{E}_1)k^2v_{Te}^2\frac{\nabla T_0}{T_0}$$

$$+\frac{iev_{Te}^2}{\omega m_e\omega_0^2}\frac{\nabla(E_{1x}n_0')}{n_0} + \frac{iev_{Te}^2}{\omega m_e\omega_0^2}\frac{E_{1x}n_0'}{n_0}\frac{k^2v_{Te}^2}{\omega_0^2}\frac{\nabla T_0}{T_0} + \frac{iev_{Te}^2}{\omega m_e\omega_0^2}\frac{E_{1x}n_0'}{n_0}\frac{\nabla T_0}{T_0}. \tag{3}$$

Here, $\omega_0^2 = \omega^2 - k^2v_{Te}^2$, $v_{Te}^2 = \kappa T_0(x)/m_e$, $\nabla n_0 = \vec{e}_x dn_0/dx \equiv \vec{e}_x n_0'(x)$, $\nabla T_0 = -\vec{e}_x dT_0/dx \equiv -\vec{e}_x T_0'(x)$. We have assumed a linear x-dependence of the two equilibrium quantities $n_0(x)$ and $T_0(x)$. Eq. (1) becomes

$$k^2\vec{E}_1 - \vec{k}(\vec{k}\cdot\vec{E}_1) - \frac{\omega^2}{c^2}\vec{E}_1 + \frac{\omega_{pe}^2+\omega_{pi}^2}{c^2}\vec{E}_1 + \frac{\omega_{pe}^2 v_{Te}^2}{c^2\omega_0^2}\vec{k}(\vec{k}\cdot\vec{E}_1)$$
$$-\frac{i\omega_{pe}^2 v_{Te}^2}{c^2 n_0\omega_0^2}\,\vec{k}E_{1x}n_0' - \frac{ik^3 v_{Te}^4\omega_{pe}^2}{c^2\omega_0^4 T_0}E_{1z}T_0'\vec{e}_x = 0. \tag{4}$$

The y-component of the vector equation (4) gives the transverse electromagnetic mode which is not of interest here.

The z and x components are

$$\left(-\omega^2 + \omega_{pe}^2 + \omega_{pi}^2 + \frac{k^2\omega_{pe}^2 v_{Te}^2}{\omega_0^2}\right)E_{1z} - \frac{ikv_{Te}^2\omega_{pe}^2 n_0'}{\omega_0^2 n_0}\,E_{1x} = 0, \tag{5}$$

$$\left(k^2 + \frac{\omega_{pe}^2+\omega_{pi}^2-\omega^2}{c^2}\right)E_{1x} - \frac{ik^3 v_{Te}^4\omega_{pe}^2 T_0'}{c^2\omega_0^4 T_0}\,E_{1z} = 0. \tag{6}$$

Eqs. (5) and (6) describe the coupling (due to the small density/temperature gradients) between the longitudinal, E_{z1}, and the transverse electric field perturbation, E_{x1}. They also determine the transverse, perturbed magnetic field component $B_{y1} = kE_{x1}/(i\omega)$. The dispersion equation reads:

$$\left(\omega_1^2 - \frac{k^2 v_{Te}^2}{\omega_{pe}^2}\right)^2\left[\omega_1^2\left(\frac{\omega_{pi}^2}{\omega_{pe}^2}+1-\omega_1^2\right) - \frac{k^2 v_{Te}^2}{\omega_{pe}^2}\left(\frac{\omega_{pi}^2}{\omega_{pe}^2}-\omega_1^2\right)\right]\left(1+\frac{k^2c^2}{\omega_{pe}^2}+\frac{\omega_{pi}^2}{\omega_{pe}^2}-\omega_1^2\right)$$
$$+\frac{k^4 v_{Te}^6}{\omega_{pe}^6}\frac{n_0'}{n_0}\frac{T_0'}{T_0} = 0. \tag{7}$$

Here, $\omega_1 \equiv \omega/\omega_{pe}$. Our interest here is the low frequency limit $\omega/\omega_{pe} \ll 1$, which yields the mode frequency in the range of the ion sound wave:

$$\omega_{EMIA}^2 = \frac{k^2 c_s^2}{1+k^2\lambda_d^2}\left[1 + \frac{m_i}{m_e}\left(\frac{n_0'}{n_0}\right)^2\frac{1}{k^2(1+k^2\lambda_e^2)}\right]. \tag{8}$$

In the limit of small values of the wave number, there appears a lower frequency cut off for the electromagnetic ion acoustic (EMIA) wave $\omega \to \omega_c = \kappa_n^2 v_{Te}^2$, where $\kappa_n = n_0'/n_0$. The group velocity of the electromagnetic ion acoustic mode (8) appears proportional to

$$k^4\lambda_e^4 - 2k^2\lambda_e^2(\kappa_n^2\lambda_d^2 m_i/m_e - 1) + 1 - \kappa_n^2 m_i(\lambda_e^2+\lambda_d^2)/m_e.$$

The sign of this group velocity is thus determined by the wave-number, the equilibrium density scale length, and the plasma parameters, so that we can have both a direct and a backward wave. As seen from Eq. (8), for the wave-lengths much exceeding the electron Debye radius, the mode may have a frequency which is above the ion sound frequency. On the other hand, the second term in Eq. (8) describes a backward mode. As a demonstration only, these properties are presented in Fig. 1 (Vranjes et al. 2007) for the ion mass $m_i = 40$ proton masses, for the electron temperature $T = 10^4$ K, and taking $\kappa_n = 1$ m^{-1}. We plot the EMIA mode for two values of the number density, viz. $n_0 = 10^{17}$ m^{-3} (dashed line) and $n_0 = 10^{15}$ m^{-3} (full line).

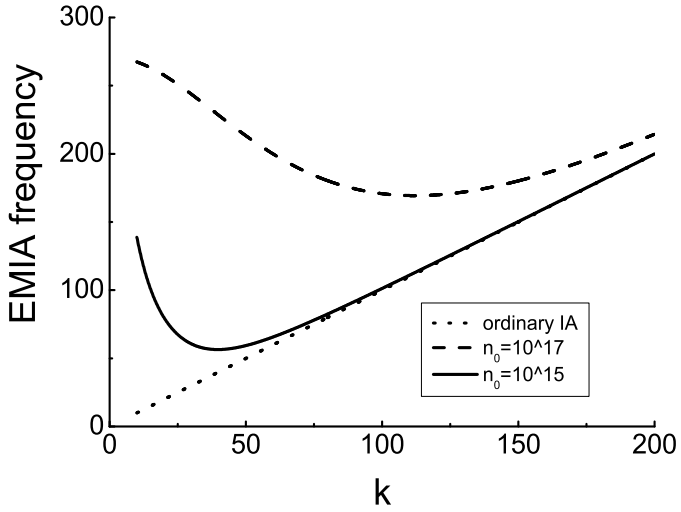

Figure 1: The electromagnetic ion sound frequency in units of $\kappa_n c_s$ for the two number densities $n_0 = 10^{17}$ m^{-3} (dashed line), and $n_0 = 10^{15}$ m^{-3} (full line) in terms of k normalized to κ_n.

The frequency is normalized to $\kappa_n c_s$ and the wave-number to κ_n. The dotted line describes the ordinary ion sound normalized to the same units. From the full and dashed lines it is seen that for small wave numbers it is a backward mode and very much different from the ordinary ion sound wave.

The linear dispersion equation Eq. (8) describes an electromagnetic wave in unmagnetized plasmas at the ion acoustic time scale, with the electromagnetic part which is due to the electron pressure gradient. However, for the electromagnetic part of the mode we do not need the electron temperature perturbation.

Acknowledgements

Results are obtained in the framework of the projects G.0304.07 (FWO-Vlaanderen), C 90205 (Prodex), GOA/2004/01 (K.U.Leuven), and the Interuniversity Attraction Poles Programme -Belgian State - Belgian Science Policy.

References

Jones, R. D.: 1983, *Phys. Rev. Lett.*, **51**, 1269.
Nycander, J., Pavlenko, V. P., Stenflo, L.: 1987, *Phys. Fluids*, **30**, 1367.
Stamper, A. A., Tidman, D. A.: 1973, *Phys. Fluids*, **16**, 2024.
Vranjes, J., Saleem, H., Poedts, S.: 2007, *Phys. Plasmas*, **14**, 034504.
Yu, M. Y, Stenflo, L.: 1985, *Phys. Fluids*, **28**, 3447.

Publ. Astron. Obs. Belgrade No. 84 (2008), 507 - 510 *Contributed paper*

COUPLED GAS ACOUSTIC AND ION ACOUSTIC WAVES IN WEAKLY IONIZED PLASMA

J. VRANJES[1,2], B. P. PANDEY[3] and S. POEDTS[1]

[1] *Center for Plasma Astrophysics, and Leuven Math. Modeling and Comp. Science Center, Celestijnenlaan 200B, 3001 Leuven, Belgium*

[2] *Faculté des Sciences Appliquées, Avenue F.D. Roosevelt 50, 1050 Bruxelles, Belgium*

[3] *Department of Physics, Macquarie University, Sydney, NSW 2109, Australia*

Abstract. Gas acoustic and ion acoustic modes are investigated in a collisional, weakly ionized plasma in the presence of un-magnetized ions and magnetized electrons. In such a plasma, an ion acoustic mode, driven by an electron flow along the magnetic field lines, can propagate almost at any angle with respect to the ambient field lines as long as the electrons are capable of participating in the perturbations by moving only along the field lines. The electron-ion collisions are shown to modify the previously obtained angle dependent instability threshold for the driving electron flow. The inclusion of the neutral dynamics implies an additional neutral sound mode which couples to the current driven ion acoustic mode, and these two modes can interchange their identities in certain parameter regimes.

1. INTRODUCTION

Weakly ionized plasmas with three or more plasma/gas species include a plethora of effects that are normally absent in the simpler one-fluid or two-fluid models. If such a plasma-gas mixture is placed in an external magnetic field, it may result in the un-magnetized ions while the electrons may remain magnetized. An example of such plasma-gas mixture is the solar atmosphere where, for protons, the ratio Ω_i/ν_i changes between $\sim 10^{-4}$ and 0.2 for the altitudes $h = 0$ km and $h = 1000$ km, respectively. In the same time, for electrons the value of the ratio Ω_e/ν_e varies between $\sim 10^{-2}$ and 16 (see e.g. Vranjes et al. 2007a, 2008).

In our recent works Vranjes and Poedts (2006a,b), Vranjes et al. (2006), the excitation of the dust-acoustic (DA) and ion-acoustic (IA) modes by a parallel or perpendicular (with respect to the ambient magnetic field) flow of the light plasma species (electrons in the case of IA mode and ions in the DA case) has been studied. The driving current instability is associated with the collisions and represents a purely fluid effect. In the IA case, the electron collisions are shown to be necessary for the instability to develop, while the ion collisions introduce an angle dependent dip in the profile for the threshold value of the flow. In the present study we investigate the behavior of an ion acoustic (IA) mode driven by an equilibrium electron flow along the magnetic field lines, in the presence of the ion-neutral, electron- neutral, and electron-ion collisions. Neutrals can also be perturbed due to various external reasons

(a common situation in the lower solar atmosphere, in the terrestrial atmosphere, etc.), or due to interaction with the perturbed plasma species. This introduces an additional (neutral) gas acoustic (GA) mode.

2. MODEL AND RESULTS

Acoustic perturbations of the neutral gas component include the friction force due to collisions with the ions of the form $-m_n n_{n0}\nu_{ni}(\vec{v}_{n1}-\vec{v}_{i1})$, with the momentum conservation due to friction $m_\alpha n_{\alpha 0}\nu_{\alpha\beta}=m_\beta n_{\beta 0}\nu_{\beta\alpha}$. Using the neutral momentum and continuity equations, one finds that the perturbed velocity of neutrals is coupled to the perturbed ion velocity as $v_{n1}=[i\omega\nu_{ni}/(\omega\omega_n-k^2v_{Tn}^2)]v_{i1}$. This describes an acoustic wave in the neutral gas which is coupled to the ions due to collisions. We have assumed small longitudinal perturbations of the form $\sim\exp(-i\omega t+i\vec{k}\cdot\vec{r})$, propagating in an arbitrary direction $\vec{r}$ which makes an angle ψ with the magnetic field vector $\vec{B}_0=B_0\vec{e}_z$. Here, $\omega_n\equiv\omega+i\nu_{ni}$, $v_{Tn}^2=\kappa T_n/m_n$, and v_{i1} is the perturbed ion velocity in the same $\vec{r}$ direction.

The ion momentum equation reads

$$m_i n_{i0}\frac{\partial v_{i1}}{\partial t}=-en_{i0}\frac{\partial\phi_1}{\partial r}-\kappa T_i\frac{\partial n_{i1}}{\partial r}-m_i n_{i0}\nu_{in}(v_{i1}-v_{n1})+\mu_{\scriptscriptstyle L}\frac{\partial^2 v_{i1}}{\partial r^2}. \tag{1}$$

The ions are not magnetized, $\nu_{in}\gg\Omega_i$, and hence there is no Lorentz force term ($\sim\vec{v}_i\times\vec{B}$) in this equation. Here, $\mu_{\scriptscriptstyle L}\nabla^2\vec{v}_i$ is an effective viscosity term that accounts for the Landau damping (D'Angelo et al. 1979). The parameter $\mu_{\scriptscriptstyle L}$ is chosen to quantitatively describe the well-known properties of the Landau effect. Taking note of the fact that the ratio between the attenuation length δ and the wavelength λ is independent both of the wavelength and the plasma density n, and dependent on the electron/ion temperature ratio $\tau=T_e/T_i$ in a prescribed way, one writes $\mu_{\scriptscriptstyle L}=m_i n_{i0}v_s\lambda/(2\pi^2\delta/\lambda)$. Here, $v_s=(c_s^2+v_{Ti}^2)^{1/2}$ is the ion sound speed, $c_s^2=\kappa T_e/m_i$, while the dependence of the ratio δ/λ on τ is such that the attenuation is strong at $\tau\approx 1$ and weak for higher values of τ. The 'fluid' attenuation length can be expressed by the following approximate fitting formula to give the same damping as the corresponding kinetic expression: $d\equiv\delta/\lambda\approx 0.2751+0.0421\,\tau+0.089\,\tau^2-0.011785\,\tau^3+0.0012186\,\tau^4$. Using the ion continuity we obtain:

$$\frac{n_{i1}}{n_{i0}}=\frac{ek^2}{m_i(\omega\omega_2-k^2v_{Ti}^2)}\,\phi_1. \tag{2}$$

Here $\omega_2=\omega+i(\nu_{in}+\mu_0k^2)+\nu_{in}\nu_{ni}\omega/(\omega\omega_n-k^2v_{Tn}^2)$, $\mu_0=\mu_{\scriptscriptstyle L}/(m_i n_{i0})$.

Electron collisions with both neutrals and ions should be included in the momentum equation which is of the form

$$m_e n_e\left[\frac{\partial\vec{v}_e}{\partial t}+(\vec{v}_e\cdot\nabla)\vec{v}_e\right]=en_e\nabla\phi-en_e\vec{v}_e\times\vec{B}-\kappa T_e\nabla n_e$$
$$-m_e n_e\nu_{en}(\vec{v}_e-\vec{v}_n)-m_e n_e\nu_{ei}(\vec{v}_e-\vec{v}_i). \tag{3}$$

The electrons are assumed to be magnetized, i.e., $\Omega_e>\nu_{ei}+\nu_{en}$. In this case, their perpendicular dynamics is negligible and the electron continuity yields

$$\frac{n_{e1}}{n_{e0}}=\frac{\nu_e\omega_0}{\nu_e\omega_0+ik_z^2v_{Te}^2}\left(\frac{iek_z^2}{m_e\nu_e\omega_0}\,\phi_1+\frac{\nu_{en}}{\nu_e}\frac{k_z^2}{k\omega_0}\,v_{n1}+\frac{\nu_{ei}}{\nu_e}\frac{k_z^2}{k\omega_0}\,v_{i1}\right). \tag{4}$$

Here, $\omega_0 = \omega - k_z v_0$, $\nu_e = \nu_{ei} + \nu_{en}$, and the electron inertia terms are omitted implying a Doppler shifted wave frequency below the electron collision frequency, and a Doppler shifted wave phase velocity below the electron thermal speed. We have assumed a constant equilibrium electron flow $\vec{v}_0 = v_0 \vec{e}_z$. Using the quasi-neutrality, we finally obtain the following dispersion equation:

$$\left[\omega^2 - k^2 c_s^2 \left(1 + \frac{1}{\tau}\right)\right](\omega\omega_n - k^2 v_{Tn}^2) = -\nu_{ni}\omega^2 \left(\nu_{in} + \nu_{en}\frac{m_e}{m_i}\right)$$

$$-i(\omega\omega_n - k^2 v_{Tn}^2)\left\{\omega(\nu_{in} + \mu_0 k^2) + \frac{m_e}{m_i}\left[\omega\left(\nu_{ei}\left(\frac{k^2}{k_z^2} - 1\right) + \nu_{en}\frac{k^2}{k_z^2}\right)\right.\right.$$

$$\left.\left. - k_z v_0(\nu_{ei} + \nu_{en})\frac{k^2}{k_z^2}\right]\right\}. \quad (5)$$

We discus first the case of static neutrals. From Eq. (5) we find a modified ion sound mode that is unstable provided that

$$V > \frac{\kappa}{1+\nu}\left(1 + \frac{1}{\tau}\right)^{1/2}\left[\nu\left(\frac{1}{\kappa^2} - 1\right) + \frac{1}{\kappa^2} + \frac{\mu}{\widehat{\nu}_{en}}\left(\frac{\widehat{\nu}_{en} b}{(\mu\tau)^{1/2}} + \frac{(1 + 1/\tau)^{1/2}}{\pi d}\right)\right]. \quad (6)$$

Here, $V = v_0/c_s$, $\widehat{\nu}_{en}$ is normalized to $\omega_r \simeq k c_s$ and should be chosen in accordance with the model. From $\nu_{en} = \sigma_{en} n_{n0} v_{Te}$ and $\nu_{in} = \sigma_{in} n_{n0} v_{Ti}$, we obtain $\widehat{\nu}_{in} = \widehat{\nu}_{en} b/(\mu\tau)^{1/2}$, where $\mu = m_i/m_e$, $b = \sigma_{in}/\sigma_{en}$, $\kappa = k_z/k$, $\nu = \widehat{\nu}_{ei}/\widehat{\nu}_{en}$, $\widehat{\nu}_{ei}$ is also given in units of $k c_s$. For larger values of ν, the second and third terms in Eq. (6) are reduced, the latter implying that the minimum in the threshold velocity profile reduces. This behavior is presented in Fig. 1 (left) for a hydrogen plasma in a neutral hydrogen gas (Vranjes et al. 2007b). Here, $\tau = 1$, and it follows that $\sigma_{en} = 2.5 \cdot 10^{-19}$ m^2, $\sigma_{in} = 9.24 \cdot 10^{-19}$ m^2 at the temperature of 1 eV, and we have chosen $\widehat{\nu}_{en} = 30$. For these parameters $d \simeq 0.4$, and $\widehat{\nu}_{in} = 2.6$. The electron-ion collisions drastically reduce the velocity threshold at small angle of propagation (i.e., for k_z/k close to 1). The limit $\nu \sim 1$ still implies a much larger neutral number density, and the neutral hydrogen gas can be assumed as a static non-moving background. This is due to the much larger collision cross section for Coulomb collisions.

When the neutral gas is perturbed or when the perturbations in the ionized component induce (due to the friction) perturbations of the neutral background, Eq. (5) in dimensionless form becomes

$$\widehat{\omega}^2 = 1 + \frac{1}{\tau} - \frac{\widehat{\omega}^2 \widehat{\nu}_{ni}\widehat{\nu}_{en}\left[b(\mu\tau)^{-1/2} + \mu^{-1}\right]}{\widehat{\omega}(\widehat{\omega} + i\widehat{\nu}_{ni}) - \frac{\mu_n}{\tau_n}}$$

$$-i\left\{\widehat{\omega}\left[\widehat{\nu}_{in} + \frac{(1+\tau^{-1})^{1/2}}{\pi d}\right] + \frac{1}{\mu}\left[\widehat{\omega}\widehat{\nu}_{en}\left(\nu\left(\frac{1}{\kappa^2} - 1\right) + \frac{1}{\kappa^2}\right) - \frac{V\widehat{\nu}_{en}(1+\nu)}{\kappa}\right]\right\}. \quad (7)$$

All frequencies are normalized to $k c_s$, and we have introduced new parameters $\tau_n = T_e/T_n$, $\mu_n = m_i/m_n$. The number of parameters can be reduced by using as before $\widehat{\nu}_{in} = \widehat{\nu}_{en} b/(\mu\tau)^{1/2}$, and from the momentum conservation in the friction force terms here we have $\widehat{\nu}_{ni} = \mu_n X\, b\widehat{\nu}_{en}/(\mu\tau)^{1/2}$, $X = n_{i0}/n_{n0}$. As a demonstration Eq. (7) is solved for $\tau = 4$, $\tau_n = 4$, $\mu = 1838$, $\mu_n = 1$, $\widehat{\nu}_{en} = 30$, and $V = 30$, $n_{e0} = n_{i0} =$

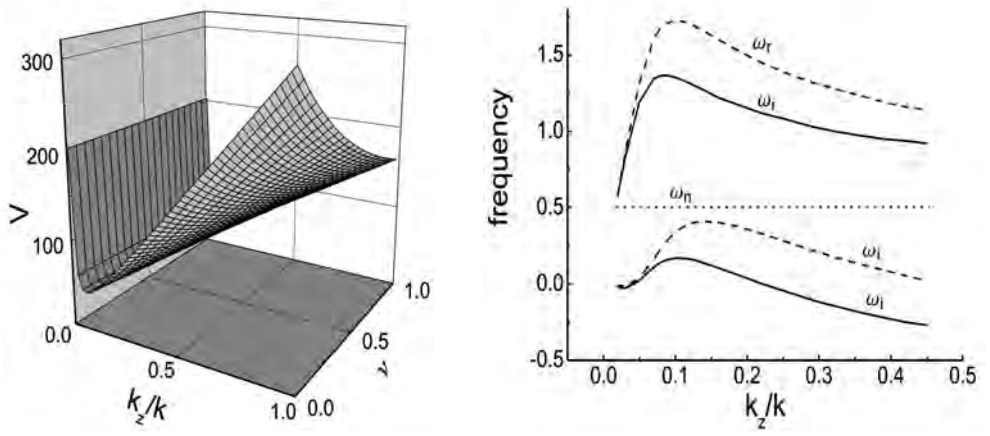

Figure 1: *Left:* The normalized threshold velocity $V \equiv v_0/c_s$ for the instability in terms of k_z/k and $\nu \equiv \nu_{ei}/\nu_{en}$. The unstable values are located above the surface. *Right:* Normalized real ω_r and imaginary ω_i parts of the angle dependent ion acoustic frequency for $\nu = 0$ (full lines) and $\nu = 0.916$ (dashed lines), in terms of k_z/k. The dotted line ω_n describes the neutral acoustic mode.

$6 \cdot 10^{16}$ m^{-3} and $n_{n0} = 10^{19}$ m^{-3}, which yields $X = 0.006$ and $\nu = 0.916$. The results are presented in Fig. 1 (right), with the remarkable angle dependent behavior of the IA mode. The neutral acoustic mode has nearly a constant frequency $\omega_n \simeq 0.5$ and a very small decrement $\simeq -0.005$. The real and imaginary parts of the ion acoustic mode frequency change in the presence of electron-ion collisions ν although the ionization is relatively small. Note that the assumed value of $\widehat{\nu}_{en} = 30$ in principle fixes the wavelength of fluctuations. For example, assuming $T = 5000$ K, one has $c_s = 6.4$ km/s and $\nu_{en}/(kc_s) = 30$ implies a wavelength of 0.7 m.

Some additional features of the mode behavior is given in Vranjes et al. (2007b). These include the interchange of their identities in certain parameter regimes.

Acknowledgements

Results are obtained in the framework of the projects G.0304.07 (FWO-Vlaanderen), C 90205 (Prodex), GOA/2004/01 (K.U.Leuven), and the Interuniversity Attraction Poles Programme -Belgian State - Belgian Science Policy.

References

D'Angelo, N., Joyce, G., Pesses, M. E.: 1979 *Astrophys. J.*, **229**, 1138.
Vranjes, J., Pandey, B. P., Poedts, S.: 2007b, *Phys. Plasmas*, **14**, 032106.
Vranjes, J., Poedts, S.: 2006a, *Eur. Phys. J. D*, **40**, 257.
Vranjes, J., Poedts, S.: 2006b, *Phys. Plasmas* **13**, 052103.
Vranjes, J., Poedts, S., Pandey, B. P.: 2007a, *Phys. Rev. Lett.*, **98**, 049501.
Vranjes, J., Poedts, S., Pandey, B. P., De Pontieu, B.: 2008, *Astron. Astrophys.*, **478**, 553.
Vranjes, J., Tanaka, M. Y., Poedts, S.: 2006, *Phys. Plasmas*, **13**, 122103.

Publ. Astron. Obs. Belgrade No. 84 (2008), 511 - 514 *Contributed Paper*

ON THE CONNECTION BETWEEN THE MULTIFRACTALITY AND THE PREDICTABILITY FROM THE AURORAL INDEX TIME SERIES

T. ŽIVKOVIĆ, L. ØSTVAND and K. RYPDAL
Faculty of physics, University of Tromsø, Norway
E–mail: tatjana@phys.uit.no

Abstract. We analyze the Auroral Electrojet (AE) index data from the period of Solar minimum and maximum, with respect to their predictability and intermittency. Neural networks are employed to predict the behavior of the AE- data for the different intermittent intervals, as well as recurrence plots where these intervals are visualized. We also compute the multifractal singularity spectrum as additional evidence for the existence of intermittency, and show that this spectrum is independent of the Solar activity.

1. INTRODUCTION

The Auroral Electrojet (AE) index is a measure of the aurora-related magnetic activity around the auroral oval of the Northern hemisphere. The horizontal field variations are measured at observatories along the auroral zone, and are meant to estimate the total amplitude of the ionospheric current system. This index is introduced by Sugiura and Davis, 1966, and is supposed to monitor the auroral substorm events. Since their discovery, AE index time series have been extensively studied as part of the effort to understand the dynamics of magnetosphere-ionosphere coupling. In addition to the obvious plasma physics based theories, more complex systems based approaches have attracted considerable interest. Depending on the measured AE index characteristics, one has found signatures of self-organized criticality (e.g. Kozelov et al., 2004), turbulence (Consolini et al., 1996), and low dimensional chaos (Vassiliadis, 1990, Athanasiu et al., 2001). In this brief report, we present results from an ongoing study of the AE index predictability and its connection to the intermittent intervals of the same data. We analyze the AE index minute data downloaded from the Kyoto database (http:// swdcwww. kugi. kyoto-u. ac. p/wdc/Sec3. html). We were interested in the years 1979 and 1986, since these years had the highest and lowest Solar activity, respectively. Particularly, we analyze the data from disturbed conditions, i.e., when an auroral substorm was identified. First, we use neural networks to identify the time scale of the AE index predictability. Then, we apply recurrence plot analysis which clearly shows different dynamic regimes, where the boundaries between these regimes coincide with the time scales on which the predictability from the neural network was achievable. These boundaries also match with the increase of the wavelet coefficient

energy calculated for the intermittent part of the AE index time series. Finally, we show by applying multifractal singularity spectrum analysis that our time series have the signatures of the intermittent turbulence.

2. NEURAL NETWORKS

Neural networks (NNs) are often used in the analysis of the AE index (see e.g. Hernandez et al., 1993, Pallocchia et al., 2008). Generally speaking, NNs have a training and test set of data, where the first set establishes the NN, and the other is classified through the NN. NNs consist of the input, output, and layers of neurons in between. These layers learn the relationship between the input and output (training set), such that later a new input (the test set) can be added in the network and, according to the rules of the NN, can produce a new output. We use the AE index data as the input, the AE index data sampled with a time lag as the output, and one layer of 4 neurons between the input and the output. We iterate the neural network until the error $\epsilon = \frac{1}{2}\sum_{i=1}^{M}(O_i - \widetilde{O}_i)^2 \to 0$, where O_i is the desired output, $\widetilde{O}_i$ is the real output from the network and M is the number of the AE index samples. After such a network has learnt the relationship between two AE index time series, where there is a time lag between their measurements, we can predict the future of other AE index time series after the same time lag. Fig. 1(a) and Fig. 1(b) shows the original and the predicted AE index time series for the period of the Solar minimum, when the length of the series was 900 min.

For the time series lengths $\geq$ 900 min, different NN has to be used. In other words, this means that the data has changed its character and the rules that governed the NN up to 900 min, can not be applied anymore. Very similar results are obtained for the data in the Solar minimum as well.

3. THE LINK BETWEEN THE RECURRENCE PLOT AND THE INTERMITTENCY

Recurrence plot (RP) analysis was introduced in Eckmann et al., 1987, and has been extensively used in the last twenty years. The essential steps of the method are as follows: First the phase space is reconstructed by time-delay embedding (see Takens, 1981), where vectors $\mathbf{x}_i$ $(i = 1, \ldots, T)$ are produced. Then a $T \times T$ matrix consisting of elements 0 and 1 is constructed. The matrix element (i, j) is 1 if the distance is $\|\mathbf{x}_i - \mathbf{x}_j\| \leq R$ in the reconstructed phase space, and otherwise it is 0. The recurrence plot is simply a plot where the points (i, j) for which the corresponding matrix element is 1 are marked by a dot. The radius R is fixed and chosen such that a sufficient number of points are found to reveal the fine structure of the plot. On the RP, periodic states are visualized as diagonal, continuous lines, where the distance between the lines indicate the period. Vertically and horizontally spread black areas represent states with short laminar behavior, while abrupt changes in the dynamics as well as extreme events cause white areas in the RP. On Fig. 1(d) we show RP for the Solar minimum, obtained for the embedding dimension $D = 6$. We see that RP consists of some small black rectangular as well as white areas, which indicate changes in the dynamics (probably from laminar to intermittent states). Particularly, for $\tau \sim 10^3$ we see that mid-rectangular area finishes and exchanges with the different pattern for the larger time scales. On Fig. 1(c), we also plot

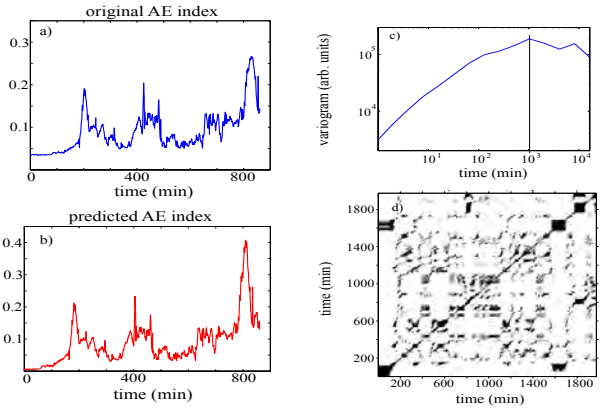

Figure 1: Data for the Solar minimum: a) original , b) predicted from NN, c) variogram, d) recurrence plot.

variogram ($V(\tau) = \frac{1}{2\ (M-\tau)} \sum_{t=0}^{M-\tau} (s(t+\tau) - s(t))^2$, where $s(t)$ is the AE index time series, and τ is a time lag), and notice that the greatest change in the variogram occurs for $\tau \sim 10^3$, which is also in agreement with the results of the neural network analysis. The differences between RP patterns are even better exposed in Fig. 2(b), where the RP for the AE index of the Solar maximum is plotted. In Fig. 2(a) on the upper part of the plot, the first 2000 points of the original AE index data for the Solar maximum are plotted. By applying mexican-hat wavelet analysis and after keeping the wavelet coefficients for the smallest scales, we are able to exclude the intermittent part of the signal, which we plot below the original signal. We also plot energies of the wavelet coefficients, which correspond to the intermittent signal. It seems like the boundaries between different patterns on the RP correspond to the peaks of the wavelet energies of the intermittent signal.

Additional evidence that AE index is intermittent is provided by direct computation of the multifractal spectrum of generalized dimensions and the singularity spectrum. First, we calculate generalized dimension spectrum $D_q = \frac{1}{q-1} \frac{\log M_q(r)}{\log r}$ when $r \to 0$. Here $M_q = \sum p_i^q$ and p_i is the probability that some point is in the box i. The generalized dimension is independent of q if the time series is monofractal. In Fig. 2 (c), we plot D_q vs. q for the AE index data at Solar maximum. Since D_q varies with q, we conclude that the time series is multifractal. Further, we define the singularity spectrum $f(\alpha)$ vs. α from the Legendre transform $(q-1)D_q = \inf\{q\alpha - f(\alpha)\}$. Here α is the Hölder exponent characterizing the local variation around a given point in the time series and $f(\alpha)$ can be thought of as the fractal dimension of the set of points which are characterized by the particular exponent α. For a monofractal, $f(\alpha)$ vanishes except for the the value of α corresponding to the (mono-) fractal dimension (see Hilborn et al., 2000). However, Fig. 2(d) shows a considerable spread in α-values for which $f(\alpha) > 0$. Very similar plots are produced for the AE index data for the Solar minimum. Since the singularity spectrum and spectrum of generalized dimensions show very little variation between the Solar maximum and Solar minimum data, it seems like solar activity does not represent a significant influence on the intermittency properties of the turbulence which give rise to the fluctuations in the AE index.

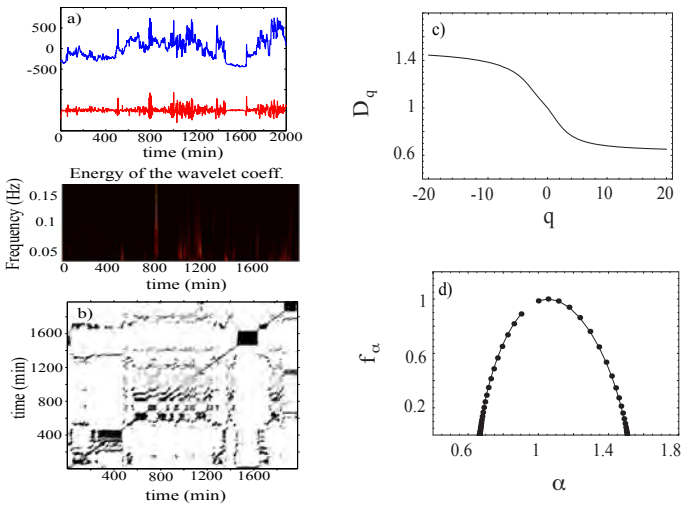

Figure 2: Data for the Solar maximum: a) original and intermittent time series with energy of the wavelet coefficients, b) Recurrence plot, c) Generalized dimension, d) Singularity spectrum.

4. CONCLUSION

We have analyzed AE index data from periods of Solar minimum as well as maximum. We investigate the predictability of the data by using neural networks, and conclude that the same neural network can not be used for all the lengths of the time series. This indicates that different dynamics govern different part of the time series, which can be clearly demonstrated via the recurrence plots. We further contemplate that these different dynamics are due to intermittent burst, which can be pictured through the wavelet energy of the small-scale wavelet coefficients. Singularity spectrum and generalized dimension also confirm that intermittent turbulence governs the dynamics of our data.

References

Athanasiu, M. A, Pavlos, G. P.: 2001, *Nonlinear Processes in Geophysics*, **8**, pp. 95.
Consolini, G, Marcucci, M. F., and Candidi, M.: 1996, *Physical Review Letters*, **76**, 21.
Davis, T., Sugiura, M.: 1966, *Journal of Geophyscal Research*, **71**, 785.
Eckmann, J. P., Kamphorst, S. O, and Ruelle, D.: 1987, *Europhysics Letters*, **5**, pp. 973.
Hernandez, J. V., Tajima, T, and Horton, W.: 1993, *Geophysical Research Letters*, **20**, 23.
Hilborn, R. C.: 2000, Chaos and nonlinear dynamics, An introduction for scientists and engineers, Oxford University Press, Second Edition.
Kozelov, B, Uritsky, V. M, and Klimas, A. J.: 2004, *Geophysical Research Letters*, **31**, 20.
Pallocchia, G., Amata, E., Consolini, G., Marcucci, M. F., and Bertello, I.: 2008, *Journal of Atmospheric and Solar-Terrestrial Physics*, **70**, pp. 663.
Vassiliadis, D. V, Sharma, A. S , Eastman, T. E., Papadopoulos, K.: 1990, *Geophysical Research Letters*, **17**, pp. 1841.
Takens, F.: 1981, In: Dynamical Systems and Turbulence, edited by Rand. D. and Young, L. S., Springer, Berlin.

CIP – Каталогизација у публикацији
Народна библиотека Србије, Београд

537.56 (082) (0.034.2)
539.186.2 (082) (0.034.2)
539.121.7 (082) (0.034.2)
533.9 (082) (0.034.2)

SUMMER School and International Symposium on the Physics of Ionized Gases (24 ; 2008 ; Novi Sad)
Proceedings and Photos [Elektronski izvor] / 24th Summer School and International Symposium on the Physics of Ionized Gases - [SPIG 2008], August 25-29, 2008, Novi Sad, Serbia ; organized by Astronomical Observatory Belgrade ; edited by Gordana Malović, Luka Č. Popović and Milan S. Dimitrijević. - Belgrade : Astronomical Observatory, 2008 (Belgrade : Astronomical Observatory). - 1 elektronski optički disk (DVD) : tekst, slika, zvuk, video ; 12 cm

Naslov sa naslovnog ekrana. - Tiraž 200

ISBN 978-86-80019-29-1
1. Malović, Gordana [уредник] 2. Astronomska opservatorija (Beograd)
a) Јонизовани гасови - Зборници - Мултимедији b) Атоми - Интеракција - Зборници - Мултимедији c) Плазма - Зборници - Мултимедији
COBISS . SR-ID 154228492